Advanced Structured Materials

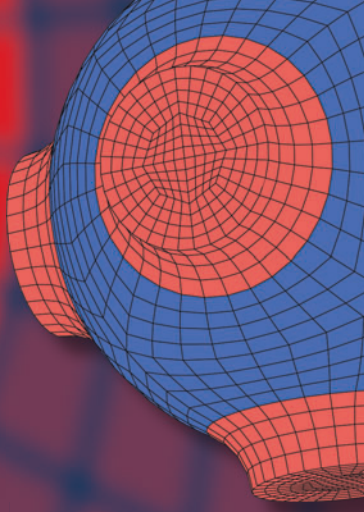

Zishan Husain Khan *Editor*

Nanomaterials and Their Applications

Springer

Advanced Structured Materials

Volume 84

More information about this series at http://www.springer.com/series/8611

Zishan Husain Khan
Editor

Nanomaterials and Their Applications

Springer

Editor
Zishan Husain Khan
Department of Applied Sciences &
Humanities
Jamia Millia Islamia
New Delhi, Delhi
India

ISSN 1869-8433 ISSN 1869-8441 (electronic)
Advanced Structured Materials
ISBN 978-981-10-6213-1 ISBN 978-981-10-6214-8 (eBook)
https://doi.org/10.1007/978-981-10-6214-8

Library of Congress Control Number: 2017951428

Printed on acid-free paper

This Springer imprint is published by Springer Nature
The registered company is Springer Nature Singapore Pte Ltd.
The registered company address is: 152 Beach Road, #21-01/04 Gateway East, Singapore 189721, Singapore

Preface

Technology of making small structures has developed greatly over the last few years from simpler methods for the fabrication of simple structures to the much advanced technologies to design complex devices within the nanoscale dimensions. Due to their peculiar and fascinating properties, as well as applications superior to their bulk counterparts, the nanomaterials have received a lot of interest. To keep pace with modern science and technology, the ability to produce nanomaterials is essential when fabricating new types of nanostructures or reducing the size of the existing microstructures into nanoscale regime. Microelectronics is the most successful example, where "smaller" means greater performance. The direct application of nanotechnology in integrated circuits is in the form of more components per chip, which results in lower cost, faster operation and less power consumption. Miniaturization has become a trend for other developing technologies also. In the area of data storage, there are many efforts to develop magnetic and optical storage components with critical dimensions as small as tens of nanometres. It is also well known that a new phenomenon is associated with nanometre-sized structures, which includes size-dependent excitation of the quantum dot structures and quantization of conductance in the metal contacts. The optical, electrical, magnetic and thermoelectric properties of nanomaterials have been explained with the help of quantum confinement effect. The fabrication of large quantities of nanomaterials from a diversified range of materials at reasonably low cost is desirable for the exploration and development of new technologies.

Since nanomaterials possess unique chemical, physical and mechanical properties, they can be used for a wide variety of applications. These applications include next-generation computer chips, battery insulation materials, phosphors for high-definition TV, low-cost flat-panel displays, tougher and harder cutting tools, elimination of pollutants, high-energy-density batteries, high-power magnets, high-sensitivity sensors, information and communication and medical sciences.

For devices and systems, the present focus of the microelectronics industry is miniaturization, which requires that the circuits, such as transistors, resistors and capacitors, are reduced in size. By achieving a significant reduction in their size, the microprocessors, which contain these components, can run much faster, thereby

enabling computations at far greater speeds. Solgel synthesis of nanomaterials results in foam-like structures called aerogels, which are porous and extremely lightweight. Due to the porosity in these nanomaterials, air is trapped at the interstices, providing good insulation. These aerogels are currently being used for insulation in offices, homes, etc. The resolution of a television, or a monitor, depends largely on the size of the pixel. With the reduction in the size of the pixel or the phosphors, the resolution improves dramatically. Nanocrystalline zinc selenide, zinc sulphide, cadmium sulphide, lead telluride and nanophosphors are best materials for improving the resolution of monitors. The use of these nanomaterials is expected to provide the low-cost high-definition televisions (HDTVs) and personal computers. Cutting tools made of nanocrystalline materials, such as tungsten carbide, tantalum carbide and titanium carbide, are much harder, much more wear-resistant, erosion-resistant and last longer than their conventional (large-grained) counterparts. All applications that require electric power use conventional and rechargeable batteries. The energy density (storage capacity) of these batteries is quite low requiring frequent recharging. The life of conventional and rechargeable batteries is also low. Nanocrystalline materials are candidates for separator plates in batteries because of their foam-like (aerogel) structure, which can hold considerably more energy than their conventional counterparts. The coatings of nanomaterials (nanocoating) may be envisioned to have resistance for the attack of pollutants or have self-cleaning properties. There are wide applications of nanomaterials in medical sciences, which include new diagnostic tools; imaging agents and methods; drug delivery systems and pharmaceuticals; therapies; implants and tissue-engineered constructs.

This book presents the latest advancements in nanomaterials with their applications, thereby providing an overview of the current status of this rapidly developing field. This book includes fourteen chapters authored by the experts in nanotechnology. Chapter 1 presents a review of the research work reported on the synthesis and characterization of nanodiamond with future applications. This chapter presents all the major techniques used for the synthesis of nanodiamond particles as well as thin films. Due to its excellent mechanical and optical properties, high surface area, non-toxicity and tenability of its surface structure, nanodiamond has been widely used in various applications. Some interesting applications of nanodiamond, especially the recent ones, have also been included in this chapter. Chapter 2 presents the review on potential two-dimensional material, i.e. carbon nanowalls for field emission and energy-related applications. The growth of CNWs by various methods is discussed in this chapter with an emphasis on plasma-enhanced chemical vapour deposition (PECVD) method. In addition, potential applications of CNWs such as field emitters and energy application including CNWs as negative electrode in lithium-ion batteries, as catalytic supports in fuel cells and solar cells, etc., have also been reviewed in the light of their unique morphology and structure. Chapter 3 highlights the role of nanostructured materials towards remediation of heavy metals/metalloids. This chapter provides a widespread analysis on the enduring research and progress activities in the field of remediation of toxic heavy metals/metalloids from contaminated water by using

nanomaterials in order to achieve environmental detoxification, using adsorption process. It also includes the discussion on the essential aspects of heavy metals' problems on environment and their effects on human health through polluted water. Chapter 4 presents the recent trends in the processing and applications of carbon nanotubes and C-MEMS-based carbon nanowires. This chapter includes a review of the processing of carbon nanotubes from the first reported work to the present and covers a myriad of CNT applications. For CNT processing, the three most used techniques, i.e. arc discharge, laser ablation and chemical vapour deposition for both multiwall and single-wall CNTs, are detailed. It is understood that these fabrication techniques often need to be adapted to serve a specific application. The processing techniques for CNT application in gas sensors, biosensors, optical sensors, supercapacitors, micro-/nanoelectronics and in nanoelectromechanical systems have been analysed and discussed in this chapter. Since the poor adhesion between CNTs and substrates often limits their application, a survey the work of researchers who developed surface modification techniques has also been reviewed. Chapter 5 presents an overview of the use of metal nanoparticles for glucose sensors. The most recent as well as conventional fabrication methods are discussed in detail. The linearity range and limit of detection of the glucose sensors are described in detail to justify the fabrication process. The chapter will also provide in-depth review of metal nanoparticles-based glucose sensors which would be beneficial to all researchers, scientists, engineers and students who are in direct contact of developing and using glucose sensors. Chapter 6 is focused on the applications of nanomaterials in civil engineering. In this chapter, the potential use of carbon nanotubes, SiO_2, TiO_2, Fe_2O_3, CuO, ZrO_2, ZnO_2, Al_2O_3, $CaCO_3$, Cr_2O_3 and Ag nanoparticles in the construction industry has been explored. The authors have also included some preliminary results on the corrosion behaviour of graphene and nano-TiO_2-incorporated steel-reinforced cementitious composite.

Chapter 7 focuses on design, development and application of nanocoatings. This chapter discusses the various processing techniques for nanocoatings along with the effect of nanocoatings on structural, mechanical and corrosion behaviour. It is expected that this chapter will provide a better understanding about the designing and developing of nanocoatings for wide industrial applications. Chapter 8 focuses on overview of solid biopolymer electrolytes-based battery and dye-sensitized solar cell. It includes the application of biopolymer electrolytes in battery and dye-sensitized solar cell (DSSC) area. Chapter 9 presents an overview of electronic behaviour of nanocrystalline silicon thin film transistors. The authors have provided a physical insight into the nc-Si TFT device characteristics and device non-idealities which may be an important step for the production of high-performance large area display devices. A review on molecular electronics has been included in Chap. 10. It includes the importance and challenges in molecular electronics. The important fabrication techniques for molecular electronics have also been touched in this review. Chapter 11 presents a review on light-emitting diodes (LEDs). The present chapter deals with introduction and working of both inorganic and organic LEDs. The emphasis has been given on organic LEDs. The present state of the art has been given in detail since its inception. Starting from basic single layer, single colour

OLEDs to present day multilayer, colour tunable OLEDs, author has elaborately discussed the development in the field of OLEDs. The fabrication, relevant characterization techniques and analysis have also been included. Chapter 12 focuses on quantum dot-sensitized solar cells (QDSSCs). It includes the basic strategies of enhanced photovoltaic characteristics that depend on factors like suppressed charge carrier recombination at the interfaces, improved photon absorption and construction of tandem structures. The prevalent challenges which have to overcome in order to develop efficient functioning QDSSC are also discussed in this chapter. Chapter 12 is aimed at understanding the haematological complications and rouleaux formation of blood components (leucocytes and platelet cells) and parameters. It provides detailed and depth knowledge about the haematological complications and rouleaux formation of blood components (leucocytes and platelet cells) and parameters. The purpose of this chapter is to determine the changes in three parameters i.e. cells count, shape of cells and size of cells, prior and after addition of three analytes i.e. sugar, sodium chloride and pure water, for varying concentration of these analytes admixed in blood.

New Delhi, India Zishan Husain Khan

Acknowledgements

Thanks to Almighty, merciful Lord for bestowing on me the wisdom, health and wherewithal to accomplish this challenging work.

I extend my heartfelt thanks to the authors, who have contributed to this book for the comprehensive coverage of current research in nanomaterials, including the synthesis and applications. Their insightful articles and research papers have undoubtedly opened up new vistas for the young researchers in the field of nanotechnology. I am truly grateful to their valuable contribution, timely response and constructive suggestions without which this book could not have seen the light of the day.

I express my deep sense of indebtedness to Prof. Talat Ahmad, Vice Chancellor, Jamia Millia Islamia, New Delhi (India), for his constant support and encouragement throughout the process of completion of this book. His words of inspiration always goad me to bring out what is best in me.

My gratitude is due to Prof. Mushahid Husain, Vice Chancellor, MJP Rohilkhand University, Bareilly (Uttar Pradesh), India, and Prof. Haroon Sajjad, Department of Geography, Jamia Millia Islamia, New Delhi (India), for their constructive criticism, suggestions and motivation during the compilation of this book. I acknowledge their role in shaping the very essence of the book.

I am grateful to all who saw me through this book and to all those who provided support, talked things over, read, wrote, offered comments and assisted in the editing, proofreading and design. My thanks are due to all of my Ph.D. students, especially Mohd. Bilal Khan, Sultan Ahmad and Mohd. Parvaz, who assisted me throughout this project.

I would also like to acknowledge the support and guidance provided by editorial team of Springer, without whom this endeavour would not have been a reality.

Last but not least, my deepest gratitude goes to my family members for their unflinching love and support. They have been a constant source of inspiration, and I dedicate this book to them. I am also indebted to my mother for her encouragement and allowing me to follow my ambitions throughout my childhood. I am grateful to my beloved soulmate, Rubina Mirza, for her constant support and for standing

beside me throughout my career. Her comforting words and innumerable sacrifices have been a source of inspiration for me and keep me on the move to improve my knowledge and move my career forward. I also thank my loving children Ayanab, Alina and Ali for always making me smile and bearing with me on those weekend mornings when I was working on this book instead of playing games with them. I hope that one day they may read this book and understand why I had spent so much time in front of my computer.

As an editor, I would look forward to receive suggestions and feedbacks from the readers at zishan_hk@yahoo.co.in.

Contents

About the Editor

Dr. Zishan Husain Khan is a Professor (Applied Physics) at the Department of Applied Sciences and Humanities, Faculty of Engineering and Technology, Jamia Millia Islamia University, New Delhi, India. He specializes in nanotechnology with special emphasis on carbon nanotubes, semiconducting nanostructures and nanochalcogenides. His work on the fabrication of a field-effect transistor (FET) based on an individual carbon nanotube using e-beam lithography and its I–V characteristics was significant. He has also studied the electrical transport properties and field emission properties of bulk carbon nanotubes and has contributed to the field of oxide semiconductors and synthesized zinc oxide (ZnO) nanostructures for various applications.

His recent work on organic light-emitting diodes (OLEDs) based on organic semiconductors and nanomemory devices based on nanochalcogenides is expected to have a significant impact on the emerging field of nanotechnology. Dr. Khan received his Ph.D. in Amorphous Semiconductors from Jamia Millia Islamia University, New Delhi, India, in 1996. He subsequently served as a postdoctoral researcher at the Center for Nanoscience and Nanotechnology, National Tsing Hua University (NTHU), Hsinchu, Taiwan, from 2001 to 2005. While pursuing his postdoctoral studies, Dr. Khan worked extensively on different types of nanostructures with a special focus on carbon nanotubes. He has published 84 research papers in outstanding and high-impact-factor journals and made over 40 presentations at conferences and symposia. Dr. Khan is one of the founder members of the Center of Nanotechnology, King Abdulaziz University, Jeddah (Saudi Arabia). He has served as guest editor for the International Journal of Nanoparticles (UK), International Journal of Nano-Biomaterials (UK), International Journal of Nanomanufacturing (UK), Journal of Nanomaterials (USA) and Advanced Science Letters (USA). He is also a regular reviewer for many reputed international journals.

Chapter 1
Nanodiamonds: Synthesis and Applications

Mohd Bilal Khan and Zishan H. Khan

Abstract The present chapter is devoted to the synthesis and applications of nanodiamond. Nanodiamond or nanocrystalline diamond is actually an allotrope of carbon which has nanosized carbon crystallites having well-known diamond structure. Although it is present in nature since long, the realization of its artificial production occurred in the 1960s by the Russian scientists. Due to the policy of secret research, it was in dark until 1980s, when the first formal report of its synthesis was published. Since then, it has been remained in the focus of scientists and researchers worldwide. Several techniques for the synthesis of nanodiamond have been developed. This chapter presents all the major techniques used for the synthesis of nanodiamond particles as well as thin films. Due to its excellent mechanical and optical properties, high surface area, non-toxicity and tenability of its surface structure, nanodiamond has been widely used in various applications. This chapter reviews some interesting applications of nanodiamond, especially, the recent ones.

1.1 Introduction

Carbon is unique among all the elements in the diversity of short-, medium- and long-range configurations it forms with itself and with other elements. Two pure carbon crystalline forms, graphite (sp^2, threefold planar bonding) and (cubic) diamond (sp^3, fourfold tetrahedral bonding), have been known and utilise by mankind for centuries, along with other less clearly identified carbon materials (coals). Hydrocarbons (oils) and organic materials have also been known for a long time. With the advancement of science and technology at nanoscale, some other forms of carbon such as carbon nanotubes (CNTs), graphene and nanodiamond were discovered and explored. Nanodiamonds are actually carbon nanostructures in which

M.B. Khan · Z.H. Khan (✉)
Department of Applied Sciences and Humanities, Jamia Millia Islamia, New Delhi 110025, India
e-mail: zishanhk@jmi.ac.in; zishan_hk@jmi.ac.in

Z.H. Khan (ed.), *Nanomaterials and Their Applications*,
Advanced Structured Materials 84, https://doi.org/10.1007/978-981-10-6214-8_1

carbon atoms are arranged in diamond-like manner. These structures have been found in different meteorites [1–3], proto-planetary nebulae, interplanetary dust [4] and several earth sediments existed since 13,000 years. Although these nanoscale diamond particles were produced, accidentally, several times in 1960s, by Russian scientists, when they were synthesizing diamond from non-diamond carbon using explosion energy [5, 6], but the first formal report on their synthesis was published in the late 1980s [7]. Since then, a lot of work has been reported on synthesis, properties and applications of nanodiamonds.

Nowadays, many techniques are available for the synthesis of nanodiamonds. The nanodiamonds are being synthesized using detonation technique [7], laser assisted synthesis [8], high temperature high pressure (HTHP) high energy ball milling of microcrystalline diamond [9], hydrothermal synthesis [10], chemical vapour deposition (CVD) synthesis [11], ion bombardment on graphite [12], chlorination of carbides [13] and ultrasonic cavitation [14] etc. These methods are entirely different from each other in their mechanisms and choice of precursors. The first three methods i.e. detonation technique, HTHP high energy ball milling and laser assisted synthesis are used for the industrial production of nanodiamonds. Due to its extraordinary properties, nanodiamond can be used for field emission and light emitting applications [15]. Nanodiamond shows high mechanical hardness, inertness and high fracture strength and high surface smoothness, which make it a strong candidate for high-end micro and nanosystems [16]. Fluorescent nanodiamonds are widely being used in bio-imaging as a successful non-toxic replacement of semiconducting nanoparticles and for other medical applications [17–20]. In addition to this, high reactive surfaces of nanodiamond allow its surface modification easily via chemical approaches and make it suitable for synthesizing high performance composites for various applications [21–28].

1.2 Synthesis of Nanodiamond

1.2.1 Detonation Techniques

Detonation methods are the most popular and widely used methods for the production of nanodiamond. In these methods, energy of explosion is used for the synthesis of nanodiamond. According to the carbon precursor used, detonation technique has three variants.

(i) In the first variant, nanodiamond is achieved by the phase transformation of graphite using the energy of shock waves originated by the detonation of explosives. This technique was initially introduced by DeCarli and Jamieson in 1961 and has been used as one of the popular techniques for the synthesis of polycrystalline diamond particles [29]. This technique was later patented by DeCarli in 1966 [30] and, later on, its improved version was patented by Cowan et al. in 1968 [31]. This technique was parallely developed by scientists in former USSR at the VNIITF Institute (Snezhinsk) in the early

1960s but remained in veil because of secrecy [32]. In this method, graphite is filled in a closed chamber, surrounded by the explosives. The whole system is confined in another closed chamber. The detonation of explosives generates high temperature (>2000 K) and high pressure. This high temperature and high pressure is sufficient to transform graphite into micrometre-sized polycrystalline diamond particles. Copper is mixed with graphite to improve the local heating [33].

(ii) In the second variant, explosives such as pure Trinitrotoluene (TNT), hexogen, octogen, a mixture of TNT/RDX or a mixture of all or some of these materials with a negative oxygen balance is detonated in a closed chamber. These explosives provide necessary carbon and high energy for the formation of nanocrystalline carbon particles [34]. The closed chamber containing the explosives is usually filled with argon, nitrogen, CO_2, hydrogen or water (ice), which act as the coolants. Depending upon the choice of coolant, the processes are called wet or dry processes [35]. In the resultant detonation soot, almost 75% are nanosized diamonds with the average size of 4–5 nm [36]. Due to such small size, nanodiamonds synthesized by detonation are called ultradispersed diamonds or UDD. The amount of nanodiamonds in detonation soot depends upon the coolant used. It has been confirmed that the yield increases in series as hydrogen < argon < nitrogen < CO_2. Another controlling factor is the amount of coolant per unit mass of explosives, which determine the inertial pressure of the detonation process. The specific heat of coolant also decides the yield of nanodiamond [37]. This method was developed in former USSR in the early 1960s [32] and further improved subsequently. The ultradispersed nanodiamond produced by this method is also covered by graphite, thus requires purification process. In the purification process, usually mineral acids are used. The purified detonation soot contains around 98% ultradispersed diamond particles of size around 4–5 nm [38].

(iii) The third variant of nanodiamond synthesis is less known. It was also invented in former USSR [39]. Various compositions of different explosives can be used in this method and these compositions produce the Nanodiamonds having different structures and sizes. Tatsii et al. [40] analyzed the products obtained by using different explosives/carbon precursor compositions and summarized the results. They used three compositions i.e.; RDX/Carbon Black, RDX/Graphite and Gunpowder/RDX/Graphite and compared the products obtained by these compositions. The detonation pressure measured was 7.5–14.5 GPa. It was observed that the product obtained by the mixture of RDX and carbon black precursor contained cubic nanodiamond particles of average size 20–80 nm while the products obtained by the RDX/Graphite mixture contained microsized particles of mixed crystal structures (diamond, lonsdaleite and graphite). The product extracted from the mixture of Gunpowder, RDX and Graphite contained single-phase particles having homogeneous grain structure with grain size of approximately 1–3 nm. These smaller grains were found to form onion-shaped aggregates [40] (Fig. 1.1).

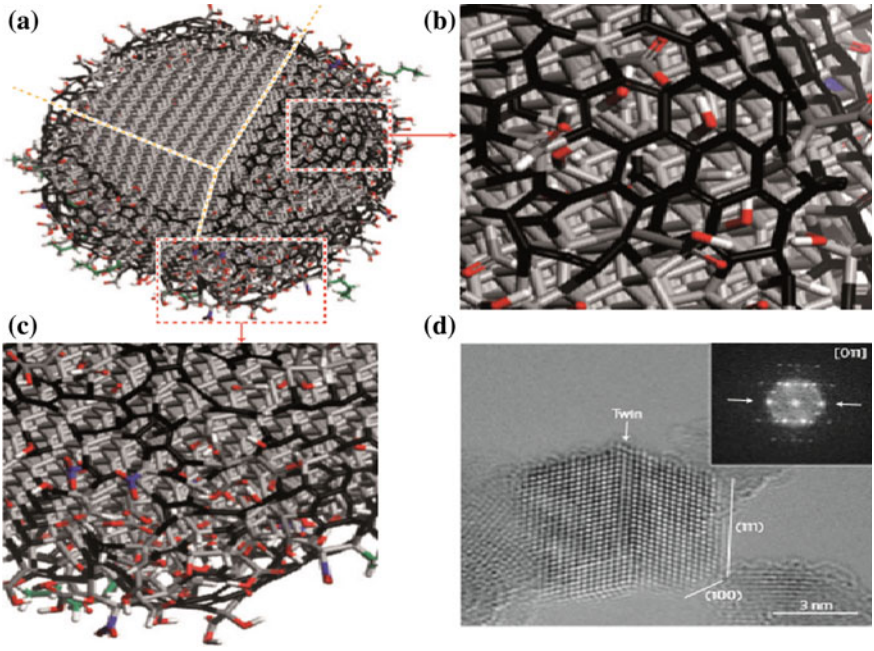

Fig. 1.1 Structure of a single nanodiamond particle, **a** schematic model illustrating the structure of a single ~5-nm nanodiamond after oxidative purification. The diamond core is covered by a layer of surface functional groups, which stabilize the particle by terminating the dangling bonds. The surface can also be stabilized by the conversion of sp^3 carbon to sp^2 carbon. A section of the particle has been cut along the amber dashed lines and removed to illustrate the inner diamond structure of the particle. **b**, **c**, Close–up views of two regions of the nanodiamond shown in (**a**). The sp^2 carbon (shown in *black*) forms chains and graphitic patches **b** the majority of surface atoms are terminated with oxygen-containing groups (**c** oxygen atoms are shown in *red*, nitrogen in *blue*). Some hydrocarbon chains (*green*, *lower left* of **a**, **c**) and hydrogen terminations (hydrogen atoms are shown in *white*) are also seen (**d**). Each nanodiamond is made up of a highly ordered diamond core. Some nanodiamonds are faceted, such as the one shown in this transmission electron micrograph, whereas most have a *rounded shape*, as shown in (**a**). The *inset* is a fast Fourier transform of the micrograph, which confirms that this nanodiamond has a highly ordered diamond core (Reprinted with permission from [5])

The growth mechanism for the synthesis of nanodiamond via detonation technique can be understood by the phase diagram of carbon (Fig. 1.2) [5]. From the phase diagram, it is evident that the most stable form of carbon is graphite at low pressure, while at high pressure, diamond is the most stable form. Both the graphite and diamond transforms into liquid at the temperature higher than 4500 °C. The diamond-liquid transition temperature is less in the case of nanosized diamond particles and the stability shifted to higher pressures. The detonation (pressure and temperature at Jouguet point (point A in Fig. 1.2)) does not provide enough high pressure and temperature which is required for the formation of bulk liquid, rather it transforms carbon into nanosized liquid droplets of size 1–2 nm. When the pressure

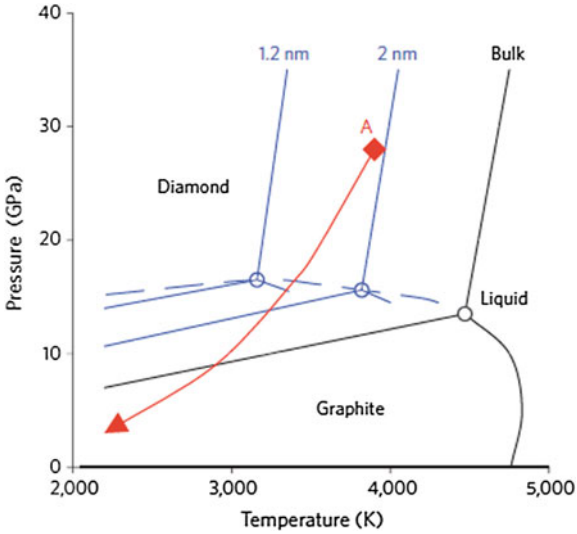

Fig. 1.2 Phase diagram of carbon (Reprinted with permission from [5])

and temperature is reduced along the isentrope (red line), these liquid droplets further condense and crystallize into nanodiamond particles [41–50]. Figure 1.3 shows different stages of nanocarbon formation in detonation technique. Region (I) corresponds to the zone of explosion, the region (II) is the zone of chemical

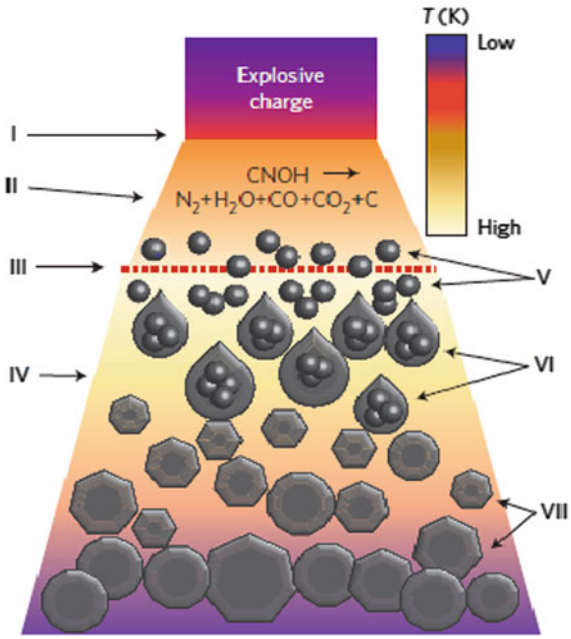

Fig. 1.3 Different stages of nanodiamond synthesis by detonation (Reprinted with permission from [5])

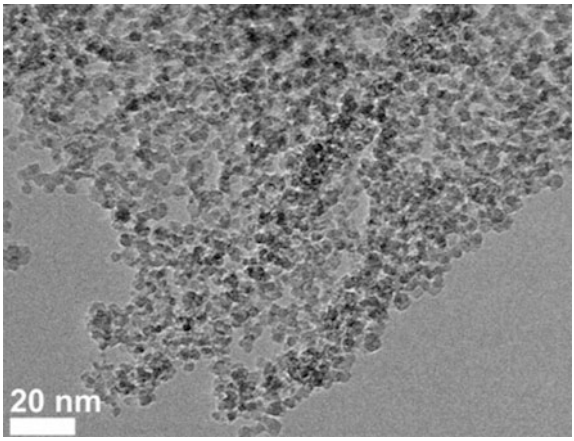

Fig. 1.4 TEM image of ultra small nanodiamonds synthesized using detonation of nanosized explosives (Reprinted with permission from [51])

decomposition of explosives (in case explosives are present as the precursors), the region (III) corresponds to Chapman-Jouguet plane (where pressure and Temperature correspond to point A in Fig. 1.2),the region (IV) is the region of expansion of detonation products, the zone (V) is the region of formation of nanosized carbon clusters, zone (VI) is the region of coagulation into nanosized liquid diamond droplets and region (VII) is the region where nanodiamond particles crystallize and grow.

Detonation methods are well established methods for the synthesis of nanodiamonds. Recently, some reports have been published on the modified detonation synthesis of nanodiamonds. Pichot et al. [51] reported the synthesis of ultrasmall nanodiamonds by the explosion of nanosized explosives. For the synthesis of nanosized explosives, they used spray flash-evaporation process. Using this new approach, they were able to synthesize nanodiamonds having average size of 2.8 nm (Fig. 1.4). Nanodiamond particles synthesized by detonation usually contain hydrogen. In their study, Batsanov et al. [52] chose benzotrifuroxan (BTF) as the required explosive for the detonation synthesis of nanodiamonds. The nanodiamond particles obtained by this process were free from hydrogen impurities (Fig. 1.5).

1.2.2 Synthesis of Nanodiamond by CVD

Chemical vapour deposition method is one of the most popular methods used for the synthesis of films of carbon nanostructures such as carbon nanotubes [53], graphene [54] and nanodiamonds [55]. In this method, cabonaceous precursors are used in the gaseous form for the deposition of nanodiamond films. The use of chemical vapour deposition for the synthesis of diamond dates back to 1956 when diamond films were produced using precursor mixture containing hydrogen [56]. This method was patented in 1967. Diamonds films were further reported to be

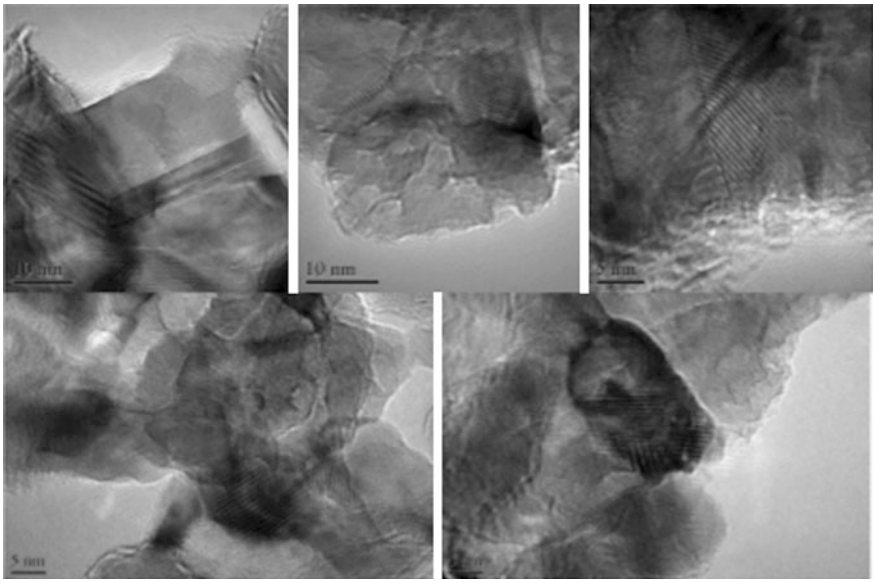

Fig. 1.5 TEM images of hydrogen-free nanodiamond particles synthesized from benzotrifuroxan (BTF) [52]

synthesized using HF-CVD [57], Microwave assisted CVD [58] and radio plasma enhanced CVD [59] by Japanese researchers. In 1989, Frenklach et al. [60] produced nanodiamond powder in gas phase using microwave CVD employing different hydrocarbons diluted in the mixture of oxygen, hydrogen and argon as the precursors. By this process, diamond nanocrystals of average size around 50 nm were produced. In another study, Frenklach et al. [61] demonstrated the formation of nanodiamond particles of size ranging from 5 nm to several hundred nm, induced by the addition of diborane (B_2H_6). These methods involve the generation of nanodiamond from activated gaseous phase and used to understand the formation of nanodiamond particles present in space dust. Other methods such as laser induced CVD synthesis of nanodiamond using methane precursor at high temperature and high pressure [62] and microwave plasma torch system using methane with Ar and nitrogen were reported. Recently, there have been several reports published on the improved CVD synthesis of nanodiamond. Park et al. [63] demonstrated the synthesis of nanodiamond using hot filament CVD reactor (Fig. 1.6).

They observed that the size of single crystalline nanodiamond particles formed by this method lying between 4 and 6 nm, which increased with the capture time. (Fig. 1.7). They did not find other allotropes of carbon, such as graphite or amorphous carbon with nanodiamonds.

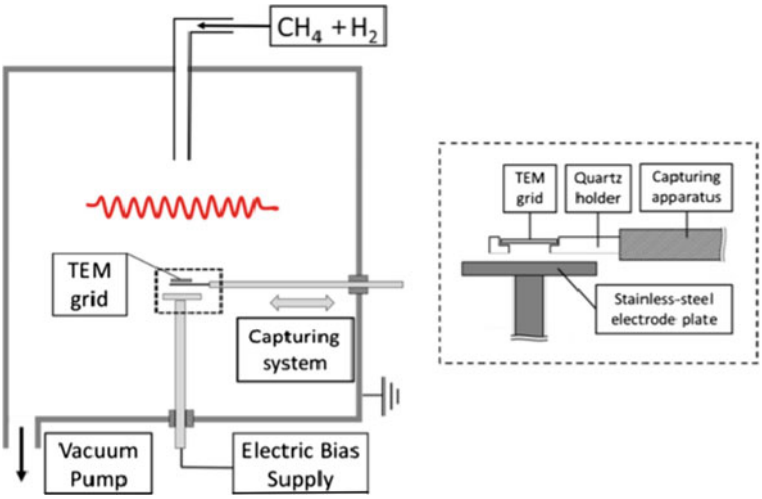

Fig. 1.6 Schematic diagram of hot filament reactor used for the synthesis of nanodiamond (Reprinted with permission from [63])

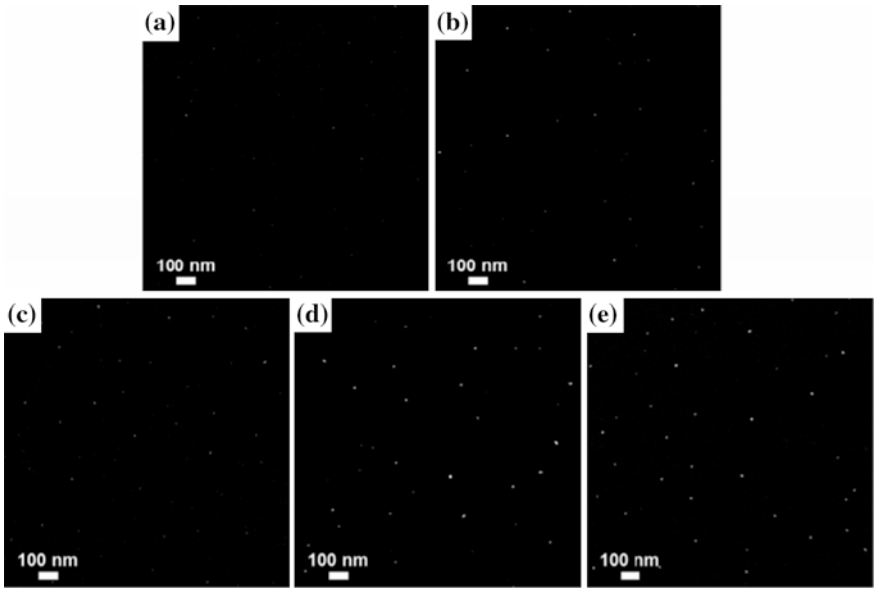

Fig. 1.7 STEM images of CVD processed nanodiamonds obtained with increasing capture time from *left to right* (Reprinted with permission from [63])

1.2.3 High Energy Milling of Microsized Diamond Particles

Nanodiamond can be obtained by high energy milling of microsized diamond particles. Usually, these nanosized diamond particles have haphazard shape which resemble with the smashed glass [64], but in the year 2009, Boudou et al. [9] synthesized quasi-spherical nanosized diamond particles of size below 10 nm. Boudou et al. [65] synthesized uniform nanodiamonds using nitrogen jet milling followed by bead milling of microcrystalline diamond powder. They further purified and sorted out the product obtained by this process to get nanodiamond particles of size below 10 nm. In 2015, Boudou et al. [66] were granted a patent on the process of cubic nanodiamond synthesis using nitrogen jet ball milling. Their process involved the nitrogen jet milling of microcrystalline diamonds followed by the nanomilling using tungsten carbide ball mill. A subsequent acid treatment was used to get rid of unnecessary traces of tungsten carbide powder. After the centrifugation, they obtained round shaped cubic nanocrystalline diamond particles of less than 10 nm (Fig. 1.8).

1.2.4 Laser Assisted Synthesis of Nanodiamond

Laser assisted synthesis is relatively new technique for the synthesis of nanostructures [67]. Nanostructures prepared by chemical methods contain different chemical impurities. Additional purification steps are required to remove these impurities. These purification steps increase the complexity of these processes. Laser ablation is a process in which high energy of laser radiation is used to synthesize high purity nanostructures that do not need any subsequent purification process (Fig. 1.9).

In 2005, Wang et al. [68] presented a detailed analysis of nanocrystal nucleation and growth in liquid medium using laser ablation taking nanodiamond as specific example. They proposed that the synthesis of nanodiamond by laser ablation in liquid medium takes place in following steps (Fig. 1.10).

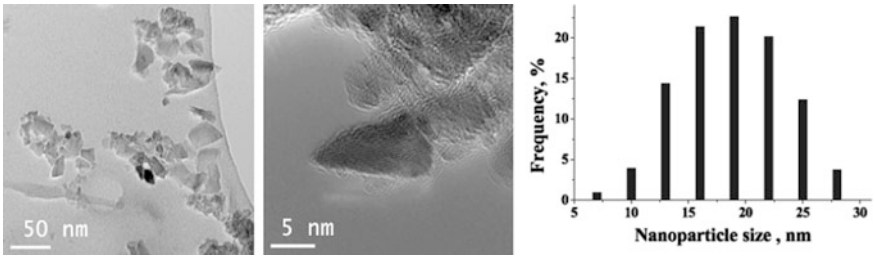

Fig. 1.8 TEM image of diamond nanoparticles prepared by milling of microcrystalline diamonds (Reprinted with permission from [65])

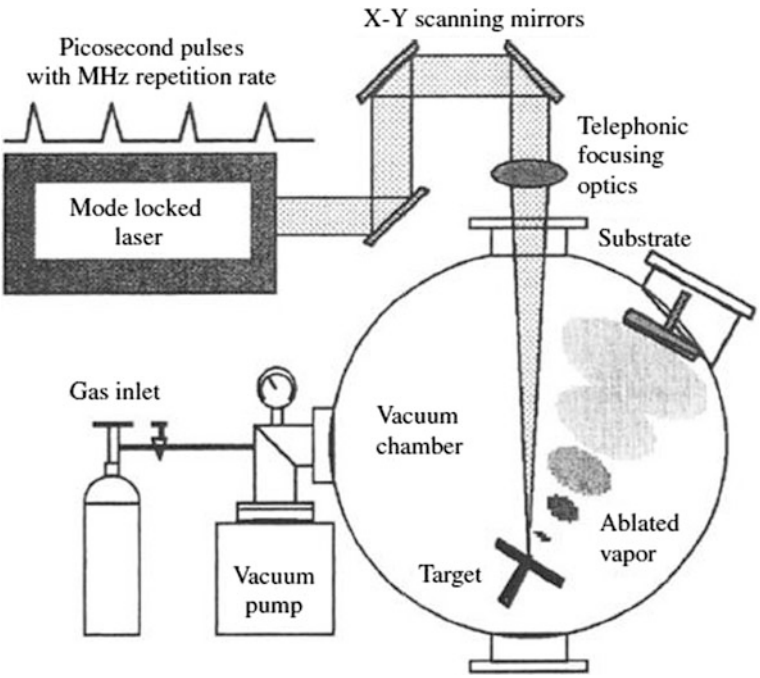

Fig. 1.9 Schematic of laser ablation setup used for the synthesis of nanomaterials (Courtesy www.understaiulingnano.com)

- Formation of plasma plume of carbon atoms with peak pressure and temperature of 15 GPa and 5000 K, respectively (Fig. 1.10a).
- Steady nucleation of carbon clusters from the carbon atoms due to condensation of plasma as the temperature and pressure drop down from the peak values. This nucleation process continues until the size of these clusters reach the critical nucleation size of diamond (Fig. 1.10b).
- With the steady nucleation, diamond nuclei are formed followed by the synthesis of diamond crystals. After some time, the growth of nanodiamond seizes due to further decrease in temperature and pressure (Fig. 1.10c).

Yang et al. [69] synthesized diamond nanocrystals using pulsed laser ablation of graphite in liquid medium (Fig. 1.11). They reported that the size of the nanocrystalline diamonds increases with increase in reaction time.

Tarasenkha et al. [70] reported the one step synthesis of nanodiamond by laser ablation of graphite in liquid medium. They obtained different carbon nanostructures using different solvents. Nanodiammond particles were formed by using aqueous diethylenetriaminepentaacetic acid [DTPA] solution as the liquid medium. Gorrini et al. [71] synthesized nanodiamond by laser ablation of graphite dispersed in aqueous medium. Further, they argued that the water acts as a confining medium which is essential for typical confined pulse laser ablation (CPLA) process. They

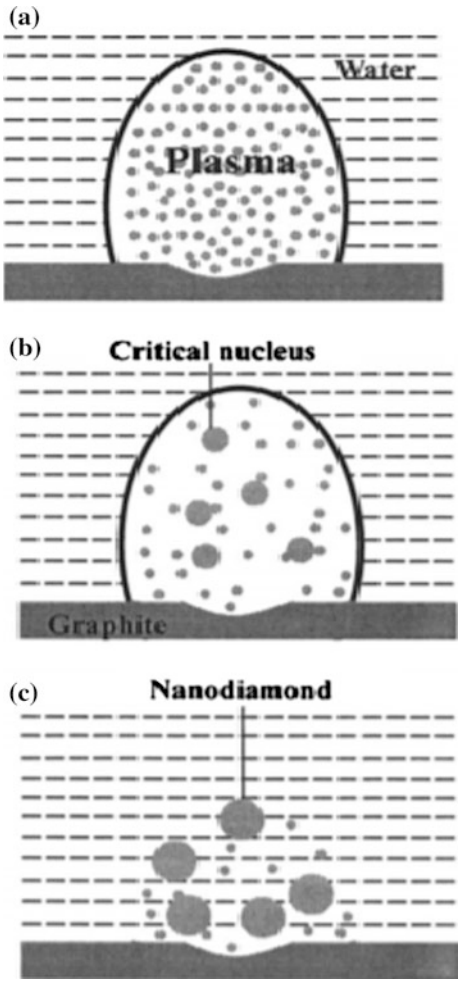

Fig. 1.10 Schematic diagram of the formation of nanodiamond by laser ablation in liquid medium; **a** formation of high pressure high temperature plume; **b** formation of diamond nuclei; **c** formation of diamond nanocrystals (Reproduced with permission from [65])

further stated that high pressure and high temperature condition provided by the laser irradiation fall in the liquid region of carbon phase diagram and induces phase change of graphite into liquid carbon. The melted carbon cools immediately due to its contact with the bulk graphite and liquid. The cooling of melted carbon favours the nucleation of diamond phase. In a review article published in 2017, Amans et al. [72] reviewed the reports published on the synthesis of carbon allotropes using laser ablation in liquid medium. They concluded that different carbon nanostructures including nanodiamond can be produced using laser ablation in liquid medium.

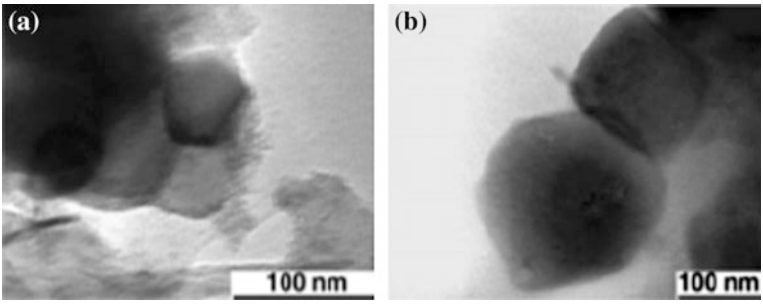

Fig. 1.11 TEM images of diamond nanocrystals synthesized using pulsed laser ablation of graphite with different reaction tune of **a** 1/2 h **b** 1 h (Reprinted with permission from [69])

1.2.5 Synthesis of Nanodiamonds Using High Energy Particles Irradiation

High energy particle radiation can also be used for the formation of nanodiamond. Banhart et al. [73] used an unconventional method for the synthesis of nanodiamond. They used high energy electron beam to compress the layers of carbon onions towards the centres. This compression allows the conversion of their cores into nanodiamonds. On the other hand, Wesolowski et al. [74] synthesized nanodiamond using the same procedure with minor modification. They used Ne^+ ion radiation to convert graphitic onion cores into nanodiamonds. Higher energy transfer, higher beam current, higher displacement cross section due to high energy ion irradiation induced the formation of higher nanodiamond yield in comparison with that in the case of high energy electron radiation. Daulton et al. [75] used high energy Kr^+ ions to produce nanodiamond particles inside graphite. In another report published in 2001, Meguru et al. [76] synthesized nanodiamond using irradiation of highly charged ions on highly oriented pyrolytic graphite followed by the surface treatment either by the electron injection from scanning electron microscope or by laser irradiation with He–Cd laser. They reported that the one-time impact of highly charged ion produces one nanodiamond particle without creating any defect in the area surrounding the region of direct impact.

1.2.6 Ultrasound Assisted Synthesis of Nanodiamonds

Synthesis of nanodiamond requires appropriate temperature and pressure conditions. These temperature and pressure conditions may be obtained by ultrasound cavitation. Ultrasound cavitation bubbles are generated in liquid medium. These ultrasonic bubbles collapse and generate a relatively bigger cavity. The temperature and

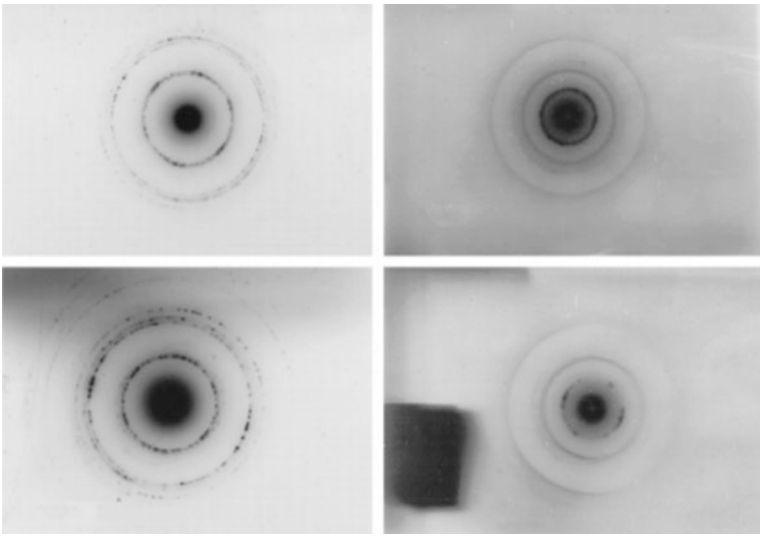

Fig. 1.12 Electron diffraction patterns of solid carbon species obtained by ultrasound cavitation; *left side* diffraction patterns represent the diamond phase while the *right side* diffraction patterns represent the graphite phase (Reprinted with permission from [14])

pressure inside the cavity reach at the high values which are required for the formation of nanodiamond under suitable experimental conditions [77] (Fig. 1.12).

Galimov et al. [14] explored the possibility of synthesis of nanodiamond by ultrasound cavitation of hydrocarbon liquid. They used benzene as the working liquid. The ultrasound cavitation in benzene resulted in the synthesis of organic polymers and solid carbon particles. Their experimental investigations suggest that these solid carbon particles consist of nanodiamond particles (Fig. 1.14).

1.2.7 Synthesis of Nanodiamonds Using Carbides

Selective etching of carbides in the presence of etchant gases gives rise to the synthesis of different carbon allotropes including nanocrystalline diamond. Gogotsi et al. [78] demonstrated the synthesis of nano and microcrystalline diamond using silicon carbide at the relatively low temperature about 1000 °C. In their experiment, silicon carbide was exposed to the mixture of chlorine, hydrogen and argon gases in appropriate ratio. Chlorine reacts with Si present in silicon carbide to form $SiCl_4$ as it is thermodynamically more stable than CCl_4. In this way, chlorine present in the gaseous mixture selectively etches Si from SiC leaving carbon on SiC substrate. Gogotsi et al. [78] argued that these carbon films have the diamond structure when the etching mixture contains the Cl_2/H_2 ratio more than or equal to 2:1 and the

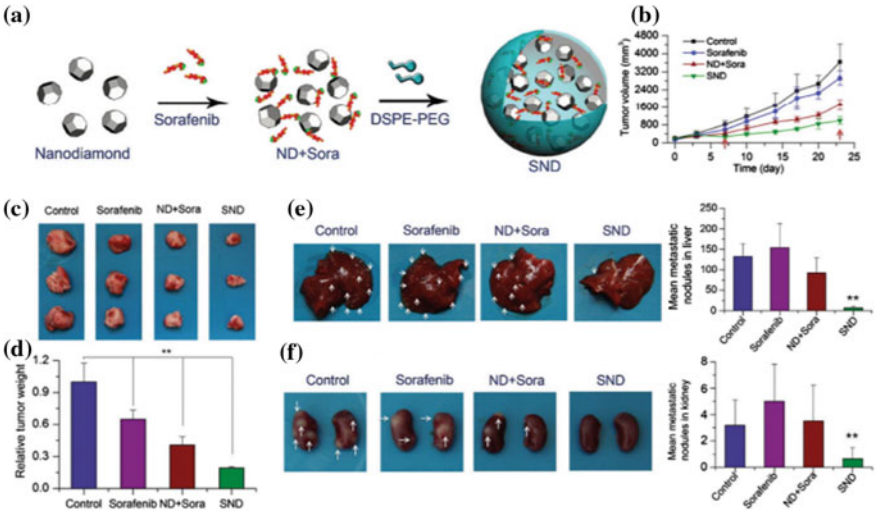

Fig. 1.13 **a** Illustration of the preparation of lipid-coated diamond nanoparticle clusters loaded with water insoluble sorafenib. **b–d** Tumour growth inhibition effects m BGC-823 gastric cancer cells induced tumour xenograft mice (20 mg kg^{-1}). **b** The relative tumour volumes in tumour xenograft models treated with saline, sorafenib suspension, nanodiamond (ND) + sorafenib (Sora) and lipid-coated diamond nanoclusters loaded with sorafenib (SND) by oral gavage (20 $mgkg^{-1}$). **c** The photographs of tumours from each group excised on day 23 after oral administration. **d** The relative tumour weight in mice with treatment of sorafenib, ND + Sora and SND in comparison with saline group. **e** and **f** Therapeutic efficacy of SND on suppressing the distant metastasis to liver (**e**) and kidney (**f**) in BGC-823 gastric cancer cells induced tumour xenograft mice. Mice were daily treated with saline, sorafenib suspension, ND + Sora and SND at 20 mg kg^{-1} of sorafenib by oral gavage. At the end point, the visually detected metastatic nodules in each tissue of liver and kidney were counted (Reprinted with permission from [103])

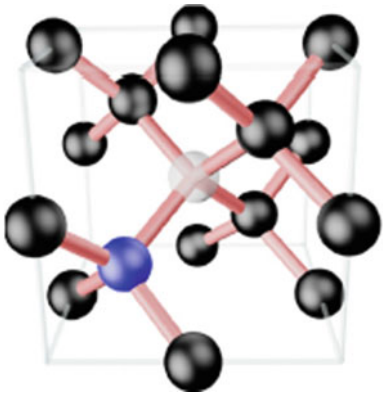

Fig. 1.14 A typical structure of NV centre in nanodiamond. The substituted nitrogen atom (*blue*) is bound to a vacancy (*white*) in diamond lattice (Reprinted with permission from [117])

temperature of about 1000 °C. Some other workers also reported the synthesis of nanodiamond by selective etching of silicon carbide using fluorocarbon plasma [79] and bombardment with hydrogen or carbon ion [80, 81].

1.3 Applications of Nanodiamonds

1.3.1 Polishing and Lubrication

The most basic feature of diamond is its structure in which sp^3 hybridized carbon atoms are arranged in tetragonal arrangement. Dense packing and stable hybridization make diamond incredibly strong and hard material [82]. Because of extraordinary hardness, diamond is used in polishing applications since long [64]. For ultrafine polishing, abrasive materials with sub-100 nm grain size are ideal. Because of sub-100 nm size and extraordinary hardness, nanodiamonds are used in fine polishing applications with the finishing better than 4 Å. Liu et al. [83] used nanodiamond suspensions for the polishing of glass ceramics. The polishing of glass ceramics is difficult due to their inconsistency. In their study, Liu et al. used the suspension of nanodiamond particles having different sizes. They found that the suspension of nanodiamonds of average size 54.9 nm performed with highest removal rate and better surface roughness. A superior surface roughness of 0.208 nm was achieved. Usually nanodiamonds are made up of nanosized diamond core and with the graphite existed on the surface [5]. This unique feature makes nanodiamond an attractive lubrication agent. It is assumed that the graphite present at the surface of nanodiamond provides lubrication and its core reduces friction by polishing away the surface roughness. However, purified nanodiamonds were also observed to enhance the lubricantion properties when it is used in grease or oil with PTFE or metal nanoparticles [84]. It is well established that the mechanism of lubrication for nanodiamond is different for different systems. When, it is used in carbon steel system, nanodiamond gets embedded into carbon steel from the lubricant reducing the friction and wear. The wear mechanism is dominated by the viscosity of nanodiamond suspension when it is used for aluminium. Shirwani et al. [85] numerically analyzed the ability of detonation-synthesized nanodiamonds to improve the lubrication and reduce friction in elastohydrodynamic lubrication. Due to the increase in the viscosity of the lubricant in the EHL contact zone, diamond nanoparticles in the lubricant polish the surfaces at the nanoscale which decreases the composite roughness of the contacting surfaces. The reduced composite roughness results in an increased film thickness ratio which yields lower friction. Wang et al. [85] filed a patent describing the method of chemical mechanical planarization of GaN using a chemical mechanical polishing slurry containing ultradispersed diamonds sized below 10 nm suspended in water with a complexing and a passivating agent. Although the exact mechanism behind the improvement of lubrication by addition of nanodiamonds is not completely known, it is a well proven lubrication additive. A detailed study is needed to understand the

mechanism of lubrication improvement using nanodiamond. It will be helpful to engineer more efficient lubrication systems.

1.3.2 Nanodiamond Nanocomposites

Extraordinary mechanical hardness, stability and thermal properties of nanodiamond enable them to be used as the filler materials in different composite systems [5]. Nanodiamond has been proved to enhance the adhesive properties [86], electromagnetic shielding properties [87], wear resistance [88], mechanical strength [89–91] and thermal conductivity [89, 92] of polymers when used as the filler material in the matrix of polymers. Recently, Zhang et al. [93] prepared a composite using biodegradable polymer, poly(lactic-co-glycolic acid) (PLGA), loaded with nanodiamond phospholipid compound (NDPC). They modified the original hydrophobic surface of nanodiamonds to be amphipathic with phospholipid. The filling of 10% NDPC into PLGA significantly improved the mechanical properties of PLGA. Nanodiamonds have also been used with other filler materials in polymers matrix. Zhang et al. [94] used nanodiamond nanocluster-decorated graphene oxide as filler material to improve the mechanical strength of epoxy. They observed that epoxy samples containing 0.1% hybrid filler material showed high mechanical stability in comparison with the epoxy composite containing 0.2% filler material. The epoxy composite prepared by ND/GO filler material also exhibited enhanced thermal properties such as decomposition temperature and activation energy. The authors argued that the presence of nanodiamonds not only prevented the agglomeration of GO sheets but also acted as the pinning agent in polymer composite which significantly enhanced the fracture toughness. Choi et al. [95] prepared a nanodiamond grafted nylolon 6,6 (PA66) reinforced PA66 nanocomposites. The tensile strength of this composite increased by 11% and 20.8%, respectively. Even PA66/pristine ND composite showed higher mechanical properties. Kausar [96] synthesized waterborne polyurethane composites with increased thermal properties and observed that the thermal stability of waterborne polyurethane increased significantly after the reinforcement. Vesna et al. [97] prepared Poly(ethylene terephthalate) composite with 1% nanodiamond terminated with carboxylic group and nanodiamond/0.3% graphene platelets by simple melt blending for radiation resistance. They observed that composites with nanodiamond-graphene hybrid filler exhibited high radiation resistivity. Nanodiamond has also been used with different metal and metallic systems to improve different properties of nanocomposites. Neito et al. [98] synthesized WC-ND nanocomposites using thermal spray method. They observed that the addition of nanodiamonds enhances the wear performance. The wear resistance was found to be increased at room temperature, while they observed poor wear resistance at 300 °C. They attributed the decrease in wear resistance at 300 °C to the degradation of carbon phase at this temperature. Yin et al. [99] produced nanodiamond reinforced copper matrix composite film on aluminium alloy substrate using cold spray. They observed that the composites

exhibited excellent wear resistance properties. Murugesan et al. [100] presented a concept of novel Ni–B–ND coating for increasing the lifetime of gas and oil equipment. Ni is an excellent coating material and is used to increase the corrosion, abrasion and wear resistance. Boron was introduced in Ni matrix to improve the corrosion resistance of the coating. The addition of ND enhanced the wear behaviour of the coating without affecting its corrosion resistance properties. This relatively new concept has the promise to improve the lifetime of oil and gas equipments. Nanodiamond has been proven to increase the mechanical and thermal properties of different matrices. Therefore, ND reinforced nanocomposites have the potential to be used in different applications. Although nanodiamond reinforced composites have been studied since long, their excellent properties and wide range of applications are continuously adding fuel to the research and development in this area.

1.3.3 Bio-medical Applications

Targeted drug delivery is one the most widely researched and promising topic of research. Different nanomaterials have been tested to act as the drug carrier in targeted drug delivery systems. The main attributes of the material to be used as drug carriers include biocompatibility, ability to carry wide range of drugs, scalability and dispersibility in water [82]. The excellent bio-imaging properties make nanodiamond an excellent drug carrier. Nanodiamond has been demonstrated to be used to carry Doxorubicin (DOX) [101]. Doxorubicin complexes are drugs which are used to treat a wide range of cancers. Chow et al. [102] demonstrated that nanodiamond-DOX complexes can be efficiently used to treat drug resistant breast and liver cancer. The effectiveness of DOX complex-nanodiamond was found to be 10 times more effective than Doxorubicin alone. Nanodiamond can also be used to increase the dispersibility of various drugs which are insoluble in water [103]. In their study, Chen et al. [104] argued that carboxyl groups functionalized nanodiamond particles absorb drug molecules via physisorption or electrostatic interaction. In this way, these molecules may be dispersed in aqueous solution. Using this procedure, several poor water soluble drugs have been dispersed. These drugs include purvalanol A (used in liver cancer treatment), 4-hydroxytamoxifen (used in breast cancer therapy) and dexamethasone (for anti-inflammation) [105]. In another study, Sorafenib, a potential drug to be used in gastric cancer therapy, is mixed with nanodiamonds to form clusters. These clusters were then coated with an amphiphilic lipid, distearoylphosphatidylethanolamine–poly(ethylene glycol) (DSPE–PEG), and tested at mice as animal model. Sorafenib delivered by this procedure was observed to be more effective than it was delivered alone. The Sorafenib-ND clusters coated with DSPE–PEG also reduced metastatic nodules in mice's liver and kidneys which are responsible for 90% cancer-related deaths [106] (Fig. 1.13).

On the other hand, nanodiamonds can be used to deliver more than one drug at a time. Wang et al. [107] showed that the combination of nanodiamond–DOX,

nanodiamond–mitoxantrone, nanodiamond–bleomycin and free paclitaxel can be used efficiently to treat breast cancer.

In other experiment, nanodiamond was used to make vascular barrier leaky, which helped DOX to penetrate the vascular barrier. Therefore, nanodiamond indirectly helped DOX to be delivered. In this study, $–NH_2$ modified nanodiamond was proven to be more effective for vascular barrier leaky [108].

Gene therapy is one of the modern methods to treat different deceases. In these methods, DNA or siRNA is transported to the cytoplasm or nuclei of the cell. Various methods have been developed so far, for the delivery of genes [109–112]. In their study, Zhang et al. modified nanodiamond with polyethyleneimine and used it for the delivery of DNA. They found 70% increase in performance as compared to that of polyethyleneimine alone [113]. Chen et al. [114] demonstrated the ability of nanodiamond to act as a carrier for the delivery of small interfering RNA (siRNA). siRNA has significant therapeutic properties and a number of carriers exist for their delivery but their biocompatibility is not up to mark. Nanodiamond presents an excellent platform for siRNA delivery. In their another report, Zhang et al. [115] used fluorescent nanodiamonds (FCN) for targeting siRNA to down regulate the expression of polo-like kinase-1 (Plk1) which is a master regulator of mitosis. The amount of FCN required for this process was 1/30 times of the amount of gold nanoparticles earlier used for this purpose. Alwani et al. [116] examined the gene targeting properties of lysine-functionalized nanodiamonds. They observed that lysine functionalization of nanodiamonds improved the dispersivity and stability of nanodiamond-gene complex. Gene therapy is an emerging field which has the promise of treating complex diseases such as genetic disorders and different types of cancers. Extensive research work is needed for the development of therapeutic agents and their delivery platforms. Nanodiamond with appropriate functionalization have been proven as the promising material for targeted delivery of these therapeutic agents.

1.4 Nitrogen Vacancy Centers (NV Centres) in Nanodiamonds and Their Applications in Bio-imaging

Nitrogen vacancy (NV) center is a type of point defect present in diamond lattice. NV centre is composed of one substitutional nitrogen atom bounded with a lattice vacancy [117] (Fig. 1.14). These nitrogen vacancy centres act as the luminescent colour centres. The NV centres absorb in the wavelength range of 460–600 nm. Diamond nanoparticles emit radiation ranging from 550 to 800 nm, when excited by green light [104].

In the nanodiamonds having negligible concentration of nitrogen, these nitrogen defects are created by the implantation of N^+ ion followed by the annealing procedure. While, in nanodiamond having substantial amount of nitrogen impurities,

the NV centres are created by the electrons or high energy radiation, followed by annealing [104]. Some other processes have also been reported for the production of nitrogen vacancies in nanodiamonds. In the process reported by Baranov et al. [118], the NV centres (with high concentration 1 NV centre per nm^3) in nanodiamonds are created by HPHT sintering of nanodiamonds.

These NV centres are classified into two categories i.e. negative NV centres (NV^-) and neutral NV centres (NV^0). Neutral NV centres have single unpaired electron while, a negative NV vacancy has two unpaired electrons. Therefore, negative NV centres have integer spin (S = 1) and the electronic states associated with these vacancies have triplet ground and excited levels. The triplet levels correspond to three different values of m_s spin states of −1, 0 and +1. In the absence of magnetic field, ground state corresponds to two degenerate states (for m_s = +1 and −1) and one state for m_s = 0. Upon excitation, the electrons are excited from triplet ground state to triplet excited state. During the transition between triplet ground level and triplet excited level, the spins are conserved. Occasionally, non-radiative transitions occur from triplet exited state to singlet metastable state and then electrons return from metastable state to ground state through non-radiative transition [1]. $m_s = \pm 1$ levels have the higher probability to undertake this type of inter-system crossing. When external resonant magnetic field is applied, the electrons make transition from m = 0 sublevel to $m = \pm 1$ sublevel in the ground state. This leads to 30% decrease of fluorescence emission intensity because, from excited $m = \pm 1$ level, the preferred transitions are non-radiative. So, the spin states present in NV centres can be determined by measuring the fluorescence variations under resonant magnetic field. This process is typically called the optically detected magnetic resonance (ODMR) [117] (Fig. 1.15).

The sensitivity of spin states of nanodiamonds with respect to external magnetic field is particularly useful in magnetic resonance imaging (MRI) and optically detected magnetic resonance imaging (ODMRI) of different species particularly, the biomolecules. Use of nanodiamonds in MRI drastically enhances the resolution of MRI [104]. Grinolds et al. [119] demonstrated the very first 3-D spatial mapping

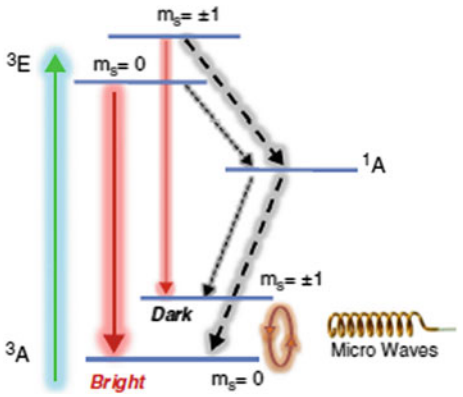

Fig. 1.15 Energy level structure of NV defect and the spin sublevels, optical excitation at 532 nm (*green arrow*), Fluorescence emission (*red arrows* 637–750 nm) non-radiative decay processes (*black dashed lines*) and spin transitions driven by MW fields (*Orange lines*) (Reprinted with permission from [117])

technique to sense the dark electronic spins on and near the nanodiamond surface with high resolution. They also employed nanodiamond to sense nuclear spins, whose magnetic moments are 600 times smaller than that of electrons. McGuinness et al. [120] demonstrated the detection of single nanodiamond particle within HeLa cell via probing its magnetic resonance. Nanodiamond-assisted MRI has also been used to imaging and sensing of biomolecules [121–123]. ODMRI has also been employed to probe the external parameters that can affect the spin states of NV^- vacancies. Kucsko et al. [124] demonstrated the ability to monitor local temperature variations in a living human embryonic fibroblast using nanodiamonds as probes.

The negative NV centres possess strong excitation and emission at 560 and 700 nm, respectively. The absorption cross section of negative NV centre at this wavelength range is 5×10^{-17} cm^2, which is comparable to that of dye molecule [104, 125, 126]. On the other hand, the fluorescence decay lifetime of negative NV centre has two components, i.e. one faster component of 1.7 ns and the other slower component of 17 ns. The latter value is beneficial for isolating the emission of nanodiamonds from background signals [104] during fluorescent imaging. Due to extraordinary fluorescence properties and biocompatibility, nanodiamonds have been used for fluorescent imaging of biomolecules and biospecies. In their report, Chen et al. [127] demonstrated the monitoring of the movement of individual nanodiamond within living HeLa cell up to 200 s. Epperla et al. [130] employed diamond nanoparticles as fluorescent trackers to monitor the intracellular transport of proteins through tunnelling membrane nanotubes. Bovine serum albumin (BSA) and green fluorescent protein (GFP) were coated on diamond nanoparticles of approximately 100 nm in diameter by means of physical adsorption. The motion of the protein-decorated diamond nanoparticles through the tunnelling nanotubes could be continuously monitored for longer than 10 min. These studies and some other recent studies [128, 129] suggest that the nanodiamonds can be used in in vivo bio-imaging and as biomarkers. Biocompatibility and extraordinary spin and fluorescent behaviour of nanodiamonds make them a promising material to be used in advanced bio-imaging. Several research groups are working in this area, and it is expected that the world will see many extraordinary applications of nanodiamonds in the field of bio-imaging especially in vivo bio-imaging which is an important aspect of targeted drug delivery.

1.5 Conclusion

As the other allotrope of carbon, nanodiamond also has various extraordinary properties. Due to these extraordinary properties, nanodiamond has remained in the focus of researchers working in the field of nanotechnology and its applications. There are several well established methods of nanodiamond synthesis such as detonation synthesis, and CVD. Recently, some new techniques and procedures, such as laser ablation, for the synthesis of nanodiamonds have been developed. These newly developed methods have the advantage of high purity over the

traditional methods. As these newly methods are not cost effective, there is a need of the development of cost effective methods that can deliver high purity nanodiamonds. Nanodiamonds have been exploited to act as the promising material for a number of applications. Some traditional applications of diamond, such as polishing and lubrication, have been improved by the use of nanodiamonds while some new applications have been emerged due to interesting properties of nanodiamonds, which arise due to size reduction. These new applications particularly involved the applications of nanodiamonds in the field of drug delivery and in vivo bio-imaging. Some recent studies proved that the nanodiamond is one of the fastest emerging materials in the field of drug delivery, bio-imaging and bio-marking. There is a need of more intense research to understand the ethical and compatibility related aspects related to the use of nanodiamonds in human disease management.

References

1. R.S. Lewis, T. Ming, J.F. Wacker, and E. Steel. Interstellar diamonds in meteorites. In *Lunar and Planetary Science Conference*, vol. 18. 1987
2. Roy S. Lewis, Edward Anders, Bruce T. Draine, Properties, detectability and origin of interstellar diamonds in meteorites. Nature **339**(6220), 117–121 (1989)
3. Sachiko Amari, Roy S. Lewis, Edward Anders, Interstellar grains in meteorites: I. Isolation of SiC, graphite and diamond; size distributions of SiC and graphite. Geochim. Cosmochim. Acta **58**(1), 459–470 (1994)
4. C.W. Bauschlicher Jr., Y. Liu, A. Ricca, A.L. Mattioda, L.J. Allamandola, Electronic and vibrational spectroscopy of diamondoids and the interstellar infrared bands between 3.35 and 3.55 μm. Astrophys. J **671**(1), 458 (2007)
5. Vadym N. Mochalin, Olga Shenderova, Dean Ho, Yury Gogotsi, The properties and applications of nanodiamonds. Nat. Nanotechnol. **7**(1), 11–23 (2012)
6. V.V. Danilenko, On the history of the discovery of nanodiamond synthesis. Phys. Solid State **46**(4), 595–599 (2004)
7. N.R. Greiner, D.S. Phillips, J.D. Johnson, F. Volk, Diamonds in detonation soot. Nature **333** (6172), 440–442 (1988)
8. Guo-Wei Yang, Jin-Bin Wang, Qui-Xiang Liu, Preparation of nano-crystalline diamonds using pulsed laser induced reactive quenching. J. Phys. Condens. Matter **10**(35), 7923 (1998)
9. J.P. Boudou et al., High yield fabrication of fluorescent nanodiamonds. Nanotechnology **20**, 235602 (2009)
10. Y.G. Gogotsi et al., Structure of carbon produced by hydrothermal treatment of β-SiC powder. J. Mater. Chem. **6**, 595–604 (1996)
11. M. Frenklach et al., Induced nucleation of diamond powder. Appl. Phys. Lett. **59**, 546–548 (1991)
12. T.L. Daulton, M.A. Kirk, R.S. Lewis, L.E. Rehn, Production of nanodiamonds by high-energy ion irradiation of graphite at room temperature. Nucl. Instrum. Meth. B **175**, 12–20 (2001)
13. S. Welz, Y. Gogotsi, M.J. McNallan, Nucleation, growth, and graphitization of diamond nanocrystals during chlorination of carbides. J. Appl. Phys. **93**, 4207–4214 (2003)
14. É. Galimov et al., Experimental corroboration of the synthesis of diamond in the cavitation process. Dokl. Phys. **49**, 150–153 (2004)

15. O.A. Shedorova, D.M. Gruen (eds.), *Ultrananocrystalline diamond: synthesis, properties and applications* (William Andrew Publishing, Norwich, NY, 2006)
16. V.P. Adiga et al., Phys Rev B **79**, 245403 (2009)
17. Y.R. Chang et al., Mass production and dynamic imaging of fluorescent nanodiamonds. Nature Nanotech. **3**, 284–288 (2008)
18. V.N. Mochalin, Y. Gogotsi, Wet chemistry route to hydrophobic blue fluorescent nanodiamond. J. Am. Chem. Soc. **131**, 4594–4595 (2009)
19. R.A. Shimkunas et al., Nanodiamond–insulin complexes as pH-dependent protein delivery vehicles. Biomaterials **30**, 5720–5728 (2009)
20. K.V. Purtov, A.I. Petunin, A.E. Burov, A.P. Puzyr, V.S. Bondar, Nanodiamonds as carriers for address delivery of biologically active substances. Nanoscale Res. Lett. **5**, 631–636 (2010)
21. A. Krueger, Diamond nanoparticles: jewels for chemistry and physics. Adv. Mater. **20**, 2445–2449 (2008)
22. W.W. Zheng et al., Organic functionalization of ultradispersed nanodiamond: synthesis and applications. J. Mater. Chem. **19**, 8432–8441 (2009)
23. B.V. Spitsyn et al., Mater. **15**, 296–299 (2006)
24. K.D. Behler et al., Nanodiamond–polymer composite fibers and coatings. ACS Nano **3**, 363–369 (2009)
25. Q. Zhang et al., Fluorescent PLLA–nanodiamond composites for bone tissue engineering. Biomaterials **32**, 87–94 (2011)
26. D.H. Wang, L.S. Tan, H.J. Huang, L.M. Dai, E. Osawa, In-situ nanocomposite synthesis: arylcarbonylation and grafting of primary diamond nanoparticles with a poly(ether–ketone) in polyphosphoric acid. Macromolecules **42**, 114–124 (2009)
27. J.L. Cheng, J.P. He, C.X. Li, Y.L. Yang, Facile approach to functionalize nanodiamond particles with V-shaped polymer brushes. Chem. Mater. **20**, 4224–4230 (2008)
28. V.N. Mochalin et al., Covalent incorporation of aminated nanodiamond into an epoxy polymer network. ACS Nano **5**, 7494–7502 (2011)
29. P.S. DeCarli, J.C. Jamieson, Formation of diamond by explosive shock. Science **133**(3467), 1821–1822 (1961)
30. P.S. DeCarli, Method of making diamond, US Patent, 3238019 (1966)
31. G.R. Cowan, N.J. Woodbury, B.W. Dunnington, P. Wood, A.H. Holtzman, Process for synthesizing diamond, US Patent 3401019 (1968)
32. V.V. Danilenko, On the discovery of detonation nanodiamond, in *Ultrananocrystalline Diamond*, ed. by O.A. Shenderova, D.M. Gruen (Norwich, WilliamAndrew, 2006), pp. 335–344
33. L.F. Trueb, J. Appl. Phys. **39**, 4707 (1968). b) G. Burkhard, H. Tamura, Y. Tanabe, A.B. Sawaoka, K. Yamada, Appl. Phys. Lett. **66**, 3131 (1995)
34. M. Vanthiel, F.H. Ree, J. Appl. Phys. **62**, 1761 (1987)
35. V.Y. Dolmatov, Detonation synthesis ultradispersed diamonds: properties and applications. Usp. Khim. **70**, 687–708 (2001)
36. V.V. Danilenko, *Synthesis and Sintering of Diamond by Explosion* (Energoatomizdat, Moscow, 2003)
37. V.Y. Dolmatov, M.V. Veretennikova, V.A. Marchukov, V.G. Sushchev, Currently available methods of industrial nanodiamond synthesis. Phys. solid state **46**(4), 611–615 (2004)
38. J.B. Donnet, C. Lemoigne, T.K. Wang, C.-M. Peng, M. Samirant, A. Eckhardt, Bull. Soc. Chim. Fr. **134**, 875 (1997)
39. G.A. Adadurov, A.V. Baluev, O.N. Breusov, V.N. Drobyshev, A.I. Rogacheva, A.M. Sapegin, V.F. Tatsii, Some properties of diamonds produced by an explosive method. Izv. Akad. Nauk SSSR Ser. Neorg. Mater. **13**(4), 649–653 (1977)
40. V.F. Tatsii, A.V. Bochko, G.S. Oleinik, Structure and properties of Dalan detonation diamonds. Combust. Explos. Shock Waves **45**(1), 95–103 (2009)

41. V.V. Danilenko, in Synthesis, Properties and Applications of Ultrananocrystalline Diamond (Proceedings of NATO Advanced Research Workshop), ed. by D. Gruen, O. Shenderova, A. Vul (Springer, Heidelberg, 2005), pp. 181–198
42. P. Badziag, W.S. Verwoerd, W.P. Ellis, N.R. Greiner, Nanometre-sized diamonds are more stable than graphite. Nature **343**, 244–245 (1990)
43. A.S. Barnard, S.P. Russo, I.K. Snook, Structural relaxation and relative stability of nanodiamond morphologies. Diamond Relat. Mater. **12**, 1867–1872 (2003)
44. A.S. Barnard, M. Sternberg, Crystallinity and surface electrostatics of diamond nanocrystals. J. Mater. Chem. **17**, 4811–4819 (2007)
45. J.Y. Raty, G. Galli, Ultradispersity of diamond at the nanoscale. Nature Mater. **2**, 792–795 (2003)
46. L. Lai, A.S. Barnard, Modeling the thermostability of surface functionalisation by oxygen, hydroxyl, and water on nanodiamonds. Nanoscale **3**, 2566–2575 (2011)
47. L. Lai, A.S. Barnard, Stability of nanodiamond surfaces exposed to N, NH, and NH_2. J. Phys. Chem. C **115**, 6218–6228 (2011)
48. A. Aleksenskiy, M. Baidakova, V. Osipov, A. Vul, Nanodiamonds, in *Applications Biology and Nanoscale Medicine*, ed. by D. Ho (Springer, Berlin, 2010), pp. 55–79
49. I.I. Vlasov et al., Nitrogen and luminescent nitrogen-vacancy defects in detonation nanodiamond. Small **6**, 687–694 (2010)
50. O.A. Shenderova, D.M. Gruen, *Ultrananocrystalline Diamond: Synthesis, Properties, and Applications* (William Andrew, New York, 2006)
51. Vincent Pichot, Benedikt Risse, Fabien Schnell, Julien Mory, Denis Spitzer, Understanding ultrafine nanodiamond formation using nanostructured explosives. Sci. Rep. **3**, 2159 (2013)
52. Stepan S. Batsanov, Alexander N. Osavchuk, Stepan P. Naumov, Alexander E. Efimov, Budhika G. Mendis, David C. Apperley, Andrei S. Batsanov, Synthesis and properties of hydrogen-free detonation diamond. Propellants Explos. Pyrotech. **40**(1), 39–45 (2015)
53. Z.Y. Juang, J.F. Lai, C.H. Weng, J.H. Lee, H.J. Lai, T.S. Lai, C.H. Tsai, On the kinetics of carbon nanotube growth by thermal CVD method. Diamond and related materials **13**(11), 2140–2146 (2004)
54. Xianbao Wang, Haijun You, Fangming Liu, Mingjian Li, Li Wan, Shaoqing Li, Qin Li et al., Large-scale synthesis of few-layered graphene using CVD. Chem. Vap. Deposition **15**(1–3), 53–56 (2009)
55. James E. Butler, Anirudha V. Sumant, The CVD of nanodiamond materials. Chem. Vap. Deposition **14**(7–8), 145–160 (2008)
56. B.V. Spitsyn, B.V. Deryaguin, USSR Inventor's Certificate No. 339134, Application No. 964957/716358 (July 10, 1956)
57. S. Matsumoto, Y. Sato, M. Kamo et al., Jpn. J. Appl. Phys. **21**(4A), L183 (1982)
58. M. Kamo, Y. Sato, S. Matsumoto et al., J. Cryst. Growth **62**(3), 642 (1983)
59. S. Matsumoto, J. Mater. Sci. Lett. **4**(5), 600 (1985)
60. M. Frenklach, R. Kematick, D. Huang, W. Howard, K.E. Spear, A.W. Phelps, R. Koba, Homogeneous nucleation of diamond powder in the gas phase. J. Appl. Phys. **66**, 395–399 (1989)
61. M. Frenklach, W. Howard, D. Huang, J. Yuan, K.E. Spear, R. Koba, Induced nucleation of diamond powder. Appl. Phys. Lett. **59**(5), 546–548 (1991)
62. P.R. Buerki, S. Leutwyler, Homogeneous nucleation of diamond powder by CO_2 laser-driven reactions. J. Appl. Phys. **69**, 3739–3745 (1991)
63. Jin-Woo Park, Kun-Su Kim, Nong-Moon Hwang, Gas phase generation of diamond nanoparticles in the hot filament chemical vapor deposition reactor. Carbon **106**, 289–294 (2016)
64. O.A. Shenderova, A.C.H. Suzanne, Nanodiamonds. In Springer Handbook of Nanomaterials, (Springer, Berlin, 2013), pp. 263–300
65. Jean-Paul Boudou, Julia Tisler, Rolf Reuter, Alain Thorel, Patrick A. Curmi, Fedor Jelezko, Joerg Wrachtrup, Fluorescent nanodiamonds derived from HPHT with a size of less than 10 nm. Diam. Relat. Mater. **37**, 80–86 (2013)

66. P. Curmi, J.-P. Boudou, A. Thorel, F. Jelezko, M. Sennour. Method for manufacturing cubic diamond nanocrystals. U.S. Patent 8,932,553, issued January 13, 2015
67. G.W. Yang, Laser ablation in liquids: applications in the synthesis of nanocrystals. Progr. Mater. Sci. **52**, 648–698 (2007)
68. C.X. Wang, P. Liu, H. Cui, G.W. Yang, Nucleation and growth kinetics of nanocrystals formed upon pulsed-laser ablation in liquid. Appl. Phys. Lett. **87**(20), 201913 (2005)
69. L. Yang, P.W. May, L. Yin, J.A. Smith, K.N. Rosser, Growth of diamond nanocrystals by pulsed laser ablation of graphite in liquid. Diam. Relat. Mater. **16**(4), 725–729 (2007)
70. N. Tarasenka, A. Stupak, N. Tarasenko, D. Mariotti, S. Chakrabarti. Structure and optical properties of carbon nanoparticles generated by laser treatment of graphite in liquid. *ChemPhysChem* (2016)
71. F. Gorrini, M. Cazzanelli, N. Bazzanella, R. Edla, M. Gemmi, V. Cappello, J. David, C. Dorigoni, A. Bifone, A. Miotello. On the thermodynamic path enabling a room-temperature, laser-assisted graphite to nanodiamond transformation. *Sci. Rep.* **6** (2016)
72. David Amans, Mouhamed Diouf, Julien Lam, Gilles Ledoux, Christophe Dujardin, Origin of the nano-carbon allotropes in pulsed laser ablation in liquids synthesis. J. Colloid Interface Sci. **489**, 114–125 (2017)
73. F. Banhart, P.M. Ajayan, Carbon onion as nanoscopic pressure cell for diamond formation. Nature **382**, 433–437 (1996)
74. P. Wesolowski, Y. Lyutovich, F. Banhart, H.D. Carstanjen, H. Kronmüller, Formation of diamond in carbon onions under MeV ion irradiation. Appl. Phys. Lett. **71**, 1948–1951 (1997)
75. T.L. Daulton, M.A. Kirk, R.S. Lewis, L.E. Rehn, Production of nanodiamonds by high-energy ion irradiation of graphite at room temperature. Nucl. Instrum. Methods Phys. Res. B **175**, 12–18 (2001)
76. T. Meguro, M. Hida, M. Suzuki, Y. Koguchi, H. Takai, Y. Yamamoto, K. Maeda, Y. Aoyagi, Creation of nanodiamonds by single impacts of highly charged ions upon graphite. Appl. Phys. Lett. **79**, 3866–3870 (2001)
77. C.E. Chapter, *Brennen: Cavitation and Bubble Dynamics* (Oxford Univ, Oxford, 1995)
78. Yury Gogotsi, Sascha Welz, Daniel A. Ersoy, Michael J. McNallan, Conversion of silicon carbide to crystalline diamond-structured carbon at ambient pressure. Nature **411**(6835), 283–287 (2001)
79. K.J. Grannen, R.P.H. Chang, Diamond growth on carbide surfaces using a selective etching technique. J. Mater. Res. **9**, 2154–2163 (1994)
80. J.M.J. Lannon, J.S. Gold, C.D. Stinespring, Hydrogen ion interactions with silicon carbide and the nucleation of diamond thin films. J. Appl. Phys. **77**, 3823–3830 (1995)
81. V. Heera, W. Skorupa, B. Pecz, L. Dobos, Ion beam synthesis of graphite and diamond in silicon carbide. Appl. Phys. Lett. **76**, 2847–2849 (2000)
82. N. Nunn, T. Marco, G. McGuire, O. Shenderova, Nanodiamond: a high impact nanomaterial. Curr. Opin. Solid State Mater. Sci. **21**(1), 1–9 (2016)
83. X. Liu, X. Xu. Ultra-fine polishing of glass-ceramics by disaggregated and fractionated detonation nanodiamond. Ceramics International (2017)
84. K.B. Holt, Diamond at the nanoscale: applications of diamond nanoparticles from cellular biomarkers to quantum computing. Phil. Trans. Roy. Soc. A **365**, 2845–2861 (2007)
85. Khosro A. Shirvani, Mohsen Mosleh, Sonya T. Smith, Nanopolishing by colloidal nanodiamond in elastohydrodynamic lubrication. J. Nanopart. Res. **18**(8), 248 (2016)
86. A. Stravato, R. Knight, V. Mochalin, S.C. Picardi, HVOF-sprayed nylon-11 + nanodiamond composite coatings: Production and characterization. J. Therm. Spray Technol. **17**, 812–817 (2008)
87. O. Shenderova et al., Detonation nanodiamond and onion-like carbon: applications in composites. Phys. Status Solidi A **205**, 2245–2251 (2008)
88. J.Y. Lee, D.P. Lim, D.S. Lim, Tribological behavior of PTFE nanocomposite films reinforced with carbon nanoparticles. Composites B **38**, 810–816 (2007)

89. I. Neitzel, V. Mochalin, I. Knoke, G.R. Palmese, Y. Gogotsi, Mechanical properties of epoxy composites with high contents of nanodiamond. Compos. Sci. Technol. **71**, 710–716 (2011)
90. U. Maitra, K.E. Prasad, U. Ramamurty, C.N.R. Rao, Mechanical properties of nanodiamond-reinforced polymer-matrix composites. Solid State Commun. **149**, 1693–1697 (2009)
91. Q. Zhang, K. Naito, Y. Tanaka, Y. Kagawa, Grafting polyimides from nanodiamonds. Macromolecules **41**, 536–538 (2008)
92. O. Shenderova et al., Nanodiamond and onion-like carbon polymer nanocomposites. Diamond Relat. Mater. **16**, 1213–1217 (2007)
93. Fan Zhang, Qingxin Song, Xuan Huang, Fengning Li, Kun Wang, Yixing Tang, Canglong Hou, Hongxing Shen, A novel high mechanical property PLGA composite matrix loaded with nanodiamond-phospholipid compound for bone tissue engineering. ACS Appl. Mater. Interfaces. **8**(2), 1087–1097 (2016)
94. Y. Zhang, K.Y. Rhee, S.-J. Park, Nanodiamond nanocluster-decorated graphene oxide/epoxy nanocomposites with enhanced mechanical behavior and thermal stability. Compos. Part B Eng. **114**, 111–120 (2017)
95. E.-Y.Choi, K. Kim, C.-K. Kim, E. Kang. Reinforcement of nylon 6, 6/nylon 6, 6 grafted nanodiamond composites by in situ reactive extrusion. Sci. Rep. **6** (2016)
96. Ayesha Kausar, Thermal and rheological properties of waterborne polyurethane/nanodiamond composite. Nanosci. Nanotechnol. **6**(1), 6–10 (2016)
97. V. Borjanović, L. Bistričić, I. Pucić, L. Mikac, R. Slunjski, M. Jakšić, G. McGuire, A.T. Stanković, O. Shenderova, Proton-radiation resistance of poly (ethylene terephthalate)–nanodiamond–graphene nanoplatelet nanocomposites. J Mater. Sci. **51**(2), 1000–1016 (2016)
98. A. Nieto, J. Kim, O. Penkov, D.-E. Kim, J.M. Schoenung, Elevated temperature wear behavior of thermally sprayed WC-Co/nanodiamond composite coatings. Surf. Coat. Technol. **315**, 283–293 (2017)
99. S. Yin, Y. Xie, J. Cizek, E. Ekoi, T. Hussain, D. Dowling, R. Lupoi, Advanced diamond-reinforced metal matrix composites via cold spray: properties and deposition mechanism. Compos. Part B Eng. **113**(15), 44–54 (2017)
100. S. Murugesan, O.R. Monteiro, V.N. Khabashesku, Extending the Lifetime of Oil and Gas Equipment with Corrosion and Erosion-Resistant Ni-B-Nanodiamond Metal-Matrix-Nanocomposite Coatings. Offshore Technology Conference. (2016). doi:10.4043/26934-MS
101. H. Huang, E. Pierstorff, E. Osawa, D. Ho, Active nanodiamond hydrogels for chemotherapeutic delivery. Nano Lett. **7**, 3305–3314 (2007)
102. Chow et al., Nanodiamond therapeutic delivery agents mediate enhanced chemoresistant tumor treatment. Sci. Transl. Med. **3**, 73ra21 (2011)
103. Xianfeng Chen, Wenjun Zhang, Diamond nanostructures for drug delivery, bioimaging, and biosensing." Chemical Society Reviews (2017), R. Lam, D. Ho., Nanodiamonds as vehicles for systemic and localized drug delivery. Expert Opin. Drug Deliv. **6**(9), 883–895 (2009)
104. X. Chen, W. Zhang, Diamond nanostructures for drug delivery, bioimaging, and biosensing. Chem. Soc. Rev. **46**, 734–760 (2017)
105. M. Chen, E.D. Pierstorff, R. Lam, S.-Y. Li, H. Huang, E. Osawa, D. Ho, ACS Nano **3**, 2016–2022 (2009)
106. Z. Zhang, B. Niu, J. Chen, X. He, X. Bao, J. Zhu, H. Yu, Y. Li, Biomaterials **35**, 4565–4572 (2014)
107. H. Wang, D.-K. Lee, K.-Y. Chen, J.-Y. Chen, K. Zhang, A. Silva, C.-M. Ho, D. Ho, ACS Nano **9**, 3332–3344 (2015)
108. M.I. Setyawati, V.N. Mochalin, D.T. Leong, ACS Nano **10**, 1170–1181 (2016)
109. Y. Wong, K. Markham, Z.P. Xu, M. Chen, G.Q. Lu, P.F. Bartlett, H.M. Cooper, Biomaterials **31**, 8770–8779 (2010)
110. M. Ladewig, ZPXu Niebert, P.P. Gray, G.Q.M. Lu, Biomaterials **31**, 1821–1829 (2010)

111. L. Feng, S. Zhang, Z. Liu, Nanoscale **3**, 1252–1257 (2011)
112. X. Wang, K. Liu, G. Yang, L. Cheng, L. He, Y. Liu, Y. Li, L. Guo, Z. Liu, Nanoscale **6**, 9198–9205 (2014)
113. X.-Q. Zhang, M. Chen, R. Lam, X. Xu, E. Osawa, D. Ho, ACS Nano **3**, 2609–2616 (2009)
114. M. Chen, X.-Q. Zhang, H. Man, R. Lam, E.K. Chow, D. Ho, Nanodiamond vectors functionalized with polyethylenimine for siRNA delivery. The Journal of Physical Chemistry Letters **1**(21), 3167–3171 (2010)
115. L. Zhang, W. Zheng, R. Tang, N. Wang, W. Zhang, X. Jiang, Gene regulation with carbon-based siRNA conjugates for cancer therapy. Biomaterials **104**, 269–278 (2016)
116. S. Alwani, R. Kaur, D. Michel, J.M. Chitanda, R.E. Verrall, K. Chithra, I. Badea, Lysine-functionalized nanodiamonds as gene carriers: development of stable colloidal dispersion for in vitro cellular uptake studies and siRNA delivery application. Int. J. Nanomed. **11**, 687 (2016)
117. G. Balasubramanian, A. Lazariev, S.R. Arumugam, D.-W. Duan, Curr. Opin. Chem. Biol. **20**, 69–77 (2014)
118. P.G. Baranov, A.A. Soltamova, D.O. Tolmachev, N.G. Romanov, R.A. Babunts, F.M. Shakhov, S.V. Kidalov, A.Y. Vul, G.V. Mamin, S.B. Orlinskii, N.I. Silkin, Small **7**, 1533–1537 (2011)
119. M.S. Grinolds, M. Warner, K. De Greve, Y. Dovzhenko, L. Thiel, R.L. Walsworth, S. Hong, P. Maletinsky, A. Yacoby, Nat. Nanotechnol. **9**, 279–284 (2014)
120. L.P. McGuinness, Y. Yan, A. Stacey, D.A. Simpson, L.T. Hall, D. Maclaurin, S. Prawer, P. Mulvaney, J. Wrachtrup, F. Caruso, R.E. Scholten, L.C.L. Hollenberg, Nat. Nanotechnol. **6**, 358–363 (2011)
121. F.C. Ziem, N.S. Goetz, A. Zappe, S. Steinert, J. Wrachtrup, Nano Lett. **13**, 4093–4098 (2013)
122. S. Steinert, F. Ziem, L.T. Hall, A. Zappe, M. Schweikert, N. Goetz, A. Aird, G. Balasubramanian, L. Hollenberg, J. Wrachtrup, Nat. Commun. **4**, 1607 (2013)
123. L.T. Hall, G.C.G. Beart, E.A. Thomas, D.A. Simpson, L.P. McGuinness, J.H. Cole, J.H. Manton, R.E. Scholten, F. Jelezko, J. Wrachtrup, S. Petrou, L.C.L. Hollenberg, Sci. Rep. **2**, 401 (2012)
124. G. Kucsko, P.C. Maurer, N.Y. Yao, M. Kubo, H.J. Noh, P.K. Lo, H. Park, M.D. Lukin, Nature **500**, 54–58 (2013)
125. S.J. Yu, M.W. Kang, H.C. Chang, K.M. Chen, Y.C. Yu, J. Am. Chem. Soc. **127**, 17604–17605 (2005)
126. R. Schirhagl, K. Chang, M. Loretz and C.L. Degen, in Ann. Rev. Phys. Chem. ed. by M.A. Johnson, T.J. Martinez, vol. 65 (2014), pp. 83–105
127. X. Chen, C. Zou, Z. Gong, C. Dong, G. Guo, F. Sun, Light. Sci Appl. **4**, e230 (2015)
128. C.-C. Fu, H.-Y. Lee, K. Chen, T.-S. Lim, H.-Y. Wu, P.-K. Lin, P.-K. Wei, P.-H. Tsao, H.-C. Chang, W. Fann, Proc. Natl. Acad. Sci. U. S. A. **104**, 727–732 (2007)
129. O. Faklaris, D. Garrot, V. Joshi, J.-P. Boudou, T. Sauvage, P.A. Curmi, F. Treussart, J. Eur. Opt. Soc. Rapid **4**, 09035 (2009)
130. C.P. Epperla, N. Mohan, C.-W. Chang, C.-C. Chen, H.-C. Chang, Small **11**, 6097–6105 (2015)

Chapter 2
Carbon Nanowalls: A Potential 2-Dimensional Material for Field Emission and Energy-Related Applications

Sanjay Kumar Srivastava, Vikram Kumar and V.D. Vankar

Abstract Carbon, an abundant material in the earth crust, is also the most attracting, in particular, owing to variety of fascinating materials it forms. It can appear as a transparent crystal (such as diamond), but also as black amorphous soot. It is associated with a rich and diverse chemistry. Carbon materials, in general, can be classified into different dimensional categories such as three-dimensional (3-D), two-dimensional (2-D), one-dimensional (1-D), and zero-dimensional (0-D) depending on the relative sizes in different spatial directions. Fullerenes are 0-D whereas carbon nanotubes (CNTs), nanofibres, or nanorods are 1-D nanostructures. Graphite nanosheets or nanowalls are considered as 2-D structures. A great attention has been given to the 0-D and 1-D carbon nanostructures, but studies on the growth and the properties of 2-D carbon nanowalls (CNWs) are not so abundant as in the case of fullerene or CNTs. The CNWs are very promising class of 2-D nanomaterials since the CNWs are characterized by an open boundary structure. On the other hand, fullerene and CNTs are closed boundary structures. Each CNW is made of several graphene sheets stacked over each other. The CNWs have a large surface area, which makes them very attractive for various potential applications such as chemical and biosensors or energy storage devices. Moreover, the CNWs have sharp edges normal to the substrate which make them very useful for field emission applications. In this chapter, growth of CNWs by various methods is discussed with an emphasis on plasma-enhanced chemical vapor deposition (PECVD) method. This is followed by the morphological and structural characterization of the CNWs by different techniques. The formation mechanism of CNWs will be described. In addition, properties of CNWs in respect to their

S.K. Srivastava (✉)
CSIR-National Physical Laboratory, New Delhi 110012, India
e-mail: srivassk@nplindia.org; sksrivastava78@gmail.com

S.K. Srivastava
Academy of Scientific & Innovative Research (AcSIR),
CSIR-NPL Campus, New Delhi 110012, India

V. Kumar · V.D. Vankar
Department of Physics, Indian Institute of Technology Delhi,
Hauz Khas, New Delhi 110016, India

Z.H. Khan (ed.), *Nanomaterials and Their Applications*,
Advanced Structured Materials 84, https://doi.org/10.1007/978-981-10-6214-8_2

potential applications in field emission and energy related devices including lithium ion batteries, fuel cells and solar cells, is also reviewed in the light of their unique morphology and structure.

2.1 Introduction

Carbon, which is abundantly found in the earth crust, is the most attracting materials in present era, in particular owing to variety of fascinating materials it forms. It can appear as a transparent crystal (such as diamond), but also as black amorphous soot. It is associated with a rich and diverse chemistry. Prior to 1985, there were only two known crystalline forms of solid carbon: diamond and graphite. The discovery of buckminsterfullerene (C_{60}) by Kroto et al. [1] followed by its macroscopic synthesis by Krätschmer [2] gave a new direction in the field of carbon research. The subsequent discovery of carbon nanotubes (CNTs) [3] added a new dimension to the knowledge of carbon technology [4].

2.1.1 Carbon Nanostructures: An Overview

The synthetic graphite was observed even in the nineteenth century; however, synthetic diamonds were realized only in the later half of the twentieth century. Since then, both graphite- and diamond-related carbon materials have attracted lots of interests in scientific communities. With the discoveries/advancements of new synthesis techniques, these two materials have renewed their importance. In the graphite-based group, new materials such as carbon fibers, glassy carbons, pyrolytic carbon were developed in the early 1960s [5] and found wide commercial applications. The most significant and relatively recent application of this carbon material is in lithium-ion rechargeable batteries, wherein nanostructured carbon-based anodes are used and has lead to feasibility of portable electronic devices [6].

A new era in carbon materials began when the family of buckminsterfullerene (C_{60}) [1] was discovered in 1985. Multi-walled carbon nanotubes (MWNTs) were discovered in 1991 by Sumio Iijima of NEC Corporation, Fundamental Research Laboratories, Japan, as a by-product of fullerenes called as helical microtubules of graphite carbon which was produced by arc discharge process [3]. The discovery of these carbon structures lead to a new worldwide research boom that seems still growing with the discovery of exciting materials and their properties. But a fundamental question was prompted that why were CNTs or fullerenes not discovered many years ago? Even all of the techniques required to synthesize and characterize these nanomaterials have been available for decades. In fact, there were evidences for the existence of CNTs before 1991, but they could not be recognized as a new and important form of carbon. The 2-D carbon nanosheets or carbon nanowalls are

relatively new. The 2-D graphite sheets have an open boundary structure whereas fullerene and CNTs have the closed boundary structures. The 2-D CNWs have a much larger surface area as compared to that of fullerene or CNTs which makes them very attractive for chemical, biosensor, and energy storage applications. Moreover, they have sharp edges almost normal to the substrate which could be very useful for field emission applications. Some of the significant developments and discoveries of the nanoscale carbon structures are summarized in Table 2.1.

Table 2.1 Summary of the developments in the field of carbon nanostructures [6, 7]

Year	Development	Remarks	Reference
1960	Production of carbon tubes with graphite layer structures	Arc discharge method, 5 μm in diameter tubes	Bacon [8]
1966	Theoretical prediction of a large hollow cage molecule	Assumed that the molecule can be fashioned out of graphite	Jones [9]
1970	The soccer ball-shaped C_{60} molecule is suggested		Osawa [10]
1973	Prediction that C_{60} would be stable	Huckel calculations, closed shell electronic configuration is predicted	Bochvar and Galperin [11]
1980	First experimental observation of carbon nanotubes by arc discharge process	By high-resolution transmission electron microscopy observation	Iijima [12]
1984	Report on the preferential stability of even-atom carbon clustery especially of a sixty carbon species	Mass spectroscopy study on laser-ablated carbon plumes. Abundance of sixty carbon species in spectrum is reported	Rohlfling et al. [13]
1985	Discovery of C_{60}	C_{60} and C_{70} detected in the mass spectrum of laser-evaporated graphite. C_{60} was named as Buckminsterfullerene	Kroto, Smalley et al. [1]
1990	Mass production of Fullerene	By evaporation of graphite electrodes in an arc discharge process	Kratehmer et al. [2]
1991	Discovery of MWNTs	Observation of helical MWNTs of graphite with closed ends deposited on cathode during the DC arcing of graphite	Iijima [3]
1992	Observation of carbon onions	Spherical shells of graphite obtained by heating of CNTs by the electron beam in a microscope	Ugarte [14]
1992	Mass production of MWNTs	Arc discharge process	Ebbesen and Ajayan [15]
1993	Discovery of SWNTs	By arc process in the presence of catalyst such as Fe or Co	Iijima et al. [16], Bethune et al. [17]

(continued)

Table 2.1 (continued)

Year	Development	Remarks	Reference
1996	Ropes of SWNTs	By laser ablation method	Smalley et al. [18]
1998	CVD synthesis of aligned MWNT films	By plasma-enhanced hot-filament CVD in the presence of catalyst film	Ren et al. [19]
1998	CVD synthesis of SWNTs	Using catalyst	Kong et al. [20], Hafner et al. [21]
2001	Ordered arrangement of SWNTs	Ordered arrangement of SWNTs of micron size called nanotube single crystals	Schilttler et al. [22]
2002	Growth of carbon nanowalls/nanosheets (CNWs)	By microwave plasma-enhanced CVD method observed especially on insulating substrates coated with NiFe under the influence of intense plasma on the biased substrate CNWs was observed as a by-product of CNTs	Wu et al. [23]
2004	Discovery of graphene-a monolayer of graphite/carbon atoms	Professor Geim and professor Novoselov of University of Manchester, UK, extracted the graphene from a piece of graphite such as is found in ordinary pencils. Using regular adhesive tape, they managed to obtain a flake of carbon with a thickness of just one atom. This was achieved at a time when many believed it was impossible for such thin crystalline materials to be stable.	Novoselov et al. [24]
2010	Nobel Prize in Physics for the year 2010 to Professor Andre Geim and Professor Konstantin Novoselov for their 'groundbreaking experiments regarding the two-dimensional material graphene'		

2.1.2 Structural Properties

2.1.2.1 Bonding Configuration of Carbon Atoms

In order to understand the structure of carbon nanostructures such as CNTs, graphene, or carbon nanowalls and other related nanostructures, understanding of carbon atoms' bonding structure and properties is essential. A carbon atom has six electrons with electronic configuration $1s^2$, $2s^2$, $2p^2$. The four valence shell

electrons fill the sp^3 or sp^2 and sp hybrid orbital and are responsible for the different bonding configurations of graphite, diamond, CNTs, fullerenes, or carbon nanowalls. For example, in diamond, four valence electrons of each carbon atom occupy the sp^3 hybrid orbitals and form four equivalent 'σ' covalent bonds to connect four other carbon atoms tetrahedrally and therefore making diamond the hardest known material and electrically insulating [25]. The diamond is transparent in the visible or infrared region, and opaque in the ultraviolet region. It also has high refractive index and unusually high thermal conductivity. Thermodynamically, diamond is metastable at room temperature. In graphite, the three valence electrons of each carbon occupy the planar sp^2 hybridized orbital to form three in-plane σ-bonds and the fourth electron forms an out-of-plane π bond which results in a planar hexagonal network. The hexagonal sheets are held parallel to each other by weak van der Waal's force with an interplanar spacing of 0.34 nm. In sp^2 bonding, σ-bond length and bond energy are 0.14 nm and 420 kcal/mol, respectively, whereas in sp^3 bonding they are 0.15 nm and 360 kcal/mol, respectively. Therefore, graphite is stronger in-plane than diamond. Graphite is stable at room temperature. It is electrically conductive because of the distribution of the out-of-plane π electron over its plane. These loose π electrons' interaction with light causes the graphite optically black. Also, the weak van der Waal's interaction among its parallel sheets makes the material soft because the sheets can easily glided relative to each other and hence making graphite as an ideal lubricant applications [25].

Fullerenes (C_{60}) are made by joining 20 hexagons and 12 pentagons made out of carbon atoms forming a spherical shell-like structure. Each carbon atoms in C_{60} is bonded with three neighboring C atoms in sp^2 bonding configuration. However, there may be small fraction of sp^3 character in these bonds due to the associated curvature. Also, the strain is evenly distributed over the molecule since all the 60 carbon atoms are identical [7].

A carbon nanotube (CNT) is hollow cylinder formed by rolling graphite sheets. Carbon–carbon bonding in CNT is sp^2. However, circular curvature of the nanotubes may cause rearrangement of σ and π bonding leading to σ–π rehybridization, in which three σ bonds are slightly out of plane causing the π orbital to delocalized outside the tube for compensation. This bonding arrangement makes CNTs mechanically stronger, electrically and thermally more conductive, and chemically and biologically more active than graphite. This also causes the incorporation of topological defects into the hexagonal network to form capped, bend, or helical tubes [25]. Based on number of sheets rolled up, nanotubes are classified as single-walled nanotubes (SWNTs) and multi-walled nanotubes (MWNTs). Different allotropes of carbon and their structure are shown in Fig. 2.1.

2.1.2.2 Single-Walled Nanotubes

A SWNT is defined as a hollow cylinder of a single graphite sheet. The inner diameter of SWNT is extremely narrow typically 1 nm. SWNTs were discovered in 1993 by arc discharge evaporation method [16, 17]. Generally, SWNTs produced

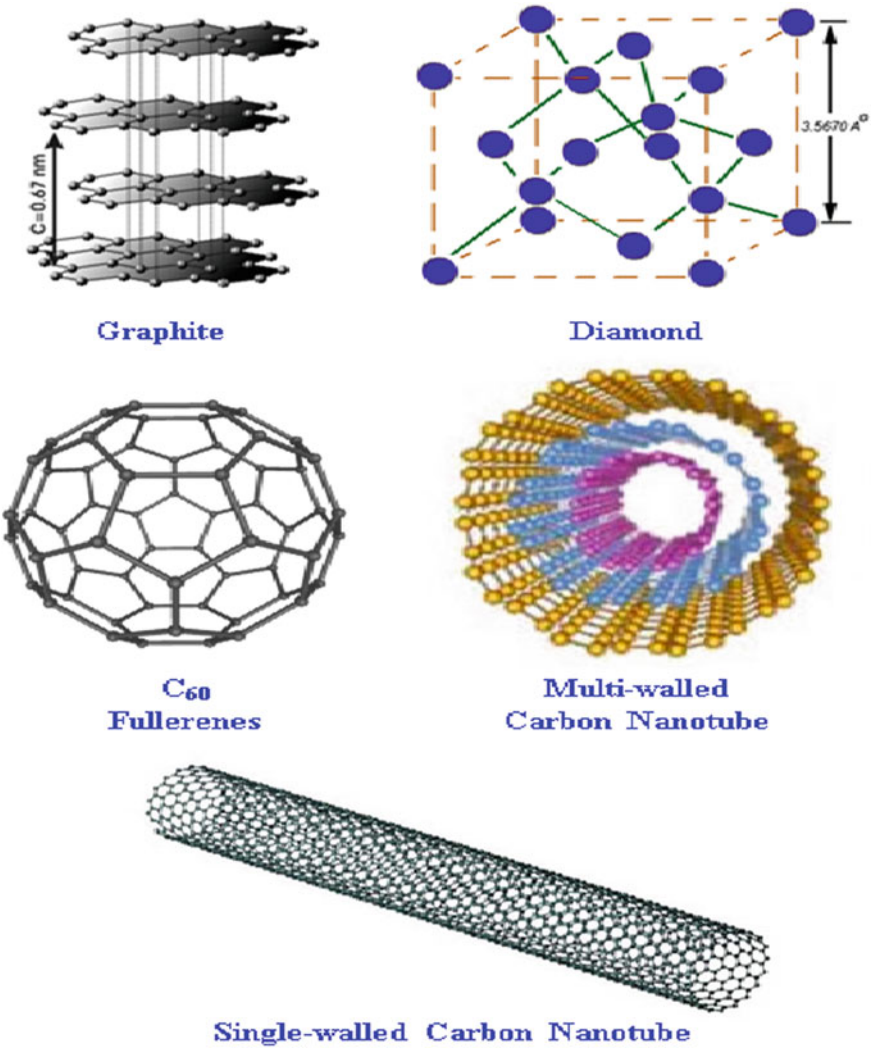

Fig. 2.1 Different allotropes of carbon and their structure

by conventional arc discharge method are capped. They appear in the form of bundles of tubes or ropes of tubes. The growth of SWNTs is believed to be essentially catalytic. Iron group metals such as iron, nickel, cobalt are used as the catalysts. The catalytically produced SWNTs have a number of interesting features different from those produced by arc evaporation. The catalytic tubes generally have small metal particles attached to one of its ends. The tubes have relatively larger diameters (typically 1–5 nm) dependent on the size of associated catalytic

particle. Also, the catalytically formed SWNTs are generally isolated rather than grouped into bundles as often observed in tubes produced by arc evaporation [26].

2.1.2.3 Multi-walled Nanotubes

A MWNT consists of many concentric seamless cylinders or SWNTs. The intertube spacing in MWNTs is typically $\sim$0.34 nm which is close to interplanar spacing of (002) planes of graphite. Diameter of MWNTs ranges from 2.5 to 100 nm depending on the process condition used for their synthesis. Figure 2.1 shows the computer generated models of a SWNT and a MWNT. Both the SWNTs and MWNTs have extremely unique structural, mechanical, electrical, electronic, thermal, and field emission properties. However, structure and hence properties of the CNTs are strongly dependent on the synthesis processes.

2.1.2.4 Carbon Nanowalls

A thin graphite sheet is a typical example of a 2-D system, whereas a single layer of graphite sheet, otherwise known as 'graphene,' is the most ideal 2-D system [24]. Graphene is a hexagonal arrangement of carbon atoms forming monoatomic planar sheet. It is a promising electronic material due to its high electrical conductivity, chemical and physical stability [27]. In addition, graphene possesses several extraordinary properties such as high ballistic electron mobility (>200,000 $cm^2V^{-1}s^{-1}$) [28], high thermal conductivity (5000 $W\ m^{-1}K^{-1}$) [29], Young's modulus ($\sim$1150 GPa), fracture strength (125 GPa) [30], and a high specific surface area ($\sim$2600 m^2g^{-1}) [31]. These properties are quite attractive for various applications.

Similar to graphene, the carbon nanowalls (CNWs) is another class of 2-D materials which is described as self-assembled and vertically standing few-layered graphene sheets. These are also called as carbon nanosheets and carbon nanoflakes. The walls are curved and have a height of approximately 1–2 μm with average thickness of few to several nanometers. They stand vertically to form a self-supported network structures. As illustrated in Fig. 2.2, each CNW consists of several stacked graphene sheets. CNWs were first reported by Wu et al. in 2002 [23] wherein they observed wall-like carbon nanostructures perpendicular to a substrate and therefore named them as CNWs. Since then, several groups have reported growth of CNWs by different chemical vapor deposition (CVD) methods mainly by plasma-enhanced CVD (PECVD). The CNWs have a high density of atomic-scale graphitic edges normal to the substrates (so-called as nanowalls) that are potential sites for electron field emission. The 2-D CNWs have a large surface area (theoretically twice that of the fullerenes or CNTs) [32] which makes them very attractive for chemical, biosensor, or energy storage applications. Moreover, each CNW has a domain structure which consists of nanographite domains which are several tens of nanometers in size. Such unique morphology and structure of

CNWs have lead to both fundamental as well as applied research. Few of the leading applications of CNWs are as electron field emitters, as the electrodes in lithium-ion batteries, as catalyst supports in fuel cells, and as an electrode or active material in solar cells.

In this chapter, basic properties of CNWs, growth, and their potential applications are described. PECVD due to its relatively low-temperature processing and feasibility for scalability has been one of the most promising techniques for the growth of carbon nanomaterials including aligned or nonaligned CNT films and CNWs. Here, growth of CNWs using microwave plasma-enhanced chemical vapor deposition (MPECVD) is featured. In addition, growth of CNWs by inductively coupled plasma (ICP)-enhanced CVD and capacitively coupled plasma (CCP)-enhanced CVD, DC-PECVD, and few more CVD methods is briefly described. The structural characteristics of CNWs, using TEM/HR-TEM and Raman spectroscopy techniques and possible growth mechanism, are also discussed. Owing to their large density of nanoscale graphitic edges vertically aligned to the substrates, CNWs are potential candidates for electron field emission applications. Few examples of their field emission applications would be discussed. Further, due to the large surface area of CNWs, different electrochemical applications using CNWs such as batteries have been proposed in the literatures. Few examples of such applications would also be discussed briefly along with application of CNWs as electrode for fuel cell and solar cells.

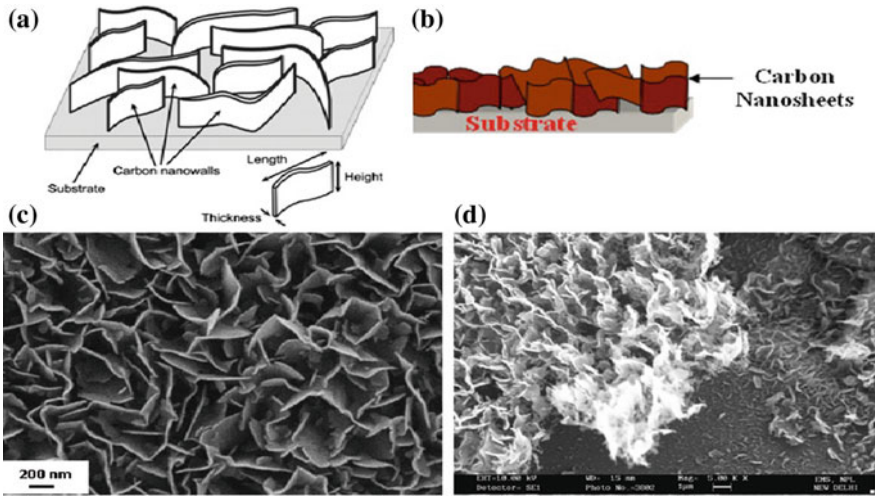

Fig. 2.2 **a** Schematic illustration of CNWs and definition of their size. Reprinted from Ref. [53] Copyright (2005), with the permission of AIP Publishing; **b** schematic illustration of CNW in cross-sectional view, **c** SEM image of typical carbon nanowalls (prepared by microwave plasma-enhanced CVD method, **d** SEM image of CNWs in cross-sectional view

2.2 Growth of Carbon Nanowalls

Carbon sheets were initially observed as the by-product of CNTs by arc discharge evaporation of graphite [15, 33]. Later, Iijima et al. [34] reported production of graphite sheets or flakes coexisting with MWNTs and other form of carbon by laser ablation method. Moreover, the relative amount of sheets was very little. In this series, Ando et al. [35] proposed mass production of petal-like graphite sheets by DC-arc discharge evaporation of graphite in hydrogen gas atmosphere. However, in addition, several other forms of carbon such as MWNTs and carbon nanoparticles were also obtained. Graphite sheets were observed only in the region outside the flame of arc discharge and on the graphite wall surrounding the anode and cathode. They observed decrease in area of deposit containing petal-like sheets with increase in H_2 pressure and arc current. Also, growth mechanism of such graphite sheets by the above methods was not very well understood. In addition, both the arc discharge and the laser ablation methods are high-temperature processes. The control of the process parameters to have carbon nanosheets or nanowalls of required morphology on a support material is difficult. The PECVD technique has several advantages suiting to simple and scalability to large area growth.

2.2.1 Main Approaches for the Growth of CNWs and Current Status

2.2.1.1 Microwave Plasma-Enhanced CVD (MPEVCD) Method

For the first time in the year 2002, Shang et al. [36] reported growth of uniformly distributed carbon nanoflakes interlaced together perpendicularly on silicon (Si) substrates by hot-filament chemical vapor deposition (HF-CVD) process using C_2H_2 + H_2 gas mixture at substrate temperature (400–700 °C). They suggested that asymmetric non-Maxwellian distribution of carbon clusters and asymmetric distribution of dangling bonds of carbon atom might have favored the formation of 2-D carbon nanosheets. The same year (2002) Wu et al. [23] reported growth of 2-D CNWs standing vertically on catalyzed (NiFe) substrates (Si, SiO_2/Si and sapphire) by MPECVD under additional DC biasing during the growth of CNTs. It was the very first report on the growth of 2-D CNWs vertically standing on the substrates by a PECVD method. They used a MPECVD system, equipped with a 500-W microwave (MW) source and a traverse rectangular cavity to couple the MW to a quartz tube for generating the plasma. Two parallel-plate electrodes were placed (2 cm away from each other) inside the tube and in the longitudinal direction of the tube for applying a DC bias to promote the aligned growth of the both nanotubes and nanowalls. Schematic of the MPECVD system used by Wu et al. [23] for CNW growth is shown in Fig. 2.3. They used mixtures of CH_4 and H_2 gases with typical flow rates of 10 and 40 sccm, respectively. The substrate was preheated to ~650–

700 °C (which was basically limited by the MW power) in H_2 plasma without any substrate biasing. Thereafter, the CH_4 was introduced to the quartz tube for the growth of nanotubes. The discharge pressure was kept at 1 Torr during both pre-heating and the growth process. During the growth process, a DC bias of −185 V was applied to the substrate. It is interesting to mention that these experiments were designed to grow CNTs for scanning probe applications and therefore various types of substrates (Si, stainless steel, Cu, GaAs, and sapphire) coated with different types of catalysts (NiFe, CoFe, FeMn, FeMn, and CoCrPt) film were tried for the optimization of the CNTs growth process. Typically thicknesses of the catalysts used were from 20 to 100 nm and were deposited using sputtering system under a base pressure of 3×10^{-9} Torr. They found CNTs growth where the substrates were electrically connected to the biased support electrode. However, growth of CNWs without CNTs was observed when substrates were electrically cutoff or isolated from the biased supporting electrode. They accounted this due to the development of strong traverse (lateral) electric field on the sample surface due to charging of the catalyst islands (without any electrical connection between catalyst and supporting biased electrode). Typical SEM images of CNWs and HR-TEM images of CNTs obtained by Wu et al. [23, 32] are shown in Fig. 2.4.

2.2.1.2 Effect of Microwave Power (Density and Dimensions)

Similarly, Srivastava et al. [37] reported growth of uniformly distributed carbon nanopetals/nanowalls almost normal to the substrate on Ni- and Fe-coated Si as well as on bare Si substrates by MPECVD technique (schematic illustration of experimental setup is shown in Fig. 2.5) without any additional substrate biasing and at relatively low temperature (350–650 °C). They used mixture of argon (Ar) and methane (CH_4) (9:1) as precursor gas during growth of 2-D CNWs. The Si substrates coated with Ni or Fe films (∼20 nm thick deposited by thermal evaporation technique) were used for the deposition of CNW films. In this approach, the

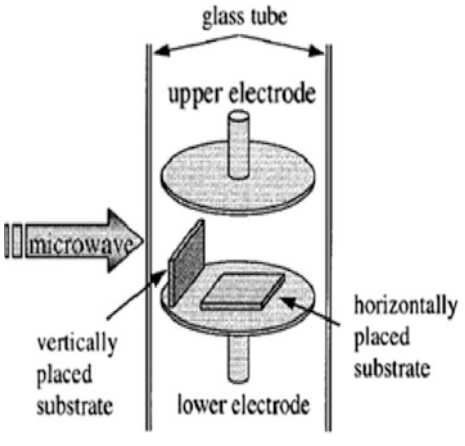

Fig. 2.3 Schematic of the MPECVD system used by Wu et al. [67] for CNW growth. Reprinted with permission from Ref. [67], Copyright (2002) American Chemical Society

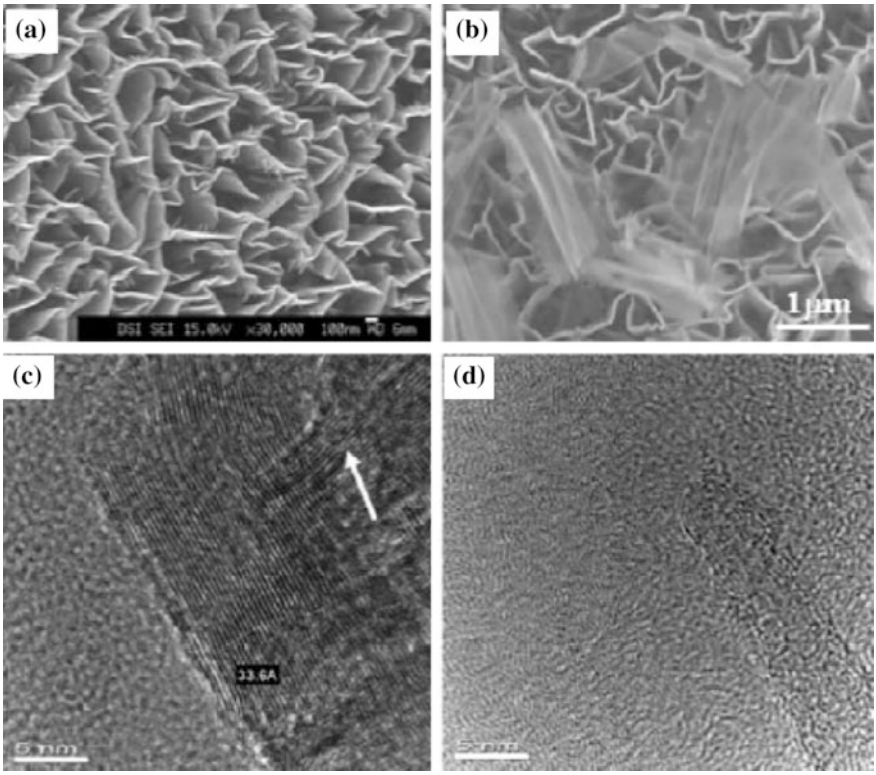

Fig. 2.4 SEM images (**a**, **b**) and HR-TEM (**c**, **d**) images of carbon nanowalls/scale bars: **a** 100 nm, **b** 1 μm, and **c** and **d** 5 nm. **a** was taken at a tilt angle of 25°. Reproduced ('adapted') from Ref. [32] with permission of The Royal Society of Chemistry

Ni-, Fe-coated, or bare Si substrates were pretreated in H_2 plasma for 10 min before introducing the precursor gas (Ar + CH_4::9:1). The process chamber pressure was maintained at 5 Torr during both preheating and the growth processes. It is to be noted that no additional heater was needed for substrate heating in this setup. The substrate heating occurred automatically by microwave induction and plasma species collisions. They investigated the effect of input MW power from 300 to 450 W on the growth and microstructures of the CNWs. The corresponding substrate temperature (T_s) was found to vary in the range of 350–550 °C.

Typical SEM images of CNWs deposited under MW power of 300, 350, 400, and 450 W, respectively, are shown in Fig. 2.6a–d. These carbon films consist of high density of uniformly distributed self-sustained rose petal-like CNWs nanostructures. These petal-like CNWs have sharp edges mostly normal to the substrate. On increasing MW power and hence substrate temperature 'T_s', density of petal-like CNWs increased while their size decreased (Fig. 2.6d). In addition, the petals became aligned almost normal to the substrate for higher MW power. The

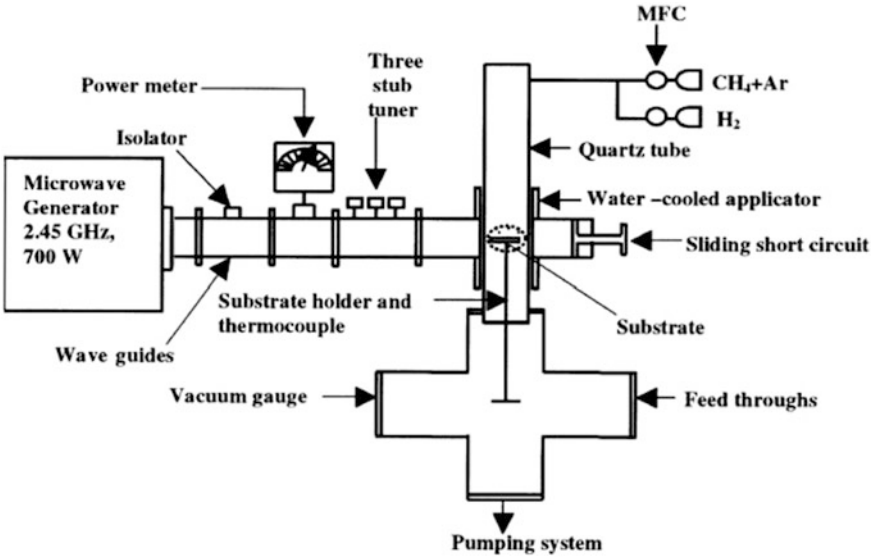

Fig. 2.5 Schematic of the tubular MPECVD system used by Srivastava et al. [37] for CNW growth. Reprinted from Ref. [37], Copyright (2005), with permission from Elsevier

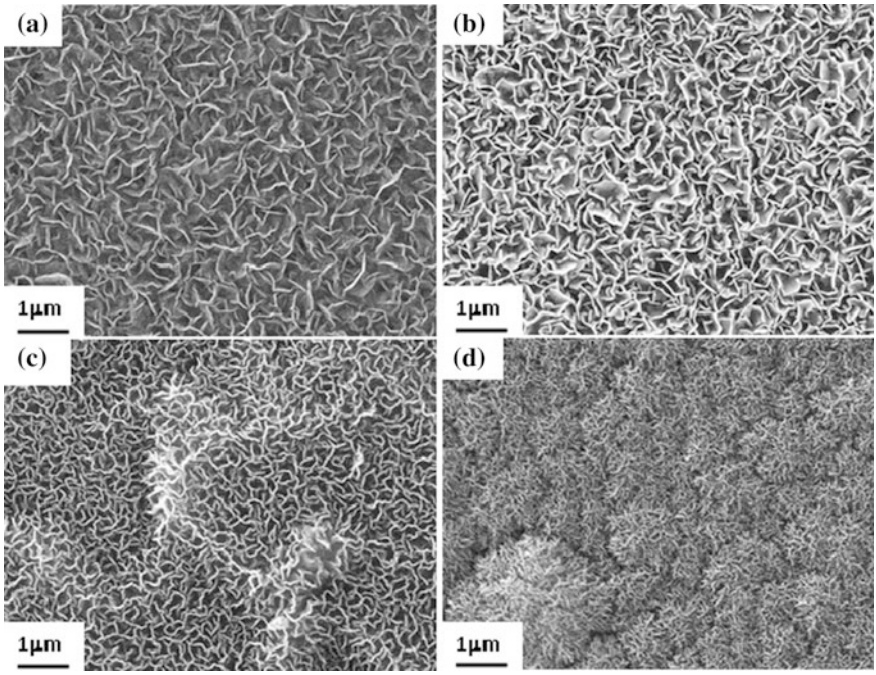

Fig. 2.6 SEM micrographs of samples **a** 300 W, **b** 350 W **c** 400 W, and **d** 450 W. Reprinted from Ref. [37], Copyright (2005), with permission from Elsevier

thickness of these petal-like carbon sheets for sample 300 W is estimated to be 50–80 nm which is reduced to 20–40 nm for sample 450 W. Similarly, lateral dimensions (length and width) of these nanopetals are 800–1000 nm for CNW sample deposited at 300 W and became 400–600 nm for sample deposited at 450 W.

On further increase of MW power produced no petal-like nanosheets but thick layer of amorphous carbon (a-C) with cauliflower morphology as shown in Fig. 2.7a, b for carbon films deposited at microwave power of 500 and 550 W, respectively. Similar kind of cauliflower-like structure was also observed for carbon films deposited at high discharge pressure (20 Torr) keeping MW power at 350 W and other parameters identical to that of 350 W sample (Fig. 2.7c). These results are consistent to Wu et al. [23] by MPECVD process with $CH_4 + H_2$ mixture. However, they found CNTs/carbon nanofibers mixed with a-C for low CH_4/H_2 flow rate ratio ($\sim$1:30), pure CNWs for an intermediate flow rate ratio ($\sim$1:4–1:8) and a-C films for further increase of flow rate ratio at a T_s of $\sim$650 °C and discharge

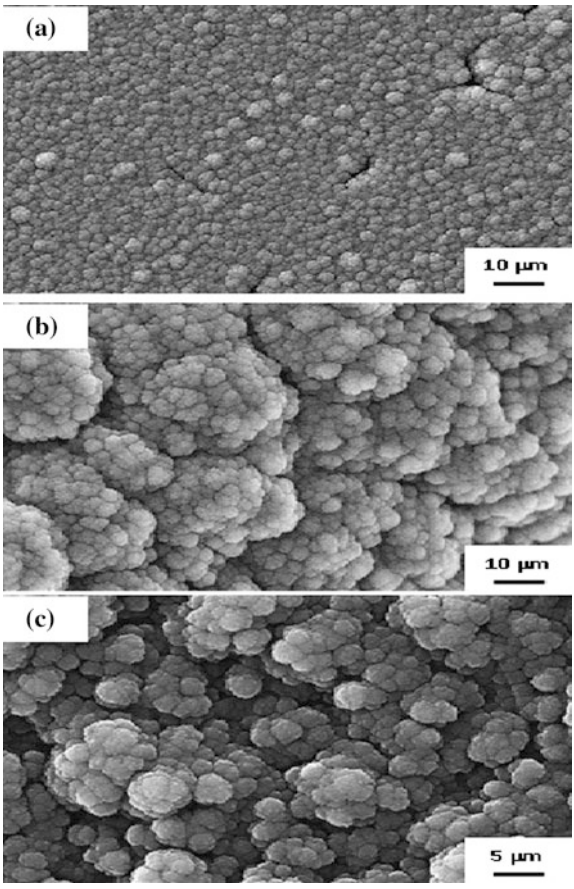

Fig. 2.7 SEM micrograph samples deposited at **a** MW 500 W and **b** MW 550 W **c** gas pressure of 20 Torr showing cauliflower type of growth of carbon films

pressure of 1 Torr. It is interesting to note that under the similar experimental conditions as used by Wu et al. [23], Srivastava et al. [37] did not observe any CNTs growth/tubular nanostructures even in the presence of metal catalysts.

2.2.1.3 Effect of Catalyst and Nature of Substrates

In order to understand the role of the catalyst film on the growth of petal-like carbon nanosheets or CNWs, films were also deposited on Fe-coated Si and bare Si substrates under the same conditions as used for sample deposited at 350. In this section, samples deposited on Ni/Si, Fe/Si, and bare Si substrates are named as NP–Ni, NP–Fe, and NP–Si, respectively. Figure 2.8a–d shows the morphological features of carbon films on Fe-coated Si and bare Si substrates. The 2-D sheet morphology is also observed on these two substrates. Carbon nanosheets on Fe-coated Si are more straight and have very sharp edges normal to the substrate. Few sharp corners like whiskers are shown in Fig. 2.8a, b. On the other hand, carbon sheets on bare Si have wavy nature and surface looks uneven (Fig. 2.8c, d) compared to that on catalyzed substrates. In addition, growth rate of CNWs nanostructures was found slightly higher on Ni-coated substrates compared to Fe/Si substrate and was found the lowest on bare Si substrates.

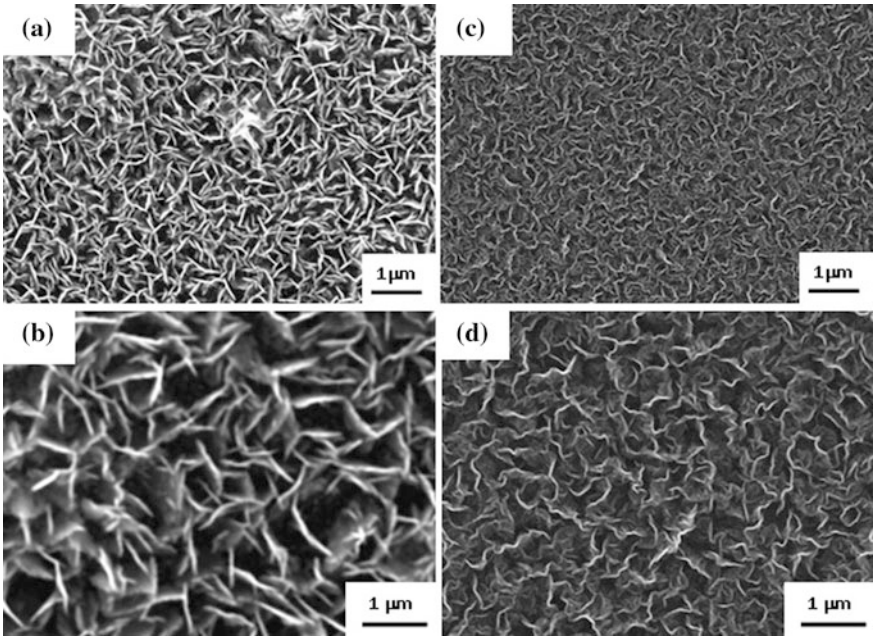

Fig. 2.8 SEM micrographs of nanostructured carbon films showing CNWs deposited on **a** Fe/Si (sample NP–Fe) and **c** bare Si substrates (sample NP–Si). The corresponding magnified images are shown in **b** and **d**, respectively

Tanaka et al. [38] used SiO_2 substrates (500 nm SiO_2 on Si wafers) to investigate the growth of CNWs by using tubular MPECVD system quite similar to that used by Wu et al. [23] and Srivastava et al. [37]. The MPECVD apparatus consisted of a 2.45 GHz, 500 W of MW source, a rectangular waveguide coupled to a cylindrical glass chamber (51 mm in inner diameter and 240 mm in length). Circular parallel-plate electrodes, placed apart in the longitudinal direction of the chamber for DC biasing of the substrate. A gaseous mixture of CH_4 and H_2 with flow rates of H_2:CH_4 of 80:20 sccm or 80:5 sccm at total gas pressure of 1.7 Torr was used for the growth of CNWs for different time. Similar to Wu et al. [23], a voltage of −185 V, was applied to the substrate. Prior to CNWs growth, the substrate was exposed to hydrogen plasma for ∼15 min. Typical morphology of CNWs grown by Tanaka et al. [38] is shown in Fig. 2.9a, b. They established that the CNWs could be grown at the fine-textured structure on the SiO_2 even in the absence of any catalyst. The height, thickness, and mesh size of the CNWs increased with growth time. They also could achieve very high growth rate of CNWs, ∼10 μm/h (as shown in Fig. 2.9c), and the height of CNWs as a function of time obeys the square root law. Similarly, Wang et al. [39] used a high-power MWPCVD method to grow flat nanocarbon sheets standing vertically on Si wafers and intersecting each other at large angles. They used a MW power of 2 kW, for 3 h at substrate temperatures of ∼950 °C, CH_4/H_2 (15/85) gas compositions at gas pressure of 70 Torr. It is noted here that deposition rate (deposition time of 3 h) seems to be very slow in their case despite using very high substrate temperature (∼950 °C) as well as MW power and pressure in this case as compared to Wu et al. [23] and Srivastava et al. [37].

In this series, Chuang et al. [40, 41] achieved a milestone in growing three-dimensional CNWs structures. The group reported growth of CNWs by MPECVD method as freestanding structures on a metallic stage using a gas mixture of C_2H_2 and NH_3 without metal catalyst. They also used MPECVD setup quite similar to that of Srivastava et al. [37], but they used external DC biasing of substrates. The growth stage (as shown in Fig. 2.10a) consisted of a small cube/block of Cu or Ta mounted on the substrate holder placed in the process chamber. In this approach, the growth was metal catalysts free; however, a metal growth stage (of Cu or Ta block) was used to facilitate energy-intensive, localized plasma for the growth of CNWs. The MW plasma of H_2 was ignited around the four top corners of a cubic growth stage at MW power of 500 W for 3 min, and for CNWs, growth of H_2 was replaced by gas mixture of C_2H_2 and NH_3 maintaining the chamber pressure at 10 Torr for 10 min. Figure 2.10b shows the CNW sample attached to the Cu stage at the roots. Figure 2.10c shows a detached CNW sample against a ruler to illustrate its size. They obtained CNWs materials (both freestanding and attached to growth stage) over a wide range of growth conditions. However, formation of CNWs occurred only when a growth stage with corners were used to induce a localized, concentrated MW discharge. The normal MW plasma without metal stage was not capable of depositing such CNWs on the Si substrates. It was suggested that the formation of CNWs is energy intensive, confining the discharge to a smaller volume on the corners of the growth stage.

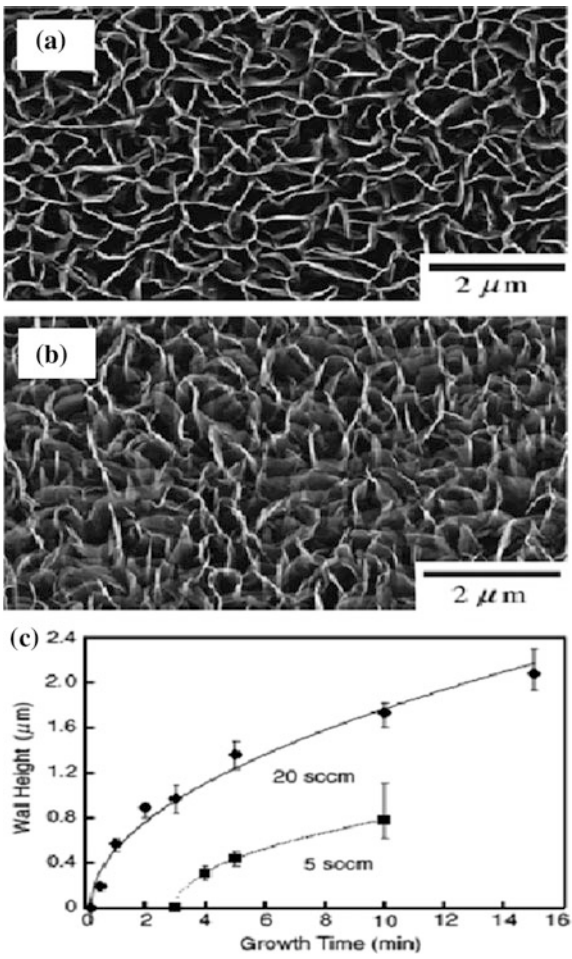

Fig. 2.9 Typical SEM images of CNWs from a top view (**a**) and from perspective view (**b**), and **c** growth time dependence of CNWs height. Reprinted with permission from Ref. [38], Copyright 2005 The Japan Society of Applied Physics

Typical SEM images of CNWs balls are shown in Fig. 2.11. It was observed that the surface-bound CNWs were more uniformly distributed and had larger wall thickness ranging 30 to 50 nm (Fig. 2.11a, b). The freestanding CNWs, on the other hand, had much smaller feature sizes, with thickness ~15 nm, embedded in grape-like small spheres (Fig. 2.11c, d).

In summary, MPECVD has been shown a very effective PECVD technique for the growth of high-quality CNWs in a controlled manner. Since the very first report of CNWs growth by Wu et al. [23] in 2002 by MPECVD as a by-product of CNTs, several groups have successfully synthesized high-quality CNWs on different substrates by MPECVD process under various process parameters. On the basis of above experimental observations and discussions, it can be concluded that CNWs can be grown by MPECVD method in a wide range of parameters of growth temperature (as low as 350 °C to as high as 950 °C), gas composition, microwave

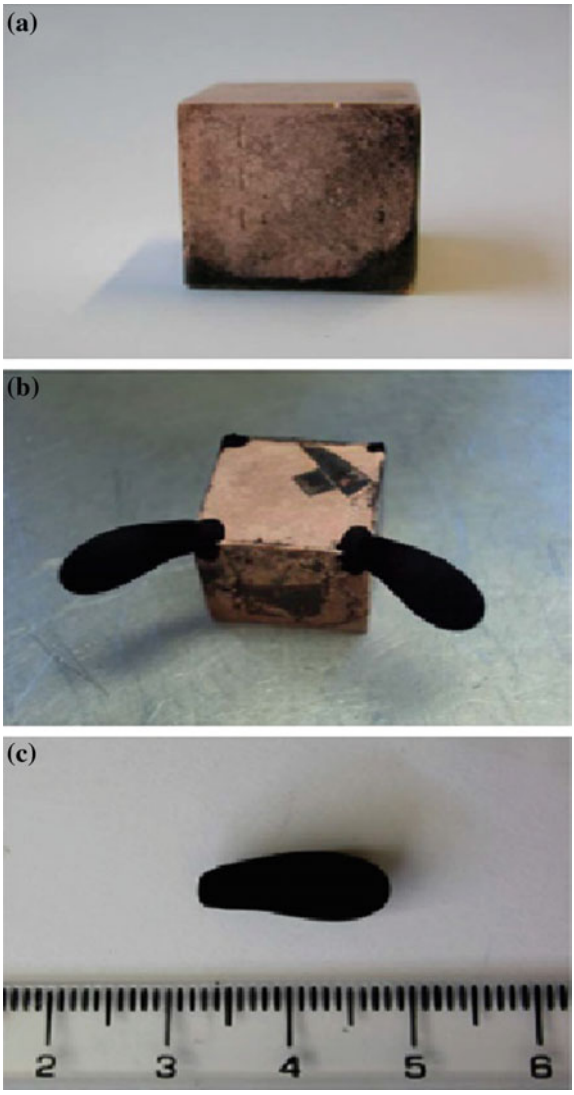

Fig. 2.10 **a** 15-mm cubic copper growth stage, **b** Nonsurface-bound carbon nanowall samples still attached to the copper growth stage at the roots, **c** A detached nonsurface-bound (freestanding) carbon nanowall sample measures to 15 mm. Reprinted from Ref. [40], Copyright (2006), with permission from Elsevier

power, and discharge pressure. In general, CNWs prepared by all the approaches have similar morphological features. It is confirmed that growth of CNWs does not require any catalyst and can be grown on both conducting and insulating substrates. This is advantageous if compared with CNTs which essentially requires transition metal catalyst by MPECVD process. Density and lateral dimensions of the CNWs can also be tailored by judiciously controlling the process parameters.

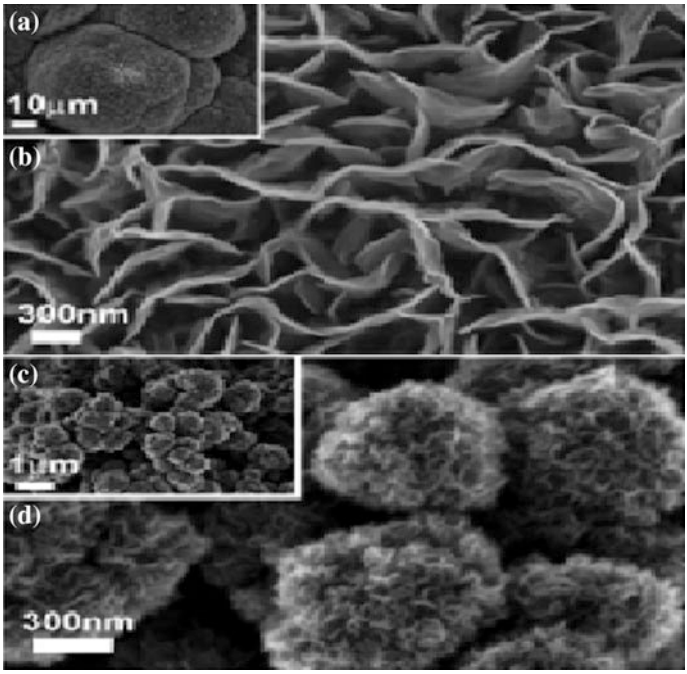

Fig. 2.11 **a** SEM image of surface-bound carbon nanowall. Overall morphology shows spherical aggregation of nanowall structures, **b** SEM image of surface-bound carbon nanowall, showing some secondary wall-like structures, **c** SEM image of freestanding carbon nanowalls shows nanowall spheres stack to form grape-like structures, **d** SEM image of freestanding carbon nanowalls shows spheres with carbon nanowall features. Reprinted from Ref. [40], Copyright (2006), with permission from Elsevier

2.2.2 Growth of Carbon Nanowalls by Rf-PECVD

Radio frequency (rf)-based PECVD is another powerful technique for low temperature, large area, and controlled growth of carbon nanomaterials such as CNTs. Hiramatsu et al. [42] fabricated vertically aligned carbon nanowalls on Si, SiO_2, and sapphire substrates without any catalyst by capacitively coupled plasma (CCP)-enhanced CVD in 2004 for the first time using H radical injection into the plasma. The rf-PECVD system consisted of a circular parallel-plate rf (13.56 MHz) CCP region and a remote radical source which uses an inductively coupled H_2 plasma (H_2 ICP). The circular parallel-plate electrodes were 5 cm apart. A variety of fluoro- and hydrocarbons such as C_2F_6, CH_4, or CF_4 (as carbon source) into the rf-CCP region were used, and H_2 was fed through a 20-cm-long and 26-mm-diameter quartz tube. A five-turn rf coil connected to the rf generator of 13.56 MHz was mounted on the quartz tube. The typical process parameters for the growth of CNWs by this method were kept as follows: (a) carbon source: H_2 flow rates: 30:15 sccm; total gas pressure: 100 mTorr; substrate temperature: 500 °C; CCP rf power:

100 W; and ICP rf power: 400 W. In the case using C_2F_6/H_2 system, aligned CNWs were grown vertically on the substrate, while CNWs grown using CH_4/H_2 system were waved and thin (10 nm). However, no CNW growth was observed in the case of the deposition without H radical injection. The group has carried out pioneering work on fabrication of vertical CNWs using rf-PECVD under various gas composition and other process parameters [42–46] mostly using fluorine-based carbon sources such as C_2F_6, CF_4, CHF_3, C_4F_8 under similar conditions as those used for the C_2F_6/H_2 system including CH_4/H_2 system. They also investigated the correlation between CNWs growth and fabrication conditions under different carbon source gases. Typical morphology of the CNWs grown using the CH_4/H_2, CF_4/H_2, and CHF_3/H_2 gas systems is shown in Fig. 2.12a, b and c, respectively. The morphology of the CNWs grown using a CF_4/H_2 and CHF_3/H_2 system was similar to those using the C_2F_6/H_2 system with marginal differences in the spacing between the walls. But CNWs could not be grown with C_4F_8/H_2 system. The growth rates (wall height vs. growth period) of CNWs had almost linear relationship with the growth period for C_2F_6, CH_4, CF_4, or CHF_3 systems as presented in Fig. 2.13. It was found to be the highest for the C_2F_6/H_2 system and the lowest for the CF_4/H_2 system. Therefore, the CF_3 radicals were proposed to be important species responsible for the formation of CNWs in any fluorocarbon/hydrogen systems. Similarly, the CH_3 radicals generated by a CH_4-CCP in the CH_4/H_2 system were also considered to be important species for CNWs growth for CH_4/H_2 system. Based on extensive investigations, the group concluded that H atoms play an important role in the formation of the CNWs. Injected H atoms react effectively with fluorocarbon radicals in the gas phase as well as at the surface by the reaction of F abstraction. At a substrate temperature of 500 °C, H atoms play key role in producing sp^2-bonded carbons at the surface and hence a continuous sp^2 network, which eventually results in the formation of CNWs. Later, the group also measured [43] H atom density in the plasma using vacuum ultraviolet absorption spectroscopy (VUVAS), in order to confirm the role of H atoms on the growth of CNWs.

Similarly, another group [47, 48] reported the growth of freestanding and ultrathin graphitic sheets ($\sim$1 nm thick) using an inductively coupled rf-PECVD method on variety of substrates including metals, semiconductors, and insulators (Si, SiO_2, Al_2O_3, Mo, Zr, Ti, Hf, Nb, W, Ta, Cu, and 304 stainless steel), without catalyst, and under various growth conditions using CH_4/H_2 system. They also confirmed H incorporation into the CNWs by means of infrared and thermal desorption spectroscopies and suggested that a combination of high plasma electron density and large atomic H density of the ICP accounted for CNWs formation. Similarly, several other groups have also demonstrated growth of CNWs by using rf-based PECVD method (CCP, ICP or in any other modes) [49–51]. It is also worth mentioning that among PECVD methods, not only high-frequency sources (such as rf or MW) have been used for the growth of CNWs but other simpler PECVD techniques such as DC-PECVD [52–57] have also been used for high-quality CNWs growth. In addition, there are few examples of CNWs growth by hotwire CVD (HW-CVD) and hot-filament CVD (HF-CVD) methods (with or

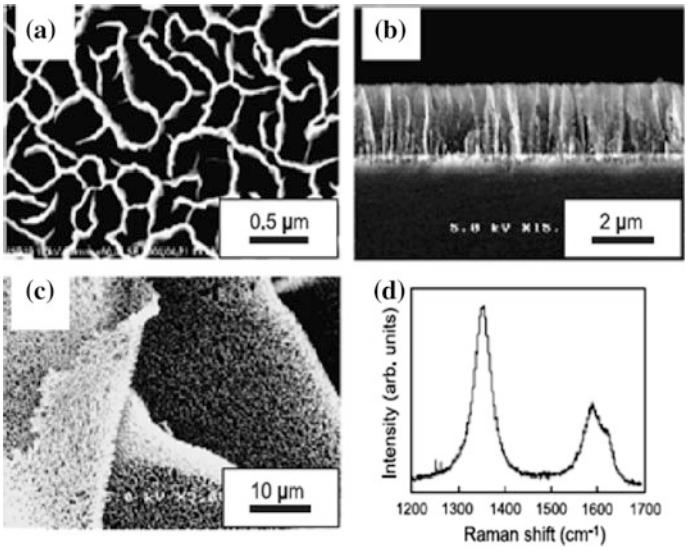

Fig. 2.12 SEM images of the carbon nanowalls grown on Si substrate using C_2F_6 rf-CCP assisted by H atom injection for 8 h; **a** top view and **b** cross-sectional view, **c** An SEM image of carbon nanowall that was scratched from a Si substrate, **d** Raman spectrum for the carbon nanowalls in (**a**). Reprinted from Ref. [43], Copyright (2005), with permission from Elsevier

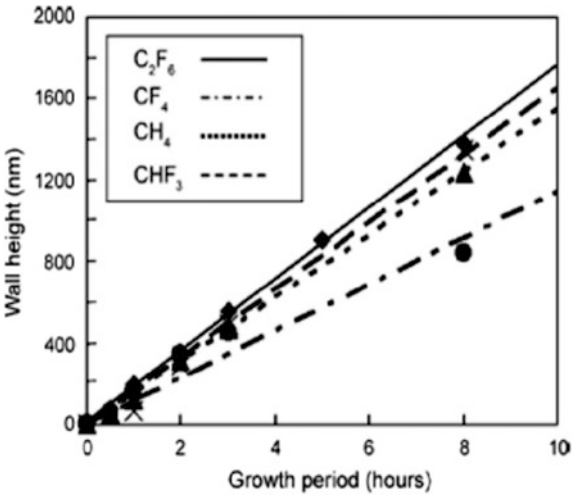

Fig. 2.13 Carbon nanowall height, as a function of the growth period. Growth data was obtained from the samples grown using C_2Fg (*solid line*), CF_4 (*dash-dot line*), CH_4 (*dotted line*), and CHF_3 (*broken line*) as the carbon source gas. Reprinted from Ref. [43]. Copyright (2005), with permission from Elsevier

without DC plasma assisted) [58, 59] also. However, growth of CNWs by conventional thermal CVD is rarely reported and efforts are being made. Nevertheless, PECVD has been a proven method for CNWs growth and can be scaled up on large area as well.

2.3 Characterization of CNWs

The CNWs synthesized by any methods so far have mainly characterized by scanning electron microscopy (SEM), transmission electron microscopy (TEM) and high-resolution TEM (HR-TEM), and Raman spectroscopy. The SEM has been used for morphological and growth characteristics of the CNW films whereas TEM and HR-TEM and Raman spectroscopy techniques have been used very efficiently for the structural characteristics of the CNWs irrespective of the growth methods (plasma or nonplasma-based techniques).

2.3.1 CNW Structure by HR-TEM

Figure 2.14 shows a typical HR-TEM micrograph of 2-D CNWs prepared by MPECVD method [38]. The nanowalls, as shown in Fig. 2.14a, are made up of many individual graphite/graphene walls. The HR-TEM image reveals the crystallinity as well as interplanar spacing of the walls in each CNW. The interplanar spacing is $\sim$0.34 nm confirming that the CNWs are made of few to several layers of graphene. Also, since mostly, growth of CNWs is carried out by PECVD route which is a relatively low-temperature growth process, it results in the presence of defects in the CNWs. Such defects can be observed from the HR-TEM images. The HR-TEM image of CNWs shows regions of highly graphitized and disordered amorphous phases (Fig. 2.14b).

2.3.2 CNWs Structure by Raman Spectroscopy

The Raman spectroscopy is a very powerful, nondestructive technique for the structural characterization of different carbon nanomaterials. This technique is also used extensively for the quality of the CNWs irrespective of growth technique. For example, first-order Raman spectra of CNWs samples grown at input MW powers of 300, 350, 400, and 450 W by MPECVD method are shown in Fig. 2.15 [37]. In these spectra, two characteristic signals are observed. Strong peaks at $\sim$1350 and 1580 cm^{-1} are typical D and G bands of microcrystalline graphite [60]. The strong D peak indicates that CNWs consists of a more nanocrystalline structure and defects such as distortion, vacancies, and strain in graphitic networks, which are typical features in CNWs. An additional peak at $\sim$1620 cm^{-1} called as D' is also observed as shoulder to G peak. The Raman spectra of CNWs are similar to those of the MWCNTs [61]. The CNWs deposited at different MW powers essentially have both D and G bands. However, the intensity ratio of the D to G bands [$R = I(D)/I(G)$], full width at half maximum (FWHM) of the D and G bands as well as the intensity of the D' band increased considerably with higher input MW power in

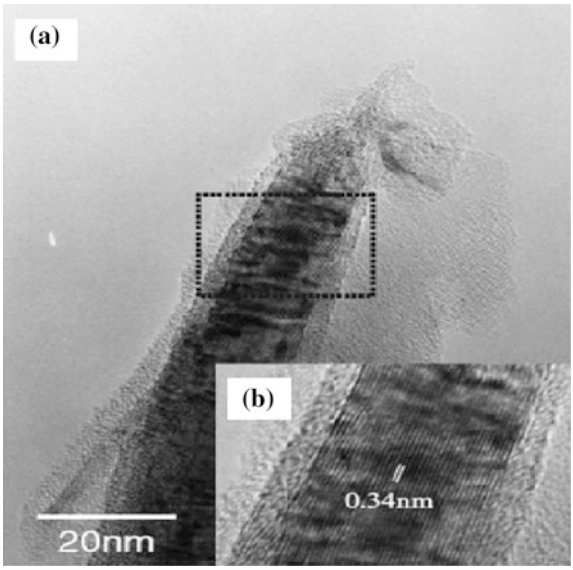

Fig. 2.14 Typical **a** high-resolution TEM image of CNW, **b** enlarged TEM image for the rectangular section in (**a**). Reprinted with permission from Ref. [38], Copyright *2005* The Japan Society of Applied Physics

MPECVD process. Typical variation of intensity ratio of *D* and *G* bands [*I*(*D*)/*I*(*G*)] and FWHM of *D* band versus MW power is shown in Fig. 2.16 [37] and is also in accordance with the observation by Tuinstra and Koenig [62]. The shift in *G* peak from 1581 to $\sim$1600 cm^{-1} [63, 64] and increase in *I*(*D*)/*I*(*G*) ratio correspond to transformation from graphite to nanocrystalline graphite phase. This shift of *G* peak to higher wave number is also due to evolution of *D*′ band, at $\sim$1620 cm^{-1}. For smaller crystallites, the *D*′ peak merges into the *G* peak and a net of the intensity of *G* feature is observed as a result of overlapping of the intensity of *G* + *D*′ feature [63]. The position of the maximum in the *G* + *D*′ feature is also observed to shift to higher wave number with higher MW power. This again indicates that the CNWs grown at higher MW power consist of higher degree of disorders and relatively smaller size or nanographitic crystallites. In general, the CNWs grown by any PECVD technique have these Raman characteristic peaks, *D*, *G,* and *D*′ peaks [37, 38, 40, 41, 53, 54, 65, 66] and are established that CNWs consist of graphitic nanostructures/small crystallites with high degree of defects.

2.4 Growth Mechanisms of CNWs

The above experimental investigations suggest that 2-D CNWs can be fabricated by variety of PECVD techniques irrespective of the growth process and conditions. It means there has to be a common mechanism of nucleation and growth of these 2-D carbon nanostructures, which is not fully understood. It has been proposed by Wu and coworkers that the electrical field is the most important factor in a MPECVD

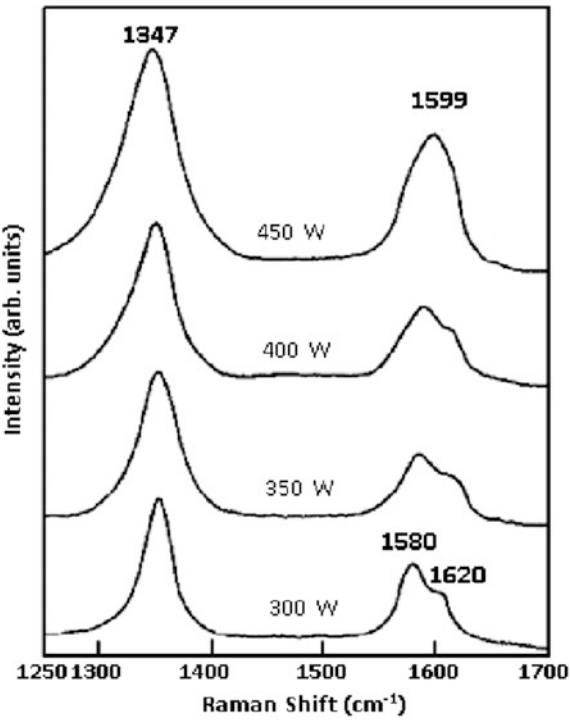

Fig. 2.15 Raman spectra of the petal-like nanostructured carbon films deposited at different microwave power. Reprinted from Ref. [37], Copyright (2005), with permission from Elsevier

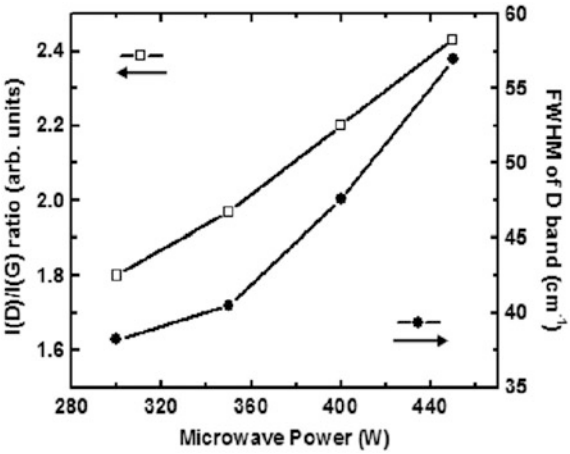

Fig. 2.16 Variation of $I(D)/I(G)$ ratio and FWHM of D band of carbon films deposited at different microwave power. Reprinted from Ref. [37]. Copyright (2005), with permission from Elsevier

process [23, 67]. However, the same may be valid in case of the other plasma assisted CVD processes such as rf-PECVD, DC-PECVD. The source of the electrical field in a MPECVD setup is first due to applied DC bias. The nonuniform charging up of the substrate in the plasma which can be altered by the existence of

metallic particles and other types of sharp features such as metal slabs/block as used by Chuang et al. [40, 41] also plays critical role. It has been found that in metallic particles presence which act both as a catalyst as well as field modulator, both CNTs and CNWs can be formed depending on the strength of the lateral electrical field and other growth parameters such as the gas flow rates, temperature, and pressure [23]. However, in the absence of catalytic metal particles or on bare substrates, it is more likely that only CNWs will be formed. To understand the mechanism of CNWs formation, Srivastava et al. [37] investigated growth of CNWs with varying growth time keeping all other parameters constant. Figure 2.17 shows the representative SEM images of the CNWs at different growth stages on the Ni (20 nm)/Si as well as on bare Si substrates. During the preheating stage, the Ni thin film changed to isolated nanoparticles. The image in Fig. 2.17a shows the initial stage of the growth process wherein formation of large size clusters of Ni as a result of H_2 plasma pretreatment are observed. The time evolution of surface morphology suggests that in the initial stage of growth of carbon films, tiny sheets are formed (Fig. 2.17a, b) which grow in size (both lateral and vertical directions) as the deposition time is increased (Fig. 2.17c–e). This resulted in carbon nanosheets as large as $\sim$600–800 nm as shown in Fig. 2.17f. The observation is consistent with the observations by Wu and co workers using Au, and other transition (Ni, Fe, etc.) metals as catalyst which implies that the existence of a strong lateral field is the key to growing CNWs. Wu and Yang have done detailed investigation on the role of electrical field in the growth of CNWs [67]. An important observation of Srivastava et al. [37]'s investigation is that without any external biasing the petal-like CNWs were obtained almost normal to the substrate surface. This suggests that the growth of CNWs could be influenced by the self-bias potential established on the immersed substrate surface in the high-frequency plasma, the field lines of which are invariably terminated normal to the surface [68, 69]. The electrostatic force would help the carbon sheets to align with the field direction which is perpendicular to the substrate surface and an energetically favorable orientation. Demonstration of growth of three-dimensional macroscopic freestanding CNWs structure purely catalyst-free and unconstrained by substrate surfaces [40, 41] is another example of electric field-driven growth of CNWs. Other detailed growth mechanisms proposed by different groups also emphasize the important role of electric field in the controlled growth of CNWs [70, 71].

With increase in MW power in a tubular MPECVD setup and hence the higher substrate temperature, CNWs are found to grow, with sharp edges further aligned normal to the substrate surface. It is expected that increase in MW power causes higher degree of ionization of the gas, increasing the density of relatively high-energy plasma species and hence higher magnitude of the self-bias of the substrate surface. Increased nucleation of graphitic clusters is expected to occur, and this leads to the formation of CNWs of relatively smaller size and higher density at increased MW power (as shown in Fig. 2.6d). Further increase of input MW power leads to deposition of disordered amorphous carbon structures. Increase of discharge pressure also leads to higher density of plasma species and hence higher substrate temperature resulting in disordered amorphous cauliflower

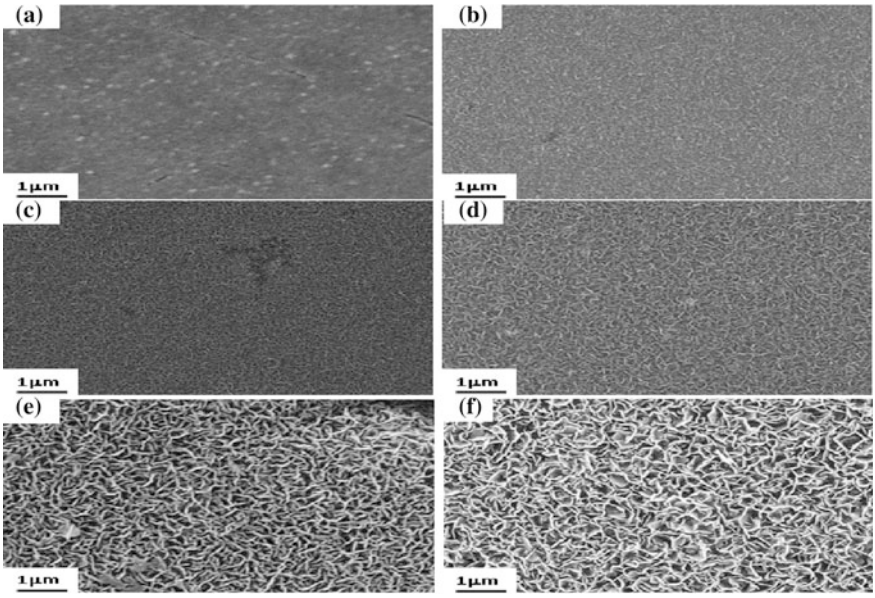

Fig. 2.17 SEM micrograph of **a** H_2-plasma-treated Ni film and carbon films deposited at microwave power of 350 W for **b** 2, **c** 5, **d** 10, **e** 20, and **f** 30 min. Reprinted from Ref. [37]. Copyright (2005), with permission from Elsevier

structures. These observations also suggest that the CNWs can be grown only for a moderate rate of carbon supply at a given substrate temperature in the tubular MPECVD setup. This is confirmed by low-magnification SEM image of sample grown at 550 W of MW power. The image is recorded near the boundary of the highest intensity plasma (HIP) ball (Fig. 2.18). The magnified images were taken from different portions of the same substrate (as shown in Fig. 2.18) which was placed on the substrate holder in such a way that the growth rate would vary from one side to the other due to the offset from the optimum position. The figure shows relative decrease of growth rate of film with increasing distance from the optimum position (HIP zone). The corresponding morphologies of the sample are shown by magnified images as presented in Fig. 2.18. It is clear that CNWs are formed only in the edge region of the HIP zone where plasma density and hence substrate temperature is supposed to be lower relative to that within HIP zone. On increasing the distance from the HIP zone, density of the sheets decreases and is the least at the outermost region of the plasma. The dimensions of the CNWs first increase and then decrease toward outer zone. The decrease of the dimensions at the outer most regions could be due to very slow growth rate. The observation further confirms the important role of input MW power and hence the self-biasing/electric field in the growth of CNWs in PECVD process.

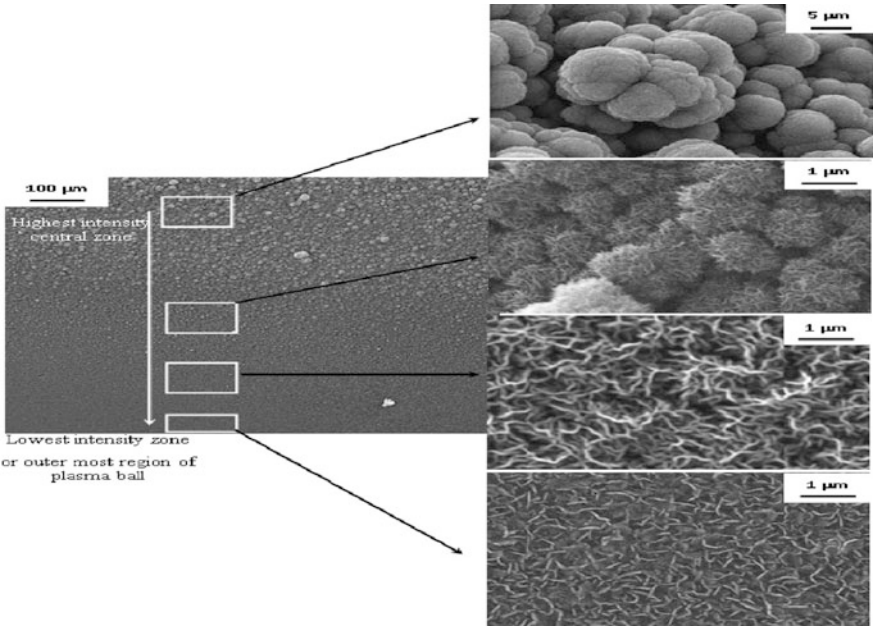

Fig. 2.18 Low-magnified SEM micrograph of a sample deposited at 550 W of MW power near the boundary of the highest intensity plasma (HIP zone) of tubular MPECVD showing variation of growth rate and morphology with distance from the HIP central zone and the corresponding magnified images

2.5 Field Emission Properties of Carbon Nanowalls

2.5.1 Field Emission

Field emission (FE) is the ejection of electrons from a solid surface under the effect of high electric field of the order of 10^9 V/m. When such a field is applied to a solid surface with a negative bias, electrons inside the solid are emitted into vacuum by quantum mechanical tunneling effect [72]. Such high field can be obtained on a sharp tip of a very thin needle where electric field lines concentrate. The schematic of quantum mechanical tunneling of electrons from a solid surface under the applied electric field is shown in Fig. 2.19 [73]. Microwave generators, X-rays, e-beam evaporators, mass spectrometers, display devices, etc., rely on thermionic electron emitters operating in a temperature range of 1000–2000 °C. Due to the high operating temperatures, miniaturization of thermionic emitters is strongly limited. Field electron emitters operating at room temperature, on the other hand, have great potential for miniaturization and hence portability of a device. This opens up several new applications such as flat panel displays, data storage devices. However, the development of FE electron sources remained hampered for about half a century due to the fact that tip-like field-enhancing structures needed to create

local high electric fields for FE to take place were under investigation. Critical life time and high operating voltages are additional intriguing factors [74]. An ideal electron source, in a micrometer sized device, has to meet several important requirements: For example, it should have a high mechanical strength and melting point, good electrical and thermal conductivity, low work function, stable chemical properties, and be inexpensive and easy to process [75]. A variety of field emitting thin films such as microcrystalline diamond films, nanodiamond films, diamond like carbon films [76] have been proposed as an alternative to the conventional tip arrays of emitters for reduced fabrication cost and improved robustness [77]. In this series of carbon materials, a lot of attentions have been paid to CNT (both SWNTs and MWNTs)-based field emitters. The potential of CNTs for FE was first reported in 1995. FE from an isolated single MWNT was first reported by Rinzler et al. [78] and that from a MWNT film was reported by de Heer et al. [79]. Since then, a number of experimental studies on FE aspects of both MWNTs [80–97] and SWNTs [98–101] have been carried out. FE from CNTs has shown to be one of the most promising properties as far as its practical application is concerned. This is because CNTs present many advantages over conventional emitters due to their unique structure and properties such as (i) high chemical stability (resistance to oxidation or other chemical species) and high mechanical strength (Young' modulus $\sim$1 TPa), (ii) high melting point ($\sim$3550 °C) and reasonable conductivity (resistivity $\sim 10^{-7}$ Ωm), (iii) high aspect ratios (>1000) with very small tip radius to greatly enhance the local electric field, and (iv) large-scale production at low cost, have longer life time, and are capable of low operating voltages [75].

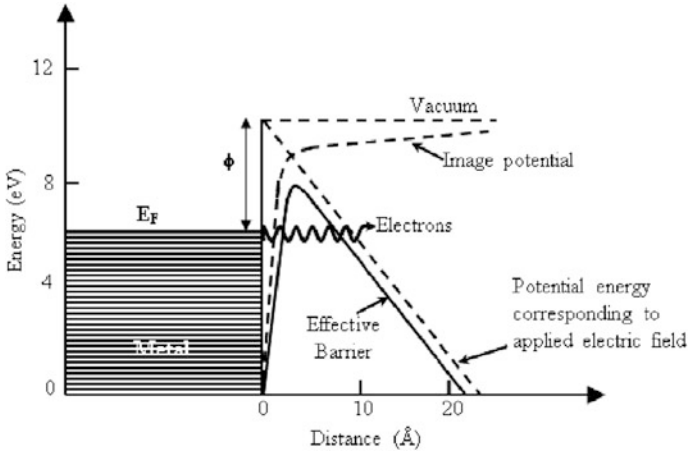

Fig. 2.19 Potential energy diagram illustrating the quantum mechanical tunneling of electrons under an external electric field. Reprinted from Ref. [73]

2.5.2 Field Emission Properties of Carbon Nanowalls

The unique morphology and geometrical shape of carbon nanowalls (as described in the earlier sections) can bring about many fascinating properties such as field emission. Moreover, the intrinsic disorders and defects of CNWs are likely to alter these properties and are ideal candidates for electron transport studies. Previously, field emissions have been studied. In the following section, brief description of a basic experimental setup for field emission measurements, basics of field emission process and related parameters, and finally the state of the art of the FE properties of CNWs are being presented.

2.5.3 Field Emission Measurement Setup

The FE measurements of nanostructured carbon films are carried out in a high-vacuum chamber using a simple diode configuration. The schematic diagram of FE measurement setup is shown in Fig. 2.20. It consists of a high-vacuum chamber the base of which is connected to a 6-inch-diameter diffusion pump (model 160/700 M, Edwards, UK) backed by a mechanical rotary pump (Edwards). Pressure in the chamber was monitored by a Pirani/Penning gauge (model PRL10 K, Edwards, UK). The electrodes of the assembly are made of circular Cu plates or any other vacuum compatible and conducting metal. Lower electrode was made as cathode (CNW films), and the sample was fixed to it with the help of silver paste. The electrode holding the sample was connected to a high-voltage power supply through an electrometer in series. Sometimes, a high resistance (of 1 MΩ) is also connected in series with the electrometer to limit the current in maximum range of the electrometer. The upper electrode which was movable in the *Z*-direction was connected to the positive terminal of the supply. It also had graduated circular plate with the help of which the gap between the electrodes could be adjusted. The upper electrode assembly could be removed for mounting the sample. The distance (d) between the top emitting surface of the film and anode was determined by first lowering the anode to the sample until electrical contact was observed then lifting the plate to a certain value with the help of the scale made on the anode. The value of d was adjusted between 300 and 500 μm as per the nature of the sample of CNWs. Several groups also use separation layer of Teflon sheet/tape of different thickness between cathode (CNWs samples and the anode). The FE measurement is generally performed in high vacuum (at a pressure of $\leq 2.0 \times 10^{-6}$ Torr) at room temperature. The variable positive voltage is applied to the anode in steps and the emission current is measured by the suitable electrometer. It is to be noted that conditioning of each sample is crucial and essential before the final measurements of emission current by applying a high voltage to remove any kind of impurity such as adatoms or adsorbates on the surface of the CNWs. The macroscopic electric field (E) applied between the electrode is estimated by dividing the applied voltage

(V) by the sample-anode separation (d) ($E = V/d$). The emission current density (J) can be calculated by dividing measured current with the area of the CNWs sample exposed to the anode.

The field emission characteristics is usually analyzed by Fowler–Nordheim (F–N) theory [72], according to which the emission current density (J) from a metal tip/surface is dependent on the local electric field (E_{loc}) and chemical state of the (i.e., work function, ϕ) of the emitter surface as $J \propto (E_{loc}^2/\phi)\ \exp(-B\phi^{3/2}/E_{loc})$, where $B = 6.83 \times 10^9$ V eV$^{-3/2}$ m^{-1}. The schematic of electron emission methodology from an emitter under the applied electric field and relation between the E_{loc} and the E and corresponding F–N formula are shown in Fig. 2.21a. In case of CNW-based cathode films, electron emission occurs from the multiple emitters and an average or integrated current is measured. There is lot of variation of local field on emitters tip in CNW films due to variation in local morphology/nanoscale emitter geometries. Also, the work function of each emitter may not be the same due to which the exact analysis of FE characteristics of CNW films is a difficult task. Nevertheless, F–N theory is the most suitable one and has been used for interpretation of emission properties of not only CNWs but also various other carbon nanomaterials including SWNTs and MWNTs. In this model, there are two key parameters in F–N formula, ϕ and E_{loc}, where E_{loc} is related to E by geometrical enhancement factor (β) as $E_{loc} = \beta E$. The value of β can be determined experimentally from the slope of F–N plot between ln (I/V^2) versus $1/V$, provided ϕ is known. The slope of F–N plot is given by,

$$\text{Slope} = -\frac{B\phi^{3/2}d}{\beta}. \tag{1}$$

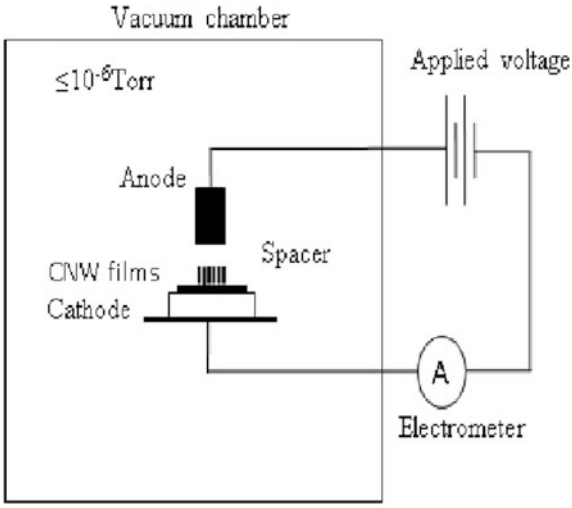

Fig. 2.20 Schematic of field emission measurement setup

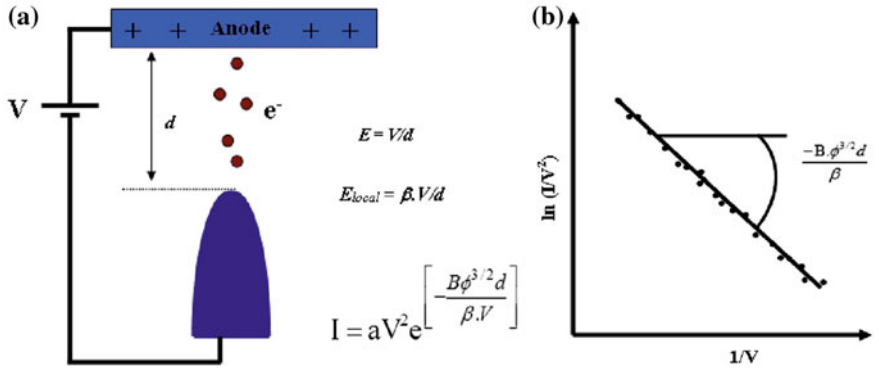

Fig. 2.21 **a** Principle of FE from a curved surface and the F–N formula. **b** An ideal F–N plot for FE showing *straight line* with negative slope

An ideal F–N plot for electron field emission characteristics is shown in Fig. 2.21b. Typically, field emission quality of emitter is quantified with respect to two parameters called as turn-on field (E_{to}) and threshold field (E_{th}). Typically, E_{to} is the field (in $V/\mu m$) required for emission current density of 10 $\mu A/cm^2$ and E_{th}, is the field required to achieve 1 mA/cm^2 emission current density from the emitter. Third parameter is related to the stability and uniformity, reproducibility, and lifetime of emission current (at E_{to} and E_{th}) for as long as possible duration.

2.5.3.1 Field Emission Characteristics of CNW-Based Carbon Films

Since CNW films contain a high density of uniformly distributed vertical carbon nanosheets or nanowalls, with sharp graphitic edges normal to the substrate, the CNWs are supposed to exhibit high geometrical enhancement factor for the electric field and hence a very good electron emission. Herein, few examples of FE properties of CNW films prepared by MPECVD process are illustrated. Also, the effect of various process parameters on the FE properties of such CNW-based emitters is briefly presented.

2.5.3.2 Effect of Catalyst–Substrate Interaction on the Field Emission

Field emission measurements of CNW films deposited on Ni/Si, Fe/Si, and bare Si (samples NP–Ni, NP–Fe, and NP–Si, respectively) by MPECVD method at MW power of 350 W under CH_4/Ar gas composition for deposition time of 30 min and discharge pressure of 5 Torr (please see morphology of such CNW films in Fig. 2.8) are shown in Fig. 2.22. It is shown that catalytically grown samples exhibited superior emission characteristics to that on bare Si-based CNW films. The emission current density (J) versus the macroscopic electric field (E) plot of these

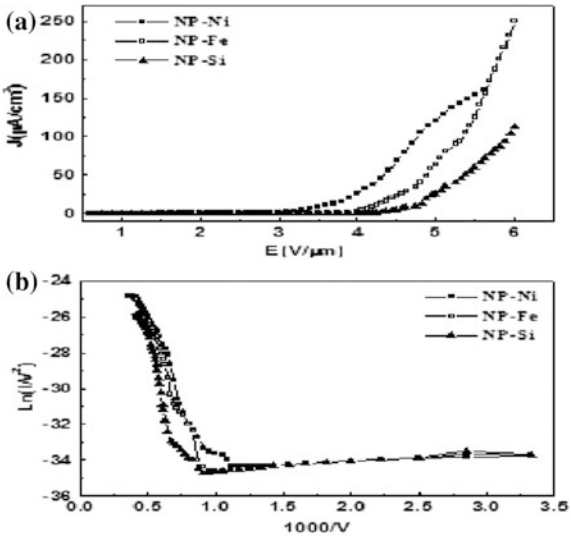

Fig. 2.22 **a** Emission current density versus macroscopic field of nanostructured carbon films grown on Ni/Si, Fe/Si, and bare Si **b** corresponding F–N plots

Table 2.2 Comparison of FE parameters (E_{to} and E_{th}) of CNW films grown on Ni/Si, Fe/Si, and bare Si substrates

Sample	Turn-on field (E_{to}) ($V/\mu m$)	Field enhancement factor (β)
NP–Ni	3.60	2428
NP–Fe	4.25	2110
NP–Si	4.75	1926

samples is shown in Fig. 2.22a and the corresponding F–N plot in Fig. 2.22b. The corresponding E_{to} and E_{th} values are listed in Table 2.2. The CNW films on Ni-coated Si substrate were found to have the lowest E_{to} while those on bare Si had the highest among these films. It indicates that the interface resistance between the film and the substrate may have significant role in the FE process in addition to the density and morphological features (density of sharp edges in the CNWs). It is known that formation of $NiSi_x$ occurs at lower temperature (>300 °C) [96] while reaction between Fe and Si substrate is a high-temperature process. Therefore, $FeSi_x$ formation is unlikely to occur at temperatures ($\sim$400 °C, the substrate temperature corresponding to 350 W of MW power) [102]. Formation of $NiSi_x$ may lower the interface resistance and hence facilitate the transport of electrons across the CNWs/$NiSi_x$ interface. This could be the possible reason for the good FE characteristics of CNW films on Ni/Si substrates compared to that on Fe/Si or bare Si substrates despite almost identical surface morphological features.

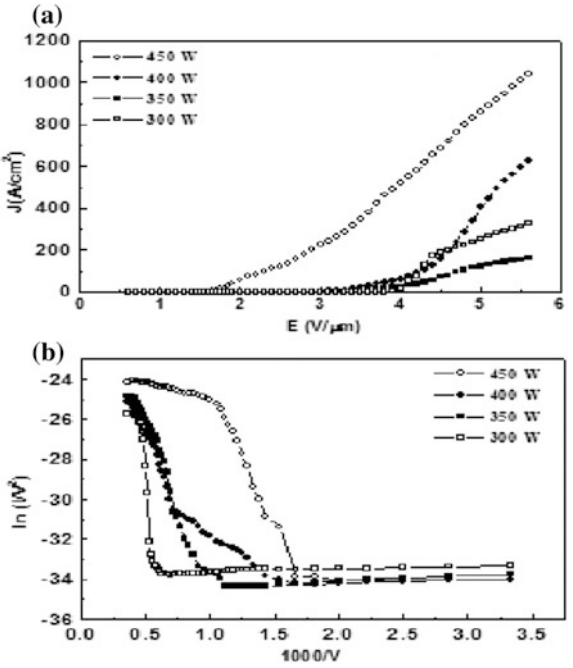

Fig. 2.23 a Emission current density versus macroscopic field of petal-like nanostructured carbon films with varying microwave power **b** corresponding F–N plots. Reprinted from Ref. [37], Copyright (2005), with permission from Elsevier

Table 2.3 Comparison of FE parameters (E_{to} and E_{th}) of petal-like CNW films

Sample	Turn-on field (E_{to}) ($V/\mu m$)	Threshold field (E_{th}) ($V/\mu m$)
NP300	4.00	–
NP350	3.60	–
NP400	3.35	–
NP450	1.75	~5.60

2.5.3.3 Effect of Microwave Power (Density and Dimensions of CNWs)

Srivastava et al. [37] investigated the effect of microwave power on the growth and field emission characteristics of CNW films by MPECVD method. The J versus E plots of CNW-based films prepared for microwave power of 300, 350, 400, and 450 (named as NP300, NP350, NP400, and NP450, respectively) by MPECVD are given in Fig. 2.23a. Among these, the best emission characteristics were observed in 450 W sample. The observed E_{to} and E_{th} values for these samples are given in Table 2.3. The observed E_{to} values are much lower than the values (17–35 V/μm) reported by Shang et al. [36] for such films by HF-CVD process. The E_{to} values decreased for samples deposited at higher MW power and the lowest E_{to} value was observed for sample 450 W. The increased density, smaller size, and improved alignment of CNWs are possibly responsible for the decreased E_{to} values for samples deposited at higher MW power. The corresponding F–N plots for the four

CNWs samples (as shown in Fig. 2.23b) have straight line with negative slopes in the high field region indicating that the emission process from the CNW films is primarily governed by the F–N model.

Similarly, other groups have also shown excellent FE properties from CNW films [32, 39, 58, 103–115] with turn-on fields as low as 1 V/μm or lower, which are comparable to the turn-on fields for CNTs or graphene films [80–101].

2.5.3.4 Effect of Temperature on the FE Properties of CNWs

Wu et al. [32] also have reported FE properties of CNWs prepared by MPECVD grown on Cu substrates (on 1 cm × 1 cm area). The FE properties of CNWs were measured at different temperatures so as to investigate the effect of absorbates on the CNWs surfaces. Also, the measurements were carried out at a relatively high base pressure ($\sim 1 \times 10^{-5}$ Torr). The FE characteristics of CNW films measured at temperatures of 20, 200, 300, and 400 °C, and at an interelectrode distance of 50 μm are shown in Fig. 2.24. The current densities at 20 °C were 0.19 and 9.53 mA/cm^2 corresponding to electric fields of 0.32 and 0.62 V/μm, respectively. The E_{to} obtained decreased to 0.26, 0.2, and 0.16 V/μm, respectively, with the temperature increasing to 200, 300, and 400 °C. The maximum J values obtained was 17.6 mA/cm^2 at an applied electric field of 0.32 V/μm at 400 °C. The corresponding F–N plots of the FE curves are shown in Fig. 2.24b confirming that the emitted current resulted from field emission mechanism. It is to be noted that in case of measurements done at 300 and 400 °C, a perfect straight line is fitted in plots of ln (I/V^2) versus $1/V$. However, the low-temperature measurements, the curve deviates from the straight line fitting particularly in the higher applied field segments (see Fig. 2.24b for 20 and 200 °C), and therefore, F–N plots have been divided into two straight line segments. The two slopes clearly suggest that at lower temperatures there exist two energy barriers for electrons. These barriers could be caused by the absorbates on the surface of CNWs. It was confirmed by the fact that higher field slope disappeared at higher temperatures (see Fig. 2.24b for 300 and 400 °C). It is easy to understand that absorbates get desorbed by heating the CNWs samples. The field enhancement factor β was determined to be as 31,400, 46,200, 54,800, and 62,900 for four measurements done at 20, 200, 300, and 400 °C, respectively, assuming a constant work function ϕ of 5 eV. Almost threefold enhancement in β value for 400 °C measurements as compared to that of 20 °C one's was observed. It was found that the four lines (extrapolating the lower field curves for temperatures at 20 and 200 °C) intersect at the same point. Based on this, it was concluded that increase in β value was not due to the decrease of ϕ [32]. Therefore, the CNWs are superior field emitters at higher temperatures.

Similar results were also reported by Jiang et al. [112]. By using thermal desorption spectroscopy and thermal desorption mass spectroscopy, they evaluated the surface adsorbates and their desorption behaviors of CNWs. They found that that the hydrocarbon materials were the main contents adsorbed on CNWs, and the absorption of H_2O and O_2, to a large degree, associated with the surface

hydrocarbon. The major species desorbed from CNW surface at 350–400 °C. CNW surface after heating in vacuum desorbs most of the surface adsorbates; CNWs exhibited the distinctly enhanced FE properties. The threshold field, E_{th}, was found 30% lower, and the emission current density increased 20 times as shown in Fig. 2.25 which shows the FE characteristics of CNWs before and after heat treatment. As discussed earlier, the larger the β, the higher the emission current and the CNWs usually have the equivalent height (h) value in μm, while their thickness (d) on the sharp edge tips is only $\sim$2 nm. Such sharp edge tips are prone to capture more adsorbates around them as they have extremely high surface energy. Even few layer adsorptions of hydrocarbons around them will strongly increase their relative thickness, resulting in a huge decrease of β factor and therefore the poor FE efficiency. On the other hand, if these adsorbates could be removed effectively, it will lead to a larger β factor enabling enhanced FE efficiency. The heating of CNWs samples certainly causes effective desorption of adsorbates and therefore was primarily accounted for the distinctly enhanced FE properties of CNWs [112].

2.5.3.5 Effect of Different Gas Environments for FE of CNWs

Wu et al. [32] also conducted FE measurements of CNWs under different gas environment such as O_2, H_2, N_2, and CH_4 and observed that the FE property in H_2 and N_2 ambient was similar to that of in the vacuum ambient. In the presence of O_2,

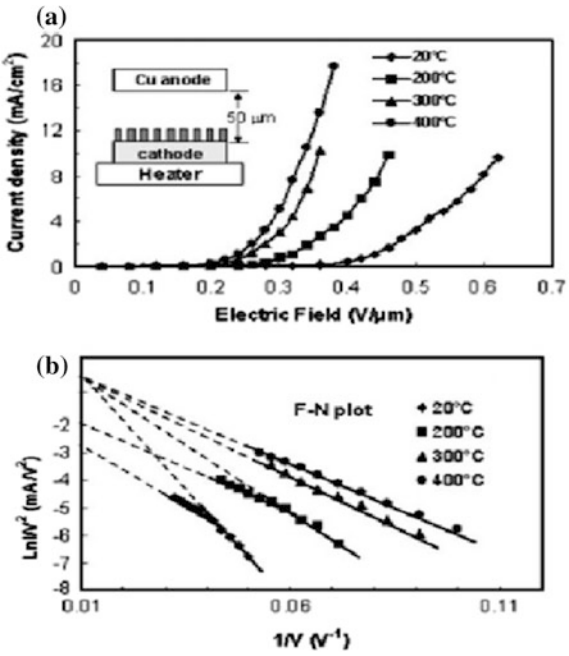

Fig. 2.24 **a** Emission current density as a function of the electrical field at different temperatures for carbon nanowalls, and **b** the corresponding F–N plots of the curve in (**a**). Reproduced (Adapted) from Ref. [32] with permission of The Royal Society of Chemistry

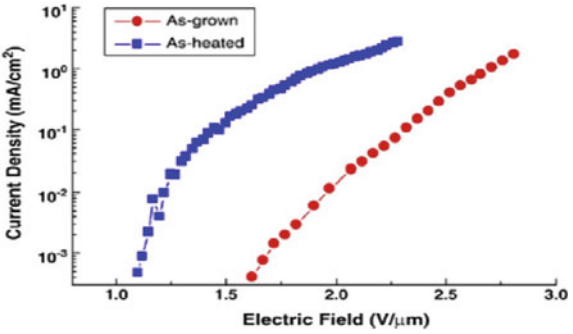

Fig. 2.25 Field emission current curves of as-grown and as-heated CNWs. Reprinted from Ref. [112]. Copyright (2010), with permission from Elsevier

the turn-on field was higher than the vacuum condition by ∼>30% at 1 V/μm. Similarly, the FE properties in O_2 environment were also inferior to the results measured in CH_4 environment. Emission stability was observed to degrade in O_2 and CH_4 ambient. Therefore, measurement environment also has strong influences on the FE properties of the CNWs.

2.6 Carbon Nanowalls for Energy-Related Applications

As mentioned earlier, the CNWs have large surface area and high aspect ratio and therefore have potential application in several energy harvesting applications. Few groups have successfully demonstrated variety of such applications of CNWs; a very brief summary of few of the representative work is presented below.

2.6.1 As Effective Electrodes in Lithium-Ion Batteries

Lithium-ion battery with high power density has been in great demands in many fields. Nanostructured materials have been recently focused a lot for the high-rate use of the battery because of their potential to provide efficient and shorter conductive path for lithium ions enabling to achieve lower internal resistivity of the electrode and hence the high power of the battery [116, 117]. Tanaike et al. [55] studied the lithium insertion behavior of CNWs by cyclic voltammetry and charge/discharge measurements. The CNWs were found to have >200 mAh/g reversible capacities with stable charge/discharge potential. Further, the CNWs had good responses of lithium insertion/extraction reaction primarily attributing to their nanoscale and uniform size consisting of well-oriented graphene. The charge/discharge property of CNWs could be further improved by heat treatment of CNWs as heat treatment removes the by-products like amorphous carbon phase or any foreign adsorbates from CNWs surface [55]. The CNWs are also suggested as a

promising nanostructured substrate for 3-D anodes of lithium-ion batteries. Krivchenko et al. [118] showed that CNWs with sputtered silicon clusters onto them produced improved electrochemical performance which was also accounted to large surface area of freestanding CNWs and improved adhesion of silicon clusters via the SiC interface layer formation. It was proposed that the 3-D silicon-decorated CNWs had the potential to minimize the lithium diffusion length and make charge collection more effective yielding better cycling performance at high rates (>2000 mAh/g) of silicon in the range of 0.05–2.00 V at 1.5 C rate [118].

2.6.2 As Catalyst Supports in Fuel Cells

Fuel cells, an environmentally green technology, are attracting significant interest for producing electricity by direct electrochemical conversion of hydrogen and oxygen into water [119]. Generally, platinum (Pt) nanoparticles are used as anode and cathode catalysts and carbon materials as catalyst supports. Also, the activity of a catalyst increases with the increase in the reaction surface area, therefore the diameter of catalyst particles should be as low as possible to increase the active surface area [119–122]. The support (carbon materials) for a fuel cell catalyst must have high surface area and sufficient electric conductivity for enhanced activity and efficient flow of electrons [120, 121]. Moreover, the carbon support should also have a high density of mesopores (20–40 nm region) to provide a high surface area to catalyst, to monomeric units of the Nafion ionomer and to boost the diffusion of chemical species [120, 122]. Also, any modification in electronic characteristics and geometrical dimensions of the carbon support can potentially affect the activity of the catalysts [120]. Therefore, new carbon nanostructures with unique morphology and structure have attracted much attention for the improvement of the electrochemical activity of the catalysts [120–123]. The CNWs are a potential catalyst supports owing to their unique structure, morphology, high surface area, and aspect ratio [124]. A number of groups have demonstrated application of CNWs as an effective catalysts support for Pt particles in the fuel cells. For example, Giorgi et al. [125] electrodeposited Pt nanoparticles on CNWs (grown by HF-CVD) by galvanostatic polarization to test the effectiveness of their use as electrocatalyst substrates. They found that the CNWs acted as a good substrate for Pt electrocatalyst for methanol oxidation and had remarkable enhancement as compared to standard carbon powder [125]. Machino et al. [126] demonstrated synthesis of dispersed Pt nanoparticles of 2 nm diameter on surface of CNWs by using supercritical fluid-CVD employing metal-organic compound. Similarly, Shin and coworkers [127] prepared well-dispersed Pt nanoparticle catalysts of diameter $\sim$3 nm supported on CNWs by a solution reduction method. The Pt/CNWs had high electrochemical active surface area and utilization, comparable to those for commercially available T–Pt/CB with good performance. Such high electrocatalytic activity was

attributed to the high electric conductivity of CNW and the improvement of electronic properties of Pt nanoparticles on the domain boundaries of CNWs, in addition to the high dispersion of Pt particles [127].

2.6.3 CNWs in Solar Cells

Recently, CNWs have started finding its application in solar cells also. For example, Wang et al. demonstrated that vertically aligned CNWs (they named it as carbon nanosheets, CNSs) with bi- and tri-layer graphene can be fabricated on various metal substrates from solid carbon sources by irradiation with H_2 and Ar plasma. They further used few-layered CNWs by transferring them on n-Si/SiO_2 to form a heterojunction solar cell and demonstrated a power conversion efficiency of 0.9% (under a simulated 100 mW/cm^2 AM 1.5G illumination) [128]. In this application, an n-type crystalline Si (100) wafer (resistivity: 2–10 Ω cm) with 200 nm insulating SiO_2 film was etched in HF solution selectively to open a window of dimension of 3 × 3 mm^2. The front and back contacts were thermally sputtered Ag on the SiO_2 and Cr/Au on the back side of n-Si, respectively. Subsequently, the CNS film (1 μm in height) was directly transferred on the top of the patterned Si wafer and was naturally dried to achieve a heterojunction solar cell. The testing of the cell was performed under a solar simulator at AM 1.5G (100 mW/cm^2) [128]. Figure 2.26 shows the schematic of the CNS/n-Si heterojunction solar cell. The charge separation mechanism on the interface between the CNSs and the Si substrate is shown in Fig. 2.26b. The energy band diagram of the fabricated solar cell is illustrated in Fig. 2.26c and photocurrent density (*J*)–voltage (*V*) characteristics in the dark and a 100 mW/cm^2 (AM 1.5 G) illumination is shown in Fig. 2.26d. The other solar cell parameters such as short circuit density (J_{sc}), open circuit voltage (V_{oc}), fill factor (*FF*), photoconversion efficiency (*PCE*), and a representative SEM image of CNSs used for solar cell are shown in the *inset* of Fig. 2.26d.

In another solar cell application of CNWs, Ho and coworkers [129] demonstrated the use of plasma-treated CNWs as counterelectrodes in dye-sensitized solar cells (DSSCs). They fabricated CNWs on a fluorine-tin-oxide (FTO) glass substrate via MPECVD using CH_4 gas. Then, post-plasma treatments were performed on the CNWs in different plasma environments (using O_2, H_2, and N_2 gas) under the same conditions, after which DSSCs were fabricated using the plasma-treated CNWs as counterelectrodes. They found that photoconversion efficiency (PCE) of the DSSC for which the as-deposited CNW was used as a counterelectrode showed an energy conversion efficiency of 1.64%, and the DSSC with the H_2 post-plasma-treated CNW counterelectrode showed an energy conversion efficiency of 2.23%. Thus, the DSSC with the H_2-treated electrode presented a 36% higher efficiency than the DSSC with the as-deposited CNW electrode.

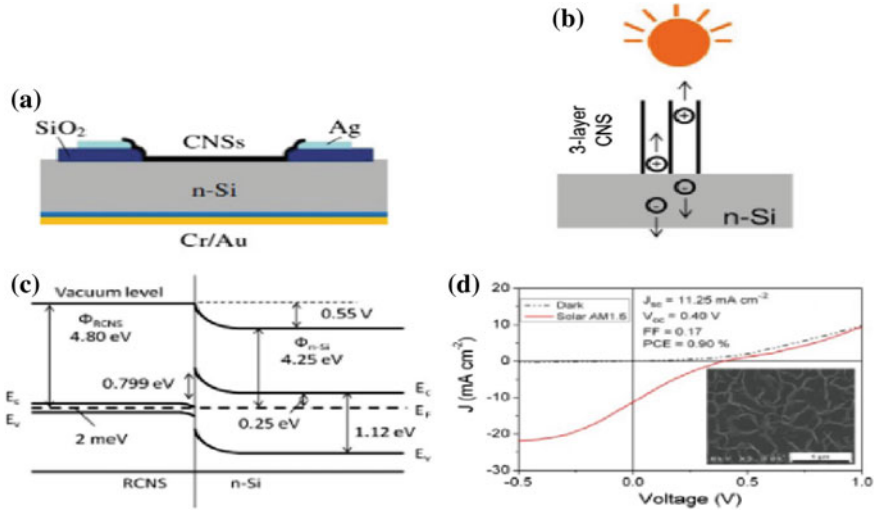

Fig. 2.26 **a** Schematic diagram of the CNS/n-Si heterojunction solar cell, **b** illustration of the charge separation existed on the interface between the CNSs and the Si substrate, **c** the energy band diagram of the fabricated solar cell, **d** *J–V* characteristics in the dark and under a 100 mW cm^{-2} AM 1.5 G illumination. Inset the corresponding data of J_{sc}, V_{oc}, *FF*, *PCB*, and SEM image of the RCNSs used for solar cell. Reprinted from Ref. [128]. Copyright (2014), with permission from Elsevier

2.7 Conclusions and Future Prospects

This chapter has shown that carbon nanowalls is another, very promising class of carbon materials like graphite, diamond, C60, CNTs, or graphene. Tremendous development is made toward controlled growth of CNWs by PECVD methods. Advantage with CNWs is that their growth does not need any catalyst like the one in case of CNTs and therefore, CNWs have several advantageous features over CNTs. However, although the thickness of the nanowalls is found to be approximately few nanometers, it is difficult to control the thickness of the nanowalls with precision. Moreover, even though single layer of graphene can be obtained from the growth, present technologies and skills have not enabled us to accurately isolate the nanowall of interest. Patterned growth of CNWs is also not an easy task. Each CNW exhibits the domain structure that consists of small crystallites or nanographite domains with high degree of graphitization. Several promising applications of CNWs have been demonstrated. The CNWs are shown to be promising electron field emitters owing to high density of atomic-scale graphitic edges and good electrical conductivity. In general, excellent FE results for the CNWs are obtained; it is still too early to conclude that the CNWs could be superior to the CNTs for field emission applications. A detailed comparative and critical experiments need to be carried out under similar conditions so as to find out the real potential of the two types of nanocarbon materials as field emitter. Nevertheless,

further research has to be done to promote field emission on different substrates as well as to enhance emission reliability of CNWs.

The CNWs show quick electrochemical response for lithium insertion/extraction, which is expected for high-rate use of lithium-ion battery. Such quick response is also an evidence for small graphite domains in CNWs. In addition, the CNWs serve as catalyst support in fuel cells where Pt nanoparticles are well dispersed along the domain boundaries in CNWs. The Pt particles on the domain boundaries also exhibit relatively high electrocatalytic activity. Thus, the domain structure of CNWs is useful for negative electrodes in high-rate lithium-ion batteries and catalyst supports in fuel cells. The electrode properties might be further improved since the size of graphite domains in CNWs can be controlled by the growth condition. Such unique structure and morphology of CNWs can lead to further applications. Photovoltaic applications of CNWs have also been demonstrated though the results are preliminary but pave the way to move forward for more exciting investigations and developments in the field.

References

1. H.W. Kroto, J.R. Heath, S.C. O'Brien, R.F. Curl, R.E. Smalley, C_{60}: buckminsterfullerene. Nature **318**, 162 (1985)
2. W. Kratschmer, L.D. Lamb, K. Fostiropoulos, D.R. Huffman, Solid C_{60}: a new form of carbon. Nature **347**, 354 (1990)
3. S. Iijima, Helical microtubules of graphitic carbon. Nature **354**, 56 (1991)
4. Y. Ando, X. Zhao, T. Sugai, M. Kumar, Growing carbon nanotubes. Mater. Today p. 22 (2004)
5. M. Inagaki, *New carbons-Control Of Structure and Functions*, 2nd edn. (Elsevier, Netherlands, 2000)
6. O.A. Shenderova, V.V. Zhirnov, D.W. Brenner, Carbon nanostructures. Crit. Rev. Solid State Mater. Sci. **27**, 227 (2002)
7. P.J.F. Harris, *Carbon Nanotubes and Related Structures: New Materials for the Twenty-first Century* (Cambridge University Press, UK, 1999)
8. R. Bacon, Growth, structure, and properties of graphite whiskers. J. Appl. Phys. **31**, 283 (1960)
9. D.E.H. Jones, New Scientist **32**, 245 (1966)
10. E. Osawa, Kagaku **25**, 854 (1970). (in Japanese)
11. D.A. Bochvar, E.G. Galperin, Huckel (4N + 2) rule and some poly-condensed systems. Dokl. Acad. Sci. SSSR **209**, 610 (1973)
12. S. Iijima, High resolution electron microscopy of some carbonaceous materials. J. Microsc **119**, 99 (1980)
13. E.A. Rohlfling, D.M. Cox, A. Kaldor, Production and characterization of supersonic carbon clusters. J. Chem. Phys. **81**, 3322 (1984)
14. D. Ugarte, Curling and closure of graphitic networks under electron-beam irradiation. Nature **359**, 707 (1992)
15. T.W. Ebbesen, P.M. Ajayan, Large-scale synthesis of carbon nanotubes. Nature **358**, 220 (1992)
16. S. Iijima, T. Ichihashi, Single-shell carbon nanotubes of 1-nm diameter. Nature **363**, 603 (1993)

17. D.S. Bethune, C.H. Kiang, M.S. DeVries, G. Goman, R. Savoy, R. Beyers, Cobalt-catalysed growth of carbon nanotubes with single-atomic-layer walls. Nature **365**, 605 (1993)
18. A. Thess, R. Lee, P. Nikolaev, H. Dai, P. Petit, J. Robert, C. Xu, Y.H. Lee, S.G. Kim, A.G. Rinzler, D.T. Colbert, G.E. Scuseria, D. Tománek, J.E. Fischer, R.E. Smalley, Crystalline ropes of metallic carbon nanotubes. Science **273**, 483 (1996)
19. Z.F. Ren, Z.P. Huang, J.W. Wang, P. Bush, M.P. Seigal, P.N. Provencio, Synthesis of large arrays of well-aligned carbon nanotubes on glass. Science **282**, 1105 (1998)
20. J. Kong, H.T. Soh, A.M. Cassel, C.F. Quate, H. Dai, Synthesis of individual single-walled carbon nanotubes on patterned silicon wafers. Nature **395**, 878 (1998)
21. J.H. Hafner, M.J. Bronikowski, B.R. Azamian, P. Nikolaev, A.G. Rinzler, D.T. Colbert, K. A. Smith, R.E. Smalley, Catalytic growth of single-wall carbon nanotubes from metal particles. Chem. Phys. Lett. **296**, 195 (1998)
22. R.R. Schilttler, J.W. Seo, J.K. Gimzewski, C. Durkan, M.S.M. Saifullah, M.E. Welland, Single crystals of single-walled carbon nanotubes formed by self-assembly. Science **292**, 1136 (2001)
23. Y. Wu, P. Quia, T. Chong, Z. Shen, Carbon nanowalls grown by microwave plasma enhanced chemical vapor deposition. Adv. Mater. **14**, 64 (2002)
24. K.S. Novoselov, A.K. Geim, S.V. Morozov, D. Jiang, Y. Zhang, S.V. Dubonos, I.V. Grigorieva, A.A. Firsov, Electric field effect in atomically thin carbon films. Science **306**, 666 (2004)
25. J. Han, in *Carbon Nanotubes Science and Applications*, ed. by M. Meyyappan (CRC Press, Boca Raton, 2005), p. 1
26. K.B.K. Teo, C. Singh, M. Chhowalla, W.I. Milne, in *Encyclopedia of Nanoscience and Nanotechnology* ed by H.S. Nalwa, vol. 1 (American Scientific Publishers, 2004), p. 665
27. A.K. Geim, K.S. Novoselov, The rise of graphene. Nat. Mater. **6**, 183 (2007)
28. J.-H. Chen, C. Jang, S. Xiao, M. Ishigami, M.S. Fuhrer, Intrinsic and extrinsic performance limits of graphene devices on SiO_2. Nat. Nanotechnol. **3**, 206 (2008)
29. A.A. Balandin, S. Ghosh, W. Bao, I. Calizo, D. Teweldebrhan, F. Miao, C.N. Lau, Superior thermal conductivity of single-layer grapheme. Nano Lett. **8**, 902 (2008)
30. C. Lee, X. Wei, J.W. Kysar, J. Hone, Measurement of the elastic properties and intrinsic strength of monolayer graphene. Science **321**, 385 (2008)
31. M.D. Stoller, S. Park, Y. Zhu, J. An, R.S. Ruoff, Graphene-based ultracapacitors. Nano Lett. **8**, 3498 (2008)
32. Y. Wu, B. Yang, B. Zong, H. Sun, Z. Shen, Y. Feng, Carbon nanowalls and related materials. J. Mater. Chem. **14**, 469 (2004)
33. Y. Ando, S. Iijima, Preparation of carbon nanotubes by arc-discharge evaporation. Jpn. J. Appl. Phys. **32**, L107 (1993)
34. S. Iijima, T. Wakabayashi, Y. Achiba, Structures of carbon soot prepared by laser ablation. J. Phys. Chem. **100**, 5839 (1996)
35. Y. Ando, X. Zhao, M. Ohkohchi, Production of petal-like graphite sheets by hydrogen arc discharge. Carbon **35**, 153 (1997)
36. N.G. Shang, F.C.K. Au, X.M. Meng, C.S. Lee, I. Bello, S.T. Lee, Uniform carbon nanoflake films and their field emissions. Chem. Phys. Lett. **358**, 187 (2002)
37. S.K. Srivastava, A.K. Shukla, V.D. Vankar, Vikram Kumar, Growth, structure and field emission characteristics of petal like carbon nano-structured thin films. Thin Solid Films **492**, 124 (2005)
38. K. Tanaka, M. Yoshimura, A. Okamoto, K. Ueda, Growth of carbon nanowalls on a SiO_2 substrate by microwave plasma-enhanced chemical vapor deposition. Jpn. J. Appl. Phys. **44**, 2074 (2005)
39. J. Wang, T. Ito, CVD growth and field emission characteristics of nano-structured films composed of vertically standing and mutually intersecting nano-carbon sheets. Diamond Relat. Mater. **16**, 589 (2007)
40. A.T.H. Chuang, B.O. Boskovic, J. Robertson, Freestanding carbon nanowalls by microwave plasma-enhanced chemical vapour deposition. Diamond Relat. Mater. **15**, 1103 (2006)

41. A.T.H. Chuang, J. Robertson, B.O. Boskovic, K.K.K. Koziol, Three-dimensional carbon nanowall structures. Appl. Phys. Lett. **90**, 123107 (2007)
42. M. Hiramatsu, K. Shiji, H. Amano, M. Hori, Fabrication of vertically aligned carbon nanowalls using capacitively coupled plasma-enhanced chemical vapor deposition assisted by hydrogen radical injection. Appl. Phys. Lett. **84**, 4708 (2004)
43. K. Shiji, M. Hiramatsu, A. Enomoto, M. Nakamura, H. Amano, M. Hori, Vertical growth of carbon nanowalls using rf plasma-enhanced chemical vapor deposition. Diamond and Relat. Mater. **14**, 831 (2005)
44. M. Hiramatsu, M. Hori, Fabrication of carbon nanowalls using novel plasma processing. Jpn. J. Appl. Phys. **45**, 5522 (2006)
45. S. Kondo, M. Hori, K. Yamakawa, S. Den, H. Kano, M. Hiramatsu, Highly reliable growth process of carbon nanowalls using radical injection plasma-enhanced chemical vapor deposition. J. Vacuum Sci. Techno. B **26**, 1294 (2008)
46. T. Mori, M. Hiramatsu, K. Yamakawa, K. Takeda, M. Hori, Fabrication of carbon nanowalls using electron beam excited plasma-enhanced chemical vapor deposition. Diamond Relat. Mater. **17**, 1513 (2008)
47. J. Wang, M. Zhu, R.A. Outlaw, X. Zhao, D.M. Manos, B.C. Holloway, Synthesis of carbon nanosheets by inductively coupled radio-frequency plasma enhanced chemical vapor deposition. Carbon **42**, 2867 (2004)
48. M. Zhu, J. Wang, R.A. Outlaw, K. Hou, D.M. Manos, B.C. Holloway, Synthesis of carbon nanosheets and carbon nanotubes by radio frequency plasma enhanced chemical vapor deposition. Diamond Relat. Mater. **16**, 196 (2007)
49. J.J. Wang, M.Y. Zhu, R.A. Outlaw, X. Zhao, D.M. Manos, B.C. Holloway, V.P. Mammana, Free-standing subnanometer graphite sheets. Appl. Phys. Lett. **85**, 1265 (2004)
50. G. Sato, T. Morio, T. Kato, R. Hatakeyama, Fast growth of carbon nanowalls from pure methane using helicon plasma-enhanced chemical vapor deposition. Jpn. J. Appl. Phys. **45**, 5210 (2006)
51. H.G. Jain, H. Karacuban, D. Krix, H.W. Becker, H. Nienhaus, V. Buck, Carbon nanowalls deposited by inductively coupled plasma enhanced chemical vapor deposition using aluminum acetylacetonate as precursor. Carbon **49**, 4987 (2011)
52. A. Yoshimura, S. Kurita, M. Tachibana, K. Kojima, P.M. Morales, H. Nakai, Fabrication of carbon nanowalls by dc plasma-enhanced chemical vapor deposition and characterization of their structures, Proceedings of 2005 5th IEEE Conference on Nanotechnology Nagoya, Japan (2005)
53. S. Kurita, A. Yoshimura, H. Kawamoto, T. Uchida, K. Kojima, M. Tachibana, P. Molina-Morales, H. Nakai, Raman spectra of carbon nanowalls grown by plasma-enhanced chemical vapor deposition. J. Appl. Phys. **97**, 104320 (2005)
54. K. Kobayashi, M. Tanimura, H. Nakai, Nanographite domains in carbon nanowalls. J. Appl. Phys. **101**, 094306 (2007)
55. O. Tanaike, N. Kitada, H. Yoshimura, H. Hatori, K. Kojima, M. Tachibana, Lithium insertion behavior of carbon nanowalls by dc plasma CVD and its heat-treatment effect. Solid State Ionics **180**, 381 (2009)
56. Z. Bo, K. Yu, G. Lu, P. Wang, S. Maoa, J. Chen, Understanding growth of carbon nanowalls at atmospheric pressure using normal glow discharge plasma-enhanced chemical vapor deposition. Carbon **49**, 1849 (2011)
57. H. Yoshimura, S. Yamada, A. Yoshimura, I. Hirosawa, K. Kojima, M. Tachibana, Grazing incidence X-ray diffraction study on carbon nanowalls. Chem. Phys. Lett. **482**, 125 (2009)
58. T. Itoh, S. Shimabukuro, S. Kawamura, S. Nonomura, Preparation and electron field emission of carbon nanowall by Cat-CVD. Thin Solid Films **501**, 314 (2006)
59. N. Lisi, R. Giorgi, M. Re, Carbon nanowall growth on carbon paper by hot filament chemical vapour deposition and its microstructure. Carbon **49**, 2134 (2011)
60. R.J. Nemanich, S.A. Solin, First- and second-order Raman scattering from finite-size crystals of graphite. Phys. Rev. B **20**, 392 (1979)

61. J. Yu, Q. Zhang, J. Ahn, S.F. Yoon, Y.J. Rusli, B. Li, K. Gan, K.H.Tan Chew, Synthesis of carbon nanostructures by microwave plasma chemical vapor deposition and their characterization. Mater. Sci. Eng. B **90**, 16 (2002)
62. F. Tuinstra, J.L. Koenig, Raman spectrum of graphite. J. Chem. Phys. **53**, 1126 (1970)
63. A.C. Ferrari, J. Robertson, Interpretation of Raman spectra of disordered and amorphous carbon. Phys. Rev. B **61**, 14095 (2000)
64. A.C. Ferrari, J. Robertson, Resonant Raman spectroscopy of disordered, amorphous, and diamond like carbon. Phys. Rev. B **64**, 075414 (2001)
65. H. Wang, Y. Wu, C.K.S. Choong, J. Zhang, K.L. Teo, Z. Ni, Z. Shen, Disorder induced bands in first order Raman spectra of carbon nanowalls, Nanotechnology, 2006. IEEE-NANO 2006. Sixth IEEE Conference, vol. 1, pp. 219–222
66. Z.H. Ni, H.M. Fan, X.F. Fan, H.M. Wang, Z. Zheng, Y.P. Feng, Y.H. Wu, Z.X. Shen, High temperature Raman spectroscopy studies of carbon nanowalls. J. Raman Spectrosc. **38**, 1449 (2007)
67. Y. Wu, B. Yang, Effects of localized electric field on the growth of carbon nanowalls Nano Lett. **2**, 355 (2002)
68. B. Chapman, *Glow Discharge Process* (Wiley, New York, 1980)
69. C. Bower, W. Zhu, S. Jin, O. Zhou, Plasma-induced alignment of carbon nanotubes. Appl. Phys. Lett. **77**, 830 (2000)
70. M. Zhu, J. Wang, B.C. Holloway, R.A. Outlaw, X. Zhao, K. Hou, V. Shutthanandan, D.M. Manos, A mechanism for carbon nanosheet formation. Carbon **45**, 2229 (2007)
71. I. Levchenko, K. Ostrikov, A.E. Rider, E. Tam, S.V. Vladimirov, S. Xu, Growth kinetics of carbon nanowall-like structures in low-temperature plasmas. Phys. Plasmas **14**, 063502 (2007)
72. R.H. Fowler, L.W. Nordheim, Electron emission in intense electric fields. Proc. R. Soc. London A **119**, 173 (1928)
73. Y. Cheng, O. Zhou, Electron field emission from carbon nanotubes. C.R. Physique **4**, 1021 (2003)
74. Z.P. Huang, Y. Tu, D.L. Carnahan, Z.F. Ren, in Encyclopedia of Nanoscience and Nanotechnology ed. by H.S. Nalwa, vol. 3 (American Scientific Publishers, 2004), p. 401
75. P. Gröning, L. Nilsson, P. Ruffieux, R. Clergereaux, O. Gröning, in Encyclopedia of Nanoscience and Nanotechnology, ed. by H.S. Nalwa, vol. 1 (American Scientific Publishers, 2004), p. 547
76. W. Zhu, C. Bower, G.P. Kochanski, S. Jin, Electron field emission from nanostructured diamond and carbon nanotubes. Solid-State Electron **45**, 921 (2001)
77. C.A. Spindt, A thin-film field-emission cathode. J. Appl. Phys. **39**, 3504 (1968)
78. A.G. Rinzler, J.H. Hafner, P. Nikolaev, L. Lou, S.G. Kim, D. Tomanek, P. Nordlander, D.T. Colbert, R.E. Smalley, Unraveling nanotubes: field emission from an atomic wire. Science **269**, 1550 (1995)
79. W.A. de Heer, A. Châtelain, D. Ugarte, A carbon nanotube field-emission electron source. Science **270**, 1179 (1995)
80. P.G. Collins, A. Zettl, A simple and robust electron beam source from carbon nanotubes. Appl. Phys. Lett. **69**, 1969 (1996)
81. P.G. Collins, A. Zettl, Unique characteristics of cold cathode carbon-nanotube-matrix field emitters. Phys. Rev. B **55**, 9391 (1997)
82. Y. Saito, K. Hamaguchi, K. Hata, K. Uchida, Y. Tasaka, F. Ikazaki, M. Yumura, A. Kasuya, Y. Nishina, Conical beams from open nanotubes. Nature **389**, 554 (1997)
83. Q.H. Wang, T.D. Corrigan, J.Y. Dai, R.P.H. Chang, A.R. Krauss, Field emission from nanotube bundle emitters at low fields. Appl. Phys. Lett. **70**, 3308 (1997)
84. J.M. Bonard, F. Maier, T. Stoeckli, A. Chatelain, W.A. de Heer, J.P. Salvetat, L. Forro, Field emission properties of multiwalled carbon nanotubes. Ultramicroscopy **73**, 7 (1998)
85. S. Fan, M.G. Chapline, N.R. Franklin, T.W. Tombler, A.M. Cassell, H. Dai, Self-oriented regular arrays of carbon nanotubes and their field emission properties. Science **283**, 512 (1999)

86. O.M. Kuttel, O. Groening, C. Emmenegger, L. Schlapbach, Electron field emission from phase pure nanotube films grown in a methane/hydrogen plasma. Appl. Phys. Lett. **73**, 2113 (1998)
87. Y. Saito, S. Uemura, Field emission from carbon nanotubes and its application to electron sources. Carbon **38**, 169 (2000)
88. M. Chhowalla, C. Ducati, N.L. Rupesinghe, K.B.K. Teo, G.A.J. Amaratunga, Field emission from short and stubby vertically aligned carbon nanotubes. Appl. Phys. Lett. **79**, 2079 (2001)
89. K.B.K. Teo, M. Chhowalla, G.A.J. Amaratunga, W.I. Milne, G. Pirio, P. Legagneux, F. Wyczisk, D. Pribat, D.G. Hasko, Field emission from dense, sparse, and patterned arrays of carbon nanofibers. Appl. Phys. Lett. **80**, 2011 (2002)
90. S.H. Jo, Y. Tu, Z.P. Huang, D.L. Carnahan, D.Z. Wang, Z.F. Ren, Effect of length and spacing of vertically aligned carbon nanotubes on field emission properties. Appl. Phys. Lett. **82**, 3520 (2003)
91. S.H. Jo, Y. Tu, Z.P. Huang, D.L. Carnahan, J.Y. Huang, D.Z. Wang, Z.F. Ren, Correlation of field emission and surface microstructure of vertically aligned carbon nanotubes. Appl. Phys. Lett. **84**, 413 (2004)
92. S.K. Srivastava, V.D. Vankar, D.V. Sridhar Rao, V. Kumar, Enhanced field emission characteristics of nitrogen-doped carbon nanotube films grown by microwave plasma enhanced chemical vapor deposition process. Thin Solid Films **515**, 1851 (2006)
93. S.K. Srivastava, V.D. Vankar, V. Kumar, Excellent field emission properties of short conical carbon nanotubes prepared by microwave plasma enhanced CVD process. Nanoscale Res. Lett. **3**, 25 (2008)
94. S.K. Srivastava, V.D. Vankar, V. Kumar, Effect of catalyst film thickness on the growth, microstructure and field emission characteristics of carbon nanotubes. In Physics of Semiconductor Devices, 2007. IWPSD 2007. International Workshop on, Physics of Semiconductor Devices, 2007. IWPSD 2007. International Workshop on, pp. 836–839, IEEE
95. S. Chhoker, S.K. Srivastava, V.D. Vankar, Field emission properties of carbon nanostructures: a review, physics of semiconductor devices, 2007. IWPSD 2007. International Workshop on, Physics of Semiconductor Devices, 2007. IWPSD 2007. International Workshop on, pp. 820–826, IEEE
96. S.K. Srivastava, V.D. Vankar, V. Kumar, V.N. Singh, Effect of substrate morphology on growth and field emission properties of carbon nanotube films. Nanoscale Res. Lett. **3**, 205 (2008)
97. H. Sharma, V. Kaushik, P. Girdhar, V.N. Singh, A.K. Shukla, V.D. Vankar, Enhanced electron emission from titanium coated multiwalled carbon nanotubes. Thin Solid Films **518**, 6915 (2010)
98. Y. Saito, K. Hamaguchi, T. Nishino, K. Hata, K. Tohji, A. Kasuya, Y. Nishina, Field emission patterns from single-walled carbon nanotubes. Jpn. J. Appl. Phys. **36**, L1340 (1997)
99. J.-M. Bonard, J.-P. Salvetat, T. Stockli, W.A. de Heer, L. Forro, A. Châtelain, Field emission from single-wall carbon nanotube films. Appl. Phys. Lett. **73**, 918 (1998)
100. W.B. Choi, D.S. Chung, J.H. Kang, H.Y. Kim, Y.W. Jin, I.T. Han, Y.H. Lee, J.E. Jung, N.S. Lee, G.S. Park, J.M. Kim, Fully sealed, high-brightness carbon-nanotube field-emission display. Appl. Phys. Lett. **75**, 3129 (1999)
101. W. Zhu, C. Bower, O. Zhou, G. Kochanski, S. Jin, Large current density from carbon nanotube field emitters. Appl. Phys. Lett. **75**, 873 (1999)
102. S.M. Sze, *VLSI Technology* (McGraw Hill, New York, 1988), p. 309
103. J. Wang, T. Ito, Improved field emission characteristics of nano-structured carbon films deposited on polycrystalline CVD diamond. Diam. Relat. Mater. **16**, 364–368 (2007)
104. E. Stratakis, R. Giorgi, M. Barberoglou, Th Dikonimos, E. Salernitano, N. Lisi, E. Kymakis, Three-dimensional carbon nanowall field emission arrays. Appl. Phys. Lett. **96**, 043110 (2010)

105. W. Takeuchi, H. Kondo, T. Obayashi, M. Hiramatsu, M. Hori, Electron field emission enhancement of carbon nanowalls by plasma surface nitridation. Appl. Phys. Lett. **98**, 123107 (2011)
106. Y. Tzeng, C.-L. Chen, Y.-Y. Chen, C.-Y. Liu, Carbon nanowalls on graphite for cold cathode applications. Diamond & Relat. Mater. **19**, 201 (2010)
107. P.H. Talemi, G.P. Simon, Field emission study of graphene nanowalls prepared by microwave-plasma method. Carbon **49**, 2875 (2011)
108. M.Y. Zhu, R.A. Outlaw, M. Bagge-Hansen, H.J. Chen, D.M. Manos, Enhanced field emission of vertically oriented carbon nanosheets synthesized by C_2H_2/H_2 plasma enhanced CVD. Carbon **49**, 2526 (2011)
109. S.A. Evlashin, Y.A. Mankelevich, V.V. Borisov, A.A. Pilevskii, A.S. Stepanov, Victor A. Krivchenko, N.V. Suetin, A.T. Rakhimov, Emission properties of carbon nanowalls on porous silicon. J. Vac. Sci. Technol. B **30**, 021801 (2012)
110. S. Shimada, K. Teii, M. Nakashima, Low threshold field emission from nitrogen-incorporated carbon nanowalls. Diamond & Relat. Mater. **19**, 956 (2010)
111. A. Malesevic, R. Kemps, A. Vanhulsel, M.P. Chowdhury, A. Volodin, C.V. Haesendonck, Field emission from vertically aligned few-layer graphene. J. Appl. Phys. **104**, 084301 (2008)
112. N. Jiang, H.X. Wang, H. Sasaoka, T. Deno, K. Nishimura, Thermal desorption and its effects on field emission properties of carbon nanowalls. Mater. Lett. **64**, 2025 (2010)
113. S. Chhoker, S.K. Arora, P. Srivastava, V.D. Vankar, Electron field emission from graphitic nanoflakes grown over vertically aligned carbon nanotubes. J. Nanosci. Nanotech. **8**, 4309 (2008)
114. V. Kaushik, A.K. Shukla, V.D. Vankar, Microwave plasma CVD-grown graphene–CNT hybrids for enhanced electron field emission applications. Appl. Phys. A **117**, 2197 (2014)
115. V. Kaushik, A.K. Shukla, V.D. Vankar, Improved electron field emission from metal grafted graphene composites. Carbon **62**, 337 (2015)
116. P.R. Bueno, E.R. Leite, Nanostructured Li ion insertion electrodes. 1. Discussion on fast transport and short path for ion diffusion. J. Phys. Chem. B **107**, 8868 (2003)
117. L. Taberna, S. Mitra, P. Poizot, P. Simon, J.M. Tarascon, Nature Mater. **5**, 567 (2006)
118. V.A. Krivchenko, D.M. Itkis, S.A. Evlashin, D.A. Semenenko, E.A. Goodilin, A.T. Rakhimov, A.S. Stepanov, N.V. Suetin, A.A. Pilevsky, P.V. Voronin, Carbon nanowalls decorated with silicon for lithium-ion batteries. Carbon **50**, 1422 (2012)
119. J. Larminie, A. Dicks, *Fuel Cell Systems Explained*, 2nd edn. (John Wiley & Sons, New York, 2003)
120. E. Antolini, Carbon supports for low-temperature fuel cell catalysts. Appl. Catal. B: Environ. **88**, 1 (2009)
121. A.L. Dicks, The role of carbon in fuel cells. J. Power Sources **156**, 128 (2006)
122. S.H. Joo, S.J. Choi, I. Oh, J. Kwak, Z. Liu, O. Terasaki, R. Ryoo, Ordered nanoporous arrays of carbon supporting high dispersions of platinum nanoparticles. Nature **412**, 169 (2001)
123. T.W. Kim, I.S. Park, R. Ryoo, A synthetic route to ordered mesoporous carbon materials with graphitic pore walls. Angew Chem. Int. Ed. **42**, 4375 (2003)
124. M. Tachibana, in *Structural Characterization of Carbon Nanowalls and Their Potential Applications in Energy Devices* (Chapter 6). *Book: Two-Dimensional Carbon: Fundamental Properties, Synthesis, Characterization, and Applications,* ed. by Yihong Wu, Zexiang Shen, and Ting Yu, Copyright © 2014 Pan Stanford Publishing Pte. Ltd., pp. 121–152
125. L. Giorgi, T.D. Makris, R. Giorgi, N. Lisi, E. Salernitano, Electrochemical properties of carbon nanowalls synthesized by HF-CVD. Sens. Actuators B: Chemical **126**, 144 (2007)
126. T. Machino, W. Takeuchi, H. Kano, M. Hiramatsu, M. Hori, Carbon nanostructures with an ultrahigh aspect ratio employing supercritical fluid chemical vapor deposition process. Appl. Phys. Express **2**, 025001 (2009)

127. S.C. Shin, A. Yoshimura, T. Matsuo, M. Mori, M. Tanimura, A. Ishihara, K. Ota, M. Tachibana, Carbon nanowalls as platinum support for fuel cells. J. Appl. Phys. **110**, 104308 (2011)
128. Z. Wang, M. Shoji, K. Baba, T. Ito, H. Ogata, Microwave plasma-assisted regeneration of carbon nanosheets with bi- and trilayer of graphene and their application to photovoltaic cells. Carbon **67**, 326 (2014)
129. Y.H. Jung, W.S. Choi, B. Hong, Post-plasma treatment of a carbon nanowall for use as a counter electrode in a dye-sensitized solar cell. J Korean Phys. Soc. **65**, 291 (2014)

Chapter 3
Role of Nanostructured Materials Toward Remediation of Heavy Metals/Metalloids

Yana Bagbi, Arvind Pandey and Pratima R. Solanki

Abstract In recent scenarios, the development of nanotechnology with novel size, shape, and surface dependent properties has revealed incredible prospective for the treatment of environmental problems especially toxic heavy metals from contaminated water. As compared with traditional materials, a nanosized particle exhibits to a large extent efficiency and faster remediation rates in water treatment. Many kinds of nanomaterials such as carbon, nanometal/metal oxides, and polymer based have high selectivity and adsorption potential for the remediation of heavy metals/metalloids such as As^{5+}, As^{3+}, Pb^{2+}, Cr^{3+}, Cr^{6+}, Hg^{2+}, Co^{2+}, Ni^{2+}, Cd^{2+}, and Cu^{2+} from contaminated water. This chapter gives a widespread analysis on the enduring research and progress activities in the field of remediation of toxic heavy metals/metalloids from contaminated water by using nanomaterials in order to achieve environmental detoxification, using adsorption process. We have also discussed the essential aspects of heavy metals problems on environment; their effects on human health through polluted water are reviewed.

Keywords Water pollution · Toxicity · Heavy metals/metalloids
Nanomaterials · Adsorption

3.1 Introduction

Water is the most valuable substance on this earth. All the life entities need water to survive. Without water then there would be no life on the earth. Drinking water quality is a common concern for people all over the world. We can survive days or

Y. Bagbi · P.R. Solanki (✉)
Special Centre for Nanoscience, Jawaharlal Nehru University,
New Delhi 110067, India
e-mail: pratimarsolanki@gmail.com

Y. Bagbi · A. Pandey
Department of Physics, North Eastern Regional Institute of Science
and Technology, Nirjuli 791109, Arunachal Pradesh, India

Z.H. Khan (ed.), *Nanomaterials and Their Applications*,
Advanced Structured Materials 84, https://doi.org/10.1007/978-981-10-6214-8_3

even weeks without food, but cannot survive for long without water. Water quantity and quality is an important issue for public health. It is a well-known fact that clean drinking water is absolutely essential for healthy living. Water covered 326 million cubic miles on the Earth; however, only 3/10,000 is fresh water that can use for bathing, washing, cooking, and drinking. The rest percent is sheltered in oceans, icecaps glaciers, atmosphere, and ground water. But this 3% of water is also getting polluted by human deeds.

The contagion of water bodies such as oceans, rivers, aquifers, lakes, oceans, and groundwater is called water pollution. This water pollution occurs when pollutants are directly or indirectly discharged into natural water without proper treatment. Water pollution not only affects plants and animals but also affect the aquatic life. Approximately, the effect of water pollution is dangerous not only to human beings but also to the entire biosphere communities [1–3]. The problem of water pollution becoming severe day by day due to increase in population and increasing industrial activities. Many areas of surface water and groundwater are now contaminated with pathogens, harmful chemicals, and toxic heavy metals. Worldwide diseases like cancer, congenital malformation, and endocrine disturbances are associated with the contaminated drinking water.

Heavy metal toxicity is one of the leading problems in the current industrialized era. Wastewater from numerous industries, tanneries, battery manufacturing, metallurgical activities, electroplating, chemical manufacturing, and mining industries hold huge quantity of heavy metal ions [4, 5]. These wastewaters are discharged into water bodies directly, threatening not only the aquatic organisms, but also harming human and animals through their food chain. In numerous parts of the world, heavy metal concentration in drinking water is higher than the international guidelines values provided by the World Health Organization (WHO) and Bureau of Indian Standard (BIS).

Heavy metal is defining by the density of the metals in most of the cases. It is, thus, defined as those metals having a specific density in excess of 5 g/cm^3 and toxic even in low concentration in contact with water and can have lethal effect on human bodies [6, 7]. It has been reported that about 1.6 million children die every year by consuming contaminated water. In the country like India, 80% of people are dying because of drinking toxic heavy metal contaminated water [6, 7]. The effects of these metals on human health are regularly reviewed by global bodies such as the World Health Organization [WHO]. Thus, the elimination of heavy metal ions from water bodies is vital to safeguard the environment and public health. To improve the quality of drinking water, the development of sustainable and robust technologies, chips, etc., has become of fundamental importance.

Several methods have been introduced to eradicate heavy metal ions from water such as chemical precipitation [8], membrane filtration [9], ion exchange [10], reverse osmosis [11], extraction [12], electrochemical treatment techniques [13], irradiation [14], coagulation [15], and adsorption [16]. But adsorption [17] shows most potential method to eliminate heavy metal ions from water as compared to others due to being inexpensive and extremely flexible. Carbon, zeolites, clay minerals, and chitosan have been explored for the adsorption of heavy metals by

numerous researchers but the less adsorption ability and elimination competence restricts its application.

Current advancement in nanotechnology provides a hopeful way to resolve the environmental problems and offers protective dealings for future problems resulting from the exchanges of energy and resources with the environment [18, 19]. The most important environmental applications of nanotechnology could be elimination of toxic heavy metals ions from polluted water.

The major demerits of traditional sorbents in removal of heavy metals from wastewater could be solved by nanostructured materials. These nanomaterials have size ranging from 1 to 100 nm. As compared with traditional materials, nanomaterials show advanced effectiveness and quicker adsorption rates of heavy metals due to its novel size, large surface area, and shape dependent properties resulting in high reactivity to various heavy metals ions.

3.2 Heavy Metals/Metalloids and Their Sources

Water pollution caused by hazardous heavy metals and metalloids can occur from both natural as well as anthropogenic sources [20, 21]. Commonly known natural sources of heavy metals are mainly volcanic activities, rocks, ore minerals that are hidden in the crust, forest fires, etc., [21]. Anthropogenic sources of heavy metals pollution are increasing due to industrial waste, use of fertilizers, pesticides, sewage sludge, mining, combustion of coal and other fossil fuels. The toxic waste occurs due to both industrial production and end-used products landing into water bodies. Many industries like metal smelting, leather tanning, semiconductor, chemical manufacturing, etc., directly discharge heavy metal ions contaminated wastewater into natural water without adequate treatment [20, 21]. Thus, industrialized countries are more often faced with the impact of toxic heavy metals. Table 3.1 provides the anthropogenic sources of heavy metal pollutants provided by Dr. Gautam SP, CPCB New Delhi [22].

As discussed above about the sources of pollution by toxic heavy metals into the environment, mining is yet another such major source. There are many reports in this regard. For example, the effluents released in water bodies from Zawar mines in Udaipur district found to have higher levels of hazardous zinc and lead [23] causing toxicity of water. In another study by Shulka [24] of the water samples of northeast coalfield region of Chhattisgarh, it was found that level of cadmium, lead, iron, zinc, chromium, copper in the water was beyond the permissible limit. Hu et al. [25] have reported extensively in their study on the pollution of heavy metals in China. Their study suggests mining is one of the prime reasons of the heavy metal pollution in China. In gold mining, mercury (Hg) is used for amalgamation of gold. Most of the mercury is removed in this process and reused; however, some of the mercury enters in the river system. The gold mining activity is prime reason for the Amazon basin system to pollute [26].

Table 3.1 Sources of heavy metals (*Source* provided by Gautam SP, CPCB New Delhi)

Metals	Industries
Chromium (Cr)	Mining, industrial coolants, chromium salts, manufacturing, leather tanning
Lead (Pb)	Lead acid batteries, paints, E-waste, Smelting operations, coal based thermal power plants, ceramics, bangle industry
Mercury (Hg)	Chlor-alkali plants, thermal power plants, fluorescent lamps, hospital waste (damaged thermometers, barometers, sphygmomanometers), electrical appliances etc.
Arsenic (As)	Geogenic/natural processes, smelting operations, thermal power plants, fuel burning
Copper (Cu)	Mining, electroplating, smelting operations
Cadmium (Cd)	Zinc smelting, waste batteries, e-waste, paint sludge, incinerations & fuel combustion
Molybdenum (Mo)	Spent catalyst
Zinc (Zn)	Smelting, electroplating
Nickel (Ni)	Smelting operations, thermal power plants, battery industry
Vanadium (Va)	Spent catalyst, sulphuric acid plant

Since ages, the agriculture has remained a prime economic activity for human beings to survive. Because of the ever increasing population, the demand for food is increasing at rapid rate, therefore, need to produce more is need of hour. In order to produce more, the increase in use of fertilizers and pesticides have taken place. For healthy growth of crops, heavy metals like Cu, Zn, Mo, Ni, Fe, Mn, and Co are also essential apart from macronutrient like N, P, K, etc. The compounds via which these elements are supplied also contain some amount of Cd and Pb, which upon prolonged use are deposited in the soil [27]. These metals enter the ground water via interconnection between soil and groundwater and hence causing water pollution [26].

Biosolid waste is another source of heavy metal contamination to the soil and hence the groundwater and water bodies. Biosolids like livestock manure, sewage sludge, etc., contain heavy metals such as Sb, Cr, Cd, and As. When these solids are used over the land in the activities such as agriculture, then over a period of time they could accumulate and hence may contaminate water [23].

3.3 Effects of Heavy Metals/Metalloid in Human Health

Heavy metals are very dangerous for both human health and aquatic life, if, it crosses the maximum permissible limit because heavy metals are inclined to bioaccumulate [28]. Bioaccumulation indicates an increase of a chemical in living bodies eventually, compared to the concentration of chemicals in the environment [28]. Accumulation of heavy metals in living things is faster in rate than the

substance is lost by catabolism and excretion. Five most common heavy metals that are very toxic to both human and aquatic life even at low concentration and reviewed by WHO many times which are discussed in brief are: lead, cadmium, chromium, mercury, and arsenic [29, 30]. Severe exposures to heavy metals have been known and it continues to grow unabated in many parts of the world. Particularly, the exposure is increasing in less developed countries like Pakistan, India, and Bangladesh [22]. Too much of heavy metal consumption can damage different systems of the body together with the reproductive system, nervous, kidneys and it can cause cancer, high blood pressure, and anemia [30, 31]. The symptoms consist of headache, abdominal pain, irritability, confusion, and in severe cases it can cause coma, seizures, and death [5, 31, 32].

Arsenic is classified as a heavy metal but it is actually a metalloid. It is abundant in our environment with both natural and anthropogenic sources [33, 34]. In water, arsenic has leading forms of inorganic species such as arsenate [As^{5+}] and arsenite [As^{3+}] [33, 34]. Maximum permissible limit of arsenic in drinking water set by the WHO and BIS is at 0.01 mg/L [35, 36]. Arsenic consumption is mostly due to intake of seafood and drinking water. Its long-standing exposure enhances risk of skin cancer, lesions, hyperkeratosis, and pigmentation changes [37, 38]. Results show occasional exposure to arsenic can have risk of lung cancer [38].

Lead is a poisonous heavy metal that is dangerous to human health. In contact with water, lead is colorless, odorless, and tasteless. In drinking water, the maximum permissible limit of lead set by the WHO and the BIS is 0.01 mg/L [35, 36]. In child, the high level of lead exposure can result with neurological damage, coma, organ failure, and ultimately death [39]. The exposure in low level can affect learning disabilities; inhibit growth, and hearing loss [31, 39]. The symptoms show poor appetite, vomiting, sleep disorder, cramps, irritability, fatigue, and constipation [39]. It can easily accumulate within the body for a long time, i.e., bioaccumulate [21], which possibly is stored in the kidney, bones, brain, and other main organs. Lead can also store in the blood and bones of child's for several decades [31, 39].

Mercury is exceptionally toxic heavy metals and it must be handled properly. The permissible limit of mercury in drinking water set by the WHO and the BIS is at 0.006 mg/L and 0.001 mg/L, respectively [35, 36]. The exposure of mercury can harm the nervous system, impair hearing, speech, vision and gait, involuntary muscle movements, corrodes skin, and mucous membranes. It can also cause the problem of chewing and swallowing of food [40]. In India, the general population is exposed to mercury due to intake of seafood and drinking contaminated water [41]. The pregnant women need to avoid a high intake of seafood, such as fish, shark, tuna, and swordfish, taken from polluted waters [40].

The maximum permissible limit of **cadmium** in drinking water set by the WHO and BIS is at 0.003 mg/L [35, 36]. It was first reported in Japan that extended exposure of cadmium might give rise to dangerous bone disease, called itai-itai ("ouch-ouch"). It was first reported from the Jinzu river basin in Japan [29, 31]. Cadmium exposure can also lead to harmful effects such as renal damage, emphysema, chronic disorders, and skeletal malformation in fetus, hypertension,

kidney damage, and testicular atrophy [29]. Cadmium is also considered as carcinogenic reported by the International Agency for Research on Cancer (IARC, 1993). The IARC's study was based on occupationally exposed workers [31]. In India, many people have already exceeding cadmium exposure levels, and the edge is very thin. Therefore, proper treatment should be taken to decrease the cadmium hazard to diminish the unpleasant health effects.

In contact with water, **chromium** forms two stable oxidation states, Cr^{3+} and Cr^{6+} [42]. Cr^{6+} is far more poisonous than Cr^{3+} to living things for its carcinogenicity, toxicity, and high aqueous solubility. Currently, the WHO has set a permissible limit for chromium in drinking water at 0.1 mg/L and the BIS at 0.05 mg/L [35, 36]. The exposures to Cr^{6+} occasinally raises the risk of cancers in the respiratory system. Zhang and Li [43] recently reported that in China (resident in the Liaoning), the death due to stomach cancers increased. The reasons behind this are drinking water in resident Liaoning was greatly contaminated with Cr^{6+} which are released by the ore smelting industries.

Copper is a reddish metal and is a crucial element for all the living organisms. It is vital in diet to assure good health. On the other hand, too much absorption of copper can be root of adverse health effects, including stomach cramps, nausea, vomiting, diarrhea, etc., [44]. It has also been reported that too much exposure of copper can cause liver and kidney damage [31]. In drinking water, the maximum permissible limit of copper set by the WHO is at 2 mg/L and by the BIS is at 0.05 mg/L [35, 36]. Therefore, removal of these heavy metals is very necessary for clean and healthy environment. Table 3.2 provides the maximum permissible limits of heavy metals set by the WHO and BIS in drinking water (Sources provided by the WHO and BIS). Figure 3.1 shows the six hazardous heavy metals in drinking water.

Table 3.2 Maximum permissible limit of heavy metal in drinking water by WHO and BIS

Sl. No.	Heavy metal/metalloids	World Health Organization (WHO) (mg/L)	Bureau of Indian Standards (BIS) (mg/L)
1	Arsenic (As)	0.01	0.01
2	Lead (Pb)	0.01	0.01
3	Chromium (Cr)	0.1	0.05
4	Cadmium (Cd)	0.003	0.003
5	Copper (Cu)	2	0.05
6	Mercury (Hg)	0.006	0.001
7	Zinc (Zn)	5	5
8	Nickel (Ni)	0.07	0.02
9	Molybdenum (Mo)	0.07	0.07
10	Selenium	0.01	0.01
11	Uranium	0.015	–
12	Barium	0.7	0.7
13	Silver	0.1	0.1

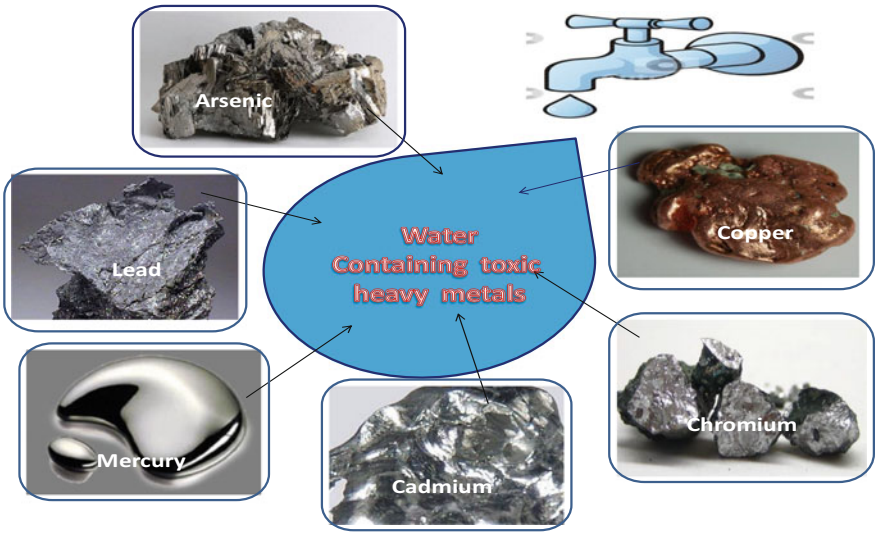

Fig. 3.1 Drinking water contains heavy metals

3.4 Nanomaterials as Adsorbent for Heavy Metals/Metalloids

Nanomaterials as sorbents for elimination of heavy metals/metalloids ions from wastewater should have following criteria. The nanosorbents should be nontoxic and have high sorption capacities. The adsorbed metal ions could be detached easily from the surface of the nanoadsorbents and could be infinitely recycled [29]. So far, a varieties of nanomaterials such as carbon, metal and metal oxides, and polymer supported nanoadsorbents have been studied for the removal of heavy metal from water, and the results indicate that highest explored nanoadsorbents were carbon, nanozero-valent iron and iron oxide-based nanoadsorbents due to their large surface area volume ratio, low cost, easy availability, nontoxic, and recyclable [29, 45]. Few metal oxide nanoadsorbents such as TiO_2, CeO, MnO, and AlO were also explored for the removal of heavy metals from water [46]. Polymer supported nanoadsorbents have also been explored by the researcher in this field [47]. Figure 3.2 shows the pie chart of explored utilization of different nanomaterials as sorbents for heavy metal remediation from water.

3.4.1 Carbon-Based Nanomaterials

Undoubtedly, carbon-based nanomaterials are the most admired and broadly used adsorbent for the applications in wastewater treatment all over the world. In recent

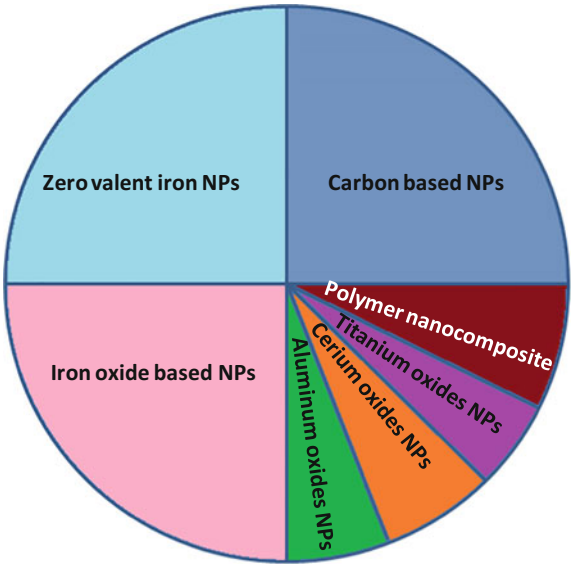

Fig. 3.2 Pie chart of explored utilization of different nanomaterials absorbents for heavy metal remediation from water

decades, carbon-based adsorbent [48] is extensively used for the removal of heavy metals from waste water due to its nontoxic, low-cost, and high sorption capacities [6]. Firstly, activated carbon was used as sorbents for heavy metal remediation but have demerits to remove heavy metals at ppm [parts per million (mg/L)] level [6]. To overcome these demerits, nanotechnology recently designs graphene, carbon nanotubes, and fullerene used as nanosorbents for the remediation of heavy metals [6, 48].

Lijima was the first who discovered carbon nanotubes (CNTs). Owing to their exclusive structural, mechanical, optoelectronic, semiconducting, electronic, chemical, and physical properties, CNTs have been used extensively to eliminate heavy metals from wastewater [6]. CNTs have two forms, single-walled carbon nanotubes (SWCNTs) and multi-walled carbon nanotubes (MWCNTs). Many studies have revealed that CNTs have outstanding adsorption capacity and have high adsorption effectiveness for various heavy metals as compared with other adsorbent [49, 50]. Li et al. [49] have reported CTNs have excellent adsorption capacity for Pb^{2+} from water. Li et al. [50] again reported thermodynamics studies of Pb^{2+} adsorption on carbon nanotubes in a range of temperatures; 280, 298, and 321 K and calculate all the thermodynamic constant such as equilibrium constant, standard entropy change, and standard-free energy. The desorption result also reveals that Pb^{2+} can be removed easily from CNTs by varying the solution pH using HNO_3 and HCl, which signifies that CNTs can be reused again. Hu et al. [51] reported chromium removal using oxidized MWCNTs. The result indicates that chromium adsorption mostly depends on the redox reaction of Cr^{6+} ions on the surface of oxidized MWCNTs to form Cr^{3+}, and ensuing Cr^{3+} sorption on MWCNTs appears as the foremost mechanism for the uptake of chromium on MWCNTs.

Pillay et al. [52] reported the adsorption capabilities of Cr^{6+} using three carbon-based adsorbents that are: activated carbon, functionalized MWCNTs, and unfunctionalized MWCNTs. The results revealed that unfunctionalized MWCNTs showed the highest adsorption capability with up to 98% out of 100 mg/L of Cr^{6+} solution being adsorbed. Pyrzyńska and Bystrzejewski [53] reported comparative study of heavy metals ion Co^{2+} and Cu^{2+} adsorption onto activated carbon, carbon nanotubes, and carbon-encapsulated magnetic nanoparticles. The results indicate CNTs have less sorption capacity as compared with carbon nanomaterials. In the meantime, Stafiej and Pyrzynska [54] reported solution pH, including metal ions concentrations, could affect the adsorption distinctiveness of CNTs, and the experimental data agreed well with the Freundlich adsorption isotherm model. Kosa et al. [55] reported modified carbon nanotubes with 8-hydroxyquinoline and used it for the removal of Cu^{2+}, Pb^{2+}, Cd^{2+}, and Zn^{2+}. The results revealed that the modification of CNTs with 8-hydroxyquinoline improved the removal efficiency of heavy metals.

Graphene is an additional parts of carbon nanomaterials, having one or more atomic layered graphite. It has two-dimensional structure having excellent thermal and mechanical properties. Zhao et al. [56] reported synthesis of few-layered graphene oxide nanosheets using modified Hummers method and used these graphene nanosheets as sorbents for the elimination of Cd^{2+} and Co^{2+} ions from water. The results signify that sorption of heavy metal on graphene nanosheets is dependent on solution pH, ionic strength, and the abundant oxygen-containing functional groups on the surfaces of graphene oxide nanosheets. Zhang et al. [57] reported composites graphene oxide/magnetite (GO/Fe_3O_4) synthesized via a copper catalyzed azide-alkyne cyclo addition reaction. Further, GO/Fe_3O_4 was modified with polyacrylic acid (PAA) to obtain $PAA/GO/Fe_3O_4$ which was used for the removal of Cu^{2+}, $Cd^{2+,}$ and Pb^{2+} ions from water. It is found that the $PAA/GO/Fe_3O_4$ nanocomposite shows extraordinary removal effectiveness for Cu^{2+}, $Cd^{2+,}$ and Pb^{2+} ions. Chandra et al. [58] reported a size of 10 nm magnetite-graphene adsorbents for the removal of As^{3+} and As^{5+} from water. The outcome signifies the high uptake of arsenic as a result of the increased adsorption sites in composite of graphene. Yang et al. [59] reported aggregation of Graphene oxide (GO) by Cu^{2+} in aqueous solution, indicates enormous Cu^{2+} absorption capacity. The study characterized by atomic force microscopy and confocal microscopy reported that Cu^{2+} ions folded GO sheets and creates large aggregation along with increased adsorption sites. The results demonstrate 10 times adsorption capacity then activated carbon. Table 3.3 shows the carbon-based nanoadsorbents explored for the remediation of heavy metals from water. Figure 3.3 shows the different shapes of carbon-based nanoadsorbents.

3.4.2 Nanosized Metal and Metal Oxides

Recently, metal and metal oxide nanoadsorbents (NMO) such as nanosized zero-valent iron (NZVI), ferric oxides, titanium oxides, cerium oxides, manganese

Table 3.3 Carbon-based nanoadsorbents used for heavy metal remediation

Carbon-based nanoadsorbents	Heavy metal	References
CNTs	Pb^{2+}	[49]
CNTs	Pb^{2+}	[50]
Oxidized MWCNTs	Cr^{6+}, Cr^{3+}	[51]
MWCNTs	Cr^{6+}	[52]
Activated carbon, CNTs, and carbon-encapsulated Fe_3O_4	Co^{2+}, Cu^{2+}	[53]
CNTs	Cu, Co, Cd, Zn, Mn, Pb	[54]
MWCNTs modified 8-hydroxy quinoline	Cu^{2+}, Pb^{2+}, Cd^{2+}, Zu^{2+}	[55]

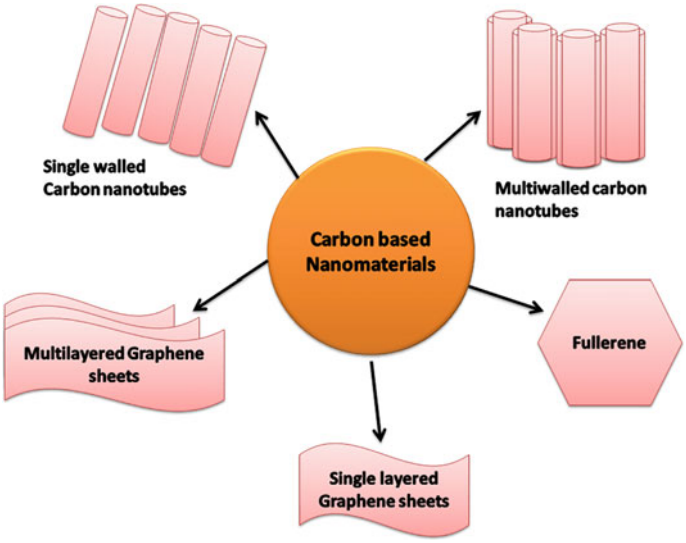

Fig. 3.3 Different shapes of carbon-based nanomaterials

oxides, aluminum oxides were explored as the most gifted adsorbent for the remediation of heavy metals from water [45, 46, 60–64]. The motivation behind this is due to their large surface areas and high adsorption capacity caused by the size-quantization effect [65, 66]. The study reported that NMOs show evidence of very favorable sorption to heavy metals in terms of high capacity and selectivity. On the other hand, the surface energy increases as the size of NMOs decreases from micrometer to nanometer levels, which reduces their stability. Therefore, NMOs can easily aggregate due to Van der Waals forces and other interactions [66], which very much decreases the high adsorption capacity and selectivity of NMOs. Additionally, NMOs have poor mechanical strength and too much pressure drops which leads to unfeasible in fixed beds. To overcome this all problems, many researchers have impregnated NMOs into porous supports to obtain composite nanoadsorbents [47], which include amino acids, polymers, activated carbon,

natural materials, etc. Above and beyond as compared with all traditional NMOs, magnetic nanoadsorbents create a center of attention because of their large surface area, ecofriendly, availability, low cost and it can be simply separated from water applying magnetic field [60, 61]. Furthermore, magnetic composite adsorbents can easily be regenerated or recycled [61], which reduces the cost of wastewater management (Fig. 3.3).

3.4.2.1 Iron-Based Nanoparticles as Nanoadsorbents for Heavy Metals

The exploitation of iron-based nanoadsorbents have been acknowledged to a great extent in the field of heavy metals remediation from water due to their exceptional properties, for instance small size, high surface area to volume ratio, ecofriendly, excellent magnetic properties, and great ability of surface modification.

Zero-Valent Iron: Among all the metal/metal oxide nanomaterials, nanoscale zero-valent iron (NZVI) has distinguished itself by its unique properties that include low cost, low toxicity, ecofriendly, larger surface to volume ratio, diminish the chemicals consumption, no secondary pollutant, strong adsorption ability, and easy separation under external magnetic field [60, 67]. Therefore, these properties make NZVI as the excellent adsorbent for the treatment of heavy metals from water. Ponder et al. [67] reported quick removal of Cr^{6+} and Pb^{2+} from aqueous solution using supported NZVI ("Ferragels"). The result indicates supported NZVI, while oxidizing the Fe to goethite (R-FeOOH) reduced the Cr to Cr^{3+} and the Pb to Pb^{0}. Kanel et al. [33, 34] reported that NZVI rapidly removes As^{3+} and As^{5+} from groundwater. The maximum adsorption capacity of As^{3+} obtained from Freundlich adsorption model was 3.5 mg/g. Boparai et al. [68] investigated NZVI for the removal of Cd^{2+} (conc. range 25–450 mg/L). The results recommend the competent removal of Cd^{2+} from contaminated water. Zhang et al. [69] reported that NZVI has limitation to remediate contaminated groundwater due to lack of durability and mechanical strength. To overcome these problems, NZVI was loaded onto kaolinite as a support material (K-NZVI) and used for the remediation of Pb^{2+} from water. The results show 96% of Pb^{2+} was removed within 30 min using 10 g/L K-NZVI in 500 mg/L Pb^{2+}. Kim et al. [70] reported the Zeolite supported NZVI for the removal of Pb^{2+} from aqueous water and the results designated immense potential of Pb^{2+} elimination from water. Su et al. [71] reported the removal of NZVI to the co-contaminants Cd^{2+} and nitrates. The result indicates increase in solution pH and negative charge of NZVI increases the removal of Cd^{2+} from 40 to 188 mg/g with nitrate present and 30% of nitrate was reduced by NZVI within 2 h. Liu et al. [43] reported NZVI supported on pumice (P-NZVI) successfully removed Hg^{2+} and Cr^{6+} from wastewater. The maximum uptake of Hg^{2+} and Cr^{6+} onto P-NZVI was 332.4 and 306.6 mg/g, respectively. Table 3.4 shows the NZVI adsorbents for the removal of heavy metals from water.

Iron Oxide-based nanoadsorbents exist in various forms in nature such as Goethite (γ-FeOOH), Maghemite (γ-Fe_2O_3), Hematite (α-Fe_2O_3), and Magnetite (Fe_3O_4) [72]. Recently, the majority of research for the applications of wastewater

Table 3.4 Zero-valent iron NPs for the removal of heavy metals

Zero-valent iron nanoadsorbents	Heavy metals	References
NZVI	Pb^{2+}, Cr^{6+}	[67]
NZVI	As^{5+}	[33]
NZVI	As^{3+}	[34]
(K-NZVI)	Pb^{2+}	[69]
Zeolite/NZVI	Pb^{2+}	[70]
NZVI	Cd^{2+}	[68]
NZVI	Cd^{2+}	[71]
P-NZVI	Hg^{2+}, Cr^{6+}	[43]

treatment has focused on iron oxide nanoadsorbents [72, 73]. Nasser [73] reported the maximum adsorption capacity for Pb^{2+} ions was obtained as 36.0 mg/g by Fe_3O_4 NPs, which was much higher than that of reported low-cost adsorbents. The small size of Fe_3O_4 NPs was favorable for the diffusion of metal ions from solution on to the active sites of the adsorbents surface. The result indicates that Fe_3O_4 nanosorbents were effective and economical adsorbents for rapid removal and recovery of metal ions from wastewater effluents. Sarkar and Sarkar [74] investigated the applicability of polyethylene glycol (PEG-4000) coated Fe_3O_4 magnetic nanoparticles for the selective removal of toxic Pb^{2+} ion from wastewater. The result indicates maximum adsorption of Pb^{2+} at optimum pH 6, and the equilibrium contact time is 10 min. Wang et al. [75] reported synthesized water-soluble Fe_3O_4 NPs through a hydrothermal method and found excellent removal of Pb^{2+} and Cr^{6+} ions from waste water. The result indicates more than 90% of Pb^{2+} and Cr^{6+} ions were removed within 2 min.

Xin et al. [76] reported amine-functionalized mesoporous Fe_3O_4 NPs (AF-Fe_3O_4) used for the removal of Pb^{2+}, Cd^{2+}, and Cu^{2+} ions from water. The result indicates the adsorption of these heavy metals agreed well with Langmuir isotherm model and the maximum adsorption capacities for Pb^{2+}, Cd^{2+}, and Cu^{2+} from 369.0 to 523.6 mg/g, which is superior to other reported work. Liu et al. [77] reported Humic acid (HA) coated Fe_3O_4 NPs (Fe_3O_4/HA) successfully removed toxic heavy metals Hg^{2+}, Pb^{2+}, Cd^{2+}, and Cu^{2+} from water. The maximum removal efficiency of the heavy metals reached equilibrium within 15 min, and agreed well with Langmuir isotherm adsorption with maximum uptake from 46.3 to 97.7 mg/g. The result indicates 99% removal of Hg^{2+}, Pb^{2+}, and almost 95% of Cd^{2+}, and Cu^{2+}. Bagbi et al. [78] reported monodispersed Fe_3O_4 NPs synthesized by chemical co-precipitation and used for successful removal of Pb^{2+} from water (Fig. 3.4). The result indicated 100% removal of Pb^{2+} within 30 min. Pseudo-second-order rate equation shows better fitted data. Spent Fe_3O_4 NPs were regenerated using 0.005 M HNO_3. Grossl et al. [79] investigate Cu^{2+} adsorption/desorption studies using goethite (a-FeOOH) NPs applying pressure-jump relaxation technique. The relaxations rate of Cu^{2+} decreased with an increase in pH. The results indicate that the rate of adsorption of divalent metal cations on goethite was directly related to the rate of removal of a water molecule from the primary hydration sphere of a

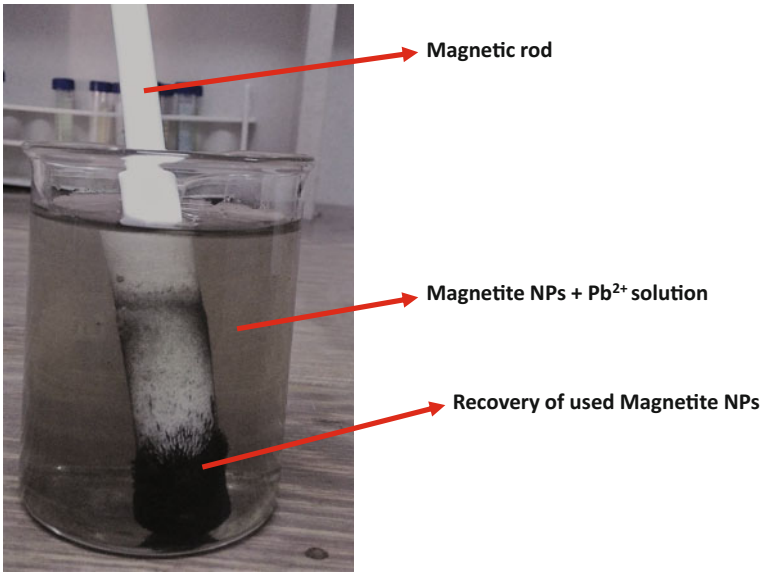

Fig. 3.4 Demonstration of manipulating magnetite NPs using a simple magnet [78]

particular divalent metal cation. Chen et al. used Goethite and hematite nanoadsorbents for the removal of Cu^{2+}. It was reported that both the nanoadsorbents show high adsorption uptake of Cu^{2+} [80]. The obtained maximum adsorption capacity of Cu^{2+} is 149.25 and 84.46 mg/g for goethite and hematite nanoadsorbents, respectively. It also indicates that adsorption of Cu^{2+} was fitted well with Langmuir adsorption isotherm as compared with Freundlich model. Hu et al. [81] investigated maghemite NPs for the removal of Cr^{6+} from waste water. The removal of heavy metal was very fast and within 15 min adsorption equilibrium reached. The adsorption data were analyzed and fitted well by Freundlich isotherm. Cr^{6+} adsorption capacity of maghemite nanoparticles was compared favorably with other adsorbents like activated carbon and clay. Regeneration studies of maghemite underwent six successive adsorption desorption processes. Hu et al. [82] reported the applicability of maghemite (γ-Fe_2O_3) NPs for the removal of Cr^{6+}, Cu^{2+}, and Ni^{2+} from electroplating wastewater. The result indicated adsorption of heavy metals reached equilibrium rapidly within 10 min and Langmuir adsorption isotherm fitted well. Regeneration studies of γ-Fe_2O_3 NPs adsorption desorption processes undergo successfully retained metal removal capacity.

3.4.2.2 Nanosized Titanium Oxides

Titanium dioxide (TiO_2) was recently explored as the adsorbent for the application of heavy metals remediation from water. It has three different crystal structures such as anatase, rutile, and brookite. The brookite type cannot be used in industries due

to its low stability at room temperature and rutile type is easily coagulated at room temperature and its band gap energy is larger than that of anatase type [83]. Therefore, anatase-type TiO_2 used as an adsorbent to investigate the photo adsorption effect was selected. It was reported that bulk and nanoparticle TiO_2 anatase exhibit different chemical behavior, catalytic reactivity, and surface acidity based on their different surface planes [83, 84]. Engates and Shipley [45] investigated adsorption of metals (Pb^{2+}, Cd^{2+}, Cu^{2+}, Ni^{2+}, Zn^{2+}) using TiO_2 nanoparticles and bulk particles. The result indicates successful removal of multiple metals (Pb^{2+}, Cd^{2+}, Cu^{2+}, Ni^{2+}, Zn^{2+}) at solution pH 8 and spiked San Antonio tap water.

Liang et al. [85] investigated new method using TiO_2 nanoadsorbents as solid-phase extractant coupled with Flame atomic absorption spectrometry (FAAS) was proposed for preconcentration and determination of trace Zn^{2+} and Cd^{2+}. The removal of Zn^{2+} and Cd^{2+} at different pH, contact time, elution solution and interfering ions was investigated. Kim et al. [83] performed an experiment for the removal of Cu^{2+} using suspended anatase-type titanium dioxide nanoadsorbents. The adsorption amount increased rapidly with an increasing solution pH and temperature. The obtained adsorption equilibrium constant (K_{ads}) was 0.854 and adsorption isotherm of Cu^{2+} adsorption fitted well to Langmuir adsorption isotherm. Skubal et al. (2002) reported removal of aqueous Cd^{2+} from waste water using TiO_2 nanoadsorbents [86]. More than 90% of Cd^{2+} was removed by both adsorption and reduction processes onto the TLA-modified TiO_2. These removal and reduction processes were catalytic in nature.

3.4.2.3 Nanosized Cerium Oxides

Nano cerium oxides (CeO_2) have been explored as the excellent nanoadsorbents for heavy metals removal from water due to specific surface area, less toxicity, good catalytic activity [87], blue shift in absorption spectra [88], lattice expansion [88], phase transformation [89], and photovoltaic response [90]. Cao et al. [91] developed, hollow ceria nanospheres via microwave assisted hydrothermal method. These ceria hollow nanospheres then were examined for the removal of As^{5+} and Cr^{6+} from water. The obtained maximum adsorption capacity for As^{5+} is 22.4 mg/g and 15.4 mg/g Cr^{6+}, and these values were extremely higher than other ceria nanostructures reported in data. Recillas et al. [92] investigated suspended CeO_2 NPs stabilized with hexamethylenetetramine and used for the removal of dissolved chromium (VI) from water. Several concentrations of adsorbent and adsorbate were tested, trying to cover a large range of possible real conditions. These results can be used to propose this treatment sequence for a clean and simple removal of drinking water or wastewater reuse when a high toxicity heavy metal such as Cr^{6+} is responsible for water pollution. Di et al. [93] synthesized CeO_2 NPs supported on aligned carbon nanotubes (ACNTs) nanoadsorbents and investigated these for the removal of Cr^{6+} from drinking water. The result indicated that CeO_2/ACNTs nanoadsorbents show excellent adsorption of Cr^{6+} and the maximum adsorption

capacity obtained as 30.2 mg/g. These studies put forward that CeO_2/ACNTs have enormous prospective applications in water treatment.

Haron et al. [94] developed cerium modified zeolite P (CeZP) nanoadsorbents and used these for the removal of As^{5+} from aqueous solution. The sorption capacity increased with increasing temperature 25–90 °C. The adsorption of As^{5+} onto CeZP follows Langmuir model and the obtained maximum sorption capacity was 8.72 mg/g (25 °C) and increased to 23.42 mg/g (90 °C), indicating an endothermic process. The results show that nanoadsorbents' CeZP has excellent removal efficiency of As^{5+} from wastewater (wood treatment industry).

3.4.2.4 Nanosized Magnesium Oxides

Recently, numerous works have focused on the synthesis of nanosized magnesium oxides (MgO) of various morphologies for the removal of heavy metals from water. Gao et al. (2008) reported a facile method to fabricate MgO of different morphologies and investigated their influence on the removal of Cr^{6+} and the result indicates excellent adsorption of Cr^{6+}. Also the flowerlike morphology of mesoporous MgO was synthesized and investigated for the adsorption capabilities of Cd^{2+} and Pb^{2+} [95]. The concentration of Cd^{2+} and Pb^{2+} decreased from 100 to 0.007 and 0.05 mg/L, respectively (at equilibrium time: 120 min). It shows that removal of Cd^{2+} and Pb^{2+} using flowerlike MgO was much lower than the Pollutant Dischargeable Standard in China ($Cd^{2+} < 0.01$ mg/L, $Pb^{2+} < 0.1$ mg/L). Koivula et al. [96] reported the used of Cryptomelane type MnO for the removal of Cu^{2+} from wastewaters. The cryptomelane has ion exchange properties for weak acidic ion exchangers that show high-quality selectivity toward transition metals. This shows obtained capacity of 1.3 m mol/g for Cu^{2+} and distribution coefficient as high as $\sim 10^4$ ml/g, promising future application for the removal of metal ions from water. Pakarinen et al. [97] reported two tunnel-structured oxides of nanoporous manganese oxides (OMS-1 and OMS-2) using hydrothermal method for the removal of metals ions and acid using kinetic measurements at different metal ion concentrations. This results show that OMS materials selectively adsorb Cu^{2+}, Ni^{2+}, and Cd^{2+} in the presence of Ca and Mg. The study shows that both the nanoadsorbents were stable and their maximum Cu^{2+} uptake capacity was obtained as 0.9–1.3 m mol/g.

3.4.2.5 Nanosized Aluminum Oxides

Recently, alumina (Al_2O_3) has been explored as the adsorbent for heavy metals, and α-Al_2O_3 is anticipated to be more adsorptive active than Al_2O_3 [98–100]. Its chemical or physical modification of γ-Al_2O_3 nanoparticles with certain functional groups shows donor atoms such as oxygen, nitrogen, sulfur, and phosphorus and is expected to improve their sorption toward heavy metals [100, 101]. Fan et al. [102] reported hydrous amorphous nanoadsorbents Al (HAO), Fe (HFO), and Mn (HMO) oxides show high affinity for heavy metal ions. These nanoadsorbents then

have been investigated for the removal of Pb^{2+} from water, the results show excellent removal efficiency. Pu et al. [103] reported fixing γ-mercaptopropyl-trimethoxysilane (γ-MPTMS) on the surface of γ-Al_2O_3 improve its selectivity toward Cu, Hg, Au, and Pd ions rather than other ions. The mechanism responsible for the selectivity adsorption of metal ions was through the affinity of -SH group, the hydrolyzation of metal ions, and electrostatic adsorption. The result shows the obtained adsorption capacity of modified γ-Al_2O_3 nanoadsorbents were found as 10.4, 16.3, 15.3, and 17.4 mg/g for Hg, Cu, Au, and Pd, respectively. Furthermore, Afkhami et al. [104] reported nanoγ-Al_2O_3-coated sodium dodecyl sulfate modified with 2, 4-dinitrophenylhydrazine (DNPH) was used as adsorbent for removal of heavy metals Pb^{2+}, Cr^{3+}, Cd^{2+}, Ni^{2+}, Co^{2+}, and Mn^{2+}. The result indicates that Freundlich isotherms sorption model fitted well for the adsorption of Mn^{2+}, Pb^{2+}, Cr^{3+}, and Cd^{2+}, ions whereas, Langmuir model fitted well for Ni^{2+} and Co^{2+} ions. The obtained maximum Langmuir adsorption capacity values for Pb^{2+}, Cr^{3+}, and Cd^{2+} ions were 100, 83.33 and 100 mg/g, respectively. Table 3.5 shows various nanoadsorbents for the removal of heavy metals/metalloids from water.

Table 3.5 Comparison of various nanoadsorbents used for aqueous Pb^{2+} remediation

Nanoadsorbents	Heavy metals	References
Fe_3O_4	Pb^{2+}	[74]
Water-soluble Fe_3O_4	Pb^{2+} and Cr^{6+}	[75]
AF-Fe_3O_4	Pb^{2+}, Cd^{2+} and Cu^{2+}	[76]
Fe_3O_4/HA	Hg^{2+}, Pb^{2+}, Cd^{2+} and Cu^{2+}	[77]
Monodisperse Fe_3O_4	Pb^{2+}	[78]
α-FeOOH	Cu^{2+}	[79]
Goethite and hematite (α- Fe_2O_3)	Cu^{2+}	[80]
γ-Fe_2O_3	Cr^{6+}	[81]
γ-Fe_2O_3	Cr^{6+}, Cu^{2+} and Ni^{2+}	[82]
TiO_2	Pb, Cd, Cu, Zn, and Ni	[45]
TiO_2, NPs	Zu^{2+}, Cd^{2+}	[85]
Anatase-type TiO_2	Cu^{2+}	[83]
Acid-modified TiO_2	Cd^{2+}	[86]
Hollow nanospheres CeO_2	As^{5+} and Cr^{6+}	[91]
CeO_2	Cr^{6+}	[92]
CeO_2/ACNTs	Cr^{6+}	[93]
CeZP	As^{5+}	[94]
Mesoporous flowerlike MgO	Cr^{6+}, Cd^{2+}, Pb^{2+}	[95]
Cryptomelane type MnO	Cu^{2+}	[96]
OMS-1 and OMS-2	Cu^{2+}, Ni^{2+} and Cd^{2+}	[97]
Hydrous amorphous Al oxides	Pb^{2+}	[102]
γ-MPTMS modified γ-Al_2O_3	Cu^{2+}, Hg^{2+} and Pb^{2+}	[103]
DNPH modified γ-Al_2O_3	Pb^{2+}, Cd^{2+}, Cr^{3+}, Co^{2+}, Ni^{2+} and Mn^{2+}	[104]

3.5 Polymer and Amino Acid Supported Nanomaterials for Heavy Metals/Metalloid

The fast adsorption and high uptake of heavy metals of nanoadsorbents mainly depend on functional groups and large surface area [47, 105]. Metal and metal oxide and carbon-based nanomaterials have high surface area but don't have to adsorb functional group. To overcome these problems, organic polymer, polyphenylenediamine, holds a large amount of polyfunctional groups (amino and imino groups) can effectively adsorb heavy metal ions, whereas their small specific area and low adsorption rate limit their application [47]. Therefore, new sorbents with both polyfunctional groups and high surface area are still expected. The development of hybrid sorbents has opened up the new opportunities of their application in fast removal of heavy metals from water [47, 106]. Chen et al. [107] prepared magnetite coated 3-aminopropyl trimethoxysilane (APTES). Then, the modified nanoparticles further grated by different heterocyclic groups (HCG) (Fe_3O_4@SiO_2-NH-HCGs). This Fe_3O_4@SiO_2-NH-HCGs were used for the removal of heavy metal cations such as Cu^{2+}, Hg^{2+}, Pb^{2+}, and Cd^{2+}. The result shows 96% removal of heavy metals within 20 min at normal temperature and has good stability and reusability.

Huang and Chen [108] investigated magnetic nanoadsorbent by the covalent binding of polyacrylic acid (PAA) on the surface of Fe_3O_4 nanoparticles and then followed amino-functionalization using diethylenetriamine (DETA) via carbodi-imide activation. This amino-functionalized magnetic nano-adsorbent shows excellent capability for the rapid and efficient adsorption of metal cations and anions from aqueous solutions via the chelation or ion exchange mechanisms. The maximum adsorption capacities and Langmuir adsorption constants were 12.43 mg/g and 0.06 L/mg for Cu^{2+} and 11.24 mg/g and 0.0165 L/mg for Cr^{6+}, respectively.

Cai et al. [109] used polyacrylic acid stabilized amorphous calcium carbonate nanoparticles and used it for the application of heavy metal removal from water. The maximum removal capacities for Cd^{2+}, Pb^{2+}, Cr^{3+}, Fe^{3+}, and Ni^{2+} ions were found to be 514.62, 1028.21, 258.85, 320.5, and 537.2 mg/g, respectively.

Pavlidou and Papaspyrides [110] reported a review on recent advances in the field of polymer-layered silicate nanocomposite. These nanocomposites have attracted both academic and industrial attention because they exhibited dramatic improvement in properties at very low filler contents.

Liu et al. [111] reported hybrid polymers from the ring-opening polymerization of pyromellitic acid dianhydride (PMDA) and phenylaminomethyl trimethoxysilane (PAMTMS) and used it for the removal of Cu^{2+} and Pb^{2+} from water. The result indicates excellent removal efficiency due to novel size and shape dependent properties of nanoparticles. Table 3.6 shows the polymer-based nanoadsorbents.

Table 3.6 Polymer and amino acid supported nanoadsorbents for heavy metal removal from water

Polymer and amino acid supported nanoadsorbents	Heavy metals	References
Fe_3O_4@SiO_2-NH-HCGs	Cu^{2+}, Hg^{2+}, Pb^{2+} and Cd^{2+}	[107]
PAA coated Fe_3O_4	Cu^{2+} and Cr^{6+}	[108]
Polyacrylic Acid Stabilized Amorphous Calcium Carbonate Nanoparticles (ACC)	Cd^{2+}, Pb^{2+}, Cr^{3+}, Fe^{3+} and Ni^{2+}	[109]
Hybrid polymers from the ring-opening polymerization of PMDA and PAMTMS	Cu^{2+} and Pb^{2+}	[111]

3.6 Conclusion

Recent development in nanotechnology has provided much more opportunities to develop nontoxic, cost-effective and environmentally friendly water treatment technology. Nanomaterials have blessed with a numerous numbers of physico-chemical properties that make them attractive for wastewater purification. Many researchers have investigated nanomaterials as sorbents and reported that it is best tools for heavy metal removal, due to their small size unique structure and surface modification. These nanomaterials rapidly remove heavy metals/metalloids ions even at low concentration, with high selectivity and adsorption capacity. The exploitation of new efficient adsorption materials is essential and will continue infinitely, the future of nanomaterials in removal heavy metal ions in wastewater treatment is fairly bright.

References

1. X. Qu, P.J. Alvarez, Q. Li, Applications of nanotechnology in water and wastewater treatment. Water Res. **47**(12), 3931–3946 (2013)
2. T. Rajeswari, N. Sailaja, Impact of heavy metals on environmental pollution. J. Chem. Pharm. Sci. **42**(3), 175–181 (2014)
3. R. Kundra, R. Sachdeva, S. Attar, M. P, Studies on the removal of heavy metal ions from industrial waste water by using titanium electrodes. J Curr. Chem. Pharm. Sc. **2**(1), 11 (2012)
4. M. Jamil, M.S. Zia, M. Qasim, Contamination of agro-ecosystem and human health hazards from wastewater used for irrigation. J. Chem. Soc. Pak. **32**(3), 370–378 (2010)
5. S. Khan, Q. Cao, Y. Zheng, Y. Huang, Y. Zhu, Health risks of heavy metals in contaminated soils and food crops irrigated with wastewater in Beijing. China. Environ. pollut. **152**(3), 686–692 (2008)
6. M.S. Mauter, M. Elimelech, Environmental applications of carbon-based nanomaterials. Environ. Sci. Technol. **42**(16), 5843–5859 (2008)
7. F. Fu, Q. Wang, Removal of heavy metal ions from wastewaters: a review. J. Environ. Manage. **92**(3), 407–418 (2011)

8. L.K. Wang, Y.-T. Hung, N.K. Shammas, *Physicochemical treatment processes* (Springer, 2005)
9. M.E. Ersahin, H. Ozgun, R.K. Dereli, I. Ozturk, K. Roest, J.B. van Lier, A review on dynamic membrane filtration: materials, applications and future perspectives. Biores. Technol. **122**, 196–206 (2012)
10. Y. Xing, X. Chen, D. Wang, Electrically regenerated ion exchange for removal and recovery of Cr (VI) from wastewater. Environ. Sci. Technol. **41**(4), 1439–1443 (2007)
11. A. Bodalo-Santoyo, J. Gómez-Carrasco, E. Gomez-Gomez, F. Maximo-Martin, A. Hidalgo-Montesinos, Application of reverse osmosis to reduce pollutants present in industrial wastewater. Desalination **155**(2), 101–108 (2003)
12. I. Rykowska, W. Wasiak, J. Byra, Extraction of copper ions using silica gel with chemically modified surface. Chem. Pap. **62**(3), 255–259 (2008)
13. F.C. Walsh, G.W. Reade, Electrochemical techniques for the treatment of dilute metal-ion solutions. Stud. Environ. Sci. **59**, 3–44 (1994)
14. G. Batley, Y. Farrar, Irradiation techniques for the release of bound heavy metals in natural waters and blood. Anal. Chim. Acta **99**(2), 283–292 (1978)
15. P. Zhang, H.H. Hahn, E. Hoffmann, Different behavior of iron (III) and aluminum (III) salts to coagulate silica particle suspension. Acta Hydrochim. Hydrobiol. **31**(2), 145–151 (2003)
16. V. Srivastava, C. Weng, V. Singh, Y. Sharma, Adsorption of nickel ions from aqueous solutions by nano alumina: kinetic, mass transfer, and equilibrium studies. J. Chem. Eng. Data **56**(4), 1414–1422 (2011)
17. D. Zamboulis, E.N. Peleka, N.K. Lazaridis, K.A. Matis, Metal ion separation and recovery from environmental sources using various flotation and sorption techniques. J. Chem. Technol. Biotechnol. **86**(3), 335–344 (2011)
18. J. Lee, S. Mahendra, P.J. Alvarez, Nanomaterials in the construction industry: a review of their applications and environmental health and safety considerations. ACS Nano **4**(7), 3580–3590 (2010)
19. I. Ali, New generation adsorbents for water treatment. Chem. Rev. **112**(10), 5073–5091 (2012)
20. H. Pekey, D. Karakaş, M. Bakoglu, Source apportionment of trace metals in surface waters of a polluted stream using multivariate statistical analyses. Mar. Pollut. Bull. **49**(9), 809–818 (2004)
21. R. Verma, P. Dwivedi, Heavy metal water pollution-A case study. Recent Res. Sci. Technol. 5(5) (2013)
22. B.Z. Marg, in *Hazardous metals and minerals pollution in India: Sources, toxicity and management*, (A position paper, Indian National Science Academy, New Delhi, 2011)
23. S.K. Agarwal, *Heavy metal pollution* (APH publishing, India, 2009)
24. A.K. Shukla, Toxicity of heavy metals in the water samples of North-Eastern coal field region of Chhattisgarh. Dermatitis **5**(25), 20 (2014)
25. H. Hu, Q. Jin, P. Kavan, A study of heavy metal pollution in China: Current status, pollution-control policies and countermeasures. Sustainability **6**(9), 5820–5838 (2014)
26. H. Bradl, *Heavy metals in the environment: Origin, interaction and remediation* (Academic Press, 2005)
27. R.A. Wuana, F.E. Okieimen, Heavy metals in contaminated soils: a review of sources, chemistry, risks and best available strategies for remediation. Isrn Ecol. (2011)
28. N. Pourang, Heavy metal bioaccumulation in different tissues of two fish species with regards to their feeding habits and trophic levels. Environ. Monit. Assess. **35**(3), 207–219 (1995)
29. X. Wang, Y. Guo, L. Yang, M. Han, J. Zhao, X. Cheng, Nanomaterials as sorbents to remove heavy metal ions in wastewater treatment. J. Environ. Anal. Toxicol. (2012)
30. X. Wang, T. Sato, B. Xing, S. Tao, Health risks of heavy metals to the general public in Tianjin, China via consumption of vegetables and fish. Sci. Total Environ. **350**(1), 28–37 (2005)
31. L. Järup, Hazards of heavy metal contamination. Br. Med. Bull. **68**(1), 167–182 (2003)

32. J. Pronczuk, M. Bruné, F. Gore, Children's environmental health in developing countries. Encycl. Environ. Health. 601–610 (2011)
33. S.R. Kanel, J.-M. Greneche, H. Choi, Arsenic (V) removal from groundwater using nano scale zero-valent iron as a colloidal reactive barrier material. Environ. Sci. Technol. **40**(6), 2045–2050 (2006)
34. S.R. Kanel, B. Manning, L. Charlet, H. Choi, Removal of arsenic (III) from groundwater by nanoscale zero-valent iron. Environ. Sci. Technol. **39**(5), 1291–1298 (2005)
35. W.H. Organization, *Guidelines for drinking-water quality* (World Health Organization, Geneva, 2011) 2011
36. (BIS) BOIS. Indian standard drinking water speciation. New Delhi 110002 (2012)
37. P. Smedley, D. Kinniburgh, A review of the source, behaviour and distribution of arsenic in natural waters. Appl. Geochem. **17**(5), 517–568 (2002)
38. T.S. Choong, T. Chuah, Y. Robiah, F.G. Koay, I. Azni, Arsenic toxicity, health hazards and removal techniques from water: an overview. Desalination **217**(1), 139–166 (2007)
39. R.A. Goyer, Lead toxicity: current concerns. Environ. Health Perspect. **100**, 177 (1993)
40. H.E. Ratcliffe, G.M. Swanson, L.J. Fischer, Human exposure to mercury: a critical assessment of the evidence of adverse health effects. J. Toxicol. Environ. Health **49**(3), 221–270 (1996)
41. M. Castro-González, M. Méndez-Armenta, Heavy metals: implications associated to fish consumption. Environ. Toxicol. Pharmacol. **26**(3), 263–271 (2008)
42. X. Lv, J. Xu, G. Jiang, X. Xu, Removal of chromium (VI) from wastewater by nanoscale zero-valent iron particles supported on multiwalled carbon nanotubes. Chemosphere **85**(7), 1204–1209 (2011)
43. T. Liu, Z.-L. Wang, X. Yan, B. Zhang, Removal of mercury (II) and chromium (VI) from wastewater using a new and effective composite: pumice-supported nanoscale zero-valent iron. Chem. Eng. J. **245**, 34–40 (2014)
44. F. Pizarro, M. Olivares, R. Uauy, P. Contreras, A. Rebelo, V. Gidi, Acute gastrointestinal effects of graded levels of copper in drinking water. Environ. Health Perspect. **107**(2), 117 (1999)
45. K.E. Engates, H.J. Shipley, Adsorption of Pb, Cd, Cu, Zn, and Ni to titanium dioxide nanoparticles: effect of particle size, solid concentration, and exhaustion. Environ. Sci. Pollut. Res. **18**(3), 386–395 (2011)
46. M. Hua, S. Zhang, B. Pan, W. Zhang, L. Lv, Q. Zhang, Heavy metal removal from water/wastewater by nanosized metal oxides: a review. J. Hazard. Mater. **211**, 317–331 (2012)
47. B. Pan, B. Pan, W. Zhang, L. Lv, Q. Zhang, S. Zheng, Development of polymeric and polymer-based hybrid adsorbents for pollutants removal from waters. Chem. Eng. J. **151**(1), 19–29 (2009)
48. J. Ruparelia, S. Duttagupta, A. Chatterjee, S. Mukherji, Potential of carbon nanomaterials for removal of heavy metals from water. Desalination **232**(1), 145–156 (2008)
49. Y.-H. Li, S. Wang, J. Wei, X. Zhang, C. Xu, Z. Luan et al., Lead adsorption on carbon nanotubes. Chem. Phys. Lett. **357**(3), 263–266 (2002)
50. Y.-H. Li, Z. Di, J. Ding, D. Wu, Z. Luan, Y. Zhu, Adsorption thermodynamic, kinetic and desorption studies of Pb^{2+} on carbon nanotubes. Water Res. **39**(4), 605–609 (2005)
51. J. Hu, C. Chen, X. Zhu, X. Wang, Removal of chromium from aqueous solution by using oxidized multiwalled carbon nanotubes. J. Hazard. Mater. **162**(2), 1542–1550 (2009)
52. K. Pillay, E. Cukrowska, N. Coville, Multi-walled carbon nanotubes as adsorbents for the removal of parts per billion levels of hexavalent chromium from aqueous solution. J. Hazard. Mater. **166**(2), 1067–1075 (2009)
53. K. Pyrzyńska, M. Bystrzejewski, Comparative study of heavy metal ions sorption onto activated carbon, carbon nanotubes, and carbon-encapsulated magnetic nanoparticles. Colloids Surf., A **362**(1), 102–109 (2010)
54. A. Stafiej, K. Pyrzynska, Adsorption of heavy metal ions with carbon nanotubes. Sep. Purif. Technol. **58**(1), 49–52 (2007)

55. S.A. Kosa, G. Al-Zhrani, M.A. Salam, Removal of heavy metals from aqueous solutions by multi-walled carbon nanotubes modified with 8-hydroxyquinoline. Chem. Eng. J. **181**, 159–168 (2012)
56. G. Zhao, J. Li, X. Ren, C. Chen, X. Wang, Few-layered graphene oxide nanosheets as superior sorbents for heavy metal ion pollution management. Environ. Sci. Technol. **45**(24), 10454–10462 (2011)
57. W. Zhang, X. Shi, Y. Zhang, W. Gu, B. Li, Y. Xian, Synthesis of water-soluble magnetic graphene nanocomposites for recyclable removal of heavy metal ions. J. Mater. Chem. A. **1**(5), 1745–1753 (2013)
58. V. Chandra, J. Park, Y. Chun, J.W. Lee, I.-C. Hwang, K.S. Kim, Water-dispersible magnetite-reduced graphene oxide composites for arsenic removal. ACS Nano **4**(7), 3979–3986 (2010)
59. S.-T. Yang, Y. Chang, H. Wang, G. Liu, S. Chen, Y. Wang et al., Folding/aggregation of graphene oxide and its application in Cu 2 + removal. J. Colloid Interface Sci. **351**(1), 122–127 (2010)
60. F. Fu, D.D. Dionysiou, H. Liu, The use of zero-valent iron for groundwater remediation and wastewater treatment: a review. J. Hazard. Mater. **267**, 194–205 (2014)
61. J.E. Van Benschoten, B.E. Reed, M.R. Matsumoto, P. McGarvey, Metal removal by soil washing for an iron oxide coated sandy soil. Water Environ. Res. **66**(2), 168–174 (1994)
62. F. Zhang, Q. Jin, S.-W. Chan, Ceria nanoparticles: size, size distribution, and shape. J. Appl. Phys. **95**(8), 4319–4326 (2004)
63. A. Agrawal, K. Sahu, Kinetic and isotherm studies of cadmium adsorption on manganese nodule residue. J. Hazard. Mater. **137**(2), 915–924 (2006)
64. J.A. Coston, C.C. Fuller, J.A. Davis, Pb^{2+} and Zn^{2+} adsorption by a natural aluminum-and iron-bearing surface coating on an aquifer sand. Geochim. Cosmochim. Acta **59**(17), 3535–3547 (1995)
65. A. Henglein, Small-particle research: physicochemical properties of extremely small colloidal metal and semiconductor particles. Chem. Rev. **89**(8), 1861–1873 (1989)
66. M.A. El-Sayed, Some interesting properties of metals confined in time and nanometer space of different shapes. Acc. Chem. Res. **34**(4), 257–264 (2001)
67. S.M. Ponder, J.G. Darab, T.E. Mallouk, Remediation of Cr (VI) and Pb (II) aqueous solutions using supported, nanoscale zero-valent iron. Environ. Sci. Technol. **34**(12), 2564–2569 (2000)
68. H.K. Boparai, M. Joseph, D.M. O'Carroll, Kinetics and thermodynamics of cadmium ion removal by adsorption onto nano zerovalent iron particles. J. Hazard. Mater. **186**(1), 458–465 (2011)
69. X. Zhang, S. Lin, Z. Chen, M. Megharaj, R. Naidu, Kaolinite-supported nanoscale zero-valent iron for removal of Pb^{2+} from aqueous solution: reactivity, characterization and mechanism. Water Res. **45**(11), 3481–3488 (2011)
70. S.A. Kim, S. Kamala-Kannan, K.-J. Lee, Y.-J. Park, P.J. Shea, W.-H. Lee et al., Removal of Pb (II) from aqueous solution by a zeolite–nanoscale zero-valent iron composite. Chem. Eng. J. **217**, 54–60 (2013)
71. Y. Su, A.S. Adeleye, Y. Huang, X. Sun, C. Dai, X. Zhou et al., Simultaneous removal of cadmium and nitrate in aqueous media by nanoscale zerovalent iron (nZVI) and Au doped nZVI particles. Water Res. **63**, 102–111 (2014)
72. P. Xu, G.M. Zeng, D.L. Huang, C.L. Feng, S. Hu, M.H. Zhao et al., Use of iron oxide nanomaterials in wastewater treatment: a review. Sci. Total Environ. **424**, 1–10 (2012)
73. N.N. Nassar, Rapid removal and recovery of Pb (II) from wastewater by magnetic nanoadsorbents. J. Hazard. Mater. **184**(1), 538–546 (2010)
74. Z. Khayat Sarkar, F. Khayat Sarkar, Selective removal of lead (II) ion from wastewater using superparamagnetic monodispersed iron oxide (Fe_3O_4) nanoparticles as a effective adsorbent. Int. J. Nanosci. Nanotechnol. **9**(2), 109–114 (2013)
75. L. Wang, J. Li, Q. Jiang, L. Zhao, Water-soluble Fe_3O_4 nanoparticles with high solubility for removal of heavy-metal ions from waste water. Dalton Trans. **41**(15), 4544–4551 (2012)

76. X. Xin, Q. Wei, J. Yang, L. Yan, R. Feng, G. Chen et al., Highly efficient removal of heavy metal ions by amine-functionalized mesoporous Fe_3O_4 nanoparticles. Chem. Eng. J. **184**, 132–140 (2012)
77. J.-F. Liu, Zhao Z-s, Jiang G-b, Coating Fe_3O_4 magnetic nanoparticles with humic acid for high efficient removal of heavy metals in water. Environ. Sci. Technol. **42**(18), 6949–6954 (2008)
78. Y. Bagbi, A. Sarswat, D. Mohan, A. Pandey, P.R. Solanki, Lead (Pb^{2+}) adsorption by monodispersed magnetite nanoparticles: Surface analysis and effects of solution chemistry. J. Environ. Chem. Eng. **4**(4), 4237–4247 (2016)
79. P.R. Grossl, D.L. Sparks, C.C. Ainsworth, Rapid kinetics of Cu (II) adsorption/desorption on goethite. Environ. Sci. Technol. **28**(8), 1422–1429 (1994)
80. Y.-H. Chen, F.-A. Li, Kinetic study on removal of copper (II) using goethite and hematite nano-photocatalysts. J. Colloid Interface Sci. **347**(2), 277–281 (2010)
81. J. Hu, G. Chen, I.M. Lo, Removal and recovery of Cr (VI) from wastewater by maghemite nanoparticles. Water Res. **39**(18), 4528–4536 (2005)
82. J. Hu, G. Chen, I.M. Lo, Selective removal of heavy metals from industrial wastewater using maghemite nanoparticle: performance and mechanisms. J. Environ. Eng. **132**(7), 709–715 (2006)
83. M.-S. Kim, K.-M. Hong, J.G. Chung, Removal of Cu (II) from aqueous solutions by adsorption process with anatase-type titanium dioxide. Water Res. **37**(14), 3524–3529 (2003)
84. M.-S. Kim, J.G. Chung, A study on the adsorption characteristics of orthophosphates on rutile-type titanium dioxide in aqueous solutions. J. Colloid Int. Sci. **233**(1), 31–37 (2001)
85. P. Liang, T. Shi, J. Li, Nanometer-size titanium dioxide separation/preconcentration and FAAS determination of trace Zn and Cd in water sample. Int. J. Environ. Anal. Chem. **84**(4), 315–321 (2004)
86. L. Skubal, N. Meshkov, T. Rajh, M. Thurnauer, Cadmium removal from water using thiolactic acid-modified titanium dioxide nanoparticles. J. Photochem. Photobiol., A **148**(1), 393–397 (2002)
87. S. Carrettin, P. Concepción, A. Corma, J.M. Lopez Nieto, V.F. Puntes, Nanocrystalline CeO_2 increases the activity of Au for CO oxidation by two orders of magnitude. Angew. Chem. Int. Ed. **43**(19), 2538–2540 (2004)
88. S. Tsunekawa, T. Fukuda, A. Kasuya, Blue shift in ultraviolet absorption spectra of monodisperse $CeO_2 - x$ nanoparticles. J. Appl. Phys. **87**(3), 1318–1321 (2000)
89. Z. Wang, S. Saxena, V. Pischedda, H. Liermann, C. Zha, In situ x-ray diffraction study of the pressure-induced phase transformation in nanocrystalline CeO_2. Phys. Rev. B. **64**(1), 012102 (2001)
90. A. Corma, P. Atienzar, H. Garcia, J.-Y. Chane-Ching, Hierarchically mesostructured doped CeO_2 with potential for solar-cell use. Nat. Mater. **3**(6), 394–397 (2004)
91. C.-Y. Cao, Z.-M. Cui, C.-Q. Chen, W.-G. Song, W. Cai, Ceria hollow nanospheres produced by a template-free microwave-assisted hydrothermal method for heavy metal ion removal and catalysis. J. Phys. Chem. C. **114**(21), 9865–9870 (2010)
92. S. Recillas, J. Colón, E. Casals, E. González, V. Puntes, A. Sánchez et al., Chromium VI adsorption on cerium oxide nanoparticles and morphology changes during the process. J. Hazard. Mater. **184**(1), 425–431 (2010)
93. Z.-C. Di, J. Ding, X.-J. Peng, Y.-H. Li, Z.-K. Luan, J. Liang, Chromium adsorption by aligned carbon nanotubes supported ceria nanoparticles. Chemosphere **62**(5), 861–865 (2006)
94. M.J. Haron, F. Ab Rahim, A.H. Abdullah, M.Z. Hussein, A. Kassim, Sorption removal of arsenic by cerium-exchanged zeolite P. Mater. Sci. Eng., B **149**(2), 204–208 (2008)
95. C. Gao, W. Zhang, H. Li, L. Lang, Z. Xu, Controllable fabrication of mesoporous MgO with various morphologies and their absorption performance for toxic pollutants in water. Cryst. Growth Des. **8**(10), 3785–3790 (2008)

96. R. Koivula, J. Pakarinen, M. Sivenius, K. Sirola, R. Harjula, E. Paatero, Use of hydrometallurgical wastewater as a precursor for the synthesis of cryptomelane-type manganese dioxide ion exchange material. Sep. Purif. Technol. **70**(1), 53–57 (2009)
97. J. Pakarinen, R. Koivula, M. Laatikainen, K. Laatikainen, E. Paatero, R. Harjula, Nanoporous manganese oxides as environmental protective materials—Effect of Ca and Mg on metals sorption. J. Hazard. Mater. **180**(1), 234–240 (2010)
98. J. Li, Y. Shi, Y. Cai, S. Mou, G. Jiang, Adsorption of di-ethyl-phthalate from aqueous solutions with surfactant-coated nano/microsized alumina. Chem. Eng. J. **140**(1), 214–220 (2008)
99. M. Hiraide, J. Iwasawa, S. Hiramatsu, H. Kawaguchi, Use of surfactant aggregates formed on alumina for the preparation of chelating sorbents. Anal. Sci. **11**(4), 611–615 (1995)
100. G. Chang, Z. Jiang, T. Peng, B. Hu, Preparation of high-specific-surface-area nanometer-sized alumina by sol-gel method and study on adsorption behaviors of transition metal ions on the alumina powder with ICP-AES. Acta Chim. Sin. Chin. Ed. **61**(1), 100–103 (2003)
101. S. Dadfarnia, A.H. Shabani, H.D. Shirie, Determination of lead in different samples by atomic absorption spectrometry after preconcentration with dithizone immobilized on surfactant-coated alumina. Bull. Korean Chem. Soc. **23**(4), 545–548 (2002)
102. M. Fan, T. Boonfueng, Y. Xu, L. Axe, T.A. Tyson, Modeling Pb sorption to microporous amorphous oxides as discrete particles and coatings. J. Colloid Interface Sci. **281**(1), 39–48 (2005)
103. X. Pu, Z. Jiang, B. Hu, H. Wang, γ-MPTMS modified nanometer-sized alumina micro-column separation and preconcentration of trace amounts of Hg, Cu, Au and Pd in biological, environmental and geological samples and their determination by inductively coupled plasma mass spectrometry. J. Anal. At. Spectrom. **19**(8), 984–989 (2004)
104. A. Afkhami, M. Saber-Tehrani, H. Bagheri, Simultaneous removal of heavy-metal ions in wastewater samples using nano-alumina modified with 2, 4-dinitrophenylhydrazine. J. Hazard. Mater. **181**(1), 836–844 (2010)
105. M.-R. Huang, S.-J. Huang, X.-G. Li, Facile synthesis of polysulfoaminoanthraquinone nanosorbents for rapid removal and ultrasensitive fluorescent detection of heavy metal ions. J. Phys. Chem. C. **115**(13), 5301–5315 (2011)
106. X. Zhao, L. Lv, B. Pan, W. Zhang, S. Zhang, Q. Zhang, Polymer-supported nanocomposites for environmental application: a review. Chem. Eng. J. **170**(2), 381–394 (2011)
107. D. Chen, T. Awut, B. Liu, Y. Ma, T. Wang, I. Nurulla, Functionalized magnetic Fe_3O_4 nanoparticles for removal of heavy metal ions from aqueous solutions. e-Polymers (2016)
108. S.-H. Huang, D.-H. Chen, Rapid removal of heavy metal cations and anions from aqueous solutions by an amino-functionalized magnetic nano-adsorbent. J. Hazard. Mater. **163**(1), 174–179 (2009)
109. G.-B. Cai, G.-X. Zhao, X.-K. Wang, S.-H. Yu, Synthesis of polyacrylic acid stabilized amorphous calcium carbonate nanoparticles and their application for removal of toxic heavy metal ions in water. J. Phys. Chem. C. **114**(30), 12948–12954 (2010)
110. S. Pavlidou, C.D. Papaspyrides, A review on polymer–layered silicate nanocomposites. Prog. Polym. Sci. **33**(12), 1119–1198 (2008). doi:http://dx.doi.org/10.1016/j.progpolymsci.2008.07.008
111. J. Liu, Y. Ma, T. Xu, G. Shao, Preparation of zwitterionic hybrid polymer and its application for the removal of heavy metal ions from water. J. Hazard. Mater. **178**(1–3), 1021–1029 (2010). doi:http://dx.doi.org/10.1016/j.jhazmat.2010.02.041

Chapter 4
Recent Trends in the Processing and Applications of Carbon Nanotubes and C-MEMS-Based Carbon Nanowires

Bidhan Pramanick, Merin Mary Meyn, Kavita Shrivastava, Sergio O. Martinez-Chapa and Marc J. Madou

Abstract In this chapter, we review the processing of carbon nanotubes from the first reported work to the present and cover a myriad of CNT applications. For CNT processing, the three most used techniques, i.e., arc discharge, laser ablation, and chemical vapor deposition for both multiwall and single-wall CNTs are detailed. We will learn that these fabrication techniques often need to be adapted to serve a specific application. We analyze processing techniques for CNT application in gas sensors, biosensors, optical sensors, supercapacitors, micro-/nanoelectronics, and in nano-electromechanical systems. Since the poor adhesion between CNTs and substrates often limits their application, we also survey the work of researchers who developed surface modification techniques. Although CNT research is quite a mature field, it still faces major challenges, including making ohmic contacts, selecting for a precise tube diameter and a precise tube length as well as problems with nanotube positioning accuracy. This explains why the large-scale manufacture of CNT devices remains a daunting task. Due to these limitations in the use of CNTs in a manufacturing environment, we propose an alternative, i.e., C-MEMS or carbon-MEMS.

B. Pramanick (✉) · S.O. Martinez-Chapa · M.J. Madou
School of Engineering and Sciences, Tecnologico de Monterrey,
64849 Mexico, N.L, Mexico
e-mail: bidhan.pramanick@gmail.com

S.O. Martinez-Chapa
e-mail: smart@itesm.mx

M.M. Meyn · K. Shrivastava
Avionics, IIST Valiamala, Thiruvananthapuram 695547, Kerala, India
e-mail: merinmeyn@gmail.com

K. Shrivastava
e-mail: kavitashrivastava998@gmail.com

M.J. Madou
Department of Mechanical and Aerospace Engineering, UC Irvine
CA 92697-3975, USA
e-mail: mmadou@uci.edu

Z.H. Khan (ed.), *Nanomaterials and Their Applications*,
Advanced Structured Materials 84, https://doi.org/10.1007/978-981-10-6214-8_4

A common C-MEMS fabrication process starts with photolithography of a high-carbon content photosensitive polymer precursor and it is followed by carbonization, also called pyrolysis, of the patterned polymer. Carbon nanowires (CNWs), fabricated by electrospinning of suspended polymer nanowires and photolithography of the contact pads for the suspended wires to attach too and the subsequent pyrolysis of this hybrid construct, have the potential of alleviating some of the aforementioned problems with CNTs. We review the C-MEMS fabrication process of CNWs in detail, compare their properties with CNTs, and discuss their various applications in this chapter.

Keywords CNT · Arc discharge · Laser ablation · Chemical vapor deposition C-MEMS · CNW · Electrospinning · EMS

4.1 Introduction

Carbon-based micro- or nanostructures are the strongest in nature because of the strength of the carbon–carbon chemical bond and crystallinity that is maintained even down to the molecular scale of a benzene ring. Carbon nanotubes (CNTs), one of the allotropes of carbon, have, compared to diamond, graphite, glassy carbon, buckyballs, and amorphous carbon, the highest electrical and thermal conductivity and are also the strongest and stiffest allotrope to be discovered so far. Thus, CNTs are the obvious choice for fundamental research as well as nanoelectronics and nanoelectromechanical (NEMS) applications. The large surface-to-volume ratios of these one-dimensional structures also make them ideal candidates to solve problems in the sensing arena and heat management say in modern computer systems.

Carbon nanotubes (CNTs) can be envisioned as tiny cylinders composed of rolled-up graphite planes with sp2 hybridized carbon. They come with a length-to-diameter ratio greater than 1,000,000. CNTs were first reported by Sumio lijima in 1991 when he fabricated this carbon allotrope using the arc discharge process [1]. These CNTs are a form of crystalline carbon with extraordinary mechanical, chemical, physical, and electrical properties. They may be single-walled CNTs (SWCNTs), multiwalled CNTs (MWCNTs) or come in the form of ropes composed of arrays of CNTs, depending on how they are produced and processed. There is a wide range of applications of CNTs in electronics, polymers (e.g., as additives), structural materials, energy storage, optics, and sensing to name a few. An often touted application, exploiting the high mechanical strength of CNTs, is their proposed use for the cabling of a space elevator, a concept introduced in the late nineteenth century that allows vehicle transport from the earth surface into space [2]. Heat dissipation is becoming an increasingly crucial problem in modern-day electronic devices and among the various polymers and nanometric materials used for thermal management purposes, CNTs have attracted extensive attention due to their ultrahigh thermal conductivity; about 600–3000 W/(m K) for an individual MWCNT. CNT research still faces challenges, including

making ohmic contacts, selecting for a precise tube diameter and a precise tube length as well as problems with nanotube positioning accuracy. Therefore, we propose an alternative, i.e., carbon-MEMS or C-MEMS.

In the past 15 years, C-MEMS has received a lot of attention because of the simple and inexpensive fabrication steps that are involved. Generally, a C-MEMS fabrication process starts with photolithography of a photosensitive polymer precursor and it is followed by pyrolysis, of the patterned polymer. Carbon nanowire (CNW) devices, fabricated by photolithography of the contact pads, electrospinning of suspended polymer nanowires, and the subsequent pyrolysis of this hybrid construct, have the potential of alleviating some of the aforementioned problems with CNTs. In the process just described, the ohmic contacts between the CNWs and the suspending electrodes are automatically established during carbon–carbon bond formation in the pyrolysis process. The length of the wires is fixed by the distance between the suspending electrodes and the CNW diameter is set by the electrospinning and carbonization process parameters. Suspending the CNWs between carbon electrodes solves the problem of surface interference and makes for better sensor and electronic component performance. The smaller the diameter of the CNWs the more graphitic the microstructure with a resultant higher conductivity and higher Young's modulus (e.g., for a 200 nm CNW, Young's modulus is 350 GPa vs. 1 TPa for a SWCNT) [2]. Although the properties of the suspended CNWs are not comparable yet to those of CNTs, they get better and better as the wire diameter is further decreased. Most importantly, using a variant of electrospinning for writing the polymer precursor pattern, i.e., electromechanical spinning (EMS), we can write CNW networks with an exact control over position, ohmic contacts, length, and diameter of the CNWs.

4.2 CNT Processings

The first reported CNTs, fabricated by Sumio lijima, are shown in Fig. 4.1 [1]. In each tube, the carbon-atom hexagons are arranged in helical fashion about the tube axis. In this section, we will discuss about the most common processing methods of CNTs, which are classified as electric arc discharge, laser ablation, and chemical vapor deposition (CVD).

In the electric arc discharge method, a voltage of 20–25 V is applied between two graphite electrodes resulting in a DC current of 50–120 A and growth of CNTs. This method can easily produce straight and near perfect MWCNTs. Using a carbon anode packed with catalyst, isolated or bundled SWCNTs can also be grown in the discharge chamber by covaporization of graphite and catalyst.

In the laser ablation technique, a pulsed laser vaporizes a composite target of graphite and catalyst resulting in the high yields of SWCNTs. When only a graphite target is used, the resultant homogeneous carbon vapor condenses into capped MWCNTs. Compared with MWCNTs prepared in an arc discharge chamber, the MWCNTs grown in a laser ablation process are relatively short.

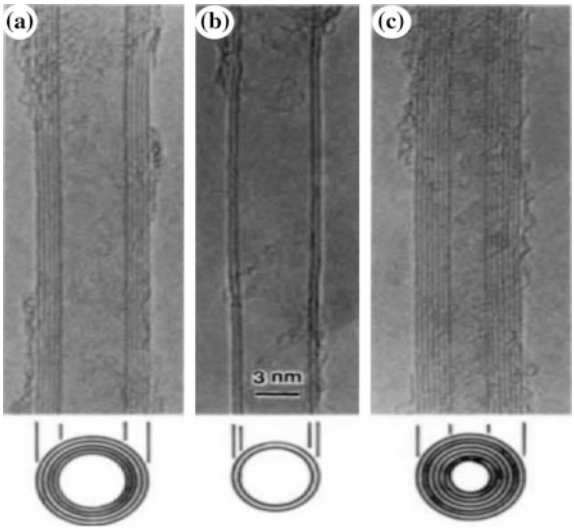

Fig. 4.1 Electron micrographs of first reported CNTs [1]

CVD is a process in which gaseous molecules, called precursors, are transformed into solid materials on a substrate via chemical reactions. For producing CNTs, a hydrocarbon vapor, such as methane, ethylene, acetylene, xylene, benzene, or toluene, is used as the precursor. Unlike the arc discharge method and the laser ablation technique, catalysts are needed in a CVD process. Low-temperature growth of CNTs is possible in CVD when a plasma source is used, called plasma-enhanced CVD (PECVD). The CVD-grown CNTs usually show poor crystallinity and a post-synthesis high-temperature treatment is often used to improve the product quality.

Various research groups have used different precursors for the above-mentioned techniques, and they also have modified the general procedures. In the following subsection, we will report few of the research works on CNT fabrication for each of the three techniques previously introduced.

4.2.1 Arc Discharge Method

In Fig. 4.2, we show a diagram of the arc discharge apparatus used by Kim et al. [2]. Pure graphite (purity of 99.999%) anodes and cathodes were used where the gap between the electrodes was maintained constant at 0.5–2 mm by advancing the consumed anode toward the cathode. A carbon plasma was generated at various currents (10–70 A) and voltages of 18–30 V and at chamber pressure of approximately 30–500 Torr. The chamber and carbon cathode were cooled by a cold water line. The catalyst, ferrocene, was introduced into the furnace by a carrying gas, and the temperature of xylene–ferrocene mixture in the jar was kept at 80 °C by using

an oil bath [2]. It was found that both SWCNT and MWCNT were obtained by this method: MWNTs are observed in the samples collected in the central area of the cathode (Fig. 4.3a) and SWNTs were detected in the flake samples collected around the cathode, and cooling water line (Fig. 4.3b).

The formation of single-walled CNTs by DC arc discharge is reported by Sato et al. [3]. CNTs form when carbon and metal are mixed in the gaseous phase after vaporization and are cooled together into liquid droplets as saturated carbon form SWCNTs during cooling precipitation. The mass synthesis of SWCNTs depends on the amount of liquid droplets formed. Carbon-saturated-metal liquid droplets form in the local thermal equilibrium of plasma, by collision between charged particles at high temperature. For the fabrication of SWCNTs using DC arc discharge, Sato et al. found that high-efficiency of graphitization catalysts, low solubility in carbon, self-assembly of metal, and growth temperature of SWCNTs were all important factors. The precipitation of carbon atoms from their saturated state in the liquid droplets leads to SWCNT growth during cooling and that growth depends on the nature of the catalyst governing both sublimation and solidification temperatures.

Researchers have tried many modifications of the arc discharge process to increase the CNTs yield and quality, and to control the CNT dimensions (diameter, length, purity). In a study, reported by Kanai et al. [4], the fabrication of CNTs is carried out in a gravity-free (0G) arc discharge and an increased yield of SWNTs was demonstrated. In a gravity-free arc discharge process, the convective flow of buffer gas during the arc discharge is reduced, which results in an increase of the high thermostatic volume of the arc flame. The yield of both soot and SWNTs in soot was increased. The SWNT yield in soot under 0G conditions was $\sim$2.2 times larger than that under 1G. In both cases, arc discharge conditions such as arc current, arc gap, and the pressure of gas were maintained constant. The analysis made by Kanai et al. revealed that the diameter distribution of SWNTs was shifted to a larger diameter regime under gravity-free conditions. The annealing process in high thermostatic atmosphere was one of the important factors to selectively synthesize a certain diameter SWNT in high yield.

Keidar et al. [5] proposed synthesis of CNTs by magnetically enhanced arc discharge (MEAD). Obtaining better control over the different properties of

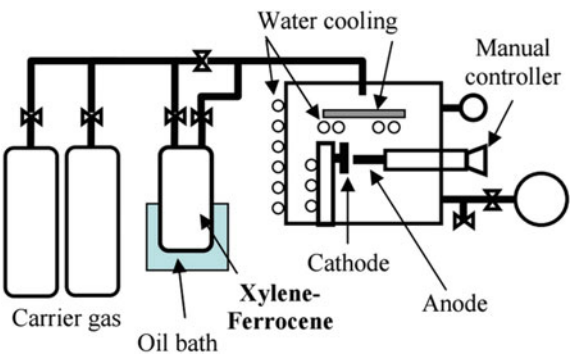

Fig. 4.2 Diagram of the arc discharge apparatus [2]

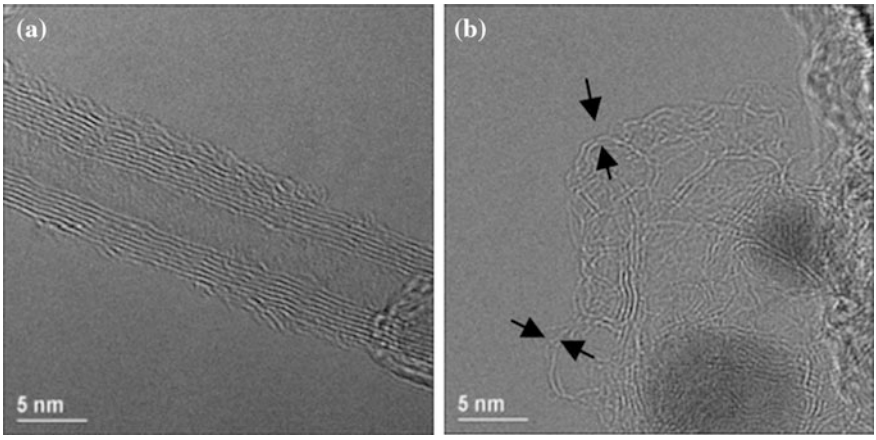

Fig. 4.3 TEM images of samples collected in **a** the central area of cathode and **b** around the cathode [2]

SWCNTs was an important objective during the production of SWCNTs. The application of a magnetic field produces higher plasma densities which lead to changes in the cathode and anode erosion rate. So the carbon deposit produced in MEAD is different from that without magnetic field. Both the length of the SWCNTs and the purity level of the carbon deposit were found to increase upon the application of a magnetic field at the time of the arc discharge. The carbon deposited by arc discharge, due to the magnetic field, mainly consists of isolated and bunched SWCNTs. In Fig. 4.4a, we show the MEAD setup, and in Fig. 4.4b, we show the schematic of an anodic arc discharge process. In Keidar et al.'s work, the interaction of CNTs and the growth phenomenon of CNTs in arc plasma were studied with an emphasis on such important effects like anode ablation that supplies the carbon plasma in an anodic arc discharge technique, and the momentum, charge, and energy transfer processes between nanotube and plasma. The length and charge density of CNTs depend on the plasma density and the electric field intensity in the electrode gap. The most important feature of CNTs produced by the arc discharge process is that they have very few structural defects compared to CNTs produced by other methods. These high-quality CNTs also exhibit a very low degradation of emissivity over time. The purity of the sample with the application of a magnetic field is also high compared to that of the conventional process because of some particular ratio between ion and neutral density may be optimal for the SWNT growth.

Sugai et al. [6] reported the fabrication of SWCNTs and fullerenes using high-temperature pulsed arc discharge. The pulse arc method for CNT production requires high temperature, long pulses, and noble inert gases like argon (Ar), helium (He), and krypton (Kr) as buffer gas. In Fig. 4.5, we show a schematic of the pulsed arc discharge used by Sugai et al. The apparatus consists of a furnace (ISUZU KRO-12K), a quartz tube, electric feedthroughs with insulation quartz tubes, carbon electrodes, a water-cooled trap, and their homemade pulsed HV power supply. The

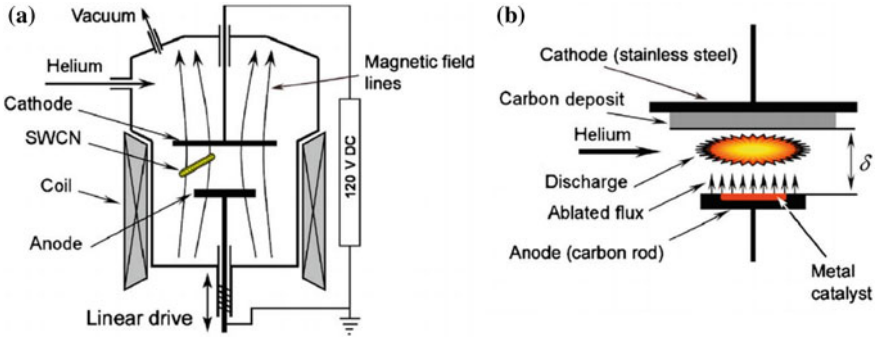

Fig. 4.4 **a** Setup of MEAD and **b** the schematic of the anodic arc discharge [5]

electrodes were located inside the quarts tube and the furnace to produce pulsed arc discharges in high-temperature buffer gases. In this method, metal-doped composite graphite rods (Ni/Co: 0.7/0.7 at. %, and Ni/Y 4.2/1.0 at. %; Toyo Tanso Co. Ltd) and pure graphite rods (Toyo Tanso Co. Ltd) were used as the electrodes. A buffer gas (He, Ar, or Kr) was passed through the quartz tube to thermally anneal carbon clusters and particles produced by the pulsed arc discharge. The temperature of the tube was varied between 25 and 1100 °C by the furnace. The fullerenes, SWNTs, and other graphitic particles drifted within the tube by the gas flow and were collected on the water-cooled copper trap. Fullerenes were identified by high-performance liquid crystal chromatography and transmission electron microscopy. Scanning electron microscopy analysis revealed the production of significant amount of SWCNTs in the carbon soot. The dependence of fullerene concentration on temperature, HV pulse duration, and buffer gas species was measured. The yield

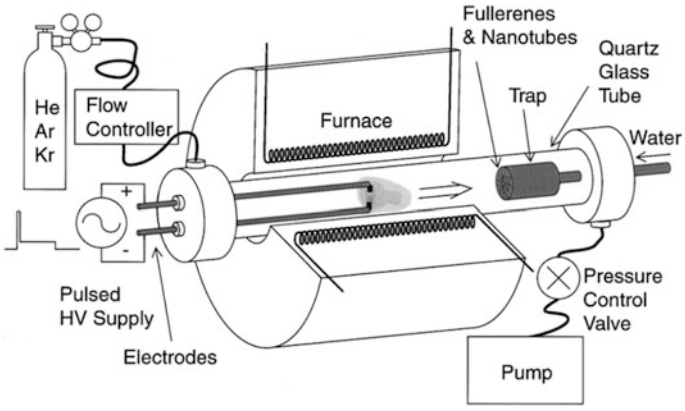

Fig. 4.5 Schematic of pulsed arc discharge [6]

Fig. 4.6 TEM image of single-wall nanotube [6]

of SWCNT production increased with an increase of pulse width duration, while the yield of fullerenes decreased when decreasing the pulse width. A TEM image of a single-wall nanotube is shown in Fig. 4.6.

Ando et al. report on the production of thick-walled CNTs by arc discharge in a hydrogen atmosphere [7]. Although SWNTs might possess very small diameter d ($0.7 < d < 2$ nm), for some applications, such as hydrogen storage and synthesis of fullerene-encapsulated SWNTs, thick SWNTs are advantageous. Ando et al. reported the preparation of thick SWNTs with diameters of 1.4–4 nm. The research group also described the growth mechanism of double-walled carbon nanotubes (DWNTs) coexisted with thick SWNTs. In the experimental setup, metal-doped carbon was used as the cathode and pure carbon was used as the anode and those electrodes were installed horizontally in the reactor. At a pressure of 60–700 Torr, a DC arc voltage was applied and the arc current was changed from 30 to 70 A. The chamber soot was collected and investigated by SEM equipped with an energy-dispersive X-ray analysis system (EDX), HR-TEM, and Raman spectroscopy. Using Fe (1 at.%) as catalyst, a large number of SWNTs were produced in H_2 gas and the yield of SWNTs in the chamber soot became higher with increasing H_2 gas pressure from 60 to 500 Torr and got saturated thereafter. However, SWNTs could not be prepared in pure H_2 gas using Co or Ni catalysts or their combination, unless 1% H_2S gas was added to the ambient.

4.2.2 Laser Ablation Method

Laser ablation method is a promising technique for producing SWCNTs and MWCNTs. This method for synthesizing CNTs was first reported by Guo et al. [8] in 1995. Schematic of their presented apparatus for laser ablation is shown in Fig. 4.7, which consists of a furnace, a quartz tube with a window, a target carbon

composite doped with catalytic metals, a water-cooled trap, and flow systems for the buffer gas to maintain constant pressures and flow rates. A laser beam (YAG or CO_2 laser) was introduced through the window and focused onto the target. The target was vaporized in high-temperature and forms SWNTs. The produced SWNTs were conveyed by the Ar buffer gas to the trap, cooled there, and collected. By this method, high-quality SWNT production, investigation of growth dynamics, and the production of new materials are done with diameter control of CNTs. The laser, having sufficiently high energy density, was capable to vaporize the target material at the molecular level.

Thess et al. [9] also produced the high-yield (>70%) SWNTs using this method by condensing laser-vaporized carbon–nickel–cobalt mixture at 1200 °C. They found that these SWNTs were nearly uniform in diameter and self-organized into ropes, forming two-dimensional triangular structures of 100–500 SWNTs.

The laser ablation method is also used to fabricate devices from separately grown SWCNTs. Chae et al. [10] reported on the concept of material-assisted laser ablation (MALA) for fabrication of SWCNTs. Single-walled carbon nanotubes were grown on quartz. Ferritin catalyst (Aldrich) diluted (1:20 by volume) with deionized water was cast onto the substrate. A high concentration of catalyst on a doublesided polished, quartz substrate was used to obtain a random network of tubes. The catalyst was oxidized in air by heating it up to 800 °C and cooling it back to room temperature. Heating to 925 °C in a 20 SCCM flow of hydrogen and 20 SCCM flow of argon, hydrogen bubbled through ethanol for 15 min producing random networks of individual single-walled tubes. After the growth, the samples were slowly cooled back to room temperature to prevent the quartz substrate from cracking. After the deposition of the target material, a photoablation assistor layer was coated on it. The Chae group used a conventional photoresist, MicroChem AZ4620 or MicroChem S1818, as the ablation assistor to coat the carbon nanotube

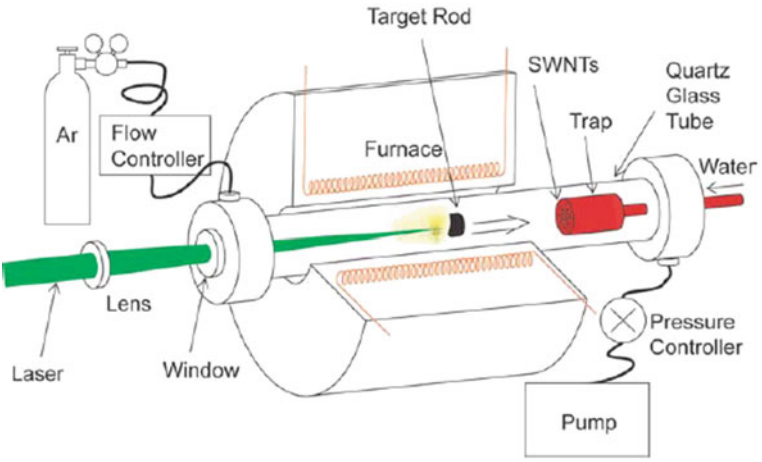

Fig. 4.7 Schematic diagram of laser-furnace apparatus [8]

layer. The concept of material-assisted excimer laser photoablation is shown in Fig. 4.8. Photoresist deposition process caused the resist to be placed under the carbon nanotubes as well as on top of the carbon nanotubes as the liquid-phase photoresist was coated and baked. After the coating of the photoablation assistor, it was ablated using pulsed excimer laser radiation (deep ultraviolet radiation from a KrF excimer laser at 248 nm wavelength). It was found that the carbon nanotube film can be patterned by the low-fluence photoablation process when a photoablation assistor is used, even though the fluence of illumination is lower than the threshold value for direct photoablation. However, the fabricated patterns were not clean as a residual layer remained after the process.

In a later work, Chae et al. found that the residue was formed because the carbon nanotubes were redeposited in the illuminated region where all of the polymer and carbon nanotubes were removed [11]. The concept of the MALA process and schematic illustration of Anvik large-area projection lithography and photoablation system are shown in Fig. 4.9a, b, respectively. Near the boundary of the patterns where some regions were illuminated and some were not, the residue layer was formed due to the exiting debris being attached to the polymer sidewalls. It was concluded that the residue layer at the edge of the pattern could be removed if a thinner polymer was used as the photoablation assistor, so that the ejected debris had a wider exiting angle from the substrate.

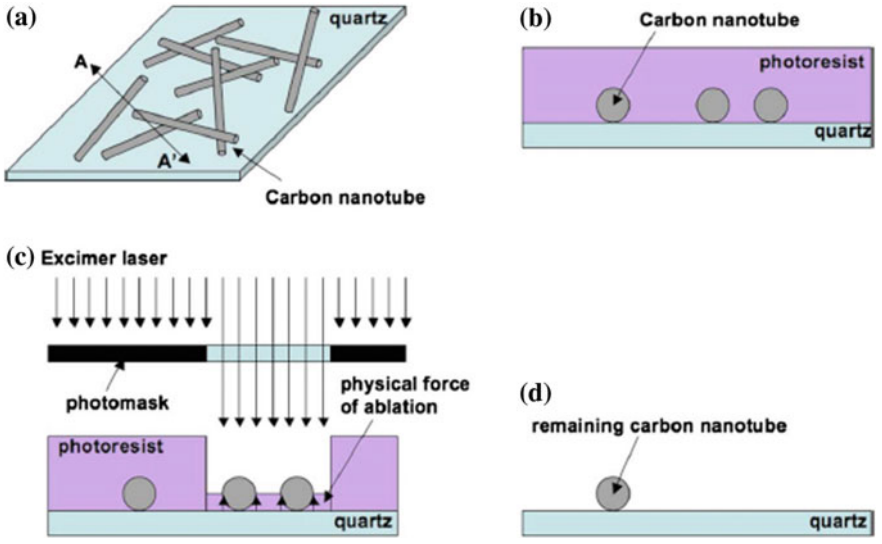

Fig. 4.8 Concept of material-assisted excimer laser photoablation. **a** Carbon nanotubes layer deposition on substrate, **b** photoablation assistor layer coating on the target material, the cross-sectional view of AA′ in **a** is illustrated, **c** ablation of the assistor layer and removal of the target material **d** patterned carbon nanotube film [10]

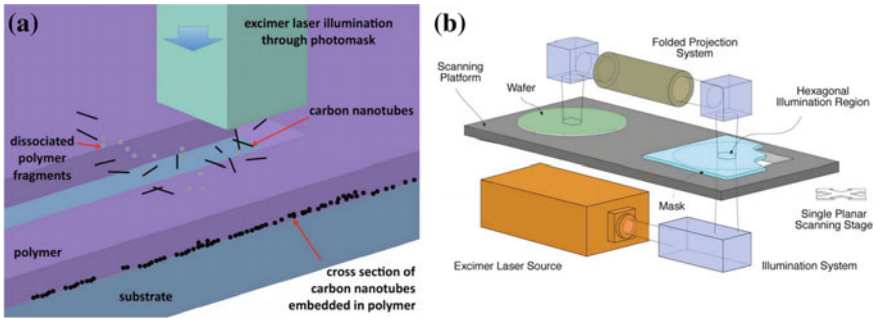

Fig. 4.9 **a** Concept of the MALA process and **b** schematic illustration of Anvik large-area projection lithography and photoablation system [11]

4.2.3 CVD Method

A method classified under CVD for the fabrication of vertically aligned CNT (VACNT) was reported by Wang et al. [12]. VACNT structure was fabricated by a thermal CVD process and metallization of Ti/Ni/Au was used to reduce the interfacial thermal resistance. The fabricated CNT structure was used as thermal interface material (TIM). Thermal conductivity achieved by this technique was about 250 W/(m. K) for bulk VACNT.

Horizontally aligned ultralong single-walled CNTs produced on silicon substrate were reported using fast-heating chemical vapor deposition by Nguyen et al. [13]. Ferric chloride ($FeCl_3$) and ethanol (C_2H_5OH) were used as catalyst and source of carbon, respectively. The fast heating of ethanol at the temperature of 900 °C for 60 min produced high-quality CNTs which were clean, ultralong, highly dense, and straight as parallel lines. The researchers did not find any CNTs on substrate at a growth temperature of 700 °C. Repeating the experiments for 800 °C, they found few CNTs, but not parallel.

The growth of a composite structure consisting of multilayered graphene which was supported by vertically aligned multiwalled CNT was reported by Matsuoka et al. [14]. The fabrication was done by chemical vapor deposition using ethanol as a source of carbon and iron layer as a catalyst. Thicker Fe films produced composite structures and thinner films produced pure vertically aligned multiwalled CNT. Medium thicknesses of Fe produced bundles of vertically aligned CNT fused together at the tip. Application of these types of composite structures includes efficient heat radiation and wiring for very large integrated circuits.

CVD growth of nanotubes, MWCNT, and graphene was affected by the thickness of catalyst film grown on the substrate. Extremely thin layer of catalyst resulted SWCNT, while thicker layer resulted MWCNT and extreme thick layer yielded graphene. For sufficiently thin film, it resulted in granulation of deposited metal film into the particles. Diameter of these particles defined the diameter of CNT and thus number of CNT walls. These particles were responsible for

significant increase in mobility, especially for metal atom near the film surface, allowing the metal film to lower its surface energy by granulation. For thick films, granulation did not occur under CVD conditions due to kinetic effect or due to lower thermodynamic driving force for granulation resulting from the smaller surface-to-volume ratio. Once the metal film was saturated with carbon, graphene formed on its surface. This process was self-limiting because the graphene prevented further carbon from reaching the catalyst (Fig. 4.10).

It is known that the yield and selectivity toward SWNTs, as well as the overall nanotube quality, depend on operating conditions (e.g., temperature, pressure, gas composition) and catalyst preparation parameters (e.g., type of metal used, total loading, addition of a second metal, type of support). Nguyen et al. reported the synthesis of single-walled carbon nanotubes over Co–Mo/Al_2O_3 catalyst by catalytic chemical vapor deposition of methane [15]. Alumina-supported Co–Mo samples prepared by the wet impregnation method were used as catalysts for the synthesis of SWNTs by CVD using CH_4 at 900 °C. The mass ratio of the bimetallic catalyst with a composition of Co: Mo: Al_2O_3 was demonstrated to play an important role in the formation of the SWCNTs obtained. The Co species mainly

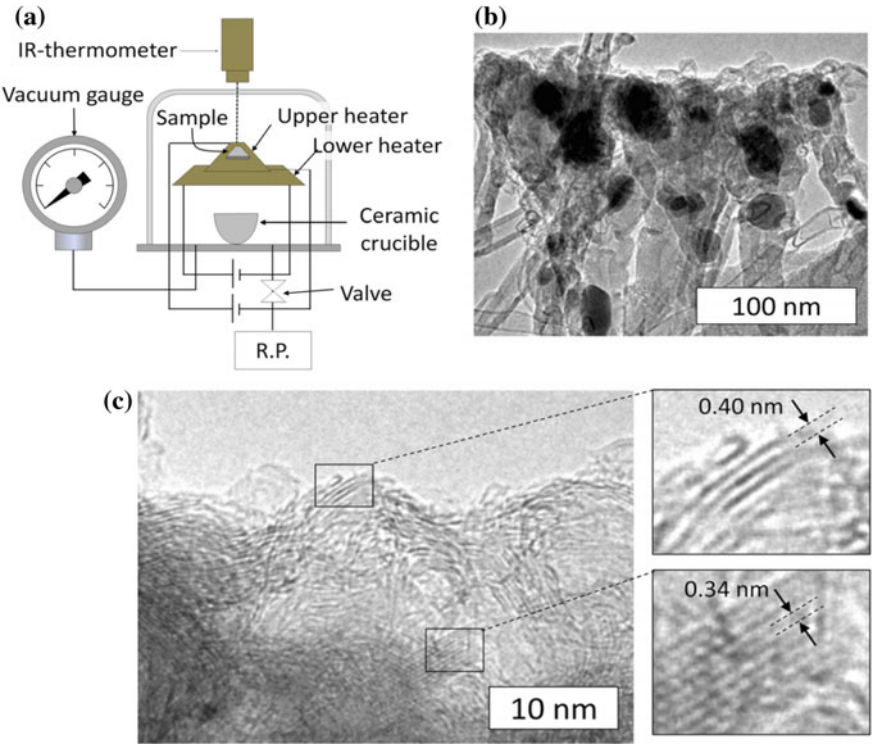

Fig. 4.10 **a** CVD apparatus for CNTs and composite synthesis, **b** TEM image of tip-bundled CNTs and **c** multilayer graphene near the surface of (**b**) [14]

generate the catalytic activity. However, with the increase of cobalt (II) nitrate hexahydrate content compared with that of ammonium heptamolubdate tetrahydrate, CNT density decreases. The diameter (d) was observed to be in the range of 0.76 to 1.69 nm. A TEM image of SWNT is shown in Fig. 4.11.

Synthesis of multiwalled CNT by radio frequency catalytic chemical vapor deposition (RF-CCVD) with bimetallic catalyst was also reported by Ramakrishnan et al. [16]. Highly pure crystalline multiwalled CNTs were synthesized by radio frequency catalytic chemical vapor deposition using acetylene as carbon source and also using bimetallic Fe–Co catalyst supported on CaO at 720 °C. Nanotubes of an average diameter of 14.7 ± 4.76 nm were produced. It was reported in the literature that induction heating is very useful for fabrication of high-quality CNT. The utilization of inductive heating in the synthesis of carbon nanotubes by CCVD significantly reduced the energy consumption, increased heating rate, and provided tighter control of the heating rate compared to external furnace methods.

Lee et al. [17] reported carbon nanotube fabrication by anodic aluminum oxide (AAO) nanotemplate. An AAO nanotemplate was deposited by two-step anodization method followed by deposition of Ni nanoparticles at bottom pore of template. Microwave plasma-enhanced CVD method was used for the growth of carbon nanotube on the template where Ni was used as catalyst and CH_4 as source of carbon. The range of diameter and density of AAO allowed using it as a microfilter template for growth of CNTs and metal or semiconductor nanowires. Planer and cross section of SEM images of CNTs are shown in Fig. 4.12a, b, respectively. AAO nanoporous templates with various pore sizes and depth were introduced to control the dimension and density of the CNTs arrays. They observed that anodization speed was dependent on voltage between anode and cathode. The grown CNTs were of 2 μm length and 50 nm diameter for the average diameter and interpore distance of 65 ± 7 nm and 82 ± 5 nm, respectively. The nanotemplate pore density and thickness were about 2.1×10^{10} pores/cm^2 and 1 μm, respectively.

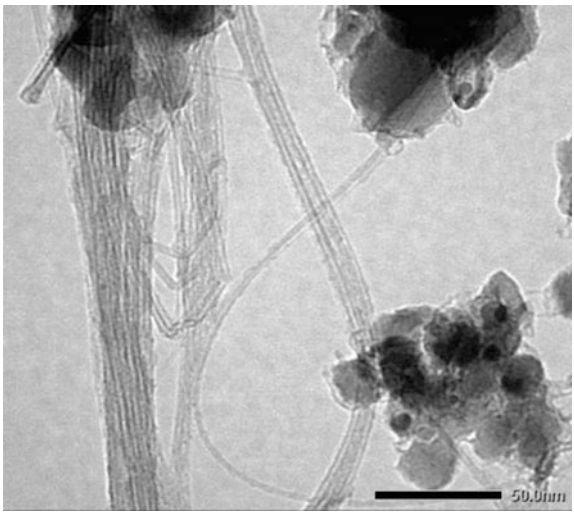

Fig. 4.11 TEM image of SWT grown onto Co–Mo/$A1_2O_3$ catalysts [15]

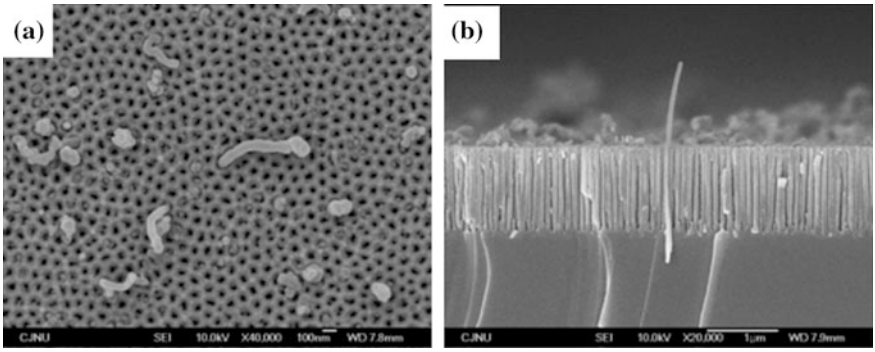

Fig. 4.12 **a** Planer and **b** cross section of SEM image of CNTs growth on AAO nanotemplate with Ni catalyst [17]

The effective methodology of combining focused ion beam and chemical vapor deposition is helpful for synthesis of carbon nanotube, triode-type multiwalled carbon nanotube and fabrication of single-walled carbon nanotube-based nanodevices. Vertically aligned CNTs show application for field emission and nanodevice interconnect. The decrease in width of interconnecting wire, usally aluminum or other metals, increases resistivity of wire which increases the delay. Therefore performance of the devices are affected. So vertically aligned CNTs are one of the replacements for this interconnecting wire. Horizontally aligned CNTs may be used as channel material between two electrodes of a FET; however, placement of CNTs is one of the challenges. Once the gate is fabricated, vertically aligned CNT can also be fabricated in each gate using plasma-enhanced chemical vapor deposition. Fabrication of vertical and horizontal CNTs using focused ion beam and chemical vapor deposition was reported in [18]. In a first step, metal-gated carbon nanotubes were fabricated on the multilayer substrate which contained a catalyst. In a second step, horizontally aligned single-walled carbon nanotubes were grown on the transmission electron microscopic grid. Bundled SWCNTs with a diameter of approximately 1–3 nm were obtained.

Wong et al. [19] reported the synthesis of multiwalled CNTs of uniform diameter using microwave plasma chemical vapor deposition method. Nitrogen (N_2) was used as carrier, and methane (CH_4) was used as carbon source. Thin iron films with different thicknesses, 0.5–5 nm, on silicon substrates acted as catalysts. Atomic force microscopy was used to investigate the relationship between the iron film thickness and the size of the iron clusters formed after the plasma treatment. Scanning and transmission electron microscopy were utilized to study the morphology, structure, and diameter of the as-grown CNTs. With the iron film thickness of 0.5 nm, the CNTs showed a remarkable structural uniformity in terms of diameter (standard deviation was 11.4% of the average diameter d).

Among all fabrication methods of CNT, plasma-enhanced chemical vapor deposition allows fabrication of different types of CNTs on a large area. This result

is difficult to be obtained on a large substrate using conventional microwave plasma source. On the other hand, if RF-excited plasma source is used with large electrodes, it has the drawback of occurrence of standing wave and skin effect which limit the plasma processing uniformity in large-area processes. A slot-excited microwave source produces CNT on plane surface of large size substrate as many slot antennas can be installed in a single waveguide and a number of waveguides can be arranged in parallel manner to produce plasma on large scale. The combination of this plasma production method and plasma-enhanced chemical vapor deposition technique of CNT gives good quality and larger area grown CNT. Fabrication of CNT by slot-excited microwave plasma-enhanced chemical vapor deposition (PECVD) was reported by Shim et al. [20]. A Schematic of experimental set up is shown in Fig. 4.13. Here plasma was produced by a slot antenna at 2.45 GHz microwave injection in CH_4/H_2 mixture. Quality of grown CNTs is controlled by optimization of one of the steps in catalyst treatment as preheating step.

A special processing technique for bulk production of CNTs was reported by Kim et al. [21] CNTs were produced in bulk by thermal induction plasma. A RF inductively coupled thermal plasma was employed to continuously synthesize SWCNT through the direct evaporation of a mixture of carbon black and metallic catalyst inside the plasma plume. The processing system consisted mainly of an RF plasma torch, which generates a plasma jet of extremely high temperature ($\sim$15,000 K), with a high energy density and abundance of reactive species (ions and neutrals). The Kim group did a parametric study which showed that the quality and purity of the SWNT produced are critically affected by the grade of carbon black, plasma gas composition, and metallic catalyst. In general, this process seems well suited for pushing SWCNT production to levels of hundreds of kilograms per year or higher.

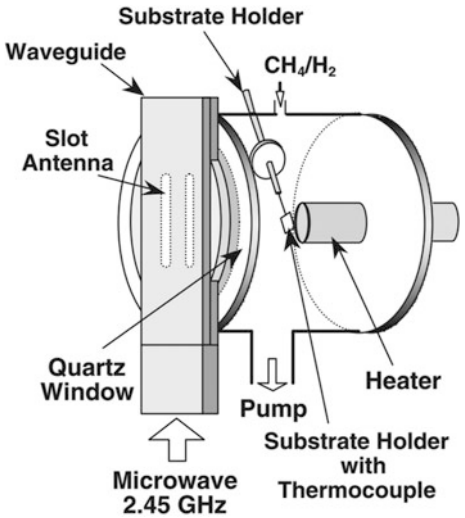

Fig. 4.13 Schematic of experimental setup [20]

4.3 Applications of CNTs

In this section, we analyze the processing techniques for various CNT applications including gas sensors, biosensors, optical sensors, supercapacitors, micro-/nanoelectronics, and nanoelectromechanical systems. Sometimes, the general techniques of CNTs processing are needed to be modified for actual applications. We will discuss in the following about the individual application and the modified fabrication technique if any used.

4.3.1 Gas Sensors

CNT-based gas sensors provide high sensitivity, low operating temperature, rapid response time, and selectivity to various gases. These sensors work on the principle of change in electrical properties caused by transfer of charges between gas molecules and CNT walls and some attached functional groups. CVD methods of fabrication are done at high temperatures and thus not within the temperature range sustainable by CMOS chips. A new low-temperature fabrication process based on "surface-programming assembly" was developed by Huang et al. [22]. Oxidized silicon surface modified to amino-terminated ($–NH_2$) self-assembled monolayer (SAM) with 3-aminopropyltriethoxysilane (APTS) was used as substrate. The substrates were cleaned with ethanol and acetone and dried with nitrogen. Then, these were soaked in the solution of APTS in acetone for 30 min to obtain amino-terminated SAM. The positive charges or amine groups cause adhesion of CNTs to the surface. The samples were cleaned again and the treatment resulted in complete coverage with APTS monolayer. By soaking in nanotube, suspended MWCNTs were deposited on the functionalized surface and samples were rinsed again. After CNTs adhered, interdigitated electrodes (IDE) were fabricated by depositing an Au layer on a SiO_2 surface and using conventional photolithography. Thus, array-type CNT-based gas sensors were developed and were tested for detection of CO and NH_3 at room temperatures. Schematic diagram of deposition of CNTs on the amino silanized SiO_2 surface and optical microscopic images of the CNT-based gas sensors are shown in Fig. 4.14a, b, respectively.

Quick and precise detection is required for highly inflammable and explosive hydrogen (H_2) gas. Metal oxide-based H_2 gas sensors have simple structure and low cost but operate at high temperatures consuming more power. Comparing pristine CNT-based gas sensors to the ones modified with acids, nanoparticles, and polymers, the former lack specificity and have low sensitivity. Dhall et al. used pristine MWCNTs (P-MWCNT) with purity >95% prepared by CVD method for functionalization process to attain increased sensitivity [23]. P-MWCNTs were heated at 400 °C to remove impurities and were dissolved in a mixture of sulfuric acid and nitric acid followed by sonication. The solution was kept at room temperature for 14 h, and then the acid was removed by centrifugation followed by washing in

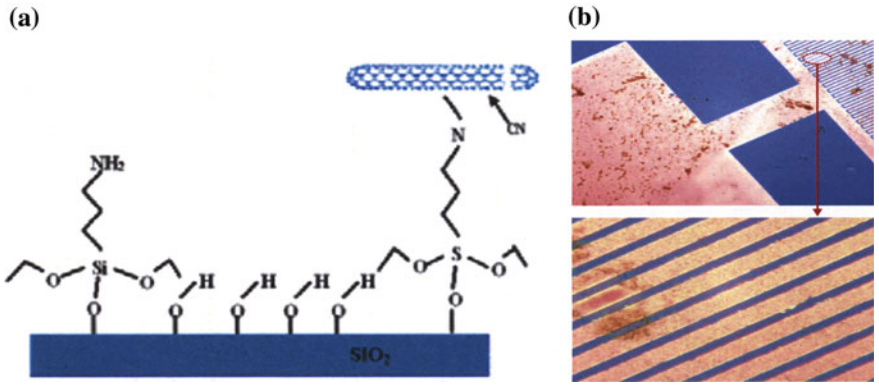

Fig. 4.14 **a** Schematic diagram of deposition of CNTs on the amino silanized SiO_2 surface and **b** Optical microscopic images of the CNT-based gas sensors [22]

deionized water. The P-MWCNTs were dried and again immersed in H_2O_2 for oxidation. In the next, H_2O_2 was removed by washing in deionized water. The functionalized MWCNTs (F-MWCNTs) were drop casted on the sensor which was fabricated on a Si/SiO_2. For the sensor fabrication, a Cr/Au layer was deposited by thermal evaporation and patterned by photolithography to get the desired patterns of interdigitated electrodes (IDEs). Solvent from the drop-casted F-MWCNTs was removed by heating the device, thereby resulting in a network of nanotubes in between electrodes. Schematic diagram of fabricated device and SEM image of fabricated interdigitated electrodes are shown in Fig. 4.15a, b, respectively. F-MWCNTs showed increased electrical conductivity and reduced crystallite size compared to P-MWCNTs. The electrical transport properties of F-MWCNTs increased to thousand times than P-MWCNTs due to the presence of functional groups that increases the number of bands close to the Fermi level, resulting in electron transfer between carbon atoms. Sensitivity of F-MWCNTs increased to 0.8% and recovery time decreases for the same concentration of H_2 gas when compared to responses of P-MWCNTs. Sensitivity of F-MWCNTs shows linear dependence of gas concentration while that of P-MWCNTs was independent of concentration. HR-TEM images of P-MWCNTs and F-MWCNTs are shown in Fig. 4.16a, b, respectively.

Yun et al. [24] reports an inkjet printing method of CNT gas sensor fabrication for massive production with reduced processing steps. SWCNTs of length shorter than 10 μm, synthesized by arc discharge, were dispersed in dimethylformamide (DMF) solution and centrifuged, and the supernatant was decanted for use in inkjet printing. A single-inkjet head equipped with a piezoelectric actuation module was used to eject SWCNT droplet on 4-in. silicon-on-insulator (SOI) wafer. Pt electrodes were patterned by e-beam evaporation followed by liftoff to remove the photoresist. SEM image of patterned CNT films under the Pt electrode and dried CNT by dropping between electrode fingers are shown in Fig. 4.17a, b, respectively. CNT droplets were observed distinctly on the finger electrode with precise

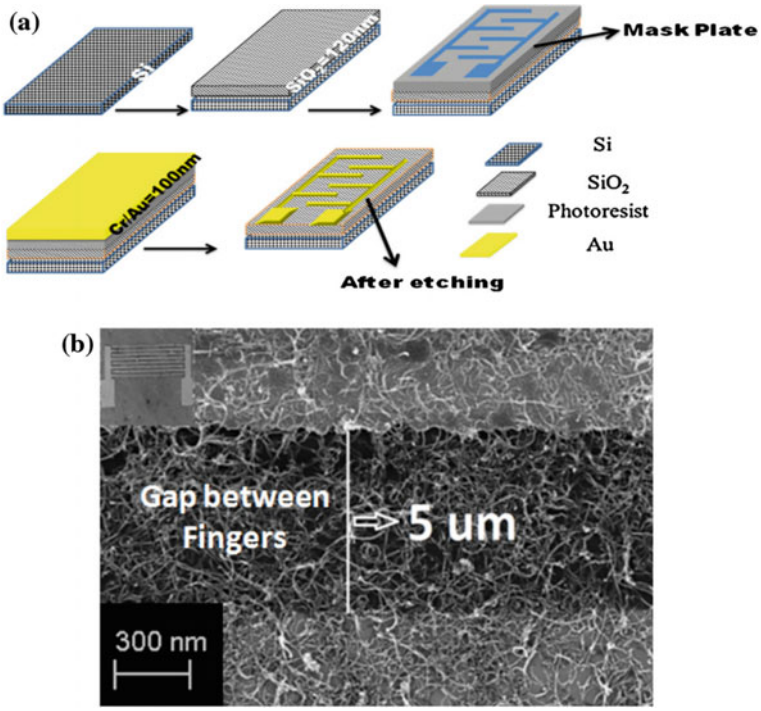

Fig. 4.15 **a** Schematic diagram of fabricated device and **b** SEM image of fabricated interdigitated electrodes [23]

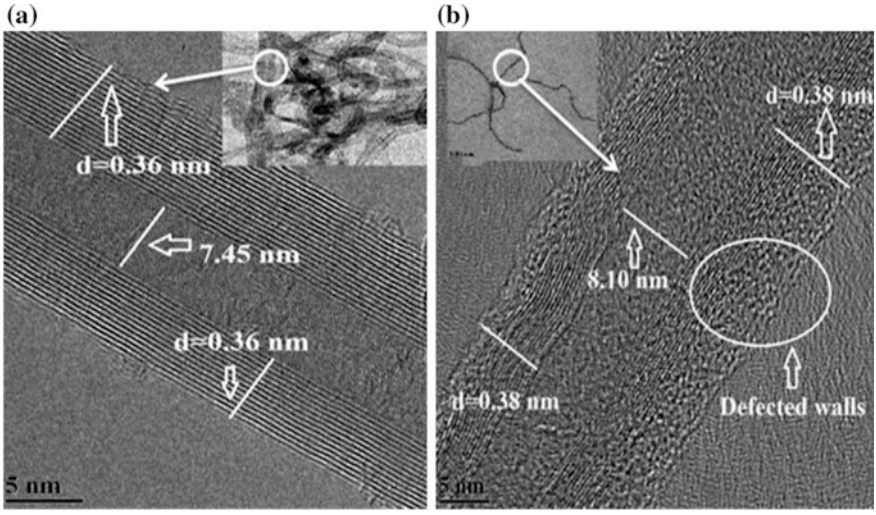

Fig. 4.16 HR-TEM images of **a** P-MWCNTs and **b** F-MWCNTs [23]

control over the number of printing drops and the dropping position. Since SWCNTs adhere to various bare surfaces without any bias due to van der Waals interactions, SWCNT arrays on SOI-wafer were not removed even after liftoff technique providing reliable assembly. Electrode patterning after inkjet printing results in uniform deposition and low contact resistance. The sensor was tested for NO_2 achieving 3% sensitivities with fast recoveries.

Applications of CNT gas sensors depending on conductance change induced by charge transfer from gas molecules absorbed on their surface are limited due to difficulty in detecting gases with low adsorption or low electronegativity. Gas sensors using CNTs have been reported, which work by fingerprinting the ionization characteristic of each individual gas regardless of adsorption energy and electronegativity [25]. The sharp tips of CNTs generate very high electric fields at relatively low voltage, about several hundred volts, which is several-fold lower than the one required with traditional electrodes. Baghgar et al. reported a new type of CNT gas sensor that works in low voltages and low pressures based on bent CNTs grown by rotating the sample relative to applied electric field during growth time. Si samples with (100) orientation for growing CNTs were first cleaned; then, a thin layer of nickel as catalyst was deposited by e-beam evaporation at a base pressure of 3×10^{-6} Torr and temperature of 250 °C. A heat treatment at 730 °C in the presence of H_2 at a pressure of 7 Torr for about 15 min was done in a PECVD system followed by application of hydrogen plasma to form nickel nanoislands. C_2H_2 was introduced as the carbon source for CNT growth at a flow rate of 50 sccm. By rotating the sample, the angle between the direction of applied electric field and the sample changes resulting in the change of growth direction of nanotubes producing bent CNTs with controllable bending angle. A few modifications to the above-discussed process allow the use of as-fabricated device as a gas sensor. A 100-nm-thick SiO_2 layer is thermally grown over Si substrate followed by deposition of a nickel layer. This allows electrical insulation of CNTs from the

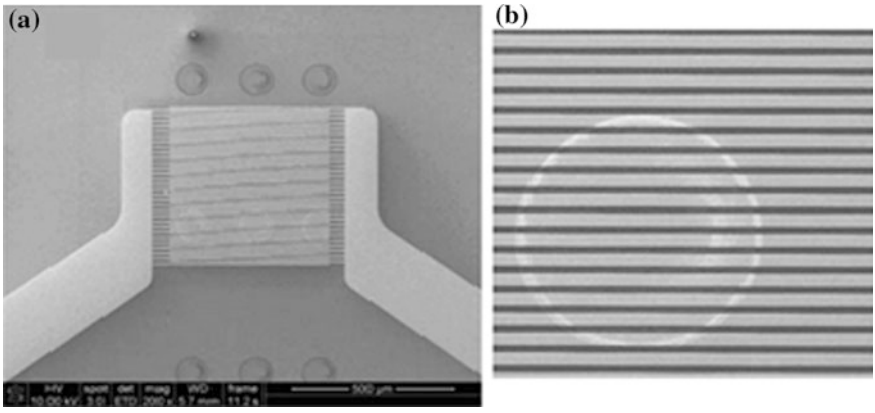

Fig. 4.17 SEM image of inkjet-printed SWCNT gas sensor **a** patterned CNT films under the Pt electrode and **b** dried CNT dropping between electrode fingers [24]

substrate. Then, a 100-nm-thick gold electrode was deposited on the nickel layer using an RF sputtering system. Gold layer was patterned by standard photolithography, over which bent CNTs were grown by the above-discussed process. It was found that by monitoring the current–voltage curve, gas can be identified with far better sensitivity than vertical CNTs due to anode–cathode spacing of less than 100 nm.

Huang et al. [26] reported use of CNTs as gas ionization sensors for ammonia detection based on fingerprinting ionization characteristics of different gases. Strong electric fields generated at the tips of positively and negatively biased CNTs were used to field-ionize or electron impact-ionize ammonia followed by measurement of prebreakdown current. Target gases were detected by monitoring the prebreakdown current. Gas ionization sensor was made of CNT film or zinc oxide (ZnO) rod as one of the electrode and an indium tin oxide (ITO) as the other electrode, both being separated by a glass insulator. The CNT film was grown on silicon substrate by CVD of diameter 30–40 nm. The sensor was placed in a shielded chamber through which air could be pumped out and ammonia could be injected in. It was found that the sensor was selective to ammonia and also showed a linear relationship between prebreakdown current and ammonia concentration with short response and recovery times. CNT films were found to be relatively stable during the measurement process.

4.3.2 Biosensors

Janagama et al. [27] demonstrated a method for fabrication of sensitive protein biosensor using MWCNTs. The developed sensors were used for early detection of prostate-specific antigen (PSA) and breast cancer. CNTs surface modified by carboxylic group was non-covalently attached to surface of clean glassy carbon electrode (GCE). Carboxylation of MWCNTs was done by mixing the carbon nanotube with concentrated nitric acid followed by reflux heating for a few hours. Acid was removed by cleaning in deionized H_2O, and later, nanotube was dried in a stream of nitrogen gas. Glassy carbon was coated on silicon wafers by a photoresist carbonization technique. Biofunctionalization of the above-mentioned structure was carried out by adding anti-S-100 antibodies. The amide group of protein molecule reacts with –COOH groups on MWCNT forming $CONH_2$ having a double bond between carbon and oxygen. The captured protein molecules were hybridized and detected by microscopy.

Higher skin penetration depth of near-infrared (NIR) region makes this frequency range useful for biomedical applications. CNTs are highly attractive for infrared sensors due to their unique structural properties. Semiconducting CNTs can be used as IR detectors as they have bandgap in the IR range. Already developed sensor based on single CNT had relatively low current response because of small sensing area. Enhancing the electric field could be of help, but doing so in the nanoscale is challenging. Fung et al. [28] reported a nanoantenna to increase response of the

sensor with a tenfold increase in photocurrent. Nanoantenna consisted of two symmetric thin metal wires separated by a nanometric gap. Illumination by an infrared source generated a standing wave current pattern along the metal wires. Field in the vicinity of electrically conducting object was enhanced and the CNT sensing element was aligned to the position of maximum estimated field near the antenna, i.e., the point perpendicular to antenna axis. For fabrication, a pair of Au microelectrodes was evaporated on quartz substrate by thermal evaporation and titanium was used to improve the adhesion of gold to the substrate. A drop of CNT suspension was dispersed on the substrate, and CNTs were formed between the electrodes by dielectrophoretic force on application of AC voltage. CNT-metal contact has to be aligned with the maximum field position of antenna. Position of CNT-metal electrode was estimated by AFM. A parylene C thin-film layer was conformally coated at room temperature on CNT for separating the antenna and sensor, also covering CNTs from contamination. The titanium layer for antenna was then patterned and aligned to the sensing region by e-beam lithography. Finally, a pair of thin metal wires was deposited over parylene C layer by thermal evaporation followed by liftoff process to form the nanoantenna. Schematic structure of a CNT-based IR detector with a nanoscale antenna is shown in Fig. 4.18a and AFM images of the fabricated CNT-based IR detector are shown in Fig. 4.18b.

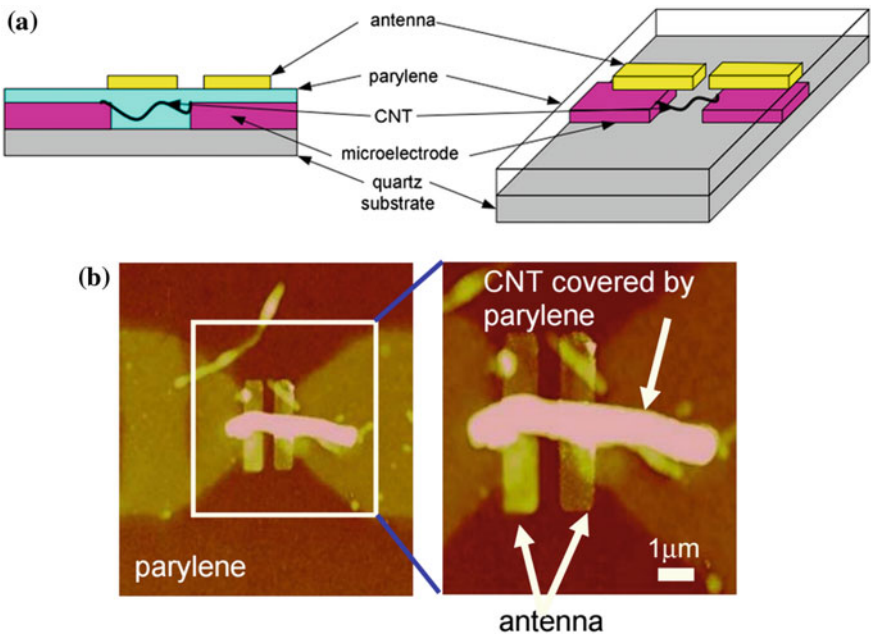

Fig. 4.18 **a** Schematic structure of a CNT-based IR detector with a nanoscale antenna and **b** AFM images of the fabricated CNT-based IR detector with the nanoantenna where parylene thin film was coated between the antenna and CNT [28]

4.3.3 Optical Sensors

Sharma et al. [29] reported near-infrared (NIR) sensors based on SWCNTs on flexible substrates. Sodium dodecyl-benzene sulfonate (SDBS) aqueous solution (formed by mixing SDBS with deionized water) was mixed with SWCNT. The solution was then sonicated for 45 min with a spherical tip at 25 °C for dispersing SWCNT in the aqueous phase. This was followed by centrifugation where heavier particles were found to settle down and then extracted for thin-film deposition on flexible polymer substrate to form the NIR sensor. Substrate was cleaned by ethanol and DI water and dried in N_2. It was covered with an isolation foil with a small window and the sonicated SWCNT was drop casted. The films were dried overnight, and the isolation foil was carefully removed. It was observed that the absorption peaks occurred at the same wavelength for all samples independent of wt % of SWCNT resulting in a uniform dispersion. Optical properties of the dispersions and films were considered. A linear response with a bias up to 5 V was shown for photocurrent. When intensity of the laser increased, more photons were absorbed and more excitons (bound electron-hole pairs) were generated resulting in large current. It was observed that low SWCNT wt% films were more sensitive to NIR illumination than the high wt% SWCNTs. The sensitivity increases with increasing NIR illumination intensity as more photons were absorbed causing large change in photocurrent. The device can be considered reliable as the film showed stable and reproducible response during long-time measurement.

4.3.4 Microelectronics

Earlier developed CNT field-effect transistors (CNFET) were mostly of p-type or ambipolar which was either due to hole doping by environmental oxygen or lower Schottky barrier for hole current at metal-CNT contact. However, to achieve operations of CMOS, well-defined n-type transistors were also needed which requires more reliable and practical methods of fabrication than those already available. Oh et al. reported that the deposition of Al layer on top of a CNT by sputtering under high vacuum gave *n*-type transport properties in CNFET [30]. A schematic of the device structure is shown in Fig. 4.19. High-purity double-walled CNT (DWCNT) and SWCNT were synthesized by hydrogen arc discharge method with diameters in the range of 2 to 4 nm and 1 to 2 nm, respectively. A droplet of dichloroethane containing CNTs was spun over Si substrate with 300-nm-thick thermally grown SiO_2 layer. 30 nm of Pd was deposited by magnetron sputtering at a base pressure of 10^{-8} Torr to form source and drain regions, followed by a standard liftoff process. Then, 30-nm-thick Al was deposited by the same method as Pd. The electrical transport properties of the device at room temperature in vacuum condition showed n-type behavior. It was found that the device formed with Al layer deposited by e-beam deposition at base pressure of

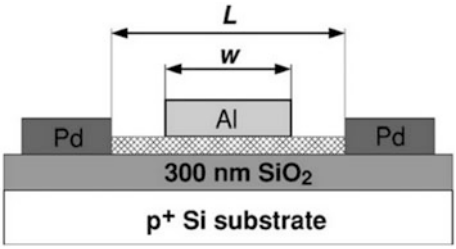

Fig. 4.19 Schematic of the device structure [30]

10^{-6} Torr did not show transfer from *p*-type behavior to *n*-type due to oxidation of Al layer during or after film deposition. This may cause holes to be induced rather than electrons, as oxidized Al surface has work function closer to that of Au. *P*-type behavior of samples is largely due to the large work function of the Pd electrodes causing the Fermi level to be located close to the valence band edge. Ambipolar behavior is due to smaller bandgap edge of large diameter CNT. However, *n*-type doping was obtained due to electron doping caused by the deposited Al layers, as electron charge transfer occurs from Al layer to CNT when unoxidized Al particles are in the vicinity of CNT. This results in the Fermi level being close to valence band edge near Pd electrode and conduction band edge under deposited Al layers causing sharp band bending near the edges of Al layers.

Field-effect transistors (FETs) using SWNTs as a channel are compatible with flexible plastic substrates in the form of thin-film transistors (TFTs) with random networks or aligned arrays of SWNTs. The SWNT films can be formed onto plastic substrates by low-temperature processes such as solution casting and transfer printing. Nouchi et al. [31] fabricated *n*- and *p*-type SWNT TFTs employing solution processes and succeeded in constructing CMOS logic circuits. In this study, *n*- and *p*-type TFTs were fabricated on different substrates by PEI (polyethyleneimine) and (tetracyano-*p*-quinodimethane) TCNQ doping, respectively. By employing an inkjet printing method, it was possible to integrate SWNT TFTs of both polarities onto the same substrate by local deposition of donor or acceptor molecules.

Transparent conductive films (TCF) find a wide range of applications as electrodes for resistive touch screen, projected capacitive touch screen, electronic paper display, as materials for organic light-emitting diode (OLED) displays, OLED lighting, and photovoltaics. CNTs are one of the alternatives for ITO, one of the widely used TCF materials, as indium is a rare metal and ITO being a brittle inorganic material oxide may result in bending, crack formation, and very low electric conductivity of ITO-based TCFs [32]. Compared to SWCNTs and MWCNTs, DWCNTs have the advantage of being transparent electrode material as they can be easily purified by simple chemical treatment. DWCNTs with purity >90% and diameter in range of 1.5 to 2 nm, synthesized by catalytic high-temperature CVD, were chosen as the starting material. Carboxyl methyl cellulose sodium salt (CMC) was chosen as the dispersant. DWCNT was dispersed in it using a tip-type sonicator and ultracentrifugated, and the sediment was

redispersed in water. The DWCNT dispersion was then diluted in water, and the solution was cast on a polyethylene terephthalate (PET) film and heated at 125 °C for 1 min. It was observed that by controlling factors such as CNT length, dispersion states, and weight-rations of the dispersant CMC/DWCNT, TCFs of low surface resistivity (320 Ω sq^{-1}) and 94% transmittance could be obtained without the use of any chemical doping for reducing surface resistivity.

For applications of nanotubes in microelectronics, the most interesting features are the ballistic transport of electrons and the extremely high thermal conductivity along the tube axis. However, high growth temperature (>600 °C) is incompatible with microelectronics along with poor adhesion between CNT and substrate. The open-ended multiwalled CNT arrays could carry higher current density than close-ended CNTs, since the internal walls can participate in the electrical transport. Multichannel ballistic transport could be achieved if the caps of the CNTs are removed (opened), improving CNT electrical conductance. Zhu et al. [33] reported a process for opening CNTs by water-assisted selective etching. They successfully applied the transfer technology to assemble the fine-pitch CNT bundles on the copper substrate with diameter, aspect ratio, and pitch of 25 μm, 4, and 80 μm, respectively. Due to the low process temperature, CNT transfer technology shows promising applications for positioning of CNTs on temperature-sensitive substrates, and for the fabrication of field emitters, electrical interconnects, thermal management structures in microelectronics packaging. Another method for improving adhesion between CNT and substrate was specified by Huang et al. [34] wherein they applied self-assembled monolayer of 3-aminopropyltriethoxysilane (APTS) to modify TSMC CMOS chip surfaces and increase adhesion. The chemical adhesion of CNTs to the surface treated was due to the presence of positive charges or amine groups on the surface. Zhu et al. claimed that the sensor device output measured with different voltage supply by using picoammeter revealed a CNT-based sensor device that could be integrated into CMOS IC at low temperature.

CNTs can function as active material in nanoelectronics and nanoelectromechanical systems for which integration of CNT with microsystems is required. CNT-microsystem integration is hindered by high process temperature required for the same, as processed MEMS/CMOS devices cannot be exposed to temperatures above $\sim$300 °C in post-processing. Existing methods of integration are not feasible as an industrial process due to factors like cost, batch production. Aasmundtveit et al. [35] proposed a method based on CVD and localized heating. A microstructure of two suspended polysilicon microbridges, 5 μm wide and 160 μm long, separated by 15 μm and suspended 3.5 μm above the substrate, was chosen. Fe and Ni were deposited to serve as catalysts. A local electric field was established between the two bridges to guide the direction of growth along with resistive heating on the growth structures. Acetylene (C_2H_2) was chosen as the carbon source as it allowed CNT CVD growth at somewhat lower temperatures than other carbon-containing gases. Temperature at the center of the microbridge was monitored by measuring the resistance, as doped Si showed temperature-sensitive resistivity. Direct Si-CNT integration depicted a potential method for a nanomaterial-based NH_3 sensor.

4.3.5 Supercapacitors

Energy storage capacity of supercapacitors can be increased by using electrodes with large specific surface area and CNT has suitable properties for such applications. CNT forests can have a vertically aligned conformation, and thus, transfer of ions between individual CNTs occurs with ease. Various methods for fabrication have already been reported, and the study by Jiang et al. [36] was advantageous in various aspects compared to previous works. The fabrication started with e-beam evaporation of molybdenum (Mo) over thermally oxidized silicon substrate followed by e-beam evaporation of catalyst (Al and Fe). Then, the substrate was placed in a vacuum quartz tube, purged with hydrogen and raised temperature to 720 °C under atmospheric pressure. Once the temperature was stabilized, hydrogen and ethylene were flown through the quartz tube and CVD was occurred at constant temperature and pressure. As a result, a vertically self-aligned CNT forest was grown and contacted by Mo, the metal current collecting layer. Preferred bending direction was obtained by mechanically pressing the CNT forest. Then, it was submerged in DI water until the CNT-Mo layer was detached from the substrate as adhesion between Mo and oxide layer was weak. The CNT-Mo structure was picked up by a flexible substrate in an aqueous environment and then dried completing the fabrication process. It was observed that there was no change in the height and morphology of CNT forests after 40 electrochemical cycling tests. Since the product supposed to function as a mechanically flexible energy storage device, change in resistance with bending was tested and was found to be essentially stable. The prototype supercapacitor was measured to have a specific capacitance of 7 mF/cm^2. The released CNT-Mo layer patterned into comb drive fingers floatingly loosely above the growth substrate is shown in Fig. 4.20.

4.3.6 Mechanical Properties of Measurements

Hu et al. [37] presented a simple molding process to realize a capacitive-type flexible sensor using 3D CNT interdigitated electrodes. These sensors can be used

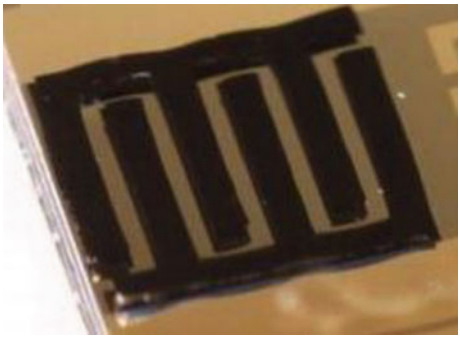

Fig. 4.20 Released CNT-Mo layer patterned into comb drive fingers [36]

for the detection of strain, bending curvature, tactile force, and proximity distance. Silicon substrate was the starting material, over which oxide was deposited and patterned for defining deep reactive ion etching (DRIE) regions. Then, Cr film was evaporated and patterned as the etching mask that defined the support structures for tactile/proximity sensors followed by patterning of photoresist that defined the shape and gap of finger electrodes, resistors, electrical routings, and supports. DRIE process patterned the trenches of the supports on the silicon substrate. Wet etching of Cr opened the finger electrode region. This substrate was the mold for the processes to follow. Fe film of 10 nm thick was deposited and patterned by a photoresist liftoff process, which acted as catalyst for CNT growth. Acetylene pyrolysis in a gas mixture of NH_3 and C_2H_2 at 800 °C made the CNT growth to a height of about 70 μm in regions with catalyst Fe film, filling the trenches and obtaining a highly structured 3D surface topography. SEM micrographs of top and cross-sectional views of the Si substrate patterned by DRIE with patterned Fe catalyst are shown in Fig. 4.21a, b, respectively. A polymer molding process was done to form CNT-polymer composite structures. Amorphous carbon, the by-product of pyrolysis process, was removed by O_2 plasma as it would increase adhesion between polymer, poly-dimethylsiloxane (PDMS), and Si and cause difficulty in their de-molding. In the polymer molding process, PDMS was poured onto Si mold with 3D CNTs, and air trapped inside the trenches was fully removed by a vacuum pump. The attached molds were cured at 100 °C for 1 h, de-molded and the composite structures were manually peeled off by tweezers and released from the Si substrate.

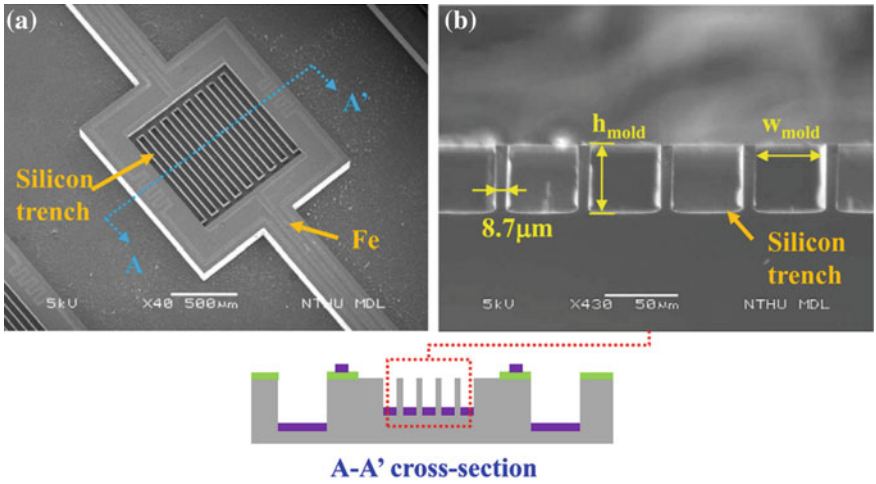

Fig. 4.21 SEM micrographs of **a** top and **b** cross-sectional views of the Si substrate patterned by DRIE with patterned Fe catalyst [37]

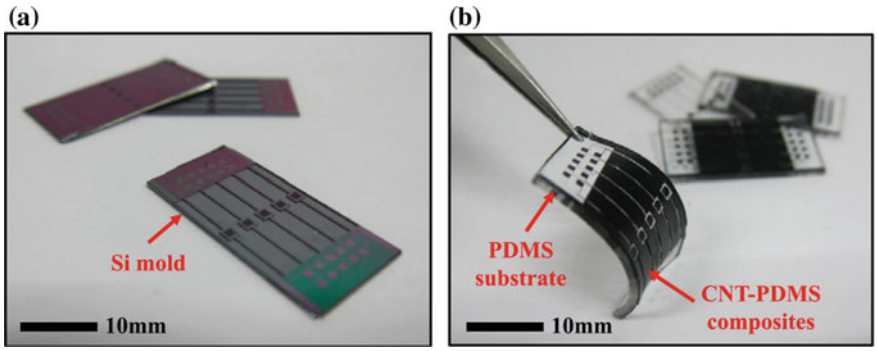

Fig. 4.22 Optical images of **a** the fabricated Si mold and **b** the flexible sensor [37]

The patterned CNTs were transferred to flexible PDMS substrate. Optical images of the fabricated Si mold and the flexible sensor are shown in Fig. 4.22a, b, respectively.

It is known that a mechanical deformation on freestanding SWCNTs leads to strong change in conductance. An AFM tip was used to deform a SWCNT, and it was found that conductance decreased by two orders of magnitude caused by change of bonding configuration from sp^2 to sp^3. The very high elasticity covalent C–C bonds return to its original state even after strong deformation. Stampfer et al. [38] reported a simple configuration of a contacted suspended SWCNT placed under a freestanding cantilever. Deformations of the cantilever due to out-of-plane forces caused the underlying CNT to deform and show change in conductance. Raw SWCNTs were dispersed in aqueous solution of sodium dodecyl sulfate (SDS) surfactant, treated in sonicator, and centrifuged. The upper 75–80% of supernatant was decanted leaving micelle-suspended SWCNT solutions. Si substrate with 1.5 μm oxide layer was spin coated with thin resist layers to enhance liftoff process and was baked at 180 °C. The surface was developed and followed by deposition of 5 nm Cr and 30 nm Au. After lifting off, The surface was functionalized with DAS, *N*-[3-(trimethoxysilyl)propyl]-ethylene-diamine (97%), prior to deposition of CNT, as the Coulomb attraction between positively charged surface due to NH_3^+ and negatively charged CNT resulting from SDS suspension (SO_3^-) enhances deposition. Spin coating followed by e-beam lithography in two steps was used to structure individual devices. First, big core structures that act as anchors in the final device were exposed followed by very fine structures. After development, 0.6 nm Ti and 30 nm (or 50 nm Au) were evaporated followed by liftoff, where Ti layer helps to reduce contact resistance of electrodes. The structure was released by HF etch followed by critical point drying to avoid sticking of freestanding caused by surface tension.

4.3.7 Carbon Electrodes

Electrochemical capacitors (ECs) or "supercapacitors" have many potential advantages in electrical devices by virtue of their large capacitance, high power, and long cycle life. CNTs are suitable materials for polarizable electrodes due to their properties. Ma et al. reported processing of CNT solid electrodes and effect of chemical treatment on the performance of these electrodes in ECs [39]. CNTs were prepared catalytically using Ni catalyst, and nanotubes of diameter 20–30 nm and length up to several tens of microns were obtained. A mixture of CNTs and phenolic resin was molded under a certain pressure. Using the new polarizable electrodes, ECs with specific capacitance of about 15–25 F cm^{-3}, low apparent leakage currents, and low DC resistance were obtained with a single-cell device when the discharge current is about 10 mA. Chemical treatment of the carbon nanotubes and the electrode enhanced the performance of the capacitors. This improvement was related to the surface condition of the carbon nanotubes. It was practical to fabricate ultrahigh capacitors by using such technique. SEM image of fabricated CNT electrode is shown in Fig. 4.23.

Sasaki et al. [40] proposed a direct, planar biological superfunctional nanoelectronic device using CNT electrodes and a standard semiconductor fabrication technique. It performed direct measurement of the electron transport between DNA molecules using as-fabricated CNT electrodes. MWCNTs prepared by arc discharge method and dispersed in solvent were used for the process. The solution containing CNT was coated on Si/SiO_2 wafer by spin-rotational method. Electrical contacts were made with Ti/Au by liftoff process. Focused ion-beam bombardment (FIBB) was used to create a very short channel between the sharply cut edges of the electrode CNT resulting in two closely spaces nanoelectrodes. DNA molecules were then placed between CNT electrodes by electrostatic trapping followed by drying the samples in vacuum and electrical measurement. The current–voltage (*I*–*V*) characteristics showed a very short hopping distance of 3.8 Å, which is similar

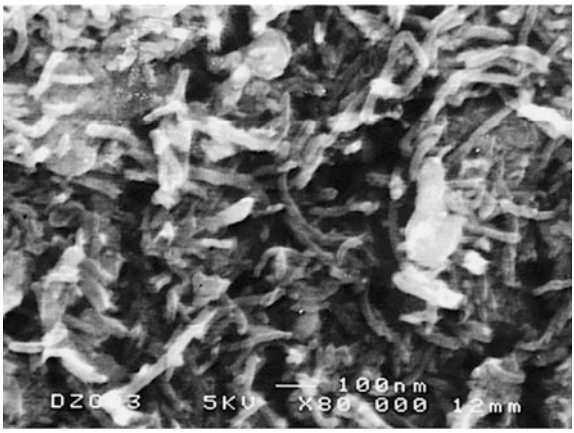

Fig. 4.23 SEM image of CNT electrode [39]

to the distance between general base pairs (~3.4 Å) of poly(*d*G)-poly(*d*C) DNA molecules. The hopping distance measured using metallic electrodes was much longer than the obtained result. Sasaki et al. concluded that the intrinsic direct transport measurement of DNA molecules had been successfully achieved by using CNT electrodes rather than metallic one.

Inanba et al. [41] reported fabrication of nanoprobe electrode-based CNTs for intracellular recording. CNTs are chosen as a potential material for cell studies because of its following properties: mechanical and electrical properties, higher spatial resolution owing to nanoscale diameter, reduction in cell damage due to tube structure, and higher current density. Intracellular recording requires nanoelectrodes insulated over the surfaces other than tips. When parylene-insulated CNT bridges were stretched, inner CNTs slipped while parylene strained. The reason was that the CNTs were grown from both sides forming a bundle structure and that friction coefficient between CNTs was low. Thus, the bridges were cut into probes and CNTs were exposed at the tips by physical stretch. Parylene was suitable as insulator of the CNT electrode, because it was deposited conformally on 3D nanostructure and also it was chemically stable and biocompatible. SEM images of before and after cutting of bare CNT bridges and a parylene-coated CNT bridge are shown in Fig. 4.24a, b, respectively.

Detection of dopamine (DA) is necessary for various biomedical needs and existing methods of detection suffers several drawbacks. The electrode surface could be modified with transition metal complexes and CNTs to enhance the electrochemical performance such as dopamine detection. Yang et al. [42] modified the electrode with $[Co(phen)_3]^{2+}$ and MWCNTs and showed good electrocatalytic activities toward oxidation of DA and possibility of DA detection. For fabrication, glassy carbon electrode (GCE) was polished to mirror-like surface, cleaned ultrasonically, and dipped in acid solution to remove residues. Suspension of MWCNTs was dropped over the electrode to modify it. Electropolymerization of Co

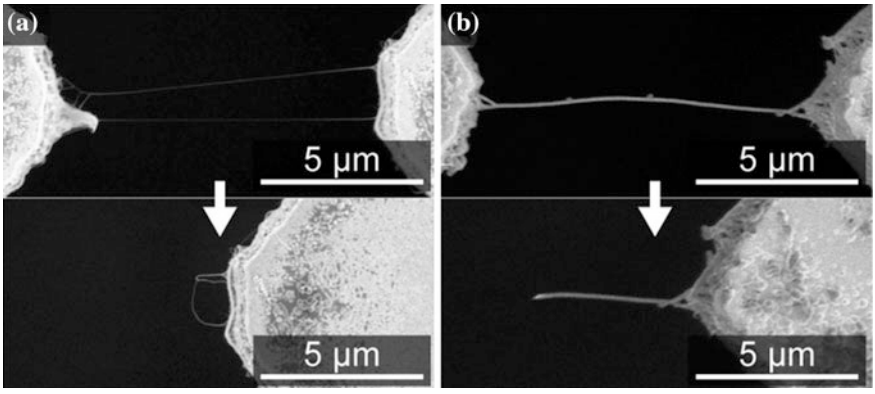

Fig. 4.24 SEM photographs of **a** before and after cutting of bare CNT bridges and **b** a parylene-coated CNT bridge [41]

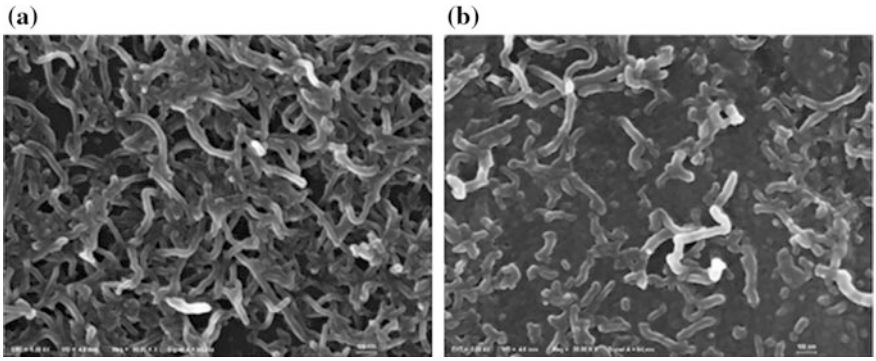

Fig. 4.25 SEM image of **a** MWCNTs/GCE and **b** [Co(phen)3^{2+}/WCNTs/GCE [42]

(II) complex was done on the surface by cyclic potential scanning to obtain the electrode $[Co(phen)_3]^{2+}$/MWCNTs/GCE. This modified electrode increased the oxidation peak current with a rapid current response, high sensitivity, good selectivity, and linear response current. SEM images of MWCNTs/GCE and $[Co(phen)_3]^{2+}$/MWCNTs/GCE are shown in Fig. 4.25.

4.4 Carbon-MEMS/NEMS

Carbon-MEMS/NEMS research is new compared to CNT research. It started 20 years ago and has received enormous attention because carbon-MEMS/NEMS provide solutions to some of the major problems presented by CNTs: the difficulty in making ohmic contact, selecting for a precise tube diameter, selecting for a precise tube length, and positioning accuracy. CNTs are typically fabricated on a flat substrate, and the interference of the substrate with the CNT proper functioning is unavoidable. Post-processing metallization on precisely positioned wires is a necessary step to make ohmic contacts to CNTs and variability of contact resistance from CNT sample to sample also remains a major problem. With C-MEMS, it is easy to fabricate CNWs suspended between carbon electrodes, solving the surface interference problem, and making for better sensor and electronic component performance. Additionally, ohmic contacts are automatically established during carbon–carbon bond formation in the carbonization process. We will discuss about some special CNW processes which enable the fine-tuning of wire thickness, length, and position. In contrast, CNTs after synthesis often come with a distribution in lengths and diameters, so they must be isolated and then carefully nanopositioned for integration. This constitutes a low-throughput technique and is unacceptable for mass manufacturing of solid-state devices [43–46].

Several microfabrication methods are available for the development of nanowire, including template methods, ion and electron beam processes, catalytic growth,

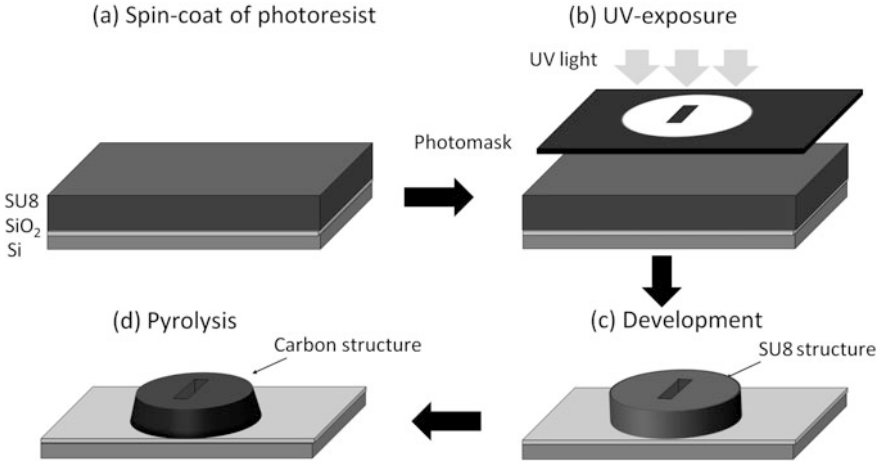

Fig. 4.26 Illustration of C-MEMS: photolithographic patterning of SU-8 photoresist and pyrolysis

Langmuir–Blodgett (LB), chemical liquid deposition (CLD) and CVD, DC arc discharge, and C-MEMS. We will discuss only about the C-MEMS method next.

Shaping of most carbon allotropes into micro- or nanodevices with mechanical machining techniques is not an easy task because the material is usually hard and brittle. Polymers, on the other hand, can be machined easily in a wide variety of machine tools and then converted to carbon devices through pyrolysis, resulting in shapes that are often impossible to make in carbon by any other means. The underlying principle of C-MEMS is to choose an easy to work with polymer precursor, machine, or photopattern this precursor material, and then convert it to carbon using a high-temperature process called pyrolysis.

An example of photolithography process to fabricate C-MEMS structures is illustrated in Fig. 4.26. The process includes spin coating, soft bake, near-ultraviolet (UV) exposure, post-bake, and development. Soft bake and post-bake are not shown in the figure. After the photolithography steps, C-MEMS architectures are obtained in a pyrolysis process. The pyrolysis is carried out in an open-ended quartz-tube furnace, where the samples are baked in an N_2 atmosphere. The pyrolysis process is as follows: first the samples are placed inside the furnace tube and N_2 gas flow is injected with high flow rate at least for initial 15 min to ensure that the environment is inert. Then, the temperature is increased to 300 °C at 5 °C/min ramp rate and is maintained it for 1 h. The temperature is further increased to 900 °C and is maintained for one more hour for carbonization. The whole process of temperature ramping and dwelling must be carried out in the presence of N_2. After that, the furnace is cooled down to 300 °C at a rate of 10 °C/min and the heater is turned off. Finally, the samples are cooled down only by the N_2 flow to reach room temperature.

The resulting microstructure of the carbon material from the process detailed above was found to be glassy carbon (GC). GC has good resistance to high temperatures, low density, low electrical resistance, and relatively high hardness and high resistance to chemical attack, and these properties make GC special for biological, chemical, and many other applications. We will see in the following that CNWs can be made from the same carbon precursor, SU8; this is a very advantageous process characteristic because the integration of CNWs with the supporting structure is rather simple. SU8 is a negative tone photoresist and has the flexibility to fabricate almost any desired design through conventional photolithography and this is followed by pyrolysis as addressed above.

4.4.1 Supporting Structure Fabrication for CNWs

In the late 1990s, Schueller, Brittain, and Whitesides first introduced carbon microstructures fabricated using pyrolysis of a micromolded precursor polymer [47]. In 2002, Singh et al. [48] fabricated C-MEMS structures using negative photoresist, SU8, on silicon wafers for the first time. Since then, various complex high aspect ratio C-MEMS structures such as posts, self-organized bunched posts, and carbon beams supporting wires, and interdigitated electrodes have been developed [46, 49, 50]. The fabrication of the supporting structures (electrodes) for suspended CNWs has already been discussed above.

4.4.2 Electrospinning for Polymer Fibers

Electrospinning is a straightforward and cost-effective method to produce CNWs with diameters ranging from less than 3 nm to more than 1 mm [51], and the electrospinning experiments can be performed by using simple setups. Electrospinning can be applied to the fabrication of NWs made from materials as diverse as synthetic and natural polymers, polymer alloys, polymer composites, as well as metals and ceramics [52]. Some of the current electrospinning applications include filtrations [53], advanced fabrics (e.g., for wound dressing [54]), scaffolds [55, 56], medical implants [57], fabrication of micro- or nanodevices such as field-effect transistors [58, 59], and gas sensors [60, 61].

4.4.2.1 Electrospinning Setup Description

A conventional electrospinning setup is shown in Fig. 4.27. It consists of four key components: a high-voltage power supply (working range between 10 and 30 kV), a polymer precursor reservoir, a conductive dispensing needle, and a conductive substrate. The reservoir maintains a constant polymer solution flow rate through

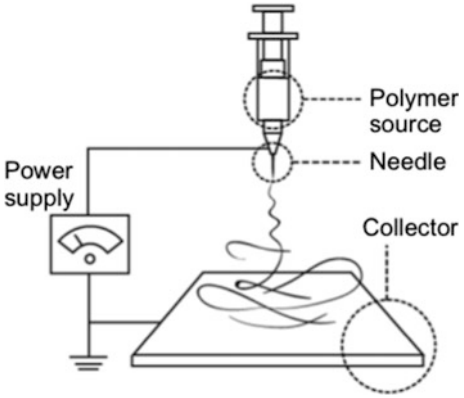

Fig. 4.27 Schematic of traditional electrospinning setup [51]

dispensing needle, a syringe, which is connected to either a mechanical or a pneumatic syringe pump. The conductive dispensing needle acts as the polymer source, which is connected to a high-voltage power supply. The needle is also sometimes called tip, nozzle, or spinneret, and its internal diameter is often in the range of hundreds of micrometers. The conductive substrate is normally grounded and serves as a collector for the electrospun NWs (Fig. 4.27).

When a voltage, higher than 10 kV, is applied to the needle, the polymer solution at the needle tip becomes unstable and a polymer jet is formed. Initially, the jet flows away from the needle in a nearly straight line, and then, it bends into a complex path during which electrical forces stretch and thin it to the nanometer scale. The initial straight section of the jet is known as near-field regime and the area where the electrical instabilities dominate is called the far-field regime. The schematic of the path of the fiber (NW) jet is shown in Fig. 4.28.

The key stages of the polymer jet formation in the electrospinning process are (a) droplet formation, (b) Taylor cone formation, (c) launching of the jet, (d) elongation of straight segment, (e) whipping instability, and (f) solidification into NW [62]. These stages are described in detail in [63].

4.4.2.2 Dimensions of the Nanowires

The morphology and dimensions of the fabricated polymer fibers depend on the composition of the electrospun polymer and the solution concentration. The more diluted solutions generate the thinner fibers and the concentrated solutions produce the thicker fibers. If the polymer concentration is too low, beads are formed instead of fibers, and with the very high concentrations, electrospinning might not be possible. Generally, the dimensions of the polymer fibers depend on the following parameters: (a) polymer precursor material, (b) polymer solution concentration, (c) needle-to-collector distance, (d) flow rate of the precursor, (e) applied voltage, and (f) mechanical stretching. A typical electrode-to-collector distance varies from

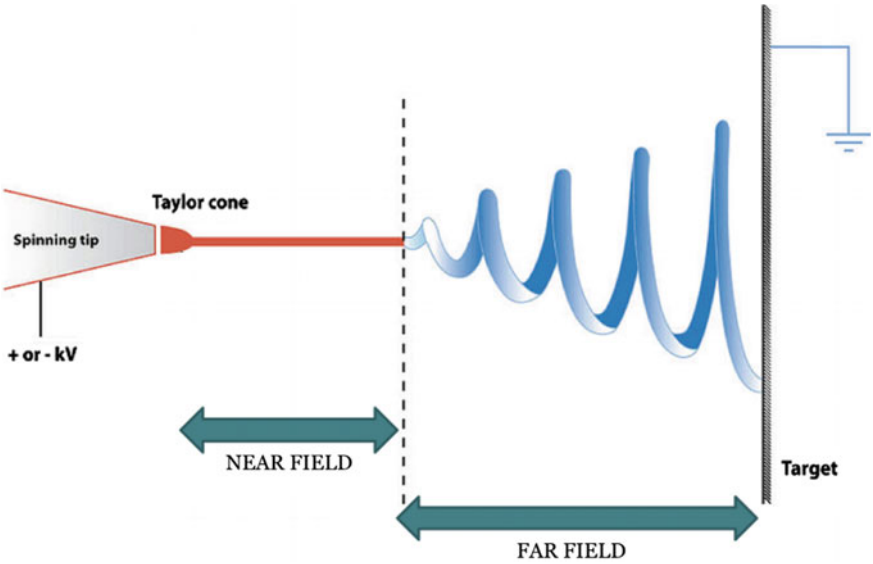

Fig. 4.28 Schematic of the path of the fiber jet. *Courtesy* Wikipedia

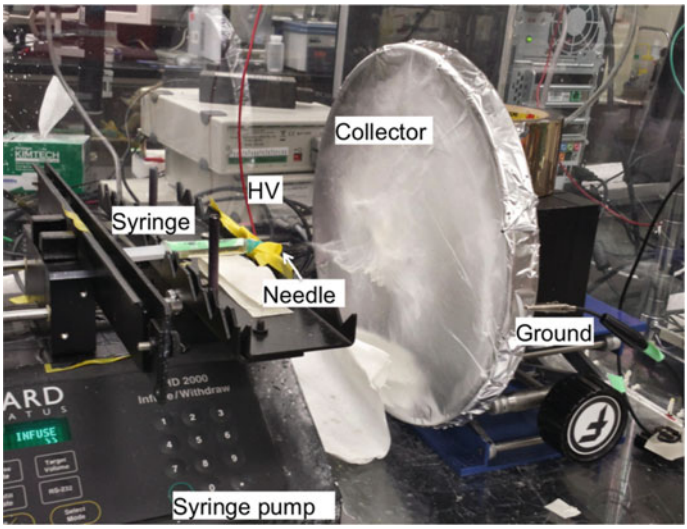

Fig. 4.29 Photographs of UCI BioMEMS Laboratory electrospinning setup [51]

8 to 30 cm. In Fig. 4.29, we show a photograph of the UCI BioMEMS Laboratory far-field electrospinning setup.

In Fig. 4.30, we show a scanning electron microscope (SEM) image of suspended NWs on carbon posts.

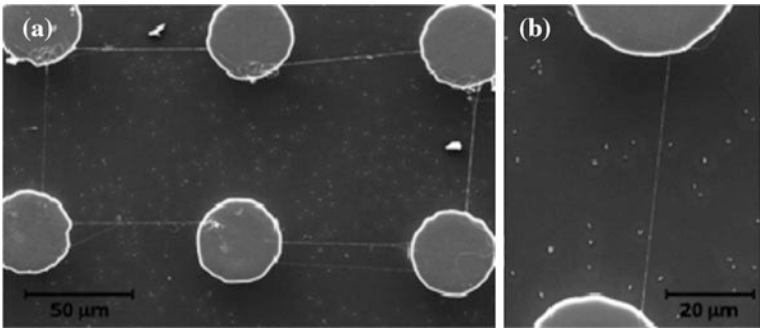

Fig. 4.30 SEM images of suspended nanowires on carbon posts **a** six carbon posts connected each other by nanowires, **b** and individual nanowire [51]

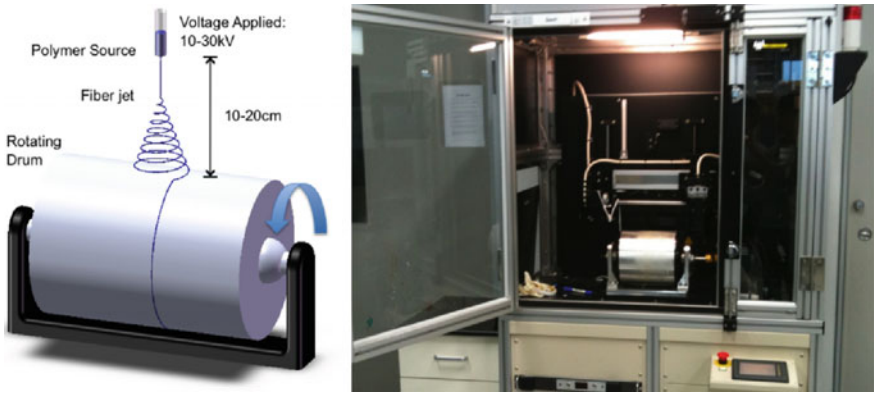

Fig. 4.31 Schematic of an FFES system with rotating drum and commercially available electrospinning setup [51]

In the far-field technique, NWs are randomly deposited on the collector. However, for many applications, highly aligned nanofibers are required. Hence, the alignment of electrospun nanofibers is the most important challenge encountered in the electrospinning field. Kim and Reneker used a rotating drum as collector electrode, aligning the collected fibers in the direction of the drum rotation and producing relatively uniform mats of oriented fibers [64]. In Fig. 4.31, we show a schematic drawing of an electrospinning setup with a rotating drum collector and a picture of a commercially available electrospinning system.

The electric instabilities inherent in FFES make this process inappropriate for a wide range of applications that require isolated NWs to be deposited in a controlled pattern or to be deposited only in predetermined locations. Near-field electrospinning (NFES) technology was developed to fill the demand for production of micro- and nanofibers with increased positioning precision [65–67]. The distance between the fiber source and the collector is significantly reduced for NFES and this

reduction in distance allows for depositing the fibers on the substrate before the onset of the whipping motion. But for NFES, the applied electric field is unable to provide enough force to stretch out the fiber jet diameter to the nanometer scale. Only micrometer-sized fibers are produced using the NFES process. Electromechanical spinning (EMS) developed by Madou et al. [68] improves the NFES by offering thinner fibers with an exceptional nanofiber deposition control. The fundamental principle behind EMS is the use of viscoelastic polymer inks in conjunction with a low-deposition voltage and a mechanical pull on the polymer fibers.

4.4.3 Setup Description of EMS

In EMS, this distance is in the range of 500 μm to 1.5 mm, and thus, EMS operates in the stable liquid jet region. Generally, the syringe in the EMS setup is mounted using a syringe holder and this can be manually or automatically positioned in the *x*–*y*–*z* directions. The target is mounted on an *X*–*Y* microstage that can be programmed to move in any desired pattern at different speeds and accelerations. A power supply, shown in Fig. 4.32, is connected to the needle to provide the high voltage and the substrate is grounded. The polymer solution flows through the needle to form a full-sized droplet at the needle tip. The polymer jet does not self-initiate upon the voltage turned, as mentioned earlier. To initiate the jet in

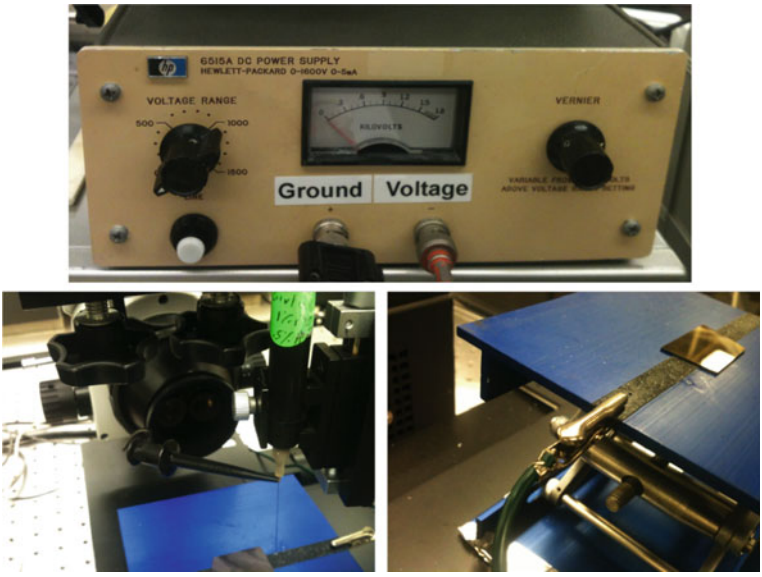

Fig. 4.32 Photographs of voltage supply, syringe, and grounded substrate of EMS setup [51]

EMS, it is necessary to introduce an artificial instability at the droplet–air interface that results in a very high local electric field and if this local electrical field is sufficient to overcome the interfacial surface tension, and then, a jet initiates. This artificial instability can be induced, for example, by poking the droplet with a glass microprobe tip (1–3 μm tip diameter). Once the jet is initiated, the system reaches a new equilibrium with a jet that continues to flow as long as the electric field is applied and new polymer solution is available.

4.4.4 Various Research Works on C-MEMS CNWs

Madou et al. [68] demonstrated far-field electrospinning to fabricate arrays of suspended CNWs by carbonization of polymeric, polyacrylonitrile (PAN) and SU8, nanowires. The nanowires were suspended between specially designed three-dimensional electrodes, posts, fabricated using organic resorcinol-formaldehyde-based xerogel. In Fig. 4.33, we show an SEM image of suspended CNWs.

In Fig. 4.34, we show SEM images of a single suspended nanowire made from SU8 and PAN, suspended between two photographically patterned C-MEMS electrodes. The linear behavior of the *I–V* curves is presented in Fig. 4.34c, showing in both cases an ohmic contact between the electrodes and the suspended nanowires. The conductance was calculated by measuring the slope of the *I–V* curves for both the cases, and it was revealed that PAN-derived CNFs are more graphitic than SU8-derived CNF and, therefore, exhibit higher conductivities.

Madou and a collaborator group in South Korea reported the fabrication of scalable suspended CNW meshes, to use as electrochemical sensing platforms, using the C-MEMS process [69]. A 6-in. silicon wafer with a thermally grown SiO_2 layer was used as the substrate material and the following three photolithography

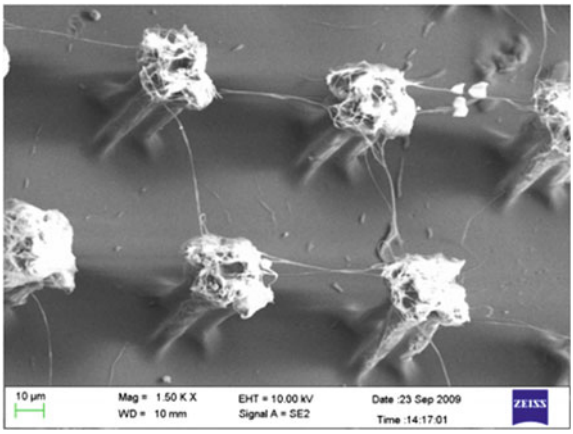

Fig. 4.33 SEM image of suspended CNW on 3D carbon post [68]

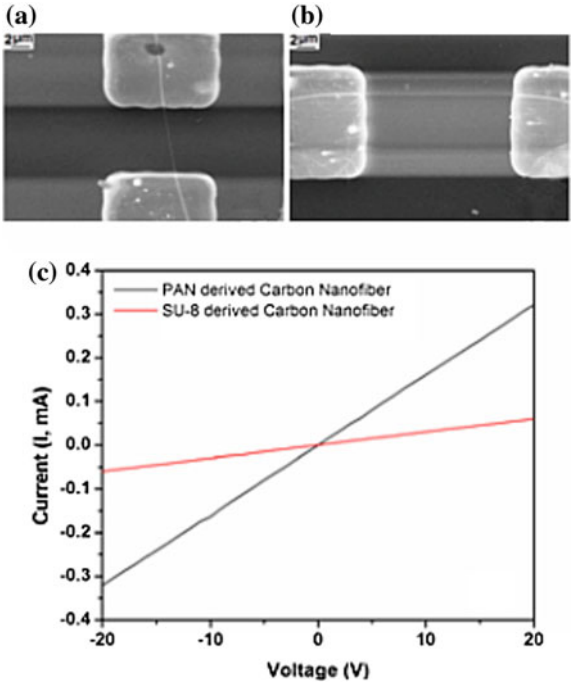

Fig. 4.34 SEM images of single suspended nanowire: **a** Su8 derived and **b** PAN derived. **c** *I–V curve* for the both cases [68]

steps were carried out using SU8 as the resist: (i) define the 4-μm-thick planar polymer pads, (ii) define the tall contact pads to support the suspended photoresist microwire meshes, and (iii) pattern the suspended photoresist microwire meshes bridging the prepatterned photoresist contact pads. Planar electrodes and suspended microwire meshes were released in a single-process step and the completed photoresist structures were converted into carbon by pyrolysis. In Fig. 4.35, we show two SEM images of a group of nanoelectrode set.

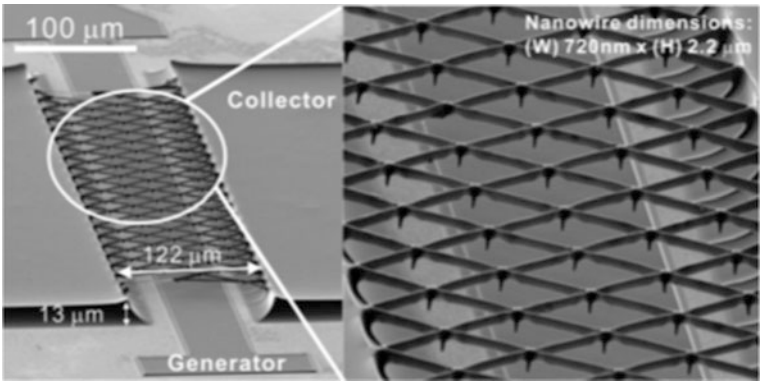

Fig. 4.35 SEM images of nanoelectrode set [69]

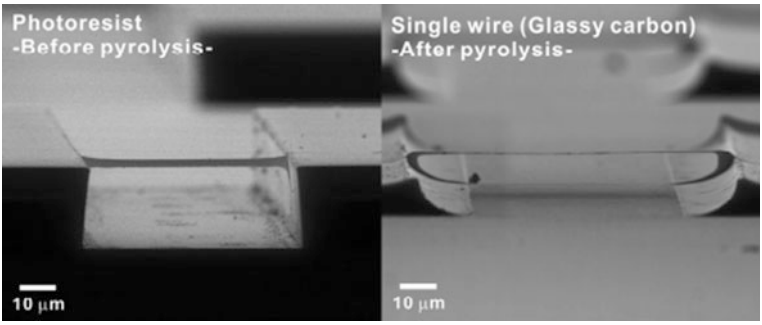

Fig. 4.36 SEM images of photoresist and suspended nanowire structure [70]

Shin et al. reported on the processing of monolithic suspended glassy carbon nanostructures. They also used two common batch processes: UV lithography and polymer pyrolysis [70] to fabricate the carbon structures which include two tall carbon pads and a suspended nanowire bridging the pads. SEM images of single CNWs are shown in Fig. 4.36. A hydrogen sensor based on the above-fabricated nanowire was also reported by the same research group [71]. For the detection of hydrogen, they deposited a thin palladium layer on the suspended CNW.

4.5 Applications of C-MEMS-Based CNWs

Some recent examples of C-MEMS/NEMS applications include electrochemical sensors, substrate for molecular electronics, batteries, fuel cells, dielectrophoretic electrodes, capacitors, scaffolds, nanoconstrictions, molds for bulk metallic glasses, and gas sensors. Here, we provide a short description of the emerging C-MEMS application of suspended carbon hot nanowires to make nanogas sensors with local CVD, nanoconstrictions, and nanogaps.

Suspended CNWs are separated from the supporting substrate, so as free from the substrate influences such as contamination and charge shunting, and this leads to significant advantages over other nanowire-based sensors typically embedded on a solid substrate. The sensing is usually a surface phenomenon and CNWs, having a high surface-to-volume ratio, are approached by analyte molecules from all directions, and this leads to an improved lower LOD. This principle is called wash cloth line sensors. By derivatizing the CNW surface with an appropriate monolayer of sensor molecules, say protein or DNA molecules, the nanowires can be turned nanoimmuno- or nano-DNA sensors. Nanogas sensors can also be made by coating the CNWs surface with metal oxide semiconductors (MOS). A SEM image of a suspended CNW and a schematic of wash cloth line are shown in Fig. 4.37.

Local CVD on the CNW occurs upon applying a direct current to the suspended CNW. The high resistance of the CNW, compared to the bulkier supporting

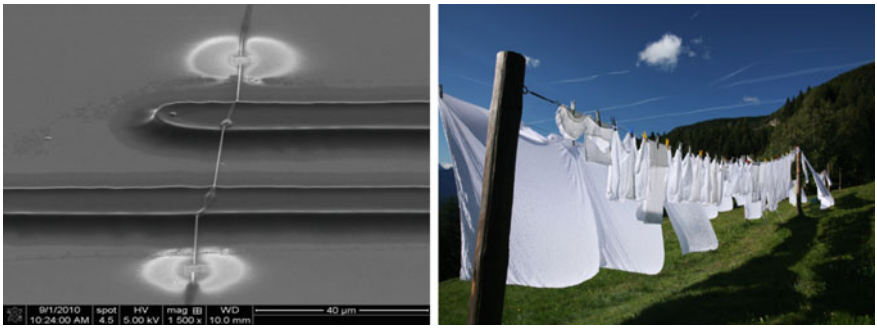

Fig. 4.37 Suspended nanowire (*left*) with a wash cloth line (*right*) [64]

electrodes, allows for its selective heating on the CNW but not on the supporting electrodes. As an example of metal-oxide-semiconductor (MOS) deposition that can be used for the fabrication of a NO_x nanogas sensor, our group has demonstrated the local CVD on CNWs by depositing a tungsten oxide (WO_3) film from tungsten hexacarbonyl [$W(CO)_6$] as the precursor. SEM images of a 358-nm-thick, 30-μm-long CNW after WO_3 deposition by local CVD of $W(CO)_6$ are shown in Fig. 4.38a, b. The thickness of the deposit follows the temperature profile expected for a heated nanowire with the center being considerably thicker (diameter of ~1.8 μm) compared to the ends of the CNW (358 nm).

The local CVD phenomenon illustrated above is not limited to WO_3 deposition. Local CVD on CNWs has the potential to become a useful tool for thermal deposition of many materials selectively on the joule-heated fibers, allowing many types of nanosensors and nanoelectronics devices.

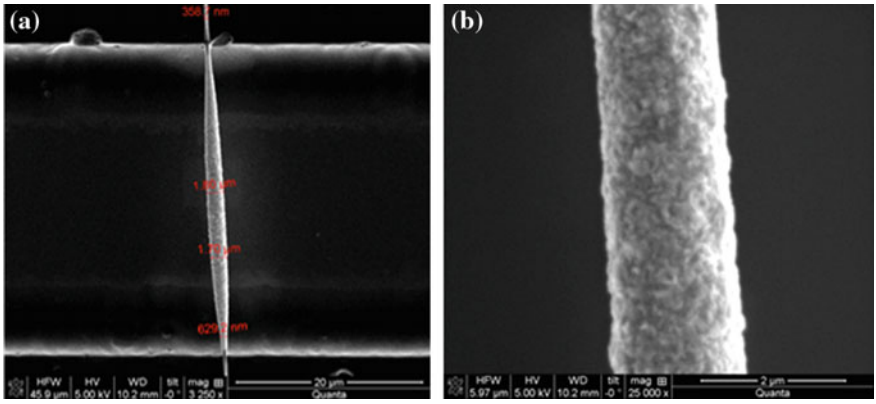

Fig. 4.38 **a** SEM images of a 358-nm-*thick* CNW with WO_3 deposited on its surface by selected area CVD, **b** a high-magnification image of the granular surface of WO_3 [72]

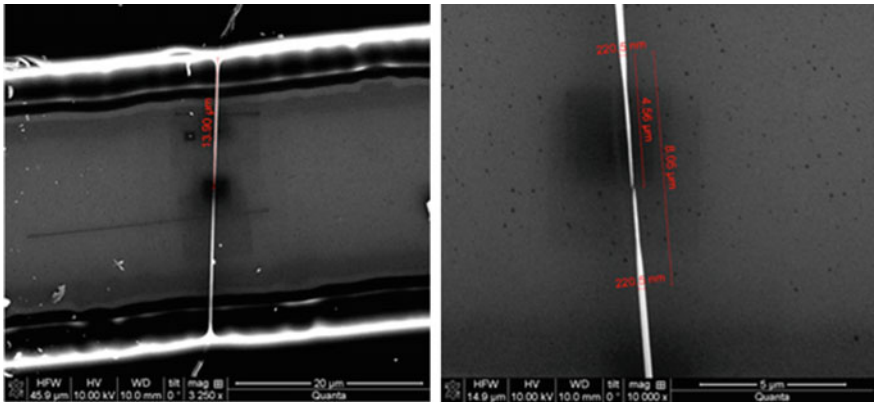

Fig. 4.39 SEM images of a CNW showing breakage due to overheating at its center [72]

Using controlled Joule heating of suspended nanowires, one can manufacture nanogap and quantum mechanical nanoconstrictions without the need for expensive equipment. At the beginning of a Joule heating experiment, a central region of the CNW attains the highest temperature which is high enough to sublimate some carbon from its surface. This thinner segment attains the sublimation temperature even faster with a constant current application, as it offers a yet higher resistance, which will lead to yet faster thinning at its center. Finally, when the center cannot withstand further thinning the nanowire breaks. We show SEM images of suspended CNW which breaks at center upon joule heating in Fig. 4.39.

Our recent study proves that the thinner and shorter CNW has the higher temperature gradient, so as the smaller nanogap in its center. Nanogaps with a dimension of less than 10 nm in a CNW might have great utility as a building block for molecular electronics, based on molecular interactions in a carbon–molecule–carbon (C–M–C) structure. There are a lot of techniques for obtaining nanogaps, but a process to totally control the gap size has not been found yet. We are currently developing an electronic control system to control the wire thickness in the center to any desired radius (nanoconstriction) and to make nanogaps of any size.

References

1. S. Iijima, Helical microtubules of graphitic carbon. Nature **314**, 56–58 (1991)
2. H.H. Kim, H.J. Kim, in *The Preparation of Carbon Nanotubes by DC arc Discharge Process Using Xylene-Ferrocene as a Floating Catalyst Precursor*. NMP47, Nanotechnology Materials and Devices Conference, IEEE, (2006), pp. 496–497
3. Y. Sato, K. Motomiya, B. Jeyadevan, K. Tohji, G. Sato, H. Ishida, T. Hirata, R. Hatakeyama, Effect of cerium ions in an arc peripheral plasma on the growth of radial single-walled carbon nanotubes. J. Appl. Phys. **98**, 094313 (2005)

4. M. Kanai, A. Koshio, H. Shinohara, T. Mieno, A. Kasuya, Y. Ando, X. Zhao, High-yield synthesis of single-walled carbon nanotubes by gravity-free arc discharge. Appl. Phys. Lett. **79**, 2967 (2001)
5. M. Keidar, I. Levchenko, T. Arbel, M. Alexander, A.M. Waas, K.K. Ostrikov, Magnetic-field-enhanced synthesis of single-wall carbon nanotubes in arc discharge. J. Appl. Phys. **103**, 094318 (2008)
6. T. Sugai, H. Omote, S. Bandow, N. Tanaka, H. Shinohara, Production of fullerenes and single-wall carbon nanotubes by high-temperature pulsed arc discharge. J. Chem. Phys. **112**, 6000 (2000)
7. Y. Ando, X. Zhao, K. Hirahara, S. Iijima, Production of thick single-walled carbon nanotubes by arc discharge in hydrogen ambience. AIP Conf. Proc. **590**, 7 (2001)
8. T. Guo, P. Nikolaev, A. Thess, D.T. Colbert, R.E. Smalley, Catalytic growth of single-walled nanotubes by laser vaporization. Chem. Phys. Lett. **243**, 49–54 (1995)
9. A. Thess, R. Lee, P. Nikolaev, H. Dai, P. Petit, J. Robert, C. Xu, Y.H. Lee, S.G. Kim, A.G. Rinzler, D.T. Colbert, G.E. Scuseria, D. Tomanek, J.E. Fischer, R.E. Smalley, Crystalline ropes of metallic carbon nanotubes. Science **273**(5274), 483–487 (1996)
10. J. Chae, X. Ho, J.A. Rogers, K. Jain, Patterning of single walled carbon nanotubes using a low-fluence excimer laser photoablation process. Appl. Phys. Lett. **92**, 173115 (2008)
11. J. Chae, K. Jain, Patterning of carbon nanotubes by material assisted laser ablation process. IEEE Trans. Nanotechnol. **9**(3), 381–385 (2010)
12. T. Wang, J. Shang, J. Liu, in *Preparation of VACNT TIM by a Novel Metallization and Chemical Bonding Process*. 13th International Conference on Electronic Packaging Technology and High Density Packaging (ICEPT-HDP) (2012), pp. 1646–1649
13. B.T. Nguyen, X.T. Than, V.C. Nguyen, T. Thanh, T. Ngo, H.T. Bui, X.N. Nguyen, H.K. Phan, N.M. Phan, Fabrication of horizontally aligned ultra-long single-walled carbon nanotubes on Si substrates using the fast-heating chemical vapour deposition method. Adv. Nat. Sci.: Nanosci. Nanotechnol. **3**, 025010 (2012)
14. Y. Matsuoka, I.T. Clark, M. Yoshimura, Growth mechanism of multilayer-graphene-capped, vertically aligned multiwalled carbon nanotube arrays. J. Vac. Sci. Technol. B **29**(6), 061801 (2011)
15. M.A. Nguyen, D.T. Ngo, V.T. Le, D.V. Cao, Synthesis of single-walled carbon nanotubes over Co–Mo/Al_2O_3 catalyst by the catalytic chemical vapour deposition of methane. Adv. Nat. Sci.: Nanosci. Nanotechnol. **4**, 035018 (2013)
16. S. Ramakrishnan, E.J. Jelmy, A. Baladandapani, M. Rangarajan, N.K. Kothurkar, Synthesis of multiwalled carbon nanotubes using RF-CCVD and a bimetallic catalyst. AIP Conf. Proc. **1447**, 275–276 (2012)
17. J. Lee, S. Choi, in *Fabrication of Carbon Nanotubes by Anodic Aluminum Oxide Nano-template*. NMP12, Nanotechnology Materials and Devices Conference, IEEE (2006), pp. 426–427
18. J. Wu, M. Eastman, T. Gutu, M. Wyse, J. Jiao, S.-M. Kim, M. Mann, Y. Zhang, K.B.K. Teo, Fabrication of carbon nanotube-based nanodevices using a combination technique of focused ion beam and plasma-enhanced chemical vapour deposition. Appl. Phys. Lett. **91**, 173122 (2007)
19. W.K. Wong, C.S. Lee, S.T. Lee, Uniform-diameter, aligned carbon nanotubes from microwave plasma-enhanced chemical-vapour deposition. J. Appl. Phys. **97**, 084307 (2005)
20. G.I. Shim, Y. Kojima, S. Kono, Y. Ohno, T. Ishijima, Fabrication of carbon nanotubes by slot-excited microwave plasma-enhanced chemical vapor deposition. Jpn. J. Appl. Phys. **47**, 5652–5655 (2008)
21. K.S. Kim, G. Cota-Sanchez, C.T. Kingston, M. Imris, B. Simard, G. Soucy, Large-scale production of single-walled carbon nanotubes by induction thermal plasma. J. Phys. D Appl. Phys. **40**, 2375–2387 (2007)
22. J.-T Huang, C.-H Lin, P.-C Chang, in *Low-temperature Fabrication Method of Carbon Nanotubes-Based Gas Sensor*. International Conference on Electronic Materials and Packaging (2008), pp. 57–60

23. S. Dhall, N. Jaggi, R. Nathawat, Functionalized multiwalled carbon nanotubes based hydrogen gas sensor. Sens. Actuators A **201**, 321–327 (2013)
24. J.-H. Yun, H. Chang-Soo, J. Kim, J.-W. Song, D.-H. Shin, Y.-G. Park, in *Fabrication of Carbon Nanotube Sensor Device by Inkjet Printing*. Proceedings of the 3rd IEEE Int. Conf. on Nano/Micro Engineered and Molecular Systems (2008), pp. 506–509
25. M. Baghgar, Y. Abdi, E. Arzi, Fabrication of low-pressure field ionization gas sensor using bent carbon nanotubes. J. Phys. D Appl. Phys. **42**, 135502 (2009)
26. J. Huang, J. Wang, C. Gu, K. Yu, F. Meng, J. Liu, A novel highly sensitive gas ionization sensor for ammonia detection. Sens. Actuators A **150**, 218–223 (2009)
27. D. Janagama, P. Goud, R. Markondeya, M. Iyer, T. Rao, in *Biofunctionalization of Multi-walled Carbon Nanotubes (MWNTs) for the Fabrication of Protein Nano Biosensors*. 11th National symposium on Advanced Packaging Materials: Processes, Properties and Interface (2006), pp. 119–121
28. C.K.M. Fung, N. Xi, B. Shanker, K.W.C. Lai, J. Zhang, H. Chen, Y. Luo, in *Design and Fabrication of Nano Antenna for Carbon Nanotube Infrared Detector*. 8th IEEE Conference on Nanotechnology (2008), pp. 205–208
29. R. Sharma, A. AI-Hamry, S. Vijayragavan, A. Benchirouf, A. Sanli, C. Miiller, O. Kanoun, in *Single-Wall Carbon Nanotubes Based Near-Infrared Sensors on Flexible Substrate*. 11th International Multi-Conference on Systems, Signals and Devices (2014), pp. 1–5
30. H. Oh, J.-J. Kim, W. Song, S. Moon, N. Kim, J. Kim, N. Park, Fabrication of *n*-type carbon nanotube field-effect transistors by Al doping. Appl. Phys. Lett. **88**, 103503 (2006)
31. R. Nouchi, H. Tomita, A. Ogura, H. Kataura, M. Shiraishi, Logic circuits using solution-processed single-walled carbon nanotube transistors. Appl. Phys. Lett. **92**, 253507 (2008)
32. N. Imazu, T. Fujigaya, N. Nakashima, Fabrication of flexible transparent conductive films from long double-walled carbon nanotubes. Sci. Technol. Adv. Mater. **15**, 025005 (2014)
33. L. Zhu, K. Moon, B. Bertram, D.W. Hess, C.P. Wong, in *Assembling Carbon Nanotube Bundles Using Transfer Process for Fine-Pitch Electrical Interconnect Applications*. Electronic Components and Technology Conference (2007)
34. J.-T. Huang, P.-C. Chang, H.-W. Chao, P.-L. Hsu, in *A Low-Temperature Fabrication Process Integrated Carbon Nanotubes-Based Sensor Device into CMOS IC*. IEEE NANO (2009)
35. K.E. Aasmundtveit, B.Q. Ta, L. Lin, E. Halvorsen, N. Hoivik, Direct integration of carbon nanotubes in Si microstructures. J. Micromech. Microeng. **22**, 074006 (2012)
36. Y. Jiang, A. Kozinda, T. Chang, L. Lin, Flexible energy storage devices based on carbon nanotube forests with built-in metal electrodes. Sens. Actuators A **195**, 224–230 (2013)
37. C.-F. Hu, J.-Y. Wang, Y.-C. Liu, M.-H. Tsai, W. Fang, Development of 3D carbon nanotube interdigitated finger electrodes on polymer substrate for flexible capacitive sensor application. Nanotechnology **24**, 444006 (2013)
38. C. Stampfer, A. Jungen, C. Hierold, *Fabrication of discrete carbon nanotube based nano-scaled force sensors* (Sensors, IEEE, 2004), pp. 1056–1059
39. R.Z. Ma, J. Liang, B.Q. Wei, B. Zhang, C.L. Xu, D.H. Wu, Study of electrochemical capacitors utilizing carbon nanotube electrodes. J. Power Sour. **84**, 126–129 (1999)
40. T.K. Sasaki, A. Ikegami, M. Mochizuki, N. Aoki, Y. Ochiai, in *Fabrication of Carbon Nanotube Electrodes for Bio-Nano-Electronic Devices*. IPAP Conference Series 6 (2005), pp. 168–170
41. A. Inaba, Y. Takei, T. Kan, K. Matsumoto, I. Shimoyama, *Nanoprobe Electrodes Cut by Physical Stretch of Parylene-insulated Carbon Nanotube Bridges, Transducers'11* (Beijing, China, 2011)
42. L. Yang, X. Li, Y. Xiong, X. Liu, X. Li, M. Wang, S. Yan, L.A.M. Alshahrani, P. Liu, C. Zhang, The fabrication of a Co (II) complex and multi-walled carbon nanotubes modified glass carbon electrode, and its application for the determination of dopamine. J. Electroanal. Chem. **731**, 14–19 (2014)

43. E.C. Walter, K. Ng, M.P. Zach, R.M. Penner, F. Favier, Electronic devices from electrodeposited metal nanowires. Microelectron. Eng. **61–62**, 555–561 (2002)
44. Y. Chai, Y. Wu, K. Takei, H.Y. Chen, S. Yu, P.C.H. Chan, A. Javey, H.S.P. Wong, *In 2010 IEEE International Electron Devices Meeting (IEDM)* (IEEE, San Francisco, CA, 2010), pp. 214–217
45. J. Huang, Q. Wan, Gas sensors based on semiconducting metal oxide one-dimensional nanostructures. Sensors **9**(12), 9903–9924 (2009)
46. S. Bibekananda, V.J. Babu, V. Subramanian, T.S.J. Natarajan, Preparation and characterization of electrospun fibers of poly(methyl methacrylate)-single walled carbon nanotube nanocomposites. J. Eng. Fibers Fabr. **3**(4), 39–45 (2008)
47. O.J. Schueller, S.T. Brittain, G.M. Whitesides, Fabrication of glassy carbon microstructures by pyrolysis of microfabricated polymeric precursors. Adv. Mater. **9**(6), 477–480 (1997)
48. A. Singh, J. Jayaram, M. Madou, S. Akbar, Pyrolysis of negative photoresists to fabricate carbon structures for microelectromechanical systems and electrochemical applications. J. Electrochem. Soc. **149**(3), E78–E83 (2002)
49. B.Y. Park, R. Zaouk, C. Wang, M.J. Madou, A case for fractal electrodes in electrochemical applications. J. Electrochem. Soc. **154**(2), 1–5 (2007)
50. J.-I. Heo, Y. Lim, M. Madou, H. Shin, in *Scalable Suspended Carbon Nanowire Meshes as Ultrasensitive Electrochemical Sensing Platforms*. IEEE 25th International Conference on Micro Electro Mechanical Systems (MEMS) (2012), pp. 878–881
51. G. Canton, in *Development of Electro-Mechanical Spinning for Controlled Deposition of Carbon Nanofibers*. PhD Thesis, UCI (2014)
52. A. Greiner, J.H. Wendor, Electrospinning: a fascinating method for the preparation of ultrathin fibers. Angew. Chem. Int. Ed. **46**(30), 5670–5703 (2007)
53. P. Gibson, H. Schreuder-Gibson, D. Rivin, Electrospun fiber mats: transport properties. AIChE J. **45**(1), 190–195 (1999)
54. H.-J. Jin, S.V. Fridrikh, G.C. Rutledge, D.L. Kaplan, Electrospinning bombyx mori silk with poly(ethylene oxide). Biomacromolecules **3**(6), 1233–1239 (2002)
55. Q.P. Pham, U. Sharma, A.G. Mikos, Electrospinning of polymeric nanofibers for tissue engineering applications: a review. Tissue Eng. **12**(5), 1197–1211 (2006)
56. R. Murugan, S. Ramakrishna, Nano-featured scaffolds for tissue engineering: a review of spinning methodologies. Tissue Eng. **12**(3), 435–447 (2006)
57. S. Agarwal, J.H. Wendor, A. Greiner, Use of electrospinning technique for biomedical applications. Polymer **49**(26), 5603–5621 (2008)
58. A. Babel, D. Li, Y. Xia, S.A. Jenekhe, Electrospun nanofibers of blends of conjugated polymers: morphology, optical properties, and field-effect transistors. Macromolecules **38** (11), 4705–4711 (2005)
59. N. Pinto, A. Johnson, A. MacDiarmid, C. Mueller, N. Theofylaktos, D. Robinson, F. Miranda, Electrospun polyaniline/polyethylene oxide nanofiber field-effect transistor. Appl. Phys. Lett. **83**(20), 4244–4246 (2003)
60. S. Sharma, M. Madou, A new approach to gas sensing with nanotechnology. Philos. Trans. R. Society A: Math. Phys. Eng. Sci. **370**(1967), 2448–2473 (2012)
61. H. Liu, J. Kameoka, D.A. Czaplewski, H. Craighead, Polymeric nanowire chemical sensor. Nano Lett. **4**(4), 671–675 (2004)
62. A.L. Andrady, *Science and technology of polymer nanofibers* (John Wiley & Sons, New York, NY, 2008)
63. M. Madou, V.H. Perez-Gonzalez, B. Pramanick, *Carbon: The Next Silicon? Book 1—Fundamentals* (Momentum Press, New York, 2016)
64. J.-S. Kim, D.H. Reneker, Polybenzimidazole nanofiber produced by electrospinning. Polym. Eng. Sci. **39**(5), 849–854 (1999)
65. D. Sun, C. Chang, S. Li, L. Lin, Near-field electrospinning. Nano Lett. **6**(4), 839–842 (2006)
66. G. Zheng, G.W. Li, X. Wang, D. Wu, D. Sun, L. Lin, Precision deposition of a nanofibre by near-field electrospinning. J. Phys. D: Appl. Phys. **43**(41), 415501 (2010)

67. C. Chang, K. Limkrailassiri, L. Lin, Continuous near-field electrospinning for large area deposition of orderly nanofiber patterns. Appl. Phys. Lett. **93**(12), 123111 (2008)
68. C.S. Sharma, H. Katepalli, A. Sharma, M. Madou, Fabrication and electrical conductivity of suspended carbon nanofiber arrays. Carbon **49**(5), 173–1727 (2011)
69. J.-I. Heo, Y. Lim, M. Madou, H. Shin, in *Scalable Suspended Carbon Nanowire Meshes as Ultrasensitive Electrochemical Sensing Platforms*. In IEEE 2012 IEEE 25th International Conference on Micro Electro Mechanical Systems (MEMS) (2012), pp. 878–81
70. Y. Lim, J. Heo, M.J. Madou, H. Shin, *Development of Suspended 2D Carbon Nanostructures: Nanowires to Nanomeshes*. The 17th International Conference on Solid-State Sensors, Actuators and Microsystems (Transducers 2013) (2013)
71. J. Heo, Y. Lim, H. Shin, in *A Stacked Electrode Set Including Suspended Carbon Nanomeshes and Planar Carbon Pads for Electrochemical/Bio Sensor Applications*. The 17th International Conference on Solid-State Sensors, Actuators and Microsystems (Transducers 2013) (2013)
72. S. Sharma, in *Microstructural Tuning of Glassy Carbon for Electrical and Electrochemical Sensor Applications*. PhD Thesis, UCI (2013)

Chapter 5
Metal Nanoparticles as Glucose Sensor

Akrema and Rahisuddin

Abstract Diabetes, a metabolic disorder, has become a major health problem in the world. According to WHO report, the number of patients is projected to 300 million in 2025. Therefore, the need of glucose detection is extremely important to the patients suffering from diabetes. Glucose oxidase (GOx) has been extensively used to construct amperometric biosensors for glucose detection owing to its high selectivity and sensitivity to glucose. However, GOx-based biosensors suffer from a stability problem due to the fundamental feature of enzymes. Therefore, it requires a need for enzyme-free glucose sensors. During last two decades, considerable attention has been paid to develop enzyme-free electrodes. Precious metals, metal alloys, and metal nanoparticles are extensively studied for advancement of non-enzymatic glucose sensors. Therefore, the need of a cost-effective, sensitive, and reliable enzyme-free glucose sensor is in great demand. In recent years, noble metal nanoparticles have found immense interest by researchers due to their potential in label-free forms of biological and chemical sensors. The high capability of these sensors is due to the novel properties of noble metal nanostructured arrays, for instance, high surface to volume ratio, localized surface plasmon resonance, excellent conductivity and anomalous transmission, and reflection of light. The amperometric technique is most widely used tool in the sensing of glucose. On the other side, some LSPR sensors are also reported which showed good sensitive to the changes in refractive index occurring at a metal/dielectric interface. Some researchers also studied fiber-optic-based glucose sensor which was based on the attenuated total reflection phenomenon. Enzymatic and non-enzymatic sensors of silver, gold, and copper nanoparticles are discussed in details in the chapter. The fabrication of glucose sensors has also been discussed with keeping in view the interest of the researchers. The objective of this chapter is to cover the bare and modified/composites of metal nanoparticles as glucose sensor. The most recent as well as conventional fabrication methods are discussed in detail. The linearity range and limit of detection of the glucose sensors are described in detail to justify the fabrication process. The chapter will provide in-depth review of metal

Akrema · Rahisuddin (✉)
Department of Chemistry, Jamia Millia Islamia, New Delhi 110025, India
e-mail: rahisuddin@jmi.ac.in

Z.H. Khan (ed.), *Nanomaterials and Their Applications*,
Advanced Structured Materials 84, https://doi.org/10.1007/978-981-10-6214-8_5

nanoparticles-based glucose sensors which would be beneficial to all researchers, scientists, engineers, and students who are in direct contact of developing and using glucose sensors. It is hoped that the chapter will bridge the common gap between the research literature and standard textbooks. The material in this chapter emphasizes on developments of sensitive, rapid, and cheap systems for identification of glucose. The fabrication techniques of metal nanoparticles as glucose sensor are also studied in connection with different methodologies like SPR, SERS, electrochemical, and paper based devices.

Keywords Nanoparticles · Glucose sensor · Amperometric sensor
Glucose oxidase · Non-enzymatic sensor

5.1 Introduction

Diabetes, a chronic disorder, is a result of partial or total deficiency of insulin and it has been known as one of the main causes of death and problems including kidney failure, heart disease, and blindness. According to World Health Organization (WHO) report, the projection of number of diabetics is measured to be 300 million in 2025 [1]. The complications of diabetes can be prohibited by proper control of the glucose concentration in blood. Therefore, there is a need for proper detection and control of blood sugar concentration. Due to this, a vast amount of research has been done regarding glucose detection.

The sensing of glucose is also important for other fields such as biochemistry, medicine, and food industry [2, 3]. Clark and Lyons [4], in 1962, had developed the first enzyme electrode to define the glucose concentration. After that much efforts have been made to develop and improve glucose sensors. Due to the high sensitivity and selectivity the glucose enzyme electrodes, based on GOx, are much researched to create various biosensors for glucose detection [5]. However, researchers faced several shortcomings of enzyme modified electrodes, such as high cost of enzymes, acute operational environment, and poor stability. Furthermore, GOx enzyme rapidly loses its activity above pH 8 and below pH 2 and temperature above 40 °C can cause serious damage [6]. Therefore, there is a high demand for enzyme-free glucose sensors which have better stability, reproducibility, and high sensibility.

Today metal nanoparticles serve as extremely intense labels for immunoassays [7–9], sensors [10–16], and surface-enhanced spectroscopies [17–23]. Metal nanoparticles also have significant potential as nanoscale optical switches, light sources, microscopes, waveguides, and lithographic tools [24–26]. Many different types of metal nanoparticles of different sizes and compositions are made easily and available to use and facilitate their application in electrochemical analysis. Metal nanoparticles, different or same kind, perform different roles in different electrochemical sensing systems, such as immunosensors, enzyme sensors and DNA sensors [27, 28]. The large surface area of metal nanoparticles is a key to the

exceptional properties of nanoparticles in which some properties like excellent conductivity and catalytic properties make the nanoparticles appropriate to enhance the electron transfer rate between electrode surface and redox centers in proteins and hence catalyst enhance the rate of electrochemical reaction.

5.2 Silver Nanoparticles-Based Glucose Sensor

In 2009, some researchers used silver nanoparticles (AgNPs) as a redox marker in a glucose sensor which was based on Ag-ISE polymeric membrane, fabricated from benzothiazole calix [4] arene [29]. Geddes and co-workers demonstrated the use of silver and gold nanoparticles (AuNPs) for glucose sensors [30]. In their study, they coated AuNPs with dextran and functionalized AgNPs with boronic acid. The sensing properties of nanoparticles were described on the basis of aggregation. The authors reported that the dextran-coated AuNPs were completely aggregated on concentration of Concanavalin A (Con A) larger than 75 μM and when the concentration of Con A was between 18.7 and 37 μM better glucose responses were observed when dextran-coated AuNPs were aggregated. In case of AgNPs, glucose interacted with boronic acid groups attached on AgNPs. The interaction of boronic acid groups and dextran caused an increase in luminescence.

In another interesting study, a film composed of AgNPs, CNTs, and chitosan (Ag/CNT/Ch) was used by researchers as a glucose sensor [31]. The resulting sensor was able to detect the glucose limited up to 0.1 μM with a linear range of 0.5–50 μM (Fig. 5.1). They also measured the possible interference by measurement of 20 μM glucose containing a specified concentration of UA and AA. 20 and 80 μM concentration of UA and AA, respectively, does not have any noticeable interference to the sensor. A current–time (*i*–*t*) plot, for the sensor on successive step changes of glucose concentration, displayed a rapid and sensitive response to

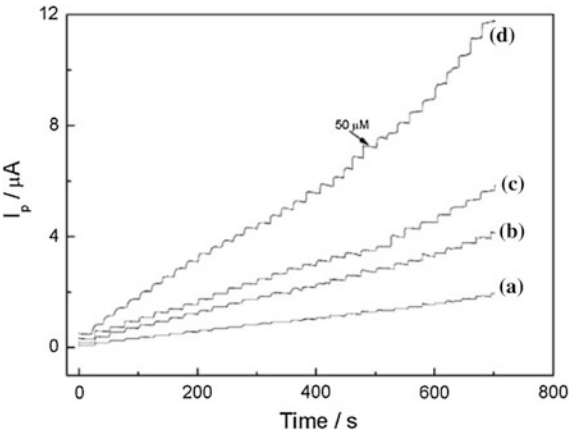

Fig. 5.1 Current–time responses of the different glucose biosensor obtained based on **a** pure chitosan, **b** Ag/Ch, **c** CNT/Ch, and **d** Ag/CNT/Ch films by successive additions of glucose at an applied potential of −0.51 V. Reprinted with permission from [41] © 2009, Elsevier

the changes in glucose concentration, and the reducing current increased to reach a relatively stable value. After optimization of results, the calculated linear range for glucose concentration was found to be in the range from 0.5 to 50 μM with a correlation coefficient R^2 = 0.9990 and LOD 0.1 μM at S/N = 3. The sensitivity of the sensor was calculated as 135.9 μA mM^{-1}. At the glucose concentrations, higher than 50 μM, the detection procedure required a suitable dilution of the serum sample.

In some reports, AgNPs were also used to enhance the current response of sensor. Tang et al. [32] optimized the direct electron transfer between electrode surface and protein to enhance the sensitivity of the electrode. In their study, they used AgNPs to enhance the sensitivity of the glucose sensors. They immobilized GOx in silver sol and cross-linked with polyvinyl butyral medium in glutaraldehyde and coated the platinum electrode with the mixed solution. The current response between an enzyme electrode and a reference electrode of Ag/AgCl was measured to test the sensitivity of biosensor. To prepare the enzyme electrode, the GOx was added to AgNPs solution and the platinum electrode was dipped in this solution for 8 min. The modified glucose sensor achieved a steady-state response which was three times less than GOx (in the absence of AgNPs). The AgNPs function as electron-conducting passages between the prosthetic groups and surface of the electrode; therefore, the rate of electron transfer between the electrode and the enzyme was increased significantly.

The localized surface plasmon resonance (LSPR) is a main tool behind all biomedical uses of metal nanoparticles as elementary optical biosensors that are able to detect interactions between recognizing and target bio-macromolecules near the particle surface [33]. There are vast advantages of using LSPR, which includes label-free and real-time detection and tunable resonant wavelengths, which can be controlled by careful adjustment of the size, shape, and material of nanoparticles [34–40]. Manno et al. [41] utilized the LSPR properties of AgNPs in glucose sensing. The AgNPs in ethanol were prepared and capped by polyvinyl alcohol. To evaluate the specificity of the LSPR-based optical sensor, different varieties of 0.1 M solutions of fructose, sucrose, phosphate buffer, and ultrapure water were introduced into the LSPR-based optical sensor solution. After the addition of ultrapure water, phosphate buffer, fructose, and sucrose solutions no changes were observed in the optical characteristics of the sensing solution; decrease in the LSPR absorbance strength could not be observed. Only after addition of glucose into the AgNPs sensor solution, the change in LSPR absorbance could be observed.

The group of Xia et al. [42] described another SPR-based glucose sensor by utilizing the special properties of homogeneous silver nanoprisms (Fig. 5.2). The group proposed an effective strategy for real-time analysis of glucose at micromole level in serum using colorimetric technique. To check the sensitivity of the colorimetric sensor, different interfering species like maltose, lactose, and fructose were also tested for any interference. The authors further examined the sensitivity and some analytical responses of the designed colorimetric glucose sensor, for which a homogeneous system was made and a series of glucose solutions with different concentrations were added and incubated for 40 min. As the concentration

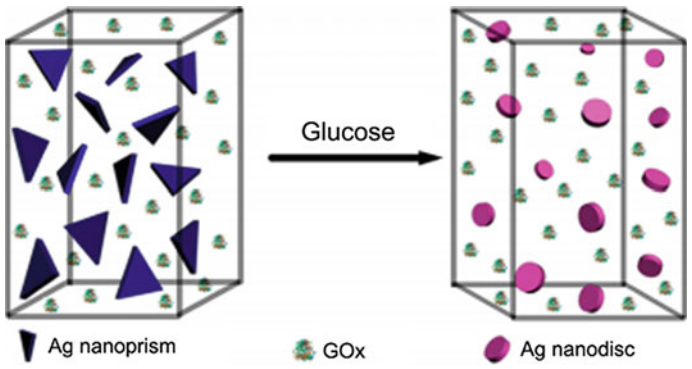

Fig. 5.2 Schematic Illustration of the (Ag Nanoprism)—GOx Homogenous System for Colorimetric Sensing of Glucose. Reprinted with permission from Xia et al. [42] © 2013, American Chemical Society

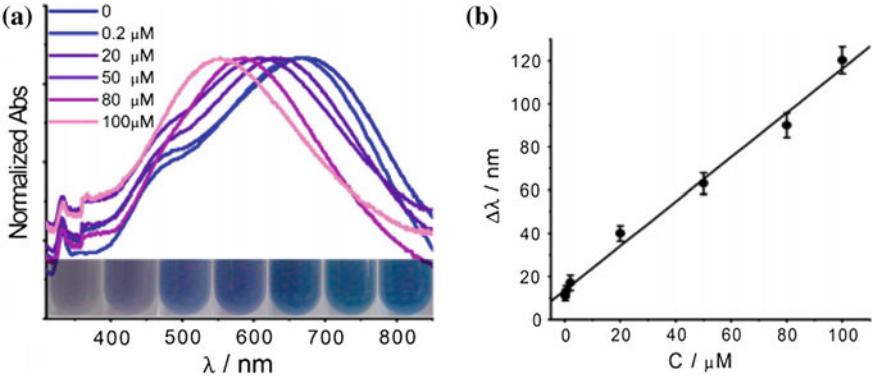

Fig. 5.3 **a** Normalized SPR absorption spectra of the (Ag nanoprism)—GOx after incubation with glucose in various concentrations for 40 min. The *inset* shows a photograph of the corresponding reaction solutions. **b** Plots of SPR peak shift ($\Delta\lambda$) versus concentrations of glucose. Reprinted with permission from Xia et al. [42] © 2013, American Chemical Society

of glucose increases, a gradual blue shift of the in-plane dipole band and a discrete color change of the Ag nanoplates can be observed (blue → purple → mauve) (Fig. 5.3a). Furthermore, a relationship between the SPR peak shift ($\Delta\lambda$) and the glucose concentration was observed which had a good linearity in the range from 0.2 to 100 μM (Fig. 5.3b). Another interesting study in the same report by Xia et al. was done to check the sensitivity of the sensor. The group tested the responses of 17 amino acids, AA, DA, and UA in serum. The linear relationship between SPR peak shifts ($\lambda\Delta$) was found to be in the range of 0.2–100 μM.

AgNPs-decorated ligands have also been used as an electrochemical sensor for glucose detection. Ensafi et al. [43] reported the fabrication process of

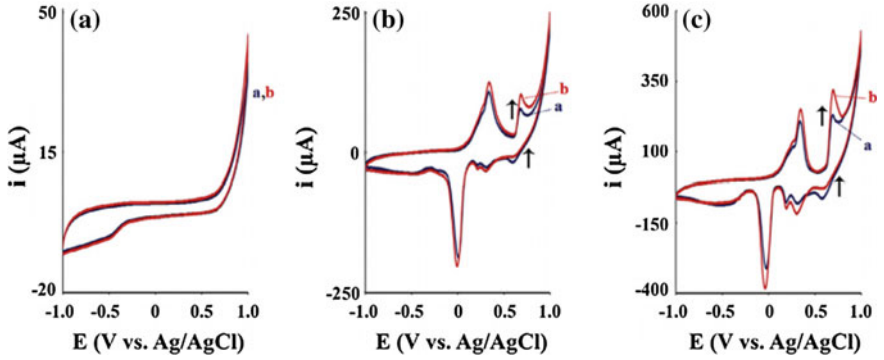

Fig. 5.4 Cyclic voltammograms of SiO_2/CPE (**a**), A/CPE (**b**), and B/CPE (**c**) in 0.1 mol/L NaOH solution in the absence of glucose (*a*) and in the presence of 2.5 mmol/L glucose solution at a scan rate of 100 mV/s (*b*). Reprinted with permission from [43] © 2016, Elsevier

electrochemical sensor based on AgNPs decorated with ligands. The amine moieties of the ligands bound to silica support (SiO_2-pro-NH-cyanuric-NH_2 and SiO_2-pro-NH_2) and attached with AgNPs to sense glucose. The authors compared A/CPE and B/CPE with unmodified electrode, i.e., SiO_2/CPE, to examine glucose sensing, as indicated in Fig. 5.4. The oxidation peaks were increased with the addition of glucose by using the modified electrodes. It was described that the intensity of current of the AgNPs-decorated electrodes was amplified in presence of glucose in comparison with the blank solution (Fig. 5.4b, c). The amperometric responses of A/CPE and B/CPE electrodes were measured with 0.70 V applied potential, versus Ag/AgCl, in 0.10 mol L^{-1} NaOH solution by sequential introduction of glucose (Fig. 5.5a, b). The linear relationship between current and successive introduction of various concentrations of glucose was obtained with a correlation coefficient of $R^2 = 0.999$. The authors found the calibration range for the detection of glucose within the range concentrations from 0.14 to 4.11 mmol L^{-1}. Additionally, the different interfering moieties, which usually co-exist in blood serum with glucose, were also examined to test the specificity of the sensor. The physiological content of glucose in plasma is found to be about 3–8 mmol/L, while UA, AA, and DA are present in quantities as small as 0.1 mmol L^{-1}, which is the ratio 30:1 for the quantity of glucose rather than interference species [44, 45]. The presence of other carbohydrate compounds rather than glucose may affect the performance of the electrodes. The authors described the effect of possible interfering compounds and they resulted that the effect of sucrose and fructose did not have any significant effect on the amperometric responses compared to other interfering species. This is the reason that AA, DA, and UA were easily oxidized in alkaline solutions [46]. Table 5.1 describes the responses for the amperometric studies of the blood serum samples, and three protein-filtered human serum samples were employed for the real sample tests.

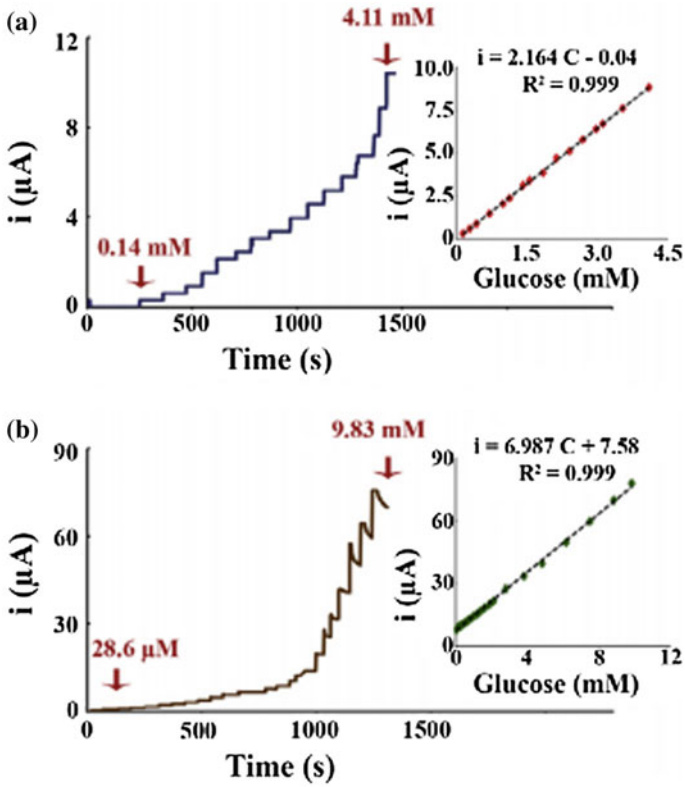

Fig. 5.5 Chronoamperometric studies of A/CPE and B/CPE versus glucose addition in 0.1 mol/L NaOH solution using hydrodynamic electrode at 1000 rmp accompanied with the corresponding calibration curves in accordance with subplots **a** and **b**, respectively. Reprinted with permission from [43] © 2016, Elsevier

Table 5.1 Determination of glucose content in real sample using the AgNPs-decorated SiO_2-pro-NH-cyanuric-NH_2/CPE sensor

Sample	Referenced values[a] (μmol/L)	Determined values[b] (μmol/L)	Relative deviation (%)
Human serum 1	78.4	78.2	−0.29
Human serum 2	49.6	49.1	−1.06
Human serum 3	134.5	136.6	+1.59

[a]Value provided by the hospital
[b]Value determined by the AgNPs-decorated SiO_2-pro-NH-cyanuric-NH_2/CPE

The electrochemical reactions under hypoxia reduce the precision of the glucose measurement. In the body, there is a noteworthy drift caused by bioelectricity which is also responsible for altering the glucose measurements. The solution to this problem was found by some researchers as implantable enzyme electrode sensor for constant glucose monitoring in clinical applications. Hence, finger puncture blood corrections are regularly needed to standardize enzymatic glucose sensors numerous times a day. Li et al. [47] designed an implantable miniaturized fiber sensor utilizing the principle of mid-infrared spectroscopy technique, called attenuated total reflection (ATR) to overcome the drawbacks. This technique was utilized to enlarge the operational optical length for sensitivity improvement (Fig. 5.6). AgNPs were grown on the cylinder-shaped surface of the sensor with a silver mirror reaction, and it has been seen that the sensitivity of the IR absorption signal was further improved. An enhancement factor of twofolds–sixfolds has been seen at different absorption wavelengths when AgNPs-modified ATR sensor used collectively with a CO_2 laser and presented a strong absorption signal from modified electrode in the presence of glucose compared with the bare ATR sensors.

A wavelength adjustable CO_2 laser was used to emit two glucose strong absorption peaks among five wavenumbers, to remove or reduce the effect of interfering species in interstitial fluid to calculate the glucose concentration. The major and isolated absorption peaks of the glucose in the "fingerprint" region differentiate glucose in vitro from interfering species in human blood [48]. Figure 5.7 shows the absorption spectrum of glucose and normalized laser emission spectrum. The ATR sensors, modified by AgNPs, were utilized to examine the characteristic of the improvement based on the ATR theory, for which a sequence of various concentrations of glucose ranging from 5 to 500 mg dL^{-1} was configured (Fig. 5.8). The linearity of the fabricated AgNPs ATR sensor was nearly equal to the bare fiber ATR sensor. Both types of ATR sensors showed linearity better than $R^2 \geq 0.98$. Bare ATR sensor showed the detection limit of glucose as 23 mg dL^{-1} and by growing AgNPs on the fiber ATR sensor showed the detection limit of glucose as 7 mg dL^{-1}, which represented that the resolution of the ATR sensor was greatly improved on modification with AgNPs.

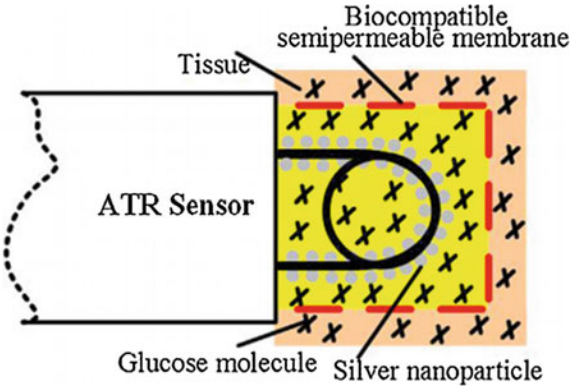

Fig. 5.6 Schematic diagram of implantable single-loop fiber ATR sensor. Reprinted with permission from [47] © 2015, Elsevier

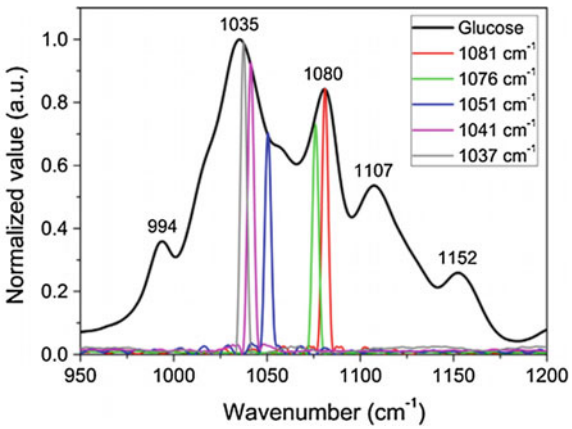

Fig. 5.7 Normalized laser emission spectrum and absorption spectrum of glucose. Reprinted with permission from [47] © 2015, Elsevier

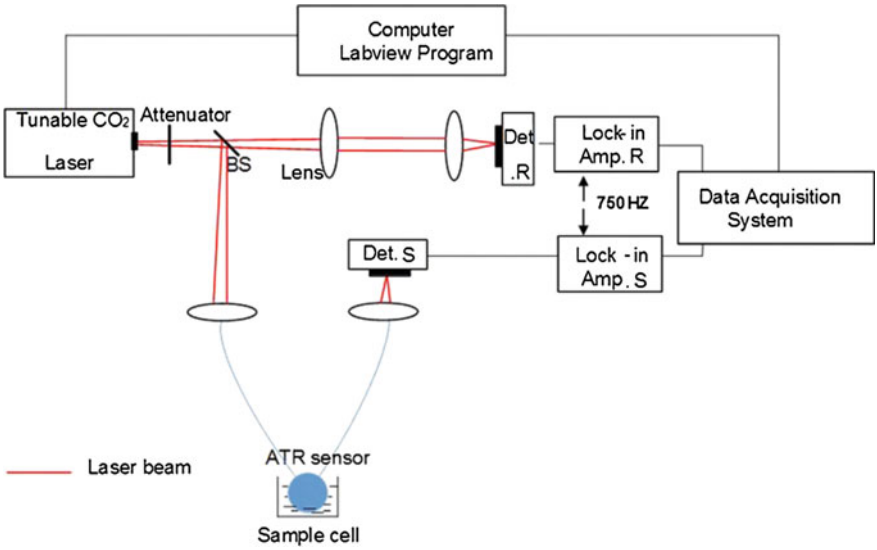

Fig. 5.8 Schematic of the measurement system of both the bare fiber ATR sensor and the fiber ATR sensor with the optimized AgNPs. Reprinted with permission from [47] © 2015, Elsevier

Another study by the Li et al. [49] describes the use of another ATR sensor for continuous glucose monitoring. This new ATR sensor was based on the AgNPs grown on the surface of the sensor. A U-shaped fiber-optic ATR sensor was fabricated which had the radius of 0.25 cm, and AgNPs were grown on the surface of the fiber ATR sensor to improve the sensitivity of the sensor. An adjustable CO_2 laser was utilized as the source of light, with emission wavelengths of glucose

absorption at 1037, 1041, 1051, 1076, and 1081 cm^{-1} to achieve accurate glucose measurements and enhance the sensitivity. The experimental observations point out that the sensitivity and magnitude of resolution of the AgNPs-modified ATR sensor were approximately three times to the conventional sensor. Two wavelengths, 1081 and 1037 cm^{-1}, were chosen to study the effect on absorption and the enhancement factor of intensity of absorption at 1081 and 1037 cm^{-1} was calculated to be $R_{1081} = 2.97$ and $R_{1037} = 3.18$, respectively. For the AgNPs-enhanced ATR sensor, the measurement resolution was approximately 15 mg dL^{-1}, whereas for the bare U-shaped ATR sensor the measurement resolution was approximately 45 mg dL^{-1}. The diabetic person will become unconscious if his/her blood glucose concentration falls below 30 mg dL^{-1} in clinics. Thus, the resolution of this AgNPs-modified ATR sensor may satisfy the clinical conditions for continuous glucose monitoring.

Graphene oxide (GO) was successfully used to fabricate the electrode using AgNPs by using electrodeposition method for sensing of glucose using amperometric technique [50]. GO-AgNPs electrode has given the current response in micro-ampere for micromolar concentration of glucose after only few mg loading of AgNPs. The authors found a linear relationship between peak height in the voltammograms and glucose concentration in the range 1–14 μM for electrochemical detection of glucose. The GO-AgNPs electrode showed the detection limit for glucose sensing as small as 4 μM. The three-electrode system was screen printed and used to verify possibility of GO-AgNPs composite as glucose sensor in human blood serum. Drop casting of composite was done on the working electrode and dried at room temperature, then the electrode was dipped in sodium hydroxide solution and background was recorded. The amperometric responses for glucose were recorded at the potential of 0.6 V by adding further blood in sodium hydroxide solution. Figure 5.9a is a clear demonstration of amperometric response of GO-AgNPs in the presence of 1–14 μM range of glucose concentration. A graph has been plotted between glucose concentration against the limiting current values,

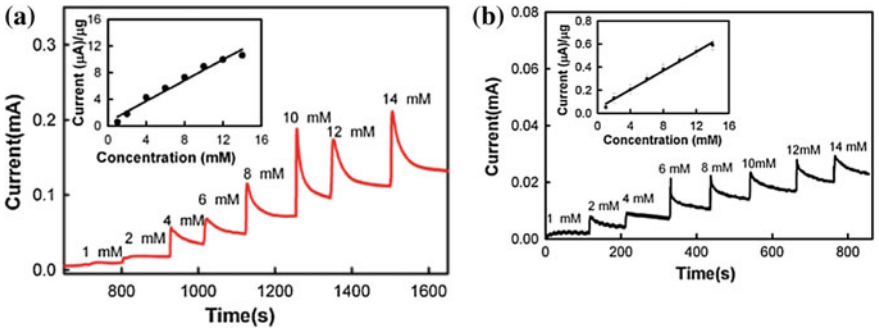

Fig. 5.9 Amperometric response for 1–14 μM glucose concentrations on **a** GO-Ag composite **b** Ag nanoparticles. *Insets* show calibration curves for respective samples showing current variation with concentration and per mg loading of silver. Reprinted with permission from [50] © 2015, Elsevier

which were recorded after each addition and normalized to current per mg of silver loaded (inset Fig. 5.9). The current responses increased linearly with glucose concentration, and data were fitted in a straight line with a correlation coefficient $R^2 = 0.9741$. The authors also checked the sensitivity and LOD and they were noted to be 11 μA mM^{-1} cm^{-2} μg^{-1} and 4 μM, respectively. In a contrary, in case of pure AgNPs (Fig. 5.9b) linear variation of current was obtained for 1–14 μM ($R^2 = 0.9986$) with sensitivity and detection limit of 0.5 μA μM^{-1} cm^{-2} μg^{-1} and 6 μM, respectively.

5.3 Gold Nanoparticles as Glucose Sensor

Chen et al. [51] described an electrodeposition method for the preparation of a chitosan–gold nanoparticles (CHI–AuNPs) nanocomposite sensor fabricated on a glassy carbon electrode (GCE) surface which was simple and controllable. The fabricated glucose sensor exhibited a LOD of 3.70×10^{-4} mol L^{-1} with a good linearity in the range from 4.00×10^{-4} mol L^{-1} to 1.07×10^{-2} mol L^{-1} of glucose concentration for the quantitative analysis of glucose. A one-step method was used to fabricate the pretreated GCE as an electrochemical non-enzyme sensor for glucose determination. The GCE was electrochemically deposited in solution containing chitosan and tetrachloroauric (III) acid at an applied potential of −1.00 V for 60 s (the electrode is denoted as GCE/Ch–AuNPs). Using the same process, an electrode was fabricated by modification with chitosan but without tetrachloroauric (III) acid (the electrode is denoted as GCE/Ch). The influences of some small biomolecules and inorganic ions have been evaluated, under optimized experimental conditions, on the current responses of 3.00×10^{-3} mol L^{-1} glucose. It has been found that UA, AA, phenylalanine and Na^+, Ca^{2+}, Zn^{2+}, Mg^{2+}, K^+ did not have any influence on the current response of glucose, but 1.00×10^{-4} mol L^{-1} cysteine has the serious effect on the sensor. Because cysteine easily adsorbs on the AuNPs surface and occupies the active sites on the surface of modified electrode. This is due to the presence of mercapto group which has better binding tendency toward AuNPs.

AuNPs-anchored nitrogen doped graphene (AuNP/NG) nanohybrids showed good stability, high sensitivity, accuracy, and reproducibility. The AuNP/NG nanohybrids presented excellent effective electrochemically active surface areas for the adsorption of biomolecules, electronic conductivity and successfully accelerated the electron transfer between the electrode and glucose, which could lead to a rapid and sensitive electrochemical current response. Lee et al. [52] evaluated the potential of AuNP/NG nanohybrid as an effective electrochemical catalyst for determination of glucose. The process for making electrode is given in Fig. 5.10.

The AuNP/NG-decorated ITO electrodes, on sequential addition of glucose, exhibited amperometric responses in a linear range from 40 μM to 16.1 mM with a correlation coefficient $R^2 = 0.9946$. The modified ITO electrode sensor showed the calculated sensitivity of to be 0.25 μA mM^{-1} cm^{-2} (Fig. 5.11a). The response time

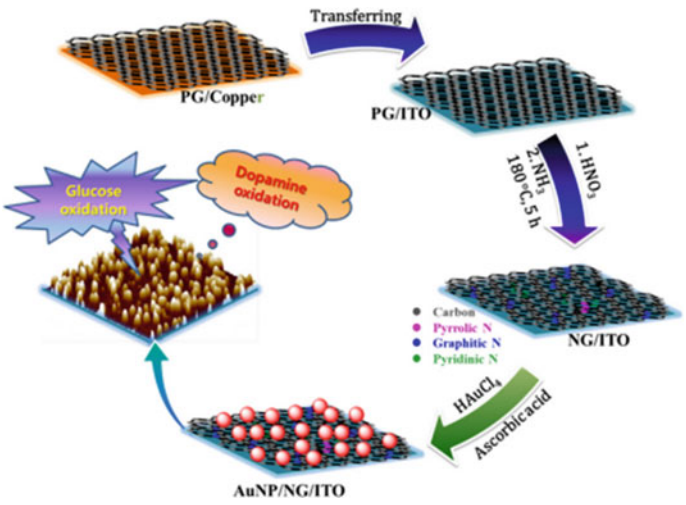

Fig. 5.10 Schematic illustration of AuNP/NG preparation. Reprinted with permission from [52] © 2016, Elsevier

was about 10 s, and the LOD was expected to be 12 μM (S/N = 3). Figure 5.11b shows the amperometric responses at a potential of 0.0 V for 4.0 mM glucose in the presence of different interfering moieties. The AuNP/NG-decorated ITO electrode showed excellent results of sensitivity by showing anti-interference behavior toward AA (0.05 mM), UA (0.05 mM), and DA (0.005 mM). The authors concluded that the non-enzymatic sensing of glucose using the fabricated electrode was performed at the potential of 0.0 V with insignificant interference. To check the long term stability of the sensor, the amperometric response was studied which reveals the current loss is up to 4.5% of the original data after operating time 700 s (Fig. 5.11c). The CV test was also conducted to check the stability of the AuNP/NG-decorated ITO electrode with 4 mM glucose in 0.1 M NaOH solution. The 90% of peak current was detected after 8 days which demonstrates the good stability of the electrode compared with the original value of glucose (Inset in Fig. 5.11c). The validity of the AuNP/NG-decorated ITO electrode was checked, and the recoveries were found to be in the range of 93.1–94.6%. The fabricated glucose sensor by the authors can find it's applications in the evaluation of glucose in real samples.

In 2006, Raj and Jena [53] designed a non-enzymatic method based on AuNPs for the detection of glucose. The 3D silica network was used to self-assemble AuNPs. In the presence of phosphate buffer solution at pH 9.2, AuNPs proficiently catalyzed the oxidation of glucose at little positive potential of 0.16 V in the absence of redox mediators or any enzymes. It has been already established that the starting potential for the oxidation of glucose at the MPTS-nAuE electrode is much more negative (<−0.3 V), which indicates the superb electrocatalytic behavior of self-assembled AuNPs. The catalytic activity of AuNPs toward the oxidation of

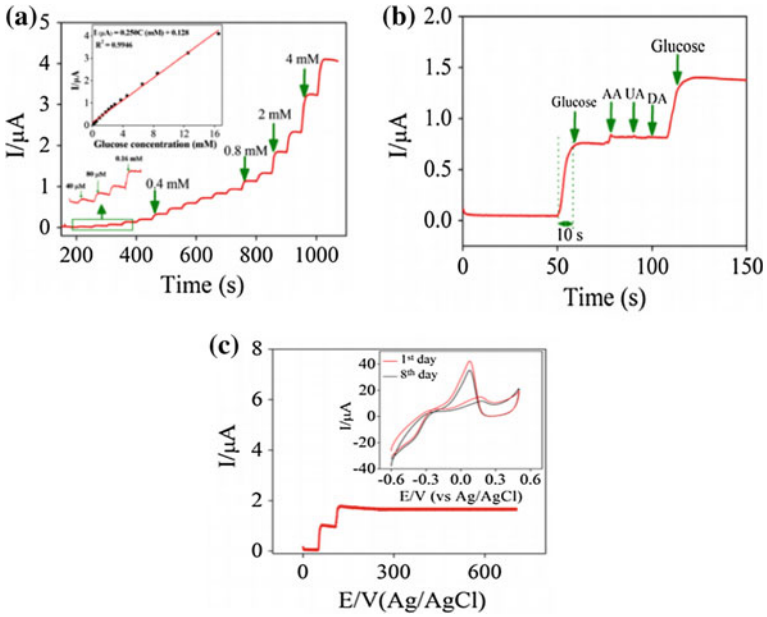

Fig. 5.11 **a** Amperometric curve of the AuNP/NG-modified ITO electrode with injection of different glucose concentrations at 0.0 V and at regular intervals of 50 s (*inset* plots of glucose concentration vs. current), **b** amperometric response of the AuNP/NG-modified ITO electrode under effect of different interferents: 0.05 mM AA, 0.05 mM UA, and 0.005 mM DA, **c** amperometric response of the AuNP/NG-modified ITO electrode toward 4 mM glucose in 0.1 NaOH solution for a running time of 700 s (*inset* CV response of the AuNP/NG-modified ITO electrode after 8 days). Reprinted with permission from [52] © 2016, Elsevier

glucose increases with the increase in surface area of MPTS-nAuE electrode with the growth of the particles. It was considered that the incipient hydrous oxide/adatom mediator model can be applied for the catalytic effect of the AuNPs [54–58]. In the report, authors recorded the amperometric response toward the detection of glucose to test the performance of the MPTS-nAuE sensor (Fig. 5.12). The electrode potential was seized at potential of 0.16 V, and glucose was injected at regular intervals. Authors recorded a speedy increment in the current response after addition of glucose to the constantly stirring the supporting electrolyte solution. The sensitivity of the sensor was calculated to be 0.179 $nAcm^{-2}$ nm^{-1} and with the increased concentration the correlation coefficient of peak current linearly was found to be $R^2 = 0.9988$. The amperometric responses were very stable and the electrode detected the glucose concentration as low as 50 nm. The amperometric response of the sensor at higher concentration was further tested as the normal physiological level of glucose is 3–8 mM (Fig. 5.13). The fabricated sensor electrode demonstrated good capability of the sensor in glucose detection, and the linear response of the sensor have applicability for an extensive array of concentrations of glucose (0–8 mM).

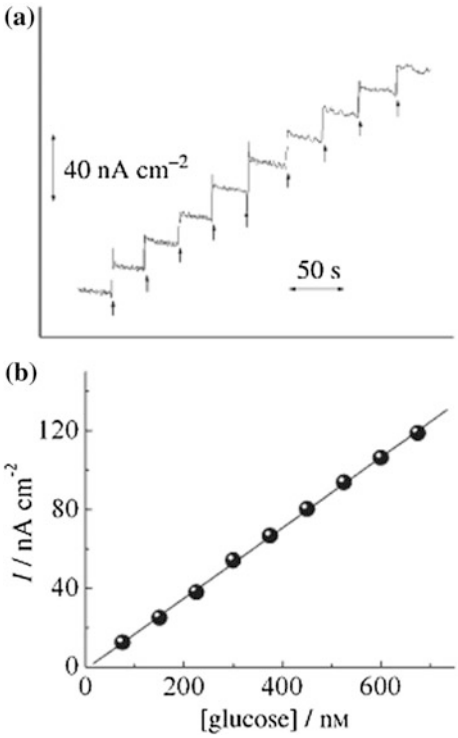

Fig. 5.12 **a** Amperometric current versus time (*i–t*) curve for the detection of glucose at the MPTS-nAuE electrode. Glucose (75 nm) was injected into the stirred 0.1 m PBS at regular intervals; *arrows* indicate the glucose injection. The potential of the electrode was held at 0.16 V. **b** Corresponding calibration plot. Reprinted with permission form [53] © 2006, John Wiley and Sons

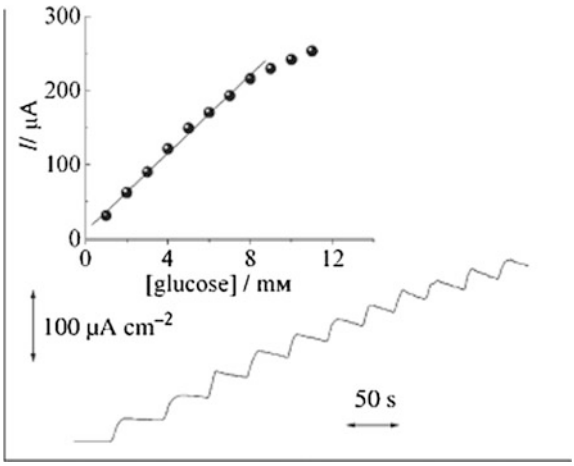

Fig. 5.13 Amperomoetric current versus time (*i–t*) curve for the detection of glucose at the MPTS-nAuE electrode. Glucose (1 mm) was injected into the stirred 0.1 m PBS at regular intervals; all other conditions are similar to those from Fig. 5.6. *Inset* shows the corresponding calibration plot. Reprinted with permission from [53] © 2006, John wiley and Sons

In 2007, Cai et al. [59] reported carbon nanotube and nanoparticle composite to fabricate high-performance electrochemical devices. Cai and group's fabricated glucose sensors demonstrated dependence of their sensitivities to the amount of AuNPs on the CNTs. The enhancement of sensitivity can be attributed to an

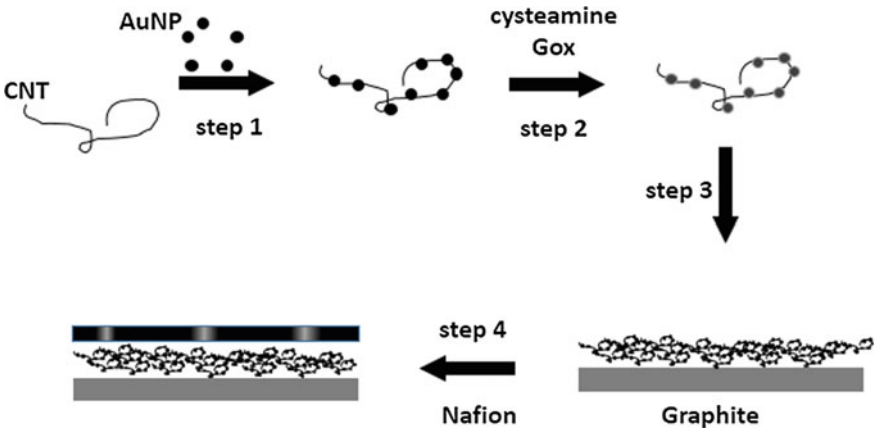

Fig. 5.14 Schematic illustration of glucose sensor made of the AuNP-CNT composite. Reprinted with permission from [59] © 2007, John Wiley and Sons

accelerated electron transfer rate from GOx to the sensing electrode. The fabrication process of AuNPs-CNT composites is shown in Fig. 5.14. The step 1 involved the formation of AuNPs-CNT composite, for which cysteamine was used to modify the surface of AuNPs on the basis of strong thiol gold interactions and in step 2, due to the amine group in cysteamine the surface of composite become positively charged and attracted the negative GOx at neutral pH [60]. In step 3, the modified electrode was dried at 4 °C after dispersion on fine polished graphite disk. Finally, the covering of whole structure of the electrode was done by Nafion in step 4 as reported [61].

In another interesting study, Ekram et al. [62] developed an enzyme-free glucose sensor by using graphite/$SrPdO_3$ electrode modified by AuNPs. According to the data, authors described the use of composite as a glucose sensor by direct oxidation of glucose through the active sites of composite, which enhanced the performance in terms of sensitivity, reproducibility, linearity response, and applicability in blood samples and real urine. The fabricated sensor was found to have linear range in the range from 100 μmol L^{-1} to 6 mmol L^{-1} with the detection limit of 10.1 μmol L^{-1}. The authors investigated three types of metal nanoparticles toward glucose oxidation. Graphite/$SrPdO_3$/Au_{nano} electrode exhibited high current response, good resolution of anodic peak, and quicker electron transfer frequency toward oxidation of glucose among graphite/SrPdO3/Au_{nano}, graphite/SrPdO3/Pt_{nano}, and graphite/SrPdO3/Pd_{nano}. The data for the anodic peak currents for oxidation of glucose are shown in Table 5.2. The electrochemical response of the fabricated electrode was further examined with the scan rate from 0.002 to 0.100 V s^{-1} in a solution containing 5 mmol L^{-1} glucose/0.1 mol L^{-1} NaOH (Fig. 5.15). The peak current was depended on the scan rate as the anodic and cathodic peak currents of glucose increased gradually by increasing the scan rate, and the anodic potential shifted to value that is more positive. The linearity was achieved by relating the anodic peak

Table 5.2 Summary of CV results obtained at different modified electrodes for 5 mmol L^{-1} glucose/0.1 mol L^{-1} NaOH, scan rate 0.050 Vs^{-1}

Electrode	E_{pa}(V)	I_{pa}(mA)	Current increase (normalized to bare graphite)
Bare graphite	−0.135	0.053	–
Graphite/$SrPdO_3$	−0.050	0.140	2.64
Graphite/Au_{nano}	+0.072	0.200	3.81
Graphite/$SrPdO_3$/Au_{nano}	+0.056	2.080	39.6
Graphite/$SrPdO_3$/Pt_{nano}	+0.003	1.270	24.2
Graphite/$SrPdO_3$/Pd_{nano}	−0.052	0.458	8.72

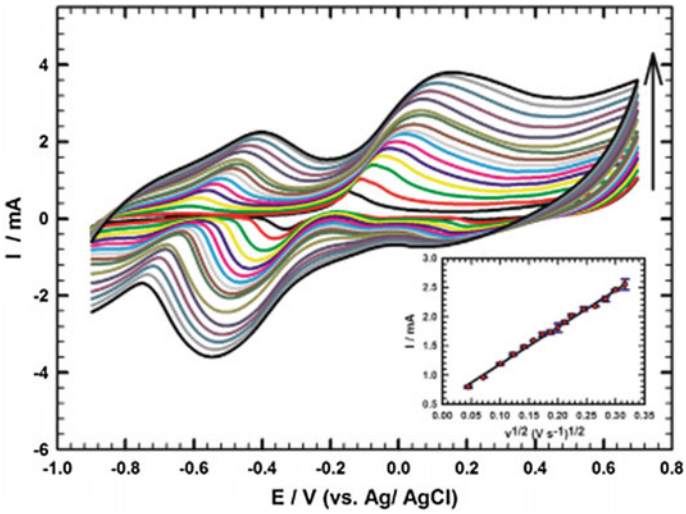

Fig. 5.15 CVs of 5 mmol L^{-1} glucose/0.1 M NaoH at graphite/$SrPdO_3$/Au_{nano} at differrent scan rates (0.002–0.100 Vs^{-1}), the *inset* the plot of the anodic peak current values versus square root of scan rate for 5 mmol L^{-1} glucose/0.1 mol L^{-1} NaoH at graphite/$SrPdO_3$/Au_{nano}. Reprinted with permission from [62] © 2015, Elseiver

current and square root of scan rate using the best fit with the standard error bar (inset of Fig. 5.15) having the correlation coefficient $R^2 = 0.996$ and a linear regression equation of

$$I_{\text{pa}} = 5.51 \times 10^{-4} + 6.35 \times 10^{-3} v^{1/2},$$

where I_{pa} is anodic peak current A and v is the scan rate Vs^{-1}.

To check the stability of the sensor, researchers utilized an amperometric test at the steady-state potential of 0.400 V and the oxidation potential of 0.050 V of glucose in 5 mmol L^{-1} glucose/0.1 mol L^{-1} NaOH. The current response of the fabricated electrode, toward glucose oxidation, was found relatively stable for

20 min at 0.050 V and for 1 h at 0.400 V. Cyclic voltammetry study was also utilized in 5 mmol L^{-1} glucose/0.1 mol L^{-1} NaOH for 50 repeated cycles. Any noticeable decrease in current response was not found which accounts for the excellent stability. As a result, the sensor showed good reproducibility during the repetitive voltammetric measurement and did not suffer from surface contamination. The authors claimed that they did not find any observable decrease in current response by recording the current response of graphite/$SrPdO_3$/Au_{nano} electrode toward glucose after 7 weeks of storage. Thus, the fabricated graphite/$SrPdO_3$/Au_{nano} sensor can be used as non-enzymatic glucose sensor with excellent long term stability.

In another valuable study, a method was developed in which the researchers fabricated a modified gold electrode as a glucose sensor using covalent interactions between GOx and AuNPs [63]. The fabricated nanoparticle enzyme sensor showed an exceptional electrocatalytic performance and rapid and sensitive response with change in glucose concentration was recorded which reached 95% of the steady-state current within 8 s under operating potential of 0.3 V versus SCE (Fig. 5.16). The same was indicated by the current versus time data on successive step changes of glucose concentration. The stability of the fabricated glucose sensor was tested by measuring the decrease in voltammetric current during potential cycling during continuous operation. There was no decrease in I_{cat} when the sensor was subjected to 30 potential cycles from 0 to 0.50 V at a scan rate of 10 mV s^{-1}. The group tested the shelf life of the sensor by measuring glucose concentration at the interval of 2–3 days while storing the enzymatic sensor in 0.1 M phosphate buffer solution at neutral pH at 4 °C. During the first 30 days, the current response of the sensor to glucose remained nearly unaltered, and after 2 months, ~70% of the original response sustained. Thus, the AuNPs-modified electrode could be reasonably efficient for preserving the activity of GOx. The good biocompatibility of AuNPs and strong covalent interactions may be the reasons for such storage stability.

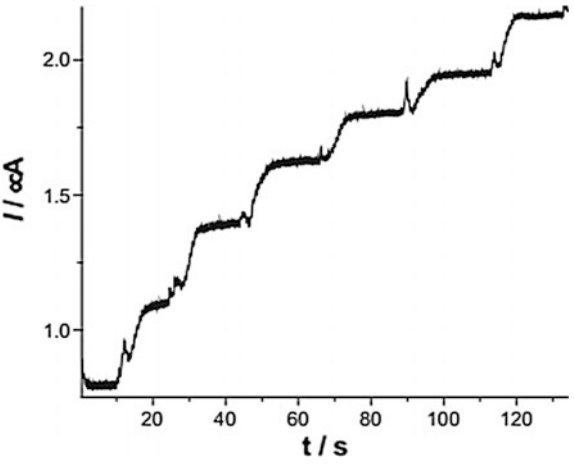

Fig. 5.16 Current–time (*i–t*) curves obtained at the nanoparticle—enzyme electrode for successive addition of 0.1 mL (100 mM) glucose to 10 mL phosphate buffer solution (pH 7.0) containing 0.1 mM ferrocene methanol; applied potential, 0.3 V versus SCE. Reprinted with permission from [63] © 2005, Elseiver

Now, it can be concluded that the assembled AuNPs can simplify the process of electron transfer between analyte and electrode surface, have tiny effect on enzyme activity, and increase the enzyme charging. Some of the advantages which AuNPs-modified sensors exhibit, are high sensitivity, higher affinity for glucose, low detection limit, good storage stability, and reproducibility, and so on. Therefore, the described methods are of interest for the improvement in the field of glucose sensors, especially for the sensors that have minimum or very little electrode area. AuNPs may be used as a favorable medium for the immobilization of enzymes and proteins with superior stability and activity for glucose sensing properties.

5.4 Copper Nanoparticles as Glucose Sensor

In the search of new materials for glucose sensing, researchers are developing new methods and materials to advance the field. In the little time span, variety of metal nanoparticles other than silver and gold have been used as the glucose sensor. Copper nanoparticles (CuNPs) have got special attention due to its low cost, sensitive, and interference-free nature [64]. Several carbon-based nanomaterials have been used as non-enzymatic amperometric sensor for determination of glucose [65–67]. CuNPs have been utilized in nanobuilding materials for sensor technology and biomolecular labeling [68]. These unusual properties of CuNPs are widely studied for potential applications [69–74].

Some researchers used CuNPs, functionalized by dimethylglycoxime (DMG) using microwave method to fabricate the electrode as a new glucose sensor [75]. The electrode was fabricated by depositing DMG-modified CuNPs dissolved in ethanol. The electrode was dried at 4 °C, and the surface was cast by Nafion solution. Figure 5.17 shows the electrochemical behavior of modified and unmodified CuNPs by potential sweep method at a scan rate of 25 mVs^{-1}. The anodic peaks of the cyclic voltammograms (A_1, B_1 and A_2, B_2) correspond to the formation of Cu^{1+} and Cu^{2+}, whereas the cathodic peaks (C_1, D_1 and C_2, D_2) represent the transformation of Cu^{2+} to Cu^{1+} and Cu^{1+} to Cu^0. These predictions are in agreement with other previously published article [76]. This is evidenced by the cyclic voltammograms that DMG has effect on the electrochemical behavior of copper ions due to the strong chelating tendency of copper ions and DMG. Another advantage of using DMG was found that it prevented copper ions from leaching during successive 500 cycles between −1.0 and 0.8 V at a scan rate of 100 mV s^{-1} when no change in anodic or cathodic peak was observed, indicating the stability of the electrode. The amperometric current response of DMG-CuNPs fabricated electrode was measured at potential +0.65 V to attain best signal-to-noise (S/N) ratio for glucose oxidation. Successive addition of glucose gives a linear relationship between current and concentration in the range of 1.0×10^{-6}–3.0×10^{-3} M of glucose concentration. The limit of detection (LOD) was found to be

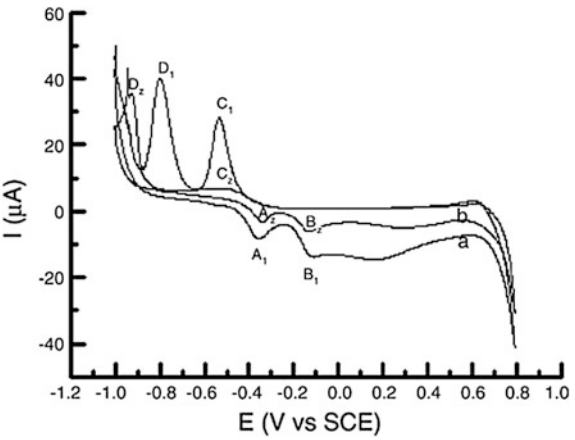

Fig. 5.17 Cyclic voltammograms of **a** a bare copper electrode and **b** DMG-CuNPs chemically modified electrode in 0.1 M NaOH. Scan rate is 25 mVs^{-1}. Reprinted with permission from [75] © 2006, Elseiver

5.0×10^{-7} M at $S/N = 3$. This suggests the high activity of DMG-CuNPs electrode to the oxidation of glucose.

The major advantage of using Nafion coating on the DMG-CuNPs-modified electrode was to reduce the interference caused by the substances such as UA and AA. For this purpose, the property of Nafion as ion change polymer has been used to immobilize electrocatalyst [77]. The coating of Nafion was done as this as possible to exclude the effect of interfering biomaterials because high concentration may cause the reduction of current signal. The fabricated DMG-CuNPs electrode had no observable effect of interfering moieties but hydroxyl containing carbohydrates influence the determination of glucose. Table 5.3 shows the current responses of carbohydrates. The interference caused by carbohydrates can be due to electrocatalytically oxidized CuO(OH) generated at positive potential [78].

The unique properties of CNTs are due to its tube structure and some of the properties are good electrical conductivity, strong adsorptive ability, and excellent bioconsistency. The properties of CNTs are leading the field of glucose sensor with new technical advancements [79–82]. In 2008, some researchers utilized the properties of CNTs in making a composite of CuNPs dispersed in CHI. This composite provided remarkable synergistic effect toward the reduction of H_2O_2

Table 5.3 Amperometric current responses to the other carbohydrates (10–5 M) of the sensor at 0.65 V with 0.1 M NaOH as a supporting electrolyte (the response to glucose was 1.13 μA)

Compounds	Response current for 10^{-5} M compounds (μA)	% Response with respect to glucose ($I_{glucose}$ = 1.13 μA)
Fructose	0.617	54.6
Lactose	0.643	56.9
Sucrose	0.627	55.48
Ribose	1.72	152.2
L-cysteine	0.193	17.08

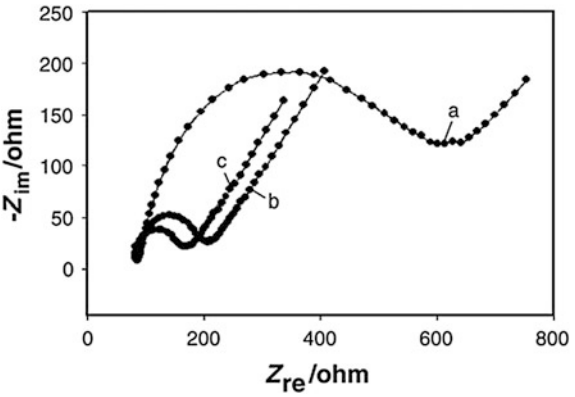

Fig. 5.18 Nyquist plots for different electrodes in 5 mM $[Fe(CN)_6]^{3-/4-}$ containing 0.1 MKCl. **a** Bare GC electrode, **b** CNTs modified GC electrode, **c** Cu/CHI/CNT-modified GC electrode. Reprinted with permission form [83] © 2008, Springer

[83]. At first, GCE was modified with CNTs and then CuNPs, dispersed in CHI, were electrodeposited on the modified electrode. The fabricated electrode is abbreviated as Cu/Ch/CNT in this chapter. The electrochemical impedance spectroscopy (EIS) and current−time curve have been used to test the electrochemical performance of the electrode. Different types of electrodes were prepared to check the electrochemical impedance performance and Nyquist plots of a bare GCE, CNT-modified GCE and a Cu/Ch/CNT-modified GCE are plotted in a 5 mM $[Fe(CN)_6]^{3-/4-}$ redox probe solution (Fig. 5.18).

From Fig. 5.18, it is clear that the radius of the semicircles, curve "a" and curve "b", located near the origin reduced with the modified process of the GC electrode. The change in the semicircle radius indicates the acceleration of electron transfer of the electrochemical probe due to CNTs. The semicircle radius of curve "c" was much smaller which means that the CuNPs and CNTs simplified the electron transfer process on the electrode surface. Therefore, it was obvious that the Cu/Ch/CNT-modified electrode is more suitable for electrochemical sensing due to its smaller resistance of electron transfer. For glucose detection, the fabricated Cu/Ch/CNT-modified electrode was further modified by immobilizing GOx through cross-linking of glutaraldehyde and bovine serum albumin. The fabricated sensor electrode established a linear relationship between current and glucose concentration in the range from 0.05 to 12 mM with LOD 0.02 mM and correlation coefficient of $R^2 = 0.9964$ at S/N 3.

As reported in the literature, CuNPs on modification with poly (3,4-ethylenedioxythiophene) (PEDOT), doped by GO, can be used for high-performance non-enzymatic glucose sensing [84]. CuNPs were electrodeposited on GO and PEDOT nanocomposite through electrochemical reaction in $CuSO_4$ and Na_2SO_4 solution. The process of electrodeposition was carried out for 200 s at a potential of −1.0 V (vs. SCE). GCEs modified with the PEDOT/GO nanocomposite and further electrodeposited CuNPs were denoted as PEDOT/GO and CuNP/PEDOT/GO, respectively. Here again EIS analysis was done to characterize the electrodes. Figure 5.19 shows the Nyquist plots, and it is known that

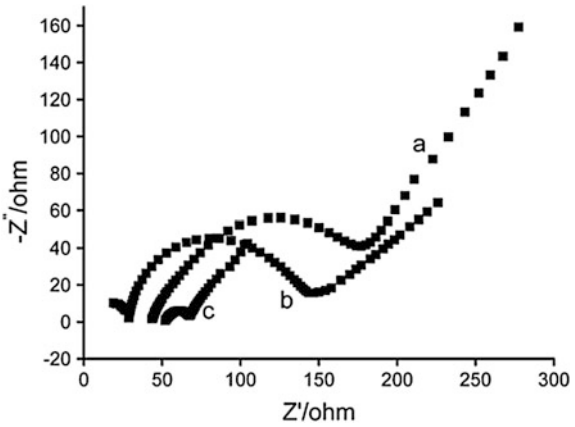

Fig. 5.19 Nyquist plots of **a** the bare GCE, **b** the PED OT/GO, and **c** the CuNP/PEDOT/GO in 50 mM $[Fe(CN)_6]^{4-/3-}$ solution containing 0.1 M KCl. Reprocuced from Ref. [84] with permission from The Royal Society of Chemistry

the Nyquist plot is composed of a semicircle portion and a linear portion, and the semicircle radius is directly proportional to the charge transfer resistance (R_{ct}) [85]. From the figure, it is clear that the radius of PEDOT/GO electrode is much smaller than bare electrode, indicating the electrodeposition of PEDOT/GO on electrode and better charge transfer. On depositing CuNPs on PEDOT/GO electrode, the radius is reduced to even smaller vale. This concludes that CuNPs with good electrical conductivity were deposited successfully and further improved the charge transfer. In this report, CuNP/PEDOT/GO electrode showed a significant oxidation peak at peak potential of 0.55 V.

As expected, the amperometric response of glucose in 0.1 M NaOH showed an extremely sensitive response to the addition of glucose at a concentration as low as 100 nM with response time of 1 s. The good conductivity and huge surface area of CuNP/PEDOT/GO electrode can be the reason for fast diffusion of glucose for the ultrafast response. The fabricated sensor electrode exposed a linear response to glucose concentration in the range of 0.1 μM–1.3 mM having correlation coefficient $R^2 = 0.9986$. The detection limit of the sensor was 47 nM, and sensitivity was 911.96 μA mM^{-1}. The sensor retained about 92% of original response after 30 days which shows the good stability nature of the sensor.

5.5 Conclusions

On the basis of above discussion, metal nanoparticles have found their enormous applications in glucose sensing. As the technology advances, various nanomaterials have been investigated as glucose sensor without interference from other species. Metal nanoparticles possess very high surface area in comparison with bulk metal and can provide much more active sites to immobilize GOx and high electron transfer rate. Amperometric sensors play an important role in sensing of glucose. Researchers are finding this field very attractive due to growing numbers of diabetic

patients. However, there are many challenges which researchers are facing with respect to utilization in the human body, before the commercialization of these techniques is possible. In the future, researchers will lead their work toward sensing of infinitesimally small concentrations of glucose and implantable informing sensors which can be implanted on body and are portable, subcutaneous, and miniaturized. Therefore, there are many challenges for researchers which can be exposed in near future. The search of new materials with high selectivity, low detection limit, a wide detection range, and fast response time will go on and attempts to make these sensors ready for continuous glucose measurement will be made simultaneously. The discussed metal nanoparticles are being able to detect micromolar to nanomolar concentrations of glucose with some modifications. The researchers also checked the effects of interfering species and stability of the sensor. Some fabricated sensors showed excellent anti-interference properties with greater stability. These types of sensors can be further developed and tested for any toxicity toward human body. Overall, metal nanoparticles are the future of glucose sensing which can improve the current technology and reduce the cost of sensor.

References

1. Y. Lin, F. Lu, Y. Tu, Z. Ren, Glucose biosensors based on carbon nanotube nanoelectrode ensembles. Nano Lett. **4**, 191–195 (2004)
2. P. D'Orazio, Biosensors in clinical chemistry. (2003)
3. J.D. Newman, A.P.F. Turner, Home blood glucose biosensors: a commercial perspective. (2005)
4. L.C. Clark, C. Lyons, Electrode systems for continuous monitoring in cardiovascular surgery. Ann. N. Y. Acad. Sci. **102**, 29–45 (1962)
5. C. Deng, J. Chen, X. Chen, C. Xiao, L. Nie, S. Yao, Direct electrochemistry of glucose oxidase and biosensing for glucose based on boron-doped carbon nanotubes modified electrode. Biosens. Bioelectron. **23**, 1272–1277 (2008)
6. R. Wilson, A.P.F. Turner, Glucose oxidase: an ideal enzyme. (1992)
7. S. Schultz, D.R. Smith, J.J. Mock, D.A. Schultz, Single-target molecule detection with nonbleaching multicolor optical immunolabels. Proc. Natl. Acad. Sci. U S A **97**, 996–1001 (2000)
8. J. Yguerabide, E.E. Yguerabide, Light-scattering submicroscopic particles as highly fluorescent analogs and their use as tracer labels in clinical and biological applications. Anal. Biochem. **262**, 157–176 (1998)
9. J.-M. Nam, C.S. Thaxton, C.A. Mirkin, Nanoparticle-based bio-bar codes for the ultrasensitive detection of proteins. Science **301**, 1884–1886 (2003)
10. Rahisuddin Akrema, Biomediated unmodified silver nanoparticles as a green probe for Cu^{2+} ion detection. Sens. Lettors. **13**, 953–960 (2015)
11. C.R. Yonzon, D.A. Stuart, X. Zhang, A.D. McFarland, C.L. Haynes, R.P. Van Duyne, Towards advanced chemical and biological nanosensors—An overview. (2005)
12. A.J. Haes, L. Chang, W.L. Klein, R.P. Van Duyne, Detection of a biomarker for Alzheimer's disease from synthetic and clinical samples using a nanoscale optical biosensor. J. Am. Chem. Soc. **127**, 2264–2271 (2005)
13. A.B. Dahlin, J.O. Tegenfeldt, F. Hŏŏk, Improving the instrumental resolution of sensors based on localized surface plasmon resonance. Anal. Chem. **78**, 4416–4423 (2006)

14. A.D. McFarland, R.P. Van Duyne, Single silver nanoparticles as real-time optical sensors with zeptomole sensitivity. Nano Lett. **3**, 1057–1062 (2003)
15. G. Raschke, S. Kowarik, T. Franzl, C. Sönnichsen, T.A. Klar, J. Feldmann, A. Nichtl, K. Kürzinger, Biomolecular recognition based on single gold nanoparticle light scattering. Nano Lett. **3**, 935–938 (2003)
16. R. Elghanian, J.J. Storhoff, R.C. Mucic, R.L. Letsinger, C.A. Mirkin, Selective colorimetric detection of polynucleotides properties of gold nanoparticles selective colorimetric detection of polynucleotides based on the distance-dependent optical properties of gold nanoparticles. Science **80**, 1078–1081 (2010)
17. J.A. Dieringer, A.D. McFarland, N.C. Shah, D.A. Stuart, A.V. Whitney, C.R. Yonzon, M.A. Young, X. Zhang, R.P. Van Duyne, Introductory lecture surface enhanced Raman spectroscopy: new materials, concepts, characterization tools, and applications. Faraday Discuss. **132**, 9–26 (2006)
18. D.L. Jeanmaire, R.P. Van Duyne, Surface Raman spectroelectrochemistry: part I. heterocyclic, aromatic, and aliphatic amines adsorbed on the anodized silver electrode. J. Electroanal. Chem. Interfacial Electrochem. **84**, 1–20 (1977)
19. K.L. Haller, L.A. Bumm, R.I. Altkorn, E.J. Zeman, G.C. Schat, R.P. Van Duyne, Spatially resolved surface enhanced second harmonic generation: theoretical and experimental evidence for electromagnetic enhancement in the near infrared on a laser microfabricated Pt surface. J. Chem. Phys. **90**, 1237–1252 (1989)
20. T.R. Jensen, R.P. Van Duyne, S.A. Johnson, V.A. Maroni, Surface-enhanced infrared spectroscopy: a comparison of metal island films with discrete and nondiscrete surface plasmons. Appl. Spectrosc. **54**, 371–377 (2000)
21. M. Moskovits, Surface-enhanced spectroscopy. Rev. Mod. Phys. **57**, 783–826 (1985)
22. K. Aslan, J.R. Lakowicz, H. Szmacinski, C.D. Geddes, Enhanced ratiometric pH sensing using SNAFL-2 on silver Island films: metal-enhanced fluorescence sensing. J. Fluoresc. **15**, 37–40 (2005)
23. Y. Chen, K. Munechika, D.S. Ginger, Dependence of fluorescence intensity on the spectral overlap between fluorophores and plasmon resonant single silver nanoparticles. Nano Lett. **7**, 690–696 (2007)
24. A. Sundaramurthy, P.J. Schuck, N.R. Conley, D.P. Fromm, G.S. Kino, W.E. Moerner, Toward nanometer-scale optical photolithography: utilizing the near-field of bowtie optical nanoantennas. Nano Lett. **6**, 355–360 (2006)
25. E. Ozbay, Plasmonics: merging photonics and electronics at nanoscale dimensions. Science **311**, 189–193 (2006)
26. H.A. Atwater, The promise of plasmonics. Sci. Am. **296**, 56–62 (2007)
27. J. Wang, Nanoparticle-based electrochemical DNA detection. Anal. Chim. Acta. pp. 247–257 (2003)
28. E. Katz, I. Willner, J. Wang, Electroanalytical and bioelectroanalytical systems based on metal and semiconductor nanoparticles. Electroanalysis. **16**, 19–44 (2004)
29. W. Ngeontae, W. Janrungroatsakul, P. Maneewattanapinyo, S. Ekgasit, W. Aeungmaitrepirom, T. Tuntulani, Novel potentiometric approach in glucose biosensor using silver nanoparticles as redox marker. Sens. Actuators, B Chem. **137**, 320–326 (2009)
30. K. Aslan, J. Zhang, J.R. Lakowicz, C.D. Geddes, Saccharide sensing using gold and silver nanoparticles—a review. J. Fluoresc. **14**, 391–400 (2004)
31. J. Lin, C. He, Y. Zhao, S. Zhang, One-step synthesis of silver nanoparticles/carbon nanotubes/chitosan film and its application in glucose biosensor. Sens. Actuators, B Chem. **137**, 768–773 (2009)
32. X. Ren, X. Meng, D. Chen, F. Tang, J. Jiao, Using silver nanoparticle to enhance current response of biosensor. Biosens. Bioelectron. **21**, 433–437 (2005)
33. T. Chung, S.Y. Lee, E.Y. Song, H. Chun, B. Lee, Plasmonic nanostructures for nano-scale bio-sensing. Sensors **11**, 10907–10929 (2011)

34. X.Y. Zhang, A. Hu, T. Zhang, W. Lei, X.J. Xue, Y. Zhou, W.W. Duley, Self-assembly of large-scale and ultrathin silver nanoplate films with tunable plasmon resonance properties. ACS Nano **5**, 9082–9092 (2011)
35. J.J. Mock, D.R. Smith, S. Schultz, Local refractive index dependence of plasmon resonance spectra from individual nanoparticles. Nano Lett. **3**, 485–491 (2003)
36. Y. Shao, S. Xu, X. Zheng, Y. Wang, W. Xu, Optical fiber LSPR biosensor prepared by gold nanoparticle assembly on polyelectrolyte multilayer. Sensors **10**, 3585–3596 (2010)
37. N. Cennamo, G. D'Agostino, A. Donà, G. Dacarro, P. Pallavicini, M. Pesavento, L. Zeni, Localized surface plasmon resonance with five-branched gold nanostars in a plastic optical fiber for bio-chemical sensor implementation. Sensors (Basel). 13, 14676–14686 (2013)
38. W. Ma, H. Yang, W. Wang, P. Gao, J. Yao, Ethanol vapor sensing properties of triangular silver nanostructures based on localized surface plasmon resonance. Sensors **11**, 8643–8653 (2011)
39. T. Zhang, Y. Song, X. Zhang, J. Wu, Synthesis of silver nanostructures by multistep methods. Sensors **14**, 5860–5889 (2014)
40. A.J. Haes, S. Zou, G.C. Schatz, R.P. Van Duyne, A nanoscale optical biosensor: the long range distance dependence of the localized surface plasmon resonance of noble metal nanoparticles. J. Phys. Chem. B. **108**, 109–116 (2004)
41. A. Serra, E. Filippo, M. Re, M. Palmisano, M. Vittori-Antisari, A. Buccolieri, D. Manno, Non-functionalized silver nanoparticles for a localized surface plasmon resonance-based glucose sensor. Nanotechnology **20**, 165501 (2009)
42. Y. Xia, J. Ye, K. Tan, J. Wang, G. Yang, Colorimetric visualization of glucose at the submicromole level in serum by a homogenous silver nanoprism-glucose oxidase system. Anal. Chem. **85**, 6241–6247 (2013)
43. M. Ghiaci, M. Tghizadeh, A.A. Ensafi, N. Zandi-Atashbar, B. Rezaei, Silver nanoparticles decorated anchored type ligands as new electrochemical sensors for glucose detection. J. Taiwan Inst. Chem. Eng. **63**, 39–45 (2016)
44. C. Apetrei, I.M. Apetrei, J.A. De Saja, M.L. Rodriguez-Mendez, Carbon paste electrodes made from different carbonaceous materials: application in the study of antioxidants. Sensors (Basel) **11**, 1328–1344 (2011)
45. A.A. Ensafi, M.M. Abarghoui, B. Rezaei, A new non-enzymatic glucose sensor based on copper/porous silicon nanocomposite. Electrochim. Acta **123**, 219–226 (2014)
46. T.G.S. Babu, T. Ramachandran, Development of highly sensitive non-enzymatic sensor for the selective determination of glucose and fabrication of a working model. Electrochim. Acta **55**, 1612–1618 (2010)
47. D. Li, Y. Sun, S. Yu, C. Sun, H. Yu, K. Xu, A single-loop fiber attenuated total reflection sensor enhanced by silver nanoparticles for continuous glucose monitoring. Sens. Actuators, B Chem. **220**, 1033–1042 (2015)
48. S. Yu, D. Li, H. Chong, C. Sun, K. Xu, Continuous glucose determination using fiber-based tunable mid-infrared laser spectroscopy. Opt. Lasers Eng. **55**, 78–83 (2014)
49. D. Li, S. Yu, C. Sun, C. Zou, H. Yu, K. Xu, U-shaped fiber-optic ATR sensor enhanced by silver nanoparticles for continuous glucose monitoring. Biosens. Bioelectron. **72**, 370–375 (2015)
50. A.C. Joshi, G.B. Markad, S.K. Haram, Rudimentary simple method for the decoration of graphene oxide with silver nanoparticles: their application for the amperometric detection of glucose in the human blood samples. Electrochim. Acta **161**, 108–114 (2015)
51. D. Feng, F. Wang, Z. Chen, Electrochemical glucose sensor based on one-step construction of gold nanoparticle-chitosan composite film. Sens. Actuators, B Chem. **138**, 539–544 (2009)
52. T.D. Thanh, J. Balamurugan, S.H. Lee, N.H. Kim, J.H. Lee, Effective seed-assisted synthesis of gold nanoparticles anchored nitrogen-doped graphene for electrochemical detection of glucose and dopamine. Biosens. Bioelectron. **81**, 259–267 (2016)
53. B.K. Jena, C.R. Raj, Enzyme-free amperometric sensing of glucose by using gold nanoparticles. Chem. A Eur. J. **12**, 2702–2708 (2006)

54. R.R. Adzic, M.W. Hsiao, E.B. Yeager, Electrochemical oxidation of glucose on single crystal gold surfaces. J. Electroanal. Chem. Interfacial Electrochem. **260**, 475–485 (1989)
55. M.W. Hsiao, R.R. Adžić, E.B. Yeager, Electrochemical oxidation of glucose on single crystal and polycrystalline gold surfaces in phosphate buffer. J. Electrochem. Soc. **143**, 759–767 (1996)
56. L.D. Burke, P.F. Nugent, The electrochemistry of gold: II the electrocatalytic behaviour of the metal in aqueous media. Gold Bull. **31**, 39–50 (1998)
57. L.A. Larew, D.C. Johnson, Concentration dependence of the mechanism of glucose oxidation at gold electrodes in alkaline media. J. Electroanal. Chem. **262**, 167–182 (1989)
58. L.D. Burke, Scope for new applications for gold arising from the electrocatalytic behaviour of its metastable surface states. Gold Bull. **37**, 125–135 (2004)
59. D. Cai, Y. Yu, Y. Lan, F.J. Dufort, G. Xiong, T. Paudel, Z. Ren, D.J. Wagner, T.C. Chiles, Glucose sensors made of novel carbon nanotube-gold nanoparticle composites. BioFactors **30**, 271–277 (2007)
60. Q. Chen, G.L. Kenausis, A. Heller, Stability of oxidases immobilized in silica gels. J. Am. Chem. Soc. **120**, 4582–4585 (1998)
61. H. Tang, J. Chen, S. Yao, L. Nie, G. Deng, Y. Kuang, Amperometric glucose biosensor based on adsorption of glucose oxidase at platinum nanoparticle-modified carbon nanotube electrode. Anal. Biochem. **331**, 89–97 (2004)
62. E.H. El-Ads, A. Galal, N.F. Atta, Electrochemistry of glucose at gold nanoparticles modified graphite/$SrPdO_3$ electrode—towards a novel non-enzymatic glucose sensor. J. Electroanal. Chem. **749**, 42–52 (2015)
63. S. Zhang, N. Wang, H. Yu, Y. Niu, C. Sun, Covalent attachment of glucose oxidase to an Au electrode modified with gold nanoparticles for use as glucose biosensor. Bioelectrochemistry **67**, 15–22 (2005)
64. X. Kang, Z. Mai, X. Zou, P. Cai, J. Mo, A sensitive nonenzymatic glucose sensor in alkaline media with a copper nanocluster/multiwall carbon nanotube-modified glassy carbon electrode. Anal. Biochem. **363**, 143–150 (2007)
65. J. Yang, L.C. Jiang, W.D. Zhang, S. Gunasekaran, A highly sensitive non-enzymatic glucose sensor based on a simple two-step electrodeposition of cupric oxide (CuO) nanoparticles onto multi-walled carbon nanotube arrays. Talanta **82**, 25–33 (2010)
66. J. Yang, W. De Zhang, S. Gunasekaran, An amperometric non-enzymatic glucose sensor by electrodepositing copper nanocubes onto vertically well-aligned multi-walled carbon nanotube arrays. Biosens. Bioelectron. **26**, 279–284 (2010)
67. J. Luo, S. Jiang, H. Zhang, J. Jiang, X. Liu, A novel non-enzymatic glucose sensor based on Cu nanoparticle modified graphene sheets electrode. Anal. Chim. Acta **709**, 47–53 (2012)
68. J. Wang, G. Chen, M. Wang, M. Chatrathi, Carbon-nanotube/copper composite electrodes for capillary electrophoresis microchip detection of carbohydrates. Analyst. **129**, 512 (2004)
69. L. Lu, M.L. Sui, K. Lu, Superplastic extensibility of nanocrystalline copper at room temperature. Science (80-.). 287, 1463–1466 (2000)
70. J.A. Eastman, S.U.S. Choi, S. Li, W. Yu, L.J. Thompson, Anomalously increased effective thermal conductivities of ethylene glycol-based nanofluids containing copper nanoparticles. Appl. Phys. Lett. **78**, 718–720 (2001)
71. T. You, O. Niwa, M. Tomita, H. Ando, M. Suzuki, S. Hirono, Characterization and electrochemical properties of highly dispersed copper oxide/hydroxide nanoparticles in graphite-like carbon films prepared by RF sputtering method. Electrochem. Commun. **4**, 468–471 (2002)
72. S.T. Farrell, C.B. Breslin, Oxidation and photo-induced oxidation of glucose at a polyaniline film modified by copper particles. Electrochim. Acta **49**, 4497–4503 (2004)
73. K.B. Male, S. Hrapovic, Y. Liu, D. Wang, J.H.T. Luong, Electrochemical detection of carbohydrates using copper nanoparticles and carbon nanotubes. Anal. Chim. Acta **516**, 35–41 (2004)
74. J.Z. Xu, J.J. Zhu, H. Wang, H.Y. Chen, Nano-sized copper oxide modified carbon paste electrodes as an amperometric sensor for amikacin. Anal. Lett. **36**, 2723–2733 (2003)

75. Q. Xu, Y. Zhao, J.Z. Xu, J.J. Zhu, Preparation of functionalized copper nanoparticles and fabrication of a glucose sensor. Sens. Actuators, B Chem. **114**, 379–386 (2006)
76. C.H. Pyun, In situ spectroelectrochemical studies on anodic oxidation of copper in alkaline solution. J. Electrochem. Soc. **133**, 2024 (1986)
77. S. Dong, T. Kuwana, Cobalt-porphyrin-Nafion film on carbon microarray electrode to monitor oxygen for enzyme analysis for glucose. Electroanalysis **3**, 485–491 (1991)
78. Y. Xie, C.O. Huber, Electrocatalysis and amperometric detection using an electrode made of copper oxide and carbon paste. Anal. Chem. **63**, 1714–1719 (1991)
79. L. Jiang, R. Wang, X. Li, L. Jiang, G. Lu, Electrochemical oxidation behavior of nitrite on a chitosan-carboxylated multiwall carbon nanotube modified electrode. Electrochem. Commun. **7**, 597–601 (2005)
80. S. Hrapovic, Y. Liu, K.B. Male, J.H.T. Luong, Electrochemical biosensing platforms using platinum nanoparticles and carbon nanotubes. Anal. Chem. **76**, 1083–1088 (2004)
81. Y.C. Tsai, S.C. Li, J.M. Chen, Cast thin film biosensor design based on a nafion backbone, a multiwalled carbon nanotube conduit, and a glucose oxidase function. Langmuir **21**, 3653–3658 (2005)
82. M. Zhang, A. Smith, W. Gorski, Carbon nanotube-chitosan system for electrochemical sensing based on dehydrogenase enzymes. Anal. Chem. **76**, 5045–5050 (2004)
83. Y. Wang, W. Wei, J. Zeng, X. Liu, X. Zeng, Fabrication of a copper nanoparticle/chitosan/carbon nanotube-modified glassy carbon electrode for electrochemical sensing of hydrogen peroxide and glucose. Microchim. Acta **160**, 253–260 (2008)
84. N. Hui, W. Wang, G. Xu, X. Luo, Graphene oxide doped poly(3,4-ethylenedioxythiophene) modified with copper nanoparticles for high performance nonenzymatic sensing of glucose. J. Mater. Chem. B. **3**, 556–561 (2015)
85. M. Xu, X. Luo, J.J. Davis, The label free picomolar detection of insulin in blood serum. Biosens. Bioelectron. **39**, 21–25 (2013)

Chapter 6
Application of Nanomaterials in Civil Engineering

Md Daniyal, Ameer Azam and Sabih Akhtar

Abstract The potential use of carbon nanotubes, SiO_2, TiO_2, Fe_2O_3, CuO, ZrO_2, ZnO_2, Al_2O_3, $CaCO_3$, Cr_2O_3 and Ag nanoparticles in the civil engineering has been explored in this article. Most of the studies showed that addition of nanomaterials in appropriate quantity improved the strength and durability properties but decreased setting time as well as workability of cementitious composites. The other challenges include high cost, environmental and health risks associated with nanomaterials. That is why the comprehensive recommendations for the utilization of nanomaterials in day-to-day construction practice are still awaited. Also, a study to evaluate the corrosion behaviour of graphene and nano-TiO_2-incorporated steel-reinforced cementitious composite has been undertaken. The nanoadmixed composite showed lower corrosion rate compared to uninhibited specimens at early ages. However, more results are required involving fairly longer period of time to establish graphene and nano-TiO_2 as corrosion inhibitors.

Keywords Nanomaterials · Cementitious composites · Strength · Durability Civil engineering

M. Daniyal · S. Akhtar (✉)
Department of Civil Engineering,
Aligarh Muslim University, Aligarh 202002, India
e-mail: sabihced@yahoo.co.in

M. Daniyal
e-mail: daniyalzhcet@gmail.com

A. Azam
Department of Applied Physics,
Aligarh Muslim University, Aligarh 202002, India
e-mail: azam2288@gmail.com

Z.H. Khan (ed.), *Nanomaterials and Their Applications*,
Advanced Structured Materials 84, https://doi.org/10.1007/978-981-10-6214-8_6

6.1 Introduction

Nanotechnology was first introduced by physicist Richard P. Feynman in his famous lecture in a meeting of the American Physical Society at the California Institute of Technology in 1959 [1]. However, after two decades, it was defined as the manufacture of materials using sizes and accuracy of between 0.1 and 100 nm by Drexler [2]. Therefore, this is not a new science or technology but became a hot research topic in last two decades. Hence, nanotechnology refers to the development of devices, structures and systems by controlled manipulation of size and shape with at least one typical dimension measured in nanometres (atomic, molecular and macromolecular scale) [3]. In fact, the size of particles plays an important role in this technology because the properties of materials are significantly affected at nanometre level. This is because of the fact that at nanoscale, electrostatic forces and quantum effects begin to prevail over gravity. Also, as particles of matter turn into nanosized, the quantity of atoms on the surface relative to those inside increases and this leads to improve the properties. Moreover, nanomaterials may be obtained either through chemical synthesis or by high milling energy. These materials may be in the form of layers (if only one characteristics dimension in the nanoscale like surface coatings or thin films, graphene), nanowires or nanotubes (if two dimensions are in nanoscale) or particles (if all the dimensions are in nanoscale such as quantum dots, precipitates and colloids). The two most important factors which cause the properties (such as reactivity, strength and electrical characteristics) of nanomaterials to differ extensively from other materials are increased surface area to volume ratio and quantum effects [4, 5].

The use of nanomaterials is increasing in the various fields such as biomedicine, automobile, electronics, robotics, construction industry because of their unique mechanical, chemical, electronic and optical properties. However presently, use of nanotechnology and nanomaterials in civil engineering particularly in construction industry is very less [6–8]. This is mainly due to the lack of comprehensive information regarding the suitable construction nanomaterials, highly expensive and health risks associated with nanomaterials [9–21]. Therefore, in order to use the nanomaterials in the construction sector effectively, researches and investigations are required to find out various facts like performance of nanomaterials and their reactive mechanism with composite materials like cement, the preference of nanomaterials with possible use in construction, characteristics and behaviour of the building elements that have nanomaterials under different loading conditions. However, only few studies are reported in literature on the application of nanotechnology and nanomaterials in the area of construction. This article reviews the advancement made with the use of nanomaterials in civil engineering and particularly in construction field. Moreover, there is not any published study on the corrosion behaviour of steel in cementitious composite containing nanomaterials. Therefore, to fill this gap a proposal has been made in order to evaluate the corrosion behaviour of graphene and nano-TiO_2-incorporated steel-reinforced cementitious composite.

6.2 Nanomaterials Used in Civil Engineering

After growing the use of nanotechnology in various fields such as biomedical sciences, automobile and electronic industries, recently construction industries also started to use nanomaterials in conventional construction materials. Currently, these materials are mainly used to give stronger structural composites, lighter structure, enhanced properties of cementitious materials, low maintenance coating, better pipe joining materials, better heat and sound insulation, improved reflectivity of glass, water repellents, self-cleaning and antifogging surfaces, ultraviolet light protector, nanosized sensors to monitor construction safety and structural health and solar cells. Hence, the application of some nanomaterials in civil engineering and their effects are listed in Table 6.1 [22–84].

6.2.1 Carbon Nanotubes (CNTs)

Carbon nanotubes are allotropes of carbon with a cylindrical tubular geometry of diameter that ranges from 1 to 100 nm and lengths up to a few millimetres. They can have single layer of graphene rolled in a cylindrical shape, called as single-wall carbon nanotube (SWCNT), or more than one layer, called as multiwall carbon nanotube (MWCNT). They are the strongest and stiffest material known to date and hold great promise for reinforcing cement-based composites [22–27]. They show unique electrical, thermal and mechanical properties because of their geometry and covalent sp^2 bonds formed between the individual carbon atoms. For instance, they have eight times the strength, 1/6th times the density and five times Young's modulus of elasticity of steel.

Some expected benefits of use of carbon nanotubes in concrete along with some dispersion agents includes enhancement in strength, durability and crack prevention in concrete, improvement in mechanical and thermal properties in ceramics and ability of real-time health assessment of structures [28]. Dispersion agents or techniques are used for deagglomeration and subsequent distribution of CNTs within matrices because they have strong tendency to agglomerate due to the presence of attractive forces (Van der Waals). Therefore, various researches have been conducted and highlighted the potential use of carbon nanotubes in cementitious matrix with different types of dispersion techniques as shown in Table 6.2.

Recently, sensors like nano- and microelectrical mechanical systems (MEMS) have been developed and used in concrete structures for accurate real-time health assessment of material or structures such as cracking, corrosion, wear and stress. These sensors could be easily fixed into the structures during the period of construction. Also smart aggregate (piezoceramic-based multifunctional device) has been used to observe properties of concrete at early age like temperature, moisture, strength and relative humidity [29, 30]. Further, CNT/polycarbonate nanocomposite provides an early warning on the probable structural health damage because it

Table 6.1 Nanomaterials used in constructions with possible benefits

Nanomaterials	Base materials	Possible benefits	References
Carbon nanotube (CNT)	Cement and concrete	Improvement in mechanical strengths and durability	[22–27, 33–42]
	Ceramics	Enhancement in thermal and mechanical properties	[28]
	Nanoelectrical mechanical systems	Real-time health assessment of structures	[29–31]
	Solar cell	Efficient electron mediation	[32]
Silicon dioxide (SiO_2)	Cement and concrete	Enhancement in mechanical Strengths and durability	[43–54]
	Glass	Antireflective and heat isolation	[55]
Titanium dioxide (TiO_2)	Solar cell	Non-utility power production	[56]
	Glass	Antifogging, hydrophilicity, fouling resistance	[57, 58]
	Cement and concrete	Self-cleaning, rapid hydration and improvement in mechanical strengths	[57–61]
Ferric oxide (Fe_2O_3)	Cement and concrete	Improvement in mechanical strengths and durability	[62–65]
Copper oxide (CuO)	Cement and concrete/steel	Improved mechanical strengths and durability, enhanced weldability and corrosion resistance of steel	[66–68]
Aluminium oxide (Al_2O_3)	Cement and concrete	Enhancement in mechanical strengths	[69–72]
Zirconium oxide (ZrO_2)	Cement and concrete	Improvement in mechanical strengths	[73–75]
Zinc dioxide (ZnO_2)	Cement and concrete	Improvement in mechanical strengths	[76, 77]
Calcium carbonate ($CaCO_3$)	Cement and concrete	Enhancement in mechanical strengths	[78–81]
Chromium oxide (Cr_2O_3)	Cement and concrete	Improvement in mechanical strengths	[82, 83]
Silver (Ag)	Paints	Antimicrobial properties	[84]

produces quick changes in the electrical resistance when the device senses strain inputs [31]. Furthermore, one of the most important applications of CNTs is to enhance the performance of fuel and solar cells that produce renewable energy because of its remarkable electron transfer properties [32].

Table 6.2 Techniques used for CNT dispersion and their effects on composite

Type and CNTs (wt%)	Dispersion techniques	Effects	References
MWCNT (0.045)	Superplasticizer	Compressive and tensile strength increased by 26.69 and 66.3%, respectively	[26]
SWCNT (0.06)	Superplasticizer	Compressive strength increased by 29.7%	[27]
MWCNT (1.0)	Ultrasonication	Total porosity decreased by 16%	[33]
SWCNT (1.0)	Ultrasonication	Compressive strength improved by 10%	[34]
MWCNT (0.2)	Ultrasonication and Superplasticizer	Ductility and flexural strength improved by 81 and 26.9%, respectively	[35]
MWCNT (0.08)	Ultrasonication and surfactant	Flexural strength and modulus of elasticity improved by 25 and 45%, respectively	[36]
SWCNF (0.048)	Ultrasonication and surfactant	Flexural strength and Young′s modulus improved by 50 and 75%, respectively	[37]
MWCNT (0.5)	Ultrasonication and Solvent	Compressive strength improved by 11%	[38]
MWCNT (0.2)	Ultrasonication, magnetic stirring and surfactant	Compressive and flexural strength improved by 29.5 and 35.4%, respectively	[39]
MWCNT (0.5)	Ultrasonication, magnetic stirring and polycarboxylate	Compressive strength improved by 25%	[40]
MWCNT (0.045)	Carboxylic acid, ultrasonication and polyacrylic acid	Compressive strength improved by 50%	[41]
SWCNF (0.5)	Acetone, ultrasonication and surfactant	Load-carrying capacity and failure strain improved by 54 and 44%, respectively	[42]

6.2.2 *Silicon Dioxide (SiO_2) Nanoparticles*

Silica fume or microsilica is a by-product of silicon and ferrosilicon alloys. This is a grey powder having surface area in the order of 20 m^2/g and particle sizes in the range of 100–200 nm. It has been observed that the addition of silica fume (by weight in the concrete mix) could increase compressive strength, tensile strength and abrasion resistance compared to the reference samples. These improvements are in fact due to the closed packing achieved in the cement paste system that reduces the overall porosity and improves the interfacial transition zone (ITZ). The reduction of porosity produces a concrete more durable and resistant to chemical

degradation processes like chloride ion diffusion, alkali silica reaction and calcium leaching, which preserves the material from mechanical degradation and protects reinforcing steel from corrosion [43]. Furthermore, several recent researchers report on the significant advantages of nano-SiO_2 (NS) as compared to silica fume (SF). The results of one such research are shown in Fig. 6.1 [44].

Therefore, it is evident from the results that the incorporation of nano-SiO_2 with silica fume or fly ash in the concrete could considerably enhance the mechanical strengths by filling the tiny pores between cement particles and silica fume/fly ash. It also reduces setting time of mortar, segregation and bleeding of concrete due to improved cohesiveness [45–48]. It was also observed that the addition of 3% nanosilica in cement mortar enhanced chloride ion diffusion resistance up to 43% whereas incorporation of silica fume improved 15% only [49]. However, most of the study reported that the addition of nanosilica alone up to 2% weight of cement enhanced the mechanical strengths and durability of cementitious composites [50–53]. Conversely, the flowing characteristics of fresh concrete may be affected due to the large surface area of nanosilica, which decreases the amount of lubricating water. Thus, it is essential to use some superplasticizers with nanosilica, so as to avoid air entraining in the fresh concrete and benefiting from the above-described performance [54]. Further, nanosilica can be used for the production of fire-protective glass. This is achieved by providing a layer of nanosilica in between two glass panels, which turns into a dense and rigid fire protector. Therefore, these glass panels control exterior light as an antireflection coating and hence conserve the energy (air conditioning) [55]. Hence, the microstructure of the cementitious composites can be enhanced with the aid of nanosilica and consequently producing more durable and sustainable materials.

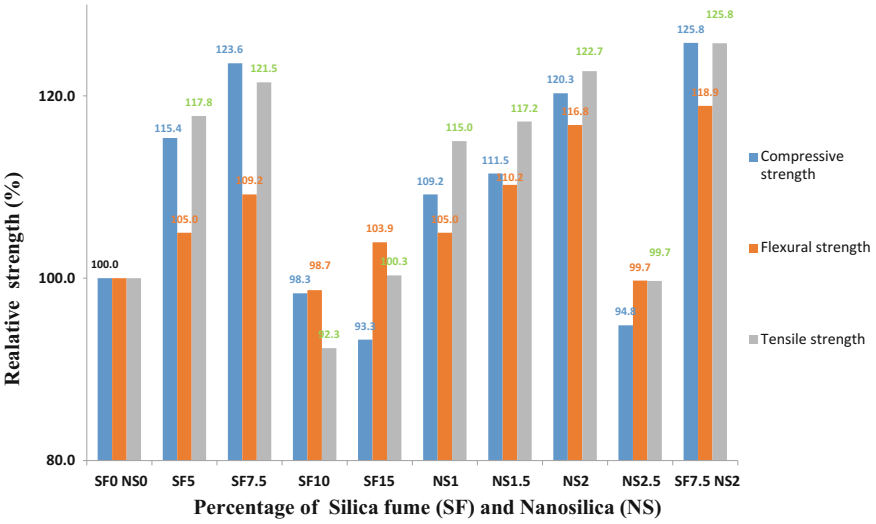

Fig. 6.1 Mechanical strengths of concrete containing silica fume and nanosilica

6.2.3 Titanium Dioxide (TiO_2) Nanoparticles

Recently, titanium dioxide nanoparticles have gained significant attention in the construction industry due to their self-cleaning properties and the ability to remove air pollutants through photocatalytic reactions. TiO_2 are semiconductors that act as photocatalysts when irradiated by ultraviolet (UV) light in the presence of gas or liquid [56]. When mixed with cement, it can photocatalytically degrade organic pollutants that are, after neutralization, washed away through the hydrophilic nature of the surface and hence maintaining the aesthetic characteristics of concrete structures, particularly those constructed with white cement [57]. Thus, TiO_2 nanoparticles are added to tiles, windows, cements, paints, etc., because of sterilizing and deodorizing properties and when included into outdoor construction materials can considerably decrease concentrations of airborne pollutants. Moreover, TiO_2 nanoparticles have proven very efficient in the removal of pollutants such as NOx, aromatics, aldehydes, ammonia and currently used in various infrastructure projects like pavements, tunnels, buildings [58].

Furthermore, it has been reported that TiO_2 nanoparticles can be used as a partial replacement of cement in the concrete mix. In one such research, it is found that the TiO_2 nanoparticles (up to 2.0%) could be advantageously used in place of cement, although the addition of TiO_2 nanoparticles not only increased the compressive, flexural and split tensile strength of concrete but also decreased its workability and setting time as shown in Fig. 6.2 [59, 60]. In another investigation, it was observed that the incorporation of 1% TiO_2 nanoparticles enhanced the compressive strength and durability performance of high-performance concrete [61]. Hence, TiO_2 nanoparticles can be advantageously used in construction industry.

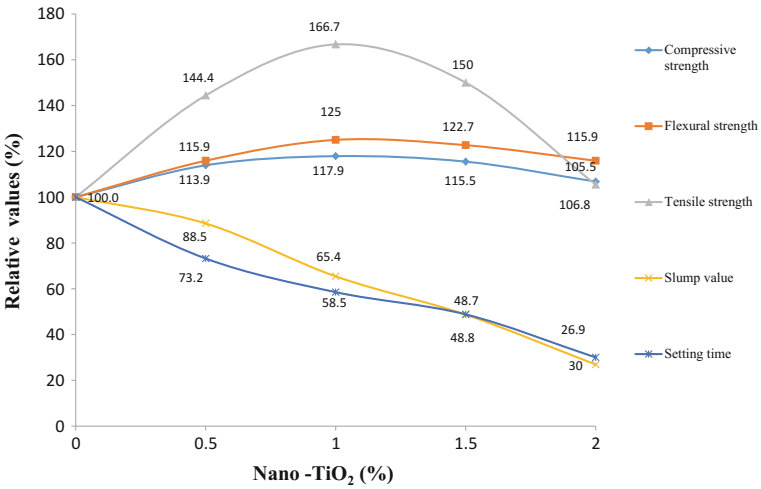

Fig. 6.2 Properties of 0.5–2% nano-TiO_2 incorporated cementitious composite relative to control composite

6.2.4 Ferric Oxide (Fe_2O_3) Nanoparticles

The use of Fe_2O_3 nanoparticles for enhancing the mechanical characteristics of cement and concrete has been carried out by few researchers. In one such investigation, it is observed that Fe_2O_3 nanoparticles could be used in concrete as a partial replacement of cement. The results of investigation show that the addition of Fe_2O_3 nanoparticles improved the strength properties of concrete but decreased its setting time and workability [62, 63]. The results of a similar study show that the properties of samples containing up to 3% Fe_2O_3 nanoparticles are desirable than the conventional cement mortar [64]. In another experiment, it was found that Fe_2O_3 nanoparticles could be advantageously used in high-performance self-compacting concrete as shown in Fig. 6.3 [65].

These increments in mechanical characteristics of concrete are due to the quick reaction between calcium hydroxide and Fe_2O_3 nanoparticles. Consequently, the hydration of cement is increased and larger amounts of reaction products are formed. However, some superplasticizer should be used while adding Fe_2O_3 nanoparticles for increasing the workability of fresh concrete.

6.2.5 Copper Oxide (CuO) Nanoparticles

The use of CuO nanoparticles in cement and concrete has been carried out by few investigators. It has been reported that CuO nanoparticles can be used in concrete as a partial replacement of cement. The results indicate that the addition of CuO nanoparticles improved the mechanical strengths and reduced the porosity of concrete as shown in Fig. 6.4 [66–68].

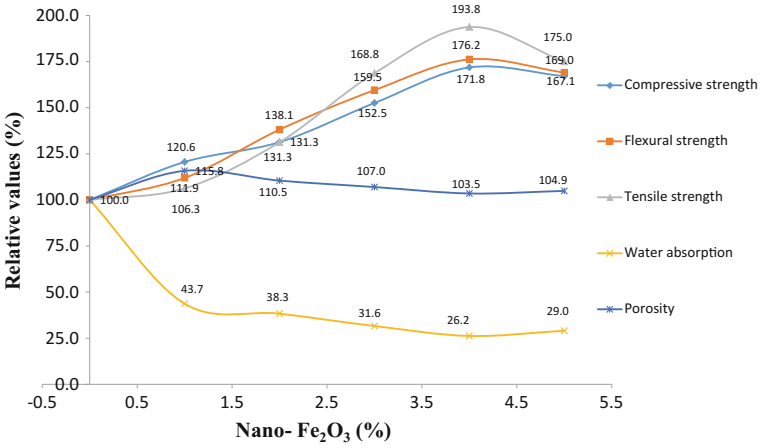

Fig. 6.3 Properties of 1–5% nano-Fe_2O_3 incorporated cementitious composite relative to control composite

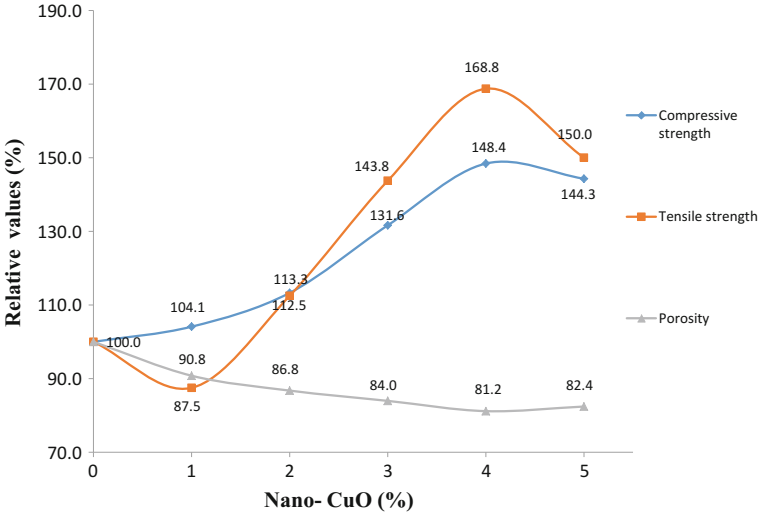

Fig. 6.4 Properties of 1–5% nano-CuO incorporated cementitious composite relative to control composite

This occurred mainly because of rapid reaction between CuO nanoparticles and calcium hydroxide. Consequently, the amount of crystalline $Ca(OH)_2$ at the early ages of hydration of cement is increased and larger amounts of calcium silicate hydrate (C-S-H gel) are formed. However, more than 4.0% addition of CuO nanoparticles reduced the mechanical strengths and increased the porosity of concrete. This may be due to inappropriate dispersion of CuO nanoparticles in the matrix that causes weak zones. Also, it may be due to the amount of CuO nanoparticles available in the concrete mix is more than the quantity needed to combine with the liberated $Ca(OH)_2$ during the hydration process.

6.2.6 *Aluminium Oxide (Al_2O_3) Nanoparticles*

The application of Al_2O_3 nanoparticles for enhancing the characteristics of cement and concrete has been carried out by few researchers. It has been reported that Al_2O_3 nanoparticles with average particles size of 15 nm can be used in the concrete as a partial replacement of cement. The results show that the Al_2O_3 nanoparticles could be advantageously used in place of cement although the addition of Al_2O_3 nanoparticles not only increased the compressive, flexural and split tensile strength of concrete but also decreased its workability and setting time as shown in Fig. 6.5 [69, 70].

These enhancements are mainly due to the rapid reaction between Al_2O_3 nanoparticles and calcium hydroxide, $Ca(OH)_2$ (formed during the hydration

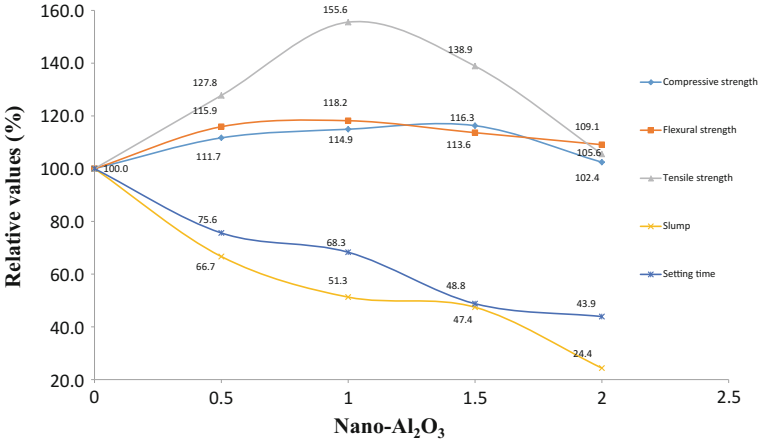

Fig. 6.5 Properties of 0.5–2% nano-Al_2O_3 incorporated cementitious composite relative to control specimen

cement). As a result, the hydration of cement is increased and larger amounts of reaction products (C-S-H gel) are formed. Moreover, the addition of Al_2O_3 nanoparticles improves the particle packing density of the mixed cement. Furthermore, the replacement of cement by Al_2O_3 nanoparticles decreased the workability of fresh concrete; thus, the use of some superplasticizer is essential [69–71]. The role of nanoalumina as a superfine aggregate was confirmed through SEM (scanning electron microscope) and EDS (energy-dispersive X-ray spectroscopy) studies, stating that the nano-Al_2O_3 fills the ITZ of cement, sand and some pores in the matrix, and hence, the compressive strength and elastic modulus of mortars is improved [72].

6.2.7 Zirconium Oxide (ZrO_2) Nanoparticles

The application of ZrO_2 nanoparticles for improving the properties of concrete and cement has been carried out only by a particular group of researchers. Possibility of enhancing mechanical characteristics of concrete by adding ZrO_2 nanoparticles as a partial replacement of cement is investigated. They reported that inclusion of ZrO_2 nanoparticles (up to 2.0% by weight) increased the compressive, flexural and split tensile strength of concrete but decreased its setting time and workability as shown in Fig. 6.6 [73–75]. These enhancements in mechanical characteristics of concrete are due to the rapid reaction between calcium hydroxide and ZrO_2 nanoparticles. As a result, the hydration of cement is increased and larger amounts of reaction products are formed. Moreover, the replacement of cement by ZrO_2 nanoparticles decreased the workability of fresh concrete, and therefore, some superplasticizer must be used.

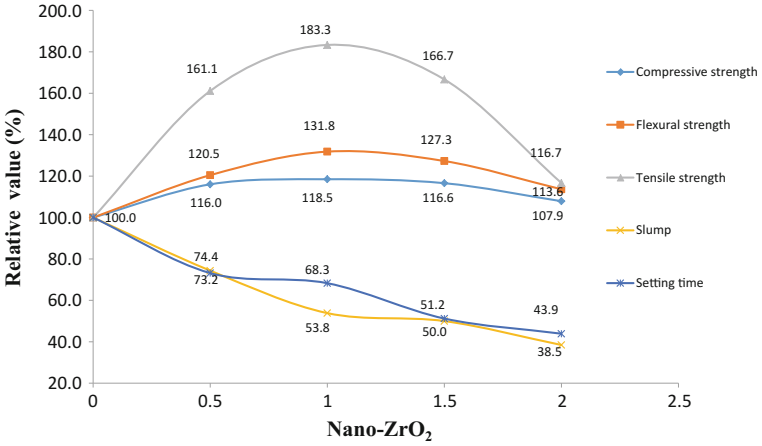

Fig. 6.6 Properties of 0.5–2% nano-ZrO_2 incorporated cementitious composite relative to control composite

6.2.8 Zinc Dioxide (ZnO_2) Nanoparticles

The use of ZnO_2 nanoparticles for influencing the properties of concrete and cement has been investigated by a particular group of researchers only. The results of a study indicate that ZnO_2 nanoparticles as a partial replacement of cement up to 4% are able to improve the flexural strength and pore structure of self-compacting concrete and recover the negative effects of polycarboxylate superplasticizer [76]. The results of another experiment indicate that the cement could be advantageously replaced with nano-ZnO_2 particles up to maximum limit of 2.0% as shown in Fig. 6.7 [77]. These enhancements in mechanical characteristics of concrete are due to the rapid reaction between calcium hydroxide and ZnO_2 nanoparticles. As a result, the hydration of cement is increased and larger amounts of reaction products are formed.

6.2.9 Calcium Carbonate ($CaCO_3$) Nanoparticles

The use of $CaCO_3$ nanoparticles for enhancing the characteristics of cement and concrete has been carried out by few researchers, though limestone ($CaCO_3$) powder is usually considered as inert and traditionally used as a filler material to improve rheological properties of concrete. However, current investigations have found that they can increase rate of hydration of ordinary Portland cement (OPC) when added as nanoparticles [78, 79]. The results of another research showed that $CaCO_3$ nanoparticles as a partial replacement of cement up to 5% could accelerate the rate of hydration, setting time and improve compressive

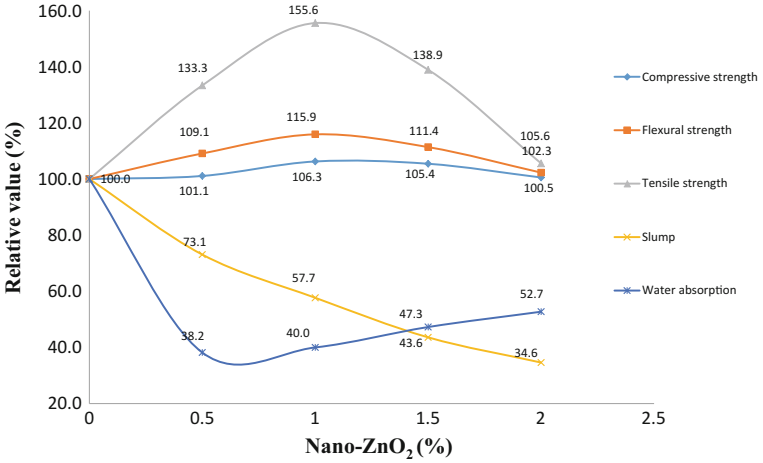

Fig. 6.7 Properties of 0.5–2% nano-ZnO_2 incorporated cementitious composite relative to control composite

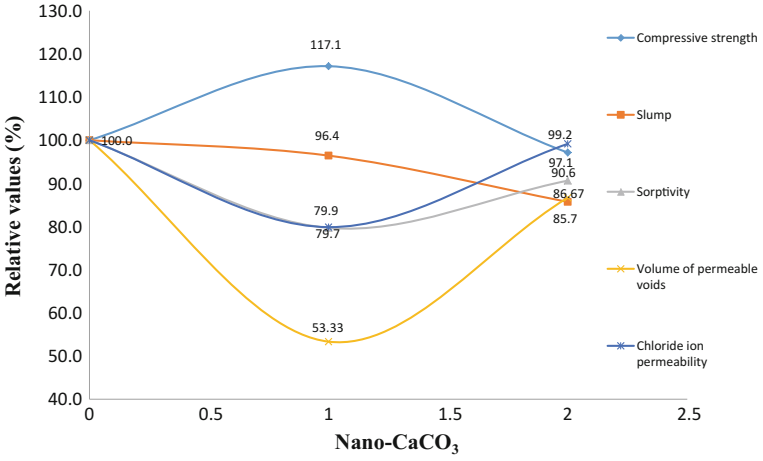

Fig. 6.8 Properties of 0.5–2% nano-$CaCO_3$ incorporated cementitious composite relative to control composite

strength [80]. In a similar study, the effects of $CaCO_3$ nanoparticles on the properties of concrete are shown in Fig. 6.8. The optimum content of nano-$CaCO_3$ is observed to be 1%. Also, it has been observed that the concrete containing 39% fly ash and 1% nano-$CaCO_3$ as a replacement of cement showed enhanced strength and durability properties compared to control concrete [81].

6.2.10 Chromium Oxide (Cr_2O_3) Nanoparticles

The utilization of Cr_2O_3 nanoparticles for influencing the properties of cementitious composites has been investigated by a particular group of researchers only. The results of a study showed that Cr_2O_3 nanoparticles as a partial replacement of cement up to 2% could improve the properties of concrete. Also, it has been found that the concrete cured in saturated lime water (LW) produced higher mechanical strength and durability properties compared to those cured in tap water (W) at all the ages; the 28-day properties are shown in Fig. 6.9. This may be due to the formation of excessive strengthening gel in the presence of saturated limewater in which the amount of nano-Cr_2O_3 particles (pozzolan) available in the composite is nearly equal to the quantity needed to combine with the liberated lime during the hydration process, thus lesser amount of silica leaching out compared to the specimens cured in water. Furthermore, the optimal level of cement replacement with nano-Cr_2O_3particles was found to be 2% and 1% for the specimens cured in saturated limewater and water respectively [82, 83].

6.2.11 Silver (Ag) Nanoparticles

The silver nanoparticles can be used as an additive in paints to inactivate pathogenic microorganisms and give antimicrobial properties to the surfaces for instance hospital walls. This is because of the fact that the silver nanoparticles have inherent properties to reduce the growth and multiplication of fungi, viruses and bacteria, which causes itchiness, infection, odour and sore [84].

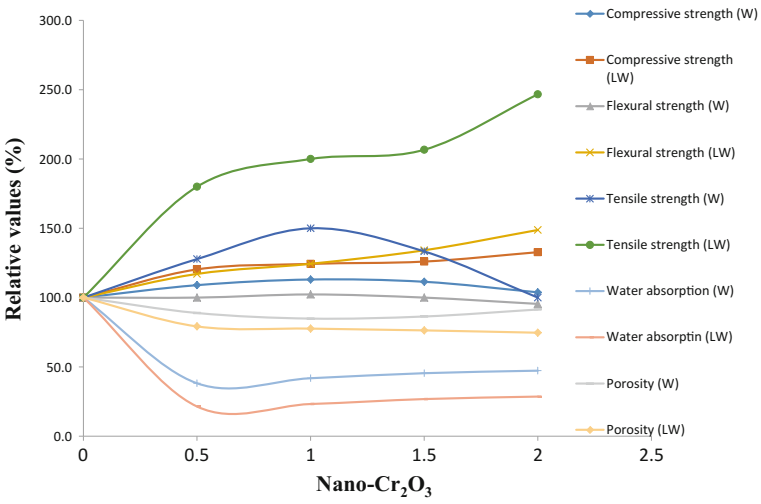

Fig. 6.9 Properties of 0.5–2% nano-Cr_2O_3 incorporated cementitious composite cured in water

6.3 Environmental and Economical Aspect

All the building and maintenance materials must be compatible to the natural environment, and their effects should not be harmful. Therefore, the consequence of different nanomaterials on the environment is discussed hotly in environmental and nanotechnology researches. Many recent investigations have focused on the ambiguity concerning the potential adverse impacts of nanomaterials. Some researches in this regard show that the unique properties that make nanomaterials in the construction sector so promising may also create unexpected human health and environmental problems. These possible problems may occur by releasing nanomaterials into air because of the production of dust, leaching of nanomaterials into the groundwater and exposing potentially hazardous materials at the time of construction and maintenance works. For example, both carbon nanotubes (SWNT and MWNT) can show antibacterial properties and pose a potential hazard because they exert side effects on the lungs, damage the cell membrane, slow down the respiratory functions, harm the mitochondrial deoxyribonucleic acid (DNA), etc. [9–12]. Similarly, TiO_2 nanoparticles irradiated through ultraviolet light or sunlight produce reactive oxygen species (ROS), which cause DNA damage, cytotoxicity and inflammation in mammals [13–15]. Likewise, SiO_2 nanoparticles have been reported to exert carcinogenic activity, harm the bacteria due to ROS productions and are toxic to marine algae, etc. [16, 17]. Also, the copper oxide or copper nanoparticles induce oxidative stress and DNA damage in human, algae, bacteria and yeasts cells [18–20]. Hence, the use of nanomaterials in civil engineering or construction industry becomes a double-edged sword. Therefore, more researches and investigations are required with well planned and designed so that building projects can be made environment-friendly and sustainable.

Currently, the cost of nanomaterials and nanotechnology equipments are quite high. This is essentially because of the novel technology and the complex equipments used for synthesis and characterization of the materials, although it is expected that cost of materials will reduce in due course with the upgradation of manufacturing technologies and equipments. However, recent view is that the nanotechnology and nanomaterials should be used in some special cases (e.g. for treating the complex problems) to give unique solutions with effective cost. In other cases, the conventional materials and methods may be used for treating the problems with effective cost. Therefore, it is a challenge to the construction or civil engineers and researchers to solve expenditure problems associated with nanomaterial-based constructions and give a service to the common public at a minimum cost [21].

6.4 Nanomaterials as Corrosion Inhibitors

Improvement in mechanical strength and durability properties of the concrete by the addition of nanomaterials is reported in literature. Yet another novel use of nanomaterial in controlling the corrosion of steel in concrete is proposed by the authors. A comprehensive study involving nanomaterials as corrosion inhibitors is under way. Some of the early results are included in this article. To compare the effectiveness of the chosen nanomaterials and their application methodology, one of the established chemical corrosion inhibitor, namely calcium nitrite, has also been included in this study.

The present investigation deals with the performance assessment of protective coatings on steel reinforcement. These coatings were made with plain cement slurry (SC), calcium nitrite (CN)-inhibited cement slurry, titanium dioxide (TO) and graphene (GP)-admixed cement slurry. Electrochemical tests were conducted on these specimens in normal and saline water (4% NaCl solution). Cyclic sweep tests using ACM (applied corrosion monitoring) potentiostat having inbuilt software for the data acquisition and post-processing was used for the study. Tafel plots for all these specimens in normal and saline water are shown in Figs. 6.10 and 6.11, respectively. Corrosion kinematic parameters were also obtained and are presented in Tables 6.3 and 6.4.

The results included here are observed at early stage of exposure. To establish the worthiness of the system in controlling and/or delaying reinforcement corrosion, longer duration exposure is required. Reduced corrosion current density and thereby very low corrosion rates were observed for all the systems investigated as compared

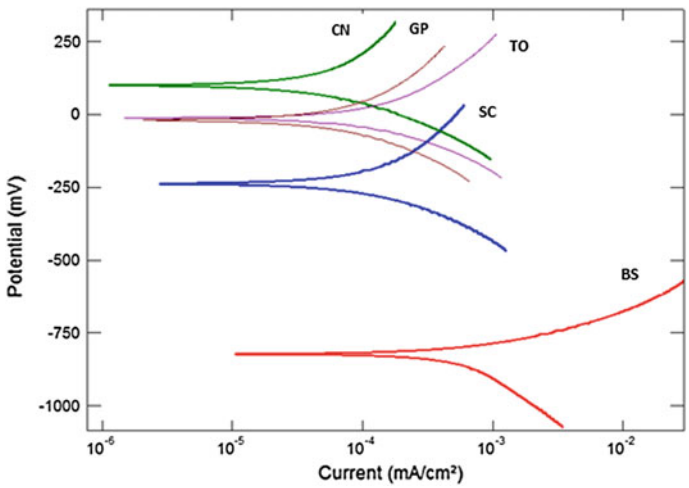

Fig. 6.10 Tafel plots of the specimens under normal exposure

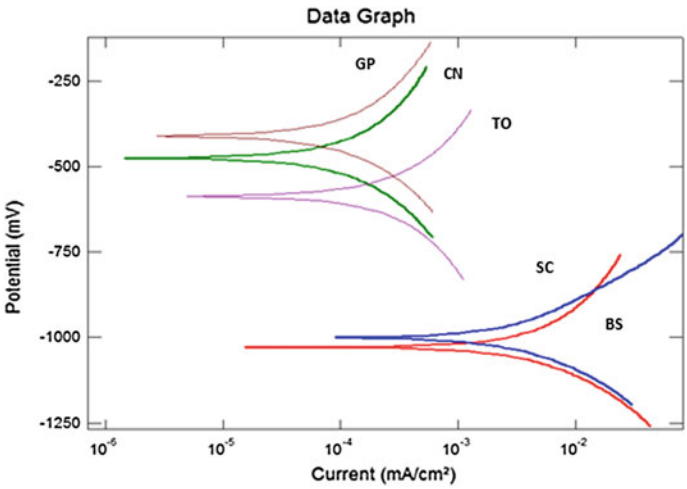

Fig. 6.11 Tafel plots of the specimens under saline exposure

Table 6.3 Corrosion kinematic parameters for the specimens under normal exposure

System	Rest potential, R_P (mV)	Anodic tafel constant, B_a (mV)	Cathodic tafel constant, B_c (mV)	Corrosion current, I_{corr} (mA/cm^2)	Corrosion rate (mm/year)
BS	−830.69	144.97	324.87	0.0020005	0.0231857
SC	−235.08	367.13	242.7	0.0001627	0.0018853
CN	101.56	444.91	192.85	0.0000847	0.0009817
TO	−19.283	289.02	162.65	0.0001302	0.0015087
GP	−10.651	333.88	206.85	0.0000886	0.0010275

Table 6.4 Corrosion kinematic parameters for the specimens under saline exposure

System	Rest potential, R_P (mV)	Anodic tafel constant, B_a (mV)	Cathodic tafel constant, B_c (mV)	Corrosion current, I_{corr} (mA/cm^2)	Corrosion rate (mm/year)
BS	−1030.3	387.09	236.78	0.0056604	0.0656045
SC	−998.4	184	157.79	0.0024881	0.0288372
CN	−473.94	304.16	268.05	0.0001291	0.0014958
TO	−587.95	263.95	283.6	0.0002736	0.0031707
GP	−410.09	310.61	256.06	0.0001212	0.0014046

to the bare steel (BS) specimens both in normal and saline water. Results are quite comparable with the calcium nitrite-inhibited systems. In most of the systems, results comparable to that of the calcium nitrite were obtained.

6.5 Conclusions

The use of nanomaterials in civil engineering or construction industries presents numerous opportunities and challenges. The mechanism and function of various nanomaterials with the conventional building materials have been reviewed and discussed in detail. Further, the following conclusion may be drawn:

(i) The addition of nanomaterials considerably reduced the initial setting time (IST) as well as final setting time (FST) of cementitious composite. This is due to its large specific surface areas, unambiguously more number of atoms on the surface, which are highly unstable and active, and consequently, speed up the cement hydration reaction and eventually reduces the setting time.

(ii) The addition of nanomaterials considerably reduced the workability of cementitious composites. This may be because of the fact that the replacement of cement with nanoparticles increased the overall surface area and thus requires more lubricating water to wet the particles. However, this can be overcome with the use of superplasticizers and supplementary cementitious materials such as fly ash, silica fume, rice husk ash along with nanomaterials.

(iii) The mechanical strengths and durability properties of cementitious composite are significantly improved with the use of appropriate amount of nanomaterials. This is mainly because of the fact that nanomaterials act as ultrafine aggregate which not only fills the tiny voids in the composite but also acts as kernel which reduces the size of $Ca(OH)_2$ and accelerate the hydration process resulting more consumption of $Ca(OH)_2$ and produced large quantity of C-S-H gel.

(iv) The mechanical strengths and durability properties of cementitious composite were found to be decreased at higher dosages of nanomaterials. It may be because of the formation of weak zones due to inappropriate dispersion of nanoparticles.

(v) Also, the suitable type and amount of nanomaterials to be added to the cementitious composite is still contradictory. Therefore, more researches and investigations are required in order to decide the appropriate quantity and type of nanomaterials to be used for a particular type of construction work.

(vi) Furthermore, there are some other challenges to use nanomaterials in civil engineering like their impacts on human health and environment and high cost. All these issues seek attention from scientific community working in this area.

(vii) A novel use of nanomaterials has been suggested by the authors. The results of the electrochemical tests clearly indicated the effectiveness of nanomaterials in controlling corrosion. The calcium nitrite-inhibited as well as graphene and nano-TiO_2-admixed cement slurry coating exhibited appreciable level of corrosion inhibition as compared to uninhibited systems. However, more tests are required involving fairly longer period of time to establish nanomaterials as corrosion inhibitors.

References

1. R. Feynman, There's plenty of room at the bottom (reprint from the speech given at the annual meeting of the west coast section of the American Physical Society). Eng. Sci. **23**, 22–36 (1960)
2. K. Drexler, Molecular engineering: An approach to the development of general capabilities for molecular manipulation. Proc. Natl. Acad. Sci. **78**, 5275–5278 (1981)
3. W.A. Goddard, D.W. Brenner, S.E. Lyshevski, G.J. Iafrate, Handbook of nanoscience engineering and technology, second ed., CRC Press, (2007)
4. S. Lee, W. Kriven, Synthesis and hydration study of Portland cement components prepared by organic steric entrapment method. Mater. Struct. **38**, 87–92 (2005)
5. K. Sobolev, M.F. Gutierrez, How nanotechnology can change the concrete world: Part 2. Am. Ceram. Soc. Bull. **84**, 16–19 (2005)
6. Z. Ge, Z. Gao, Applications of nanotechnology and nanomaterials in construction, *First International Conference on Construction in Developing Countries (ICCIDC–I), Advancing and Integrating Construction Education, Research & Practice*, (Karachi, Pakistan 2008), pp. 235–240
7. G.Y. Li, Properties of high-volume fly ash concrete incorporating nano-SiO_2. Cem. Concr. Res. **34**, 1043–1049 (2004)
8. H. Irie, K. Sunada, K. Hashimoto, Recent developments in TiO_2 photocatalysis: Novel applications to interior ecology materials and energy saving systems. Electrochem. **72**, 807–812 (2004)
9. C.W. Lam, J.T. James, R. McCluskey, S. Arepalli, R.L. Hunter, A review of carbon nanotube toxicity and assessment of potential occupational and environmental health risks. Crit. Rev. Toxicol. **36**, 189–217 (2006)
10. L.H. Ding, J. Stilwell, T.T. Zhang, O. Elboudwarej, H.J. Jiang, J.P. Selegue, P.A. Cooke, J.W. Gray, F.Q.F. Chen, Molecular characterization of the cytotoxic mechanism of multiwall carbon nanotubes and nano-onions on human skin fibroblast. Nano Lett. **5**, 2448–2464 (2005)
11. S. Kang, M. Pinault, L.D. Pfefferle, M. Elimelech, Single walled carbon nanotubes exhibit strong antimicrobial activity. Langmuir **23**, 8670–8673 (2007)
12. C. Blaise, F. Gagne, J.F. Ferard, P. Eullaffroy, Ecotoxicity of selected nano-materials to aquatic organisms. Environ. Toxicol. **23**, 591–598 (2008)
13. A. Rincon, C. Pulgarin, Bactericidal action of illuminated TiO_2 on pure escherichia coli and natural bacterial consortia: Post-irradiation events in the dark and assessment of the effective disinfection time. Appl. Catal. B **49**, 99–112 (2004)
14. E.J. Wolfrum, J. Huang, D.M. Blake, P.C. Maness, Z. Huang, J. Fiest, W.A. Jacoby, Photocatalytic oxidation of bacteria, bacterial and fungal spores, and model biofilm components to carbon dioxide on titanium dioxide coated surfaces. Environ. Sci. Technol. **36**, 3412–3419 (2002)
15. L.K. Adams, D.Y. Lyon, P.J.J. Alvarez, Comparative ecotoxicity of nanoscale TiO_2, SiO_2, and ZnO water suspensions. Water Res. **40**, 3527–3532 (2006)
16. K. Fujiwara, H. Suematsu, E. Kiyomiya, M. Aoki, M. Sato, N. Moritoki, Size dependent toxicity of silica nanoparticles to chlorella kessleri. J. Environ. Sci. Health A. **43**, 1167–1173 (2008)
17. D. Dutta, S.K. Sundaram, J.G. Teeguarden, B.J. Riley, L.S. Fifield, J.M. Jacobs, S.R. Addleman, G.A. Kaysen, B.M. Moudgil, T.J. Weber, Adsorbed proteins influence the biological activity and molecular targeting of nanomaterials. Toxicol. Sci. **100**, 303–315 (2007)
18. Z. Chen, H.A. Meng, G.M. Xing, C.Y. Chen, Y.L. Zhao, G.A. Jia, T.C. Wang, H. Yuan, C. Ye, F. Zhao, Z.F. Chai, C.F. Zhu, X.H. Fang, B.C. Ma, L.J. Wan, Acute toxicological effects of copper nanoparticles. Toxicol. Lett. **163**, 109–120 (2006)

19. V. Aruoja, H.C. Dubourguier, K. Kasemets, A. Kahru, Toxicity of nanoparticles of CuO, ZnO and TiO_2 to microalgae *Pseudokirchneriella subcapitata*. Sci. Total Environ. **407**, 1461–1468 (2009)
20. K. Kasemets, A. Ivask, H.C. Dubourguier, A. Kahru, Toxicity of nanoparticles of ZnO, CuO and TiO_2 to yeast *Saccharomyces cerevisiae*. Toxicol. Vitro. **23,** 1116–112 (2009)
21. M. Holman, Nanomaterial Forecast: Vols and applications, *ICON Nanomaterial Environmental Health and Safety Research Needs Assessment*, (Lux Research: Houston, TX, 2007)
22. M.A. Ahmed, Y.A. Hassanean, K.A. Assaf, M.A. Shawkey, Fascinating improvement in mechanical properties of cement mortar using multiwall carbon nanotubes and ferrite nanoparticles. Int. J. Struct. Civ. Eng. Res. **4**, 159–170 (2015)
23. S. Iijima, Carbon nanotubes: Past, present, and future. Phys. B **323**, 1–5 (2002)
24. S. Kumar, P. Kolay, S. Malla, S. Mishra, Effect of multiwalled carbon nanotubes on mechanical strength of cement paste. J. Mater. Civ. Eng. **24**, 84–91 (2012)
25. T. Manzur, N. Yazdani, Strength enhancement of cement mortar with carbon nanotubes: Early results and potential. Transp. Res. Record. **2142**, 102–108 (2010)
26. T.C. Madhavi, P. Pavithra, B.S. Sushmita, S.B. Vamsi, P. Surajit, Effect of multiwalled carbon nanotubes on mechanical properties of concrete. Int. J. Sci. Res. **2**, 166–168 (2013)
27. L. Małgorzata, Carbon nanotubes influence on the compressive strength of cement composites. Tech. Trans. Civ. Eng. **1**, 5–11 (2014)
28. P.F. Becher, Microstructural design of toughened ceramics. J. Am. Ceram. Soc. **74**, 255–269 (1991)
29. M. Saafi, P. Romine, Nano and micro technology. Concr. Int. **27**, 28–34 (2005)
30. G.B. Song, H.C. Gu, Y.L. Mo, Smart aggregates: Multifunctional sensors for concrete structures-A tutorial and a review. Smart Mater. Struct. **17**, 1–17 (2008)
31. W. Zhang, J. Suhr, N. Koratkar, Carbon nanotube/polycarbonate composites as multifunctional strain sensors. J. Nanosci. Nanotechnol. **6**, 960–964 (2006)
32. G. Girishkumar, M. Rettker, R. Underhile, D. Binz, K. Vinodgopal, P. McGinn, P. Kamat, Single-wall carbon nanotube based proton exchange membrane assembly for hydrogen fuel cells. Langmuir **21**, 8487–8494 (2005)
33. T. Nochaiya, A. Chaipanich, Behavior of multi-walled carbon nanotubes on the porosity and microstructure of cement based materials. Appl. Surf. Sci. **257**, 1941–1945 (2011)
34. A. Chaipanich, T. Nochaiya, W. Wongkeo, P. Torkittikul, Compressive strength and microstructure of carbon nanotubes-fly ash cement composites. Mater. Sci. Eng. **527**, 1063–1067 (2010)
35. R.K.A. Al-Rub, A.I. Ashour, B.M. Tyson, On the aspect ratio effect of multi-walled carbon nanotube reinforcements on the mechanical properties of cementitious nanocomposites. Const. Build. Mater. **35**, 647–655 (2012)
36. M.S. Konsta-Gdoutos, Z.S. Metaxa, S.P. Shah, Highly dispersed carbon nanotube reinforced cement based materials. Cem. Concr. Res. **40**, 1052–1059 (2010)
37. Z.S. Metaxa, M.S. Konsta-Gdoutos, S.P. Shah, Carbon nanofiber cementitious composites: Effect of debulking procedure on dispersion and reinforcing efficiency. Cem. Concr. Compos. **36**, 25–32 (2013)
38. S. Musso, J.M. Tulliani, G. Ferro, A. Tagliaferro, Influence of carbon nanotubes structure on the mechanical behavior of cement composites. Compos. Sci. Technol. **69**, 1985–1990 (2009)
39. J. Luo, Z. Duan, H. Li, The influence of surfactants on the processing of multi-walled carbon nanotubes in reinforced cement matrix composites. Phys. Status Solidi A **206**, 2783–2790 (2009)
40. F. Collins, J. Lambert, W.H. Duan, The influences of admixtures on the dispersion, workability, and strength of carbon nanotube-OPC paste mixtures. Cem. Concr. Compos. **34**, 201–207 (2012)
41. A. Cwirzen, K. Habermehl-Cwirzen, V. Penttala, Surface decoration of carbon nanotubes and mechanical properties of cement/carbon nanotube composites. Adv. Cem. Res. **20**, 65–73 (2008)

42. A.M. Hunashyal, S.J. Lohitha, S.S. Quadri, N.R. Banapurmath, Experimental investigation of the effect of carbon nanotubes and carbon fibres on the behaviour of plain cement composite beams. IES J. Part A: Civ. Struct. Eng. **4**, 29–36 (2011)
43. M.H. Zhang, H. Li, Pore structure and chloride permeability of concrete containing nano-particles for pavement. Constr. Build. Mater. **25**, 608–616 (2011)
44. S. Hussain, K. Sastry, Study of strength properties of concrete by using micro-silica and nano-silica. Int. J. Res. Eng. Technol. **3**, 103–108 (2014)
45. Q. Ye, Z.N. Zhang, D.Y. Kong, R.S. Chen, Influence of nano-SiO_2 addition on properties of hardened cement paste as compared with silica fume. Constr. Build. Mater. **21**, 539–545 (2007)
46. L. Senff, D. Hotza, W.L. Repette, V.M. Ferreira, J.A. Labrinca, Mortars with nano-SiO_2 and micro-SiO_2 investigated by experimental design. Constr. Build. Mater. **24**, 1432–1437 (2010)
47. B.W. Jo, C.H. Kim, G.H. Tae, J.B. Park, Characteristics of cement mortar with nano-SiO_2 particles. Constr. Build. Mater. **21**, 1351–1355 (2007)
48. B. Hasan, S. Nihal, Comparative study of the characteristics of nanosilica, silicafume and fly-ash incorporated cement mortars. Mater. Res. **17**, 570–582 (2014)
49. L. Singh, S. Bhattacharyya, U. Sharma, G. Mishra, S. Ahalawat, Microstructure improvement of cementitious systems using nanomaterials: A key for enhancing the durability of concrete. Mechanical and Physics of Creep, Shrinkage and Durability of Concreate ASCE (2013) 293–300
50. A. Boshehrian, P. Hosseini, Effect of nano-SiO_2 particles on properties of cement mortar applicable for ferrocement elements. Concr. Res. **2**, 167–180 (2011)
51. H. Bahadori, P. Hosseini, Reduction of cement consumption by the aid of silica nanoparticles. J. Civil Eng. Manag. **18**, 416–425 (2012)
52. A. Heidari, D. Tavakoli, Properties of concrete incorporating silica fume and nano-SiO_2. Ind. J. Sci. Technol. **6**, 108–112 (2013)
53. P. Zhang, X. Dai, J. Gao, P. Wang, Effect of nano-SiO_2 particles on fracture properties of concrete composite containing fly ash. Curr. Sci. **108**, 2035–2043 (2015)
54. L. Senff, J.A. Labrinca, V.M. Ferreira, D. Hotza, W.L. Repette, Effect of nano-silica on rheology and fresh properties of cement pastes and mortars. Constr. Build. Mater. **23**, 2487–2491 (2009)
55. A.K. Rana, S.B. Rana, A. Kumari, V. Kiran, Significance of nanotechnology in construction engineering. Int. J. Recent Trends Eng. **1**, 46–48 (2009)
56. N. Serpone, E. Pelizzetti, *Photocatalysis: Fundamentals and applications* (Wiley, New York, 1989)
57. B. Ruot, A. Plassais, F. Olive, L. Guillot, L. Bonafous, TiO_2-containing cement pastes and mortars: Measurements of the photocatalytic efficiency using a rhodamine B-based colourimetric test. Sol. Energy **83**, 1794–1801 (2009)
58. G.L. Guerrini, Photocatalytic performances in a city tunnel in Rome: NOx monitoring results. Constr. Build. Mater. **27**, 165–175 (2012)
59. A. Nazari, R. Shadi, R. Sharin, S.F. Shamekhi, A. Khademno, Improvement in the mechanical properties of the cementitious composite by using TiO_2 nanoparticles. J. Am. Sci. **6**, 98–101 (2010)
60. A. Nazari, R. Shadi, R. Sharin, S.F. Shamekhi, A. Khademno, Assessment of the effects of the cement paste composite in presence TiO_2 nanoparticles. J. Am. Sci. **6**, 43–46 (2010)
61. E. Mohseni, M. Ranjbar, K. Tsavdaridis, Durability properties of high-performance concrete incorporating nano-TiO_2 and fly ash. Am. J. Eng. Appl. Sci. **8**, 519–526 (2015)
62. A. Nazari, R. Shadi, R. Sharin, S.F. Shamekhi, A. Khademno, Benefits of Fe_2O_3 nanoparticles in concrete mixing matrix. J. Am. Sci. **6**, 102–106 (2010)
63. A. Nazari, R. Shadi, R. Sharin, S.F. Shamekhi, A. Khademno, The effects of incorporation Fe_2O_3 nanoparticles on tensile and flexural strength of concrete. J. Am. Sci. **6**, 90–93 (2010)
64. N.A. Yazdi, M.R. Arefi, E. Mollaahmadi, B.A. Nejand, To study the effect of adding Fe_2O_3 nanoparticles on the morphology properties and microstructure of cement mortar. Life Sci. J. **8**, 550–554 (2011)

65. A. Khoshakhlagh, A. Nazari, G. Khalaj, Effects of Fe_2O_3 nanoparticles on water permeability and strength assessments of high strength self-compacting concrete. J. Mater. Sci. Technol. **28**, 73–82 (2012)
66. A. Nazari, R. Shadi, Effects of CuO nanoparticles on compressive strength of self-compacting concrete. Sadhana-Indian Academy Sci. **36**, 371–391 (2011)
67. A. Nazari, R. Shadi, Effects of CuO nanoparticles on microstructure, physical, mechanical and thermal properties of self-compacting cementitious composites. J. Mater. Sci. Technol. **27**, 81–92 (2011)
68. A. Nazari, M.H. Rafieipour, R. Shadi, The Effects of CuO Nanoparticles on properties of self compacting concrete with GGBFS as Binder. Mater. Res. **14**, 307–316 (2011)
69. A. Nazari, R. Shadi, R. Sharin, S.F. Shamekhi, A. Khademno, Influence of Al_2O_3 nanoparticles on the compressive strength and workability of blended concrete. J. Am. Sci. **6**, 6–9 (2010)
70. A. Nazari, R. Shadi, R. Sharin, S.F. Shamekhi, A. Khademno, Mechanical properties of cement mortar with Al_2O_3 nanoparticles. J. Am. Sci. **6**, 94–97 (2010)
71. M.R. Arefi, M.R. Javeri, E. Mollaahmadi, To study the effect of adding Al_2O_3 nanoparticles on the mechanical properties and microstructure of cement mortar. Life Sci. J. **8**, 613–617 (2011)
72. L. Zhenhua, W. Huafeng, H. Shan, L. Yang, W. Miao, Investigations on the preparation and mechanical properties of the nano-alumina reinforced cement composite. Mater. Lett. **60**, 356–359 (2006)
73. A. Nazari, R. Shadi, ZrO_2 nanoparticles effects on split tensile strength of self compacting concrete. Mater. Res. **13**, 485–495 (2010)
74. A. Nazari, R. Shadi, R. Shirin, F.S. Seyedeh, A. Khademno, An investigation on the strength and workability of cement based concrete performance by using ZrO_2 nanoparticles. J. Am. Sci. **6**, 29–33 (2010)
75. A. Nazari, R. Shadi, R. Shirin, F.S. Seyedeh, A. Khademno, Embedded ZrO_2 nanoparticles mechanical properties monitoring in cementitious composites. J. Am. Sci. **6**, 86–89 (2010)
76. A. Nazari, R. Shadi, The effects of zinc dioxide nanoparticles on flexural strength of self-compacting concrete. Compos. Part B: Eng. **42**, 167–175 (2011)
77. A. Nazari, S. Riahi, The effects of ZnO_2 nanoparticles on strength assessments and water permeability of concrete in different curing media. Mater. Res. **14**, 178–188 (2011)
78. T. Sato, J.J. Beaudoin, *The Effect Of Nano-Sized $CaCO_3$ Addition on the Hydration of OPC Containing High Volumes of Fly Ash*. Proceeding of the 12th International conference on the chemical of cement, Montreal, Canada, 1–12 (2006)
79. T. Sato, F. Diallo, Seeding effect of nano-$CaCO_3$ on the hydration of tricalcium silicate. J. Transp. Res. Board. **2141**, 61–67 (2010)
80. S. Kawashima, P. Hou, D.J. Corr, S.P. Shah, Modification of cement-based materials with nanoparticles. Cem. Concr. Compos. **36**, 8–15 (2013)
81. F.U.A. Shaikh, S.W.M. Supit, Mechanical and durability properties of high volume fly ash concrete containing calcium carbonate nanoparticles. Constr. Build. Mater. **70**, 309–321 (2014)
82. A. Nazari, S. Riahi, Optimization mechanical properties of Cr_2O_3 nanoparticles binary blended cementitious composite. J. Compos. Mater. **45**, 943–948 (2011)
83. A. Nazari, S. Riahi, The effects of Cr_2O_3 nanoparticles on strength assessments and water permeability of concrete in different curing media. Mater. Sci. Eng. **528**, 1173–1182 (2011)
84. A. Kumar, P.K. Vemula, P.M. Ajayan, G. John, Silver nanoparticle-embedded antimicrobial paints based on vegetable oil. Nat. Mater. **7**, 236–241 (2008)

Chapter 7
Design, Development and Application of Nanocoatings

Akash Singh, Siddhant Mittal, Deepa Mudgal and Pallav Gupta

Abstract Coatings can be defined as the application of one material on the other material usually known as substrate. They are mainly applied on the material to protect it from any degradation which occurs due to environmental conditions. They act as an interface between the substrate and the environment. Moreover, they are also used for decorative purposes. Nanocoatings are those coatings in which the size of a particle is in the range of 1–1000 nm at least in one dimension. Nanocoatings provide more wear resistance attributed to its higher toughness and hardness to the substrate as compared to other conventional coatings. They also provide antimicrobial, wrinkle resistance, stain resistance, hydrophobic and hydrophilic characteristics, UV protection and antistatic properties affecting the bulk properties of the substrate material. Nanocoatings can be manufactured by mainly two methods: vapour phase method and liquid phase method. Vapour phase method includes chemical vapour deposition, laser ablation, vapour condensation, plasma arc and flame synthesis processes. Liquid phase method includes sol–gel, precipitation, electrolysis, microemulsion and hydrothermal processes. Nanocoatings are used in aircraft (landing gears and engines), industrial rolls, hydraulic shafts, boiler tubes, turbines and pumps to prevent corrosion and erosion problems. They are also used on cars, pens, watches and cosmetics for decorative purposes. Nanocoatings are used on money bills so as to prevent forgery. This chapter discusses in detail about the nanocoatings. Efforts have also been made to summarize the various processing techniques for their fabrication. Effect of nanocoatings on structural, mechanical and corrosion behaviour is also discussed. It is expected that the present chapter will be useful in designing and developing nanocoatings for wide industrial applications.

Keywords Nanocoatings · Hydrophobic and Hydrophilic · Corrosion
Chemical vapour deposition · Thermal spray · Turbines

A. Singh · S. Mittal · P. Gupta (✉)
Department of Mechanical and Automation Engineering,
A.S.E.T, Amity University Uttar Pradesh, Noida, India
e-mail: pgupta7@amity.edu

D. Mudgal
Department of Mechanical Engineering, Thapar University, Patiala, Punjab, India

Z.H. Khan (ed.), *Nanomaterials and Their Applications*,
Advanced Structured Materials 84, https://doi.org/10.1007/978-981-10-6214-8_7

7.1 Coating and Nanocoatings

Coatings can be defined as the application of one material on the other material usually known as the substrate so as to protect it from degradation due to changing environment. They act as an interface between the substrate and the environment [1]. Coatings help in enhancing the life of materials by improving different properties like porosity, bond strength, residual stress, impact resistance, elevated temperature and erosion [2]. However, they are also sometimes used to fulfil anticorrosive and decorative purposes [3, 4]. NiCrAlY, NiCoCrAlY, Stellite-6, Al_2O_3-13% TiO_2, Cr_3C_2-25% NiCr and WC–CO–Cr are some examples of the coating powder materials. Nanocoatings are those coatings in which the size of a particle is in the range of 1–1000 nm at least in one dimension [5]. Nanocoatings provide improved wear resistance attributed to its higher toughness and hardness with low porosity to the substrate as compared to conventional coatings [6]. They also provide antimicrobial, wrinkle resistance, stain resistance, hydrophobic and hydrophilic characteristics, UV protection and antistatic behavior affecting the bulk properties of the substrate material [7, 8]. Nano-TiO_2, TiAlN, Ni–ZrO_2, nanosize magnesium aluminium-layered double hydroxides (nano-LDHs), nanostructured Ni-Mo alloys, silver nanoparticles, silver-based nanostructured materials, zinc oxide nanoparticles, copper nanoparticles and carbon nanotubes (CNTs) are some of the examples of nanocoating materials [7–10].

7.2 Techniques for Fabrication of Nanocoatings

There are mainly two types of techniques for the fabrication of nanocoatings. They are vapour phase method and liquid phase method.

7.2.1 Vapour Phase Method

Vapour phase synthesis involves evaporation of the precursor which can be either solid or liquid. This supersaturated vapour of condensable gaseous species is formed as a result of chemical reactions [11]. Rapid condensation of this vapour reduces the vapour pressure of the condensable species to create nanosized clusters. Vapour phase fabrication approach is used to make metallic and metal oxide ceramic nanoparticles [12]. Most of the synthesis methods of nanoparticles in the gas phase are based on homogeneous nucleation in gas phase and subsequent condensation and coagulation [13]. Figure 7.1 shows the schematic diagram of vapour phase method used for the synthesis of nanocoatings. Vapour phase method mainly includes five processes, i.e. physical vapour deposition, chemical vapour deposition, plasma arc, flame synthesis and laser ablation (Fig. 7.2) [14–17].

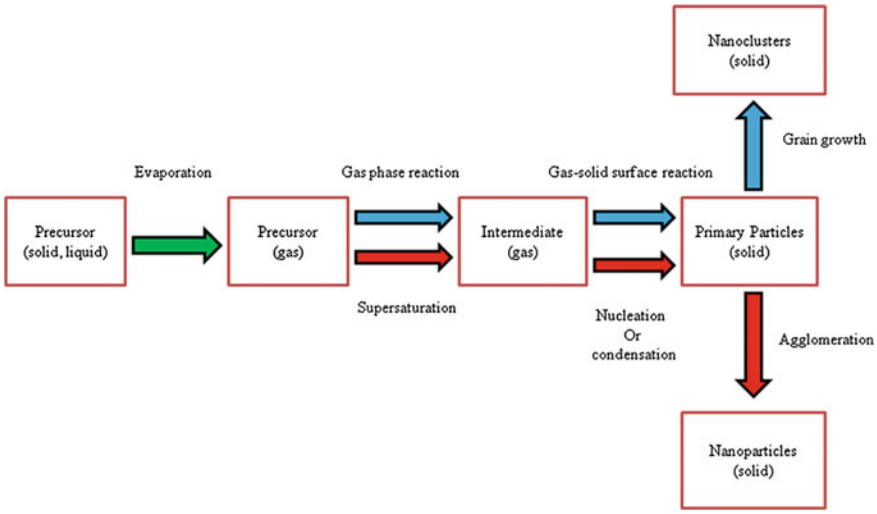

Fig. 7.1 Flow chart of vapour phase method

Fig. 7.2 Types of vapour phase method for production of nanocoatings

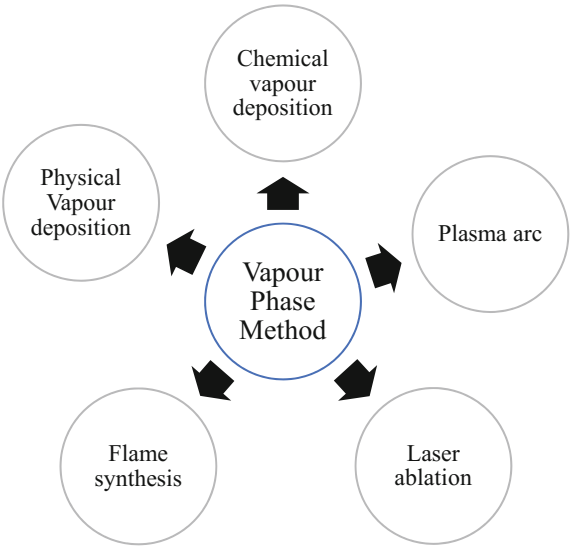

7.2.1.1 Physical Vapour Deposition

Physical vapour deposition (PVD) is a set of process used to deposit material on the substrate typically in the range of nanometres [18]. PVD uses thermodynamic or mechanical means to produce the thin film. Sputtering is a principal technique among all the mechanical methods, where energetic noble gas ion, mostly argon

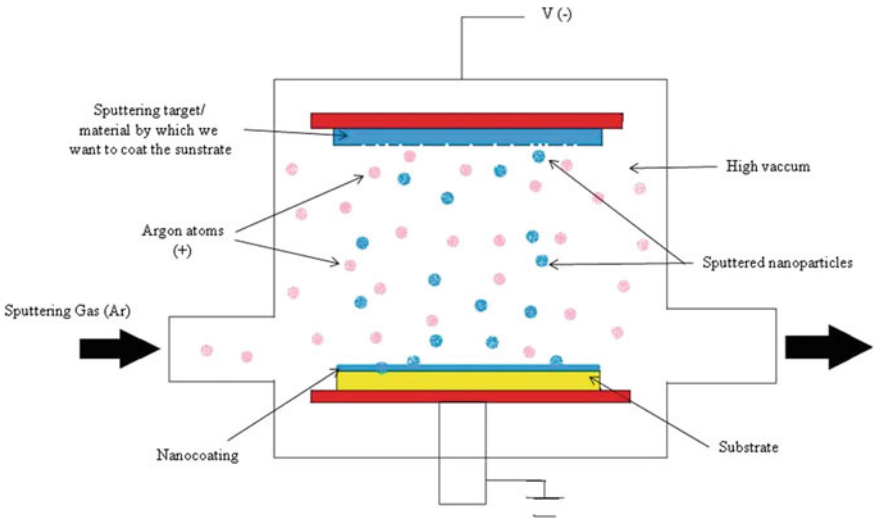

Fig. 7.3 Schematic diagram of physical vapour deposition process

which acts as the positively charged particles, is bombarded on the surface of a material. This surface acts as the anode and is preferred film material to coat the specimen [19]. Thermal evaporation (thermodynamic means) is a process in which a solid piece of the desired film material is heated until it melts or evaporates or until it sublimes. Vapours follow a direct line of sight path to the substrate in a high vacuum, where it condenses to form a thin film. The temperature in the region ranges from 70 to 500 °C [20]. Håkansson et al. [21] coated the steel substrate with TiN coating using physical vapour deposition, and it was found to show superior results with nanosize particles as compared to micron size particles (Fig. 7.3).

7.2.1.2 Chemical Vapour Deposition

Chemical vapour deposition (CVD) is a technique used to produce a wide variety of nanoparticles of varied shapes and size, typically thin films or nanocoatings [22]. Most of the procedures of this are similar to chemical vapour condensation. CVD mainly involves heterogeneous reaction between the substrate and the reactant gas. In chemical vapour deposition (Fig. 7.4), the substrate is exposed to one or more volatile precursors, which react or decompose on the substrate surface to produce the preferred deposit. Regularly, volatile by-products are also formed, which are removed from the reaction chamber by gas flow [23]. To a large extent, success of process depends on system conditions. The temperature in this process ranges from 800 to 2000 °C in the region. This process has excellent adherence and coating thickness up to 20 μm [24, 25]. Melancha Gupta et al. coated high aspect ratio (80:1) with the polymeric nanocoating with the chemical vapour deposition method. Using

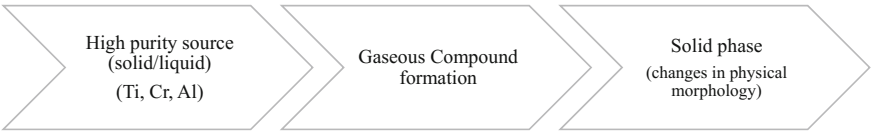

Fig. 7.4 Flow chart for physical vapour deposition

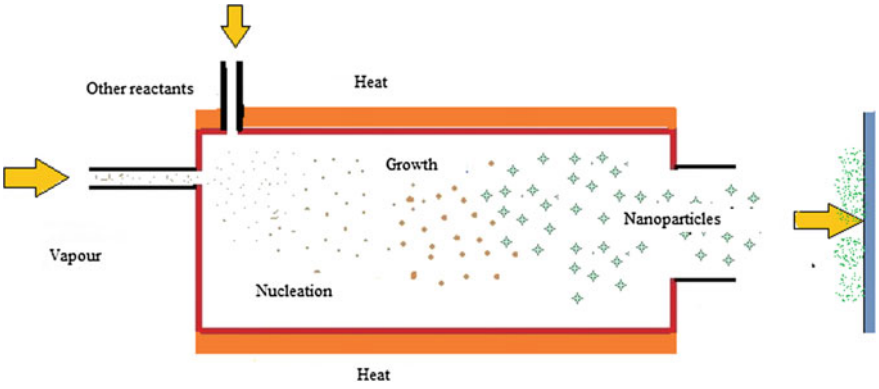

Fig. 7.5 Schematic diagram of chemical vapour deposition of nanocoatings

characterization techniques like SEM and XRD, they concluded that the CVD nanocoating has altered the surface properties of the pores [26] (Fig. 7.5).

7.2.1.3 Plasma Arc

When gases like nitrogen, argon and hydrogen are superheated and electrically ionized they form the plasma. The temperature of plasma is from 10,000 to 14,000 °C. This much high temperature is sufficient for completely melting and evaporating the particles of the precursor. It decomposes the reactants into ions and dissociating atoms into radicals [27]. The source material is mainly used in the solid form here. In other words, plasma arc spraying is a thermal spray coating process which includes heating the material (in form of powder or wire) and speeding up to high pace by gas circuit [28]. The schematic representation of the plasma arc process is shown in Fig. 7.6. Cao Qin and Sylvain Coulomb presented the synthesis of the organic layer-coated metal nanoparticles. They were synthesized by the evaporation of metal cathode surface by the plasma arc followed by capacitively coupled radio-frequency plasma polymerized from a gaseous hydrocarbon monomer [29]. J. H. Ahn et al. used Al_2O_3-8 wt% TiO_2 a wear resistance nanopowder to coat the low carbon steel substrate using plasma spray. It was found that substrate coated with low critical process spray parameter (CPSP) showed highest wear resistance as compared to high CPSP [30] (Fig. 7.7).

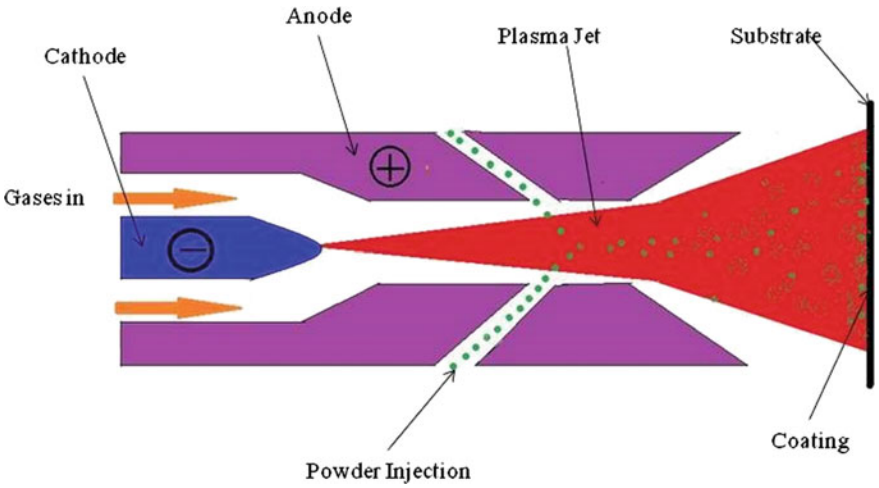

Fig. 7.6 Schematic diagram of plasma arc process

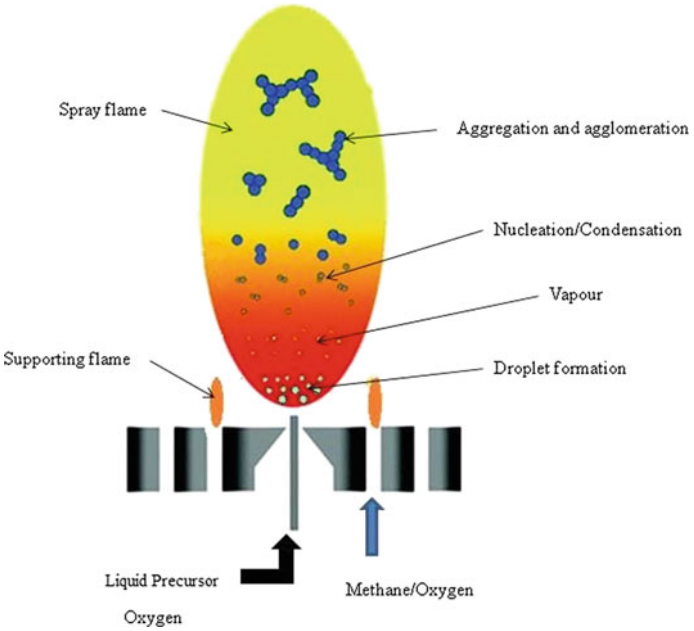

Fig. 7.7 Schematic diagram for flame synthesis process

7.2.1.4 Flame Synthesis

Flame synthesis is a most promising and versatile synthesis process for the production of nanocoatings. It is mainly used due to its low-cost production in large scale [31]. The flame process which uses liquid precursors is known as flame spray pyrolysis. Here, the main emphasis is placed on the reactant and the fuel composition [32]. The FSP processes are quite attractive as they can employ a wide array of precursors, so a broad spectrum of new nanosized powders can be synthesized. In flame synthesis, the energy required to drive the chemical reactions of the precursors is obtained from the flame. Decomposition or pyrolysis reaction at high temperatures in the flame results in the formation of atomic clusters which further grow to nanoparticles by surface growth coagulation or coalescence [33]. Judicious control of the process parameters affects the flame characteristics, thus controlling the properties of particle size, crystallinity and morphology [34]. High purity, low synthesis costs and high production rates, along with the flexibility in the production of a wide variety of nanocrystalline and/or nanostructured materials, make flame synthesis an excellent choice among the gas phase synthesis routes [32].

7.2.1.5 Laser Ablation

Laser ablation means removal of the material from the precursor or the target material with the help of laser irradiation, and this is the basic principle behind this process [35]. This process is mainly done in vacuum, but sometimes it is also carried out in liquid medium or in variety of solvents. Then, it is called laser ablation synthesis in solution [36]. Laser ablation mainly focuses on the non-equilibrium vapour conditions created at the surface of the precursor material. Schematic diagram of the laser ablation process is shown in Fig. 7.8. A pulsed laser mainly Nd YAG laser is incident on the target with the high power in the ablation

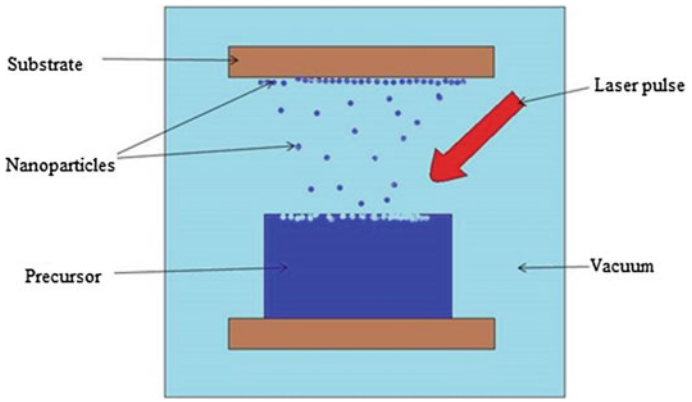

Fig. 7.8 Schematic diagram for laser ablation process for nanocoatings

chamber. This high amount of energy is absorbed by the source material which drastically increases its temperature. Due to this high temperature, the particles of the precursor vaporize. This vapour rises up and gets deposited on the substrate. And when this process continues there is a formation of thin film on the substrate of nanoparticles called as nanocoatings [37–39]. Arias et al. [40] investigated that the calcium phosphate coating deposited on metal substrate utilizing the pulsed laser deposition technique showed high adhesive strength.

7.2.2 Liquid Phase Method

Liquid phase method is a relatively new technique in which a thin ceramic film is deposited on a metal plate. Liquid phase methods have low production cost and are also environment-friendly as well. Thin films can be deposited on metallic substrates which may or may not be mechanically stable at high temperatures. Growth of the film and its corresponding microstructure make it a potential candidate for use in a wide number of applications.

Most commonly used film is of SiO_2 which can be easily hydrolyzed using aluminium metal, boric acid or metal. When a thin film is formed, there is also a generation of highly acidic solutions apart from the formation of basic solutions. Figure 7.9 shows the flow chart illustrating the liquid phase method. Figure 7.10 describes the type of liquid phase methods used for production of nanocoatings.

7.2.2.1 Electrochemical

Electrochemical deposition technique is one of the low-cost non-vacuum methods which require cheap raw materials and relatively simple instruments that consume considerably less energy than other techniques such as evaporation and sputtering technique [41]. Electrochemical deposition is the process that uses reduction reactions to deposit an element or a compound which is dissolved in the electrolyte as ions on top of an electrode [42]. Fundamental aspects of electrochemical deposition include the heterogeneous electron transfer step between the electrode and the electroactive species present in the solution as well as the transition of the discharged metal atoms into the crystalline state [43].

7.2.2.2 Precipitation

Precipitation is a technique in which a new solid surface is generated from a solution. Solid product formed after reaction in a liquid solution is called as “precipitate”. At times, formation of a precipitate indicates the occurrence of a chemical reaction. For example, if silver nitrate is added into sodium chloride, a reaction takes place which leads to the formation of white precipitate of silver

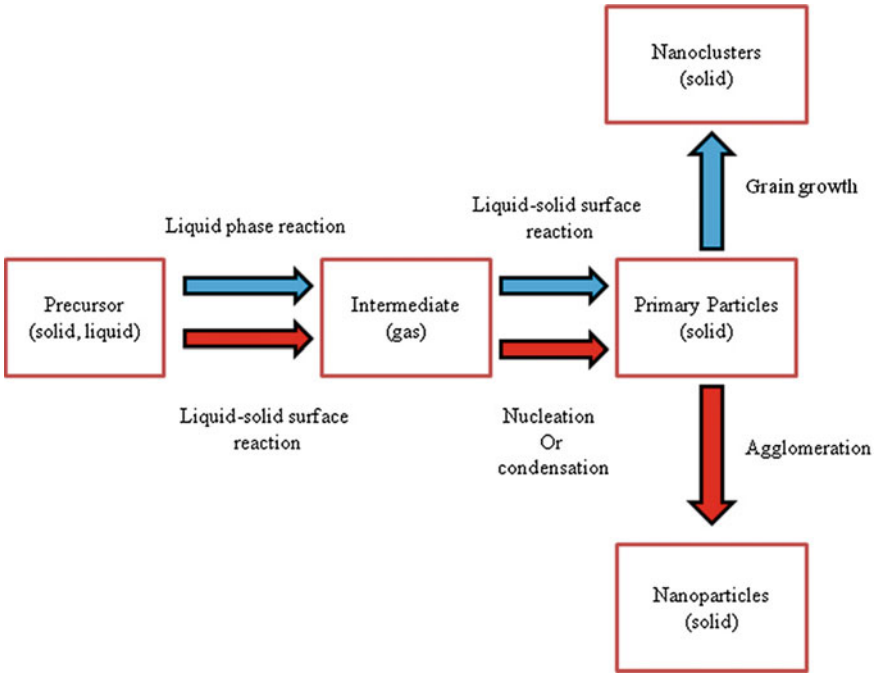

Fig. 7.9 Flow chart of liquid phase method

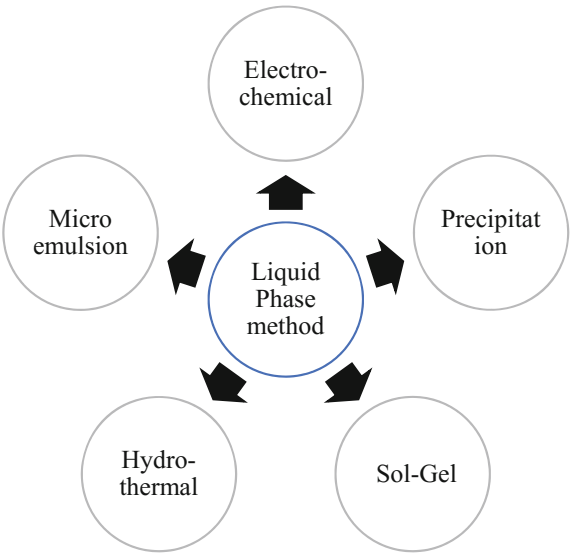

Fig. 7.10 Types of liquid phase methods for production of nanocoatings

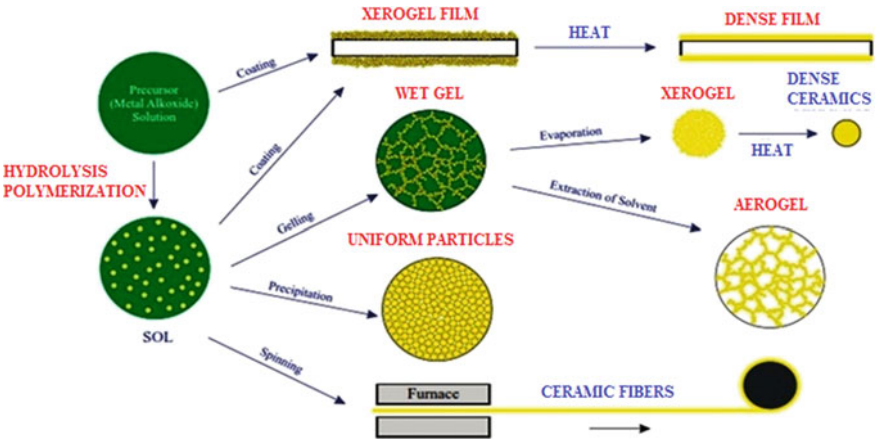

Fig. 7.11 An overview of various sol–gel processes [46]

chloride. Potassium iodide when reacts with lead (II) nitrate lead to the formation of yellow precipitate of lead (II) iodide. The onset of nucleation is an important step of precipitation technique. Generation of solid particle in precipitation technique involves development of an interface, this needs energy which based on the relative surface energy of the solid and the solution. In case, if this energy is absent and no nucleation platform is present, supersaturation takes place.

7.2.2.3 Sol–Gel

Sol–gel technique helps in the fabrication of different types of materials for wide engineering applications. This processing technique helps in developing various types of nano/microstructures [44]. It develops new porous nanomaterials, with homogeneous structures and complex shapes. It is an easy method for the synthesis of inorganic, organic–inorganic networks such as glasses, ceramics, films or powders [45]. Sol–gel process involves the transition of a solution system from a liquid "sol" (mostly colloidal) into a solid "gel" phase. A sol refers to a colloidal solution. A gel is a wet solid-like material in which solid networks of interconnected nanostructures cover the volume of a liquid medium. Continuous phase is a solid network, and the dispersed phase is a liquid. Gels tend to be mostly liquid in composition and typically exhibit the density of a liquid as a result but have cohesiveness nature like a solid [46]. Whereas in case of sol, the continuous phase is a liquid, and the dispersed phase is a solid. The difference between a sol and a non-colloidal liquid is that solid particles are dispersed throughout the liquid in a

sol. If sol is put in a centrifuge, it can force the particles dispersed in the liquid to precipitate out. This will not happen for a non-colloidal liquid solution, for example, salt dissolved in water [47]. Figure 7.11 shows an overview of various sol–gel processes.

(a) Synthesis of Sol–Gel Figure 7.12 shows steps for chemical processing of sol–gel formation which consists of hydrolysis, condensation, gelation, ageing, drying followed by densification.

There are two generic variations of the sol–gel technique at room temperature. One is called the colloidal method, and the other is called the polymeric (or alkoxide) route. Difference lies in selecting the starting materials (precursors) that are used. The first step of any sol–gel process always consists in selecting the precursors of the required materials. Precursor leads the reaction towards the formation of either colloidal particles or polymeric gels. When, the future material is composed of several components (several components are mixed together) then the use of combination of different precursors and procedures enhances different chemical synthesis and hence different products. Both routes involve suspending or dissolving the precursors in a suitable liquid, usually water for the colloidal route and alcohol for the polymeric route. The precursor is then activated by the addition of an acid (such as hydrochloric acid) or a base (such as potassium hydroxide). The activated precursors then react together to form a network. The network grows and ages with time and temperature, until it achieves the size of the container. At this point, the viscosity of the liquid increases at an exponential rate until gelation occurs [48]. Figure 7.13 shows the structure of gels formed after two different modes. Factors that affect the sol–gel chemistry are Ph value, solvent, temperature, time, catalyst and agitation.

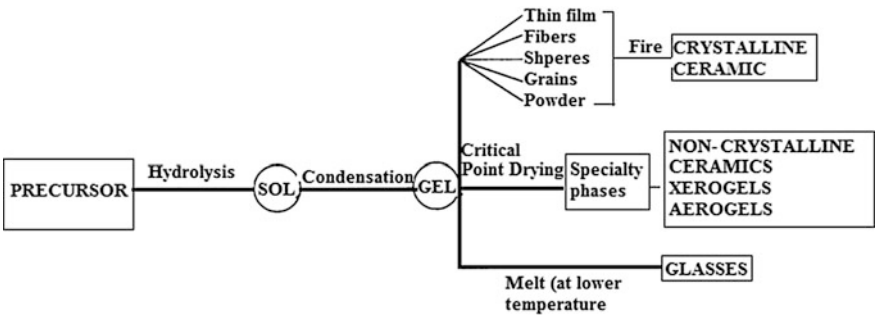

Fig. 7.12 Chemical processing of sol–gel process [60]

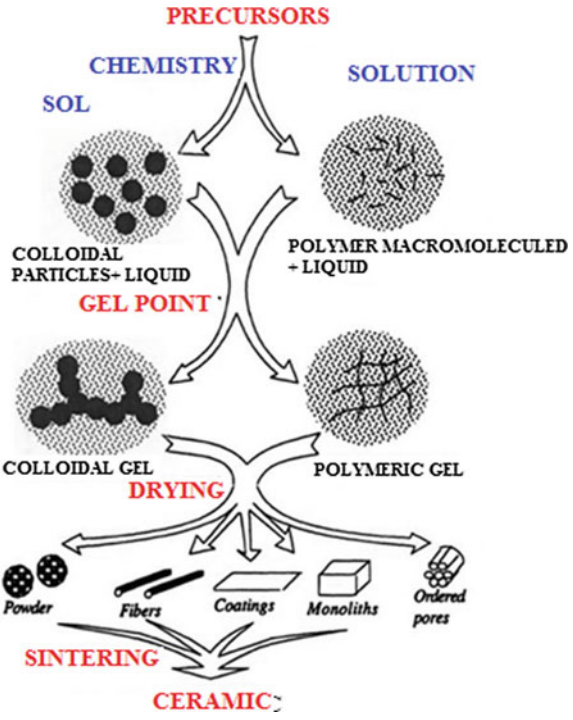

Fig. 7.13 Simplified chart of different structure of gel processing [48]

7.2.2.4 Hydrothermal

Formation of nanocoatings using hydrothermal technique is a relatively new area. This method is widely used in the synthesis of ceramic powders. By using this method, the resultant powder requires no more high-temperature calcinations, and thus there is the least possibility of agglomeration and clustering among the various particles. Pressure and reaction path opted for the hydrothermal synthesis affect the geometry of the final powder. Various benefits associated with the usage of hydrothermal technique are as follows:

- By using this technique, the various economical costs associated with the instruments and precursors are found to be reduced.
- As this technique makes use of relatively lower temperatures; therefore, there is a stoichiometric control over the various phases, and the possibility of stress induced defects is also reduced.
- A wide range of powders having different morphologies and particle size can be formed with the usage of hydrothermal processing technique.
- Some secondary phases which are difficult to achieve using other technique can be formed using hydrothermal technique.
- Hydrothermal synthesis technique can be very easily coupled with other processes such as microwave, electrochemistry, ultrasonics, hot isostatic pressing.

7.2.2.5 Microemulsion

Microemulsion is a single phase isotropic and thermodynamically stable liquid which is a combination of water and oil. In this technique, oil is used which is a combination of various hydrocarbons and olefins. In comparison to the other emulsions, microemulsions form easily when mixed with the components and also do not require high shear conditions. There are basically three types of microemulsions which are used for nanocoatings: (a) direct, (b) reversed and (c) bicontinuous. Microemulsions are also used in various applications such as dry cleaning, floor polishers, pesticides, cutting oils and drugs. There are various theories which are proposed in respect of formation, stability and phase behaviour. One concept explains that the thermodynamic stability in a system is due to the presence of surfactant, and their formation includes the presence of elastic behaviour of surfactant film at the oil/water interface.

7.3 Research and Development in Nanocoatings

With the introduction of nanomaterials, novel nanocoatings have been introduced in different technological applications as nanostructured materials have the ability to develop functional, intelligent and smart coatings which can provide specific or multiple physiochemical properties to protect the surface of the base material [49]. Advanced properties of the nanocoatings have attracted thousands of researchers to work in the area of nanocoatings which can be used in the various fields such as aerospace industries, medicine, bioimplants etc. A lot of research and development is going across the world on nanocoatings so as to develop the coatings which can be used to increase the properties of the different substrates. A large number of coating techniques are available which can be used for deposition in various applications. These techniques have already been discussed under Sect. 7.2. The current section will discuss few reported studies in the area of nanocoatings.

It was very well known that titanium-based implants have been used for reconstructions of bone anchors. However, due to the poor osteoinductive properties of titanium, it has been coated by hydroxyapatite. Plasma sprayed coating technique, ion beam sputtering, sol–gel, electrophoretic deposition and electrochemical deposition are the technique which has been used to deposit HA coating. Kuo et al. [49] suggested that compared to plasma sprayed, electrochemical deposition has capability of producing uniform coating. Zang et al. [50] studied the electrochemical deposited HA coating on titanium substrate. It was reported that HA coating was conveniently fabricated through electrochemical process with porous and actinomorphic-assembled lamellar structure. Ben-Nissan et al. [51]

investigated that bone graft material which has been used is mainly produced from coralline hydroxyapatite. However, due to certain conditions, these materials reduced durability and strength. To overcome such problems, a two stage route has been developed consisting of complete conversion of coral to pure HAp followed by application of sol–gel derived HAp nanocoatings to cover micro- and nano-pores within the intra-pore material. This resulted in improvement of biaxial strength, enhanced durability, longevity and strength.

Mazaheri et al. [52] investigated the corrosion performance of electroless-deposited Ni–P coatings and Ni–P/nano-diamond composite coating on steel substrate. They reported that the coating provides better hardness and corrosion resistance as compared to conventional Ni–P coating.

Zheludkevich et al. [53] synthesized nanostructured hybrid sol–gel coatings doped with cerium ions as a pretreatment of AA2024-T3 alloy. They reported that the coating was found to be potential candidate for the pretreatment of alloy to be used for corrosion protection. Lamaka et al. [54] developed and studied the TAP/tTMSPh-(titaniumdiisopropoxide) bis/(tris(trimethylsilyl) phosphate doped sol–gel coating) and TPOZ/GPTMS (zirconium (IV) tetra-propoxide)/((3-glycidoxypropyl)-trimethoxysilane)-based sol–gel films deposited on AZ31B alloy under 0.005 M NaCl solution. The tris(trimethylsilyl) phosphate-containing sol–gel coating confers good corrosion protection due to its chemical interaction with the magnesium substrate which, most probably, leads to the formation of a graded and stable in-depth film. Hamdy et al. [55] studied the effect of vanadia sol–gel coatings on the corrosion behaviour of Al6061 T6 in 3.5% NaCl solution. They have used vanadia as alternative to chromate. It was reported that etching together with oxide-thickening step prior to vanadia treatment plays a vital role in the corrosion protection. Vanadium can incorporate through the pores of Al-oxide layer to form thick Al–V-oxide layer. They also opined that the V-treated specimens seem very promising as an alternative to chromating.

7.4 Application of Nanocoatings

Asri et al. [56] reported in a review that a sol–gel dip coating and electrochemical deposition techniques are widely used for depositing biocompatible hydroxyapatite-based coatings on biocompatible metal substrates for biomedical applications. Electroless-deposited Ni-P coatings have been widely used in many industries like electronic board, automotive part, oil and gas instruments and as decorative applications and for corrosion/corrosion erosion application [52].

Sol–gel is a new technique which is used in several applications such as in manufacturing abrasive powder, optical fibres and nuclear industry [57].

Sol–gel technique is used in the deposition of coatings. Coatings on any surface serve one of the following purposes:

- Corrosion protection
- Abrasion resistance
- Optical properties
- Ferroelectric and conduction properties
- Catalytic activity.

It was reported that the efficient conversion of solar radiation into thermal energy depends on the solar absorber used for the collector panel. The solar absorber should have high absorptance and low emittance. Electrochemical deposition of nickel-based selective coatings were found to present good optical properties required for solar absorber along with the economic viability [58]. However, due to low thermal stability and environmental issues in chemical vapour deposition technique, researchers are looking towards physical vapour deposition technique to be used for coating mid- and high-temperature solar selective panels. Among all the PVD process, sputtering has been used successfully for coating flat plate solar collectors and receiver tubes [59].

References

1. A.A. Tracton (ed.) Coatings technology handbook. (CRC press, USA, 2005)
2. D.J. Branagan et al., High-performance nanoscale composite coatings for boiler applications. J. Therm. Spray Technol. **14**(2), 196–204 (2005)
3. L. Barchi, U. Bardi, S. Caporali, M. Fantini, A. Scrivani, A. Scrivani, Electroplated bright aluminium coatings for anticorrosion and decorative purposes. Prog. Org. Coat. **67**(2), 146–151 (2010)
4. B.P. Reinherz, *For Decorative Coating of Glass and Ceramic Articles*. U.S. Patent No. 4,892,847, 9 Jan 1990
5. J.C. Welch, S. Chakraborty, "Nano-coatings for articles." U.S. Patent Application No. 13/022,047
6. Hyung-Jun Kim, Chang-Hee Lee, Soon-Young Hwang, Superhardnano WC–12% Co coating by cold spray deposition. Mater. Sci. Eng., A **391**(1), 243–248 (2005)
7. Zhenyu Wang, Enhou Han, Wei Ke, Influence of nano-LDHs on char formation and fire-resistant properties of flame-retardant coating. Prog. Org. Coat. **53**(1), 29–37 (2005)
8. S. Radhakrishnan et al., Conducting polyaniline–nano-TiO_2 composites for smart corrosion resistant coatings. Electrochim. Acta **54**(4), 1249–1254 (2009)
9. Roya Dastjerdi, Majid Montazer, A review on the application of inorganic nano-structured materials in the modification of textiles: focus on anti-microbial properties. Colloids Surf. B **79**(1), 5–18 (2010)
10. G. Wu et al., A novel route to control refractive index of sol-gel derived nano-porous silica films used as broadband antireflective coatings. Mat. Sci. Eng.: B **78**(2), 135–139 (2000)
11. Mark T. Swihart, Vapor-phase synthesis of nanoparticles. Curr. Opin. Colloid Interface Sci. **8**(1), 127–133 (2003)
12. A.R. Gupta, V. Kant, Research article synthesis, characterization and biomedical applications of nanoparticles, Vijayta Gupta Department of Chemistry, University of Jammu, Jammu-180006, India. Sci. Int. **1**(5) (2013)

13. P. Tartaj, M.P. Morales, S. Veintemillas-Verdaguer, T. Gonzalez Carreno, C.J. Serna, Synthesis, properties and biomedical applications of magnetic nanoparticles, in *Handbook of Magnetic Materials*, ed. by K.H.J. Buschow (Elsevier, Amsterdam, 2006), pp. 403–482
14. Mark T. Swihart, Vapor-phase synthesis of nanoparticles. Curr. Opin. Colloid Interface Sci. **8** (1), 127–133 (2003)
15. F.E. Kruis, H. Fissan, A. Peled, Synthesis of nanoparticles in the gas phase for electronic, optical and magnetic applications—A review. J. Aerosol Sci. **29**(5), 511–535 (1998)
16. H. Hahn, Gas phase synthesis of nanocrystallinematerials. Nanostruct. Mat. **9**(1), 3–12 (1997)
17. S. Abbott, N. Holmes, *Nanocoatings: Principles and Practice: From Research to Production*. (DEStech Publications, Inc, USA, 2013)
18. C.F. Powell, J.H. Oxley, J.M. Blocher Jr., *Vapor Deposition* (Wiley, New York, 1967)
19. K. Reichelt, X. Jiang, The preparation of thin films by physical vapour deposition methods. Thin Solid Films **191**(1), 91–126 (1990)
20. D.M. Mattox, *Handbook of Physical Vapor Deposition (PVD) Processing*. (William Andrew, New York, 2010)
21. G. Håkansson et al., Microstructures of TiN films grown by various physical vapour deposition techniques. Surf. Coat. Technol. **48**(1), 51–67 (1991)
22. J.-H. Park, T.S. Sudarshan (ed.), *Chemical Vapor Deposition*, vol. 2. (ASM international, USA, 2001)
23. K.L. Choy, Chemical vapour deposition of coatings. Prog. Mater Sci. **48**(2), 57–170 (2003)
24. J.O. Carlsson, P.M. Martin, Chemical vapor deposition. *Handbook of Deposition Technologies for Films and Coatings* (2010), pp. 314–63
25. B.A. Campbell, A. Bryant, N.E. Miller, *Chemical Vapor Deposition Process*. U.S. Patent No. 4,547,404. 15 Oct. 1985
26. M. Gupta et al., Initiated chemical vapor deposition (iCVD) of conformal polymeric nanocoatings for the surface modification of high-aspect-ratio pores. Chem Mat **20**(4), 1646–1651 (2008)
27. F.E. Kruis, H. Fissan, A. Peled. Synthesis of nanoparticles in the gas phase for electronic, optical and magnetic applications—a review. J. Aerosol Sci. **29**(5), 511–535 (1998)
28. M. Aliofkhazraei, *Nanocoatings: Size Effect in Nanostructured Films*. (Springer Science & Business Media, Berlin, 2011)
29. Cao Qin, Sylvain Coulombe, Organic layer-coated metal nanoparticles prepared by a combined arc evaporation/condensation and plasma polymerization process. Plasma Sources Sci. Technol. **16**(2), 240 (2007)
30. J.H. Ahn, E.P. Song, S.H. Lee, N.J. Kim, Wear resistance of plasma-sprayed Al_2O_3-TiO_2 nanocoatings. Key Eng. Mater. **345–346**, 641–644 (2007)
31. Bhaskaran Manjith Kumar, Subramshu Shekar Bhattacharya, Flame synthesis and characterization of nanocrystalline titania powders. Proces Appl Ceramics **6**, 165–171 (2012)
32. Hendrik K. Kammler, Lutz Mädler, Sotiris E. Pratsinis, Flame synthesis of nanoparticles. Chem. Eng. Technol. **24**(6), 583–596 (2001)
33. Karsten Wegner, Wendelin J. Stark, Sotiris E. Pratsinis, Flame-nozzle synthesis of nanoparticles with closely controlled size, morphology and crystallinity. Mater. Lett. **55**(5), 318–321 (2002)
34. Wendelin J. Stark, Sotiris E. Pratsinis, Aerosol flame reactors for manufacture of nanoparticles. Powder Technol. **126**(2), 103–108 (2002)
35. J. Weber, *Method for Manufacturing a Medical Device Having a Coated Portion by Laser Ablation*. U.S. Patent No. 6,517,888, 11 Feb 2003
36. D.B. Chrisey, G.K. Hubler (ed.), *Pulsed Laser Deposition of Thin Films*, vol. 3 (1994)
37. Alfredo M. Morales, Charles M. Lieber, A laser ablation method for the synthesis of crystalline semiconductor nanowires. Science **279**(5348), 208–211 (1998)
38. B.N. Chichkov, et al., Femtosecond, picosecond and nanosecond laser ablation of solids. Appl. Phys. A **63**(2) (1996): 109–115
39. C. Momma et al., Short-pulse laser ablation of solid targets. Opt. Commun. **129**(1), 134–142 (1996)

40. J.L. Arias, et al., Micro-and nano-testing of calcium phosphate coatings produced by pulsed laser deposition. Biomaterials **24**(20), 3403–3408 (2003)
41. LYS Lee, *Research Summary*, (https://www.polyu.edu.hk/abct/en/staff-singledemo376a2.html?id=72). Accessed on 22 Aug 2016
42. W. Dissanayaka Wijesooriyage, *Electrochemical Deposition and Characterization of Thermoelectric Thin Films of (BixSb1-x) 2Te3*. (2011), p. 20
43. J. Eskhult, *Electrochemical Deposition of Nanostructured Metal/Metal-Oxide Coatings* (2007), p. 11
44. Gareth J. Owens, Rajendra K. Singh, Farzad Foroutan, Mustafa Alqaysi, Cheol-Min Han, Chinmaya Mahapatra, Hae-Won Kim, Jonathan C. Knowles, Sol–gel based materials for biomedical applications. Prog. Mater Sci. **77**, 1–79 (2016)
45. C.A. Milea, C. Bogatu, A. Duta, The influence of parameters in silica sol-gel process. Bull. Transilvania Univ. Brasov **4**(53), 59–66 (2011)
46. Sol-Gel Technology, *Chemat Technology A Total Sol-Gel Solution*. (http://www.chemat.com/chemattechnology/SolGel.aspx). Accessed on 22 Aug 2016
47. S. Sakka, *Handbook of Sol-Gel Science and Technology. 1. Sol-Gel Processing*, vol. 1. (Springer Science & Business Media, Berlin, 2005)
48. A.C. Pierre, *Introduction to Sol-Gel Processing*, vol. 1. (Springer Science & Business Media, Berlin, 2013), pp. 12–15
49. M.C. Kuo, S.K. Yen, The process of electrochemical deposited hydroxyapatite coatings on biomedical titanium at room temperature. Mater. Sci. Eng., C **20**(1), 153–160 (2002)
50. Y. Zhang, T.A.O. Jie, Y. Pang, W. Wei, W. Tao, Electrochemical deposition of hydroxyapatite coatings on titanium. Trans. Nonferrous Metals Soc. China **16**(3), 633–637 (2006)
51. B. Ben-Nissan, A. Milev, R. Vago. Morphology of sol–gel derived nano-coated coralline hydroxyapatite. Biomaterials **25**(20), 4971–4975 (2004)
52. Hamed Mazaheri, Saeed Reza Allahkaram, Deposition, characterization and electrochemical evaluation of Ni–P–nano diamond composite coatings. Appl. Surf. Sci. **258**(10), 4574–4580 (2012)
53. M.L. Zheludkevich, R. Serra, M.F. Montemor, K.A. Yasakau, I.M. Miranda Salvado, M.G.S. Ferreira, Nanostructured sol–gel coatings doped with cerium nitrate as pre-treatments for AA2024-T3: corrosion protection performance. Electrochimica Acta **51**(2), 208–217 (2005)
54. S.V. Lamaka, M.F. Montemor, A.F. Galio, M.L. Zheludkevich, C. Trindade, L.F. Dick, M.G. S. Ferreira, Novel hybrid sol–gel coatings for corrosion protection of AZ31B magnesium alloy. Electrochim. Acta **53**(14), 4773–4783 (2008)
55. Abdel Salam Hamdy, Advanced nano-particles anti-corrosion ceria based sol gel coatings for aluminum alloys. Mater. Lett. **60**(21), 2633–2637 (2006)
56. R.I.M. Asri, W.S.W. Harun, M.A. Hassan, S.A.C. Ghani, Z. Buyong, A review of hydroxyapatite-based coating techniques: sol–gel and electrochemical depositions on biocompatible metals. J. Mech. Behav. Biomed. Mater. **57**, 95–108 (2016)
57. T.W.I. Solgel, (http://www.twi-global.com/capabilities/materials-and-corrosion-management/surface-engineering-and-advanced-coatings/sol-gel/). Accessed on 22 Aug 2016
58. M. Lira-Cantú, A.M. Sabio, A. Brustenga, P. Gómez-Romero, Electrochemical deposition of black nickel solar absorber coatings on stainless steel AISI316L for thermal solar cells. Solar Energy Mat. Solar Cells **87**(1), 685–694 (2005)
59. N. Selvakumar, H.C. Barshilia, Review of physical vapor deposited (PVD) spectrally selective coatings for mid-and high-temperature solar thermal applications. Solar Energy Mat. Solar Cells **98**, 1–23 (2012)
60. C. Wolf, C. Rüssel, Sol-gel formation of zirconia: preparation, structure and rheology of sols. J. Mat. Sci. **27**(14), 3749–3755 (1992)

Chapter 8
Electronic Behavior of Nanocrystalline Silicon Thin Film Transistor

Prachi Sharma and Navneet Gupta

Abstract Thin film transistor (TFT) plays an important role for the fabrication of highly functional active matrix backplanes for large area display applications such as organic light emitting diodes (OLEDs). Nanocrystalline silicon (nc-Si) has recently achieved lot of interest over existing hydrogenated amorphous silicon (a-Si:H) and polycrystalline silicon (poly-Si) due to its superior properties which makes it suitable channel material for the fabrication of TFTs. In present work, the physical insight into the nc-Si TFT device characteristics and device non idealities is reported which can provide important step for the production of high performance large area display devices.

8.1 Introduction

Thin film transistor (TFT) is commonly used as a pixel addressing element and is the heart of large area electronic devices over the past few decades [1–3]. Large area electronics involves various display applications such as liquid crystal displays (LCDs) and organic light emitting diodes (OLEDs). The aim of these applications is to spread electronic components over large area substrate at low fabrication cost.

For the production of new generation large displays, an active matrix addressing scheme is required for display panels where pixels are located at row and column interactions in order to minimize capacitive losses in column and row lines. This addressing scheme basically consists of two TFTs per pixel, of which one is operated under continuous gate bias and hence requires a high electrical stability.

P. Sharma (✉) · N. Gupta
Department of Electrical & Electronics Engineering, Birla Institute of Technology and Science, Pilani, Rajasthan, India
e-mail: prachi.sharma@pilani.bits-pilani.ac.in

P. Sharma
Department of Electronics and Communication, K.I.E.T, Ghaziabad 201206, Uttar Pradesh, India

Z.H. Khan (ed.), *Nanomaterials and Their Applications*,
Advanced Structured Materials 84, https://doi.org/10.1007/978-981-10-6214-8_8

For fabricating TFTs, various materials can be used as an active channel layer. The commonly used materials are hydrogenated amorphous silicon (a-Si:H) and polycrystalline silicon (poly-Si).

Nanocrystalline silicon (nc-Si) has been proven as the best alternative material over a-Si:H and poly-Si as shown in Table 8.1. The TFTs consist of three electrodes (i.e., source, drain, and gate), gate insulator, and thin semiconductor layer. Based on the level of the gate electrode, the TFTs are divided into two types, top-gate TFT and bottom-gate TFT. In top-gate TFT, the gate electrode is located above the semiconductor layer whereas in bottom-gate TFT, the gate electrode is located below the semiconductor layer.

When the nc-Si film is deposited over the amorphous substrate like glass then its crystallinity is not very high in the initial growth phases because the nc-Si is usually grown up in the form of cone-shape that is from bottom to top. The grain size and therefore the crystallinity increase with the increase in nc-Si film thickness [6]. This structural difference in top and bottom layers of nc-Si film plays crucial role in nc-Si TFT designing.

In case of bottom-gate structure, the device performance depends on the bottom layer of nc-Si film where the channel is formed as compared to top-gate TFT, where the channel is located in highly crystalline part at the top of nc-Si film [7]. Owing to this, the top-gate nc-Si TFT provides high mobility and also the better performance as compared to bottom-gate TFT. For this reason, top-gate structure of nc-Si TFT is considered in the present work. The schematic view of top-gate nc-Si TFT shown in Fig. 8.1 consists of a glass substrate, above which a nc-Si layer is used to form the channel followed gate dielectric.

The advancement in performance of flat panel display has been realized by reducing the size of top-gate nc-Si TFT and thus of gate dielectric. However, scaling down the size of gate dielectric causes two main problems that are reliability and leakage current. To avoid the leakage current problem, the selection of gate dielectric material is necessary which must have high-k value. However, possible high-k materials impose some practical challenges and have conflicting material properties. Therefore, some material selection approaches are required to recognize the trade-offs between conflicting properties and also to select the optimal material for better device performance. Material selection approaches also help us to provide ranking to the alternatives from best to worst. Therefore, these approaches provide a platform to select and prioritize the possible materials and also provide support to perform rigorous evaluation of the possible alternatives. Sharma and Gupta [8]

Table 8.1 Comparison between different materials used for the TFT fabrication [4, 5]

Parameters	a-Si:H	nc-Si	Poly-Si
Mobility	Low	Much higher than a-Si:H	High
Circuit type	NMOS	NMOS/PMOS	NMOS/PMOS
Stability	Less stable	More stable than a-Si:H	Stable
Uniformity	High	Potentially high	Poor
Cost	Low	Low	High

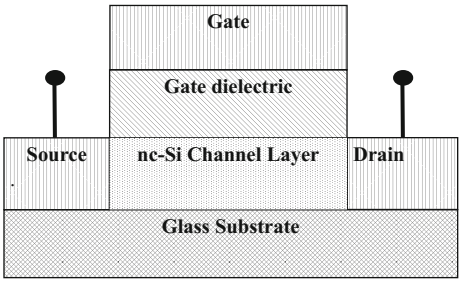

Fig. 8.1 Schematic view of top-gate nc-Si TFTs

investigated Si_3N_4, Al_2O_3, ZrO_2, Ta_2O_5, and HfO_2 materials for the gate insulator of top-gate nc-Si TFT by mean of three most popular material selection approaches i.e., Ashby's approach [9], VIKOR (VlseKriterijumska Optimizacija I Kompromisno Resenje in Serbian) [10], and TOPSIS (Technique for order preference by similarity to ideal solution) [11]. For this analysis, two performance indices (i.e., drain current and leakage current) based on four material indices (i.e., dielectric constant, band gap, conduction band offset and interface trap density) have been considered. The results (Tables 8.2 and 8.3) show that Si_3N_4 is the best suitable material and can provide high drain current and less leakage current when used as gate dielectric in top-gate nc-Si TFT.

The performance of top-gate nc-Si TFT also depends upon the various process parameters used during its fabrication and also on the conduction and instability mechanisms that occurs under electrical stress. So it is important to look into all these aspects.

The first section of this chapter explains the important outcomes and the research carried till date in the area of top-gate nc-Si TFT. In the second section, models for conduction in nc-Si TFT given by various researchers are reviewed. In third section, the mechanisms which cause the electrical instability in TFT are explained in detail.

8.2 Fabrication of nc-Si Based TFTs

The key findings of published research in the area of top-gate nc-Si TFT are as follows.

Min et al. [12] discussed that the nc-Si film in ideal condition grows quickly, provide highest mobility in minimum thickness and provide lowest conductivity under electrical stress. The lowest conductivity at room temperature in nc-Si film is achieved as low as conductivity of crystalline silicon which is around 10^{-7} S/cm. They proposed that as the film thickness increases from 50 to 350 nm, the magnitude of film conductivity increased by the order of five. This is due to the increase in magnitude of electron field-effect mobility by order of two and also increase in carrier density. The increase of electron mobility with the increase in film thickness is the key point behind the use of top-gate structure of nc-Si TFT to avail benefit of

carrier mobility which is premier at the top level of the nc-Si film. However, authors didn't present any information regarding hole mobility. Authors also discussed that in case of TFT, the leakage current is basically the conduction current which is related to channel layer under flat band situation. Therefore, it is necessary to reduce the electron carrier density present in channel in neutral condition. In TFT, the leakage current must be lowest for its possible application as switch, to provide voltage stability or in CMOS circuits to provide minimal power consumption. They have used PECVD technique for the fabrication of top-gate coplanar TFT and proposed that the compensation doping getting of water and oxygen content from mixture of base gases, or addition of chlorine content during film deposition can help in reducing the electron carrier density.

Cheng et al. [13] presented top-gate staggered nc-Si TFT deposited using PECVD at low temperature of about 150 °C. They proposed that the quality of the nc-Si material can be measured by the mobility of carriers present in the nc-Si channel in saturation condition as it directly reveals the capability of nc-Si material because saturation current is not influenced by the trapping and detrapping of charge carriers in gate dielectric. In addition to this, there is insufficient activity of doped layer under saturation condition and therefore saturation mobility reflects the lower limit of nc-Si channel capability.

In later research [14], they proposed that the structural formation of nc-Si film is based on various parameters like hydrogen dilution, temperature during deposition, nc-Si film thickness, and type of the substrate. They used both glass and plastic (Kapton E polymide) substrates for their study and fabricated both p-type and n-type staggered top-gate TFT devices on a single substrate using PECVD. They have achieved sufficient mobilities for realizing CMOS circuit on plastic but fail to achieve low off current and less threshold voltage shift due to poor quality of dielectric and the interface between gate dielectric and channel. They reported that for the better performance of the device, the substrate must have low thermal expansion coefficient, high thermal stability, low surface roughness, high chemical stability and transition temperature of glass, low permeability by oxygen and water, and low shrinkage capability to avoid misalignment during photolithography.

Lee et al. [15] proposed ambipolar transistor which worked alternatively as p-type and n-type transistor by the application of negative and positive gate voltages, respectively. The fabrication of ambipolar transistor is not reported earlier as it is difficult to realize high-quality contact between metal and semiconductor and also to deposit high-quality nc-Si film. They have used nc-Si/Cr stack as source-drain contacts in place of n^+ nc-Si for the fabrication of top-gate TFT. They proposed that hydrogen atoms clean the surface of Cr electrodes, during the initial phase of nc-Si film formation and this leads to highly crystalline nc-Si film and therefore Cr silicidation provides lower electron as well as hole injection barrier. They reported that at higher gate voltages, leakage current increases exponentially for both p- and n-type TFTs, which validates ambipolar operation. This behavior is due to accumulation of holes and electrons in n-channel and p-channel under reverse gate voltages through injection from Cr drain, this discriminates TFT with Cr silicide contacts from TFT with n^+ nc-Si contacts.

Lee et al. [16] presented the low temperature (i.e., 260 °C) fabrication of top-gate nc-Si TFT through 13.56 MHz PECVD by the use of silane diluted with hydrogen. They propose that the hydrogen dilution of silane controls the crystallinity of nc-Si layer [17], however, this increases the level of oxygen impurity in nc-Si film and at the grain boundaries. The high concentration of hydrogen atoms in the silane plasma is the main requirement for the deposition of low temperature highly crystalline nc-Si film. They reported that low dark conductivity can be achieved by providing hydrogen chemical cleaning during the deposition of nc-Si film.

In later research, Lee et al. [18] proposed that the field-effect mobility (μ_{FE}) is the ratio of free charge carriers in extended energy states, n_{band}, to the total number of induced charge carriers (which comprises of trapped carriers, n_{trap} and free carriers) times the band mobility μ_{band}, and is expressed as:

$$\mu_{FE} = \left[\frac{n_{band}}{n_{band} + n_{trap}}\right] \mu_{band} \tag{8.1}$$

The grains of nc-Si are enclosed by amorphous grain boundaries. Low temperature process provides low oxygen content in nc-Si film and thereby reduces probability of defect state creation at grain boundaries. This avoids band bending and thereby offers high mobility. This validates that low temperature is necessary for the deposition of highly crystalline nc-Si film.

Park et al. [6] presented the fabrication of top-gate nc-Si TFT using inductively coupled plasma (ICP) CVD with different channel thicknesses at the temperature of 180 °C. They proposed that ICP-CVD reduces the surface damage usually caused by ion bombardment by generating the remote plasma without causing the bombardment of ions. This reduction in surface damage provides highly crystalline growth of nc-Si film and avoids amorphization in Si deposition surface. They proposed that grain size increases with increase in film thickness because of the growth of nc-Si layer in form of cone shape i.e., from bottom to top. In addition to this, the surface roughness also increases with increase in nc-Si thickness. Lee et al. [19] proposed that the top-gate nc-Si TFT provides better stability and high on/off ratio as compared to bottom-gate nc-Si TFT. The high stability of top-gate nc-Si TFT makes it highly suitable device for display application like pixel driver in OLED to maintain low line voltages. They have used silicon nitride as the gate dielectric for the fabrication of both top-gate and bottom-gate n-channel nc-Si TFT because silicon nitride provides high reliability, high breakdown field and also allow processing at low temperature.

Kang et al. [20] also presented the effect of film thickness on the nc-Si TFT performance. They proposed that as thickness of nc-Si film increases, the field-effect mobility also increases due to increase in grain size. However, this causes the increase in leakage current. According to them, this increase in leakage current is due to the reduction in total resistance present in TFT.

Lee et al. [21] reported the mechanisms that are responsible for gate leakage current. They proposed that at high gate and low drain bias, thermal emission of charge carriers that are trapped in grain boundary regions is responsible for leakage

current whereas Poole–Frenkel emission mechanism in drain depletion state is responsible for high gate bias and high drain bias. Under low gate bias, ohmic conduction via bulk channel layer is responsible mechanism for leakage current. They presented that high leakage current causes loss of signal in pixels and also increases the power consumption of the driving circuitry. They proposed that reduction in leakage current can be attained either by using offset-gated configuration or by employing lightly doped drain regions.

Cheng et al. [22] reported the effect of contact resistance on the performance of staggered top-gate nc-Si TFT and for this study they have fabricated both n^+ and p^+ nc-Si TFT at various channel lengths. The total resistance of nc-Si TFT comprises of channel resistance R_{CH} and the contact resistance R_o. They reported that $R_o \times W$ decreases with increase in gate overdrive voltages. They also proposed that if the channel length of n-type TFT is below 10 μm and of p-type TFT is below 25 μm, then the drain current at $V_{DS} = 10$ V is restricted by the contact resistance.

Djeridane et al. [23] proposed that during the growth of nc-Si film over the amorphous like substrate, a residual amorphous phase called as incubation layer is formed at the interface between the substrate and the film. This incubation layer can be avoided by controlling the deposition plasma parameters. They also reported that silicon nitride provides better stability when used as gate dielectric for the fabrication of n-type nc-Si TFT. However, for fabrication of p-type TFT they have used SiO_2 as a gate dielectric due to its wide band gap, large conduction and valence band offset.

Subramaniam et al. [24] reported that ambipolar operation can be achieved by reducing the oxygen concentration in the nc-Si channel. The ambipolar transistor allows the production of complementary inverter using single type device. They

Table 8.2 Ranking of alternatives by VIKOR approach [8]

Gate dielectric materials	Maximum group utility, G	Ranking based on G values	Minimum regret of opponent, R	Ranking based on R values	Q ($v = 0.5$)	VIKOR ranking
Si_3N_4	0.2079	1	0.1590	1	0	A1
Al_2O_3	0.4880	4	0.4	4	0.8521	A5
ZrO_2	0.4734	2	0.1778	2	0.3730	A2
HfO_2	0.4856	3	0.1778	2	0.3880	A3
Ta_2O_5	0.6056	5	0.3	3	0.7925	A4

Table 8.3 Ranking of alternatives by TOPSIS approach [8]

Gate dielectric materials	S^*	S^-	Z	TOPSIS ranking
Si_3N_4	0.0714	0.2143	0.7501	1
Al_2O_3	0.1615	0.1848	0.5336	2
ZrO_2	0.1229	0.1280	0.5101	3
HfO_2	0.1287	0.1236	0.4898	4
Ta_2O_5	0.1881	0.1270	0.4030	5

Table 8.4 Experimental published data for top-gate nc-Si TFT

Reference	Esmaeili et al. [7]	Cheng et al. [13]	Min et al. [12]	Lee et al. [15]
Gate contact	Al 300 nm	Al 200 nm	Al 200 nm	Al 300 nm
Source/drain contact layer	–	Cr 50 nm	Cr 50 nm	Cr 50 nm
Doped layer	n^+ nc-Si 80 nm	n^+ nc-Si 60 nm	n^+ nc-Si 60 nm	n^+ a-Si:H 50 nm
Process nc-Si	PECVD 50 nm	VHF PECVD 50 nm	VHFPECVD 300 nm	PECVD 100 nm
Dielectric	SiO_2 270 nm	SiO_2 300 nm	SiO_2 370 nm	a-SiO_x
Temperature (°C)	350	150	150	260
Width to length ratio (W/L)	180 μm/45 μm	200 μm/30 μm	240 μm/40 μm	W = 200 μm L = 20, 50, 100, 200 μm
Structure type	Top-gate coplanar	Top-gate staggered	Top-gate staggered	Top-gate staggered
Substrate	Glass	Glass, Kapton	Glass	Glass
Mobility	11 cm^2/Vs (at V_{ds} = 10 V)	Glass 30 cm^2/Vs Kapton 23 cm^2/Vs	40 cm^2/Vs	100-150 cm^2/Vs
Leakage current	1×10^{-12}A	–	–	–
Sub-threshold Slope	2.5 V/dec	–	–	0.22-0.25 V/dec
On/off ratio	10^8 at V_{DS} = 10 V	–	–	10^6
Threshold voltage	2.5 V (at V_{DS} = 0.1 V)	–	–	1.5–2 V
Threshold voltage shift	–	–	–	–
Year	2002	2002	2002	2005

(continued)

Table 8.4 (continued)

Reference	Fonrodona et al. [25]	Cheng et al. [14]	Kamei et al. [17]	Fonrodona et al. [26]
Gate contact	Al Thermally evaporated	Al 300 nm	Sputtered Al 300 nm	Al Thermally evaporated
Source/Drain contact layer	–	–	–	–
Doped layer	n + or p + a-Si:H 150 nm	Cr 100 nm	Cr 100 nm	n + nc-Si 150 nm
Process nc-Si	HWCVD 200 nm	PECVD 100 nm	RF PECVD 300 nm	HWCVD 200 nm
Dielectric	SiO_2 100 nm	a- SiO_x 300 nm	SiO_2 300 nm	SiO_2 100 nm
Temperature	200 ºC	260 ºC	150 ºC	200 ºC
Width to Length ratio (W/L)	20 µm/60 µm	200 µm/50 µm	200 µm/50 µm	100 µm/20 µm
Structure	Top-gate Coplanar	Top-gate Staggered	Top-gate staggered	Top-gate coplanar
Substrate	Glass covered with 200 nm APCVD deposited SiO_2	Glass	Glass	Glass covered with APCVD deposited SiO_2
Mobility	22 cm^2/Vs	150 cm^2/Vs	450 cm^2/Vs	11.5 cm^2/Vs
Leakage current	–	–	–	–
Sub-threshold Slope	0.5 V/dec	0.3 V/dec	0.6 V/dec	0.34 V/dec
On/off Ratio	$>10^6$	10^7	10^6	–
Threshold voltage	6.3 V	2 V	2 V	5.70 V
Threshold voltage shift	–	–	–	0.5 V at $V_{GS} = -10$ V
Year	2005	2005	2006	2006

(continued)

Table 8.4 (continued)

Reference	Lee et al. [19]	Lee et al. [18]	Kang et al. [20]	Subramaniam et al. [24]
Gate contact	Al	Al 300 nm	Al 300 nm	Al Liftoff
Source/Drain contact layer	Cr	n + nc-Si	n + nc-Si	Cr or Ti
Doped layer	n + nc-Si 60 nm	–	–	n^+ nc-Si 100 nm
Process nc-Si	PECVD 80 nm	ICP-CVD 60, 90, 130 nm	ICP-CVD 60, 90, 130 nm	PECVD 250 nm
Dielectric	a-SiN_x:H 300 nm	SiO_2 150 nm	SiO_2 150 nm	SiO_2
Temperature	240 ºC	180ºC	–	250˚C
Width to Length ratio (W/L)	200 µm/50 µm	20 µm/10 µm	20 µm/10 µm	20 µm/10 µm
Structure type	Top-gate	Top-gate	Top-gate Staggered	Top-gate Staggered
Substrate	Glass	Glass	Glass	p-type silicon
Mobility Resistivity	0.5 cm^2/Vs at V_{DS} = 1 V 0.6 cm^2/Vs at V_{DS} = 10 V	69 cm^2/Vs with 60 nm film 99 cm^2/Vs with 90 nm film	26 cm^2/Vs with 60 nm film 77 cm^2/Vs with 90 nm film 119 cm^2/Vswith 130 nm film	–
Leakage current	6.75×10^{-14}Aat V_{DS} = 0.1 V 2×10^{-11}A at V_{DS} = 10 V	At V_{GS} = −4.4 V 8.4×10^{-11} A with 60 nm film 3.6×10^{-10}A with 90 nm film	7.2×10^{-10} to 1.9×10^{-8}A at V_{GS} = −4.4 V	–
Sub-threshold Slope	0.82 V/dec at V_{DS} = 1 V 0.93 V/dec at V_{DS} = 10 V	217mv/dec with 60 nm film 230 mv/dec with 90 nm film	–	–

(continued)

Table 8.4 (continued)

Reference	Lee et al. [19]		Lee et al. [18]	Kang et al. [20]	Subramaniam et al. [24]
On/off Ratio	10^6 at V_{DS} = 1 V 2×10^5 at V_{DS} = 10 V		10^7 at V_{DS} = 0.1 V	10^4 at V_{DS} = 0.1 V	–
Threshold Voltage	2.4 V at V_{DS} = 1 V 2.7 V at V_{DS} = 10 V		2.2 V with 60 nm film 2.3 V with 90 nm film	–	–
Threshold voltage shift	V_{DS} = 1 V	V_{DS} = 10 V	V_{GS}	–	–
	0.35 0.77 1.52	0.34 0.57 1.23	20 V 30 V 40 V		
Year	2007		2007	2008	2012

fabricated both n-type and p-type top-gate staggered nc-Si TFT at submicron dimensions with no short channel effects.

Table 8.4 summarized nc-Si top-gate TFT device dimensions and performance parameters of the published experimental works. So based on the literature review, it is clear that n-channel nc-Si TFT provides higher mobility compared to p-channel TFT and staggered top-gate structure of TFT provides better stability and high on-off current ratio. So in this chapter, staggered top-gate n-channel nc-Si TFT is considered and investigated for its electrical behavior.

8.3 Conduction Models

Various device models have been presented in past for explaining the electrical behavior of nc-Si TFTs. This section presents the key assumptions, their conditions of validity and range of applicability of important analytical models of nc-Si TFTs.

Dosev et al. [27] reported the physical phenomenon accountable for different operation regimes and presented an analytical model for nc-Si TFTs associated with this phenomenon. This model is based on existing models for a-Si:H TFTs, which have been extended to account for observed physical phenomena in nc-Si TFT. They proposed that the density of the defect states (i.e., DOS) is lesser in nc-Si than in a-Si:H due to higher internal order of atoms in nc-Si.

$$I_{\mathrm{Dsat}} = \mu_{\mathrm{fet}} C_{\mathrm{i}} \frac{W}{L} V_{\mathrm{DSe}} (1 + \lambda V_{\mathrm{DS}}) V_{\mathrm{GTe}} \quad (\text{for above threshold regime}) \tag{8.2}$$

where μ_{fet} is the field-effect carrier mobility, C_{i} is the capacitance of gate insulator, V_{DS} is drain to source voltage, λ is parameter relating to the effect of gate-length modulation, V_{DSe} is effective voltage from drain to source, and V_{GTe} is the effective gate overdrive voltage.

Dosev et al. [28] presented the numerical simulation results of nc-Si TFTs, using ATLAS device simulator. They examined that acceptor-like defect states in nc-Si TFTs are filled at lower gate voltages as compared to a-Si:H having similar threshold voltages. The transconductance shape of nc-Si TFTs is same as of a-Si:H TFTs before the acceptor-like states are occupied. When acceptor-like states are filled by electrons then transconductance shape of nc-Si TFTs becomes typical as of poly-Si TFTs. Due to this behavior of acceptor-like states, the nc-Si TFTs properties typically lie between a-Si:H and the poly-Si transistors. However, authors considered a gap of 1.91 eV which is not a usual value for a-Si:H as well as for nc-Si TFT devices. For nc-Si TFT devices with an optical gap of 1.72 eV, Estrada et al. [29] demonstrated that the anomalous effect of transconductance is due to trapped charge concentration and if some conditions are fulfilled related to the trapped charges concentration in defect states and concentration of free charges in the material then this effect can also observe for a-Si:H devices with acceptor tail states activation energy similar to normal values of 0.035 eV. Therefore, the behavior of nc-Si is not

necessarily suggested between a-Si:H and poly-Si. The mobility and drain current models for nc-Si TFT devices are presented by Cerdeira et al. [30] including a second region examined in above-threshold regime, which are not exist in a-Si:H TFTs.

Hatzopoulos et al. [31] proposed the model for drain current in regime of above threshold, on the basis of exponential distribution of tail states energy. Under linear region, this proposed model explained the observed super linear rise of drain current with gate voltage by the value of characteristic thermal energy of band tails being higher than 1.5 times the lattice thermal energy. When the characteristic temperature distribution of tails states is equal to 1.5 times the lattice temperature, then the derived current analytical model leads to the general quadratic metal-oxide-semiconductor (MOS) expression which is reported by Pappas et al. [32]

$$I_{\mathrm{D}} = \frac{W}{L}\mu B\left[(V_{\mathrm{G}} - V_{\mathrm{T}})^{2AkT_{\mathrm{t}}} - (V_{\mathrm{G}} - V_{\mathrm{T}} - V_{\mathrm{D}})^{2AKT_{\mathrm{t}}}\right] \quad (\text{for above threshold regime}) \tag{8.3}$$

$$I_{\mathrm{Dsat}} = \frac{W}{L}\mu B(V_{\mathrm{G}} - V_{\mathrm{T}})^{2AkT_{\mathrm{t}}} \quad (\text{for saturation regime}) \tag{8.4}$$

where

$$B = \frac{n_i}{qA^2\sqrt{2kT_{\mathrm{t}}N_{\mathrm{t}}/\varepsilon_{\mathrm{s}}}}\left(\frac{C_{ox}^2}{4\varepsilon_{\mathrm{s}}kT_{\mathrm{t}}N_{\mathrm{t}}}\right)^{AkT_{\mathrm{t}}} \tag{8.5}$$

and

$$A = \frac{1}{kT} - \frac{1}{2kT_{\mathrm{t}}} \tag{8.6}$$

$$\mu_{\mathrm{FE}} = \frac{\mu B}{C_{\mathrm{in}}}2AkT_{\mathrm{t}}(2AkT_{\mathrm{t}} - 1)(V_{\mathrm{G}} - V_{\mathrm{T}} - V_{\mathrm{D}})^{2(AKT_t - 1)} \tag{8.7}$$

where I_{D} is drained current, μ_{FE} is field-effect mobility, k is Boltzmann constant, μ is low electric field mobility of electron, T_{t} is characteristic temperature of tail state distribution, N_{t} is tail states volume density at intrinsic level, n_{i} is intrinsic carrier concentration, C_{ox} is gate dielectric capacitance, ε_{s} is silicon permittivity, kT is thermal energy at room temperature, V_{G}, V_{D} and V_{T} are gates, drain and threshold voltage respectively, W is channel width, and L is channel length.

When μ_{FE} is constant and is independent of gate voltage then from Eq. (8.6), $AkT_{\mathrm{t}} = 1$ and $T_t > 3T/2$. Under this condition Eq. (8.3), (8.4), and (8.7) becomes,

$$I_{\mathrm{D}} = \frac{W}{L} C_{\mathrm{in}} \mu_{\mathrm{FE}} \left[(V_{\mathrm{G}} - V_{\mathrm{T}}) V_{\mathrm{D}} - \frac{V_{\mathrm{D}}^2}{2} \right] \quad (\text{for } V_{\mathrm{D}} < V_{\mathrm{G}} - V_{\mathrm{T}}) \tag{8.8}$$

$$I_{\mathrm{Dsat}} = \frac{W}{2L} C_{\mathrm{in}} \mu'_{\mathrm{FE}} \left[(V_{\mathrm{G}} - V_{\mathrm{T}})^2 \right] \quad (\text{for } V_{\mathrm{D}} \geq V_{\mathrm{G}} - V_{\mathrm{T}}) \tag{8.9}$$

$$\mu'_{\mathrm{FE}} = \frac{3\mu k T n_{\mathrm{i}}}{2q\sqrt{3\varepsilon_{\mathrm{s}} k T N_{\mathrm{t}}}} \frac{C_{\mathrm{in}}}{N_{\mathrm{t}}} \tag{8.10}$$

The off current in nc-Si TFT is examined by Esmaeili-Rad et al. [33] and analyzed that the presence of fixed charges at the nc-Si/passivation nitride interface serves to increase the band bending, leading to an increase in off current by about two orders of magnitude. The reduction in leakage current can be achieved by using a-Si:H/nc-Si bilayer as the channel of nc-Si TFT device. When the nc-Si channel layer is capped with a-Si:H, the reduction in leakage current can be determined by the bulk conductivity of nc-Si because a-Si:H layer typically makes less defective interface with the nitride layer which is used for the passivation.

Ahnood et al. [34] presented a general analytical technique capable of removing contact resistance effects, both ohmic and non-ohmic based solely on *I–V* measurements, enabling the extraction of an accurate and physically meaningful mobility. They proposed that the omission of contact resistance effects can results in an incorrect extraction of the maximum μ_{FET} by a factor of 2. Mao [35] demonstrated the impact of the grain size of nc-Si on the surface potential of doped nc-Si TFTs. During the calculation of the surface potential of nc-Si, authors examined that the change in the dielectric constant of nc-Si should be considered when its diameter is smaller than 10 nm and the change in the band gap of nc-Si should be considered when its diameter is larger than 6 nm. They proposed a simplified surface potential equation for nc-Si TFTs under strong inversion conditions.

$$E(\varphi_{\mathrm{s}}) = \sqrt{\frac{2q}{\left(1 + \frac{10.4}{1 + \left(\frac{1.38}{d \times 10^9}\right)^{1.37}}\right)\varepsilon_0} \left[\frac{N_{\mathrm{ST}}}{d}\varphi_{\mathrm{s}} + \frac{1}{N_{\mathrm{Aa}}^-} \frac{4kT(2\pi kT)^3 (m_{\mathrm{e}} m_{\mathrm{h}})^{\frac{3}{2}}}{h^6} \exp\left(- \frac{E_{\mathrm{g}}(\infty) + q\left(\frac{3.4382}{d \times 10^9} + \frac{1.1483}{(d \times 10^9)^2}\right)}{kT} \right) kT \exp\left(\frac{q\varphi_{\mathrm{s}}}{kT}\right) \right]} \tag{8.11}$$

where N_{Aa}^- is active dopant concentration, d is average grain size, q is electronic charge, N_{ST} is grain boundary surface state density, $E_{\mathrm{g}}(\infty)$ is bulk band gap, k is Boltzmann constant, T is temperature, φ_{s} is surface potential, ε_o is dielectric constant of free space, m_{e} and m_{h} are effective electron and hole masses respectively, and h is Planck's constant.

Anutgan et al. [36] performed the capacitance analyzes of nc-Si TFT. They found that the conducting thin layer in nc-Si film enlarges the effective area of capacitor beyond the electrode in nc-Si TFT structure. This increase of the effective area can be related to bulk capacitance-resistance branches and also with channel resistance where the earlier is governing at higher frequencies and the latter is

accountable for the further increase in effective area at lower frequencies. Thus, they proposed that the hole conductivity along the nc-Si TFT interface is less as compared to electron conductivity.

Steinke et al. [37] presented a model for determining the threshold voltage of nc-Si TFTs by examining the multiple boundaries between neighboring crystalline grains limit the charge-carrier transport. They have calculated the macroscopic densities of free and trapped carriers and then relate these densities with the site and bond occupation probabilities of a two-dimensional percolation problem in which sites correspond to grains and bonds to grain boundaries. In the site-bond percolation problem, they determined the threshold by using Monte-Carlo simulations. However, the model only describes transistor behavior near-threshold and could not explain the linear behavior soon after the transistor is turned on at low drain bias.

Sharma et al. [38] presented an analytical model for calculating the threshold voltage using one-dimensional Poisson's equation. They have analyzed the effect of various physical parameters i.e., trapping state density, doping density, temperature, and gate insulator thickness on the threshold voltage. They proposed that the decrease in gate insulator thickness and increase in temperature causes the decrease in the threshold voltage as shown in Fig. 8.2. They also demonstrate that the

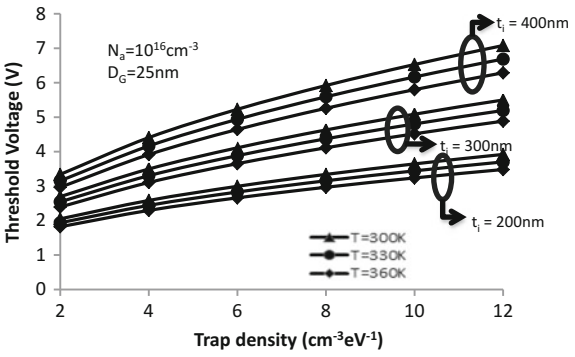

Fig. 8.2 Variation of threshold voltage as a function of trap density for different values of gate insulator thickness at different temperatures [38]

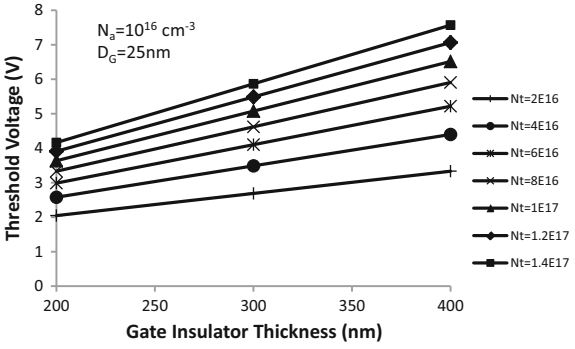

Fig. 8.3 Variation of threshold voltage as a function of gate insulator thickness for different values of trap density [38]

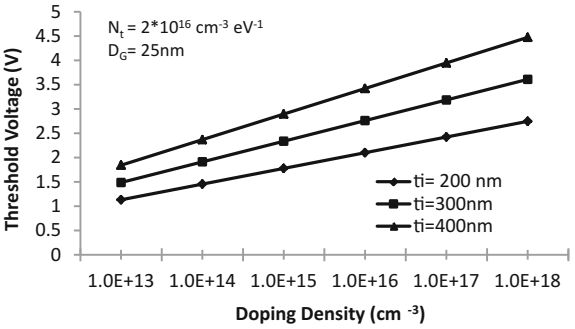

Fig. 8.4 Variation of threshold voltage as a function of doping density for different values of gate insulator thickness [38]

threshold voltage increases with increase in trap density and doping concentration for a particular value of gate insulator thickness as shown in Figs. 8.3 and 8.4.

8.4 Electrical Instability

In general, the silicon (Si) based TFT suffers from electrical instability due to two possible instability mechanisms: (a) Charge trapping in gate insulator and/or in the interface between the gate insulator and channel (b) Defect state creation in active layer. These instability mechanisms cause the shift in threshold voltage and thereby change the drain current of TFT. Esmaeili-Rad et al. [39] found that the nc-Si TFT shows less threshold voltage shift as compared to a-Si:H TFTs. In addition, Kim et al. [40] examined that in case of top-gated nc-Si TFT, the defect state creation is much lower due to the presence of well-crystallize region of the nc-Si film. Sharma and Gupta [41] further analyze the instability mechanism in top-gate nc-Si TFT and proposed the model for threshold voltage shift including the effect of various physical parameters like grain size, gate insulator thickness, doping density, and grain boundary trapping state. They provided the expression for threshold voltage as-

$$|\Delta V_T| = \left(V_{gs} - \varphi_s \left[1 + \frac{q t_i \sqrt{N_t}}{\varepsilon_i} \sqrt{1 + \frac{10.4}{1 + \left(\frac{1.38}{D_G \times 10^7} \right)^{1.37}}} \right] \right) \left\{ 1 - \exp\left[-\left(\frac{t}{\tau} \right)^{\beta} \right] \right\} \tag{8.12}$$

where V_{gs} is gate to source voltage, φ_s is surface potential, q is electronic charge, t_i is insulator thickness, ε_i is dielectric constant, N_t is density of trapping states ($cm^{-3}\ eV^{-1}$), D_G is grain size, τ is characteristic trapping time, and β is stretched-exponential exponent.

Based on the analysis, they proposed that the higher trap density, larger gate insulator thickness, and greater doping concentration provide lesser threshold

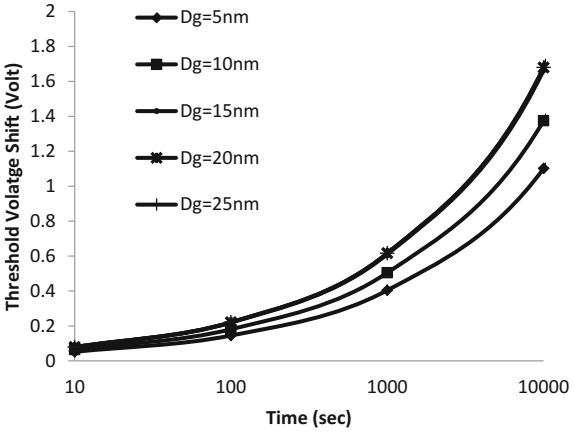

Fig. 8.5 Computed variations of threshold voltage shift in the top-gated nc-Si TFTs as a function of time for different grain sizes [41]

voltage shift. They also investigated that for smaller grain size, threshold voltage shift reduces with the reduction in grain size. But, if grain size is larger i.e., greater that 20 nm then device become shows minimal threshold voltage shift as shown in Fig. 8.5. Now, in the following section, we discuss about the attributes of instability mechanisms which are presented by the various researchers.

8.4.1 Powell's Model

Powell [42] analyzed that the electrical instability mechanism in amorphous silicon-silicon nitride TFTs, operate with low electric fields ($\sim 3 \times 10^5$ V cm^{-1}) in the dielectric, is basically the charge trapping that occurs in silicon nitride layer that causes the threshold voltage shift and thus causes drain current degradation for a given biasing condition. Since silicon nitride as a gate dielectric has a high density of trap states thus causes charge trapping instabilities in TFT. Author proposed that the rate limiting process involved in the charge transfer at low electric field is basically the conduction in the nitride by variable range hopping at Fermi level and not the supply function from the semiconductor. Since the space charge in the nitride and the variable hopping conduction both depends on density of states in silicon nitride thus the threshold voltage shift is determined by the density of states at the Fermi level.

However, author [43] further proposed that the nitride dependency of the hopping rates was due to variation in wave function rather than the trap density. The magnitude of threshold voltage shift is strongly temperature dependent with activation energy of 0.3 eV. This activation energy is determined by the mean hop energy required for charge injection deep into the silicon nitride at the low applied electric fields. The strong temperature dependency of charge trapping is due to charge redistribution in the silicon nitride by thermally activated variable hopping from occupied states.

The logarithmic time dependence of threshold voltage shift is given as-

$$\Delta V_{\mathrm{T}} = r_{\mathrm{d}} \log\left(1 + \frac{t}{t_{\mathrm{o}}}\right) \tag{8.13}$$

where r_{d} is constant and contains the density of traps and tunneling constant.

Later, Powell and his research group [44] analyzed that in addition to the existing process of charge trapping near the interface, following mechanisms are also possible: (1) tunneling into the dielectric, (2) trapping into states at semiconductor-dielectric boundary, and (3) localization in deep states within the amorphous silicon layer.

They proposed that the new mechanism responsible for instability of a-Si:H TFTs is the creation of metastable dangling bond states within the a-Si:H layer near to dielectric interface as a result of the field-effect-induced changes in electron density.

If phosphorus doping is used in order to move the Fermi level into the conduction band tail, then this makes the unstable configuration of silicon atom with five electrons. This silicon atom located just below the fermi level and thus causes the breaking of weak Si–Si bond and hence the formation of dangling bond defects:

$$2\mathrm{Si_4}^0 + \mathrm{e}^- \rightarrow \mathrm{Si_3}^- + \mathrm{Si_3}^0$$

The main difference [45] between the two instability mechanisms is that, in case of charge trapping mechanism [42], the charge carriers are slowly trapped into electron states (also known as slow states) which are in poor communication with the a-Si conduction band. This trapping process produces a fixed shift in the transfer characteristic of a-Si TFTs. However, in case of defect state creation mechanism [44], there is a slow increase of extra states (also known as fast states) which are in good communication with the a-Si conduction band.

Berkel et al. [45] analyzed the bias dependence of threshold voltage shift in amorphous silicon-silicon nitride ambipolar TFTs and reported the coexistence of both instability mechanisms. They proposed that the state creation is dominated at low positive bias whereas charge trapping is dominated at higher positive as well as negative bias. An ambipolar TFT possess electron as well as hole accumulation layers under positive and negative gate biases, respectively. In this case, the number of created dangling bonds is given as [45]

$$\Delta N_{\mathrm{dh}} = C\frac{V_{\mathrm{e}} - V_{\mathrm{h}}}{2}\left(\mathrm{cm}^{-2}\right) \tag{8.14}$$

where V_{e} is the shift of threshold voltage for electron conduction and V_{h} is the shift for hole conduction, while the density of slow states is given by

$$\Delta n_t = C\frac{V_e + V_h}{2}\left(\mathrm{cm}^{-2}\right) \tag{8.15}$$

where C in Eqs. (8.14) and (8.15) is the geometrical capacitance.

Author concludes that the extra states are created due to the absence of bonding electrons and these reactions will separately proceed whenever conduction band states or valence band states are populated and thus for bond breaking, recombination events are not required which is considered essential by Stutzmann et al. [46]. Berkel et al. [45] provide clear evidence for the charge trapping in the nitride and thus for the presence of slow states at the a-Si:H/a-SiN:H interface. Charge exchange with the nitride layer causes the net positive charge after negative bias stress and also net negative charge after positive bias stress. Under positive bias, the charge trapping mechanism is strongly field dependent.

Powell and his group [47] provide further refinement in bias dependency of the threshold voltage shift by including the effect of nitride composition. They reported that state creation is independent of the nitride composition and dominant at lower biases whereas the charge trapping is dependent on the nitride composition and dominant at higher biases. This indicates that the state creation process occurs in the a-Si:H layer whereas the charge trapping occurs in a-SiN_x:H layer. The defect states can be directly created by populating the conduction band tail states in the undoped material which moves the Fermi level up to the energy similar to these states. They also proposed that the charge trapping process is strongly field dependent which is associated with the field enhanced hopping at the Fermi level.

They also measured the time and temperature dependence of two instability mechanisms [48] and found that at the bias above which the charge trapping in the nitride dominates, the threshold voltage shift shows the logarithmic time dependence whereas at the bias below which state creation in the a-Si:H dominates, the threshold voltage shift shows the power law dependence, $\Delta V_T = \alpha(t/t_o)^{\beta}$ where β is about 0.5. They also found that the state creation is thermally activated but the charge trapping is weakly temperature dependent. The charge trapping shows logarithmic time dependence and the small temperature dependence because the rate limiting step is basically the charge injection from the a-Si:H to the silicon nitride with charge trapping close to the semiconductor interface and no charge redistribution occurs due to the conduction in the nitride. The threshold voltage shift due to the state creation is small and is given as

$$\Delta V_T = (V_G - V_T)(t/t_o)^{\beta} \tag{8.16}$$

Thus, the rate of state creation is proportional to the band tail electrons and t_o is independent of density of band tail electrons. The magnitude of $E_a \sim 0.9$ eV (i.e., activation energy of t_o) and temperature dependent β ($\sim$0.45–0.65) is uniform with dispersive hydrogen diffusion. Thus, they proposed that the state creation process is similar to that of dangling bond creation process which occurs due to the breaking of weak Si–Si bonds sustained by dispersive diffusion of hydrogen [49, 50].

Powell et al. [51] also reported that the charge trapping mechanism causes a shift of the electron and hole threshold voltages in the same direction whereas the state creation mechanism causes a shift in opposite direction. The electron threshold voltage is shifted in positive direction while hole threshold voltage is shifted in negative direction. For the transistor which uses silicon nitride as a gate dielectric, state creation in the lower part of the band gap is the dominant process at the low positive bias whereas the removal of states from the lower part of the gap dominates at the low negative bias. However, for the transistor that uses oxide as the gate dielectric, state creation is the dominant process for both positive and negative bias. For positive bias, states creation occurred in the lower portion of the band gap whereas for negative bias, it occurred in the upper portion of the band gap. In addition to this, for oxide transistor, the positive and negative bias annealing causes overall increase in the density of states whereas for nitride transistor negative bias annealing causes a decrease in the density of states due to the annealing of defect states presents below the midgap. This difference between nitride and oxide transistor is because of the different zero-bias Fermi energy position at the interface due to the existence of an electron accumulation layer in the nitride transistor.

For nitride transistor, the dominant mechanism for threshold voltage shift under the higher biases stress is the charge trapping which occurs for both high positive as well as high negative bias. The magnitude of the threshold voltage shift for state reduction is smaller than for the state creation. Authors also found that threshold voltage shows the power law time dependence for both the polarities and in addition to this the activation energy is same ($\sim$0.9 eV) for both positive and negative bias. This concludes that the state creation process for positive bias is similar to that of state removal process for negative bias.

Powell and his group [52] further proposed that the parameter β is not appropriate for measuring the TFT instability and thus a new concept known as thermalization energy concept has been proposed. According to them, defect creation during bias stress exhibits a thermal barrier for defect removal with the maximum energy around 1.1–1.4 eV based on the time and temperature at which defects were created. This barrier is not important under thermal equilibrium ($\sim$500 K) because the defect creation and removal are balanced by the formation energy of defects, however, under non-equilibrium condition, this energy barrier is important in order to identify the specific intermediate step.

They reported the expression for thermalization energy as [52]

$$E = (k_B T)\ln(\upsilon t) \tag{8.17}$$

It means that after time t, all defect-creation sites with energy $E_a \leq E$ would have converted into defects. Deane et al. [52] plotted threshold voltage shift as a function of stress time at various temperatures and then applied the thermalization concept to the bias stress data by plotting threshold voltage shift as a function of thermalization energy and found a unique curve at a single fitting parameter i.e., attempt-to-escape frequency $\upsilon(=10^{10}\ \mathrm{Hz})$. They also plotted stretched exponential as a function of thermalization energy and found that the stretched exponential curve matched well

with the experimental data for the $E < 0.95$ eV but curves show mismatched for $E > 0.95$ eV and thus they proposed that to obtain a stretched exponential, the defect state creation has to be proportional to the number of excess band tail carriers $(\Delta N_{BT})^{\alpha}$ with α between 1.5 and 1.7. For $\alpha = 1.5$, threshold voltage shift is given as equation

$$\Delta V_t \propto \left[\left(\frac{t}{t_0}\right)^{\beta} + 1\right]^{-2} \tag{8.18}$$

They provide the following comparison between defect state creation and defect removal

1. Defect state creation possesses $E_a = 0.975$ eV with $\upsilon_o = 10^{10}$ Hz whereas defect removal shows activation energy between 01.1 and 1.5 eV with υ_o of 10^{13} Hz.
2. Defect creation mechanism occurs due to the breaking of weak Si–Si bond and which results into the thermalization of SiHD complex in the H-DOS (hydrogen density of states) whereas the defect removal occurs due to the release of hydrogen from the SiHD complex. The following equation shows that thermalization of SiHD complex.

$$\mathrm{Si} - \mathrm{Si}_{\mathrm{weak}} + \mathrm{SiHD} \rightarrow \mathrm{SiHD} + \mathrm{Si} - \mathrm{Si}_{\mathrm{strong}}$$

8.4.2 Libsch's Model

Libsch et al. [53] proposed that the charge injection from the a-Si:H channel into the traps presented in the a-Si:H/a-SiN$_X$:H interface and in the nitride layer close to the interface causes the threshold voltage shift (ΔV_T) in the transfer characteristic of TFT. They proposed the stretched-exponential equation given as-

$$|\Delta V_T| = |\Delta V_0|\left\{1 - \exp\left[-\left(\frac{t}{\tau}\right)^{\beta}\right]\right\} \tag{8.19}$$

where ΔV_0 is the effective voltage drop across the insulator, $\tau = \tau_0 \exp(E_T/kT)$ is the characteristic trapping time of the carriers with τ_o being the thermal prefactor for emission over the energy barrier, $E_a = E_T\beta$ represent the thermal activation energy with β as the stretched-exponential exponent and E_T being the average effective energy barrier for the carriers enter into the insulator from the a-Si:H channel. When the shorter stress times, lower stress electric fields or lower stress temperatures are applied on the nitride gate dielectric a-Si:H TFT then the carriers inject directly into the bottom energy states of a-Si:H/a-SiN$_X$:H interface and in the a-SiN$_X$:H transitional layer near the a-Si:H/a-SiN$_X$:H interface. However, when longer stress times,

higher stress electric fields or higher stress temperatures are applied then large concentration of states in the insulator near the a-Si:H/a-SiN_X:H interface will get filled and as a result probability of emission from these states increases.

Staebler et al. [54] reported that β and τ are independent of gate bias while ΔV_0 is dependent on gate bias and is given as $\Delta V_0 \approx V_g - V_{ti}$ with no power dependence (i.e., $\alpha = 1.0$). β is given as $\beta = \left(T_{ST}/T_0^*\right) - \beta_0$ with $T_0^* \approx 229$ K and $\beta_0 \approx 1.04$ for $T_{ST} \leq 80$ °C while for $T_{ST} \geq 80$ °C, β becomes temperature independent with $\beta \approx 0.5$. A nonzero value of β_0 shows that ΔV_T is independent of gate dielectric which differs from the conclusion given by previous researchers [55].

8.4.3 Nathan's Model

Nathan and his group [56] proposed that when a bias is applied on the gate terminal with the drain and source grounded then the threshold voltage shift shows the power law dependence on gate bias stress and can be given by defect pool model [57]. According to defect pool model, the rate of defect state creation is dependent on barrier to defect state formation, number of band tail electrons and density of week Si–Si bonds. Thus, the threshold voltage shift is given as

$$\Delta V_T = A(V_{ST} - V_{Ti})(t)^{\beta} \tag{8.20}$$

where V_{ST} is the gate bias stress voltage, V_{Ti} is the threshold voltage of TFT before gate bias is applied, A and β (~ 0.3) are temperature dependent parameters, and t is the gate bias stress time. However, when both gate and drain terminals of the nitrogen rich gate dielectric TFTs are subjected to bias voltage then for small gate stress biases (≤ 15 V), where the defect state creation is the dominant instability mechanism, TFT shows less threshold voltage shift as compared to the presence of only gate bias stress. Authors reported that the increase in drain bias stress results in the increase of lateral electric field which in turn decreases the channel carrier concentration (n_{BT}) close to drain. However, in the saturation mode ($V_{DS} = V_{GS} - V_T$), the channel carrier concentration remains constant and thus causes negligible threshold voltage shift. Similarly, TFTs subjected into deeper saturation ($V_{DS} > V_{GS} - V_T$) shows less threshold voltage shift. Thus, the charge stored on the gate when TFT is subjected to both gate and drain bias stresses is given as [56]:

$$Q_G = \frac{2}{3} C_G WL \frac{(V_{GS} - V_T)^3 - (V_{GD} - V_T)^3}{(V_{GS} - V_T)^2 - (V_{GD} - V_T)^2} \tag{8.21}$$

$$\text{In linear region, } V_{GD} = V_{GS}\, Q_{G0} = C_G \cdot W \cdot L(V_{GS} - V_T) \tag{8.22}$$

$$\text{In saturation region, } V_{GD} \rightarrow V_T \quad Q_G = \frac{2}{3} C_G \cdot W \cdot L(V_{GS} - V_T) \tag{8.23}$$

Now threshold voltage shift is given as,

$$\Delta V_T = \left(\frac{Q_G}{Q_{G0}}\right) A(V_{GS} - V_{Ti})(t)^{\beta} \tag{8.24}$$

where Q_G is given by Eq. (8.21) and Q_{G0} is given by Eq. (8.22)

In constant current stressing, the drain and gate terminals of the TFTs are shorted in the diode connected configuration with the source terminal grounded. The constant drain current is maintained by the progressive adjustment of the gate bias for the compensation of threshold voltage shift. Such compensation thus maintained the constant band tail carrier density (n_{BT}) and hence threshold voltage shift shows no trend of saturation.

Nathan and his group [58] further modified the power law dependency of ΔV_T which is given as

$$\Delta V_T(t) = [V_{GS}(t) - V_T(t)]^{\gamma} \left(\frac{t}{t_0}\right)^{\beta} \tag{8.25}$$

where

$$t_0 = \left(\frac{\beta w N_{BT}}{A N_{WB} D_{00} w^{\beta}}\right)^{\frac{1}{\beta}} \tag{8.26}$$

Here, A is proportionality constant, N_{BT} is the band tail states density, w is the attempt-to-escape frequency of hydrogen, D_{00} is the microscopic diffusion coefficient, β is power law index, and γ is a power parameter having values between 1.5 and 1.9. The power law parameters β, γ, and t_0 are dependent on temperature and stress history of the TFT.

8.5 Conclusion

The purpose of this chapter is to provide a detailed progress in the area of top-gate nc-Si TFT. The performance of top-gate nc-Si TFT depends upon the various process parameters used during its fabrication and also on the conduction and instability mechanisms that occurs under electrical stress. So an extensive review is provided by covering the fabrication techniques, conduction models and electrical instability mechanisms of top-gate nc-Si TFT which can be useful for its effective application in new generation displays.

References

1. A.J. Snell, K.D. Mackenzie, W.E. Spear, P.G. LeComber, Application of amorphous silicon field effect transistors in addressable liquid crystal display panels. Appl. Phys. Lett. **24**, 357–362 (1981)
2. M. Mizukami, K. Inukai, H. Yamagata, T. Konuma, T. Nishi, J. Koyama, S. Yamazaki, 6-bit digital VGA OLED. SID Int. Symp. Dig. Tech. Papers **31**, 912–915 (2000)
3. K. Finkenzeller, *RFID Handbook: Fundamentals and Applications in Contactless Smart Cards and Identification*, 2nd edn. (Wiley, West Sussex, England, 2003)
4. P. Smith, D. Allee, C. Moyer, D. Loy, Flexible transistor arrays. Inf. Display **21**, 18–22 (2005)
5. J.J. Lih, C.F. Sung, C.H. Li, T.H. Hsiao, H.H. Lee, Comparison of a-Si and poly-Si for AMOLED displays. J. Soc. Inform. Display **12**, 367–371 (2004)
6. J.H. Park, S.M. Han, Y.H. Choi, S.J. Kim, M.K. Han, *"New In-Situ Process of Top Gate Nanocrystalline Silicon Thin Film Transistors Fabricated at 180° C for the Suppression of Leakage Current," IEEE International Electron Devices Meeting, Washington, 2007*, 10–12 Dec 10–12 2007, pp. 595–598
7. M.R. Esmaeili-Rad, *Nanocrystalline Silicon Thin Film Transistor* [PhD thesis], University of Waterloo, Canada, 2008
8. P. Sharma, N. Gupta, Investigation on material selection for gate dielectric in nanocrystalline silicon (nc-Si) top-gated thin film transistor (TFT) using Ashby's, VIKOR and TOPSIS. J. Mat. Sci.: Mat. Electron. (Springer) **26**, 9607–9613 (2015)
9. M.F. Ashby's, Multi objective optimization in material design and selection. *Acta Materialia*. **48**, 1792–1795 (2000)
10. S. Opricovic, G.H. Tzeng, Multicriteria planning of post-earthquake sustainable reconstruction. Comput.-Aided Civil Infrastruct. Eng. **17**, 211–220 (2002)
11. C. Hwang, K. Yoon, *Multiple attribute decision making methods and application survey*, vol. 186 (Business & Economics, Berlin, Springer, 2005)
12. R.B. Min, S. Wagner, Nanocrystalline silicon thin-film transistors with 50-nm-thick deposited channel layer, 10 $cm^2\ V^{-1}\ s^{-1}$ electron mobility and 108 on/off current ratio. Appl. Phys. A **74**, 541–543 (2002)
13. I.C. Cheng, W. Sigurd, Hole and electron field-effect mobilities in nanocrystalline silicon deposited at 150 C. Appl. Phys. Lett. **80**, 440–442 (2002)
14. I.C. Cheng, W. Sigurd, Nanocrystalline silicon thin film transistors. IEE Proc.-Circ., Devices Syst. **150**, 339–344 (2003)
15. C.H. Lee, A. Sazonov, A. Nathan, *"High mobility n-channel and p-channel nanocrystalline silicon thin-film transistors" IEEE International Electron Devices Meeting, IEDM Technical Digest*. Washington, 5 Dec 2005, pp. 915–918
16. C.H. Lee, A. Sazonov, A. Nathan, High-mobility nanocrystalline silicon thin-film transistors fabricated by plasma-enhanced chemical vapor deposition. Appl. Phys. Lett. **86**, 222106-1-3 (2005)
17. T. Kamei, M. Kondo, A. Matsuda, A significant reduction of impurity contents in hydrogenated microcrystalline silicon films for increased grain size and reduced defect density. Jpn. J. Appl. Phys. **37**, L265–L268 (1998)
18. C.H. Lee, S. Andrei, N. Arokia, R. John, Directly deposited nanocrystalline silicon thin-film transistors with ultra high mobilities. Appl. Phys. Lett. **89**, 2101 (2006)
19. C.H. Lee, D. Striakhilev, A. Nathan, "Stability of nc-Si: H TFTs with silicon nitride gate dielectric. IEEE Trans. Electron Devices **54**, 45–51 (2007)
20. D.W. Kang, J.H. Park, S.M. Han, M.K. Han, The effects of nanocrystalline silicon thin film thickness on top-gate nanocrystalline silicon thin film transistor fabricated at 180°C. J. Semicond. Technol. Sci. **8**, 111–114 (2008)
21. H.J. Lee, A. Sazonov, A. Nathan, Leakage current mechanisms in top-gate nanocrystalline silicon thin film transistors. Appl. Phys. Lett. **92**, 083509 (2008)

22. I. Cheng, S. Wagner, S.E. Vallat, Contact resistance in nanocrystalline silicon thin-film transistors. IEEE Trans. Electron Devices **55**, 973–977 (2008)
23. Y. Djeridane, K.H. Kim, S.H. Kim, J.H. Bae, J.Y. Jeong, J. Jang, Fabrication and characterization of ion-doped p-Type nanocrystalline silicon thin-film transistors. J. Korean Phys. Soc. **54**, 437–440 (2009)
24. A. Subramaniam, K.D. Cantley, H.J. Stiegler, R.A. Chapman, E.M. Vogel, Submicron ambipolar nanocrystalline silicon thin-film transistors and inverters. IEEE Trans. Electron Devices **59**, 359–366 (2012)
25. M. Fonrodona, J. Escarre, F. Villar, D Soler, J. Bertomeu, J. Andreu, A. Saboundji, N. Coulon, T. Mohammed-Brahim T, *Nanocrystalline top-gate thin film transistors deposited at low temperature by Hot-Wire CVD on glass*. IEEE Conference on Electron Devices, Spanish, 2–4 Feb 2005, pp. 183–186 (2005)
26. M. Fonrodona, J. Soler, F. Escarré, J. Villar, J. Bertomeu, A.S. Andreu, C. Nathalie, M.B. Tayeb, Low temperature amorphous and nanocrystalline silicon thin film transistors deposited by hot-wire CVD on glass substrate. Thin Solid Films **501**, 303–306 (2006)
27. D. Dosev, T. Ytterdal, J. Pallares, L.F. Marsal, B. Iñíguez, DC SPICE model for nanocrystalline and microcrystalline silicon TFTs. IEEE Trans. Electron Devices **49**, 1979–1983 (2002)
28. D. Dosev, B. Iniguez, L.F. Marsal, J. Pallares, T. Ytterdal, Device simulations of nanocrystalline silicon thin-film transistors. Solid-State Electron. **47**, 1917–1920 (2003)
29. M. Estrada, A. Cerdeira, L. Resendiz, B. Iniguez, L.F. Marzal, J. Pallares, Effect of localized traps on the anomalous behavior of the transconductance in nanocrystalline TFTs. Microelectron. Reliab. **45**, 1161–1166 (2005)
30. A. Cerdeira, M. Estrada, B. Iniguez, J. Pallares, L.F. Marsal, Modeling and parameter extraction procedure for nanocrystalline TFTs. Solid-State Electron. **48**, 103–109 (2004)
31. A.T. Hatzopoulos, L. Pappas, D.H. Tassis, N. Arpatzanis, C.A. Dimitriadis, F. Templier, M. Oudwan, Analytical current-voltage model for nanocrystalline silicon thin-film transistors. Appl. Phys. Lett. **89**, 193504-1-3 (2006)
32. I. Pappas, C.A. Dimitriadis, F. Templier, M. Oudwan, G. Kamarinos, Above-threshold drain current model including band tail states in nanocrystalline silicon thin-film transistors for circuit implementation. J. Appl. Phys. **101**, 84506-1-4 (2007)
33. M.R. Esmaeili-Rad, A. Sazonov, A. Nathan, Analysis of the off current in nanocrystalline silicon bottom-gate thin-film transistors. J. Appl. Phys. **103**, 074502-1-6 (2008)
34. A. Ahnood, F. Li, K. Ghaffarzadeh, M.R. Esmaeili-Rad, A. Nathan, A. Sazonov, P. Servati, Non-ohmic contact resistance and field-effect mobility in nanocrystalline silicon thin film transistors. Appl. Phys. Lett. **93**, 163503-1-3 (2008)
35. L.F. Mao, The quantum size effects on the surface potential of nanocrystalline silicon thin film transistors. Thin Solid Films **518**, 3396–3401 (2010)
36. T. Anutgan, M. Anutgan, I. Atilgan, B. Katircioglu, Capacitance analyses of hydrogenated nanocrystalline silicon based thin film transistor. Thin Solid Film. **519**, 3914–3921 (2011)
37. I.P. Steinke, P.P. Ruden, Percolation model for the threshold voltage of field-effect transistors with nanocrystalline channels. J. Appl. Phys. **111**, 014510-1-5 (2012)
38. P. Sharma, N. Gupta, Threshold voltage modeling on nanocrystalline silicon thin-film transistors. J. Electron Devices **19**, 1608–1612 (2014)
39. M.R. Esmaeili-Rad, A. Sazonov, A. Nathan, Absence of defect state creation in nanocrystalline silicon thin film transistors deduced from constant current stress measurements. Appl. Phys. Lett. **91**: 113511-1-3 (2007)
40. S.J. Kim, S.G. Park, S.B. Ji, M.K. Han, Effect of drain bias stress on stability of nanocrystalline silicon thin film transistors with various channel lengths. Jpn. J. Appl. Phys. **20**, 04DH12 (2010)
41. P. Sharma, N. Gupta, Model for threshold voltage instability in top-gated nanocrystalline silicon thin film transistor. J. Comput. Electron. (Springer) **15**, 666–671 (2016)
42. C.M. Svensson, K.I. Lundstrom, Trap-assisted charge injection in MNOS structures. J. Appl. Phys. **44**, 4657–4663 (1973)

43. S.W. Wright, J.C. Anderson, Trapping centres in sputtered SiO_2 films. Thin Solid Films **62**, 89–96 (1979)
44. H. Koelmans, H.C. De Graaff, Drift phenomena in CdSe thin film FET's. Solid-State Electron. **10**, 997–1000 (1967)
45. M.J. Powell, Charge trapping instabilities in amorphous silicon silicon nitride thin film transistors. Appl. Phys. Lett. **43**, 597–599 (1983)
46. R.A. Street, *Hydrogenated amorphous silicon* (Cambridge University Press, Cambridge, 1991)
47. R.A. Street, C.C. Tsai, Fast and slow states at the interface of amorphous silicon and silicon nitride. Appl. Phys. Lett. **48**, 1672–1674 (1986)
48. A.R. Hepburn, J.M. Marshall, C. Main, M.J. Powell, C.V. Berkel, Metastable defects in amorphous silicon thin film transistors. Phys. Rev. Lett. **56**, 2215–2218 (1986)
49. C.V. Berkel, M. Powell, Resolution of amorphous silicon thin film transistor instability mechanisms using ambipolar transistors. Appl. Phys. Lett. **51**, 1094–1096 (1987)
50. M. Stutzmann, W.B. Jackson, C.C. Tsai, Light-induced metastable defects in hydrogenated amorphous silicon: a systematic study. Phys. Rev. B. **32**, 23–47 (1985)
51. M.J. Powell, C.V. Berkel, I.D. French, D.H. Nicholls, Bias dependence of instability mechanisms in amorphous silicon thin film transistors. Appl. Phys. Lett. **51**, 1242–1244 (1987)
52. M.J. Powell, C.V. Berkel, J.R. Hughes, Time and temperature dependence of instability mechanisms in amorphous silicon thin film transistors. Appl. Phys. Lett. **54**, 1323–1325 (1989)
53. R.A. Street, The origin of metastable states in a-Si:H. Solar Cells. **24**, 211–221 (1988)
54. G. Muller, On the generation and annealing of dangling bond defects in hydrogenated amorphous silicon. Appl. Phys. A **45**, 41–51 (1988)
55. M.J. Powell, S.C. Deane, W.I. Milne, Bias stress induced creation and removal of dangling bond states in amorphous silicon thin film transistors. Appl. Phys. Lett. **60**, 207–209 (1992)
56. S.C. Deane, R.B. Wehrspohn, M.J. Powell, Unification of the time and temperature dependence of dangling bond defect creation and removal in amorphous silicon thin film transistors, Phys. Rev. B. **58**, 12 625–12 628 (1998)
57. F.R. Libsch, J. Kanicki, Bias stress induced stretched exponential time dependence of charge injection and trapping in amorphous thin film transistors. Appl. Phys. Lett. **62**, 1286–1288 (1993)
58. D.L. Staebler, C.R. Wronski, Optically induced conductivity changes in discharge-produced hydrogenated amorphous silicon. J. Appl. Phys. **51**, 3262–3268 (1980)

Chapter 9
Molecular Electronics

Subhasis Ghosh

Abstract Molecular electronics aim to create a functional electronic device using single or small assembly of molecules. It is believed that molecular electronics, not only will meet the increasing demand of more speed and more storage, but also provide a test bed to investigate mesoscopic transport phenomena and different properties at molecular level. Though there are several advantages in adopting single molecule as the active element in nanodevices, but contacting molecule with macroscopic contact in a circuit still remains a major challenge, as the conventional lithography-based contacting techniques cannot form metal contacts to a single molecule. Moreover, the absence of suitable imaging techniques at subnanometer level to look into single metal-molecule junction makes it even harder challenge. In last decade, several novel contacting techniques using nanolithography have been developed. However, the evidence that a molecule has been docked and contacted between two metal electrodes successfully can only be provided by measuring the current transport through the junctions. Out of the different mesoscopic devices in the length scale of 1–3 nm, it has been emphasized that molecular devices based on electrical break junction will be most suitable for electrical characterization with a prospect to use them in future circuits based on single molecule-based nanodevices. These investigations on the electrical transport through single or small assembly of molecules should be extremely useful for understanding quantum transport processes through the molecule, the device fabrication processes at nanoscale, and the roadmap for future nanoelectronics are essential for overcoming the "red brick wall" of Si-based microelectronics.

S. Ghosh (✉)
School of Physical Sciences, Jawaharlal Nehru University, New Delhi, India
e-mail: subhasis@mail.jnu.ac.in; subhasis.ghosh.jnu@gmail.com

S. Ghosh
Department of Physics, Shiv Nadar University, Greater Noida, India

Z.H. Khan (ed.), *Nanomaterials and Their Applications*,
Advanced Structured Materials 84, https://doi.org/10.1007/978-981-10-6214-8_9

9.1 Introduction

The number of transistors in an integrated circuit grows exponentially, approximately doubling every two years following *Moore's law* [1]. The ever-increasing demand of the number of components requires scaling down feature size. This scaling down cannot be continued without reaching a classical or semi-classical limit, and eventually being dominated by quantum mechanical effects. Though *where-is-the-limit* is the subject of intense academic debate, but transistor with gate length less than 10 nm has been demonstrated and eventually incorporated in modern microchip. In addition to reduction in source to drain distance, the demand for ever-increasing switching speed has led to reduction of thickness of the gate oxides from 100 nm down to 1–2 nm, which is potentially detrimental for uncontrolled surface roughness and unwanted charge carriers tunneling. These uncontrolled and unwanted effects due to miniaturization of electronic devices lead to extensive research activities to develop nanodevices. One of the ways could be the use of single molecule-based electronic nanodevice and eventually electronic circuits. Molecule is the smallest conductor of electricity and arguably should be most preferred choice for active component in nanodevice. Molecule-based system should be naturally fault tolerant as there cannot be defect in single molecule, and molecules can be produced reproducibly in large numbers by chemical reactions which open up the almost infinite possibilities, in particular, in organic systems. Moreover, new functionalities or existing functionalities at a simpler process level can be provided by virtue of self-organization capabilities of molecules.

Aviram and Ratner [2] first proposed the use of single molecule as active electronic devices in 1974. They proposed that an organic molecule with built-in donor–acceptor moieties separated by a tunnel barrier could act as a rectifying diode. It took more than 20 years to realize organic molecule-based rectifying diode [3]. Absence of contacting technology to nanosystems was the biggest hindrance in achieving single molecule-based devices. After this discovery, an enormous amount of experimental results were presented using different novel contacting techniques [4–7]. But, during last decade, most of the achievement is more or less limited to *proof-of-concept*, because the reproducibility at nanometer scale appears to be extremely difficult challenge to overcome. Recently, several contacting techniques have shown promising results [4–7], which have shown reproducible results in organic molecule-based devices.

9.2 What Is Molecular Electronics?

As mentioned before, according to Moore's law, to achieve desired miniaturizing in near future, it will require to position atom by atom reproducibly and controllably. However, the technology required for this has not been realized yet, whereas it has been realized that it may be possible to position molecule by molecule to achieve

desired functionalities in electronic nanodevices. The field *molecular electronics* deals with all the issues related in realizing single or small assembly of molecules-based nanodevice that would perform all linear and nonlinear functionalities deemed for electronic devices. Initially, molecular electronics are defined as technologies utilizing only single molecules; however, this definition has been broadened by including electronic devices utilizing single molecular properties in small assemble of molecules, but differentiating from the field of electronics which utilized the properties of molecular solids, known as organic electronics. Essentially, molecular electronics is to be entirely based on molecule-based nanodevices deemed to break the technological bottleneck posed by Moore's law.

The simplest device is supposed to conceive a switch which should perform similar way as in Si-based devices, i.e., with well-defined addressable ON and OFF states and remaining in the state that it is placed until its state is changed by an external trigger. The addressability of molecular switch is not an issue in case of single molecule-based devices, but an area of major concern in devices which are based on assembling of molecules due to uncertainty in the position of molecule on a surface on which a particular configuration of molecules is required for certain functionalities. Another concern is the chemical stability of molecule under a wide variety of conditions. However, the biggest challenge is how to make a molecule connect with other molecules at nanoscale, as well as macroscale, extremely important for wiring up the molecules required for molecular circuit.

9.3 First-Generation Molecular Devices

The first-generation of molecular devices was proposed by Aviram and Ratner [2], based on an organic molecule with both donor and acceptor species, expected to show rectifying behavior analogous to conventional *p-n* junction. The proposed molecule composed of tetrathiafulvalene, a donor moiety connected by a methylene bridge to tetracyanoquinodimethane, an acceptor moiety, shown in Fig. 9.1. Metzger et al. [3] have successfully demonstrated rectification in Aviram–Ratner diode based on Langmuir Blodgett (LB) films of μ-(*n*-hexadecyl) quinolinium tricyanoquinodimethanide sandwiched between metal electrodes and observed rectification behavior. In this two terminal device, LB films of μ-(*n*-hexadecyl) quinolinium tricyanoquinodimethanide were deposited on aluminum (Al)-coated quartz or Silicon. Al layer evaporated on the LB films was for top contact. Figure 9.2 shows the current–voltage (*I*–*V*) characteristics for two devices. First device which showed a rectification ratio of 40 was based on single monolayer sandwiched between two Al electrodes. Second device was based on four monolayers to enhance the stability, but the rectification was reduced to 10. In the second type of devices, current was increased by three orders of magnitude most probably due to interface states between monolayers. Since the successful demonstration of unimolecular diode, there are several efforts [4, 5] to achieve higher rectification ratio in new molecular system. Wei et al. [8] have shown a rectification ratio of 10^3

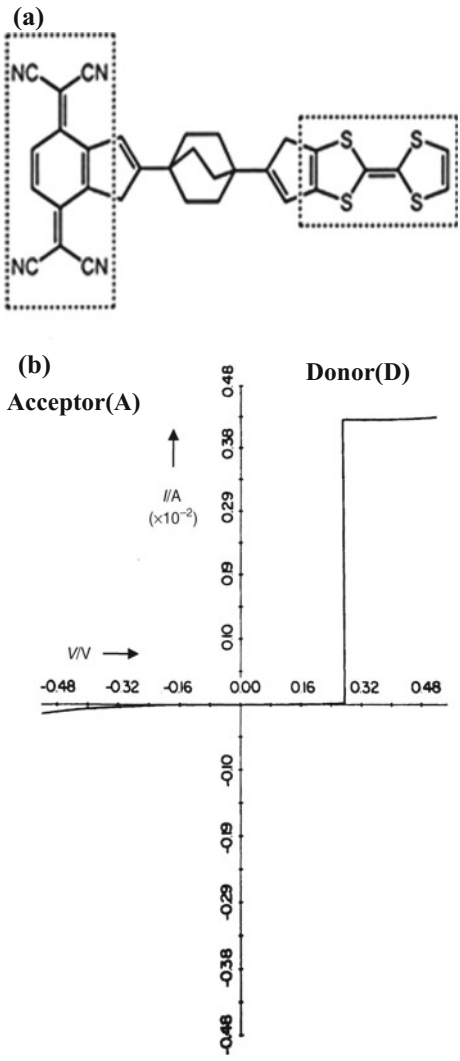

Fig. 9.1 **a** Molecule proposed by Aviram and Ratner composed of donor (D) moiety tetrathiafulvalene connected by a methylene bridge (σ) to an acceptor (A) moiety, tetracyanoquinodimethane, **b** theoretically calculated *I*–*V* characteristics of metal/molecule/metal structure with the proposed molecule. Reprinted with permission from Ref. [2] Copyright (1974) Elsevier

in devices based on carbon nanotube asymmetrically functionalized with donor and acceptor moieties. Undoubtedly, these results help in progress of molecular electronics, but exact mechanism which is extremely important for further progress responsible for the rectification is still under intense debate.

As shown in Fig. 9.1, the molecule with an electron-rich moiety, i.e., tetrathiofulvalene (TTF) as donor (D) an electron-poor moiety, i.e., tetracyanoquinodimethane (TCNQ) as acceptor (A) linked by a covalent triple-methylene bridge as insulator (σ), generalized as D–σ–A molecule is sandwiched between two metallic

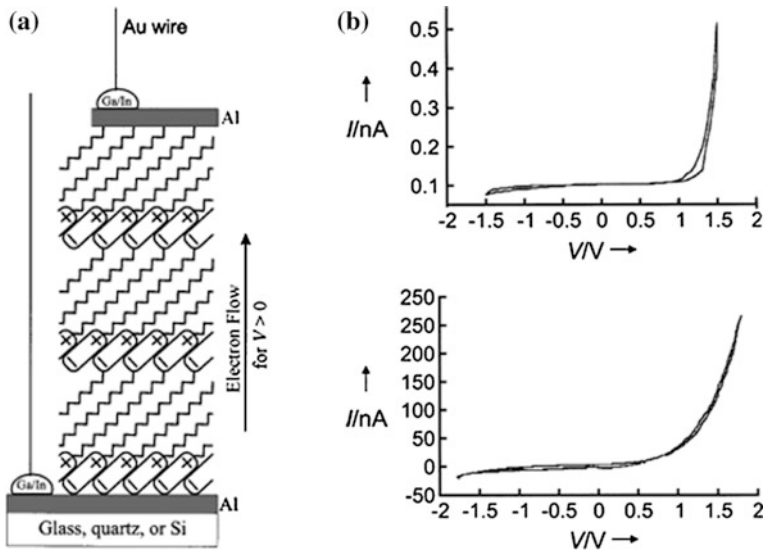

Fig. 9.2 **a** Schematic representation of the LB films structure of molecule μ-(*n*-hexadecyl) quinolinium tricyanoquinodimethanide on aluminum-coated Si or quartz. Either one or four monolayer of the molecule has been deposited. **b** *I–V* characteristics of two different devices. Al/1 LB monolayer/Al Ga/In eutectic and Al/4 LB monolayer/Al Ga/In eutectic. Reprinted with permission from Ref. [3] Copyright (1997) American Chemical Society

electrodes with two interfaces metal-D and metal-A. D and A regions of the molecular rectifiers are equivalent to *n* and *p* regions, respectively, in inorganic metallurgical p–n junction diode. However, D–σ–A molecular rectifier though appears to be a simple device, but is much more complex systems than inorganic *p–n* junctions. High and inhomogeneous electric fields resulted from the molecular dipoles in the monolayer, the screening induced by the molecules and the metallic electrodes, effect of high electric field on the electronic structure of molecules make these devices complex and require self-consistent quantum mechanical treatment for theoretical simulation. ab initio calculations have shown [9] that the direction of current flow in forward bias depends not only on the position of molecular level relative to the Fermi levels of the metal electrodes, but also on the bias-induced shift of the molecular levels resulting reverse rectification in opposite direction and may be responsible poor low rectification ratio generally observed in the these devices. It has been [10, 11] shown that any asymmetric coupling of the molecules with the electrodes or any asymmetry in the molecule could result in asymmetric *I–V* characteristics and rectification. Based on experimental observation, three different mechanisms by Aviram–Ratner (AR) [2], Kornilovitch–Bratkovsky–Williams (KBW) [12] and Datta–Paulsson (DP) [13] have been proposed to explain the rectification behaviors of molecular rectifier. These models are summarized in Fig. 9.3 [14] and described below.

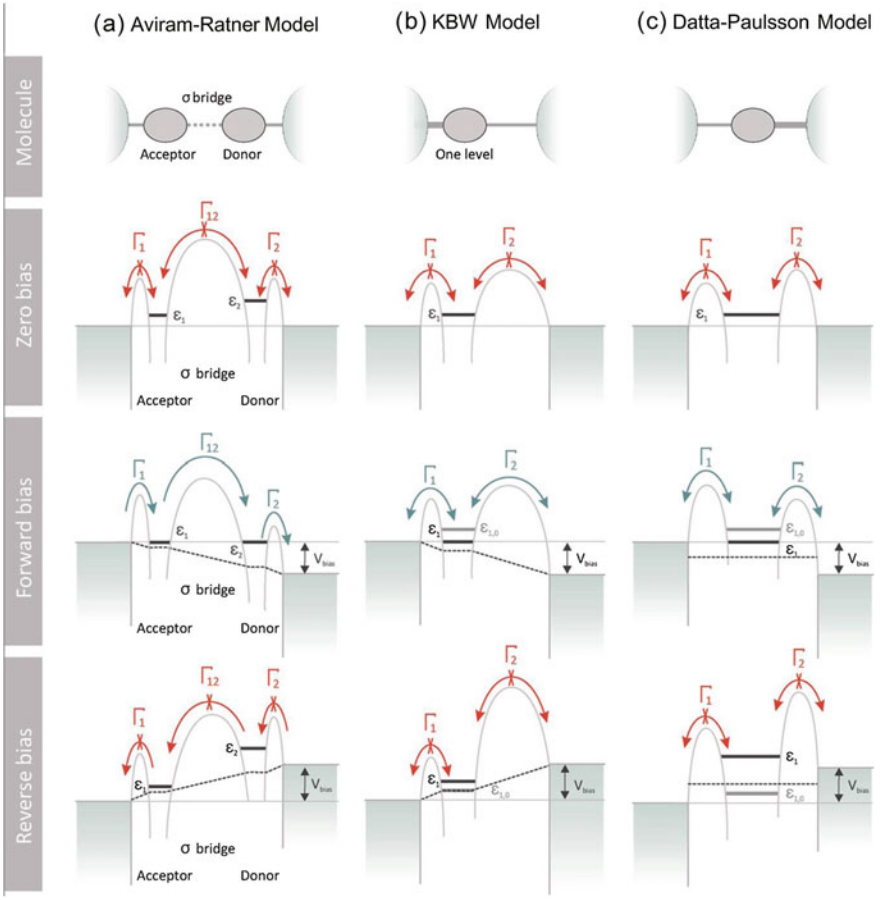

Fig. 9.3 Comparison of three models for molecular diodes (Γ_i represents the rates of tunneling steps). **a** Aviram–Ratner proposal with molecule levels shifting through the applied electric field. The subtle energy-level alignment for the donor and acceptor moieties, in combination with the large electrical spacer separating the two moieties, eventually leads to a difference in the current onset. **b** Simplified model, as proposed by Kornilovitch, Bratkovsky, and Williams (KBW), with one level. The level is shifted with respect to the applied electric field. **c** Considering the charging of the energy levels (proposed by Datta and Paulsson) can lead to diode behavior, even without level shifting by an electric field. Reprinted with permission from Ref. [14] Copyright 2012 American Chemical Society

AR Model [2]: According to this model, at a zero bias, the HOMO of the donor and the LUMO of the acceptor is slightly below and above the electrode's Fermi level, respectively. With application of positive bias, due to the alignment of the metal electrode's Fermi level with the lowest occupied molecular orbital (LUMO) of acceptor, the charge carriers are injected into acceptor from cathode, but charge cannot flow from acceptor to donor until the Fermi level of metal anode is lowered

enough so that charge can transfer from the highest occupied molecular orbital (HOMO) of donor to the metal electrode. In the reverse bias direction, charge transfer from metal electrode to acceptor will happen as the E_F of the metal electrode is lowered below the HOMO of acceptor. This will result electrons to tunnel from donor to acceptor through the barrier. The two separate energy levels ε_1 and ε_2 of the donor and acceptor, respectively, respond oppositely to the electric field resulting in energy-level alignment or misalignment responsible for the asymmetric charge transport. Essentially, according to AR model, rectification could be viewed as a different onset of resonant tunneling under forward and reverse bias directions.

KBW Model [12]: In this model, KBW applied AR mechanism to relatively simpler system with only one molecular orbital. According to this model, an essentially asymmetric tunneling barrier is responsible for rectification. Due to asymmetry in the molecule, the position of the orbital is not located symmetrically between the electrodes and most of the applied bias drops across longer insulating barrier. Hence, the conditions for resonant tunneling through the molecular levels are attained at different voltages under forward and reverse biases. Hence, alignment and misalignment of the molecular level with Fermi level of the electrodes depend on the bias directions leading to the rectification behavior. KBW model provides an important clue for choosing or designing simple molecules with asymmetry at one end or different length tails enacting different tunneling barriers compared to complex molecule required in the AR model, and it is proposed that the rectification ratio can be varied by changing the lengths of the insulating tails.

DP Model [13]: According to this model, it has been shown how the rectification can be achieved through asymmetric coupling of a symmetric molecule with the electrodes at the two ends. In this mechanism, the *I*–*V* characteristics are symmetric under low bias but become asymmetric under higher bias. Furthermore, under resonant conduction, this asymmetry results in conductance peak of different heights. According to this model, conduction through the molecule occurs through the same molecular level at opposite biases, and this is the main difference with AR and KBW models. Essentially, the induced asymmetry is due to the charging effect which is significantly high in single-molecular devices with tunneling barrier to the electrodes and the asymmetry in charging energies leads to the different tunneling rates between the molecular level and the two electrodes. Hence, the average population of the molecular level with two electrons depends on the direction of biases in the resonant tunneling condition, resulting rectification.

Experimentally, it is difficult to distinguish these three mechanisms from each other for several reasons. (1) It is difficult to chemically synthesize complex molecule required for Aviram–Ratner diode, and even it is more difficult to achieve a decoupling between donor and acceptor orbital in D–σ–A molecule. (2) It is difficult to control the coupling between the electrodes and the terminated groups of molecules due to several poorly understood interfacial interactions and random contact geometries. (3) As the molecular rectifier is mostly based on monolayer and not a single molecule, molecular dipole induces high and inhomogeneous electric

fields. (4) Compared to inorganic p-n junction diode, the operating electric field in molecular devices is at least one order of magnitude higher, so effect of high electric field on the electronic structure of molecules becomes extremely important.

9.4 Second Generation of Molecular Devices

The ultimate switching device with ON and OFF states capable of different logic operations would be based on single atom-based transistor, and such a device has been proposed by Wada et al. [15] with a switching speed of 1 THz. With present day technology, it has not been possible to achieve such ambitious device. However, similar device has been conceived using organic molecules. Stoddart and co-workers [16] have been able to demonstrate a molecular shuttle that could be switched electrostatically from one state to another using rotaxane molecule, as shown in Fig. 9.4. The rotaxane has two components, a molecular rod and a docking station based on benzidine and benzophenol, respectively. The rod has two beads based on two bulky triisopropylsilyl groups at the ends. When a proton source like trifluoro acetic acid (TFA) is added, the bead shifts toward biphenol station and can only be brought back by neutralizing the TFA with pyridine. This back and forth movement between two states can serve as controlled switch which has been configured to operate as XOR gate. Other active area of research is to conceive molecular switch based on bistable *I–V* characteristics and *I–V* characteristics with negative differential resistance (NDR). The molecular switch based on bistability and NDR has been envisaged as memory devices. Collier et al. [17] have demonstrated bistable *I–V* characteristics in two terminal molecular devices based on catenane (Fig. 9.4) with amphiphilic phospholipid counter-ions sandwiched between an *n*–Si and Ti/Al electrodes. Repeatable read–write cycles have been demonstrated [16] using this bistable device. Reed and co-workers [18] have demonstrated NDR in a device based on molecule 2-amino-4,4-de(thynylphrnyl)-5-ntro-1-benzenethilate with nitroamine redox center sandwiched between two metal contacts in a nanopore. Strong NDR with a peak-to-valley ratio of 10^3:1 has been observed (Fig. 9.5). No NDR was observed [18, 19] in control molecule (without nitro or amine moieties). Though the exact mechanism is not known yet, but phenomenologically, it has been explained [18, 19] as a two-step reduction. As bias increases, reduction of the molecule provides charge carriers, resulting increase in current which will continue to flow till the bias reaches to second reduction potential, and subsequently, the molecule is reduced to the dianion. Seminario et al. [20] have shown with ab initio calculations that current flows through the molecule only when the molecule is in reduced state because LUMO is only extended along the whole length of the molecule when it is in reduced state. But Ghosh et al. [21] have argued opposite, i.e., conduction happens resonantly with HOMO only when molecule is in oxidized state. The debate on the microscopic mechanism of NDR further fueled by another interesting work by Xue et al. [22] who have shown NDR in *I–V* characteristics of single dibenzothiophenium 5-phenyl molecule by scanning

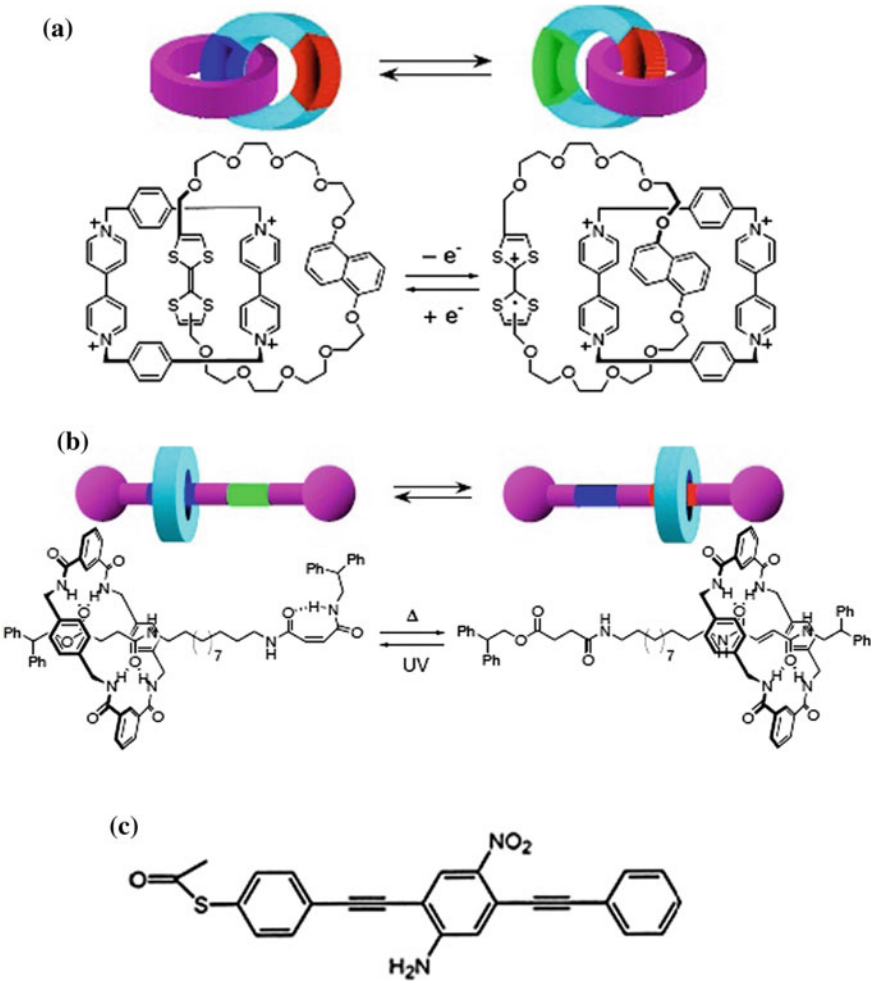

Fig. 9.4 **a** Schematic representation of two conformers of an electro active, bistable molecule catenane. **b** Schematic representation of a rotaxane which is a mechanically interlocked molecular architecture consisting of a dumbbell-shaped molecule threaded through a macrocycle. As the ends of dumbbell are larger than the diameter of the ring, rotaxane is trapped. **c** Molecule containing a nitroamine redox center [2-amino-4,4-de(thynylphrnyl)-5-ntro-1-benzenethilate] used in nanopore for two terminal-based devices [18, 19]

tunneling spectroscopy (STS). Interestingly, this molecule does not have nitroamine redox center, yet shows NDR. It has been argued [23] that reduced density of state at metal/molecule contact is prerequisite for observing NDR (Fig. 9.6). In case STS-based measurements, narrow tip of scanning tunneling microscope (STM) provides reduced density of state at tip/air/molecule contact, and since the other end of the molecule is attached to metallic substrate through a relatively

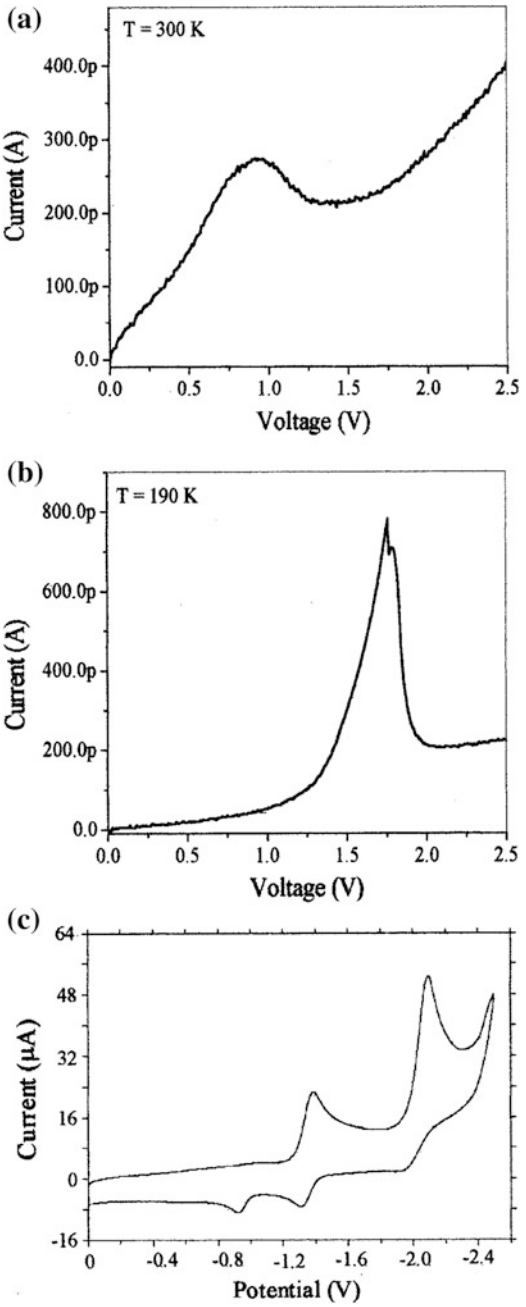

Fig. 9.5 *I–V* characteristics of two terminal devices based on molecule containing a nitroamine redox center at **a** 300 K, **b** 190 K, **c** cyclic voltammagram of the molecule showing two reduction peaks. Reprinted with permission from Ref. [19] Copyright 2000 AIP Publishing LLC

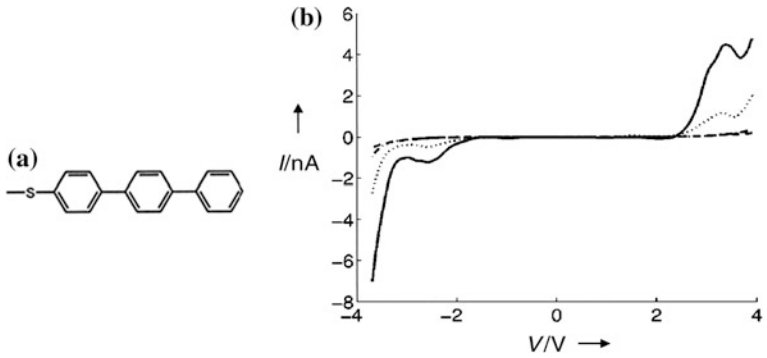

Fig. 9.6 **a** Molecule dibenzothiophenium 5-phenyl, **b** the *I–V* characteristics obtained by STS carried out on a monolayer of molecule. Reprinted with permission from Ref. [22] Copyright 1999, American Physical Society

strong thiol–gold covalent bond, the molecular orbital tends to align with the E_F of the substrate. When bias is applied, the molecular levels shift in one direction, while the tip density of states (DOS) shifts the other direction, and if the molecular levels cross the tip DOS, then one should observe NDR.

9.5 Third Generation of Molecular Devices

In third-generation molecular devices, mostly organic molecules are used as active device components and current transports through the molecules directly connected end-to-end with metal electrodes. Out of several platforms for third-generation molecular devices, single-molecule junctions based on a metal–molecule–metal architecture has received maximum attention. In addition to contemplated basic element for future molecular integrated circuit, the single-molecule junctions have immensely contributed to the fundamental understanding of mesoscopic transport by providing the most suitable platform for experimenting different predictions of quantum transport.

Efficient device fabrication based on single or few molecules requires development of suitable contact structure or pattern for characterization of molecular devices. It is difficult to study transport properties of single molecule by probing them between two symmetrical metal contacts due to lack of electrodes with separation in molecular dimension. There are two general approaches involving preformed contacts with nanometer separation between two electrodes. The first one is based on vertical device structures (VDS), where a self-assembled monolayer (SAM) of organic molecules is prepared on a metallic surface which is one contact and other contact is the tip of STM [24, 25] or conductive probe atomic force microscopy (AFM) [26], and crosswire techniques [27] belong to this class of structures in which two-crossed metallic wires separated by nanometer separation

hold the molecules vertically. These techniques are most suitable for few molecule-based devices; it is extremely difficult to employ these techniques for single molecule-based devices. The second one is based on lateral device structures (LDS), in which a pair of electrodes with nanometer separation is formed, and molecules are locked with their end groups within the gap using self-assembly technique. Such electrodes are fabricated on substrate using mechanically controlled break junction (MCEB) [28, 29], electromigration-induced break junction (EIBJ) [30–34] and electro-deposition [35–37]. In VDSs, the top contact to the molecule is made physically, whereas, only the bottom contact is chemically coupled to the molecule. It is difficult to avoid inbuilt asymmetry in VDSs due to different contact structures at the both end of the molecule. This poses great difficulty in distinguishing the cause of asymmetry in *I–V* characteristics as due to contact limited or due to asymmetry in the molecule. The devices based on LDSs can be fabricated in two different ways. In first approach, molecules are self-assembled on the metal surface before breaking and induced to migrate into the gap at low temperature. In this case, after breaking the break junctions, the residual interlink of metallic adhesion layer and the cantilever effect [38] of the suspended Au microelectrode cannot be ruled out. In the second approach [39–41], first a pair of electrode with nanometer-sized separation (nanogap) between them is created by an EIBJ technique performed at room temperature. There are several advantages of this method. The main advantage is that this method allows the break junction to be first characterized at room temperature, prior to deposition of molecules. A pair of electrodes with 1-2 nm separation can be realized with relatively high yield, as can be inferred from combined imaging and electrical characterization. This method allows the deposition of the desired molecule at the nanogap created at room temperature after initial characterization of the nanogap.

The first two methods, VDS based on scanning probe microscope (SPM) and LDS based on MCJB lack mechanical stability, as well as electrical stability required for transport measurements under different ambient conditions. It is even doubted [42] whether individual molecules are actually attached to the gap in break junctions fabricated by the methods proposed in Refs. 28, 29 and 43. In principle, our method of fabrication of two electrodes with nanometer separation is more or less similar to third method, [44, 45] except two main differences: (i) nanoelectrodes need not be fabricated at low temperature and (ii) nanoelectrodes can be fabricated without self-assembled molecules. Simplicity and reproducibility of our method stand it out of all the methods proposed or demonstrated for fabrication of nanoelectrodes. Moreover, though our method does not require sophisticated lithography, however is compatible with conventional processes for device fabrication. The fabrication of nanoelectrodes has been achieved by passing a large electrical current through a thin Au-finger with a notch at the middle, fabricated on SiO_2/Si substrates by photolithography. When high current passes through the Au-finger, electromigration driven breaking results two stable electrodes with nanometer separations, enabling transport measurements through nanometer size molecules. In order to form m–M–m junctions, organic molecules, such as 1,4 benzedithiol (BDT), 1,4 benzenedimethanedithiol (BDMT), and thiolated ds-DNA

have been strongly bonded by self-assembly technique between two electrodes which are connected to suitable contact pads to facilitate further probing with different electrical characterization techniques or integration into with array of such devices.

In our method [39–41], 3000–5000$_2$ Å thermal oxide-coated silicon (Si) substrates were first silanized with a monolayer of 3-Mercaptopropyl trimethoxysilane (MPTMS). In silanization, the SiO_2 substrate was processed in four steps, (i) piranha clean, (ii) oxygen plasma, (iii) hydroxylation, and finally (iv) four hours of exposure to the MPTMS gaseous molecules inside a vacuum desiccators. The silanized SiO_2 samples were transferred immediately into the evaporation chamber for deposition of a 200–300 Å Au layer. The silane functional group of the MPTMS forms Si–O–Si covalent bonds with the SiO_2 surface silanols, leaving the –thiol group (–SH) of the molecule on the top leading to Au–S bond strong enough to hold the Au thin film tightly. A field emission scanning electron microscope (FESEM) image of the lithographically defined Au wire is shown in Fig. 9.7. For electrical characterization, each end of the Au micro wire is connected to a thick ($\sim$5000 Å) Au pad layer. The pressure was maintained at 2–3 $\times$ 10^{-7} torr, during all depositions, and the deposition rate was maintained at 1 Å/s, monitored in situ using a quartz crystal thickness monitor. To localize the positions

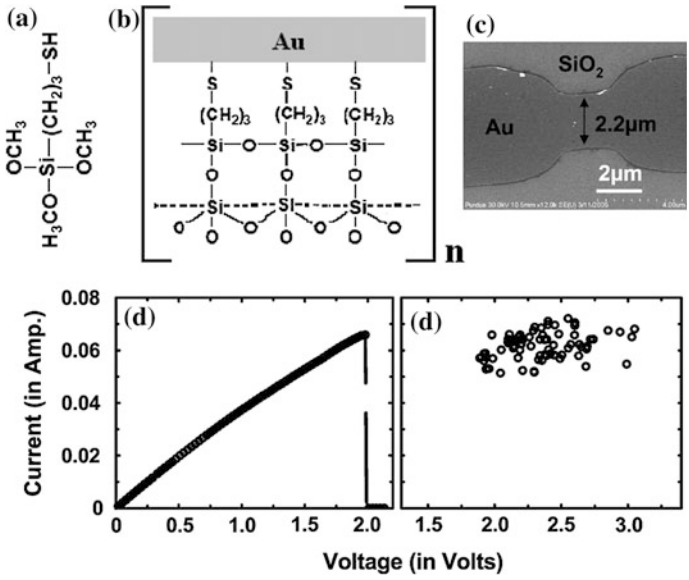

Fig. 9.7 **a** 3-Mercaptopropyl trimethoxysilane (MPTMS) molecule. **b** Schematic diagram of MPTMS monolayer adhesion that forms Si–O–Si covalent bonds with SiO_2 surface and Au–S bond with evaporated Au thin layers. **c** FESEM image of lithographically defined Au wire before electromigration. **d** *I–V* characteristics in Au wire during electromigration. **e** Threshold current and voltage at break point for some EIBJ devices. Reprinted with permission from Ref. [41] Copyright 2006, IEEE

of the nanogaps, lithographically Au-finger is notched at the middle (shown in Fig. 9.7). As voltage increases linearly across the Au-finger, at a threshold voltage V_{th}, current decreases abruptly by several orders of magnitude due to the formation of a gap which was subsequently imaged by FESEM. Initially, current through the wire increases linearly and after V_{th} Ohmic current changes to tunneling current through the nanogap created between two Au electrodes. The resistances of the Au wires, which were 30–50 μΩ before electromigration, change to MΩ–GΩ after the break. The break occurs when the driving voltage typically exceeds 1.5 V resulting in a nanogap due to the physical motion of Au atoms out of the high-current density areas, a phenomenon known as electromigration. The electromigration is the result of (i) the force due to the effect of electric field on the migrating ions and (ii) the wind force due to the scattering of the conduction electrons by the Au atoms. It has been observed that wires with longer notch width ($\sim$4 μm) give a wider gap between the electrodes compared to that of shorter ones ($\sim$2 μm). This can be explained by the threshold current density required for Joule heating for shorter width and longer width wires reaches at lower and higher bias, respectively. Higher bias makes the Au atoms move further apart with high field resulting in wider gap between the electrodes. Hence, electromigration is a combined effect of the maximum local Joule heating at the notch and the momentum transfer between the conduction electrons and diffusing metal ions.

Following electromigration, the nanogaps are characterized by FESEM. Figure 9.8 shows the FESEM image for two pairs of Au electrodes with sub-nm separation. The final gaps (the regions with shortest separation) were of length 1 nm over 5 nm width. Five chips, each having twenty five break junctions were examined under FESEM. The nanogaps with molecular dimension were mostly of 5–10 nm areas of the junctions separated by 1–5 nm and rest of the junctions showing gaps with 5–15 nm separation. The device yield is more than 20%, which is an improvement to the previously reported 10–15% device yield [46–48] using break junctions formed by electromigration. From FESEM imaging, it is difficult to estimate the exact gap length below 2 nm, but the separation of the subnanometer gap can be inferred from the conductivity measurement of nanogaps after the break. Figure 9.9 represents the histogram of the spectrum of conductance observed in nanogaps formed by EIBJ. The smallest separation has been observed to be located at one place along the whole width of the Au wire, and obviously, the observed conductivity can be attributed to the smallest gap region and cannot be affected by the other portions of the gap. We have observed at low bias the current through the smallest nanogaps is in the nanoampere to picoampere range, and the current through the gap more than 2 nm (as viewed through FESEM) is below the measurable limit of the picometer. As expected, current through the empty gap currents is in excellent agreement with the Fowler–Nordheim tunneling relation [49], as shown in Fig. 9.8. *I–V* characteristics of empty gap are reproducible in repeated scans ensuring the stability of the electrodes with nanogap with time and under high electric fields. It is extremely important that after the formation of gap, electrodes edges are not affected further due to application of high electric field. The length of

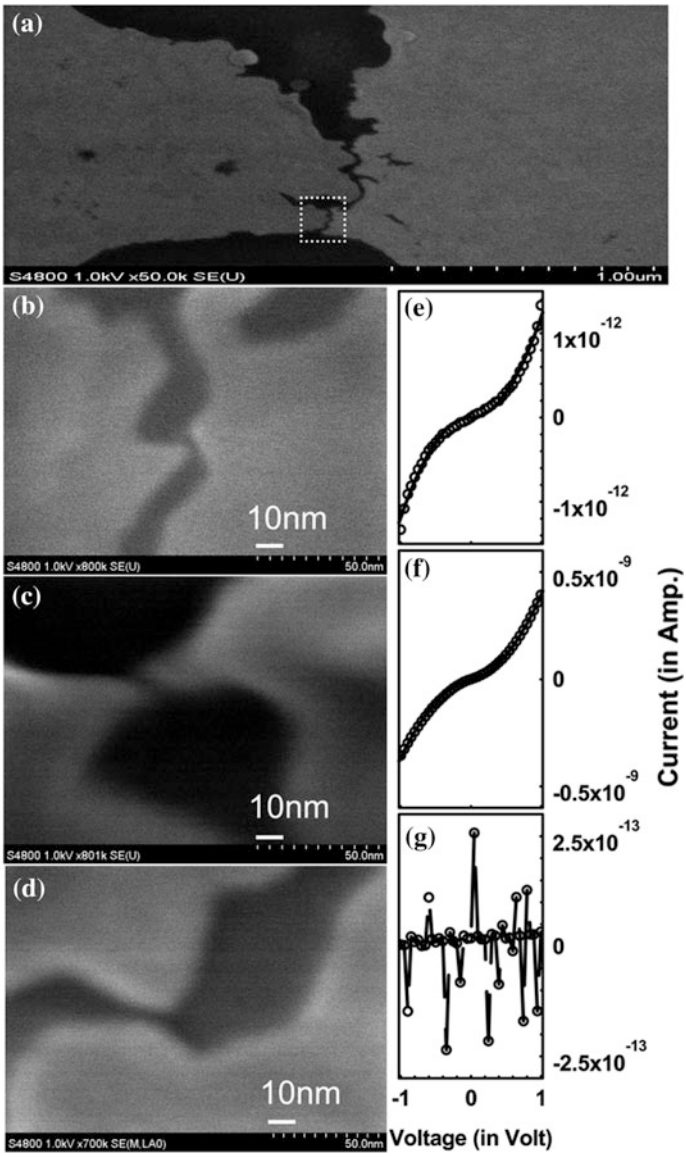

Fig. 9.8 FESEM images of EIBJ devices that show 1 nm gap created between two Au electrodes, **a** although Au wires are initially 2 μm wide, gap of length 1 nm and width 5 nm is observed **b** after break junction. Image (b) is zooming picture of selected portion in image (**a**). **e**–**g** Corresponds to empty gap *I*–*V* characteristics of EIBJ devices, respectively. *Solid lines* are Fowler—Nordheim fit to experimental data (*open circles*). Conductivity is measured (**e**), (**f**) for Au/empty gap/Au devices with gaps 2 nm, as confirmed through FESEM image (**b**) and (**c**). For devices with larger gap lengths (5 nm), conductivity falls below noise level of instrument (**g**). Reprinted with permission from Ref. [41] Copyright 2006, IEEE

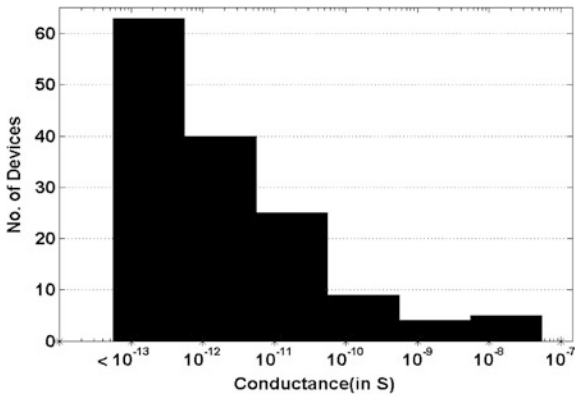

Fig. 9.9 Histogram of conductances obtained from 150 nanogap in electromigration-induced break junction (Au/empty gap/Au devices. Reprinted with permission from Ref. [41] Copyright 2006, IEEE

the gap is related to the tunneling conductance by the expression [50], $G_{tun} = \alpha \exp(-kd)$, where G_{tun} is the tunneling conductance, d is the gap length, and α and k are constants determined by the local structure. The tunneling conductance versus separation distance is reported [41] for Au–vacuum–Au structure comparable to these devices. This relationship can be described by values of $\alpha = 6.67 \times 10^{-8}$, and $k = 1.25 \times 10^{10}$ m^{-1}. From the tunneling conductance of the empty gaps, the separation of the nanogaps has been estimated [51]. As there is one order decrease in tunneling current in every 2 Å, the observed conductivity mostly is dominated by the separation localized at one point over the whole width.

9.5.1 Current Transport Through Single 1,4-Benzenedithiol (BDT) and 1,4-Benzenedimethanedithiol (BDMT) Molecules

Following the creation and subsequent characterization of the break junctions, 1 mM solutions of BDT or BDMT in dichloromethane or ethanol were used to deposit the desired molecules between the two electrodes separated with nanogap. This has been done either by immersing the whole chip in the solution or by putting a droplet on the chip. Whenever separation of the nanogap matches the length of BDT or BDMT molecules with thiol end groups, molecules dock between two electrodes and a stable chemical bond between the sulfur atom and Au surface is established. In order to verify the docking of molecular layers to Au surfaces, SAM using the same solution was grown on clean Au surfaces using the same immersion procedures and were subsequently characterized by reflection absorption infrared (RAIR) spectroscopy. RAIR spectra of BDT and BDMT are shown in the insets of Figs. 9.10 and 9.11 [39]. In case of BDT SAM, the peak at around 1500 cm^{-1} is due to stretch mode of C=C–C in benzene ring in BDT. The peaks at around 1000 cm^{-1} and 800 cm^{-1} are due to C–H in-plane and out-of-plane bends in

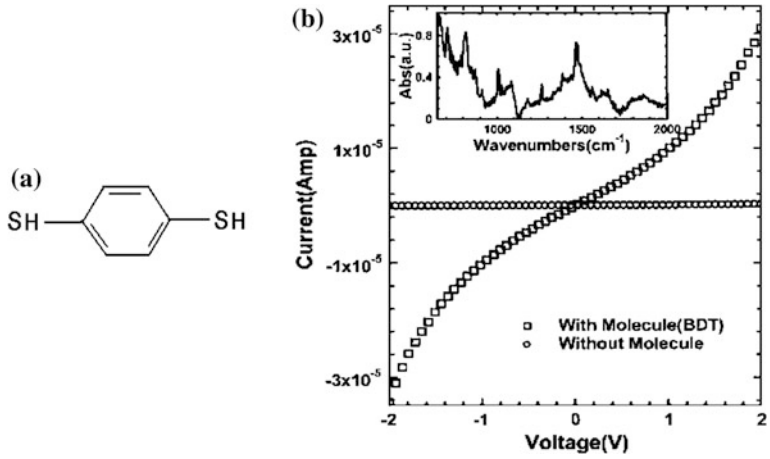

Fig. 9.10 **a** Benzene dithiol (BDT) molecule, **b** *I–V* characteristics of 1,4-benzene dithiol (BDT) at room temperature (*empty squares*), along with that of the nanogap before deposition of molecules (*empty circles*). Current through the break junction increases by more than two orders of magnitude after docking the BDT molecule. *Inset* shows the RAIR of BDT on Au. Reprinted with permission from Ref. [39] Copyright 2005 AIP Publishing LLC

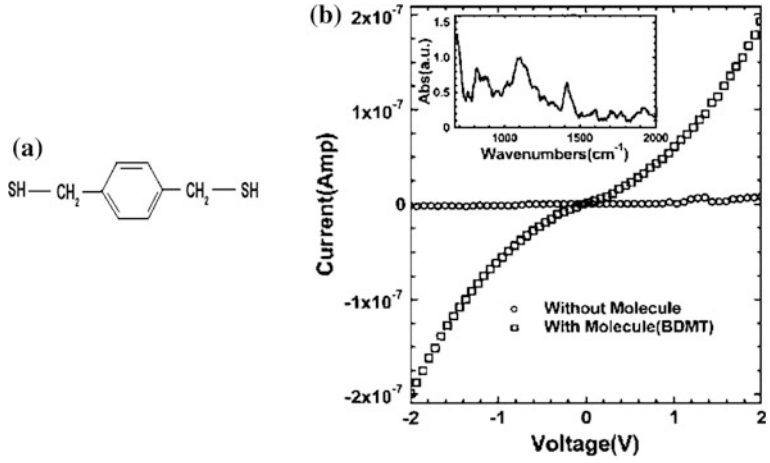

Fig. 9.11 **a** 1,4-benzenedimethanedithiol (BDMT) **b** *I–V* characteristics of BDMT at room temperature (*open squares*), along with that of the nanogap before deposition of molecules (*open circles*). Current through the break junction increases by more than two orders of magnitude after docking the BDMT molecule. *Inset* shows the RAIR of BDMT on Au. Reprinted with permission from Ref. [39] Copyright 2005 AIP Publishing LLC

BDT, respectively. The peaks in RAIR spectra of the BDMT SAM have similar origin as those in BDT.

Figures 9.10 and 9.11 show the *I–V* characteristics [39] for BDT and BDMT, respectively. The figures also show the *I–V* characteristics of the respective electrodes with nanogap before deposition of the molecules. *I–V* measurements were performed on more than 100 break junctions for each molecule. It has been observed that conductance increases with increasing deposition time of the molecules, and conductance of the nanogap electrodes increases for those structures for which the gap widths (inferred from pre-molecule conductance) were comparable to the molecular length, but there was no change in conductance with significantly larger gaps. Further, it should be pointed out here that the conductance did not systematically increase upon exposure to the only organic solvent, indicating that the observed conductance was not due to leakage paths along the oxide surface or solvent-induced reconfiguration of the contact structures. As expected, devices which show significant increase in conductivity following deposition of molecules generally exhibit similar *I–V* characteristics. Figure 9.12 shows that the *I–V* curves of six devices, each divided by an integer. When these curves are scaled by integers, they all collapse on one curve indicating that the curves observed for $N = 1$ must be due to single BDMT molecule. Similar characteristics have been observed by other groups [52–54] using SPM-based break junctions. Furthermore, *I–V* characteristics are shown in Fig. 9.10 correspond to a case in which a number of molecules can be considered to be conducted in parallel, while *I–V* characteristics shown in Fig. 9.11 correspond to the lowest observed conductance in this series, and most likely correspond to a single molecule.

Figures 9.10, 9.11 and 9.12 reveal several notable features of the *I–V* characteristics of the devices with BDT and BDMT molecules. (i) The *I–V* characteristics are linear at low bias ($\sim$0.3 V), and resistance near zero bias has been found to be 9 and 26 MΩ for single BDT and BDMT molecules, respectively. (ii) As expected due to the presence of the –CH2– groups at the two ends, the resistance of the single BDMT is higher than that of single BDT molecule. (iii) The low-field conductance is significantly higher than those observed in measurements using other contact structures, in particular using VDSs. (iv) The *I–V* characteristics

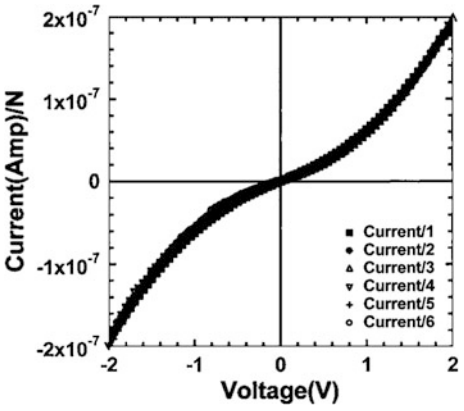

Fig. 9.12 Six representative *I–V* curves of BDMT from different groups, which are integer multiple of a fundamental curve. Curves are divided by 1, 2, 3, 4, 5, and 6. Reprinted with permission from Ref. [39] Copyright 2005 AIP Publishing LLC

over the whole range of bias are symmetric and nonlinear. (v) There is no conductance gap and this is consistent with the behavior expected from a molecule in which the density of states is broadened significantly due to strong coupling to the metallic electrodes at both ends of the molecule [55–58]. (vi) The superposition of all *I–V* traces on a curve for $N = 1$ (Fig. 9.14) provides evidence of stable Au–S contacts at both ends of the molecule and negligible in plane molecule–molecule interactions. In MCBJ, for current transport through a single molecule, contacts to the molecule are often made and broken by mechanically pulling apart the junction and then bringing the contacts back together between series of measurements. It has been suggested [51] that the current transport observed in early MCBJ structures may be through the overlapping pair of molecules bonded between two opposite facing electrodes, rather than through a single molecule attached to electrodes at both ends of the molecule. In the case of ECBJ-based devices, beyond a reasonable doubt, the Au–S bonds are stable at both ends of the molecule and the origin of symmetric and reproducible *I–V* characteristics may be different from those obtained using MCBJ.

9.5.2 Current Transport Through Single DNA

To investigate current transport through single DNA, three different 18-mer ds-DNA molecules were used for fabricating devices based on ECBJ. The molecules had thiol group attached to the 5′ end through a $(CH_2)_6$ linker, for covalent attachment to the Au electrodes. The DNA sequences were chosen carefully so that they differ by their GC content and the corresponding melting temperatures. Three sequences are Seq-1: self-complementary SH-CGT ACA TGA TCA TGT ACG with GC content of 44.4%, Seq-2: SH-CAG TCA GGC AGT CAG TCA with GC content of 55.6% and Seq-3: self-complementary SH-CGT GCA CGT ACG TGC ACG with GC content of 66.7%. DNA disulfide groups were reduced and then purified, as described in Ref. [40]. The same sequences were also used without the thiol groups to serve as control. The purified DNA was subjected to annealing at 90 °C for 10 min in appropriate buffer. Subsequently, DNA was attached to Au by immersing the chips with array of ECBJ in 10 μM solution of thiolated ds-DNA.

I–V characteristics of the devices with DNA were obtained between −1V and +1 V. Approximately, 15% of the devices showed an increase in current, attributed to the presence of covalently linked ds-DNA molecule in the nanogaps, whereas none of the control samples (DNA without thiol at ends) showed an increase in current. Figure 9.13 shows the *I–V* characteristics of two devices with sequences 1 and 3 which show about a three order increase in current when compared to the current in the control device. The devices were then subjected to a temperature ramp up to 400 K with a 30 s hold at 5 K increments, and then ramped back to room temperature. All the devices that were not exposed to any voltage stress during the temperature ramp, exhibited a reduction in current, when measured after the ramp, as shown in Fig. 9.13. It can be argued that the loss of conduction, which

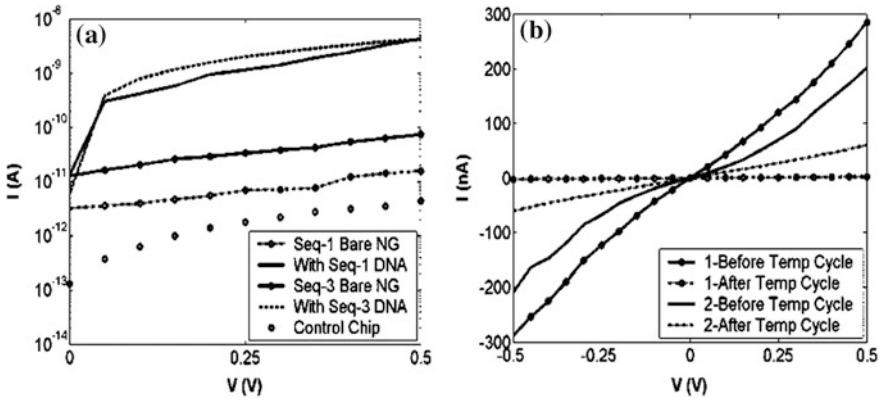

Fig. 9.13 **a** Comparision of current–voltage characterstics of conduction through bare nanogap, with DNA docked in sequence 1&3, and for the control chip after incubation in nonthiolated sequence 1, where no conduction was observed. **b** *I–V* plots for sequence 1 show decrease in conduction after temp cycling. Conduction was restored after reincubation and temp cycling. Reprinted with permission from Ref. [40] Copyright 2005 AIP Publishing LLC

was observed consistently with all different sequences, is due to the denaturing of DNA in the dry state. The melting of the DNA strands is facilitated due to the absence of significant number of counter-ions and water molecules and should occur within the 100 K temperature ramp subjected to the devices. The devices behave like electrical fuses which can be "blown" by a temperature ramp. There are two notable features observed in this set of experiments. (i) Firstly, at each temperature increment and stabilization during the ramp, *I–V* characteristics were measured and 50% of these devices did not show a decrease in current, as compared to about 20 devices which showed a decrease in current, after the temperature ramp. It can be argued that a voltage stress during the temperature ramp could reduce the denaturing of the molecule due to charging effects in the ds-DNA. (ii) Secondly, after the temperature ramp, the conduction in the devices with DNA was regained in about 10% devices when re-exposed to a buffer. It can be argued that it will be difficult to re-hybridize DNA strands in the absence of counter-ions and water molecules.

As there are three hydrogen bonds between G and C, conduction through G–C bridge would be higher compared to conduction through A and T which are bridged with two hydrogen bonds [59, 60], but this has not been demonstrated using electrical measurements in dry conditions. The DNA sequences were designed in such a way that in the linear dimension, no G and C bases were more than two bases away from each other. It has been found that resistance near zero bias for single DNA with three different sequences increases with decreasing GC content, as shown in Fig. 9.14. This can be explained by higher hopping efficiency of charge

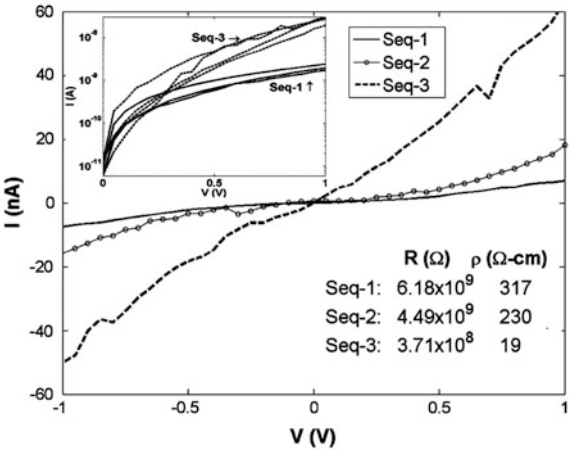

Fig. 9.14 Current–voltage plots of the three DNA sequences. Close to 0 voltage, the resistance decreases with increasing GC content. The resistivity values assume a single molecule, 6.7 nm long and 2 nm in diameter. *Inset* shows a number of *I–V* plots for sequences 1 and 3, all measured on different devices. Reprinted with permission from Ref. [40] Copyright 2005 AIP Publishing LLC

carriers between G and C. As the ionization potential of G is the lowest (G < A < C < T), it is considered the easiest path for conduction of charge carriers [60] resulting less resistance to the charge flow in the sequence containing higher G–C pairs. This is responsible for the decrease in resistance between Seq-1 and Seq-3 by an order of magnitude. The resistance and resistivity obtained from the linear region of the *I–V* curves closer to zero bias are given in Fig. 9.14. Previously reported resistivity values are (i) 0.025 Ω cm in DNA with diameter assumed to be 10 nm and length 1.7–2.9 μm, (ii) 1 Ω cm for poly(dG)-poly(dC) with average resistance value for 50 nm of self-assembled DNA networks [61], (iii) 0.41 Ω cm for h-DNA with diameter assumed to be 2 nm, and the conductivity was evaluated from the measured loss of sensitive resonant cavities operating at 100 GHz [58] and, (iv) 1 mΩ cm with assumed diameter of 2 nm and length of 600 nm [62]. Otsuka et al. have found resistance values from 109 to 106 Ω with increasing relative humidity from 30 to 100% in 1 kb to over 35 kb long molecules, indicating the dependence of resistance on water molecules in the ambient [63]. The values are shown in Fig. 9.14, assuming one ds-DNA chain of 2 nm diameter and 6.72 nm length and could be lower limit on the resistivity, as there can be more than one DNA molecules bridging the gap.

In summary, it has been shown that ECJB-based method to form electrodes with nanometer scale spacing to dock single or few molecules between the electrodes is the most efficient and reliable method to fabricate the most fundamental device for molecular electronics. The measured *I–V* characteristics of two short organic molecules and relatively long molecule such as DNA show repeatable characteristics. The absence of conductance gap and the relatively large conductance values at low bias indicate the strong coupling between molecules and electrodes. This method can be used effectively to investigate electrical transport through a large number of important organic molecules. Moreover, it has been shown that the denaturing of DNA can be studied electrically and ds-DNA molecule can be used as a fuse that can “blow” at higher temperature reversibly. In addition, it has been

shown how the resistance of DNA depends on sequence. These findings have potential to be a first toward DNA-based molecular electronics and direct label-free detection of DNA hybridization.

9.6 Theoretical Aspect for Conduction Through Single Molecule

The conductance of single molecules is a complex issue because it not only depends on electronic structure of molecule, but also depends on the coupling of individual molecule with macroscopic contacting pads. If the conduction through single or bunch of molecules is treated as mesoscopic conductor, then conductance is proportional to the transmission probability of electron from left electrode (L) to right electrode (R), between which the molecule is attached and can be expressed as

$$G = \frac{2e^2}{h}\, T$$

where e is the electron charge, h is the Planck's constant, and T is the total transmission probability over all transmission channels between L and R. If $T = 1$, i.e., when there is no molecule between L and R, G is $2e^2/h$ which is 77481 nS, equivalent to 12.9 KΩ. Hence, resistance of single molecule cannot be less than 12.8 KΩ. T which strongly depends on the coupling strength between molecule and electrode and can be given by

$$T = T_{\mathrm{R}} T_{\mathrm{L}} T_{\mathrm{mol}}$$

where $T_{\mathrm{R}}, T_{\mathrm{L}},$ and T_{mol} are the transmission coefficient of the left interface, right interface, and molecule, respectively, and G can be given by

$$G = \frac{2e^2}{h}\, T_{\mathrm{R}} T_{\mathrm{L}} T_{\mathrm{mol}}$$

The total current I from the left electrode L to the right electrode R, due to the presence of either one or many molecules in the gap, is given by

$$I = \frac{2e}{h} \int_{-\infty}^{\infty} [f_{\mathrm{L}}(E) - f_{\mathrm{R}}(E)] \mathrm{Tr}\left\{ G^a(E) \Gamma^{\mathrm{R}}(E) G^r(E) \Gamma^{\mathrm{L}}(E) \right\} \mathrm{d}E$$

where $Tr\{\}$ is the trace operator, $G_a(E)$ and $G_r(E)$ are the advanced and retarded Green's function for the molecule, respectively, and $\Gamma^{\mathrm{R}}(E)$ and $\Gamma^{\mathrm{L}}(E)$ are the matrices representing the coupling between molecule and right and left electrodes, respectively. This formalism also depends on the alignment of the molecular energy

levels, i.e., HOMO and LUMO, relative to the Fermi levels of the metal electrode. The coupling strength between the electrons in the molecules and those in the electrodes is the most important aspect of nonequilibrium Green function formalism for molecular transport [7]. There are three coupling regimes based on the relative strength of coupling (Γ) and the single-electron charging energy U which is the energy required to add or remove an electron to the molecule or from the molecule, respectively. These regimes are classified as (i) weak coupling ($\Gamma \ll U$), (ii) strong coupling ($\Gamma \gg U$), and (iii) intermediate coupling ($(\Gamma \sim U) \sim U$). Essentially, these three different coupling regimes indicate different degrees of overlap of the wave functions of the molecules and that of metal electrodes, resulting in different transport mechanisms, schematically shown in Fig. 9.15 [64]. In the weak coupling regime, an whole electron transfers from molecule to electrode or vice versa, so that the electron transport happens through a two-step process in which the electrons first hop from one electrode to the molecule, which has matching energy levels, and then hop to other electrode (Fig. 9.15a). In the absence of matching energy level, charge transport will be blocked unless an appropriate bias voltage high enough is applied so that it can overcome e–e repulsion, i.e., U to bring the Fermi energy of the electrode to the molecular energy levels. This phenomenon is also known as the Coulomb blockade. In the intermediate coupling regime, due to moderate interaction with electrode, molecular energy levels broaden and the injected electron from the electrode will be affected by the electrons on the molecule (Fig. 9.15b). In a

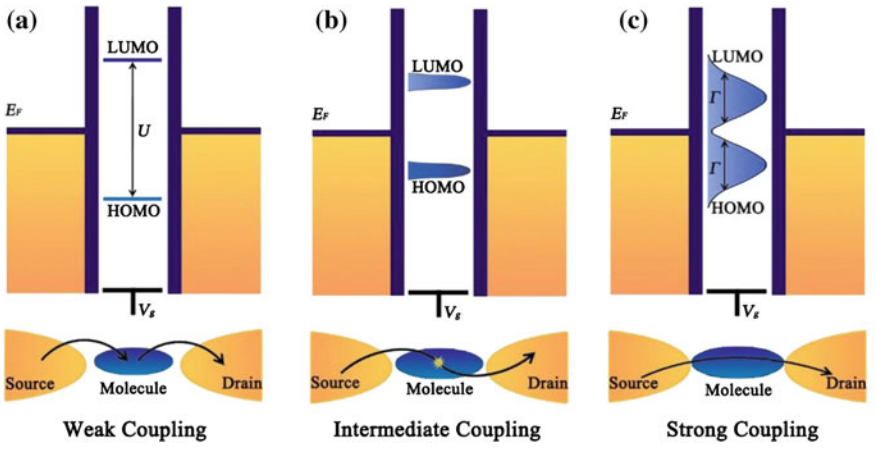

Fig. 9.15 Schematic representation of the energy levels and the charge transport processes of the molecular junctions with different coupling strengths between the molecules and the electrodes. **a** In the weak coupling regime ($\Gamma \ll U$), the HOMO and the LUMO of the molecules are well defined, and the electron transport occurs in a two-step process. **b** In the intermediate coupling regime ($\Gamma \sim U$), the HOMO and the LUMO become broader and closer to the Fermi energy of electrodes (E_F), and the electron transport occurs through the molecules interacting with the electrons on the molecules. **c** In the strong coupling regime($\Gamma \gg U$), a large broadening of the molecular energy levels occurs, and electrons move from the source to the drain through a one-step process. Reprinted with permission from Ref. [64] Copyright 2013 Royal Society of Chemistry

situation, when there is an unpaired electron on the molecule, it's spin state can be reversed by electrons injected from the electrode leading to a spin screening that could result in different transport phemena. A zero-bias Kondo resonance is the result of such spin screening. Other possibility is a simultaneously tunneling process, in which one electron tunnels into the LUMO of the molecule with another electron simultaneously tunneling out of the HOMO, leaving the molecule in the excited state. In the strong coupling regime, the energy levels of the molecules are considerably broadened due to substantial overlapping of the molecule–electrode electronic states enabling partial, i.e., fractional charger transfer between the molecules and the electrodes (Fig. 9.15c). Therefore, the electron could virtually transport from one electrode to another through a one-step coherent process without stopping on the molecules. The absence of Coulomb blockade and observation of symmetric *I–V* characteristics further support strongly coupled regime. In this case, the conductance gap $E_{gap} \sim |E_F - \varepsilon_0|$ will be reduced by the contact and thermal broadening as shown in Fig. 9.15 given by Damle et al. [56] $E_{gap} \sim [(E_F - \varepsilon_0) - (2\Gamma - 4k_BT)]$, where ε_0 is the molecular level. The strong broadening of molecular levels due to covalent bonding at both contacts and a large charging energy can account for the observed reduction of the conductance gap.

9.7 Outlook and Open Questions

To take molecular electronics further so that several single molecule-based devices demonstrated as *proof-of-concept* can be practical devices, the combination of the recently developed techniques and traditional micro-fabrication techniques perfected over the decades for Si-industry is the need of the hour. For example, gating of two terminal break junction-based single molecular device is required to achieve functionalities for ultimate molecular circuit. Further, application of novel materials, for example, fabrication of single-molecule devices using graphene electrodes separated with a variable gap will take molecular electronics to next level. However, there remains several open questions in the different aspects of molecular electronics. Though there seems to exist a consensus on transport mechanism through single molecule, but several major issues such as, (i) the relationship between the molecular structure and intra molecule quantum interference, (ii) intermolecular interactions and their effect on charge transport, (iii) exact role of electrodes on the conductance quantization of single molecule, (iv) charge transport in single molecule to multimolecule junctions, (v) transport in intermediate regime where charging energy is close to level broadening and (vi) the spin-related effect such as Kondo effect and other many body effects remain as open questions and require further experimental and theoretical investigations. Though, ultimate limit for electronic device minimization will depend on the control of device with atomic accuracy, but it is generally accepted that realistically only the molecules can provide such control in subnanometer regime. It should be emphasized that there is no reason to believe that molecular electronics will replace robust Si-based

microelecronics, but it has potential to complement Si-based technology by providing molecule-based nanodevices with novel functionalities which at present is beyond the scope of conventional solid-state devices. The experimental and theoretical research on molecular electronics in last two decades exhibited significant scientific achievement which has brought scientists and engineers from different disciplines together. But, it is worth mentioning that over hype and unrealistic enthusiasm for rapid exploration of molecular electronics may not be compatible with systematic exploration practiced with great success in microelectronics industry.

References

1. G.E. Moore, Electronics **38**, 114–117 (1965)
2. A. Aviram, M.A. Ratner, Chem. Phys. Lett. **29**, 277–283 (1974)
3. R.M. Metzger, B. Chen, U. Höpfner, M.V. Lakshmikantham, D. Vuillaume, T. Kawai, X.L. Wu, H. Tachibana, T.V. Hughes, H. Sakurai, J.W. Baldwin, C. Hosch, M.P. Cava, L. Brehmer, G.J. Ashwell, J. Am. Chem. Soc. **119**, 10455–10466 (1997)
4. Dong Xiang, Xiaolong Wang, Chuancheng Jia, Takhee Lee, Xuefeng Guo, Chem. Rev. **116**, 4318–4440 (2016)
5. R. Lloyd Carroll, C.B. Gorman, Angew. Chem. Int. Ed. **41**, 4378–4400 (2002)
6. D. Xiang, X. Wang, C. Jia, T. Lee, X. Guo, Chem. Rev. **116**, 4318–4440 (2016)
7. R.M. Metzger. Chem. Rev. **115**, 5056–5115 (2015)
8. Z. Wei, M. Kondratenko, Lê H. Dao, D.F. Perepichka, J. Am. Chem. Soc. **128**, 3134–3135 (2006)
9. C. Krzeminski, C. Delerue, G. Allan, D. Vuillaume, R.M. Metzger, Phys. Rev. B **64**, 085405–085410 (2001)
10. S. Datta, W. Tian, S. Hong, R. Reifenberger, J.I. Henderson, C.P. Kubiak, Phys. Rev. Lett. **79**, 2530–2533 (1997)
11. M. Elbing, R. Ochs, M. Koentopp, M. Fischer, C. von Hänisch, F. Weigend, F. Evers, H.B. Weber, M. l Mayor. PNAS **102**, 8815–8820 (2005)
12. P.E. Kornilovitch, A.M. Bratkovsky, R.S. Williams, Phys. Rev. B **66**, 165436–165446 (2002)
13. F. Zahid, A.W. Ghosh, M. Paulsson, E. Polizzi, S. Datta, Phys. Rev. B **70**, 245317–245321 (2004)
14. E. Lörtscher, B. Gotsmann, Y. Lee, L. Yu, C. Rettner, H. Riel, ACS Nano **6**, 4931–4939 (2012)
15. Y. Wada, T. Uda, M. Lutwyche, S. Kondo, S. Heike, J. Appl. Phys. **74**, 7321–7328 (1993)
16. R.A. Bissell, E. Cordova, A.E. Kaifer, J.F. Stoddart, Nature **369**, 133–137 (1994)
17. C.P. Collier, G. Mattersteig, E.W. Wong, Y. Luo, K. Beverly, J. Sampaio, F.M. Raymo, J.F. Stoddart, J.R. Heath, Science **289**, 1172–1175 (2000)
18. J. Chen, M.A. Reed, A.M. Rawlett, J.M. Tour, Science **286**, 1550–1552 (1999)
19. J. Chen, W. Wang, M.A. Reed, A.M. Rawlett, D.W. Price, J.M. Tour, Appl. Phys. Lett. **70**, 1224–1226 (2000)
20. J.M. Seminario, A.G. Zacarias, J.M. Tour, J. Am. Chem. Soc. **122**, 3015–3020 (2000)
21. A.W. Ghosh, F. Zahid, S. Datta, R.R. Birge, Chem. Phys. **281**, 225–230 (2002)
22. Y.Q. Xue, S. Datta, S. Hong, R. Reifenberger, J.I. Henderson, C.P. Kubiak, Phys. Rev. B **59**, R7852–R7855 (1999)
23. Y. Karzazi, J. Cornil, J.L. Bre.das. J. Am. Chem. Soc. **123**, 10076–10084 (2001)
24. S. Datta, W. Tian, S. Hong, R. Reifenberger, J.I. Henderson, C.P. Kubiak, Phys. Rev. Lett. **79**, 2530–2533 (1997)

25. E.G. Emberly, G. Kirczenow, Phys. Rev. Lett. **91**, 188301–188304 (2003)
26. D.J. Wold, C.D. Frisbie, J. Am. Chem. Soc. **123**, 5549–5556 (2001)
27. J.G. Kushmerick, D.B. Holt, J.C. Yang, J. Naciri, M.H. Moore, R. Shashidhar, Phys. Rev. Lett. **89**, 086802–086804 (2002)
28. M.A. Reed, C. Zhou, C.J. Muller, T.P. Burgin, J.M. Tour, Science **278**, 252–254 (1997)
29. C. Kergueris, J.P. Bourgoin, S. Palacin, D. Esteve, C. Urbina, M. Magoga, C. Joachim, Phys. Rev. B **59**, 12505–12513 (1999)
30. W. Linag, M.P. Shores, M. Bockrath, J.R. Long, H. Park, Nature **417**, 725–729 (2002)
31. J. Park, A.N. Pasupathy, J.I. Goldsmith, C. Chang, Y. Yaish, J.R. Petta, M. Rinkoski, J. P. Sethna, H.D. Abruña, P.L. McEuen, D.C. Ralph, Nature **417**, 722–725 (2002)
32. L.H. Yu, D. Natelson, Nano Lett. **4**, 79–83 (2004)
33. K.I. Bolotin, F. Kuemmeth, A.N. Pasupathy, D.C. Ralph, Appl. Phys. Lett. **84**, 3154–3156 (2004)
34. H. Park, A.K.L. Lim, A.P. Alivisatos, J. Park, P.L. McEuen, Appl. Phys. Lett. **75**, 301–303 (1999)
35. F. Morpurgo, C.M. Marcus, D.B. Robinson, Appl. Phys. Lett. **74**, 2084–2086 (1999)
36. Z. Li, H.X. He, N.J. Tao, Appl. Phys. Lett. **77**, 3995–3997 (2000)
37. M.M. Deshmukh, A.L. Prieto, Q. Gu, H. Park, Nano Lett. **3**, 1383–1385 (2003)
38. T.B. Gabrielson, I.E.E.E. Trans, Electron. Devices **40**, 903–909 (1993)
39. S. Ghosh, H. Halimun, A.K. Mahapatro, J. Choi, S. Lodha, D. Janes, Appl. Phys. Lett. **87**, 233509-3 (2005)
40. S.M. Iqbal, G. Balasundaram, S. Ghosh, D.E. Bergstrom, R. Bashir, Appl. Physics Lett. **86**, 153901–153903 (2005)
41. A.K. Mahapatro, S. Ghosh, D.B. Janes, I.E.E.E. Tran, NANO **5**, 232–237 (2006)
42. E.G. Emberley, G. Kirczenow, Phys. Rev. B **64**, 235412–235419 (2001)
43. J. Reichert, R. Ochs, D. Beckmann, H.B. Weber, M. Mayor, H.V. Löhneysen, Phys. Rev. Lett. **88**, 176804–176807 (2002)
44. H. Park, A.K.L. Lim, A.P. Alivisatos, J. Park, P.L. McEuen, Appl. Phys. Lett. **75**, 301–304 (1999)
45. J. Park et al., Nature (London) **417**, 722–725 (2002)
46. W. Linag, M.P. Shores, M. Bockrath, J.R. Long, H. Park, Nature **417**, 725–729 (2002)
47. J. Park et al., Nature **417**, 722–725 (2002)
48. H. Park, A.K.L. Lim, A.P. Alivisatos, J. Park, P.L. McEuen, Appl. Phys. Lett. **75**, 301–303 (1999)
49. S.M. Sze, *Physics of Semiconductor Devices* (Wiley, New York, 1969)
50. C.Z. Li, H.X. He, N.J. Tao, Appl. Phys. Lett. **77**, 3995–3997 (2000)
51. C. Kergueris, J.P. Bourgoin, S. Palacin, D. Esteve, C. Urbina, M. Magoga, C. Joachim, Phys. Rev. B **59**, 12505–12513 (1999)
52. B. Xu, N.J. Tao, Science **301**, 1221–1223 (2003)
53. X. Xiao, B. Xu, N.J. Tao, Nano Lett. **4**, 267–271 (2004)
54. X.D. Cui et al., Science **294**, 571–574 (2001)
55. W. Tian et al., J. Chem. Phys. **109**, 2874–2882 (1998)
56. P.S. Damle, A.W. Ghosh, S. Datta, Chem. Phys. **281**, 171–187 (2002)
57. P.S. Damle, A.W. Ghosh, S. Datta, Phys. Rev. B **64**, 201403–201406 (2001)
58. K.-H. Yoo, D.H. Ha, J.-O. Lee, J.W. Park, J. Kim, J.J. Kim, H.-Y. Lee, T. Kawai, H.Y. Choi. Phys. Rev. Lett. **87**, 198102–198105 (2001)
59. Ch. Adessi, S. Walch, M.P. Anantram, Phys. Rev. B **67**, 081405–081408 (2003)
60. M. Di Ventra, M. Zwolak, in *DNA Electronics in Encyclopedia of Nanoscience and Nanotechnology*, ed. by H.S. Nalwas (American Scienti®c Publishers, California, 2004)
61. Lintao Cai, Hitoshi Tabata, Tomoji Kawai, Appl. Phys. Lett. **77**, 3105–3106 (2000)
62. H.W. Fink, C. Schönenberger, Nature **398**, 407–410 (1999)
63. Y. Otsuka, H. Lee, J. Gu, J. Lee, K.-H. Yoo, H. Tanaka, H. Tabata, T. Kawai, Jpn. J. Appl. Phys. **41**, 891–894 (2002)
64. C. Jiaa, X. Guo, Chem. Soc. Rev. **42**, 5642–5660 (2013)

Chapter 10
Organic Light-Emitting Diodes—A Review

P.K. Bhatnagar

Abstract Light-emitting diodes (LEDs) have become the integral part of almost all electrical and electronic systems and gadgets. LEDs of gallium arsenide (GaAs) emitting infrared light were patented by Gary Pitman and Bob Biard of Texas instruments way back in 1961. Since then, efforts have been made continuously in the direction of developing efficient LEDs in the visible and ultraviolet range also. The literature survey shows that during 1970–1979 there was a significant development in red, green, yellow, orange, and blue LEDs. Out of these, blue LED was very expensive and could not be commercialized until 1994. Although inorganic LEDs in the visible region are in use for the past 3–4 decades as replacement of incandescent bulbs, elements in seven segment displays, large RGB displays, calculator, watches, etc., but the main problems are that (i) the processing of basic inorganic semiconductor material is not environment-friendly due to requirement of high purity (ii) non-flexibility (iii) high cost of processing. Therefore, the researchers all over the world focused their research on developing systems and devices in such a way that not only environment is protected (green systems and green devices), but also requirements like flexibility, low-power consumption, and cost effectiveness be taken care of. Conducting polymer-based organic LEDs (OLEDs) and other devices is the alternative for futuristic devices. In fact the work started extensively after Alan G Mac Diarmid, Alan J. Heeger, and Hideki Shirkawa received noble prize in the year 2000 for their research on conducting polymer (polyacetylene). The present article deals with introduction and working of both inorganic and organic LEDs. The emphasis has been given on organic LEDs. Present state of art has been given in detail since its inception. Starting from a single layer OLED to present day multilayer layer OLEDs with different color-to-color tuning have been discussed in detail. The fabrication, relevant characterization techniques and analysis have also been discussed in detail. A systematic development in terms of improvement inefficiency, luminance, stability, and low-power consumption is given which has been possible due to (i) incorporation on some nanomaterials-like carbon nanotubes, quantum dots, graphene (ii) improving and

P.K. Bhatnagar (✉)
New Delhi, India
e-mail: pk.bhatnagar@south.du.ac.in

Z.H. Khan (ed.), *Nanomaterials and Their Applications*,
Advanced Structured Materials 84, https://doi.org/10.1007/978-981-10-6214-8_10

optimizing the physical conditions of growth which include annealing temperature and its duration (iii) incorporation of electron transport layer (ETL), hole transport layer (HTL), electron blocking layer (EBL), hole blocking layer (HBL) in right sequence in the device structure (iv) improving the morphology of the spin-coated films by controlling spin speed and spin duration (v) concentration of conducting polymer in the organic solvent (vi) controlling thickness of the emissive layer, etc. Some light has also been thrown on future aspects and applications of OLEDs.

10.1 Organic Light-Emitting Diodes–A Review

With rising population and rising standard of living, the rate of demand of energy increased many fold all over the world in the past two decades, particularly from the year 2000 onwards, and as expected it will continue to do so. Researchers working in the area of energy are making untiring efforts to find environmentally friendly, cheaper, and sustainable ways to produce the energy by non-conventional energy sources in which wind and solar play an important role. The driving force behind it is that the conventional energy sources like coal, oil, and fossil fuel are depleting very fast. Also the techniques to produce electricity are neither ecofriendly, nor these sources have an unlimited stock and unlimited life, and therefore, scientists are generally looking mainly for two approaches:

(i) Finding/utilizing alternative—environmentally friendly techniques using non-conventional sources of energy
(ii) Making/ using daily use appliances and devices which consume very low power as the energy saved is equivalent to energy produced

Solar energy, wind energy, thermal energy, bio-energy are some of the examples of ecofriendly non-conventional sources of energy, whereas use of highly efficient, low-power consuming semiconducting and other useful electronic materials-based devices like light-emitting diodes (LEDs), semiconductor laser, IMPATT and GUNN diodes are examples of energy saving efficient devices. It may be pointed out that in some cases, for example, for lighting purpose researchers are looking for some new materials other than inorganic semiconductors due to the reasons discussed in the following text.

The present chapter deals mainly with organic light-emitting diodes (with special emphasis on white LEDs which may be used for lighting purpose). Here we would like to give a brief introduction and working principle of both inorganic and organic LEDs. An attempt has been made to throw light on the present state of art of organic light-emitting diodes (OLEDs) and plastic light-emitting diodes (PLEDs). The question arises: Why Organic LEDs? The answer is simple and has been explained in the next paragraph.

Although the inorganic semiconductor-based LEDs are commercially available and have become very popular for economic lighting purpose, traffic lights, etc., as

cheaper, efficient and less-power consuming alternative to conventional tube lights, bulbs, fluorescent lamps, CFL. In spite of these advantages, there are some serious environmental problems in processing inorganic semiconductor materials which need a very high level of purity (6–8 N) for device application. In case of silicon, which is highly abundant, technologically advanced and highly reliable material for devices, there is lot of carbon emission in its processing for obtaining desired level of purification. So is the case with other semiconducting materials also where toxicity level is undesirable. The higher will be the demand, the more will be damage to the environment—which has already reached the alarming level. Therefore, it is the duty of the present generation to think and take necessary measures in the interest of coming generation and must not leave an unhealthy and polluted environment for them. Therefore, wherever possible the alternative eco-friendly materials and processing techniques should be used for future applications. Organic or plastic electronics seems to have a bright future where organic semiconductors and conducting polymers are the base materials. There are also some stability and efficiency issues, which need to be addressed. In the area of lighting, the organic LEDs, WOLEDs, or WPLEDs have great potential owing to many advantages such as being environmentally friendly, economically viable, easily processed, light weight, and flexible in nature. These organic/polymer materials exhibit similar properties as that of inorganic semiconductors for similar applications. The novel idea of wearable electronics is also being materialized. Some of the popular devices/systems are folding display systems/ mobile screens and are available in the market (though expensive to start with). However, stability, cost, and efficiency are some issues which need to be dealt with. We will first introduce inorganic LEDs followed by organic LEDs in the following text.

10.2 Inorganic LEDs

These are generally fabricated from direct band gap semiconductors using GaAs in binary, ternary, or quaternary composites like InGaAs, GaAsP, InGaAsP, where the band gap of the material can be tailored by adjusting the composition so that the device could be used in visible or IR region as the requirement may be.

Working Principle: LED is a simple P–N junction device fabricated from suitable semiconducting material in which the charge carriers are injected from both sides of the junction corresponding to the type of the semiconductor used (electrons from n-side and holes from p-side as shown in Fig. 10.1. These charge carriers undergo radiative recombination (under proper optimized conditions like thickness of active layer, doping density, suitable bias) and emit light. The device is known as inorganic LED. The color tuning is possible by varying the compositions of the material as well as by changing the applied voltage for carrier injection.

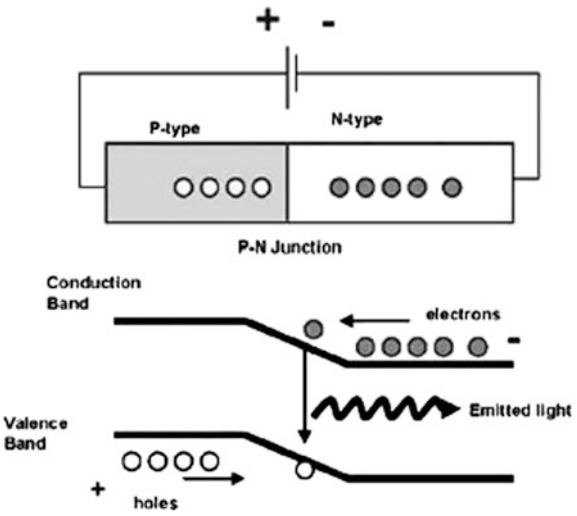

Fig. 10.1 Schematic of a p–n junction light-emitting diode [34]

10.3 Organic LEDs

These are generally fabricated from organic polymer and organic semiconducting materials like conducting/conjugated polymers (CP): polythiophene P3HT, MEH-PPV, PCDTBT, PDOT, PEDOT: PSS. In fact Alan G Mac Diarmid, Alan J. Heeger, and Hideki Shirkawa received noble prize in the year 2000 for their research on conducting polymer (polyacetylene). They showed that plastic could be made conducting or semiconducting by incorporation of alternate sigma and pi bonds. The conducting polymers can be doped like semiconductor (by oxidation and reduction) and have forbidden energy gap also. Since then, efforts are being made more vigorously to fabricate organic electronic devices like organic solar cells, organic LEDs, organic FETs, and success has been achieved. Use of LED lights is one small change that will definitely make a revolutionary difference, not only operational cost is expected to be highly reduced but the carbon emission problem will also be solved to a greater extent [1]. Lucifier™ Lights Pvt Ltd. [2] writes "energy conservation and preservation has become the need of hour that is going to define the future for the whole world, hence use of LEDs will not only help in saving energy but also reduce pollution thus helping cause of global warming to large extent."

Working Principle: As mentioned earlier that for a conducting polymer (CP) the energy values can be calculated on the basis of molecular orbital theory—one gets highest occupied molecular orbital (HOMO-similar to top of valence band of inorganic semiconductor) and lowest unoccupied molecular orbital (LUMO-same as minima of conduction band of inorganic semiconductor), and the gap between the two behaves like energy band gap of inorganic semiconductor. Typical energy level diagram for single layer OLED has been shown in Fig. 10.2 a while Fig. 10.2b, c represent band diagram for unbiased and biased OLED, respectively.

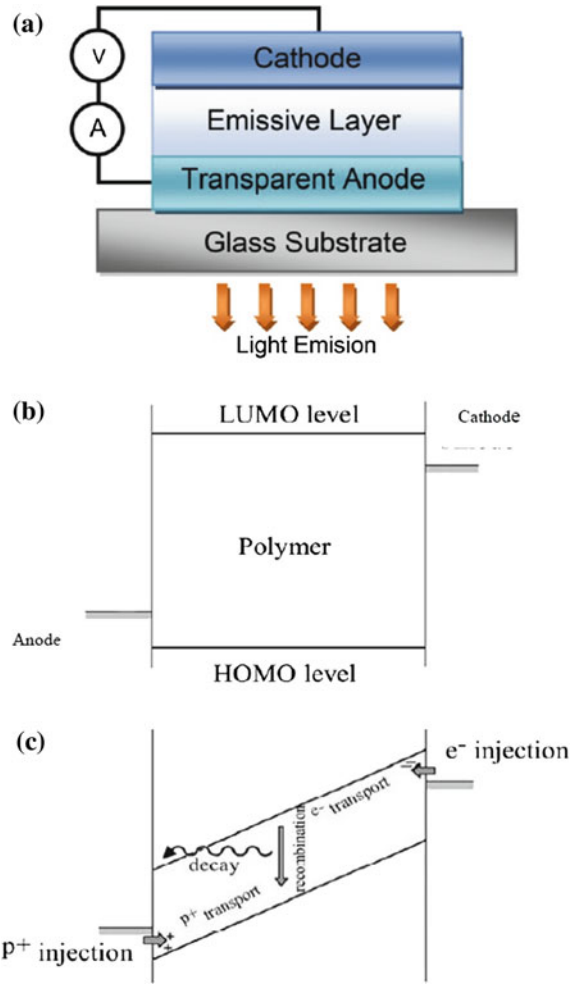

Fig. 10.2 **a** Simple single layer LED structure. **b** Band diagram of unbiased LED, **c** biased LED

When the OLED is biased suitably (+ve at ITO side and –ve at Al side), the electrons enter from cathode while the holes enter from anode to reach the emissive layer. The transport of electron and holes is via transfer reaction and hopping between polymer chains. These charge carriers make excitons (bound electron–hole pair) which decay radiatively upon recombination and one gets corresponding light emission (blue, red, orange, or mixed), but the situation in actual practice is more complicated and one has to analyze the factors which are responsible for poor efficiency of OLEDs/PLEDs. The making of device/film is simple as the active (emissive) layer can easily be spin coated but it may have morphological and stability issues if proper care is not taken. It is important to mention here that unlike inorganic semiconductors CPs have certain limitations such as:

1. The mobility of charge carriers in conducting polymers is very small ($\sim \mu_e \leq 10^{-8}$ cm^2 V^{-1} s^{-1} and $\mu_h \leq 10^{-4}$ cm^2 V^{-1} s^{-1}). Since the hole mobility is higher than that of electron hence CPs are preferentially hole transporter while the electrons have deep trapping probability.
2. Charge carriers get trapped in polymers chain if alignment is not straight or intermingled due to the presence of kinks and discontinuity.
3. Surface morphology of the film is very important as the film has to be uniform to have efficient device performance.
4. Charge imbalance at the emissive layer: in this case, the majority of the charge carriers do not recombine because of higher mobility of holes ($\mu_h \leq 10^{-4}$ cm^2 V^{-1} s^{-1}) than that of electron ($\mu_e \leq 10^{-8}$ cm^2 V^{-1} s^{-1}) [3], the holes pass through the emissive layer without recombining with electron, thereby reducing the overall efficiency. To solve this problem, there is a need to introduce buffer layers like electron blocking layer (EBL), hole blocking layer (HBL), hole transporting layer (HTL), electron transporting layer (ETL) at suitable positions.
5. Excitons quenching near cathode: this is a serious drawback and it can be taken care of by suitably introducing a buffer layer so that the recombination zone be shifted away from the cathode [4].
6. Loss of triplets in electroluminescence (EL) process: actually two types of excitons are produced on charge injection: (i) singlet excitons with spin angular momentum $s = 0$ (ii) triplet excitons with spin angular momentum $s = 1$ [5]. The singlets which are 25% of the total excitons generated contribute to EL while triplets which are 75% do not contribute as they decay non-radiatively.
7. Loss of generated photons inside the LED structure itself: it means that not all the photons emitted from the active region are able to come out of the device. Some of the factors responsible are (i) light emitted by the active region may be reabsorbed in the substrate of LEDs or (ii) part of light may be incident on the metallic contact surface may be absorbed by the metal itself (iii) total internal reflection may further reduce the possibility of light to escape from LED.

Keeping these points in mind, one can now develop efficient organic devices due to better understanding. Starting from single color LED, the efforts have been intensified to make white OLED (WOLED). In earlier days, small organic molecules were used to make WOLED, but the main problem was need of vacuum evaporation technique for their deposition which is not only an expensive technique but could not be used for making large area thin films which find application in flat band displays and flat panel lighting system. Though Sony company made world's first OLED TV in November 2008 but due to its very high cost of fabrication and problem of realizing large area films, these could not be fully commercialized.

Therefore, for real practical applications, CPs of large molecule and high molecular weight are desirable. They can be processed by much simpler and cheaper techniques like spin coating and ink-jet printing [6], because these polymers are easily soluble in organic solvents like xylene, toluene, 1,2-dichlorobenzene. Other advantages of CPs over conventional inorganic semiconductor-based devices are: [7]:

(i) While conjugated polymers can be prepared with electrical and optical properties similar to the semiconductors, they retain their original physical properties of plastics such as being light weight, flexible, and economical with environmental-friendly processing.
(ii) Doping in conjugated polymers can be achieved by simple oxidation process where some delocalized electrons are removed from the polymer chains, leading to p-type polymer, and the reduction process where an addition of electrons is done to unfilled bands leading to the formation of n-type polymer. This eliminates the need of expensive ultra-purification of the conjugated polymers, which is required for the inorganic semiconductors.
(iii) The biggest advantage of these polymers is that they are easily soluble in a large number of common organic solvents (like xylene, chlorobenzene, toluene) making their solution processing possible for device fabrication and avoiding the use of expensive vacuum evaporation techniques.
(iv) The optoelectronic devices based on these CPs do not require any p–n junctions, which is another most important advantage over inorganic semiconductors; thin films of these polymers themselves act as the active materials.
(v) Another important advantage of PLEDs over the inorganic semiconductor LEDs is the ease in tuning of emission color. Color tuning in PLEDs is possible through several routes such as variation of substituent on the conjugated polymer chains [8], multilayer device structures [9], and copolymerization with dyes [10].

Conjugated polymers have long chain of alternate single (σ) and double ($\sigma + \pi$) bonds as shown in Fig. 10.3. Electrons in σ bonds are strongly bound and are immobile, whereas the π electrons are not tightly bound and are delocalized. It is well-known fact that the σ bonds provide high mechanical strength to the polymer chain. On the other hand, delocalization of π electrons is responsible for the conducting properties of the conjugated polymers.

The molecular orbital (π bond) split into bonding and antibonding orbitals (called as π and π^* or HOMO and LUMO, respectively), which resemble with the valence band and conduction band in solid-state inorganic semiconductors [11]. The generalized band structure for semiconductors is shown here in Fig. 10.4. As we are aware that large numbers of monomers form a polymer chain, these bands consist of various energy levels corresponding to each monomer unit. The filled highest occupied molecular orbital (HOMO) and the vacant lowest unoccupied molecular orbital (LUMO) decide the optical and electrical properties in conjugated polymers. The energy difference between HOMO and LUMO is termed as the band

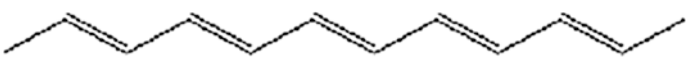

Fig. 10.3 Basic structure of conducting polymers chain structure

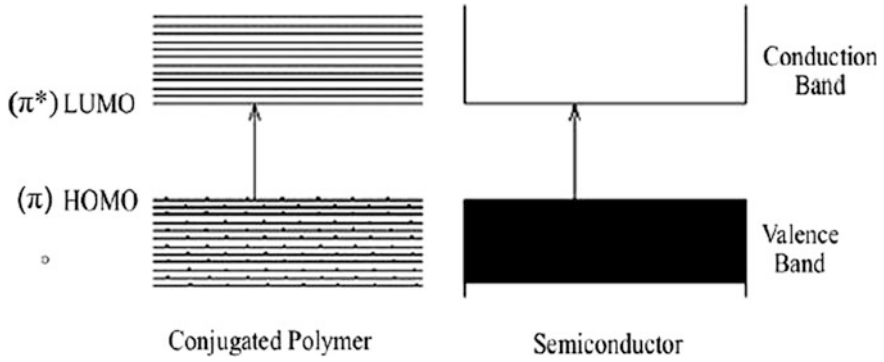

Fig. 10.4 Energy levels in conjugated polymers and inorganic semiconductors

gap of conjugated polymers. RH Friend et al. published a review article [12] and their group has done pioneering work in this area [13, 14]. A schematic diagram of an ideal OLED has been shown in Fig. 10.5a, b which shows transport mechanism of a multilayer OLED.

10.4 Characteristics of OLED

It is important to be familiar with the terminology and characteristics of OLED

1. Current density–Bias voltage characteristics (*J–V*): Here the voltage at which the current start rising rapidly is called turn-on voltage of diode (Fig. 10.15). It depends on various parameters like type of material used in making OLED, structure of OLED, type of electrodes, film thickness, solvent, spin speed, annealing temperature, and annealing duration.
2. Luminance characteristics (*L–J*): Luminance is a measure of light intensity or brightness of optical source (Fig. 10.19a). The bias voltage at which luminance of 1 Cdm^{-2} is obtained in LED is known as turn-on voltage of LED. The luminance intensity of source is measured in terms of Candela (Cd) which for a monochromatic source of light is defined as optical power of 1/683 W being emitted at 555 nm into a solid angle of 1 Steradian (Sr). Similarly, luminance flux (lm) is related to Cd by relation Cd = lm/Sr. Some typical value of luminance are given below [15, 16] in Table 10.1. Another unit of light is LUX which is lmm^{-2}
3. Electroluminescence (EL spectra Fig. 10.20). This provides information about wavelength of light emitted by OLED [17]. It also gives information about contribution of each color or wavelength in the total luminescent spectra of OLED or PLED.

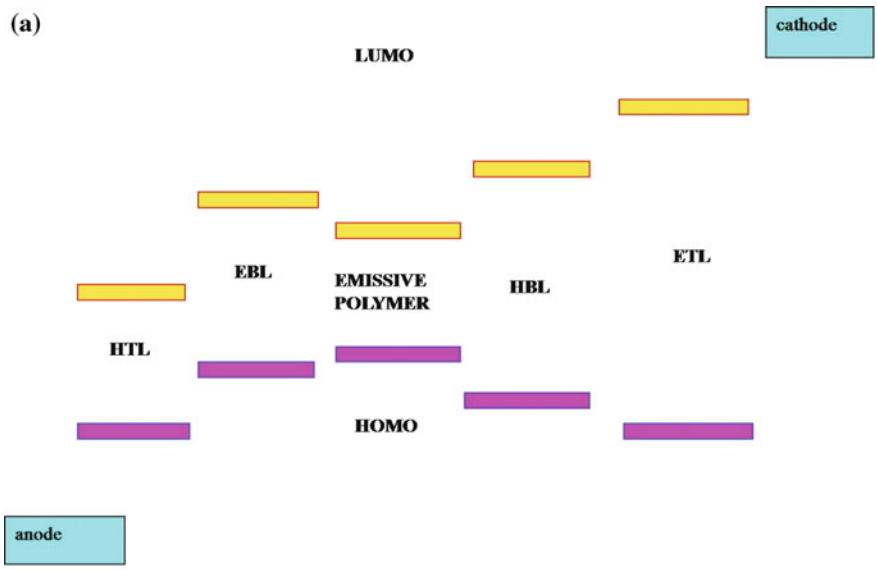

Fig. 10.5 **a** Schematic of ideal OLED. **b** Transport mechanism of a multilayer OLED

Table 10.1 Typical values of luminance of various sources of light in cd/m^2

Light sources	Luminance (cd/m^2)
Sun (at noon)	1.6×10^{-9}
Fluorescent lamp	1000–2000
Computer screen	100–200
Glow worm	~5.11 (at 555 nm)

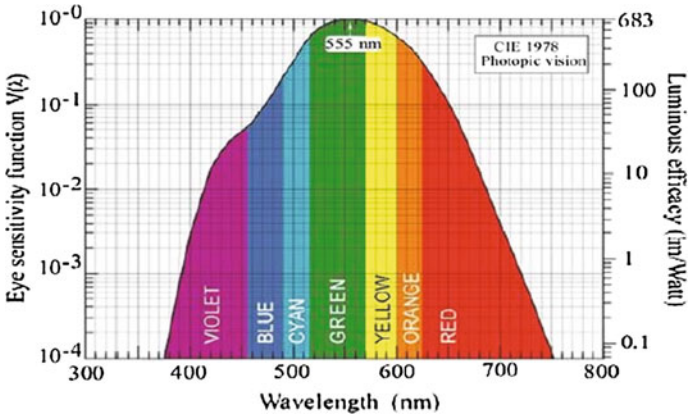

Fig. 10.6 Eye sensitivity function, $v(\lambda)$, and luminous efficacy of optical power, $V(\lambda)$ is maximum at 555 nm [7]

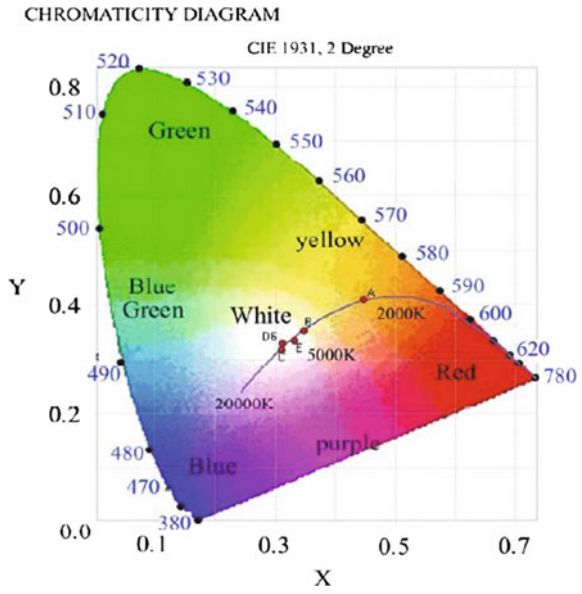

Fig. 10.7 CIE (x, y) chromaticity diagram [7]

4. Color quality (Colorimetry): It is a very important requirement which is measured in terms of color coordinates standardized by the international commission for illumination—Commission Internationaled' Eclairaze—CIE. The color in this method is measured using color matching functions (Fig. 10.6) and chromaticity diagram (Fig. 10.7).

In the standardization process, human eye sensitivity function (at wavelength 555 nm-green color) is taken as unity. For monochromatic light source, luminance efficacy (**le**) is of the order of eye sensitivity function, whereas for multicolor light source (e.g., white light source), **le** is calculated by integrating over all available wavelengths in the visible region. Three parameters are most important to define the color quality: (i) color rendering index (CRI), (ii) correlated color temperature, and (iii) chromaticity coordinate (CIE). The light source having good color rendering performance means it is emitting equivalent to a black body source at 3000–6000 K having CIE coordinates as (0.33, 0.33) corresponding to white light. Figure 10.7 shows chromaticity diagram where the boundaries represent plots of monochromatic light called spectrum loci. Area near the center of diagram is called Planckian Locus which represents plot of coordinates of black body radiation (1000–20,000 K). Most of the traditional sources emit between 2850 and 6500 K of Black Body (Table 10.2).

Some more important parameters:

1. Luminance efficiency or power efficiency (η_p): Its units are candela per ampere (CdA^{-1}) or Lumen per Watt (lmW^{-1}). It is defined as Lumen output per input electrical power (Fig. 10.19b).
2. Internal quantum efficiency (IQE): It is defined as number of photons generated inside the device per electron–hole pair injected into the device such that $\eta_{int} = \gamma\eta_s\Phi_s$ where γ is fraction of injected carriers that produce excitons and also known as charge balance factor, η_s is the fraction of singlet excitons, and Φ_s is fraction of energy released from material as light also called as quantum efficiency of fluorescence.
3. External quantum efficiency (EQE): It is defined as total number of photons emitted from the device per electron–hole pair injected into the device such that $\eta_{ext} = R_e\,\eta_{int}$ where R_e is the ratio of number of photons emitted into free space per second to number of photons emitted per second from the active layer. R_e is also known as coupling efficiency.
4. Life time: It is defined as average number of hours of operation in which the initial intensity drops to 50%.

Table 10.2 CIE coordinate and CRI for different white light sources used in daily life [15]

Light sources	CIE Coordinates		CCT(K)	CRI
	X	*Y*		
Day light	0.313	0.329	6500	90
Incandescent lamp	0.448	0.408	2854	100
Fluorescein cool white lamp	0.375	0.367	4080	89
Fluorescein warm white lamp	0.440	0.403	2940	72
Tungsten halogen lamp	0.448	0.407	2856	100
High-pressure sodium lamp	0.511	0.417	2100	24
Xenon lamp	0.324	0.324	5920	94

Some typical examples of CPs giving different colors are given below

(i) Orange—MEH-PPV
(ii) Blue—PFO

A whole list of materials and list of venders (Sigma Aldrich, graphene supermarket, etc.) is available for OLED materials on various websites for different purposes like:

Charge transport and photosensitizing materials.
Electron transport and hole blocking materials.
Hole transport (HT) and hole injection layer (HIL) materials.
Host materials.
Light emitters and dopants.
Light-emitting polymers (LEPs).

White light is a suitable combination of red, green, and blue emitters/colors. In an inorganic LED, generally GaN or InGaN is used with different compositions (binary, ternary, and quaternary materials) and phosphors like Ce:YAG is used for color tuning which also depends upon the thickness and concentration of phosphor layers, and proper color mixing will give white light. For this purpose, multilayers are used and a typical example for obtaining white light OLED/PLED is shown in Fig. 10.8.

New materials are being synthesized in various research and development laboratories all over the world to get cheaper, efficient, and long-life OLEDs.

In the following section, we will summarize some general and serious technology-based drawbacks of OLEDs and their possible solutions:

1. Charge injection barriers at the interfaces of emissive materials can be reduced by having materials with suitable (closely matched) HOMO and LUMO levels.

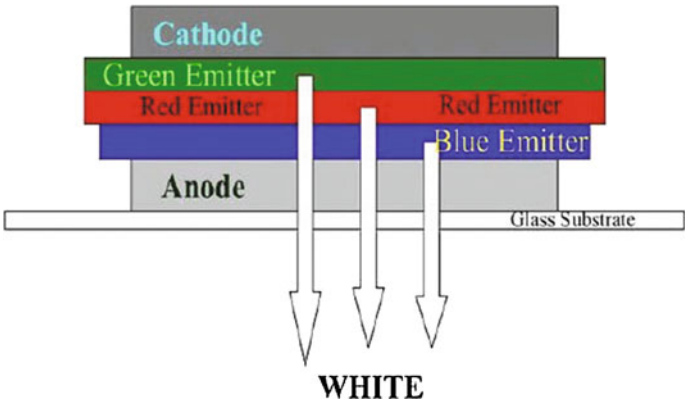

Fig. 10.8 Multilayer structure of a typical WOLED/WPLED

2. Lot of organic material waste can be avoided by precise control of parameters like thickness and composition of various layers.
3. In spin coating for multilayer structure, generally it becomes difficult; it is difficult to coat one layer over other due to common solvent problem which may result in washing away the previous layer. Float lifting technique has been used to do away with this problem [7].
4. Control of recombination zone location (which affects the CIE coordinates and efficiency) can be taken care of by incorporation of HTL, ETL, EBL, HBL; but sometimes they may result in increase in complexity.
5. High operating voltage due to thick profile of various stacked organic layer is undesirable, therefore one needs to optimize the thickness of the layers.
6. To enhance the contribution of triplet excitons toward radiative emission, one may use heavy metal elements which increase spin orbit coupling and enhance spin flip leading to more radiative decay. The other possible solution is use of phosphorent red and green dyes as guest to harvest/utilize triplet excitons [18, 19] by self-trapping mechanism.
7. For better morphology, one has to optimize very carefully parameters like concentration of solution, spin duration, spin speed, annealing temperature, and annealing duration.

For color tuning, one needs optimized concentration of dopants or blending of two or more polymers [20, 21]. Further for emission, the energy transfer should be very fast and the materials should have appropriate concentration. For a white PLED, doping ratio of blue > green > red is required and carefully balanced.

The other possibilities are to use conducting polymer as host material and red/green phosphorent dyes as guest material (Fig. 10.9). Choice of right material has been a challenge as explained below:

The problem that can be noticed in (Fig. 10.9b) is that the triplet excitons energy level of blue-color emitting polymer, say PFO is well below that of green phosphorent dye, and therefore, the energy cannot be transferred from PFO to green dye. But at the same time since the red phosphorent dye has triplet excitons level lower than blue CP (blue color CP at 2.15 eV [22] and red at 2.0 eV [23]), the triplet energy may easily be transferred to red dye. Now that the problem has partly been solved by identifying materials for blue (CP PFO) and red color (dye–Ir $(piq)_2$acac), the remaining is selection of a suitable green dye to complete RGB. Literature survey shows that a green phosphorent dye Ir $(mppy)_3$ or [Iridum (III) tris (2-(4-tolyl) Pyridinato-NC^2 is available. It has been shown by Devinder et al. [24] that even if host material is a suitable polymer (say PFO), the green dye can produce EL using self-trapping mechanism. The self-trapping mechanism (STM) and excitons formation has been shown in Fig. 10.10.

The recovery condition is that for STM the LUMO level of green dye should be well below the LUMO level of host CP while HOMO level should be well above. The electrons injected from cathode and holes from anode (during biasing) get trapped in LUMO and HOMO of guest, respectively, and excitons is formed in dye itself. These excitons can decay radiatively and produce EL in green region and

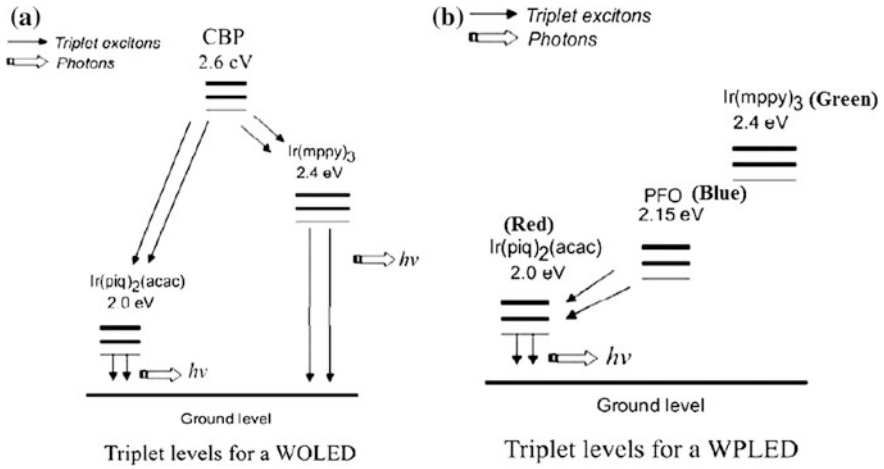

Fig. 10.9 Triplet energy levels of $Ir(mppy)_3$ and $Ir(piq)_2(acac)$ with **a** CBP as HOST (**b**) PFO as HOST

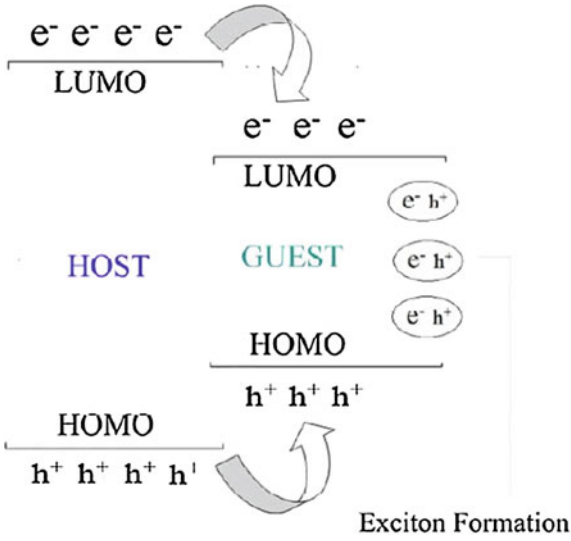

Fig. 10.10 Favorable HOMO and LUMO levels of the guest material for self-trapping

thus all the colors required for WOLED can be obtained. For efficient WOLED device, there is a need to optimize the concentration of RGB components so that their proper combination emits white EL.

To understand the experimental technique used to fabricate OLED, first we will discuss a typical structure for blue and green components [PFO + Ir $(mppy)_3$] as shown in Fig. 10.11. For full RGB, red dye can be added in the active layer in the optimized composition to obtain WOLED.

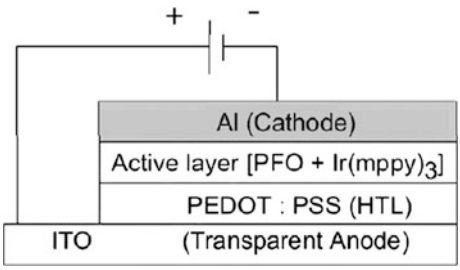

Fig. 10.11 A typical structure for OLED

The material used are PFO, Ir $(mppy)_3$, chlorobenzene, ITO/glass substrate (anode), PEDOT:PSS, aluminum, and LiF (cathode). Following steps are used:

First of all, solutions of PFO and Ir $(mppy)_3$ are made in chlorobenzene keeping PFO concentration constant as 10 mg/ml and varying dye concentration from 0 to 15 w/w%. The solutions are ultrasonicated and divided into two parts.

1. In the first part, PFO and IR $(mppy)_3$ composite films are spin coated on glass substrate for optical measurements (Absorption and PL).
2. While the other part is kept for device fabrication on patterned ITO-coated glass having sheet resistance of $\sim 15\ \Omega/\square$. Here ITO is used as anode. Over this substrate, a PEDOT:PSS layer (HTL) is spin coated keeping spin rate as 4000 rpm for 20 s. The samples are baked and dried in vacuum oven at 100 °C for ~ 1 h. Over this, an active (emissive) layer of PFO + $Ir(mppy)_3$ having different concentration of $Ir(mppy)_3$ is spin coated at spin rate of 2000 rpm for 30 s. These structures are annealed at 55 °C for 2 h. Finally, the Al contacts of 100 nm thickness are vacuum evaporated on the emissive layer as shown in Fig. 10.11.

Results of absorption and PL studies have been shown in Fig. 10.12a, b, respectively.

All the absorption and PL curves are normalized. The absorption spectra of PFO and phosphorent dye in p-xylene are shown in Fig. 10.12a. The minimum absorption of $Ir(mppy)_3$ is at 328 nm and it serves as excitation wavelength in the PL studies. Normalized PL spectra Fig. 10.12b shows that there is no significant emission in green region even at high doping concentrations which means that the entire singlet excitons energy is used to produce blue PL and there is absolutely no transfer of singlet excitonic energy from PFO to green phosphorent dye no matter what concentration of dye was taken in the given range. PL studies on PFO show that peak emission of PFO is about 30 times higher as compared to $Ir(mppy)_3$. In other words, green dye emits very weak PL as compared to PFO (for excitation wavelength of 328 nm). There may be some possibility of FRET but it is very insignificant.

The studies on effect of dye concentration in EL spectra of PLED having emissive layer of PFO + $Ir(mppy)_3$ composite indicate that with increase in green concentration, green emission goes on increasing. When the concentration of green dye

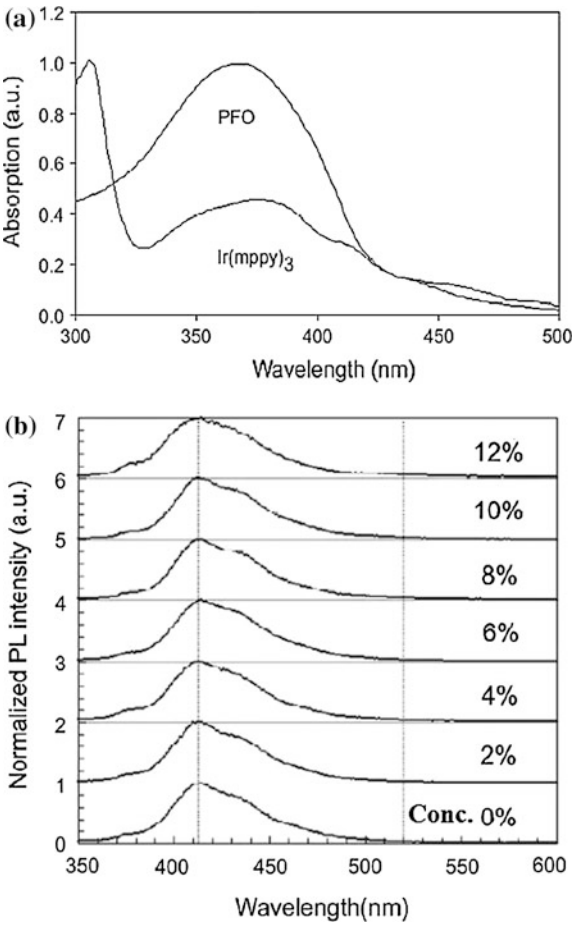

Fig. 10.12 **a** Absorption spectrum of $Ir(mppy)_3$ (normalized) and PFO (normalized). **b** PL spectra of the [PFO + $Ir(mppy)_3$ (0–12%)] composite films (excitation wavelength 328 nm)

$\geq$ 6%, the green wavelength region overshoots the blue region. This is not due to transfer of energy from PFO to dye because the dye has higher triplet level than PFO.

And therefore the EL observed in green region Fig. 10.13 along with that of blue is due to the self-trapping mechanism (described earlier) and the probability of charge trapping increases with increase in green dye concentration in the present typical case Fig. 10.14.

Self-trapping of electron will take place from LUMO of PFO to LUMO of Ir $(mppy)_3$, and self-trapping of holes takes place from HOMO of PFO to HOMO of Ir $(mppy)_3$—both to make excitons which decay radiatively. Figure 10.15 shows the effect of dye concentration on the *J–V* characteristics. Initially up to 10% of the dye concentration the turn-on voltage increases and then starts decreasing slightly as the dye concentration increase from 10 to 12%.

This may happen due to high concentration of guest molecules where the guest molecules come closer to form channel of charge carriers resulting in reduction of

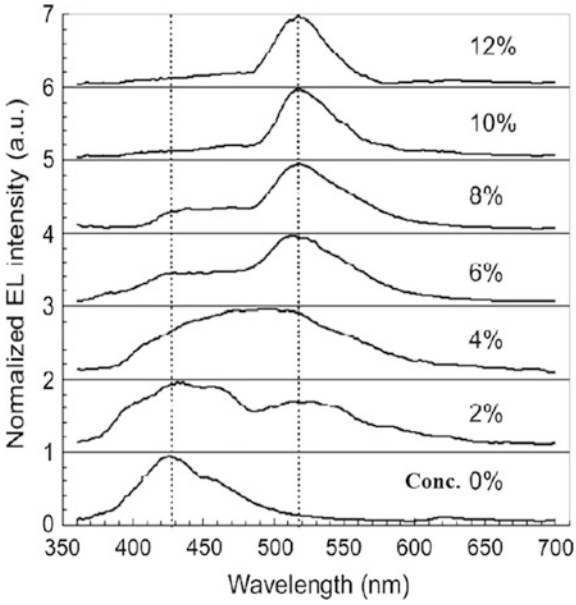

Fig. 10.13 EL spectra of the PLEDs fabricated using [PFO + $(Ir(mppy)_3$ (0–12%)] composite films as the active emissive layers (A fixed current density of 50 mA/cm^2 is used to drive all the diodes) [22]

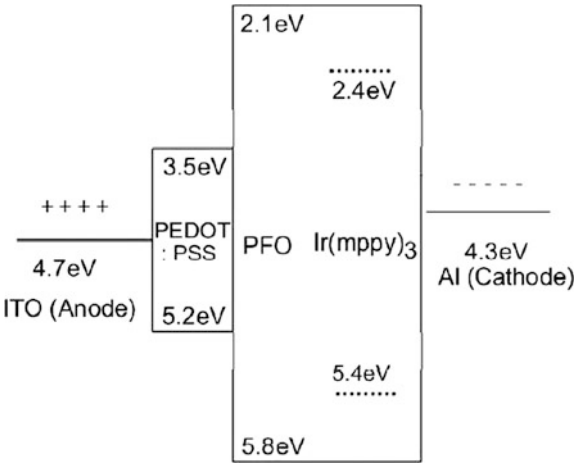

Fig. 10.14 Energy level diagram for the PFO/Ir $(mppy)_3$ composites

turn-on voltage. Finally, PLED parameters can be optimized and color tuning is possible by varying parameters like the thickness of the doped layer and dopant concentration. To get proper color coordinates [CIE (0.33, 0.33)], there is a need of optimization of concentration of various dopants. Actually as per Fig. 10.9b, it can be noticed that red dye can efficiently use triplet excitons because its triplet level is well below the PFO. Figure 10.16 is self-explanatory where normalized absorption and PL have been plotted as function of wavelength.

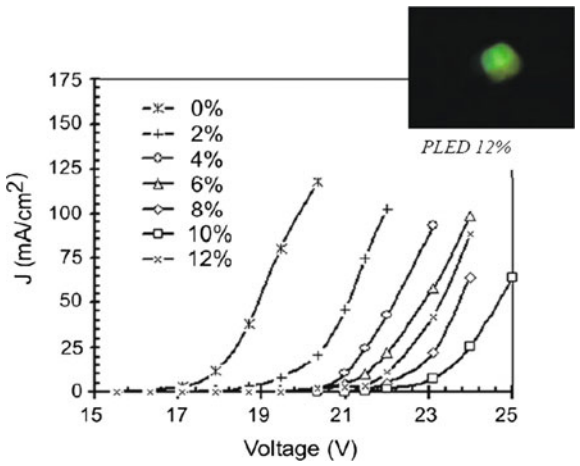

Fig. 10.15 *J–V* characteristics of the PLEDs fabricated using [PFO + $Ir(mppy)_3$ (0–12%)] composite films as active emissive layers [22]

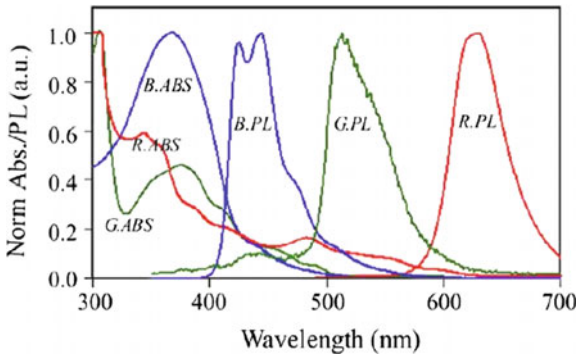

Fig. 10.16 Figure showing overlap between absorption (*ABS*) spectrum of red dye (*R*) and photoluminescence (*PL*) spectra of green dye (*G*) and PFO (*B*)

Figure 10.16 exhibits the possibility of Forster Resonance Energy Transfer (FRET), where energy transfer is possible because of overlap of absorption of donor and emission of acceptor dye. It is a distance-dependent phenomenon, i.e., distance between donor and acceptor molecule which is order of few nms and it occurs primarily due to resonance of acceptor dipole with donor dipole. The concentrations of various RGB components need to be optimized carefully. The concentration of red dye is kept lowest of the three constituents as it is most effective and gets excited by charge trapping. FRET and self-trapping phenomenons are true for green dyes also. Some bioelectric materials like salmon DNA [25, 26] have been used successfully to improve the performance of MEH-PPV and PFO-based polymer LEDs.

As mentioned earlier, the sDNA-CTMA complex incorporated in WPLED at suitable position (Fig. 10.17) acts as electron blocking layer and enhances the performance of bio-WPLED. It helps in maintaining the balance of charge carriers by preventing electron from slipping out of recombination region, thereby increasing the probability of recombination of electrons and holes in the emissive layer. Figure 10.17 is self-explanatory. If we look at various HUMO and LUMO

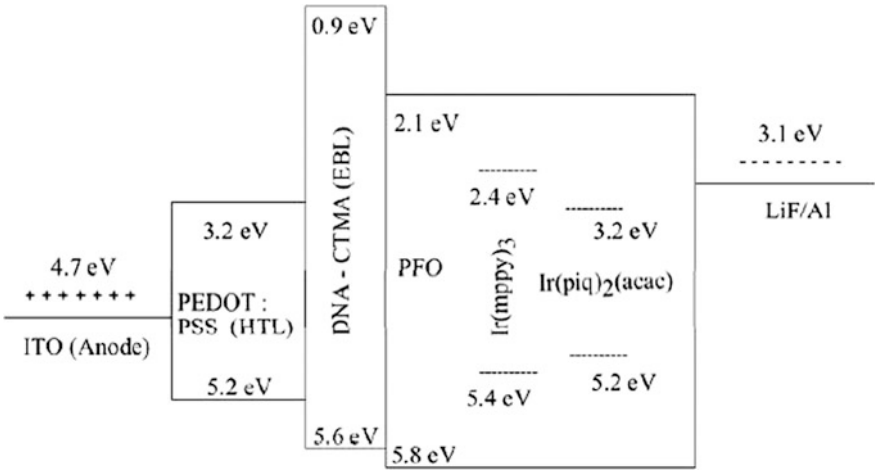

Fig. 10.17 Energy level diagram for the bio-WPLED fabricated

levels of different constituents, it can be noticed that DNA-CTMA complex due to its low LUMO level (0.9 eV) blocks efficiently electrons from going out of the emissive layer. The energy level of red dye ensures charge trapping in the dye because its LUMO level (3.2 eV) is well below that of PFO and HOMO level is well above that of PFO (5.2 eV).

10.5 Fabrication Steps of Bio-WPLED [7]

Blue-emitting conducting polymer PFO was dissolved in chlorobenzene keeping the concentration as 10 mg/ml. To this solution, green [$Ir(mppy)_3$] and red [($Ir(piq)_2(acac)$)] phosphorescent dyes were added in concentration 0.8 and 0.2% w/w, respectively. These concentrations of the solutes were obtained after series of experiments by varying the dye concentrations in the host PFO so as to obtain best possible EL spectrum. The solution was homogenized using an ultrasonicator. This solution was spin coated on a patterned ITO-coated glass (having sheet resistance $\sim$15 Ω/□), keeping the spin rate 2000 rpm for 30 s. The thickness of the film was measured with the help of talystep and is found to be 220 ± 10% nm (Figs. 10.18 and 10.19).

The resistivity of the ITO substrate is very crucial for the device. If the resistivity is too high, the device current is likely to be very low and the turn-on voltage for the device will be high. On the other hand, if the resistivity is too low, the device is likely to be shunted. A resistivity of 15–20 Ω/□ has been found to be most appropriate by most of the workers for fabrication of LED structures. The ITO-coated glass substrates have to be clearly degreased, otherwise not only the

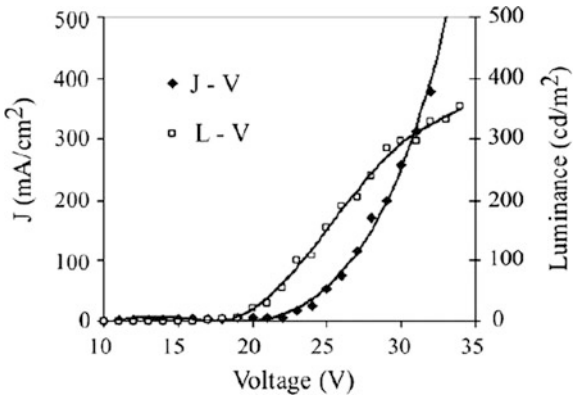

Fig. 10.18 *L–J–V* characteristics for the bio-WPLED fabricated

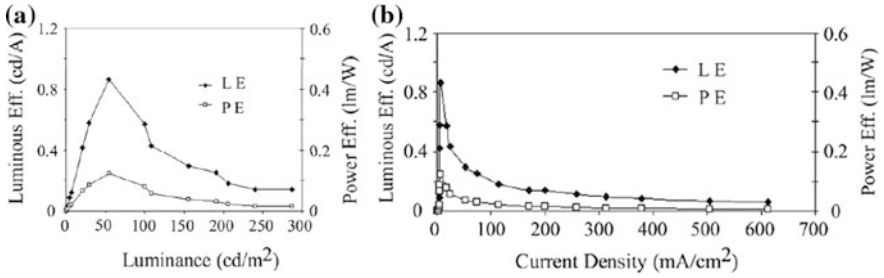

Fig. 10.19 Luminous and power efficiencies for the Bio-WPLED as a function of **a** luminance; **b** current density

emitted light will be obstructed but also spin-coated films will not stick and be non-uniform. Therefore, the substrate was first cleaned in an ultrasonic solvent bath for 10–20 min and then dried in a heating chamber at a temperature of ∼50 °C for 2 h. The morphology of the film must be improved during fabrication. For this purpose, the concentration of PFO in chlorobenzene has been optimized. If the concentration of the solute is too high, the morphology will be poor due to kinks and overlapping of the chains. On the other hand, if the concentration of the solute is too low, the luminescence intensity will be poor. Before coating the emissive layer, a PEDOT:PSS layer is spin coated on the ITO. This layer acts as HTL and also smoothen the uneven surface of the ITO. A thin layer of DNA-CTMA complex was also coated on the PEDOT:PSS layer to act as an EBL. A buffer layer of LiF 10 nm thick is vacuum evaporated on the active layer, which reduces the potential barrier at the polymer/Al interface. The LiF layer also prevents the diffusion of Al atoms into the emissive layer during vacuum evaporation of cathode contact. On the buffer layer, Al cathode contacts of 100 nm thick are vacuum evaporated at a rate of 0.6 nm/s. A shadow mask was used for the deposition of the cathode resulting in the devices area of 2 mm × 2 mm.

10.6 Characteristics of Laboratory Made Prototype Typical Device

The turn-on voltage is quite high about 20–21 V, and the maximum luminescence is of the order of 350 Cdm^{-2} at bias voltage of 34 V as reported by us [26]. The luminous and power efficiency are reported as 0.86 CdA^{-1} and 0.12 lmW^{-1}, respectively. There is a need to reduce the turn-on voltage. The color quality of bio-WPLED is also important. For a typical device fabricated by Madhwal et al. [21], all primary peaks start becoming significant beyond 25 V and become stable around 32–34 V as shown in Fig. 10.20.

The CIE obtained is (0.30, 0.34) which is close to the pure white light (0.33, 0.33). All these values are approximate and vary slightly with chemical and physical parameters like concentration, type of solvent, and the process involved. It's important to note that the concentration of red dye has to be optimized carefully because beyond a certain value (say 2 w/w % for a typical case) the dye molecule start segregating and making clusters which is not desirable (Fig. 10.21).

The general chromaticity diagram is shown in Fig. 10.22. To further increase the efficiency, it is necessary to revisit the parameters which adversely affect the performance of LED. Some of the major problems have already been discussed in this chapter viz. charge imbalance, loss of triplet excitons, morphology of the thin film, poor mobility of electron and holes in CPs, excitons quenching near the metal electrodes, the presence of metal contamination into CP after cathode evaporation [27]. Chance et al. [28] have shown that metals like Ca diffuse from cathode into the

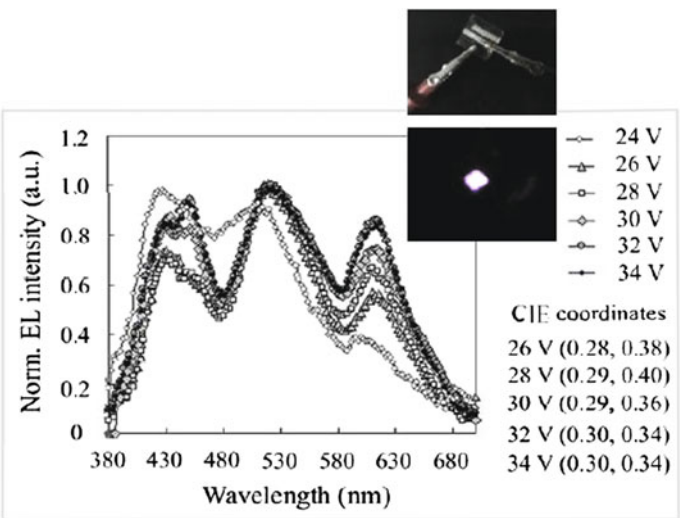

Fig. 10.20 EL spectra and corresponding CIE coordinates for the bio-WPLED [21]. *Inset* Sample picture and the working WPLED

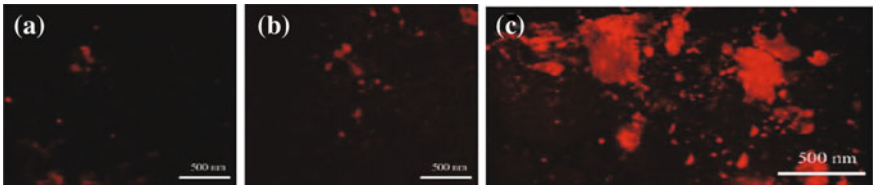

Fig. 10.21 Confocal micrograph of the films: red dye doped in PFO [**a** 2%, **b** 5%, **c** 15%] confocal (LSM 510, Carl Zeiss, Germany)

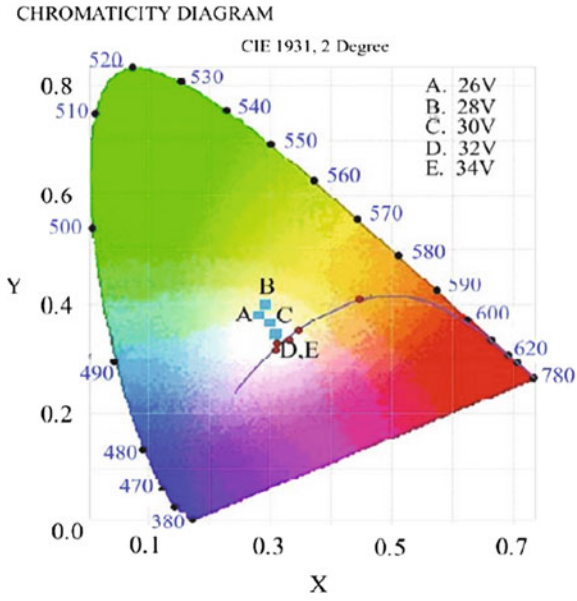

Fig. 10.22 Chromaticity diagram for the bio-WPLED Fabricated showing CIE coordinates at different bias voltages

emissive polymer and form high number of quenching centers near the cathode. Further due to proximity of metal electrode to the polymer layer, there is a possibility of a short distance non-radiative energy transfer from the fluorescent layer to metal.

Use of suitable ETL may be one of the possible solutions in order to improve the efficiency of the device. DNA-CTMA EBL alone would not be able to enhance the efficiency of WPLED to sufficient extent, and suitable ETL can enhance mobility of electron and helps in shifting the recombination zone away from metal electrode. As a result, the exciton formation will take place away from the metal electrode reducing the possibility of their quenching by metal electrode. Single-walled carbon nanotubes (SWNT) have been identified as excellent electron transporting material (ETL). It has been shown by Singh et al. [29, 30] that incorporation of CNT in CPs (concentration of 5 w/w%) matrix enhances its conductivity by 5–6 order of magnitude by making an efficient network therefore for a typical MEHPPV-SWCNT composite film-based LED the luminance increased approximately by 5

times [31]. It has been shown that incorporation of ETL not only improves charge balance between the electron and holes but also shifts the recombination zone away from the metal electrode thus, resulting in a significant improvement in luminance of the device. Therefore, the use of SWNT (ETL) in conjunction with DNA-CTMA complex (EBL) which increases the luminous efficiency of this multilayered (MEHPPV-SWNT) composite with EBL by about 20 times [7]. Some worker have suggested the use of Alq_3 as suitable ETL because it has excellent film formability and low ionization potential (5.7 eV) making it an appropriate candidate for blocking holes and transporting electrons in the emissive layer. But the two main problem with Alq_3 is that since it is a green emitter, it interferes with the emission spectra of LED and due to lower molecular weight it cannot be spin coated (because it is not soluble inorganic solvent) and needs relatively expensive vacuum evaporation technique which is not commercially viable. Therefore, Alq_3 was not used. In the case discussed above, MEHPPV-SWNT composite layer for ETL was casted over emissive layer using a special technique where extreme care was taken. This technique prohibited washing away of one layer (due to same solvent) when other layer was spin coated over it. This technique has been discussed below for a typical structure shown in Fig. 10.23.

Here MEH-PPV-SWCNT composite has been used as ETL over the emissive layer of (MEH-PPV). Since both, emissive layer and ETL (MEHPPV-SWCNT composite) had the common organic solvent, they both dissolve in common organic solvent when one layer is spin cast over the other (here thin film of MEHPPV-SWCNT composite is spin cast over MEH-PPV emissive), the MEH-PPV layer is washed out. This is highly undesirable. Therefore, to fabricate the ETL over emissive layer, float lift technique is used. In this technique, first of all MEH-PPV/DNA-CTMA complex/PEDOT:PSS/ITO structure is made by spin cast technique. Now ethylene glycol is taken in a petri dish. Over this, a few drops of MEH-PPV-SWCNT composite solution are cast which spreads uniformly over highly viscous glycol and floats over it. Now the already made dried structure MEH-PPV/DNA-CTMA complex/PEDOT:PSS/ITO is placed over the thin dried layer of MEH-PPV-SWCNT (ETL) floating on ethylene glycol for one minute

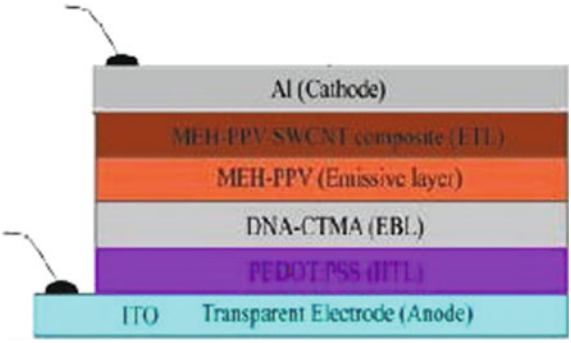

Fig. 10.23 MEH-PPV-SWCNT composite bio-LED

carefully. The floating film MEH-PPV-SWCNT will adhere itself to MEH-PPV emission layer due to non-sticking nature of ethylene glycol. The samples are then dried in vacuum oven to remove the residual ethylene glycol. Al contact (cathode) is vacuum coated over this ETL. Now the device is ready for characterization.

A comparison of LED characteristics (Current density *J* vs. Bias voltage and Luminescence vs. *J*) with and without ETL has been shown for a typical lab made device in Figs. 10.24 and 10.25. Significant improvement is observed mainly due to the fact that SWCNT improves/provides high mobility to the electrons and there is an improvement in the injection of the charge carriers. Some workers have used ZnO nanorods (NR) for increasing the emission of MEH-PPV for a typical structure shown in Fig. 10.26a, b [32]

In this structure, ZnO NR were grown by electro-chemical method over ITO (15 Ω/□), after that LiF (10 nm) and Al contact were vacuum evaporated. The overall thickness of the device was 900 nm. A comparison of *J* versus *V* and luminescence versus *J* with and without ZnO nanorods is shown in Fig. 10.27a, b

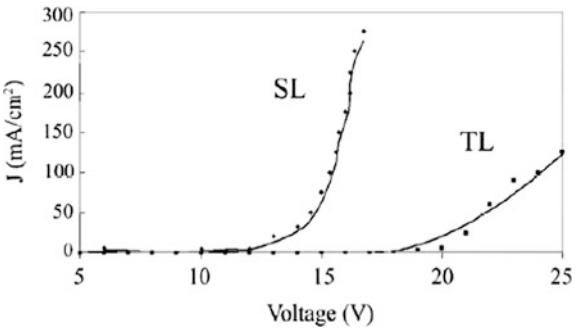

Fig. 10.24 Current density—bias voltage characteristics of SL and TL devices

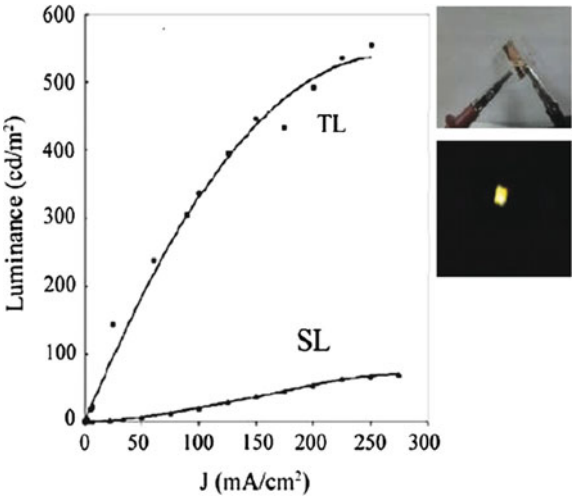

Fig. 10.25 Luminance as a function of current density for the TL and SL devices

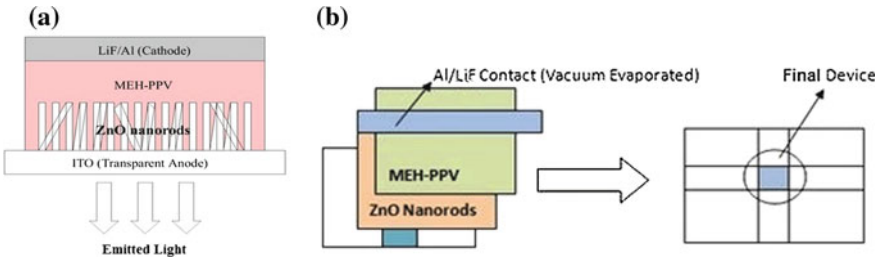

Fig. 10.26 **a** incorporation of ZnO nanorods in single layer structure. **b** final device structure

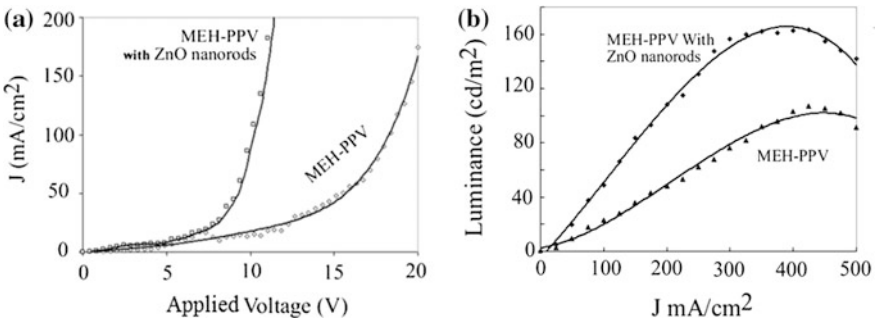

Fig. 10.27 **a** *J–V* characteristics of MEH-PPV-based PLEDs. **b** luminance characteristics for MEH-PPV PLEDs with and without ZnO nanorods

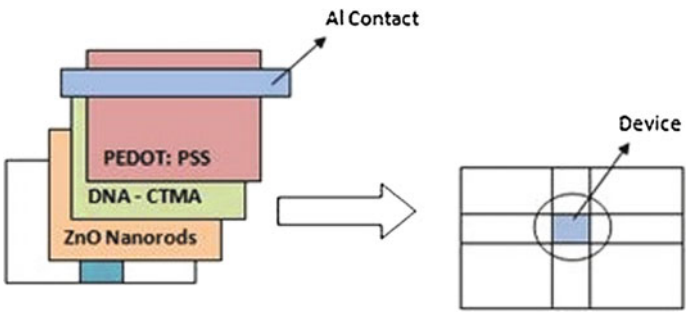

Fig. 10.28 Schematic of ZnO nanorods-based UV LED

which indicate a significant enhancement in the performance of LED. The turn-on voltage decreases and luminance increases by incorporation of ZnO NRs.

The reason is that ZnO NRs unwind the polymer chains and connect them in such a way that an alternate mechanism for charge transfer is obtained besides already present normal hopping process. Another improved structure is shown in Fig. 10.28.

Here there is an enhancement in UV emission due to Burstein Moss effect [33, 34]. Vertically aligned ZnO NRs can also be fabricated cost effectively by hydrothermal method with the help of seed layer [35]. These LEDs have been proposed to be used both for UV LED as well as UV lasers.

10.7 Conclusion

Conducting polymers and based devices is one of the hot areas of research where efforts are being made all over the world to synthesize new polymer materials to achieve higher mobility (at least one to two orders of magnitude higher) of the charge carriers so as to obtain higher efficiency and lower cost. There is a need to address the stability issues besides developing low-power consuming devices. The future of the conducting polymer-based electronics is very promising, and in the coming days, these materials may replace some of the conventional materials used in the present day electronic devices.

The prospects of OLEDs in industry are very bright. Commercialization of these OLEDs in displays, lighting, TV screens, etc., is in high progress.

References

1. Times of India page 21 'Energy conservation' dated 28 Feb. 2009, Saturday
2. Lucifer™ Lights Pvt. Ltd. (www.ledindia.com)
3. H.S. Kang, M.S. Kim, K.T. Park, K.M. Kim, T.H. Lee et al., Curr. Appl. Phys. **1**, 443 (2001)
4. C. Ulbricht, B. Beatrice et al., Adv. Mater. **21**, 4418 (2009)
5. B.W. D'Andrade, S.R. Forrest, Adv. Mater. **16**, 1585 (2004)
6. H. Youn, M. Yang, Appl. Phys. Lett. **97**, 243302 (2010)
7. D. Madhwal, in *Development of Conducting Polymer Based White Light Emitting* Diode. Ph. D. thesis, University of Delhi, p. 5
8. S.H. Jin, S.Y. Kang, I.S. Yeom, J.Y. Kim, S.H. Park, K. Lee et al., Chem. Mater. **14**, 5090 (2002)
9. C.C. Huang, H.F. Meng, G.K. Ho, C.H. Chen, C.S. Hsu, J.H. Huang et al., Appl. Phys. Lett. **84**, 1195 (2004)
10. C. Ego, D. Marsitzky, S. Becker, J. Zhang, A.C. Grimsdale, K. Muellen et al., J. Am. Chem. Soc. **125**, 437 (2003)
11. A.B. Kaiser, Rep. Prog. Phys. **64**, 1 (2001)
12. R.H. Friend et al., Nature **397**, 121 (1999)
13. H. Burroughs, D.D.C. Bradley, A.R. Brown, R.H. Friend, Nature **347**, 539 (1990)
14. A.R. Brown, D.D.C. Bradley, P.L. Burns, J.H. Burroughes, R.H. Friend, N. Greenham, A.B. Holmes, A. Kraft, Appl. Phys. Lett. **61**, 2793 (1992)
15. en.wikipedia.org/wiki/Lighting, "comparison of various light sources"
16. http://jeb.biologists.org/cgi/content/full/207/14/2373
17. https://en.wikipedia.org/wiki/Incandescent_light_bulb
18. R. Song, Y. Dduan, S. Chen, Y. Zhao, J. Hou, S. Liu, Semic. Sci. Tech. **22**, 728 (2007)
19. J.H. Seo, J.H. Seo, J.H. Park, Y.K. Kim, J.H. Kim, G.W. Hyung, Appl. Phys. Lett. **90**, 3507 (2007)

20. H.A. Al Attar, A.P. Monkman, M. Tavasli, S. Bettington, M.R. Bryce, Appl. Phys. Lett. **86**, 121101 (2005)
21. D. Madhwal, S.S. Rait, A. Kumar, A. Verma, K. Tada, M. Onoda, P.K. Bhatnagar, P.C. Mathur, J. Mater. Sci. **45**, 3300 (2010)
22. U. Scherf, D. Neher, Advances in polymer science. Polyfluorenes **212**
23. Y. Lyu, J. Kwak, W.S. Jeon, Y. Byun, H.S. Lee, D. Kim, C. Lee, K. Char, Adv. Funct. Mater. **19**, 420 (2009)
24. D. Madhwal, S.S. Rait, A. Verma, A. Kumar, M. Onoda, P.K. Bhatnagar, P.C. Mathur, PhysicaScripta **81**, 0657 (2010)
25. J.A. Hagen, W. Li, A.J. Steck, J.G. Grote, Appl. Phys. Lett. **88**, 171109 (2006)
26. D. Madhwal, S.S. Rait, A. Verma, A. Kumar, P.K. Bhatnagar, P.C. Mathur, M. Onoda, J. Lumin. **130**, 331 (2010)
27. W.R. Salaneck et al., The metal on polymer interface in polymer light emitting diodes. Adv. Mater. **8**, 48 (1996)
28. R.R. Chance, A. Prock, R. Sibey, Comments on the classical theory of energy transfer. J. Chem. Phys. **62**, 2245 (1975)
29. I. Singh, P.K. Bhatnagar, P.C. Mathur, I. Kaur, L.M. Bharadwaj, R. Pandey, Carbon **46**, 1141 (2008)
30. I. Singh, A. Verma, I. Kaur, L.M. Bharadwaj, V. Bhatia, V.K. Jain, C.S. Bhatia, P.K. Bhatnagar, P.C. Mathur. J. Polym. Sci. Part B: Polym. Phys. **48**, 89 (2010)
31. I. Singh, D. Madhwal, A. Verma, A. Kumar, S.S. Rait, I. Kaur, L.M. Bharadwaj, C.S. Bhatia, P.K. Bhatnagar, P.C. Mathur, J. Lumin. **130**, 2157 (2010)
32. R. Bhardwaj, in *Development and Characterization of Conducting Polymer/ZnO Based Bio-Light Emitting* Diode. Ph. D. thesis, University of Delhi (2013)
33. E. Burstein. Phys. Rev. **93**, 632 (954)
34. T.S. Moss, Proc. Phys. Soc. **67**, 775 (1954)
35. K. Gautam, I. Singh, P.K. Bhatnagar, K. Rao Peta, Superlattices Microstruct. **93**, 101–108 (2016)

Chapter 11
Hematological Complications and Rouleaux Formation of Blood Components (Leukocytes and Platelet Cells) and Parameters

Hafeez Ullah, Munir Akhtar and Fayyaz Hussain

Abstract This chapter has the detailed and depth knowledge about the hematological complications and Rouleaux formation of blood components (leukocytes and platelet cells) and parameters. The purpose of this chapter is to determine the changes in three parameters, i.e., cells count, shape of cells, and size of cells, prior and after addition of three analytes, i.e., sugar, sodium chloride, and pure water, for ten varying concentrations, i.e., from 0 to 450 mM, admixed in 2 ml blood for sugar [$C_6H_{12}O_6$], 3 ml blood for sodium chloride [NaCl] and 4 ml blood for pure water. We have also discussed the effects of sugar, salt, and distilled water in comparison with the preexisting literature. This chapter also contains information's about sample preparation; methodology of bright and dark field microscopy under transmission mode used for each blood cells and parameters, 2-D images of each phantom of each analyte for its normal sample and admixed sample, tables and graphs to express the variation in parameters relative to each phantom, results of each phantom and detailed discussions about changes in blood parameters and components mentioned above for each analyte.

H. Ullah (✉)
Department of Physics, The Islamia University of Bahawalpur,
Bahawalpur 63100, Pakistan
e-mail: hafeezullah79@gmail.com

M. Akhtar
Department of Physics, Laser and Optronics Laboratory,
Bahauddin Zakariya University, Multan 60800, Pakistan
e-mail: munir.akhtar126@gmail.com

F. Hussain
Department of Physics, Material Simulation Research Laboratory (MSRL),
Bahauddin Zakariya University, Multan 60800, Pakistan
e-mail: fayyazhussain248@yahoo.com

Z.H. Khan (ed.), *Nanomaterials and Their Applications*,
Advanced Structured Materials 84, https://doi.org/10.1007/978-981-10-6214-8_11

Abbreviations

HGB	Hemoglobin
RDW	Red blood cells distribution width
HCT	Hematocrit
MCV	Mean corpuscular volume
MPV	Mean platelet volume
RBCs	Red blood cells
PDW	Platelet distribution width
PCT	Platelet crit
PRP	Platelet rich plasma
WBCs	White blood cells

11.1 Introduction

Blood is a fluid in our body which is not only responsible for transportation of nutrients (proteins, fats, minerals, carbohydrates, etc.) but also waste materials (carbon dioxide) out of body [1]. Blood is composed of plasma and cells. Blood cells are red blood cells (erythrocyte), white blood cells (leukocytes), and platelet cells (thrombocytes) [2]. Each male contains 4.7–6.1 million and female contains 4.2–5.4 million erythrocytes in one microlitter, 4×10^3 to 11×10^3 leukocytes and 2×10^5 to 5×10^5 thrombocytes [3, 4]. Normally, two to three drops have 1 billion RBCs with a ratio 600:1:40 of RBCs, WBCs, and platelets [3]. This chapter has the detailed and depth knowledge about the effects of sugar, salt, and pure water on shape, size; blood parameters and cells count of both leukocytes and thrombocytes. Many laboratory techniques and methods can be used for this type of biological and hematological study such as optical diffuse reflectance (ODR) [5], mid infrared spectroscopy (MIS) [6], light polarimetry [7], Raman spectroscopy [7], photo acoustic spectroscopy (PAS) [8], computed tomography (CT), magnetic resonance imaging (MRI) [9], optical coherence tomography (OCT) [10], and light microscopy [11]. Every method has its own advantages but light microscopy has many advantages over other techniques like easy to take it from one place to another, live observation of cells or bodies with no harmful radiations, cheap without little exception, has high magnification power. It gives information's about biological activities and parameters such as cell division, cell movement, shape and size of cells, pigments, etc. There exist many microscopic techniques like infrared microscopy (IRM), scanning probe microscopy (SPM), ultraviolet microscopy (UVM),) digital holographic microscopy (DHM), digital pathology (virtual microscopy), laser microscopy (LM), optical microscopy (OM), electron microscopy (EM) and optical microscopy (OM) and amateur microscopy (AM) [11], but we used light microscopic technique (bright and dark field microscopy) under transmission mode. In our work, we use light microscopy to diagnose blood cells

and parameters, i.e., white light microscopy for WBCs and PRP under dark field microscopy for platelet cells. This type of microscopy uses beam of light that makes fluorescence in sample or slide, transmitted through it, and one can observe many times magnified view of cells through eyepiece.

11.2 Materials and Methods

In this research work, we have used two types of samples in order to diagnose the blood parameters and blood cells (leukocytes and thrombocytes only).

11.2.1 Sample Type I for Leukocytes

To diagnose the WBCs parameters, we used microscope under transmission mode for aforementioned ten concentrations of sugar, sodium chloride, and pure water from 0 to 450 mM range with difference of every 50 mM. We poured 2 ml blood for sugar, 3 ml for sodium chloride, and 4 ml for pure water in ten different heparin tubes. Heparin is used as anticoagulant. Then, we mixed each concentration of every analyte with a difference of every 50 mM in each heparin tube. Heparin works as anticoagulant agent. 0 mM means no extra analyte is admixed in first sample. Blood smear of each analyte sample was prepared by using ethanol as fixing agent and field strain (A, B) for staining. Slide for each sample was then examined after putting one drop of emersion oil under microscope model (Olympus CX41) at 100×. The images of each sample set were taken with digital camera model (Canon EOS 600D, Japan). Whole experiment was conducted at room temperature.

11.2.2 Sample Type II for Platelet Cells

Blood with blood group (**AB+)** of a healthy person was taken into ten EDTA tubes for each analyte. EDTA is an anticoagulant agent. Each tube for sugar has 2 ml blood, for salt has 3 ml blood, and for distilled water has 4 ml blood. We mixed aforementioned ten varying concentrations of each analyte into each heparin tube. We put each sample in centrifuge machine at 800 rpm for 4 min to prepare platelet rich plasma. Then, we put one drop of PRP from each sample on each slide and examined it after covering each slide with cover slip under dark field microscope at 40×. Whole experiment was conducted at room temperature. PRP of each sample of each analyte is shown in Fig. 11.1.

Fig. 11.1 Showing platelet rich plasma of each analyte

11.3 Effects of Glucose on Blood Cells

Glucose [$C_6H_{12}O_6$] has 180 molecular weight and has 180 g/L in one mole. It is one of the carbohydrates which are the best and vital source of energy. All sources of glucose are not good for health such as soft drinks and foods, although they are energy rich [12]. There exist four categories of sugar HFCS (corn starch), sucrose (table sugar), glucose (sugar in blood), and fructose (sugar in fruits). Adenosine triphosphate (ATP) which is the energy and is released when glucose is glycolysed [13]. Glucose level without and with meal is round about 70–99 mg/dL and 140 mg/dL, respectively [14]. Its level in blood constitutes either hyperglycemia (glucose more than normal level) or hypoglycemia (glucose less than normal level) [15]. The efficiency of platelet cells is increased due to resistance or less production of insulin either by hyperglycemia or by hypertriglyceridemia by the processes of glycation or osmotic burst/lyses of cells during abnormal metabolic process. Platelet cells release excess calcium by reducing the production of nitric oxide and disable the cellular endothelial by the processes like inflammation and oxidative stress. Thus, in diabetes platelet cells become more effective [16, 17].

11.3.1 Results

Two-dimensional photograph of glucose analyte under light microscope of each sample for ten varying concentrations (0–450 mM) is shown in Fig. 11.2a–j

11.3.2 Regions of Interest of WBCs for Sugar Analyte

Two-dimensional photographs of glucose analyte for platelet cells under dark field microscopy for each sample range (0–450 mM) are shown in Fig. 11.3a–j.

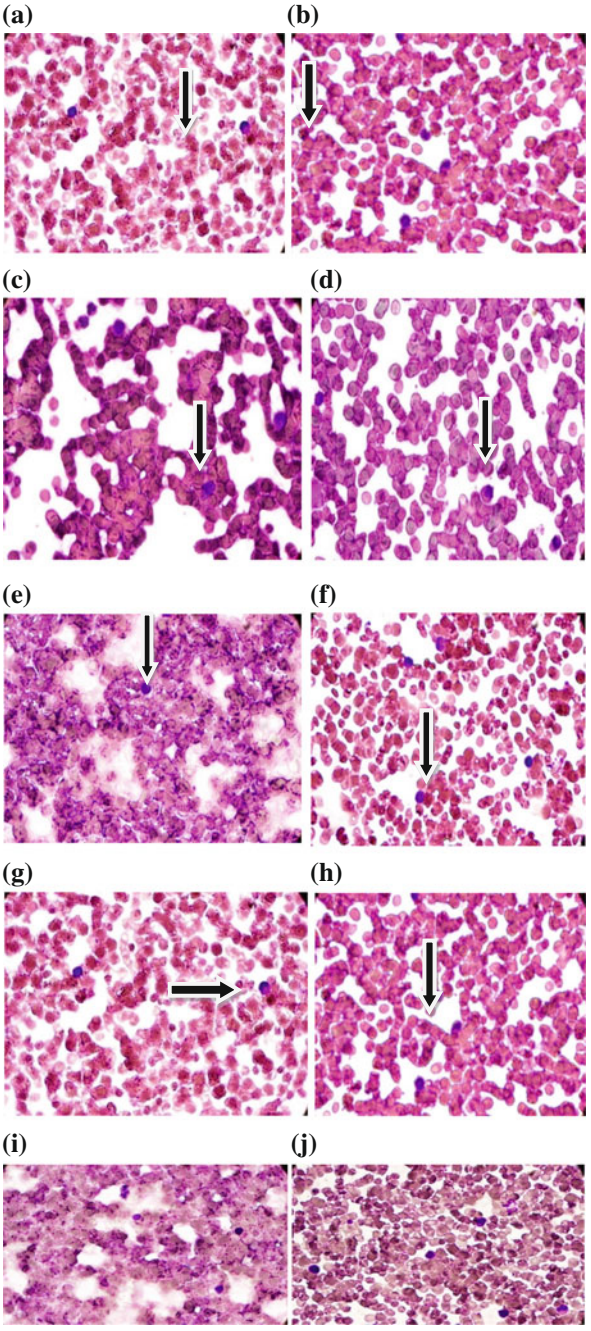

Fig. 11.2 2-D images of whole blood phantom prepared under white light microscope with 2 mL blood in heparin tube for **a** 0 mM (original sample) concentration of glucose, **b** 50 mM (18 mg) concentration of glucose, **c** 100 mM (36 mg) concentration of glucose, **d** 150 mM (54 mg) concentration of glucose, **e** 200 mM (72 mg) concentration of glucose, **f** 250 mM (90 mg) concentration of glucose, **g** 300 mM (108 mg) concentration of glucose, **h** 350 mM (126 mg) concentration of glucose, **i** 400 mM (144 mg) concentration of glucose and, **j** 450 mM (162 mg) concentration of glucose

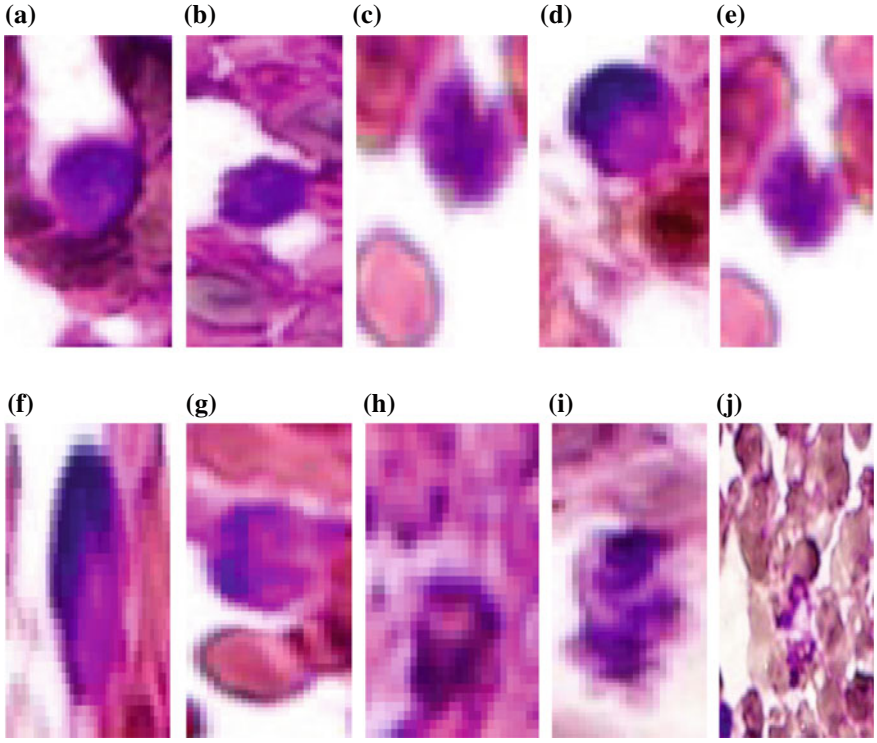

Fig. 11.3 Regions of interests (ROIs) for WBCs under sugar analyte concentrations 0–450 mM (**a**–**j**)

11.3.3 Statistical Comparison Under Glucose [$C_6H_{12}O_6$]

We admixed aforementioned ten different concentrations of sugar from 0 up to 450 mM with a step size of 50 mM into 2 ml blood, performed CBC of each sample with the help of celltac α hematological analyzer, and noted the blood components and parameters as given in Table 11.1.

11.3.4 Discussions and Conclusive Remarks

Sugar is a dietary part but its abnormal use creates metabolic disorders which further disturb many of the biological systems. Here, we focus on blood cells leukocytes and thrombocytes. Under increasing concentration of sugar, size of WBCs increases from normal size due to diffusion of sugar into cells and finally they burst/lyse as shown in Fig. 11.2a–j. Size of platelet cells starts increasing for 0–250 mM and cells clump with each other i.e. Rouleaux formation then further

Table 11.1 Change in parameters and cells count relative to glucose [$C_6H_{12}O_6$] concentrations

Sr. No.	Sugar concentration (mM)	No. of WBCs (10^3/μL)	No. of platelet cells (10^3/μL)	No. of RBCs (10^6/μL)	HGB (g/dL)	RDW (%)	PDW (%)	MCV (fL)	MPV (fL)	HCT (%)	PCT (%)
1	0	6.3	289	2.88 L	7.3 L	12.6	17.0	73.3 L	8.5	21.1 L	0.25
2	50	5.9	284	2.88 L	7.4 L	12.4	17.4	73.3 L	8.1	21.1 L	0.23
3	100	5.0	253	2.90 L	7.4 L	13.0	17.9	73.4 L	8.0	21.3 L	0.20
4	150	4.4	259	2.86 L	7.2 L	12.8	17.2	74.1 L	7.7	21.2 L	0.20
5	200	4.6	244	2.85 L	7.2 L	12.9	17.3	74.0 L	7.8	21.1 L	0.19
6	250	4.4	256	2.81 L	7.1 L	13.0	17.3	73.7 L	7.9	20.7 L	0.20
7	300	4.3	240	2.86 L	7.1 L	12.6	18.3H	74.1 L	7.6	21.2 L	0.18
8	350	4.3	247	2.79 L	7.1 L	13.1	17.3	74.2 L	7.6	20.7 L	0.19
9	400	4.4	290	2.75 L	7.0 L	12.7	17.4	73.5 L	8.2	20.2 L	0.24
10	450	4.5	307	2.79 L	7.0 L	13.1	17.9	74.2 L	8.0	20.7 L	0.25

addition of glucose from 300 to 450 mM they shrink in size as shown in Fig. 11.4. Shape of WBCs is also effected by hyperglycemia; the cells change from regular spherical to elongated up to 300 Mm and then change into elliptical shape at 450 mM as shown in Figs. 11.1, 11.2, while shape of platelet cells becomes elliptical up to 250 mM and then starts becoming normal like a plate above 300 mM as shown in Fig. 11.5. Sugar has same chemical structure like vitamin C. Vitamin C boosts up immune system by helping the leukocytes to fight against pathogens, while sugar weakens the defensive system. So, hyperglycemia not only weakens the defensive system by reducing the activity of WBCs but also count of leukocytes by destroying them. Thrombocytes count from 0 to 300 mM decreases gradually because insulin controls the sugar level, but as the sugar level increases above 300 mM then platelet cells start increasing as shown in Fig. 11.6. Thus, diabetes can cause deficiency of insulin, disorders of cellular walls, metabolic disorders, and inflammation, but platelet activity is increased by diabetes [21]. Hence, there is a suggestion about treatment of dengue with diabetes. RBCs also decrease in numbers under hyperglycemia due to bursting/lyses as shown in Fig. 11.6. HGB is a red pigment present in blood which plays a vital role to carry oxygen to different parts of body and gives red color to blood. HGB level gradually decreases with increasing concentration of glucose as shown in Fig. 11.7. HCT or PCV (packed cell volume) or EVF (erythrocytes volume fraction) is the volume percentage of RBCs. Its abnormal value is life threatening, and a low HCT or EVF value is noticed against increasing concentration of sugar as shown in Fig. 11.7. Low HCT results in anemia and leukemia. MCV is the measure of average volume of RBCs and is helpful in classification of type of anemia. MCV shows increasing trend under hyperglycemia as shown in Fig. 11.7 and thus showing trend from normocytic anemia to macrocytic anemia. RDW is the measure of range of variations of RBCs. RDW shows an increasing trend with increasing concentration of sugar as shown in Fig. 11.7. High value of RDW also causes anemia. MPV is the measure of average size of platelet cells and is useful to predict the destruction or production of platelet cells. High MPV results in destruction of platelet cells. Figure 11.7 shows decreasing trend of MPV and thus indicates production of cells. PDW is used to express the variations in size of platelet cells. PDW increases with increasing concentration of sugar. MPV and PDW are related with each other and are generally direct in relation but here is opposite condition as shown in Fig. 11.7. Low MPV with high PDW results in anemia. PCT is a source to measure quantitative disorders/abnormalities of platelet cells. PCT shows thrombocytopenia up to 350 mM and then thrombocytosis up to 450 mM as shown in Fig. 11.7. HGB, RDW, HCT, and MCV are the parameters related to RBCs, while MPV, PDW, and PCT are related with platelet cells.

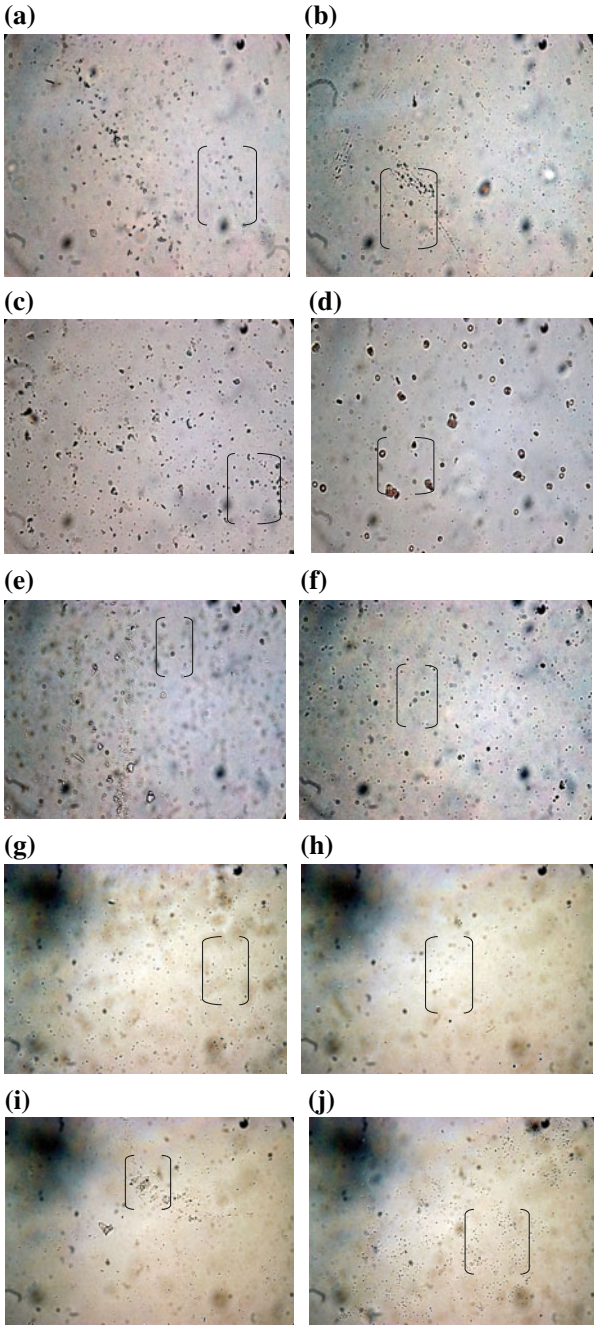

Fig. 11.4 Dark field microscopic 2-D images of PRP phantom prepared with 2 mL in EDTA tube for **a** 0 mM concentration of glucose, **b** 50 mM (18 mg) concentration of glucose, **c** 100 mM (36 mg) concentration of glucose, **d** 150 mM (54 mg) concentration of glucose, **e** 200 mM (72 mg) concentration of, glucose, **f** 250 mM (90 mg) concentration of glucose, **g** 300 mM (108 mg) concentration of glucose, **h** 350 mM (126 mg) concentration of glucose, **i** 400 mM (144 mg) concentration of glucose and, **j** 450 mM (162 mg) concentration of glucose

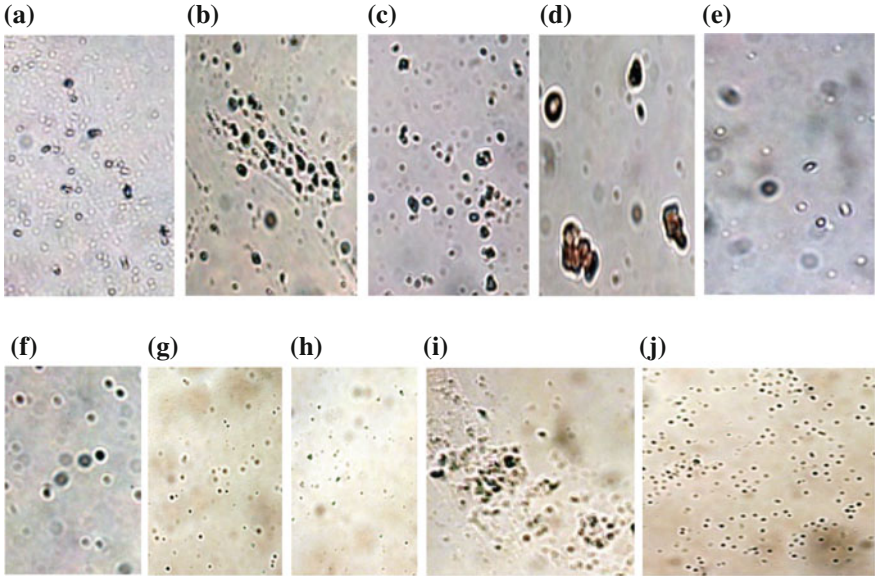

Fig. 11.5 ROIs of platelet cells for sugar analyte's concentrations (0–450 mM)

11.4 Effects of Salt (NaCl) on WBCs and Platelet Cells

Salt maintains homeostasis in body due to its vital dietary part of our routine. Its normal value is between 135 and 145 mM/L in the human body. Depending upon concentration, it has two conditions, less than normal value and higher than normal value are termed as hyponatremia and hypernatremia respectively [18–20]. NaCl is its chemical formula with 58.5 as its molecular weight. Blood pressure is associated with concentration of salt. NaCl is also used in medicine, agriculture, as cleansing agent, in food industry, and in pure form used as optical agent [21]. Hypernatremia results in production of protein-like interleukin which in turn produces large amount of helper cells which damages the defense system by destroying healthy tissues (Table 11.2). This situation is termed as autoimmunity. So, hypernatremia not only results in high blood pressure but also weakens the immune system [22, 23]. NaCl is very vital dietary part and causes high blood pressure due to its high usage. Many disorders are caused by its accumulation in blood capillaries like resistance against activities of arteries, increase in renal function, increase in mass of left ventricle, increase in number of strokes and increase in the stiffness, and disorders in cardiovascular system [19]. During hypernatremia, the platelet cells function is increased due to accumulation of (Na) [24, 25]. Hypernatremia shows Rouleaux formation (grouping or colonies formation) of platelet cells due to high blood pressure with and without family history. Molecular weight of sodium chloride is 58.5. Its chemical formula is NaCl.

Table 11.2 Change in blood parameters and cells count relative to salt (NaCl) concentrations

Sr. No.	Salt (NaCl) concentration (mM)	No. of WBCs (10^3/μL)	No. of platelet cells (10^3/μL)	No. of RBCs (10^6/μL)	HGB (g/dL)	RDW (%)	PDW (%)	MCV (fL)	MPV (fL)	HCT (%)	PCT (%)
1	0	6.3	289	2.88 L	7.3 L	12.6	17.0	73.3 L	8.5	21.1 L	0.25
2	50	4.9	325	2.73 L	6.9 L	13.2	17.4	74.4 L	8.1	20.3 L	0.26
3	100	4.5	341	2.74 L	7.0 L	13.0	17.9	74.1 L	7.8	20.3 L	0.27
4	150	4.0	327	2.80 L	7.0 L	12.5	18.0	73.9 L	8.3	20.7 L	0.27
5	200	3.8	327	2.94 L	7.4 L	12.6	17.9	74.5 L	7.9	21.9 L	0.26
6	250	3.6	306	2.92 L	7.4 L	13.2	17.2	74.7 L	7.7	21.8 L	0.24
7	300	3.9	321	3.08 L	7.8 L	12.7	17.3	74.0 L	7.7	22.8 L	0.25
8	350	3.6	318	3.02 L	7.8 L	12.8	17.8	75.2 L	7.8	22.7 L	0.25
9	400	2.2	309	2.20 L	5.5 L	13.6	18.3H	75.5 L	7.7	22.5 L	0.24
10	450	3.5	321	2.98 L	7.5 L	13.8	17.2	76.2 L	7.6	22.7 L	0.24

11.4.1 Materials and Methods

For the effects of salt on WBCs and Platelet cells, same method has been adopted as given in Sect. 1.3.1 with 3 ml blood for each phantom.

11.4.2 Results

Two dimensional photographs of WBCs of each phantom for aforementioned ten varying concentration of NaCl from 0 to 450 mM under microscope with bright field at 100X are given in Fig. 11.8.

11.4.3 Regions of Interest for WBCs Under Salt

Regions of Interest of WBCs (ROI) of each phantom for aforementioned ten varying concentration of NaCl from 0 to 450 mM under microscope with dark field at 40X are given in Fig. 11.9.

11.4.4 Regions of Interest for Platelet Cells Under Salt

ROIs of platelet cells of each phantom for aforementioned ten varying concentration of NaCl from 0 to 450 mM are given in Fig. 11.10

11.5 Discussions

Hypernatremia causes high blood pressure in general. WBCs are more affected than RBCs by NaCl because they have membrane and nucleus. Under hypernatremia water moves out of blood vessels and causes dehydration. When concentration of salt is less as compared to normal value then water will move into blood vessels. This type of changes brings renal disorders [26]. WBCs under hypernatremia concise or reduce in size and bring changes in shape from round to elliptical as shown in Fig. 11.12a–j, while platelet cells also show size shrinkage and shape deformation due to Rouleaux formations with increasing concentration of salt as shown in Fig. 11.11a–j. Under hypernatremia, count of WBCs goes high which is harmful because these cells start damaging the healthy tissues and the condition is known as autoimmunity like sclerosis (hardening of tissues) diabetes type-1 and [18, 27]. WBCs count goes on decreasing up to 400 Mm and then above 400 Mm goes on increasing as shown in Fig. 11.8. Platelet cells count is not linear factor due to Rouleaux formation for some middle concentration samples, but graphically under hypernatremia number of platelet cells increases generally as shown in Fig. 11.8. HGB is a red pigment present in

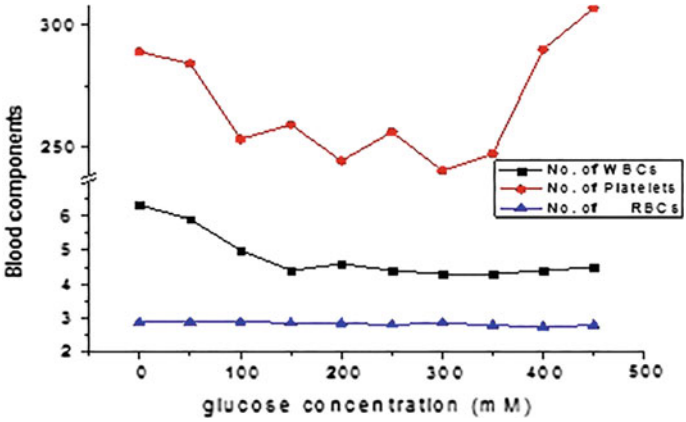

Fig. 11.6 Comparison of sugar concentrations and blood cells

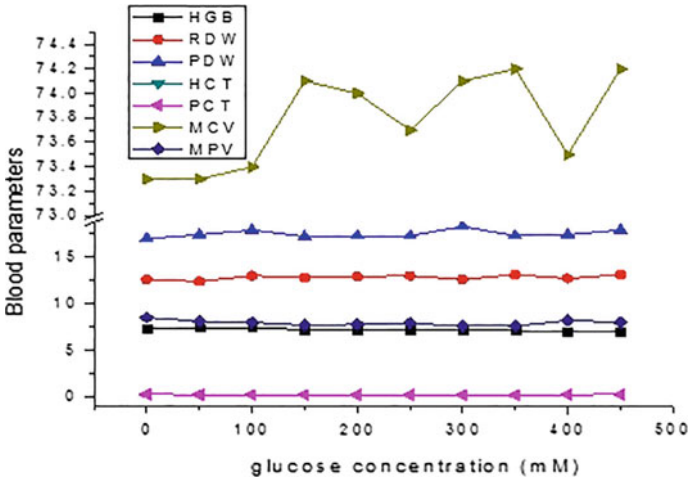

Fig. 11.7 Comparison of sugar concentrations and blood parameters

blood which plays a vital role to carry oxygen to different parts of body and gives red color to blood. HGB level is less than normal value up to 150 mM and then starts increasing with increasing concentration of NaCl up to 450 mM as shown in Fig. 11.9. So it can be suggested that high dose of salt can be used to improve HGB level in blood. HCT or PCV (packed cell volume) or EVF (erythrocytes volume fraction) is the volume percentage of RBCs. Low HCT results in anemia and leukemia. Its abnormal value is life threatening, and a high HCT or EVF value is noticed against increasing concentration of salt as shown in Fig. 11.13. MCV is the measure of average volume of RBCs and is helpful in classification of type of anemia. MCV shows increasing trend under hypernatremia as shown in Fig. 11.9 and thus showing

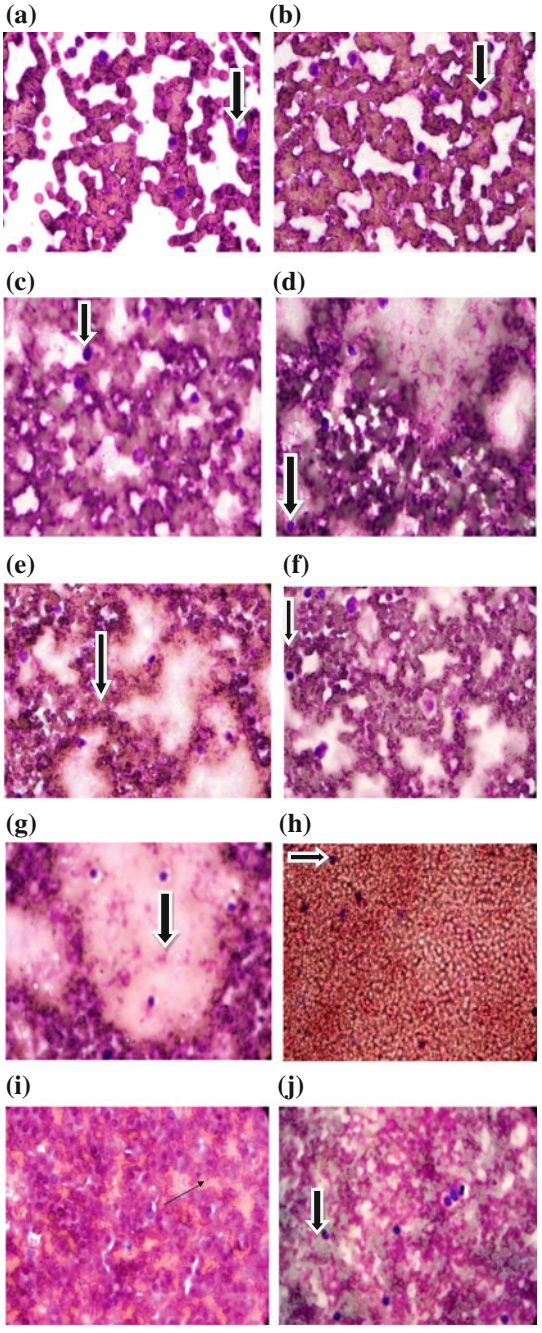

Fig. 11.8 a–j Showing photograph of WBCs of each phantom for ten varying concentrations of salt ranging from 0 to 450 mM with step size of 50 mM, respectively, under microscope at 100X

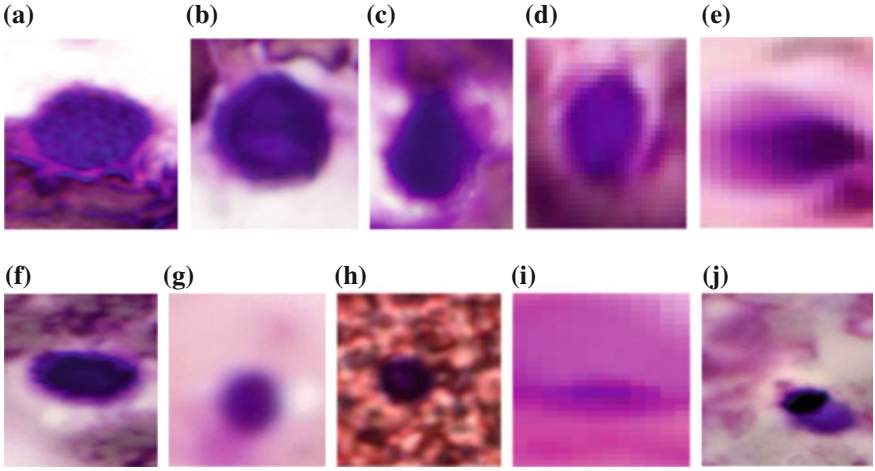

Fig. 11.9 ROIs of WBCs under salt concentrations (0–450 mM)

trend from normocytic anemia to macrocytic anemia. RDW is the measure of range of variations of RBCs. RDW shows an increasing trend with increasing concentration of salt as shown in Fig. 11.9. High value of RDW also causes anemia. MPV is the measure of average size of platelet cells and is useful to predict the destruction or production of platelet cells. High MPV results in destruction of platelet cells. Figure 11.9 shows decreasing trend of MPV and thus indicates production of cells. Thus, it can be suggested that high usage of salt is beneficial to overcome low platelet count in dengue patients. PDW is used to express the variations in size of platelet cells. PDW increases with increasing concentration of sugar. MPV and PDW are related with each other and are generally direct in relation but here is opposite condition as shown in Fig. 11.9. Low MPV with high PDW results in anemia. PCT is a source to measure quantitative disorders/abnormalities of platelet cells. PCT shows trend of thrombocytopenia up to 200 mM and then thrombocytosis up to 450 mM as shown in Fig. 11.9. HGB, RDW, HCT, and MCV are the parameters related to RBCs, while MPV, PDW, and PCT are related with platelet cells.

11.6 Effects of Distilled Water on Blood Cells

Water can move inside and outside of cells due to osmosis and diffusion because membranes of cells are made up of permeable proteins. Water due to its movement within the cells forms three types of solutions: hypertonic solution, hypotonic solution, and isotonic solution [18]. **Hypertonic solutions:** When the concentration of water is greater inside the cell than outside is called hypertonic solution. Under

hypertonic solution water will move from inside to outside and cell will shrink and unable to perform natural process of cell division [18]. **Hypotonic solutions:** When the concentration of water is greater outside the cell than inside is called hypotonic solution. Under hypotonic solution, cell will swell and finally burst/lyse [18]. **Isotonic solutions:** If concentration of water inside and outside of cells is same then solution is termed as isotonic solution. Under isotonic solution, cells remain neutral [18].

11.6.1 Results

Two dimensional photographs of WBCs of each phantom for aforementioned ten varying concentration of water from 0 to 450 mM under microscope with bright field at 100X are shown in Fig. 11.14.

11.6.2 Regions of Interest for WBCs Under Water

2-D images of dark field microscopy of each phantom for ten different concentrations (0–450 mM) of water analyte with step size 50 mM are shown in Fig. 11.15a–j

11.6.3 Regions of Interest for Platelet Cells Under Water

ROIs of platelet cells of each phantom for aforementioned ten varying concentration of H_2O from 0 to 450 mM are given in fig. 11.16.

11.7 Statistical Comparison of Blood Components and Parameters Under Pure Water (H_2O)

We admixed ten different concentrations of water from 0 up to 450 mM with a step size of 50 mM into 4 ml blood and performed CBC of each sample with the help of celltac α hematological analyzer and noted the blood components and parameters as given in Table 11.3 and have been plotted in Figs. 11.17 and 11.18.

Table 11.3 Change in parameters and cells count relative to pure water (H_2O) concentrations

Sr. No.	Water concentration (µl)	No. of WBCs (10^3/µL)	No. of platelet cells (10^3/µL)	No. of RBCs (10^6/µL)	HGB (g/dL)	RDW (%)	PDW (%)	MCV (fL)	MPV (fL)	HCT (%)	PCT (%)
1	0	6.3	289	2.88 L	7.3L	12.6	17.0	73.3 L	8.5	21.1 L	0.25
2	50	5.7	331	2.98 L	7.6L	12.5	17.9	73.2 L	8.0	21.8 L	0.26
3	100	5.7	354	2.92 L	7.5L	12.5	17.9	72.6 L	8.2	21.2 L	0.29
4	150	5.5	333	2.80 L	7.0 L	12.5	18.2	73.9 L	8.3	20.7 L	0.27
5	200	5.7	349	2.94 L	7.4 L	12.6	17.9	74.5 L	7.9	21.9 L	0.26
6	250	5.7	349	2.92 L	7.4 L	13.2	17.2	74.7 L	7.7	21.8 L	0.24
7	300	5.7	333	3.08 L	7.8 L	12.7	17.3	74.0 L	7.7	22.8 L	0.25
8	350	5.8	375	3.02 L	7.8 L	12.8	17.8	75.2 L	7.8	22.7 L	0.25
9	400	5.7	345	2.02 L	5.5 L	13.6	18.3H	75.3 L	7.7	16.7 L	0.24
10	450	5.6	344	2.98 L	7.5 L	13.8	17.2	76.2 L	7.6	22.7 L	0.24

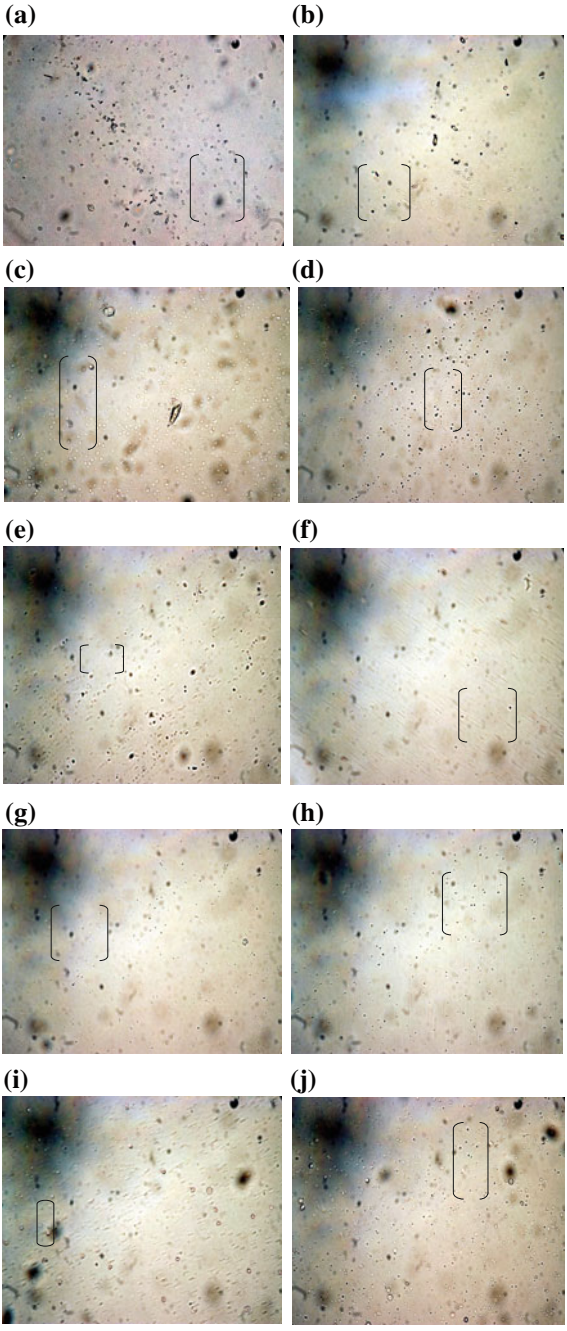

Fig. 11.10 a–j Showing photograph of platelet cells of each phantom for ten varying concentrations of salt ranging from 0 to 450 mM with step size of 50 mM, respectively, under dark field microscope at 40X

11.8 Results and Discussions

Under hypotonic solution of distilled water, the size of WBCs increases with increasing concentration of pure water. Leukocytes get swell and burst/lyse as shown in Fig. 11.15. Like leukocytes, platelet cells also grow in size with increasing concentration of distilled water as shown in Fig. 11.16 and region of interest for platelet cells under distilled water. Shape of WBCs also changes gradually from round to elliptical due to swelling by osmosis processes as shown in Fig. 11.15 and region of interest for leukocytes under distilled water. Thrombocytes also show same changes in shape as shown by leukocytes they become elongated from plate shape and finally elliptical as shown in Fig. 11.16 and region of interest for platelet cells under distilled water. Leukocytes count under hypotonic solution decreases due to bursting of cells as shown in Fig. 11.17. Platelet cells show opposite count; they increase in number up to 350 mM and then decrease as shown in Fig. 11.17. HGB is a red pigment present in blood which plays a vital role to carry oxygen to different parts of body and gives red color to blood. HGB level starts increasing from 50 mM, remains high up to 350 mM, and then starts decreasing as shown in Fig. 11.18. So it can be suggested that at very high concentration of pure water HGB level in blood becomes low and cannot perform properly [28]. HCT or PCV (packed cell volume) or EVF (erythrocytes volume fraction) is the volume percentage of RBCs. Low HCT results in anemia and leukemia. Its abnormal value is life threatening; a high HCT or EVF value is noticed against increasing concentration of water as shown in Fig. 11.18. MCV is the measure of average volume of RBCs and is helpful in classification of type of anemia. MCV shows increasing trend under hypernatremia as shown in Fig. 11.18 and thus showing trend from normocytic anemia to macrocytic anemia. RDW is the

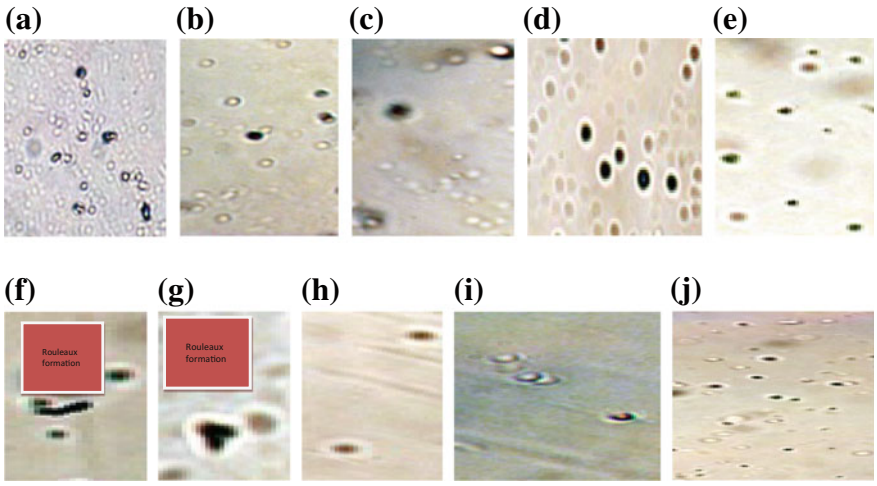

Fig. 11.11 ROIs for platelet cells under salt concentrations (0–450 mM)

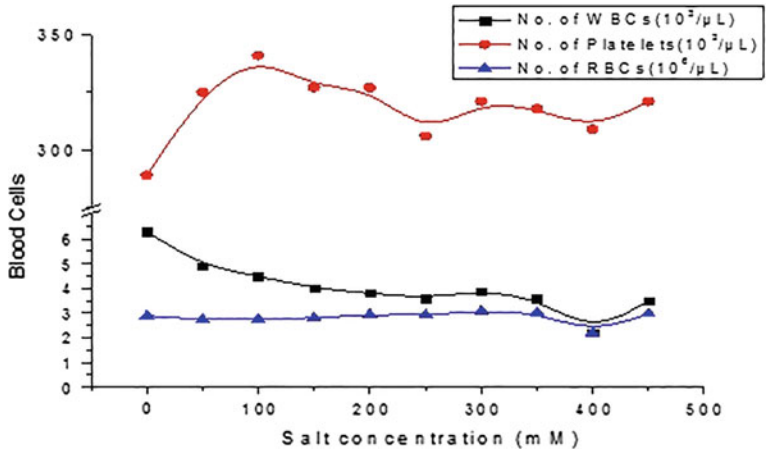

Fig. 11.12 Salt concentrations versus blood cells

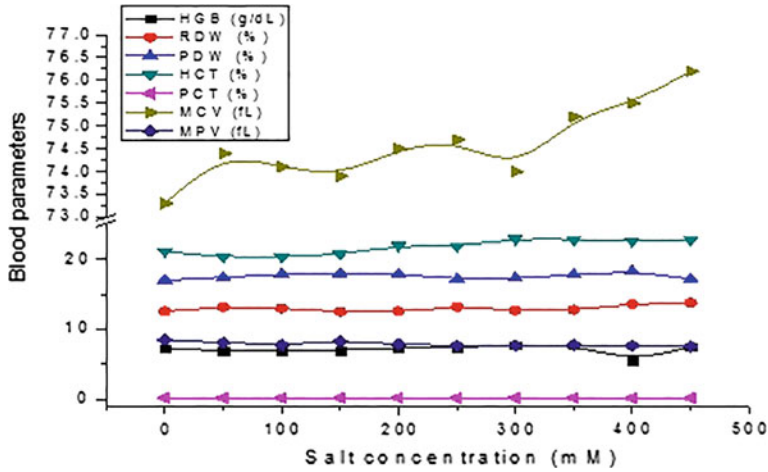

Fig. 11.13 Salt concentrations versus blood parameters

measure of range of variations of RBCs. RDW shows decreasing trend up to 150 mM, and with further increasing concentration of water it increases up to 450 mM as shown in Fig. 11.18. High value of RDW also causes anemia [29]. MPV is the measure of average size of platelet cells and is useful to predict the destruction or production of platelet cells. High MPV results in destruction of platelet cells. Figure 11.18 shows decreasing trend of MPV and thus indicates production of cells. Thus, it can be suggested that high usage of water is beneficial to overcome low platelet count in dengue patients. PDW is used to express the variations in size of platelet cells. PDW increases with increasing concentration of

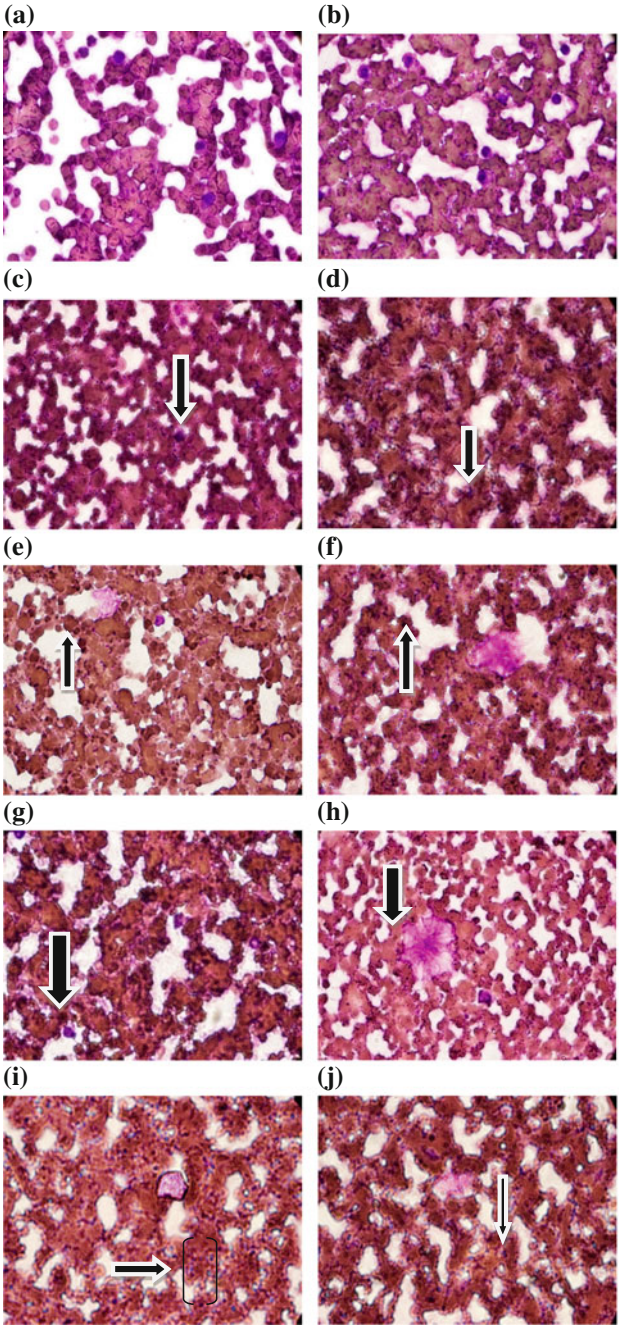

Fig. 11.14 **a–j** Two-dimensional images for each sample of WBCs ranging from 0 up to 450 mM using white field microscopy under transmission mode at 100X

water up to 400 mM. MPV and PDW are related with each other and are generally direct in relation but here is opposite condition as shown in Fig. 11.18. Low MPV with high PDW results in anemia. PCT is a source to measure quantitative disorders/abnormalities of platelet cells. PCT shows almost no change under increasing concentration of pure water as shown in Fig. 11.18 [30]. HGB, RDW, HCT, and MCV are the parameters related to RBCs, while MPV, PDW, and PCT are related with platelet cells (Fig 11.18).

11.9 Summary

Blood is composed of blood cells and plasma with many parameters. Blood in our body performs many important functions like supply of oxygen and nutrients, messenger functions, removal of waste materials, immunological functions, coagulation functions, regulation of body temperature, and pH hydraulic functions. These above given functions are disturbed by the abnormal use of these analytes. In this, we have given a detailed and depth knowledge about shape, size, and cells count of both leukocytes and thrombocytes. Under hypercondition of glucose, salt and distilled water shape of both cells changes almost from round to elliptical. Size of cells increases under hypercondition of glucose and distilled water which results

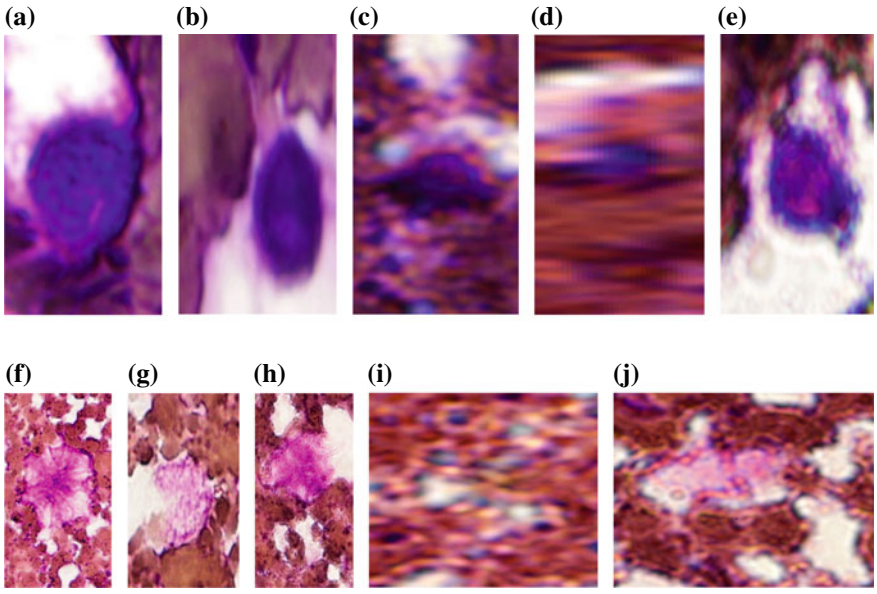

Fig. 11.15 ROIs for WBCs under pure water concentrations (0–450 mM) **a–j** Two-dimensional images of each sample range plateleting from 0 up to 450 mM showing the changes in shape and size of cells using dark field microscopy under transmission mode at ×40

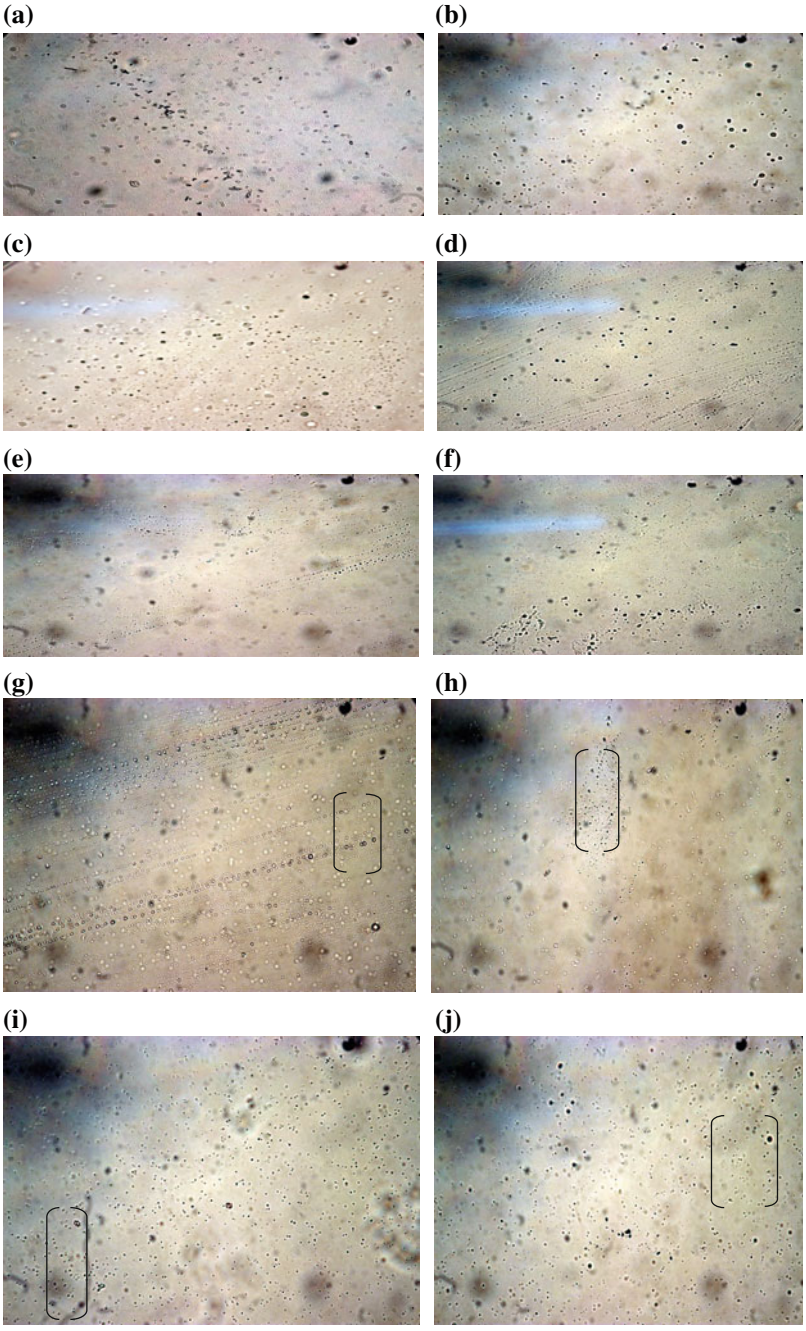

Fig. 11.15 (continued)

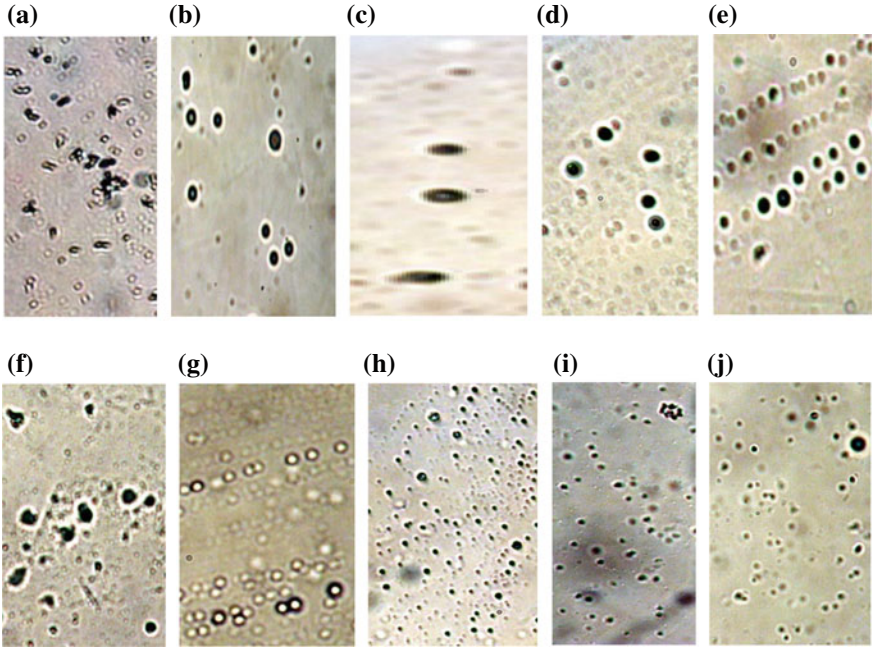

Fig. 11.16 ROIs for platelet cells under water concentrations (0–450 mM)

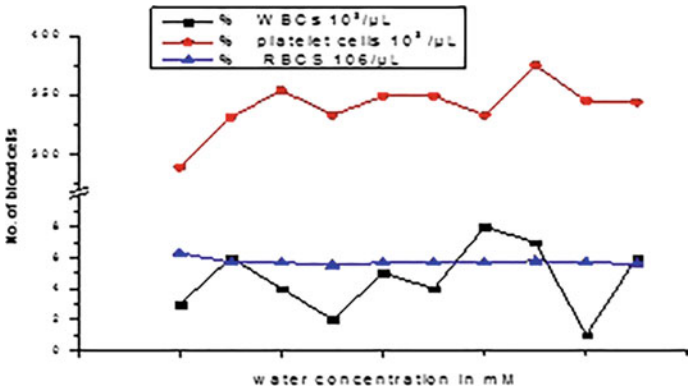

Fig. 11.17 Comparison of pure water concentrations and blood cell

lyses of cells, while leukocytes concise. Cells count of leukocytes under hypercondition of three analytes decreases for both glucose and distilled water, while under salt analyte they increase in number above 400 mM and cause autoimmune diseases. Count of thrombocytes under hypercondition of glucose and salt increases very slowly but under distilled water their count goes on increasing very sharply. HGB a red pigment in blood increases with increasing concentration of salt and

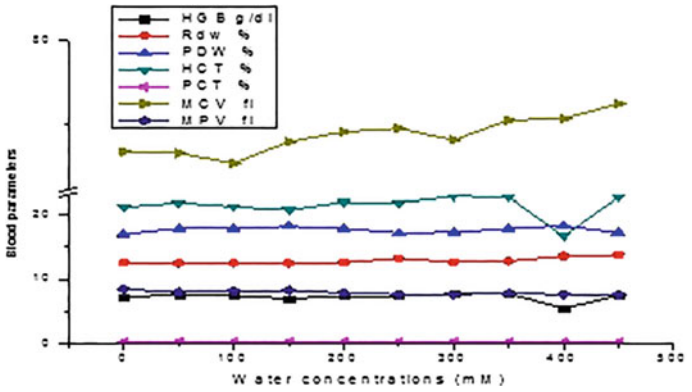

Fig. 11.18 Comparison of salt concentrations versus blood parameters and blood cells

distilled water but for sugar it decreases. HCT or PCV (packed cell volume) or EVF (erythrocytes volume fraction) decreases for sugar and increases for salt and distilled water little bit with increasing concentration. MCV in blood increases with increasing concentration of salt and distilled water but for sugar it decreases. RDW and PDW increase with increasing concentration of all three analytes. MPV decreases with increasing concentration of all three analytes. PCT which measures quantitative abnormalities of platelet cells almost remains same under increasing concentration of three analytes with few fluctuations in its values. All parameters almost have same value and same trend for each concentration. Thus, abnormal use of any of three analyte is toxic to many physiological, biochemical and metabolic processes, biological systems, and organs like immune system, respiratory system, blood circulatory system, lymphatic system, enzymes system and failures of organs like liver and heart.

References

1. C.F. Krieglstein, C. Anthoni, W.H. Cerwinka, K.Y. Stokes, J. Russell, M.B. Grisham et al., Role of blood- and tissue-associated inducible nitric-oxide synthase in colonic inflammation. Am. J. Pathol. **170**(2), 490–496 (2007)
2. A. Maton, *Human Biology and Health: Laboratory Manual* (Prentice Hall, New Jersey, 1993)
3. D.W. Ross, L.H. Ayscue, J. Watson, S.A. B. Stability of hematologic parameters in healthy subjects. Intraindividual versus interindividual variation. Am. J. Clin. Pathol. **90**(3), 262–267 (1988)
4. B. Alberts, A. Johnson, J. Lewis, P. Walter, M. Raff, K. Roberts, *Molecular Biology of the Cell*, 4th edn. (Routledge, International Student Edition, 2002)
5. S. Juds, *Photoelectric Sensors and Controls: Selection and Application*, 1st edn. (Taylor & Francis, London, 1988)
6. W.S. Lau, *Infrared Characterization for Microelectronics* (World Scientific, Singapore, 1999)
7. H. Hart, L.F. Craine, D.J. Hart, *Organische Chemie* (Wiley, London, 2002)

8. D.K. Gurton, Photoacoustic technique 'hears' the sound of dangerous chemical agents. R&D Magazine, Rockaway, NJ. Cited 19 Jan 2016. Available from: http://www.rdmag.com/news/2012/08/photoacoustic-technique-hears-sound-dangerous-chemical-agents
9. K.M. Hasebroock, N.J. Serkova, Toxicity of MRI and CT contrast agents. Expert Opin. Drug Metab. Toxicol. **5**(4), 403–416 [doi:10.1517/17425250902873796]
10. H. Ullah, M. Ikram, Monitoring of glucose levels in mouse blood with noninvasive optical methods. Laser Phys. **24**(2), 025601 (2014)
11. W. Wallace, L.H. Schaefer, J.R. Swedlow, A Workingperson's guide to deconvolution in light microscopy. Biotechniques **31**, 1076–1097 (2001)
12. A. Pan, F.B. Hu, Effects of carbohydrates on satiety: differences between liquid and solid food. Curr. Opin. Clin. Nutr. Metab. Care **14**(4), 385–390 (2011)
13. J.G. Salway, *Medical Biochemistry at a Glance* (Wiley, London, 2006)
14. M.M. Engelgau, K.M. Narayan, W.H. Herman, Screening for type 2 diabetes. Diabetes Care. **23**(10), 1563–1580 (2000)
15. R. Walker, J. Rodgers, *Type 2 Diabetes: Your Questions Answered* (Dorling Kindersley, Noida, 2006)
16. V.R. Vaidyula, G. Boden, A.K. Rao, Platelet and monocyte activation by hyperglycemia and hyperinsulinemia in healthy subjects. Platelets **17**(8), 577–585 (2006)
17. M. Yngen, A. Norhammar, P. Hjemdahl, N.H. Wallén, Effects of improved metabolic control on platelet reactivity in patients with type 2 diabetes mellitus following coronary angioplasty. Diabetes Vasc. Dis. Res. **3**(1), 52–56 (2006)
18. R.A. McPherson, *Henry's Clinical Diagnosis and Management by Laboratory Methods* (22nd edition. Elsevier/Saunders, 2011)
19. P.J. Van Soest, *Nutritional Ecology of the Ruminant* (Comstock Pub, Sacramento, 1994)
20. L. Goldman, A.I. Schafer, *Goldman's Cecil Medicine* (Elsevier Health Sciences, Amsterdam, 2011)
21. D.S. Kostick, Salts. USA2008 Cited 19 Jan 2016 Available from: http://minerals.usgs.gov/minerals/pubs/commodity/salt/myb1-2008-salt.pdf
22. C. Wu, N. Yosef, T. Thalhamer, C. Zhu, S. Xiao, Y. Kishi et al., Induction of pathogenic TH17 cells by inducible salt-sensing kinase SGK1. Nature **496**(7446), 513–517 (2013)
23. M. Kleinewietfeld, A. Manzel, J. Titze, H. Kvakan, N. Yosef, R.A. Linker et al., Sodium chloride drives autoimmune disease by the induction of pathogenic TH17 cells. Nature **496**(7446), 518–522 (2013)
24. K.N. Kornerup, C.P. Page, The role of platelets in the pathophysiology of asthma. Platelets **18**(5), 319–328 (2007)
25. T.M. Laidlaw, M.S. Kidder, N. Bhattacharyya, W. Xing, S. Shen, G.L. Milne, et al. Cysteinyl leukotriene overproduction in aspirin-exacerbated respiratory disease is driven by platelet-adherent leukocytes. Blood **119**(16), 3790–3798 (2012) [doi:10.1182/blood-2011-10-384826]
26. H.J. Adrogué, N.E. Madias, Hypernatremia. New Engl. J. Med. **342**(20), 1493–1499 (2000). doi:10.1056/NEJM200005183422006
27. J.W. Young, Gluconeogenesis in cattle: significance and methodology1. J. Dairy Sci. **60**(1), 1–15 (1977)
28. F. Homaidan, L. Kricka, T. Whitehead, Morphology of red blood cells in alcoholics. Lancet **323**(8382), 913–914 (1984). doi:10.1016/S0140-6736(84)91379-5
29. J.A. Cohen, M.M. Kaplan, The SGOT/SGPT ratio—an indicator of alcoholic liver disease. Dig. Dis. Sci. **24**(11), 835–838 (1979)
30. J. Lindenbaum, Hematologic complications of alcohol abuse. Semin. Liver Dis. **7**(03), 169–181 (1987)

Chapter 12
Quantum Dot Sensitized Solar Cells (QDSSCs)

Karan Surana and R.M. Mehra

Abstract Quantum Dot Sensitized Solar Cells (QDSSCs) are currently a field of intense research across the globe as they provide a promising cost-effective alternative for efficient energy conversion. The wide acceptance of QDs is due to their exceptional optical properties, size-tunable electro- and photoluminescence, multiple exciton generation (MEG), and broad absorption spectra. However, the progress of QDSSCs is confronted with many challenges. The basic strategies of enhanced photovoltaic characteristics depend on factors like—suppressed charge carrier recombination at the interfaces, improved photon absorption, and construction of tandem structures. Exploiting further nanoscience and nanotechnology will be essential in overcoming these hurdles for achieving better functional quantum dot sensitized solar cells. The current research work focuses on how the prevalent challenges are being overcome in order to develop efficient functioning QDSSC.

12.1 Introduction

As we strive for better technology, the urge to develop, cost effective, easily manufactured, and efficient alternative energy sources increases significantly across the globe. Among the alternative energy sources such as wind, water, biomass, solar, geothermal, significant research focus has gone into the conversion of solar energy into electrical energy using solar cells. A solar cell is a solid-state electronic device that converts the solar energy directly into electricity by photovoltaic (PV effect). Ever since the French scientist Alexandre Edmund Becquerel discovered the PV effect in 1839, the research in the field of solar cells has continuously progressed; the ongoing research has led to the fourth generation of solar cells, which are based on low-cost and easily processable materials like quantum dots

K. Surana · R.M. Mehra (✉)
Material Research Laboratory, School of Basic Sciences & Research,
Sharda University, Greater Noida, UP 201310, India
e-mail: rm.mehra@sharda.ac.in

Z.H. Khan (ed.), *Nanomaterials and Their Applications*,
Advanced Structured Materials 84, https://doi.org/10.1007/978-981-10-6214-8_12

(QDs), natural dyes, and perovskite. Among these, quantum dot sensitized solar cells (QDSSCs) have emerged as a strong PV candidate for future clean energy demands.

QDSSCs are a promising low-cost alternative to existing PV technologies such as crystalline silicon (Si) and thin inorganic films. A QDSSC makes use of quantum dots (QDs) as light absorbing material. QDs are semiconducting nanoparticles whose excitons (bound pairs of conduction band electrons and valence band holes) are confined in all three spatial directions thus showing excellent quantum confinement effect. The wide acceptance of QDs is due to their exceptional size-depended optical and electronic properties, size-tunable electro- and photoluminescence, multiple exciton generation (MEG), and broad absorption spectra. By tailoring the size of the QDs, their absorption spectrum can be tuned, thus, different sized QDs having absorption maxima peaks in the entire visible spectrum can be used in QDSSCs to harness solar energy efficiently. This could easily raise the power conversion efficiency above the Shockley–Queisser limit of 31% for conventional Si-based solar cells.

12.2 QDSSC Structure

QDSSCs comprise of four main components as shown in Fig. 12.1: (i) a 2–20 μm thick, mesoporous, wide bandgap semiconductor film (typically TiO_2 or ZnO) composed of crystalline nanoparticles abutting one another on transparent conducting oxide (TCO) glass (ii) QDs adsorbed onto the mesoporous layer (iii) a hole conductor electrolyte interpenetrating the nanocrystalline semiconductor network and (iv) a counter electrode. The interfacial properties of the QDs should be such that it gets properly adsorbed onto the wide bandgap semiconductor surface while efficiently absorbing radiation from the entire UV–Vis–IR spectrum. However, the progress of QDSSCs is confronted with many challenges including—finding appropriate hole-carriers for each type of QDs; establishing suitable redox electrolyte which is non-corrosive to the specific QDs; ensuring no path for recombination of the excited photons; determining the proper combination of QDs in

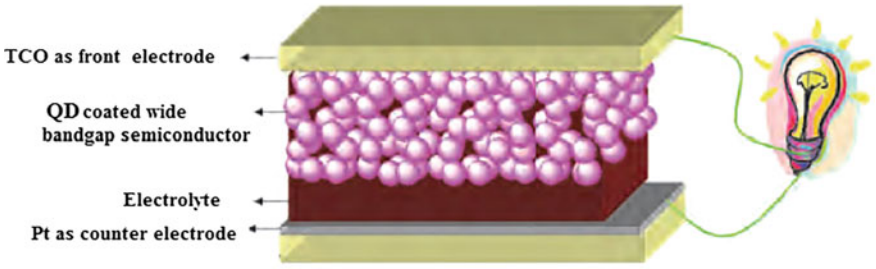

Fig. 12.1 Schematic diagram of Quantum Dot Sensitized Solar Cell [1]

multi-layered structure for optimum photovoltaic characteristics, and few others. Here on, the progress made in the performance of QDSSCs is depicted on the basis of power conversion efficiency, and emphasis is given on the importance of energy level alignment of the system in order to increase the light to electric power conversion efficiency.

12.3 Working Principle

First, let's have a general understanding of how QDSSC works. The device when irradiated under sunlight, electron–hole pairs are generated owing to photoexcitation of QDs. The excited electron is transported from the valence band (VB) or the HOMO to the conduction band (CB) or the LUMO of the QD and is swiftly injected into the LUMO of the wide bandgap semiconductor, leaving a hole in the valence band (VB) of the QD. The oxidized QD is subsequently restored by electron donation from the redox couple. Simultaneously, the injected electron in the CB of semiconductor travels through the porous structure into the conducting glass and reaches the counter electrode via the external load where it is intercepted by the redox couple. The generated voltage corresponds to the difference between the conduction band energy level of the (wide bandgap) semiconductor and the redox potential of the electrolyte. Consequently, without any perpetual chemical alteration, electrical power is generated. The schematic diagram of the above mechanism is shown in Fig. 12.2.

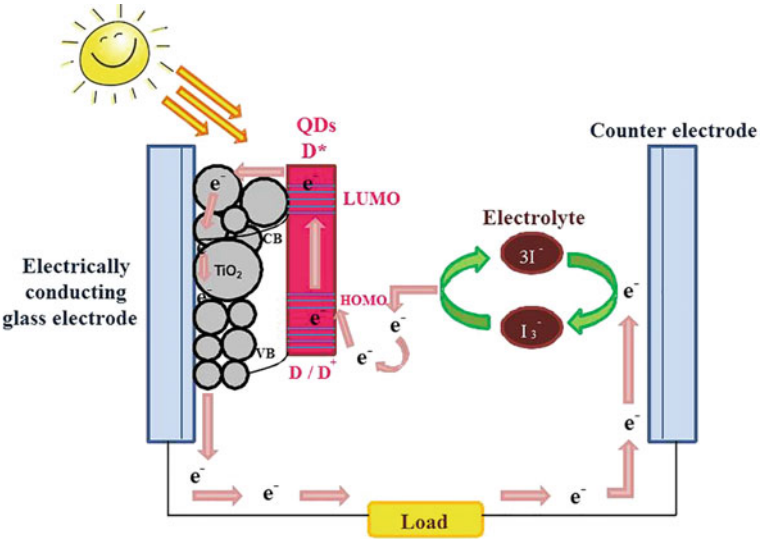

Fig. 12.2 Schematic diagram of the working mechanism of a QDSSC [1]

The QDs of groups III–V, II–VI, or IV–VI, particularly CdS, CdTe, CdSe, core-shell structures like CdSe/CdS, CdS/ZnS, CdSe/ZnS, CdSeTe/ZnS have been widely exploited for QDSSC. The highest efficiency has not yet reached an admirable figure, meaning it is still far from the one obtained with DSSC but the hope is still there as wide modifications are possible in the arena of QDSSC. With desired permutations and combinations of the various components, a sustainable efficiency can be achieved in QDSSC for commercial application.

The fabrication and study of solar cells based on CdS and CdSe QDs assembled onto 1-D TiO_2 nanofibers were presented by Sudhagar et al. [2]. In this study, TiO_2 nanofibers were electrospun on FTO substrates. The nanofibrous TiO_2 electrodes were sensitized with CdS QDs via chemical bath deposition (CBD) technique for 2–5 cycles and followed by further sensitization with CdSe QDs for half day. Finally, polysulfide electrolyte and platinum counter electrode were used to assemble the QDSSC. The coupled CdS:CdSe QDSSC showed a significantly high IPCE of 80% for the TiO_2:CdS (4 cycles):CdSe. The corresponding values of V_{oc}, J_{sc}, FF, and η were 0.64 V, 9.74 mA/cm^2, 42.3, and 2.69%, respectively. The improved photovoltaic characteristics were credited to the variation of particle size in CdS QDs, which lead to the quasi-Fermi-level alignment and consequently resulted in cascade energy level structure in the order of TiO_2 < CdS < CdSe. Hence the introduction of a CdS layer between TiO_2 and CdSe elevated the conduction band edge of CdSe, giving a higher driving force for the injection of excited electrons out of the CdSe layer.

An efficiency of $\sim$1% was published by Chen et al. [3] using oleic acid (OA) capped CdSe QDs. The QDSSC consisted of a 5 μm thick TiO_2 layer spread using doctor blade method on FTO glass. The TiO_2 surface was modified with mercaptopropionic acid (MPA) linker prior to immersion in CdSe QD solution. Compared to TOPO capped CdSe QDs, the amount of OA-capped QDs adsorbed on MPA modified TiO_2 electrode was found to be about 1.7 times greater thereby confirming improvement in the QD loading and light-harvesting capability. A platinum counter electrode was used, and the QDSSC performance was compared using two types of electrolytes, viz. iodide/triiodide and polysulfide. Iodide electrolyte showed an efficiency of 0.97% with a higher V_{oc} of 0.65 V, while the QDSSC with polysulfide electrolyte gave higher values of J_{sc} and FF.

Chen et al. [4] prepared solar cells using hydrothermally grown ZnO nanowires as photoanode. Chemical bath deposition method was used to deposit successive layers of CdS and CdSe QDs. Platinum-based counter electrode and polysulfide electrolyte formed the final solar cells. The hierarchical arrangement of ZnO < CdS < CdSe is necessary for the better transfer of electrons from the conduction band of CdSe QDs to ZnO. The parameters acquired from the *I–V* characteristics were J_{sc} = 5.19 mA/cm^2, V_{oc} = 0.66 V, FF = 0.415, and η = 1.42%. The solar cells with arrangement ZnO/CdS/CdSe showed better performance compared with that of ZnO/CdS. This was attributed to broader light absorption capability and effective charge injection kinetics in the ZnO-/CdS-/CdSe-based solar cell. Additionally, the obtained electron lifetime was 13.8 ms for

Table 12.1 Comparative study of TiO_2, CdSe, and CdS as presented by Osada et al. [5]

QDs	J_{sc} (mA/cm^2)	V_{oc} (V)	FF	η (%)
CdSe/TiO_2	8.2	0.54	0.48	2.1
CdSe/CdS/TiO_2	11.9	0.58	0.52	3.6
CdS/CdSe/TiO_2	4.4	0.50	0.51	1.1
CdS/TiO_2	2.5	0.46	0.51	0.58
TiO_2 only	0.41	0.27	0.40	0.044

the former solar cell while only 6.2 ms for the latter device suggesting lowering in interface charge recombination rate by CdSe QDs sensitization.

A thorough comparative study on various arrangements of TiO_2, CdSe, and CdS, was presented by Osada et al. [5] in 2014 using polysulfide electrolyte and the Cu_2S counter electrode. The obtained results are compiled in Table 12.1. The results clearly confirm that the appropriate band alignment for the photoanode is TiO_2/CdS/CdSe, thereby suggesting that the injected electrons were swiftly transferred to TiO_2 and the reverse electron transfer did not matter for the efficiency.

Recently few studies demonstrated the positive effect of doping ions into sulfide QDs, such as Hg^{2+} into PbS [6], and Mn^{2+} into CdS [7], which increased the current density thereby enhancing the efficiency of the solar cells. Kim et al. [8] fabricated TiO_2 electrodes sensitized with CdS, PbS/CdS, Mn-PbS/CdS, and PbS/Mn-CdS using SILAR technique followed by a coating of two cycles of ZnS passivation layer over the sensitized electrodes. Further, polysulfide electrolyte and CuS counter electrode were used. Mn-doped films showed a substantial increase in J_{SC} as compared to the corresponding photoanodes without dopants. PbS/Mn-CdS film gave an efficiency of 3.55% with a J_{sc} of 12.9 mA/cm^2 and V_{oc} of 0.56 V. The reason for the enhanced photovoltaic properties was attributed to the impact of Mn impurities on the host material, which created new energy states, thus delaying the exciton recombination time and allowing better charge separation.

Tian et al. [9] reported a chemical passivation strategy method for synthesis of mesoporous ZnO photoelectrode, which enhanced the apertures in the photoelectrode for harvesting more QDs. Also, a thin layer of TiO_2 nanoparticles was introduced on the surface of ZnO so as to reduce the surface charge recombination. The alignment under study was CdS > CdSe > ZnO > TiO_2. Under passivated condition, the obtained efficiency was 4.68% compared to 2.4% obtained under non-passivated condition. Employment of the passivation layer significantly increased the amount of harvested QDs while improving their distribution. Further, it may have triggered the enhancement in charge recombination resistance while prolonging the electron lifetime, which contributed in improving the overall efficiency and characteristics of QDSSC.

Chuang et al. [10] in 2014 reported a certified high efficiency in QDSC. Patterned ITO substrate was used to spin coat ZnO nanoparticles. Few layers of PbS-TBAI (Tetrabutylammonium iodide) and PbS-EDT (1,2-ethanedithiol) were spin coated successively. Coating of MoO_3, Al, and Au were done on the electrodes

by thermally evaporating corresponding material on the substrate, and the results were compared. The final device architecture was ITO/ZnO/PbS-TBAI/PbS-EDT/MoO_3/Al or Au. The obtained values of V_{oc}, J_{sc}, FF, and η were 0.55 V, 24.2 mA/cm^2, 63.8, and 8.55%, respectively. These characteristics were attained due to the tailoring of band alignment at the interfaces of QD/QD and QD/anode.

Hossain et al. [11] in their article established that CdSe-sensitized TiO_2 SCs show noticeably slower charge recombination at the TiO_2/CdSe interface with the superior light harvesting of long wavelength photons giving rise to enhanced overall device performance of the cascaded CdS/CdSe solar cells. This resulted in the inference that while the CdS buffer layer might actually be indispensable in few types of SCs, yet it actually is redundant and even causes a loss in efficiency in CdSe-sensitized TiO_2 SCs. The photovoltaic performance recorded for the QDSSC utilizing a scattering layer over TiO_2 with 9 layers of SILAR grown CdSe QDs, polysulfide electrolyte, and Cu_2S counter electrode was V_{oc} = 0.579 V, J_{sc} = 15.77 mA/cm^2, FF = 56.95%, and η = 5.21%.

A highly efficient QDSC based on $Cd_{1-x}Mn_xSe$ quantum dots was reported by Tian et al. [12]. Modification of TiO_2 with CdS was adopted to improve the adsorption of $Cd_{1-x}Mn_xSe$ to form a photoanode with the structure of TiO_2/CdS/$Cd_{1-x}Mn_xSe$. Maximum external quantum efficiency (EQE) of 74% at 580 nm was obtained with $Cd_{0.8}Mn_{0.2}Se$ QDs. The improved quantum efficiency was ascribed to the rise in light-harvesting, charge-transfer, and charge-collection efficiencies. An efficiency of 6.33% with a J_{sc} of 19.15 mA/cm^2 and V_{oc} of 0.58 V was achieved.

Recently Wei et al. [13] presented a high efficiency of 11.23% using $CdSe_xTe_{1-x}$ QDs decorated TiO_2 electrode passivated with ZnS layer. A polysulfide electrolyte and Cu_2S counter electrode were used. The reason for such efficiency was attributed to the SiO_2 fumed electrolyte; the existence of SiO_2 nanoparticles in the electrolyte created an energy barrier for the recombination between photo-generated electrons from the QDs as well as the recombination between the electrolyte and the injected electrons from TiO_2.

Bhattacharya et al. [14] fabricated a solar cell without the use of a mesoporous layer. The QD layer played the dual role of trapping photons as well as transporting them to the FTO layer. The efficiency obtained was low, but a decent fill factor of 66.08% and a V_{oc} of 1.41 V were obtained, which suggests superior band alignment and faster electron transfer.

12.4 Conclusions

In order to achieve a superior performing solar cell, an appropriate arrangement of QDs of different sizes has to be identified so as to harvest the maximum region of the electromagnetic spectrum, precisely the UV, Visible, and IR region. Further establishing a suitable band alignment between the stacked QDs and the mesoporous semiconductor is an unavoidable requirement, achieving which would lead

to a faster charge transfer. This also entails proper loading of the QDs on the semiconductor surface. The focus needs to be laid down on the impedance analysis of the different junctions of the solar cell, so that the configurations can be altered suitably. Such studies can identify the appropriate requirement of Fermi level of the counter electrode, thereby a suitable alternative can be chosen. As a final thought, the basic strategies of enhanced photovoltaic properties depend on the reduced carrier recombination at the various interfaces, improved light absorption by photon management, and construction of tandem structures. Exploiting further nanoscience and nanotechnology will be an essential in overcoming these hurdles for achieving better functional quantum dot sensitized solar cells.

References

1. N. Singh, A. Kapoor, R.M. Mehra, Invertis J. Renew. Energy **3**, 133–177 (2013)
2. P. Sudhagar, J.H. Jung, S. Park, Y.G. Lee, R. Sathyamoorthy, Y.S. Kang, H. Ahn, Electrochem. Commun. **11**, 2220–2224 (2009)
3. J. Chen, J.L. Song, X.W. Sun, W.Q. Deng, C.Y. Jiang, W. Lei, J.H. Huang, R.S. Liu, Appl. Phys. Lett. **94**, 153115-1–153115-3 (2009)
4. J. Chen, J. Wu, W. Lei, J.L. Song, W.Q. Deng, X.W. Sun, Appl. Surf. Sci. **256**, 7438–7441 (2010)
5. N. Osada, T. Oshima, S. Kuwahara, T. Toyoda, Q. Shen, K. Katayama, Phys. Chem. Chem. Phys. **16**, 5774–5778 (2014)
6. J.-W. Lee, D.-Y. Son, T.K. Ahn, H.-W. Shin, I.Y. Kim, S.-J. Hwang, M.J. Ko, S. Sul, H. Han, N.-G. Park, Sci. Rep. **3**(1050), 1–8 (2013)
7. P.K. Santra, P.V. Kamat, J. Am. Chem. Soc. **134**, 2508–2511 (2012)
8. H.-J. Kim, H.-D. Lee, C.S.S.P. Kumar, S.S. Rao, S.-H. Chung, D. Punnoose, New J. Chem. **39**, 4805–4813 (2015)
9. J. Tian, Q. Zhang, E. Uchaker, R. Gao, X. Qu, S. Zhang, G. Cao, Energy Environ. Sci. **6**, 3542–3547 (2013)
10. C.H.M. Chuang, P.R. Brown, V. Bulovic, M.G. Bawendi, Nat. Mater. **13**, 796–801 (2014)
11. M.A. Hossain, J.R. Jennings, C. Shen, J.H. Pan, Z.Y. Koh, N. Mathews, Q. Wang, J. Mater. Chem. **22**, 16235–16242 (2012)
12. J. Tian, L. Lv, C. Fei, Y. Wang, X. Liu, G. Cao, J. Mater. Chem. A **2**, 19653–19659 (2014)
13. H. Wei, G. Wang, J. Shi, H. Wu, Y. Luo, D. Li, Q. Meng, J. Mater. Chem. A **4**, 14194–14203 (2016)
14. K. Surana, R.M. Mehra, B. Bhattacharya, H.-W. Rhee, A.R. Polu, P.K. Singh, Renew. Sustain. Energy Rev. **52**, 1083–1092 (2015)